

# Analysis of Seismic Signatures Generated from Controlled Methane and Coal Dust Explosions in an Underground Mine

Michael M. Murphy

Dissertation submitted to the faculty of the Virginia Polytechnic Institute and State University in partial fulfillment  
of the requirements for the degree of

**Doctor of Philosophy**  
In  
**Mining and Minerals Engineering**

Committee Members:

Dr. Erik Westman, Chair

Dr. Thomas Barczak

Dr. Martin Chapman

Dr. Mario Karfakis

Dr. Michael Karmis

Dr. Peter Swanson

**November 7<sup>th</sup>, 2008**  
**Blacksburg, VA**

Keywords: instrumentation, methane and coal dust explosions, mine seals, radiated seismic  
energy, seismic monitoring, underground mines

# Analysis of Seismic Signatures Generated from Controlled Methane and Coal Dust Explosions in an Underground Mine

Michael M. Murphy

## **Abstract**

Examination of seismic records during the time interval of the Sago Mine disaster in 2006 revealed a small amplitude signal possibly associated with an event in the mine. Although the epicenter of the signature was located in the vicinity where the explosion occurred, it could not be unequivocally attributed to the explosion. More needs to be understood about the seismicity from mine explosions in order to properly interpret critical seismic information. A seismic monitoring system located at NIOSH's Lake Lynn Experimental Mine has monitored nineteen experimental methane and dust based explosions. The objective of the study was to analyze seismic signatures generated by the methane and dust explosions to begin understanding their characteristics at different distances away from the source. The seismic signatures from these different events were analyzed using standard waveform analysis procedures in order to estimate the moment magnitude and radiated seismic energy. The procedures used to analyze the data were conducted using self-produced programs not available with existing commercial software. The signatures of the explosions were found to be extremely complex due a combination of mine geometry and experimental design, both of which could not be controlled for the purposes of the study. Geophones located approximately 600 m (1970 ft) and over from the source collected limited data because of the attenuation of the seismic waves generated by

the methane explosion. A combination of the methods used to characterize the seismic signatures allowed for differentiation between experimental designs and the size of the explosion. The factors having the largest impact on the signatures were the mine geometry, size of the methane explosion, construction of the mine seal and location of the mine seal. A relationship was derived to correlate the radiated seismic energy to the size of the explosion. Recommendations were made, based upon the limitations of this study, on methods for better collection of seismic data in the future.

# Dedication

This dissertation is dedicated to my mother and father. Without their love and support throughout my whole life, I would have never reached this point.



# Acknowledgements

I would like to thank the Department of Mining and Minerals Engineering at Virginia Tech and the National Institute for Occupational Safety and Health's Pittsburgh Research Laboratory for giving me the opportunity to work on this dissertation. I would have not been able to succeed academically without the consistent guidance and encouragement from my advisor Dr. Erik Westman during both my undergraduate and graduate academic years. I would also like to thank the assistance of my other committee members: Dr. Thomas Barczak, Dr. Martin Chapman, Dr. Mario Karfakis, Dr. Michael Karmis and Dr. Peter Swanson for their assistance. Former committee members who also need to be acknowledged for their tremendous help are Dr. Anthony Iannacchione and Dr. Thomas Novak.

Without the assistance and dedication of Jerry Morrow at NIOSH-PRL, particular aspects of the project would have been much more difficult and I thank him for the effort he provided. Other co-workers at NIOSH-PRL who must be acknowledged for their kind assistance include Eric Weiss, James Addis, Sam Harteis, Kenny Jackson, Frank Karnack, Walt Marchewka, Dr. Don Sellers, Bill Slivensky, Dr. Karl Zipf, Dennis Dolinar, Ken Cashdollar, Marcia Harris, Mike Sapko and Dave Dwyer. I would also like to give sincere thanks to the support from ISS International, who manufactured the equipment used in the study, for their continual help and devotion in allowing me understand and troubleshoot the instrumentation. Despite the time zone difference between Pittsburgh and South Africa, their friendly support was seemingly always available.

I would like to thank my family, Mom, Dad, Jennen, Jason, Poppy and Granny and Grandpa and Grandma Murphy, for giving me their love and support through my whole life which has allowed me to succeed. I hope Maddy and Megan (on the way) are very proud of their Uncle Michael Michael Michael.

To my best friends from Blacksburg, Steven Dellinger, Ho-Ching Fong, Mike Jaynes, Jeanette Montrey and Seth Powers, thank you for a great two and a half years during my visits back home (and the one time all of you were able to come to Pittsburgh). These were the best times of my life up to this point. Thanks to the Chi Alpha Christian Fellowship at Virginia Tech and Peter's Creek Baptist Church in Pittsburgh, PA for their prayers throughout the years.

Above all I would like to thank God for giving me the strength and knowledge to complete all of the challenges I've had in my life. Through Him all things are possible.

# Table of Contents

<b>Dedication .....</b>	<b>iv</b>
<b>Acknowledgements .....</b>	<b>v</b>
<b>Table of Contents .....</b>	<b>vii</b>
<b>List of Figures.....</b>	<b>x</b>
<b>List of Tables .....</b>	<b>xvii</b>
<b>Chapter 1 – Introduction.....</b>	<b>1</b>
1.1 Statement of the problem .....	1
1.2 Proposed solution and objective.....	3
1.3 Scope of the study .....	4
<b>Chapter 2 – Literature Review .....</b>	<b>7</b>
History of Methane Explosions in Underground Mines .....	7
2.1 Historical summary of methane explosions from the early 1800’s – 1977 .....	7
2.2 Historical summary of documented methane explosions occurring within sealed areas (1986 – 2006) .....	10
2.3 Recent methane explosion disasters and methods of prevention.....	11
2.4 Chemistry and physics of an underground methane explosion .....	13
Background of Seismic Waves and Sources .....	15
2.5 Types of seismic waves.....	15
2.6 Velocity of seismic waves.....	17
2.7 Seismic sources .....	18
2.7.1 Frequency of seismic sources.....	19
2.7.2 General model for the displacement spectra.....	20
2.7.3 Moment magnitude and radiated seismic energy estimates of seismic sources.....	21
Seismic monitoring in underground mines .....	23
2.8 Brief history of seismic monitoring system applications in mines.....	24
2.9 Evaluation of seismic data .....	25
2.10 Components of a seismic monitoring system.....	26
2.10.1 Seismic transducers.....	26
2.10.2 Analog to digital conversion .....	29
2.11 Review of past seismic studies on underground explosions.....	31
2.11.1 Description of body and surface waves for an explosive source .....	31
2.11.2 Frequency content of body and surface waves for explosive sources .....	35
2.11.3 Moment magnitude and radiated seismic energy studies from an explosive source.....	36
2.11.4 Mine seal response to methane and dust explosions .....	38
<b>Chapter 3 – Experimental Procedures.....</b>	<b>43</b>
3.1 Lake Lynn Experimental Mine location and dimensions.....	43

3.2 Features inside of the mine .....	47
3.3 Instrumentation used during the study .....	51
3.3.1 Seismic transducers .....	51
3.3.2 Seismic monitoring system .....	55
3.3.3 Calibration of the seismic monitoring system .....	57
3.4 Data collection at the Lake Lynn Experimental Mine.....	64
3.4.1 – Geophone locations.....	64
3.4.2 – Methane and dust explosions as a seismic source .....	67
3.4.3 – Cast boosters as a seismic source .....	70
3.4.4 – Rock drops tests as a seismic source .....	73
3.5 Seismic data analysis procedures .....	74
3.5.1 Transforming the data for analysis.....	74
3.5.2 Spectral analysis of the data.....	76
3.5.3 Moment magnitude and radiated seismic energy calculations using the displacement and velocity spectra.....	78
3.6 Determination of the size of the explosion.....	83
<b>Chapter 4 – Amplitude, Attenuation and Duration of the Seismic Signatures.....</b>	<b>86</b>
4.1 Amplitude analysis of the seismic signatures.....	86
4.1.1 Method of analysis .....	86
4.1.2 Results from mine shots #503-524 and discussion.....	87
4.1.3 Results of from the cast booster experiments and discussion.....	92
4.2 Attenuation of the seismic signatures.....	93
4.2.1 Method of analysis .....	93
4.2.2 Results and discussion from mine shots #503-524.....	96
4.3 Duration of the seismic signatures .....	98
4.3.1 Method of analysis .....	98
4.3.2 Results and discussion for mine shots #506 – 509 .....	99
4.3.3 Results and discussion for mine shots #510 – 519 and 521.....	104
4.3.4 Results and discussion for mine shots #520 and 522 .....	106
<b>Chapter 5 – Velocity Analysis of the Seismic Signatures .....</b>	<b>109</b>
5.1 Method of analysis .....	109
5.2 Results and discussion from mine shots #503 – 524 .....	113
5.3 Results and discussion from mine shots #528 – 540 .....	119
<b>Chapter 6 – Frequency Analysis of the Seismic Signatures.....</b>	<b>125</b>
6.1 – Method of analysis .....	125
6.2 – Results and discussion from the analysis of a mine structure during mine shots #528 – 540 .....	126
6.3 – Results and discussion from mine shots #528 – 540 .....	131
6.4 – Results and discussion from mine shots #503 – 524 for the D-Drift geophones.....	133
6.5 – Results and discussion from mine shots #503 – 524 for the other geophones .....	137
6.6 – Observation of low-frequency content during confined explosions in a sealed area .....	139
<b>Chapter 7 – Radiated Seismic Energy and Moment Magnitude Estimates from the Seismic Signatures .....</b>	<b>144</b>
7.1 – Method of analysis .....	144
7.2 – Results and discussion on the radiated seismic energy and moment magnitude estimates .....	145
7.2.1 Estimated energy as a percentage of the original energy.....	145
7.2.2 Radiated seismic energy estimates versus moment magnitude from the geophones located over 150 m.....	146
7.2.3 Radiated seismic energy estimates versus moment magnitude from the geophones located under 150 m.....	149
7.3 – Relationship between the radiated seismic energy and size of the explosion .....	153

<b>Chapter 8 – Conclusions and Recommendations for Future Research.....</b>	<b>157</b>
<b>References.....</b>	<b>164</b>
<b>Appendix A: Mine Shot Plans and Mine Structure Descriptions .....</b>	<b>170</b>
<b>Appendix B: Pressure-Time Curves for Mine Shots .....</b>	<b>228</b>
<b>Appendix C: Maximum Ground Velocity (Amplitude) – Peak Pressure Plots.....</b>	<b>247</b>
<b>Appendix D: Attenuation Curves for the Mine Shots .....</b>	<b>267</b>
<b>Appendix E: LabVIEW Program Used for Analysis of the Seismic Signatures.....</b>	<b>282</b>
<b>Appendix F: Analysis of Secondary Events Collected During Mine Shots #510-522 .....</b>	<b>287</b>
<b>Appendix G: Distance-Time Plots for Velocity Calculations.....</b>	<b>304</b>
<b>Appendix H: Summary of Radiated Seismic Energy and Moment Magnitude Estimates from Mine Shots #503 – 524.....</b>	<b>317</b>

# List of Figures

Figure 1.1 – Seismic signature of the event at the time of the Sago Mine disaster (Chapman 2006).	2
Figure 1.2 – The epicenter location of the small amplitude signal was at the Sago Mine. If depth is unconstrained, the assumed mine explosion location (black diamond) and epicenter (blue diamond) are at the same approximate location (Chapman 2006).	2
Figure 2.1 – Number of fatalities caused by major explosions occurring in underground coal mines between 1890 and 1975.	9
Figure 2.2 – Number of incidents caused by major explosions occurring in underground coal mines between 1890 and 1975.	9
Figure 2.3 – Number of fatalities from coal methane and dust explosions for underground coal operators between 1975 and 2006.	12
Figure 2.4 – Typical time-pressure history for an explosion in a tunnel.	14
Figure 2.5 – Visual description of the types of body and surface waves: (a) P-waves, (b) S-waves, (c) Raleigh waves and (d) Love waves (adapted from Bolt 1982).	16
Figure 2.6 – Difference between low-frequency and high-frequency seismic waves.	19
Figure 2.7– Frequency ranges of common seismic sources.	20
Figure 2.8 – Simple diagram of a seismometer to monitor vertical ground motion (adapted from Havskov 2006).	26
Figure 2.9– Amplitude frequency response of mechanical and velocity transducers to kinematic variables. The asymptotic slope of each curve segment is highlighted and changes at each instruments natural frequency. The ratios of relative to actual measurements are also shown beside each curve.	28
Figure 2.10 – Example of an aliased signal which violates the Nyquist criterion (adapted from Analog Devices 1994).	30
Figure 2.11– Map of routine mining seismicity for the conterminous United States between May 1997 and March 2000 (Dewey 1998).	38
Figure 2.12 – Fourier transform from the plug seal located in crosscut 1 during mine shots #347 and 348. The seal had a thickness of 1.2 m and total cross-sectional area of 10.6 m <sup>2</sup> . The peak frequencies occur at 320-370 Hz.	40
Figure 2.13 – Fourier transform from the meshblock seal located in crosscut 2 during mine shots #347 and 348. The seal had a thickness of 0.325 m and total cross-sectional area of 13.0 m <sup>2</sup> . The peak frequencies occur at 90-115 Hz.	41
Figure 2.14 – Fourier transform from the meshblock seal located in crosscut 3 during mine shots #347 and 348. The seal had a thickness of 0.325 m and total cross-sectional area of 16.0 m <sup>2</sup> . The peak frequencies occur at 50-80 Hz.	41
Figure 2.15 – Fourier transform from the meshblock seal located in crosscut 4 during mine shots #347 and 348. The seal had a thickness of 0.175 m and total cross-sectional area of 13.5 m <sup>2</sup> . The seal failed during shot #348. The peak frequencies occur at 20 Hz and 45-60 Hz.	42
Figure 3.1 – Location of Lake Lynn Experimental Mine.	44
Figure 3.2 – Vertical borehole geology of the old workings at the Lake Lynn Experimental Mine. The layers detected in the old workings were considered to be consistent with the geology of the drift area.	45
Figure 3.3 – Lake Lynn Experimental Mine map. The crosscut numbering scheme, location of instrument rooms and bulkhead door, and explosion paths are indicated in the figure.	47
Figure 3.4 – View of the bulkhead door partially closed in E-Drift.	48
Figure 3.5 – View of the instrument room from C-Drift.	49
Figure 3.6 – View of the panels inside (left) and outside (right) of the mine which contain corresponding wire terminals.	49
Figure 3.7 – Data gathering station located in one of the mine drifts.	50
Figure 3.8 – Response curve of the Sercel L-28LB geophone (Sercel 2005).	52
Figure 3.9 – Photograph of the geophone used in the study. In the photograph, the geophone is being installed at the test site.	53
Figure 3.10 – Photograph demonstrating how the two horizontal components are seated inside of the TDC II casing.	53
Figure 3.11 – Schematic of the TDC II casing (Sercel 2008).	54

---

Unless otherwise noted in the document by a reference or footnote, all figures were created by the author.

Figure 3.12 – Response to velocity for the Guralp CMG-6TD instrument installed on the surface above the mine.....	55
Figure 3.13 – Calibration results for both MS and QS boxes.....	59
Figure 3.14 – Filter response, $G(\omega)$ , for MS box.....	60
Figure 3.15 – Complete system amplitude response to ground displacement, $d(\omega)$ . The natural frequency of the geophone is highlighted by the dotted line at 4.5 Hz.....	62
Figure 3.16 – Complete system amplitude response to ground velocity, $V(\omega)$ . The natural frequency of the geophone is highlighted by the dotted line at 4.5 Hz.....	63
Figure 3.17 – Geophone and rock drop test site location map.....	65
Figure 3.18 – Horizontal geophone orientations inside of Lake Lynn Experiment Mine. One horizontal component was oriented parallel to the drift and the other horizontal component was oriented perpendicular to the drift.....	66
Figure 3.19 – Ignition chamber located at the end of C-Drift.....	68
Figure 3.20 – Plastic diaphragm used to contain the methane within the ignition chamber.....	68
Figure 3.21 – Example of the coal and rock dust being suspended from the mine roof and placed on the mine floor.....	69
Figure 3.22 – Photograph of the structure located at crosscut 1 as viewed from B-Drift. The geophone location is circled in the figure. The post in front of the seal and geophone location contained instrumentation used for a different study by the mine staff.....	71
Figure 3.23 – Map of the experimental design for the booster detonation experiments. The black dots in A-Drift show the booster detonation locations. The structures are shown in crosscuts X1-X5 between A- and B-Drifts. In the crosscuts between B- and C-Drifts are stoppings, some of which are debris piles as indicated by broken lines. The closest geophones during these tests were on the structure in crosscut 1 and the C-Drift instrument room as indicated by the green dots.....	72
Figure 3.24 –Fourier transformation windows selected for the signal and background noise.....	75
Figure 3.25 – Example of the data observed in the frequency domain after a Fourier transformation.....	76
Figure 3.26 – Example of the Fourier amplitude spectrum of ground displacement, $D(\omega)$ . The blue line represents the signature from the event and the pink line represents the background noise.....	77
Figure 3.27 – Example of the Fourier amplitude spectrum of ground velocity, $V(\omega)$ . The blue line represents the signature from the event and the pink line represents the background noise.....	78
Figure 3.28 – Example of the Brune model superimposed on the Fourier amplitude spectrum of ground displacement to help determine $\Omega_0$ .....	79
Figure 3.29 – Example of Fourier amplitude spectrum of ground velocity to help determine the radiated seismic energy. The blue line represents the signature from the event and the pink line represents the background noise.....	80
Figure 3.30 – Example of the Fourier amplitude spectrum of ground velocity to help determine the radiated seismic energy. In this example the frequency intervals to include in the calculation is more difficult to determine. The blue line represents the signature from the event and the pink line represents the background noise.....	82
Figure 3.31 – Example of pressure-time curves used to obtain the size of the explosion, as defined by the peak pressure generated.....	83
Figure 3.32 – Example of a pressure-time curve for the confined explosions, which shows an oscillating pressure pulse.....	85
Figure 4.1 – Plot of maximum ground velocity versus maximum pressure for Geophone 5 (Channel 1).....	87
Figure 4.2 – Plot of amplitude versus distance for mine shot #506.....	94
Figure 4.3 – Plot of attenuation for mine shot #506.....	95
Figure 4.4 – Representative waveform from Geophone 2 for mine shot #507. The two lines indicate the interval which determined the duration.....	100
Figure 4.5 – Representative waveform from Geophone 2 for mine shot #509. The two lines indicate the interval which determined the duration.....	101
Figure 4.6 – Representative waveform from Geophone 3 for mine shot #507. The two lines indicate the interval which determined the duration. Past the right indicator, an event occurs at approximately 8.3 seconds. This event is believed to be the “suck-back” of the pressure wave to the mine face which was expected for the experimental design in mine shot #507, as described in more detail in Section 2.4 and in Appendix F.....	102
Figure 4.7 – Representative waveform from Geophone 3 for mine shot #508. The two lines indicate the interval which determined the duration. The interval was believed to represent a long duration because of the confinement of the pressure wave, which is described in more detail in Section 6.6.....	103

Figure 4.8 – Representative waveform from Geophone 3 for mine shot #509. The two lines indicate the interval which determined the duration. Smaller events representing debris impacts are believed to be observed within the time interval indicated. ....	103
Figure 4.9 – Simplified schematic of the experimental design for mine shots #510 – 519 and 521. The design indicates that that propagation path of the pressure wave is isolated within A-Drift. The green dots indicate the geophone locations within the bounds of the figure. ....	104
Figure 4.10 – Schematic of the experimental design for mine shots #520 and 522. The design indicates that that propagation path of the pressure wave was allowed to enter into B- and C-Drifts. The green dots indicate the geophone locations within the bounds of the figure. ....	106
Figure 4.11 – Example of a seismic signature collected during mine shot #522 by Geophone 2. The signature appears to contain multiple reflections as a result of the pressure wave from the methane and dust explosion entering into B- and C-Drifts. ....	108
Figure 5.1 – Distance-time plot for mine shot #508. ....	110
Figure 5.2 – Waveform from far away geophone which shows two distinct phase arrivals. ....	112
Figure 5.3 – Histogram of apparent average velocities based upon arrival times calculated from the mine shots. ....	113
Figure 5.4 – Plot of apparent seismic wave velocity versus initial energy for mine shots #505-520. ....	115
Figure 5.5 – Plot of apparent seismic wave velocity versus pressure from inside the ignition zone for mine shots #505-520. ....	117
Figure 5.6 – Sample particle motion diagram for mine shot #518. ....	119
Figure 5.7 – Plot of apparent seismic wave velocity for the cast booster experiments (mine shots #528-538). ....	120
Figure 5.8 – Waveform from Geophone 2 (vertical component) for mine shot #531 which shows the first break in the signature believed to be the arrival of the P-wave according to the apparent velocity calculated. The signature had to be zoomed significantly to observe the arrival. ....	122
Figure 5.9 – Waveform from Geophone 2 (vertical component) for mine shot #528 which shows the first break in the signature believed to be the arrival of the S-wave according the apparent velocity calculated. ....	123
Figure 5.10 – Waveform from Geophone 3 (horizontal component perpendicular to the drifts) for mine shot #530 which shows an instance where the first break of the signature was difficult to observe. The black arrows indicate the assumptions on where the arrival of the seismic wave is located. The red arrow indicates the location where the arrival time was eventually picked. ....	124
Figure 6.1 – Sample FFT from Geophone 3 during mine shot #507. ....	126
Figure 6.2 – FFT from the geophone attached to a mine structure during mine shot #530. ....	127
Figure 6.3 – FFT from the geophone attached to a mine structure during mine shot #529. ....	128
Figure 6.4 – FFT from the geophone attached to a mine structure during mine shot #533. ....	129
Figure 6.5 – FFT from the geophone attached to a mine structure during mine shot #540. ....	130
Figure 6.6 – FFT from the Geophone 2 during mine shot #534. ....	132
Figure 6.7 – FFT from the Geophone 5 during mine shot #534. ....	133
Figure 6.8 – FFT comparison from Geophone 3 during mine shot #506, 507 and 509. ....	134
Figure 6.9 – FFT comparison from Geophone 3 during mine shot #505 and 508. ....	135
Figure 6.10 – FFT comparison from Geophone 3 during mine shot #510, 516 and 519. ....	136
Figure 6.11 – FFT comparison from Geophone 3 during mine shot #524. ....	137
Figure 6.12 – Filtered waveform from the Guralp surface geophone during mine shot #523. ....	140
Figure 6.13 – Filtered waveform from the Guralp in-mine geophone during mine shot #523. ....	141
Figure 6.14 – Filtered waveform from Geophone 3 during mine shot #524. ....	141
Figure 6.15 – Filtered waveforms from Geophone 6 during three mine shots: (a) a seal in the entry that did not fail, (b) a seal in the entry that did fail and (c) and explosion with no seal in the entry. ....	142
Figure 7.1 – Radiated seismic energy versus moment magnitude estimates made over 150 m away from the seismic source for all the tests. ....	147
Figure 7.2 – Radiated seismic energy versus moment magnitude estimates made over 150 m away from the seismic source for just tests with no seal in the entry. ....	148
Figure 7.3 – Radiated seismic energy versus moment magnitude estimates made over 150 m away from the seismic source for just tests with a seal in the entry. ....	149



Figure 7.4 – Radiated seismic energy versus moment magnitude estimates made less than 150 m away from the seismic source for all the tests.....	150
Figure 7.5 – Radiated seismic energy versus moment magnitude estimates made less than 150 m away from the seismic source for just tests with no seal in the entry.....	151
Figure 7.6 – Radiated seismic energy versus moment magnitude estimates made less than 150 m away from the seismic source for just tests with a seal in the entry.....	152
Figure 7.7 – Linear relationship of the radiated seismic energy versus size of the explosion for all the mine shots observed.....	154
Figure 7.8 – Power relationship of the radiated seismic energy versus size of the explosion for all the mine shots observed.....	155
Figure A.1 – Experimental design for mine shot #503.....	172
Figure A.2 – Experimental design for mine shot #504.....	175
Figure A.3 – Experimental design for mine shot #505.....	178
Figure A.4 – Experimental design for mine shot #506.....	181
Figure A.5 – Experimental design for mine shot #507.....	184
Figure A.6 – Experimental design for mine shot #508.....	187
Figure A.7 – Experimental design for mine shot #509.....	190
Figure A.8 – Experimental design for mine shot #510.....	193
Figure A.9 – Experimental design for mine shot #513.....	196
Figure A.10 – Experimental design for mine shot #514.....	199
Figure A.11 – Experimental design for mine shot #516.....	202
Figure A.12 – Experimental design for mine shot #517.....	205
Figure A.13 – Experimental design for mine shot #518.....	208
Figure A.14 – Experimental design for mine shot #519.....	211
Figure A.15 – Experimental design for mine shot #520.....	214
Figure A.16 – Experimental design for mine shot #521.....	217
Figure A.17 – Experimental design for mine shot #522.....	220
Figure A.18 – Experimental design for mine shot #523.....	223
Figure A.19 – Experimental design for mine shot #524.....	226
Figure B.1 – Pressure-time curve for mine shot #503.....	229
Figure B.2 – Pressure-time curve for mine shot #504.....	230
Figure B.3 – Pressure-time curve for mine shot #505.....	231
Figure B.4 – Pressure-time curve for mine shot #506.....	232
Figure B.5 – Pressure-time curve for mine shot #507.....	233
Figure B.6 – Pressure-time curve for mine shot #508.....	234
Figure B.7 – Pressure-time curve for mine shot #509.....	235
Figure B.8 – Pressure-time curve for mine shot #510.....	236
Figure B.9 – Pressure-time curve for mine shot #513.....	237
Figure B.10 – Pressure-time curve for mine shot #514.....	238
Figure B.11 – Pressure-time curve for mine shot #516.....	239
Figure B.12 – Pressure-time curve for mine shot #517.....	240
Figure B.13 – Pressure-time curve for mine shot #518.....	241
Figure B.14 – Pressure-time curve for mine shot #519.....	242
Figure B.15 – Pressure-time curve for mine shot #520.....	243

Figure B.16 – Pressure-time curve for mine shot #521. ....	244
Figure B.17 – Pressure-time curve for mine shot #522. ....	245
Figure B.18 – Pressure-time curve for mine shot #523. ....	246
Figure C.1 – Maximum ground velocity versus maximum pressure for Geophone 1 (C-Drift instrument room floor). Mine shot #507, which generated a pressure of 21 psi, appears to be an outlier. ....	248
Figure C.2 – Maximum ground velocity versus maximum pressure for Geophone 1 (C-Drift instrument room floor). The plots have removed mine shot #507 from the dataset which results in better overall trends when compared to Figure C.1. ....	249
Figure C.3 – Maximum ground velocity versus maximum pressure for Geophone 2 (C-Drift instrument room roof). Mine shot #507, which generated a pressure of 21 psi, appears to be an outlier. ....	250
Figure C.4 – Maximum ground velocity versus maximum pressure for Geophone 2 (C-Drift instrument room roof). The plots have removed mine shot #507 from the dataset which results in better overall trends when compared to Figure C.3. ....	251
Figure C.5 – Maximum ground velocity versus maximum pressure for Geophone 3 (D-Drift instrument room). The data from Channel 2 were considered questionable for some tests due to digitizer and/or geophone malfunction, which resulted in not as many data points for that plot. ....	252
Figure C.6 – Maximum ground velocity versus maximum pressure for Geophone 4 (E-Drift entry near bulkhead door). Data were only available from this location for a very small range of maximum explosive pressures. ....	253
Figure C.7 – Maximum ground velocity versus maximum pressure for Geophone 5 (D-Drift entry). The data from Channel 1 were considered questionable due to digitizer and/or geophone malfunction, which resulted in not as many data points for that plot. ....	254
Figure C.8 – Maximum ground velocity versus maximum pressure for Geophone 6 (E-Drift middle of entry). ....	255
Figure C.9 – Maximum ground velocity versus maximum pressure for Geophone 8 (A-Drift face). Mine shot #507, which generated a pressure of 21 psi, appears to be an outlier. ....	256
Figure C.10 – Maximum ground velocity versus maximum pressure for Geophone 8 (A-Drift face). The plots have removed mine shot #507 from the dataset which results in similar trends as the other datasets, although only three tests were recorded from this location. ....	257
Figure C.11 – Maximum ground velocity versus maximum pressure for Geophone 9 (A-Drift crosscut). Mine shot #507, which generated a pressure of 21 psi, appears to be an outlier. ....	258
Figure C.12 – Maximum ground velocity versus maximum pressure for Geophone 9 (A-Drift crosscut). The plots have removed mine shot #507 from the dataset which results in similar trends as the other datasets, although only three tests were recorded from this location. ....	259
Figure C.13 – Maximum ground velocity versus maximum pressure for Geophone 1 (C-Drift instrument room floor) recalculated to allow the regression line to intersect the origin. ....	260
Figure C.14 – Maximum ground velocity versus maximum pressure for Geophone 2 (C-Drift instrument room roof) recalculated to allow the regression line to intersect the origin. ....	261
Figure C.15 – Maximum ground velocity versus maximum pressure for Geophone 3 (D-Drift instrument room) recalculated to allow the regression line to intersect the origin. ....	262
Figure C.16 – Maximum ground velocity versus maximum pressure for Geophone 5 (D-Drift entry) recalculated to allow the regression line to intersect the origin. ....	263
Figure C.17 – Maximum ground velocity versus maximum pressure for Geophone 6 (E-Drift middle of entry) recalculated to allow the regression line to intersect the origin. ....	264
Figure C.18 – Maximum ground velocity versus maximum pressure for Geophone 8 (A-Drift face) recalculated to allow the regression line to intersect the origin. ....	265
Figure C.19 – Maximum ground velocity versus maximum pressure for Geophone 9 (A-Drift crosscut) recalculated to allow the regression line to intersect the origin. ....	266
Figure D.1 – Amplitude versus distance plot (top) with resulting attenuation plot (bottom) for mine shot #503. ....	268
Figure D.2 – Amplitude versus distance plot (top) with resulting attenuation plot (bottom) for mine shot #504. ....	269
Figure D.3 – Amplitude versus distance plot (top) with resulting attenuation plot (bottom) for mine shot #505. ....	270
Figure D.4 – Amplitude versus distance plot (top) with resulting attenuation plot (bottom) for mine shot #507. ....	271
Figure D.5 – Amplitude versus distance plot (top) with resulting attenuation plot (bottom) for mine shot #508. ....	272
Figure D.6 – Amplitude versus distance plot (top) with resulting attenuation plot (bottom) for mine shot #509. ....	273

Figure D.7 – Amplitude versus distance plot (top) with resulting attenuation plot (bottom) for mine shot #510. ....	274
Figure D.8 – Amplitude versus distance plot (top) with resulting attenuation plot (bottom) for mine shot #513. ....	275
Figure D.9 – Amplitude versus distance plot (top) with resulting attenuation plot (bottom) for mine shot #514. ....	276
Figure D.10 – Amplitude versus distance plot (top) with resulting attenuation plot (bottom) for mine shot #516. ....	277
Figure D.11 – Amplitude versus distance plot (top) with resulting attenuation plot (bottom) for mine shot #517. ....	278
Figure D.12 – Amplitude versus distance plot (top) with resulting attenuation plot (bottom) for mine shot #518. ....	279
Figure D.13 – Amplitude versus distance plot (top) with resulting attenuation plot (bottom) for mine shot #519. ....	280
Figure D.14 – Amplitude versus distance plot (top) with resulting attenuation plot (bottom) for mine shot #520. ....	281
Figure E.1 – Screenshot demonstrating the main purpose of the program. A .txt file containing columns of seismic data, with a header displaying location of the geophone, is loading into the path box. The sampling rate is set in order to properly display the frequencies. The top waveform chart displays the full signature with it's FFT on the side. A yellow and green vertical line allows the selection of a window in the signature. The selected window is then displayed on the bottom waveform chart with it's FFT on the side. The transform of either FFT can be saved (depending on background code). The window also shows the time frame selected (not shown in the screenshot) which was helpful in determining the durations of the seismic signatures. The name of the saved FFT file is programmed to be the name of the input file + name of the geophone location. Another waveform chart (not shown) displays a filtered waveform (low-pass, high-pass, band-pass or band-stop optional) from the original signal based upon program code. ....	283
Figure E.2 – Screenshot displaying the code which displays a seismic signature when a different column is selected from the data. The data is passed to an FFT calculation and also passed through a lowpass filter. The lowpass filter icon can be double clicked on and for a selection of a different frequency range type of filter. ....	284
Figure E.3 – Screenshot displaying the code for selection of two vertical lines which form a time window around the seismic signature. The selected portion of the signature is then sent to a waveform chart and an FFT calculation. ....	285
Figure E.4 – Screenshot displaying the code which formats the name of the .txt file which is saved from the FFT. ....	286
Figure F.1 – Seismic signature from Geophone 2 collected during mine shot #517 which was presented during the defense proposal. ....	288
Figure F.2 – Seismic signature from Geophone 2 collected during mine shot #510. The red waveform represents the horizontal component parallel to the mine drifts, green waveform represents the horizontal component perpendicular to the drifts and the blue waveform represents the vertical component. ....	290
Figure F.3 – Pressure data obtained from the LLEM monitoring system at the A-Drift face for mine shot #510. ....	291
Figure F.4 – Seismic signature from Geophone 2 collected during mine shot #510 and 519. These waveforms represent the horizontal component parallel to the mine drifts of the geophone. ....	292
Figure F.5 – Seismic signature from Geophone 2 collected during mine shot #510 and 519. These waveforms represent the horizontal component perpendicular to the mine drifts of the geophone. ....	292
Figure F.6 – Seismic signature from Geophone 2 collected during mine shot #510 and 519. These waveforms represent the vertical component of the geophone. ....	293
Figure F.7 – Pressure data obtained from the LLEM monitoring system at the A-Drift face for mine shot #519 with the data from shot #510 superimposed for comparison. The arrows indicate peaks correlated to peaks in the seismic signature plotted in Figure F.4. ....	293
Figure F.8 – Seismic signature from Geophone 2 collected during mine shots which showed significant secondary events. These waveforms represent the horizontal component parallel to the mine drifts of the geophone. ....	295
Figure F.9 – Seismic signature from Geophone 2 collected during mine shots which showed significant secondary events. These waveforms represent the horizontal component perpendicular to the mine drifts of the geophone. ....	295
Figure F.10 – Seismic signature from Geophone 2 collected during mine shots which showed significant secondary events. These waveforms represent vertical component of the geophone. ....	296
Figure F.11 – Pressure data obtained from the LLEM monitoring system at the A-Drift face for mine shots #510 - 519. ....	297
Figure F.12 – Photograph of the mine shelves and chains used in the series of mine shots with different rock and coal dust concentrations. ....	298
Figure F.13 – Seismic signature from Geophone 2 collected during mine shots which showed some secondary events. These waveforms represent the horizontal component parallel to the mine drifts of the geophone. ....	301
Figure F.14 – Seismic signature from Geophone 2 collected during mine shots which showed some secondary events. These waveforms represent the horizontal component perpendicular to the mine drifts of the geophone. ....	301

Figure F.15 – Seismic signature from Geophone 2 collected during mine shots which showed some secondary events. These waveforms represent the vertical component of the geophone. ....	302
Figure G.1 – Distance-time plot for mine shot #505. ....	305
Figure G.2 – Distance-time plot for mine shot #506. ....	305
Figure G.3 – Distance-time plot for mine shot #507. ....	306
Figure G.4 – Distance-time plot for mine shot #509. ....	306
Figure G.5 – Distance-time plot for mine shot #510. ....	307
Figure G.6 – Distance-time plot for mine shot #513. ....	307
Figure G.7 – Distance-time plot for mine shot #514. ....	308
Figure G.8 – Distance-time plot for mine shot #516. ....	308
Figure G.9 – Distance-time plot for mine shot #517. ....	309
Figure G.10 – Distance-time plot for mine shot #518. ....	309
Figure G.11 – Distance-time plot for mine shot #519. ....	310
Figure G.12 – Distance-time plot for mine shot #520. ....	310
Figure G.13 – Distance-time plot for mine shot #528. ....	311
Figure G.14 – Distance-time plot for mine shot #529. ....	311
Figure G.15 – Distance-time plot for mine shot #530. ....	312
Figure G.16 – Distance-time plot for mine shot #531. ....	312
Figure G.17 – Distance-time plot for mine shot #532. ....	313
Figure G.18 – Distance-time plot for mine shot #533. ....	313
Figure G.19 – Distance-time plot for mine shot #534. ....	314
Figure G.20 – Distance-time plot for mine shot #535. ....	314
Figure G.21 – Distance-time plot for mine shot #536. ....	315
Figure G.22 – Distance-time plot for mine shot #537. ....	315
Figure G.23 – Distance-time plot for mine shot #538. ....	316

# List of Tables

Table 2.1 – Documented methane explosions that have occurred within sealed areas of active underground mines in the US since 1986 (Zipf 2007).....	11
Table 2.2 – Seal size and associated natural frequencies obtained from LLEM Mine Shots #347 and 348.....	40
Table 3.1 – Summary of installation dates for geophones.....	67
Table 3.2 – Summary of P- and S-wave velocities collected during the rock drop tests.....	74
Table 4.1 – Slope and offsets which relate the ground velocity to maximum pressure during methane and dust explosions. Different average coefficients were observed for data in ranges between 0-150 meters and 150-250 meters.....	89
Table 4.2 – Recalculated slopes which relate the ground velocity to maximum pressure during methane and dust explosions. Different average coefficients were observed for data in ranges between 0-150 meters and 150-250 meters.....	91
Table 4.3 – Amplitude of ground velocities collected by Geophone 5 for the boosters set off near the A-Drift face.....	93
Table 4.4 – Amplitude of ground velocities collected by Geophone 5 for the boosters set off near the A-Drift face.....	97
Table 4.5 – Average durations from Geophones 1 and 2 for mine shots #505 – 509.....	100
Table 4.6 – Average durations from Geophones 3 and 5 for mine shots #505 – 509.....	102
Table 4.7 – Average durations from the closer geophones during mine shots #510– 519.....	105
Table 4.8 – Average durations from the far away geophones during mine shots #510– 519 and 521.....	106
Table 4.9 – Average durations for the closer geophones during mine shots #520 and 522.....	107
Table 4.10 – Average durations for the closer geophones during mine shots #523 and 524.....	108
Table 5.1 – Summary of initial energy, pressure from inside of the ignition chamber and the resulting average apparent velocities based upon the first arrival in the signature found for mine shots #505-520.....	114
Table 5.2 – Summary of average apparent velocities based upon the first arrival in the signature found for the cast booster experiments (mine shots #528-538).....	120
Table 6.1 – Summary of dominant frequency ranges detected from Geophone 1 and 2 during mine shots 503 – 524.....	139
Table A.1 – Maximum pressures observed at the seals during mine shot #503.....	173
Table A.2 – Maximum pressures observed at the seals during mine shot #504.....	176
Table A.3 – Maximum pressures observed at the seals during mine shot #505.....	179
Table A.4 – Maximum pressures observed at the seals during mine shot #506.....	182
Table A.5 – Maximum pressures observed at the seals during mine shot #508.....	188
Table A.6 – Maximum pressures observed at the stoppings during mine shot #510.....	194
Table A.7 – Maximum pressures observed at the stoppings during mine shot #513.....	197
Table A.8 – Maximum pressures observed at the stoppings during mine shot #514.....	200
Table A.9 – Maximum pressures observed at the stoppings during mine shot #516.....	203
Table A.10 – Maximum pressures observed at the stoppings during mine shot #517.....	206
Table A.11 – Maximum pressures observed at the stoppings during mine shot #518.....	209
Table A.12 – Maximum pressures observed at the stoppings during mine shot #519.....	212
Table A.13 – Maximum pressures observed at the stoppings during mine shot #520.....	215
Table A.14 – Maximum pressures observed at the stoppings during mine shot #521.....	218
Table A.15 – Maximum pressures observed at the stoppings during mine shot #522.....	221
Table H.1 – Moment magnitude and radiated seismic energy summary from Geophone 1.....	318
Table H.2 – Moment magnitude and radiated seismic energy summary from Geophone 2.....	319

Table H.3 – Moment magnitude and radiated seismic energy summary from Geophone 3.....	320
Table H.4 – Moment magnitude and radiated seismic energy summary from Geophone 4.....	321
Table H.5 – Moment magnitude and radiated seismic energy summary from Geophone 5.....	322
Table H.6 – Moment magnitude and radiated seismic energy summary from Geophone 6.....	323
Table H.7 – Moment magnitude and radiated seismic energy summary from Geophone 8.....	324
Table H.8 – Moment magnitude and radiated seismic energy summary from Geophone 9.....	324
Table H.9 – Moment magnitude and radiated seismic energy summary from Geophone 10.....	324
Table H.10 – Moment magnitude and radiated seismic energy summary from Geophone 13.....	325

# Chapter 1 – Introduction

## 1.1 Statement of the problem

Seismic monitoring provides a powerful means for detection and evaluation of events resulting from mining activity or unintended explosions that cause catastrophic events. Seismic signature characteristics such as arrival times, amplitudes, duration and frequency content can give indication to the nature and location of the source. In the past, most mining-related seismic assessments have focused on events such as production blasts from quarries, roof falls and rock fractures (Iannacchione et al. 2005a; Iannacchione et al. 2005b; Swanson et al. 2002). However, little or no effort has been put towards examining the characteristics of a signature emanating from a methane and coal dust explosion in an underground mine. The Sago Mine disaster in 2006 provides an example of why these particular signatures should be researched. A small amplitude signal, shown in Figure 1.1, was identified on records of the closest regional seismic network stations (Chapman 2006). The epicentral location of the small amplitude signal, shown in Figure 1.2, was at the Sago Mine. However, it was unclear whether the signature represented the explosion itself or another type of mining-related seismicity such as a large roof fall. The current study will begin the process to understand the seismicity from methane and coal dust explosions.

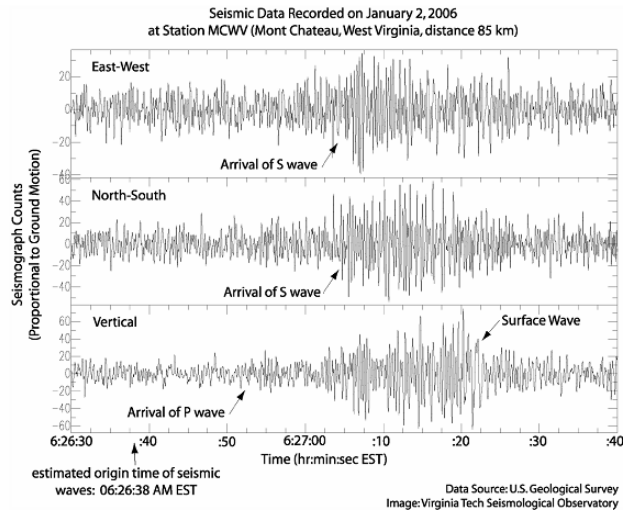


Figure 1.1 – Seismic signature of the event at the time of the Sago Mine disaster (Chapman 2006).

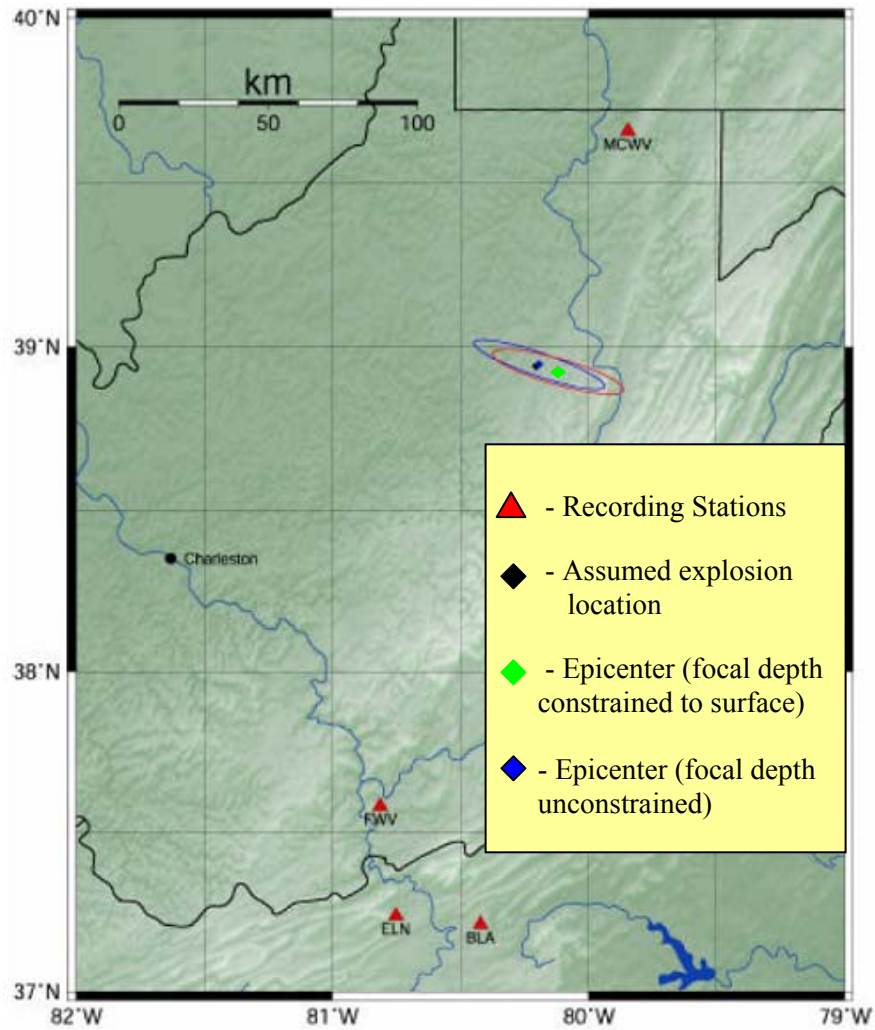


Figure 1.2 – The epicenter location of the small amplitude signal was at the Sago Mine. If depth is unconstrained, the assumed mine explosion location (black diamond) and epicenter (blue diamond) are at the same approximate location (Chapman 2006).



## 1.2 Proposed solution and objective

The Lake Lynn Experimental Mine (LLEM) is a facility associated with National Institute of Occupational Safety and Health's Pittsburgh Research Laboratory. The research mine is located approximately 96 km (60 miles) southeast of Pittsburgh, PA on the border between Pennsylvania and West Virginia. The research facility has conducted controlled methane and coal dust explosions since 1983. These experiments provide insight into the behavior and prevention of underground mine explosions (Cashdollar et al. 2006; Sapko et al. 2000). This facility provided an ideal location and opportunity to monitor the seismicity from controlled explosions in an underground mine. The objective of the study was to analyze seismic signatures generated by methane and coal dust explosions\* to begin understanding their characteristics at different distances away from the source. By analyzing the signatures at different distances away, the seismic assessments were related to the size of the explosion. These types of measurements have never been made before and characteristics found in the signatures are hoped to provide better understanding of these events when captured in the far-field.

NIOSH has also been conducting research on the design and behavior of explosion-containment seals during methane and dust explosions (Zipf et al. 2007). Therefore, the opportunity to investigate the seismicity of methane and dust explosions interacting with mine seals was made available. The focus on the current study was to analyze the seismic signatures emanating from methane and coal dust explosions for any type of experimental design, determined by the investigative interest of NIOSH. When mine seals were involved, the intent

---

\* The methane and coal dust explosions were designed and conducted by K.L. Cashdollar, E.S. Weiss, and/or S.P. Harteis as part of the mine explosion program for NIOSH, Pittsburgh Research Laboratory's Disaster Prevention and Response Branch.

was to not evaluate seal design criteria based upon the seismic signatures, but to analyze the impact of the mine seals on the seismic signature.

The accessibility of Lake Lynn Experimental Mine allowed for the unique opportunity to monitor methane and dust explosions in an underground environment; however, the control of the experimental designs was not made available. The placement of mine seals, or structures representing mine seals, in the surrounding area and blast pressures during each explosion could not be controlled for the purposes of the current study. Since the facility was occupied with many other research projects at the time of the study, including extensive seal testing for MSHA-based seal design requirements, having the experimental setups adjusted was not possible. Ideally, experiments with replicated designs would be monitored; however, this was not an option in this study due the research focus of NIOSH. This study was considered to be an exploratory project where any finding or observation through the analysis of the signatures from varying experimental designs would be considered beneficial.

### **1.3 Scope of the study**

A seismic monitoring system was installed at the Lake Lynn Experimental Mine to collect seismic signatures emanating from methane and dust explosions. Geophones were placed throughout the mine to provide observations at different distances away from the source. As the study progressed, geophones were added to the initial array at locations which were considered advantageous or where responses were lacking. Using waveform analysis procedures, seismic characteristics from the explosions were investigated. These seismic characteristics include, but are not limited, to the duration, spectral character, moment magnitude, and radiated seismic energy. A sophisticated program, previously coded by NIOSH researchers, which contained algorithms to help determine these unique characteristics was adapted and modified for this task.

A LabVIEW program was also programmed to help determine frequency content at specific portions of the seismic signature and also used for filtering of the data. Although commercial software provided by the monitoring system manufacturer was available, the more manual and “step-by-step” analysis of these signatures was more useful for this research. With the existing commercial software, certain assumptions made during the seismic analysis in background processes were unknown. Since these measurements have never been made before, these assumptions needed to be known so the analysis of the seismic signatures could progress. The development of a program geared towards controlling what algorithms are performed on the signatures in a step-by-step fashion allowed for all factors to be made identified and defined.

Opportunities to collect other types of mining-related seismic events at the Lake Lynn Experimental Mine were also be available. Drop tests using several types of material such as limestone blocks, concrete blocks and steel blocks was performed to help calibrate the system by obtaining obtain P- and S-wave velocities. A particular area at LLEM, which had been previously mined over 50 years ago and known as the old workings, has had roof stability issues dating back to 1994 (Dolinar et al. 2003). This area was monitored to capture potential rock shear events and roof falls.

The content of this study is summarized as follows. In Chapter 2, a literature review gives a brief summary of the history of methane explosions in underground mines, background information on seismic wave and source properties, and concludes with a discussion on previous seismic monitoring studies conducted in underground mines. The information in Chapter 3 documents the experimental procedures of the study. The information includes a description of the Lake Lynn Experimental Mine, the instrumentation used in the study, a summary of the data collected during the study and description of the algorithms used to analyze the seismic

signatures. Chapters 4 – 7 discusses the different ways the data were analyzed and the results of the analysis. Chapter 4 analyzes the amplitude, attenuation and duration of the seismic signatures. Chapter 5 analyzes the apparent velocities to determine what types of seismic waves were produced during the tests. Chapter 6 analyzes the frequency content of the seismic signatures and Chapter 7 analyzes the relative moment magnitude and radiated seismic energy estimates from the collected signatures. Chapter 8 provides an overall conclusion from the study and recommendations for future research. A detailed description of the explosive mine shots is reported in Appendix A and sets of charts or tables supporting the results are reported in Appendices B – H.

The final results from this study provide more fundamental understanding of seismic signatures not studied extensively in the past, specifically signatures obtained from explosions in a contained environment like an underground mine. While these results might not provide all the answers, they enhance the understanding of these complex signatures and provide a basis for more in-depth controlled experimentation in this area.

# **Chapter 2 – Literature Review**

## **History of Methane Explosions in Underground Mines**

Methane explosions in underground mines have been reported throughout the history of mining. These disasters impact the safety of underground workers, affect the underground conditions and cause a loss of production. In the early mining days, these disasters were mainly caused by ignition of methane at the active face. In recent times, these events have mostly occurred in sealed areas of abandoned parts of the mine where methane is accumulated and ignited by lightning or a spark from a roof fall (Zipf 2007). Coal dust can act as additional fuel to increase the explosive pressure. The following historical summary of methane explosions in underground mines is intended to show the impact of how devastating these events are and the importance of continued research for better understanding of how to prevent them.

### **2.1 Historical summary of methane explosions from the early 1800's – 1977**

Disasters from methane explosions have plagued the mining industry as far back as the early 1800's. The first reported occurrence of methane accumulation in an underground mine, written in 1818, described the mining environment as poorly ventilated and workers experienced a great inconvenience from “carbonic acid gas” (Grammar 1818). The letter also reported the first known U.S. explosion in a coal mine occurring in 1810 and was caused by an open light igniting the methane accumulation. Literature discussing research on prevention of these disasters have dated back to 1908 when a report requested by the Secretary of the Interior, James

Rudolph Garfield, was used to create new legislation for ensuring more efficient and careful operation of mines (Watteyne et al. 1908).

Figures 2.1 and 2.2 show the number of fatalities and incidents by year caused by major explosions occurring in underground coal mines for the U.S., respectively. A major explosion was considered to be an event that caused five or more fatalities. The chart was compiled by archived fatality data from 1890 to 1975, including mine operators, inspectors, contractors, surface workers, visitors, etc (Humphrey 1960 and Richmond et al. 1983). Between 1890 and 1900, mines became deeper with more abandoned sections where methane concentrations could accumulate. Also, during this period, the use of electric trolley locomotives was being used for the first time. Prior to 1920, it was common practice in coal mines to purposely ignite a methane concentration at the working face to remove the accumulation (Humphrey 1960). Over 50% of the explosions between 1900 and 1920 were caused by open lights. The highest number of fatalities from major explosions in a given year was 903 in 1907. Including minor explosions, which were defined as events resulting in less than five deaths, the total number of fatalities in 1907 was 960. The biggest disaster in the history of the mining industry, the Fairmont Coal Company Mining Disaster in Monongah, West Virginia where 362 fatalities resulted, also occurred in 1907. Nagy (1981) showed that the trend of these fatalities began to decline if the 15 year averages of fatalities were taken into consideration. One possible reason for the decline of fatalities was that sealing of abandoned areas became a more common practice during this time. However, this practice was conducted mainly in mines with high spontaneous combustion potential (Mitchell 1971). Eighteen major explosions occurred between 1958 and 1977. These explosions were most likely detonated within active areas of the mine, based upon the reported ignition source, and not within the abandoned seal area (Nagy 1981). In 1969, The Federal Coal

Mine Health and Safety Act of 1969 required all mines to ventilate or seal abandoned areas with explosion proof bulkheads.

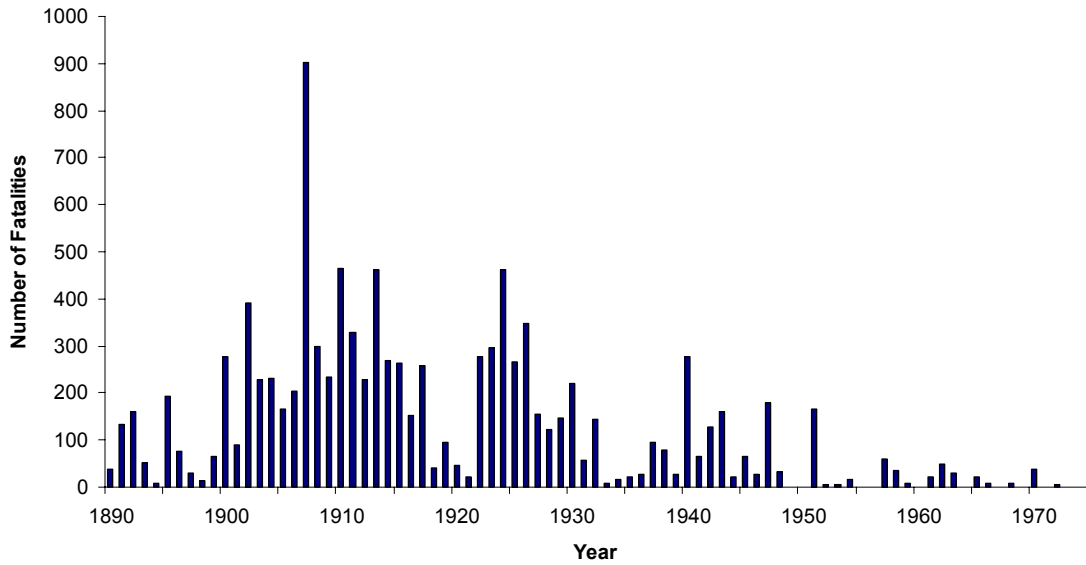


Figure 2.1 – Number of fatalities caused by major explosions occurring in underground coal mines between 1890 and 1975.

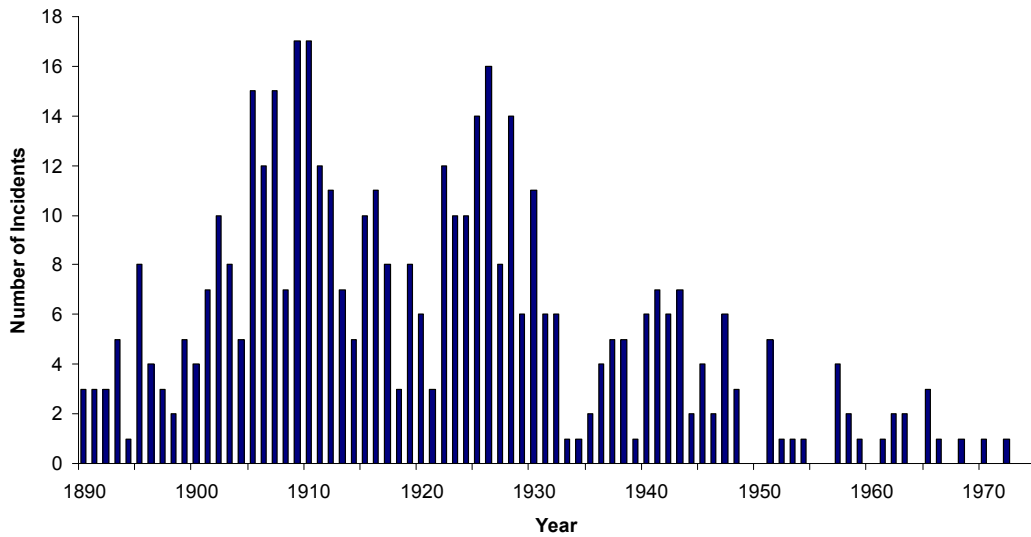


Figure 2.2 – Number of incidents caused by major explosions occurring in underground coal mines between 1890 and 1975.

## **2.2 Historical summary of documented methane explosions occurring within sealed areas (1986 – 2006)**

Investigative reports are unavailable for explosions occurring within sealed areas in underground coal mines prior to 1986. The earliest investigative report for an underground coal mine explosion within a sealed area occurred in 1986 at the Roadfork No. 1 Mine. Including the Roadfork No. 1 Mine incident, Zipf et al. (2007) tabulated twelve known explosions, recreated in Table 2.1, that have occurred within sealed areas of active underground mines in the US since 1986. The characteristics of the explosions are reported, which include the mine and year of occurrence, size of the sealed area, damage from the explosion, suspected ignition source, estimated explosive pressure and reference to the MSHA accident investigation reports. Nine documented cases, where explosions within sealed areas in underground coal mines occurred, happened before the Sago Mine disaster.

Lightning or roof falls appear to be the ignition source for the methane concentration for most of the disasters, however MSHA investigators could not establish the cause of the explosion conclusively. In the cases where lightning is a suspected ignition source, there is a conduit available for the strike to travel into the underground mine (Checca and Zuchelli 1987). The archived data from detection networks, in the form of isokeraunic maps and lightning charts, are used for analysis. The reports generated by the archived data along with physical and analytical evidence from explosions can work together to show lightning as a source. The procedure has become a standard practice for MSHA investigators, but this data only proves lightning as a suspected source and is not irrefutable.



**Table 2.1** – Documented methane explosions that have occurred within sealed areas of active underground mines in the US since 1986 (Zipf 2007).

Mine	Year	Size of Sealed Area	Damage from Explosion	Suspected Ignition Source	Estimated Explosive Pressure	Source
Roadfork No.1	1986	Several room and pillar panels	4 Seals Destroyed	Spark from rock fall	Unknown	South (1987)
Mary Lee No.1	1993	Several square miles	2 seals destroyed and shaft cap displaced	Lightning	15 kPa (2 psig)	Checca and Zuchelli (1995)
Oak Grove No. 1	1994	Several square miles	2 seals destroyed and shaft cap displaced	Unknown	Unknown	Scott and Stephan (1997)
Gary 50	1995	Several square miles	None; seals survived	Lightning or roof fall	35-48 kPa (5-7 psig)	Sumpter et al. (1996)
Oak Grove No. 1	1996	Several square miles	5 seals destroyed	Lightning	<35 kPa (<5 psig)	Scott and Stephan (1997)
Oasis	1996 (May)	Several square miles	3 seals destroyed	Lightning or roof fall	<138 kPa (<20 psig)	Ross and Schultz (1996)
Oasis	1996 (June)	Several square miles	Unknown	Lightning or roof fall	Unknown	Ross and Schultz (1996)
Oak Grove No. 1	1997	Several square miles	3 seals destroyed	Lightning	>138 kPa (>20 psig)	Scott and Stephan (1997)
Big Ridge Mine Portal No. 2	2002	Unknown	1 seal destroyed	Unknown	Unknown	Kattenbraker (2002)
Sago	2006	1 room and pillar panel	10 seals destroyed	Lightning	>642 kPa (>93 psig)	Gates et al. (2007)
Darby	2006	1 room and pillar panel	3 seals destroyed	Oxygen/acetylene torch	>152 kPa (>22 psig)	Light et al. (2007)
Jones Fork E-3	2006	Unknown	3 seals destroyed	Unknown	Unknown	Under investigation
Blacksville No. 1 <sup>1</sup>	1992	Shaft area	Shaft cap and collar destroyed	Welding sparks	6.9 MPa (1,000 psig)	Rutherford et al. (1993)

<sup>1</sup> Explosion occurred under shaft cap of abandoned shaft.

### 2.3 Recent methane explosion disasters and methods of prevention

A great deal of effort has been focused on the proper way to prevent methane and dust explosions from occurring underground mines. The first studies on how to protect sealed areas were conducted in 1914 at the U.S. Bureau of Mine’s Experimental Coal Mine. In these studies, barriers on both sides of a weak stopping limited the propagation of an explosive flame into the sealed area of the mine, despite the barriers being destroyed (Rice et al. 1922). Subsequent studies were able to develop bulkheads which were able to withstand a pressure of 50 psi; however it is important to note that these studies were to protect abandoned areas in mines because the explosions were assumed to be ignited in the active sections (Rice et al. 1931).

While there has been continued significant progress on preventing underground mine disasters, in the 2000’s there have been an increase of injuries and fatalities due to underground

explosions, as reported in Figure 2.3. Compiled from MSHA data, this figure includes all coal methane and dust explosions for underground coal operators, meaning incidents occurring outside of sealed areas are included (MSHA 2007). Most recently in 2006, two major explosions occurred within sealed areas of the mine at Sago and Darby resulting in 17 fatalities.

Due to the recent mining disasters, a great deal of research has been initiated on the prevention of underground explosions with research projects intended to expand the knowledge and technology for preventing these events. Seismic data has the ability help MSHA investigators make more conclusive assessments of the events that occurred during an underground explosion. However, seismic data can be difficult to obtain for these events. The availability of seismic records for past events is difficult to determine, because if the exact time of detonation is indefinite then processing the data to find the event, without a relatively small time frame, is very difficult. The data discussed in Chapter 1 are the only signatures obtained from a regional seismic network that may represent an underground methane explosion.

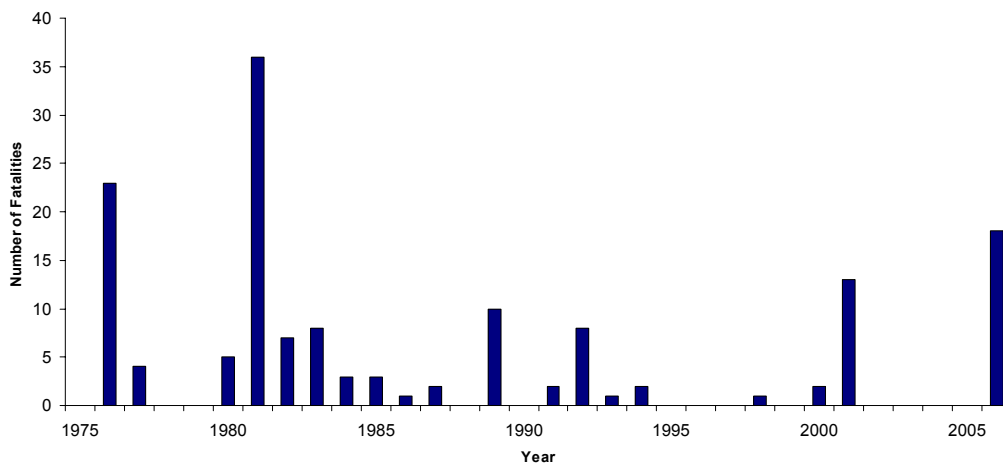


**Figure 2.3** – Number of fatalities from coal methane and dust explosions for underground coal operators between 1975 and 2006.

## **2.4 Chemistry and physics of an underground methane explosion**

In the abandoned areas of underground mines, the methane concentrations will increase within the sealed areas due to coalbed methane liberation. A methane concentration between 5 – 16% by volume is ideal conditions for an explosion. An explosion will not occur in an atmospheric condition exceeding 16% methane concentration. The explosive pressures for a coal dust-air concentration are very similar to a methane-air concentration. Thus, the volatilization of the coal dust, which occurs rapidly within the flame front of a methane explosion, can add to the maximum pressure generated by the explosion (Zipf 2007).

Zipf (2007) considers a scenario of an explosion in a mine entry with both ends closed and filled with an explosive methane-air concentration. Four cases can occur which include slow deflagration, fast deflagration, detonation and reflection of a detonation wave from a direct impact with the closed end of the tunnel. Initially, the slow deflagration stage involves an initial laminar flame speed of approximately 3 m/s (10 ft/s). As this speed accelerates, the turbulent flame speed increases to approximately 300 m/s (1,000 ft/s). The pressure in the burned gas behind the flame increases and an acoustic wave propagates to the speed of sound for that particular site. As the velocity of the unburned gas ahead of the flame front increases, the turbulence in the flow will increase causing the fast deflagration stage to occur. Factors affecting the degree of turbulence include obstructions from the roof and rib, machinery and wall roughness which increase the overall roughness of the tunnel. When the flow ahead of the flame front is turbulent, the flame speed increases from subsonic to supersonic and the detonation stage occurs. For this type of event, the flame front travels at supersonic velocity and the pressure wave no longer disturbs the unburned gas ahead of the flame front. For the explosions

conducted at the mine during this study, the experiments were in the slow deflagration stage and never reach detonation.

A typical pressure-time history for an explosion in a tunnel is plotted in Figure 2.4. The explosion comprises of a rise to a peak pressure and decline back to the ambient atmospheric pressure, which is the positive compression phase. The rapid fall below the ambient atmospheric pressure is the expansion phase, or a phenomenon known as suck-back. The positive compression phase represents the mass movement of air out of the high-pressure blast initiation zone and the movement of air back into that zone is the suck-back phenomena.

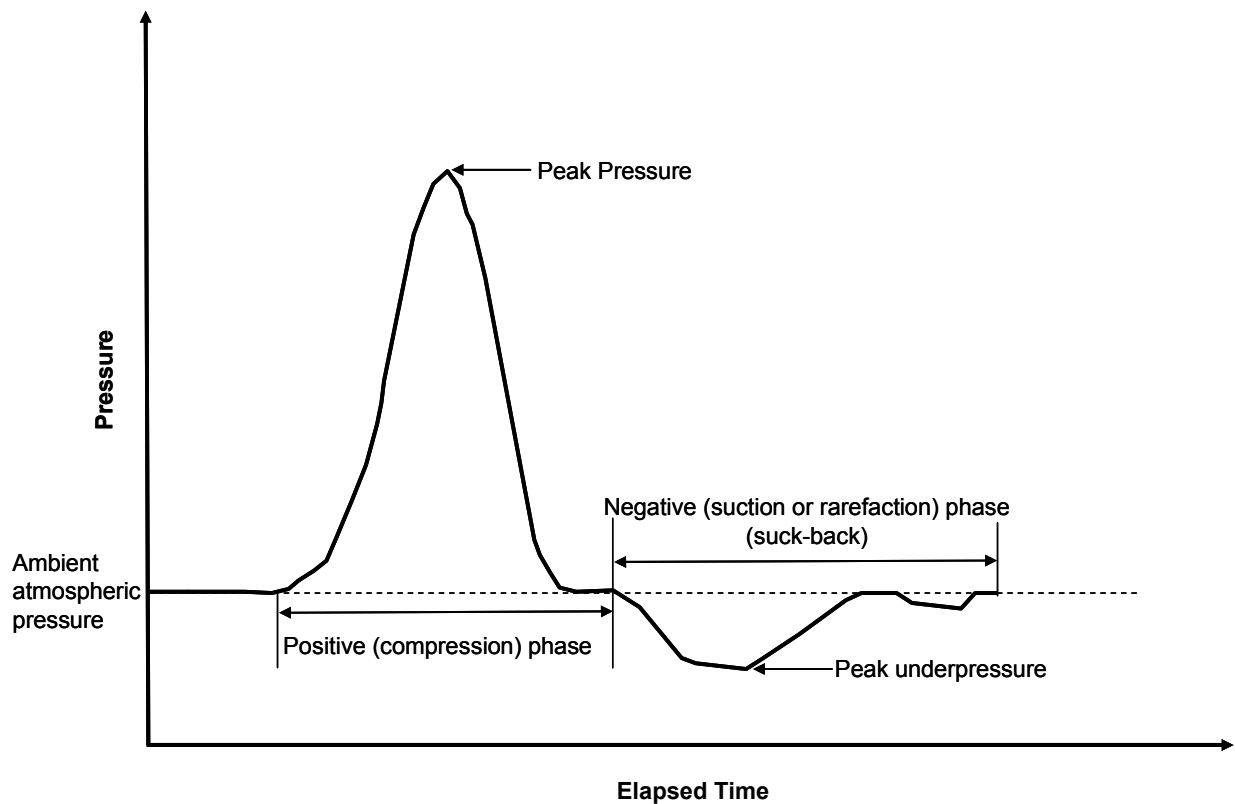


Figure 2.4 – Typical time-pressure history for an explosion in a tunnel.

## **Background of Seismic Waves and Sources**

Waveform characteristics such as elastic wave type, velocity, frequency and spectra content can all give indication towards the seismic source. These characteristics will be studied to investigate unique features in the signatures collected at the Lake Lynn Experimental Mine. The following sections review the different types of characteristics and important features within different types of signatures which will be used for analysis.

### **2.5 Types of seismic waves**

Seismic waves are transient elastic deformations propagating through a medium that can be recorded by seismic instruments. The types of seismic waves are defined by their distinctive particle motion. There are two main types of seismic waves: body waves and surface waves. Body waves travel through the interior of the medium. The two main types of body waves are P-waves and S-waves. P-waves (also known as compressional, longitudinal or primary waves) travel by compressional and dilational uniaxial strains in the direction parallel to the path of wave energy. S-waves (also known as shear, transverse or secondary waves) travel as shear strains in the direction perpendicular to the path of wave energy (Kearey et al. 2002). The two types of body waves can be visualized in Figures 2.5a and 2.5b.

Surface waves propagate along a free surface boundary of the medium. The two types of surface waves are Rayleigh waves and Love waves. Rayleigh waves (also known as “ground rolls”) have an elliptical particle motion that is perpendicular to the surface and parallel to the direction of wave energy. The Rayleigh wave propagation is also often referred to as retrograde particle motion. Love waves are comprised of horizontally polarized shear waves and have a

particle motion parallel to the surface and perpendicular to the direction of wave energy. These two types of surface waves can be visualized in Figures 2.5c and 2.5d.

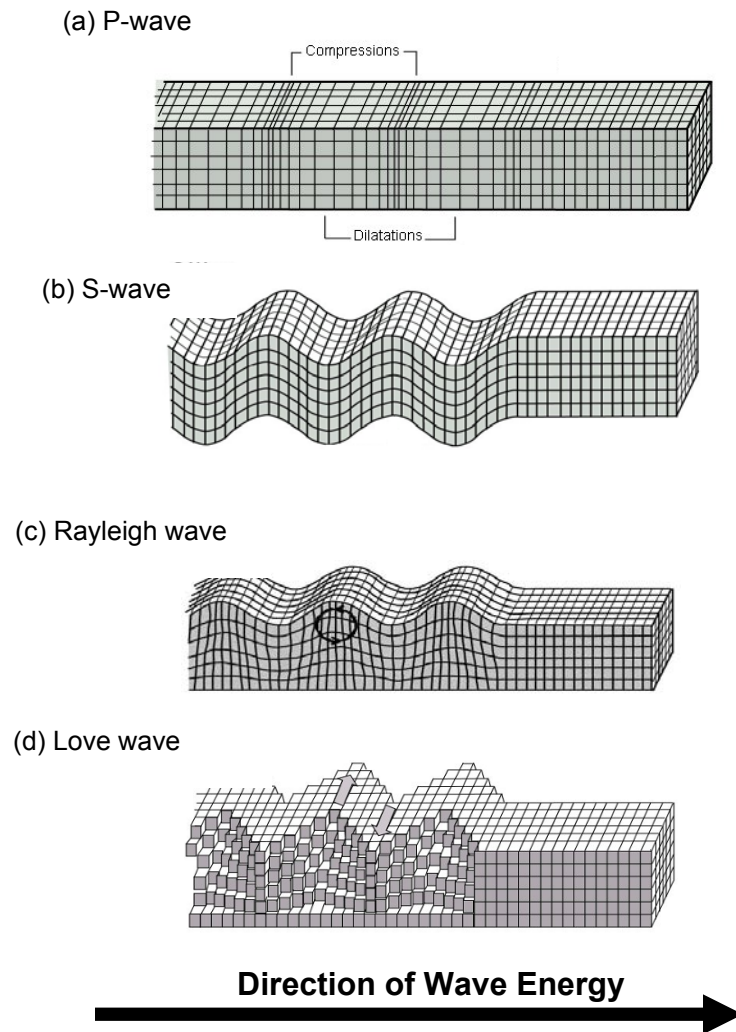


**Figure 2.5** – Visual description of the types of body and surface waves: (a) P-waves, (b) S-waves, (c) Rayleigh waves and (d) Love waves (adapted from Bolt 1982).

## 2.6 Velocity of seismic waves

The propagation velocity of a seismic wave is the velocity with which the seismic energy travels through the medium (Kearey et al. 2002). For small strains, the wave velocity is independent of the velocity of the disturbed particle motion of the medium. For larger strains, changes in material behavior occur and the particle velocity is dependent on the wave velocity. The velocity of a seismic wave through a homogeneous, isotropic material is dependent upon the appropriate elastic modulus and density of the material. For P-waves, the velocity is given by the relationship shown in Equation 2.1. The bulk modulus  $K$ , also known as the modulus of incompressibility, is the ratio of the volume stress to the volume strain. The shear modulus  $\mu$ , also known as the modulus of rigidity, is the ratio of shear stress to shear strain.

$$V_p = \left[ \frac{K + \frac{4}{3}\mu}{\rho} \right]^{1/2} \quad (2.1)$$

where:  $K$  = Bulk modulus (Pa)  
 $\mu$  = Shear modulus (Pa)  
 $\rho$  = Density ( $\text{kg/m}^3$ )

The velocity of an S-wave is represented in Equation 2.2. S-waves contain pure shear motion, thus they cannot travel through mediums such as water or air. P-waves can travel through fluids such as air or water as acoustic waves.

$$V_s = \left[ \frac{\mu}{\rho} \right]^{1/2} \quad (2.2)$$

Based upon the equations of the two body waves, it can be observed that compressional waves always travel faster than shear waves. The ratio of the velocities can be related by the

value of the Poisson's ratio, which refers to the ratio of lateral strain to longitudinal strain, for a given material. This relationship is shown in Equation 2.3.

$$\frac{V_p}{V_s} = \left[ \frac{2(1-\sigma)}{1-2\sigma} \right]^{1/2} \quad (2.3)$$

where:  $\sigma$  = Poisson's ratio

The Poisson's ratio for hard rocks is approximately 0.25 (Kearey et al. 2002). Using this value in the equation above, the relationship between P- and S-waves becomes  $V_p = \sqrt{3} V_s$ . Surface waves travel slower than shear waves through dispersion, meaning different frequency components travel at different velocities. Underground in the mining environment, surface waves diminish at a depth of three radii of the mine opening as a general rule of thumb. An air-coupled surface wave has been found to travel at the speed of sound in air, as shown by Johnston (1987) who recorded the seismicity from an air blast. Johnson found that when the source of the disturbance is in the air, air-coupled surface waves are generated and advances with the pressure wave traveling at the speed of sound in air.

## 2.7 Seismic sources

Seismic sources are the natural (earthquakes, cavity collapses or storms) or man-made (explosions, mining-induced collapses or cultural noise) events which generate seismic waves. Seismic events, such as a production blast at a mine or quarry, may have a known source location and time while other events, such as an earthquake or microfracturing in a mine roof, require mathematical techniques to determine the source location and time.



### 2.7.1 Frequency of seismic sources

The frequency of a seismic wave, measured in Hertz (Hz), is the number of cycles in the repetitive waveform per second. The wavelength of a seismic wave is the distance between two repetitive features in the waveform. Equation 2.4 relates the frequency ( $f$ ) and wavelength ( $\lambda$ ) of a waveform, where  $v$  is the wave velocity.

$$\lambda = v/f \quad (2.4)$$

Equation 2.4 shows that frequency and wavelength are inversely correlated. Figure 2.6 illustrates the difference between low-frequency and high-frequency waves in terms of wavelength. A low-frequency signal has a long wavelength and a high-frequency signal has a short wavelength. For body waves, all frequencies of the pulse travel through the medium at the same velocity. For surface waves, the propagation progressively changes causing different frequency components to travel at different velocities. Dispersion of surface waves can introduce complexity into the seismic signature when all wave types are contained within the seismic signature.

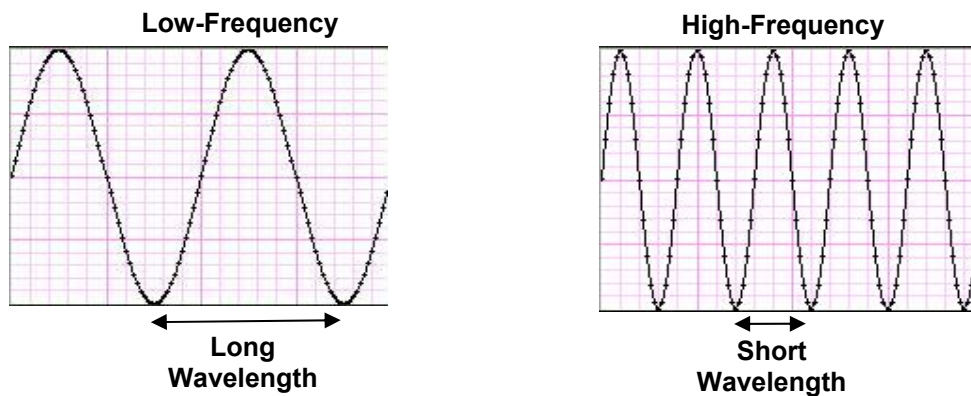


Figure 2.6 – Difference between low-frequency and high-frequency seismic waves.

Seismic sources can also be differentiated in terms of frequency content, as shown in Figure 2.7. Earthquakes have very low-frequency content, typically between 0.05 – 5 Hz (Kearey et al. 2002). Iannacchione et al. (2005a) monitored the seismicity from different types of mining-related events and found that blasts from nearby quarries (5 – 14 km away) had a frequency range between 0.5 – 75 Hz, roof fall events had a range between 1 – 400 Hz and rock drop tests had a range between 5 – 400 Hz. Higher frequency mining-induced events can be in the form of acoustic emissions prior to rockbursts, which are typically in the range of 100 – 10,000 Hz (Armstrong 1969).

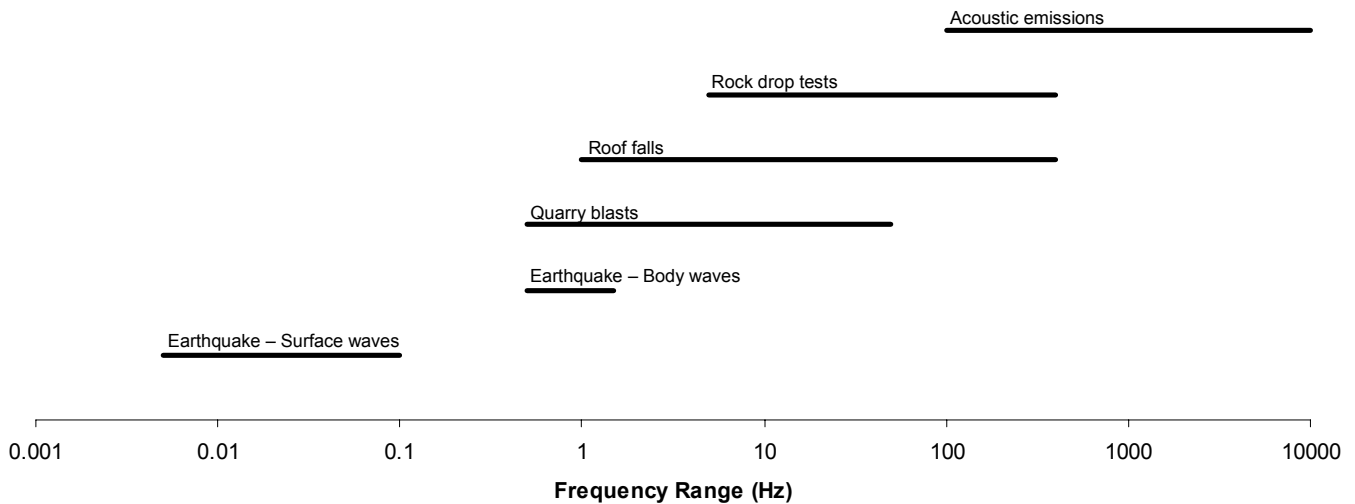


Figure 2.7– Frequency ranges of common seismic sources.

### 2.7.2 General model for the displacement spectra

The displacement spectra, also known as the Fourier amplitude displacement spectrum, for seismic events can be used to identify the moment magnitude and radiated seismic energy associated with the source. The low-frequency spectral plateau  $\Omega_0$ , also known as the long period amplitude, and the corner frequency,  $f_c$ , can be estimated using the displacement spectra (Abercrombie 1995). The low-frequency spectral plateau is used for computing the moment

magnitude and radiated seismic energy. The general model,  $\Omega(f)$ , used to fit the displacement spectra for both the P- and S-waves is shown in Equation 2.5.

$$\Omega(f) = \frac{\Omega_o e^{-\left(\frac{\pi f t}{Q}\right)}}{\left[1 + \left(\frac{f}{f_c}\right)^{\gamma n}\right]^{\frac{1}{\gamma}}} \quad (2.5)$$

where:  $\Omega_o$  = low-frequency spectral plateau of the displacement spectrum (m/Hz),  
 $f$  = frequency of the waveform (Hz),  
 $f_c$  = corner frequency of the waveform (Hz),  
 $t$  = travel time of the waveform (s),  
 $Q$  = frequency independent quality factor,  
 $n$  = high-frequency fall off rate, and  
 $\gamma$  = constant to define the spectral shape.

A spectral shape proposed by Brune using the constants  $t = 0$ ,  $n = 2$  and  $\gamma = 1$  has been known to match seismic data well (Brune 1970; Brune 1971). Using Brune's model to fit the displacement spectra, and assuming that the seismic wave does not attenuate, the equation can be reduced to Equation 2.6.

$$\Omega(f) = \frac{\Omega_o}{\left[1 + \left(\frac{f}{f_c}\right)^2\right]} \quad (2.6)$$

### 2.7.3 Moment magnitude and radiated seismic energy estimates of seismic sources

Seismic sources can be analyzed in terms of static seismic moment (Aki 1968), moment magnitude (Hanks and Kanamori 1979) and radiated seismic energy (Boatwright and Fletcher 1984). The seismic moment is often used as an indicator for the overall size of the event. The

static seismic moment,  $M_o$ , is derived from physical characteristics of the source, as shown in Equation 2.7.

$$M_o = \frac{4\pi\rho R|\Omega_o|c^3}{F_c} \quad (2.7)$$

where:  $\rho$  = density of the rock at the source (kg/m<sup>3</sup>),  
 $R$  = distance from source to receiver (m),  
 $\Omega_o$  = low-frequency spectral plateau observed in the Fourier displacement amplitude spectrum (m/Hz),  
 $C$  = P- or S-wave velocity (m/s), and  
 $F_c$  = P- or S-wave radiation pattern coefficient.

For the static seismic moment calculations, if the events, such as impacts, are assumed to produce an isotropic wave radiation pattern, then  $F_c$  would be equal to 1. If the events produce a bipolar radiation pattern, such as shear events from rock fractures, then the RMS values of 0.52 for P-waves and 0.63 for S-waves, determined by Boore and Boatwright (1984), are used. The moment magnitude,  $M$ , is a magnitude scale based on the static seismic moment and is defined in Equation 2.8.

$$M = \frac{2}{3} \log(M_o) - 6 \quad (2.8)$$

For mining-related events, the moment magnitude scale typically ranges from -4 to 4. Iannacchione et al. (2005a) conducted a study which summarized the moment magnitudes estimated for different types of sources such as rock drops and roof falls. The moment magnitude for dropping rocks (sizes between 3.7 to 17.9 tons) from a height of approximately 5 m (16.4 ft) ranged from -0.9 to 0. For roof falls, four events were calculated to have a moment magnitude ranging from 0.1 to 1.4. These events were described as massive and many individual

rocks of varying size and shape striking the mine floor at slightly different times. Iannacchione et al. (2005b) reported moment magnitudes of rock fracture events collected from three field sites, which ranged from -1.5 to 0.9. Iannacchione et al. (2005c) gives moment magnitude estimates of microseismic events collected from a longwall panel in the eastern U.S. Of the 9,580 events collected, only one had a moment magnitude above 2. Over 95% of the events had a moment magnitude between -2 and 0.

The radiated seismic energy is typically used as a measure for the strength of the event. The radiated seismic energy,  $E_s$ , is expressed in units of joules and is defined in Equation 2.9. The radiated seismic energy relationship used in this study is a simplified version from the equation derived and presented in Boatwright and Fletcher 1984. Iannacchione et al. (2005a) reported the radiated seismic energy estimates of the rock drop tests and roof falls. The radiated seismic energy estimates of the rock drop tests ranged from 0.2 to 93.1 Joules and the estimates for the roof falls ranged from 7.7 to 631.1 Joules.

$$E_s = 4\pi\rho cR^2(I_1 + I_2 + I_3) \quad (2.9)$$

where:  $\rho$  = density of the rock at the source ( $\text{kg/m}^3$ ),  
 $R$  = distance from source to receiver (m),  
 $c$  = P- or S-wave velocity (m/s), and  
 $I$  = integral of squared velocity for a geophone orientation ( $\text{m}^2/\text{s}^2/\text{Hz}$ ).

## Seismic monitoring in underground mines

The first seismic network to monitor seismicity in mines was in the Upper Silesia coal basin (originally Germany, now Poland) near the end of the mid 1920's (Gibowicz 1963). Since then, many seismic systems have aided mining engineers and researchers for development of

safer mining methods. The following section reviews the history of seismic monitoring in mines and the instrumentation involved.

## **2.8 Brief history of seismic monitoring system applications in mines**

A seismic monitoring system is used to detect the types of seismic waves discussed previously. Historically, seismic monitoring systems have been utilized to monitor earthquake activity. The first earthquake was recorded instrumentally for the first time in 1889. The first global seismic monitoring of earthquake activity occurred in 1892 when John Milne developed and installed seismometers at different observatories.

In mining, seismic monitoring systems have most extensively been used to quantify the rock mass response near excavations in order to develop safer practices and attempt to predict areas of instability. Early uses of seismic monitoring in underground mines have helped with the detection and location of seismic events. For example, in 1983 instrumentation was installed at the Campbell Mine in Red Lake, Ontario, which is an underground gold mine. A 30-hour period of events were recorded and found to be due to a progressive failure of successive pillars. The system located the events in areas where no crews were working however the vibrations could be felt in active mining areas (Blake and Hedley 2003). Use of seismic techniques implemented in underground mines continued to mostly focus on the prevention of rockbursts in failure prone areas. In the 1980s and 1990s, the U.S. Bureau of Mines conducted research on mining-induced seismicity for providing warning and insight into how to control such rockburst occurrences (Bolstad 1990). The development of instruments to monitor acoustic emissions and seismic events has helped determine the damaging types of seismic waves created. These studies have also helped delineate potential rockburst areas and assess the stability of each potential failure area in real time (Leighton 1984). Other uses of seismic monitoring systems have included

international monitoring for nuclear explosions in conjunction with the Comprehensive Nuclear-Test-Ban Treaty. Nuclear explosions from the past were studied extensively in order to discriminate from other types of seismic activity.

Mendecki (1997) describes four different application scenarios when referring to seismic monitoring systems in mining. The four applications are regional monitoring, mine or shaft wide monitoring, pillar/remnant monitoring and continuous quantification of seismic rock mass response to mining. Data from regional monitoring can be taken from the nationwide U.S. Geological Survey (USGS) stations. The closest USGS station to Lake Lynn is located at Mt. Chateau, which is approximately 10 miles south of the mine. Mine wide monitoring is typically done using a local monitoring system owned by the mine itself. In the case of the seismic monitoring system used in this study, mine wide monitoring was the method used where geophones were located inside the Lake Lynn Experimental Mine. Each of these applications have minimum system characteristics such as frequency of the source that can be obtained, sampling rate of the analog to digital converter and event rate that can be recorded by the system.

## **2.9 Evaluation of seismic data**

The efficient collection and accurate interpretation of seismic data is important to the application the seismic data is being used for. Recorded seismic signals always contain noise, whether generated by the system or from natural occurrences. Seismic data recorded in normal mining environments are always contaminated by noise (Šílený 1997). The nature and source parameters of seismic traces can be interpreted incorrectly if the noise is not observed. However, noise in the mining environment typically has characteristic frequencies which can be observed easily. The Lake Lynn Experimental Mine is inactive in terms of mining production, so no

mining background noise will affect the signatures when compared to an active, producing mine. Various maintenance activities occur at the mine, typically in the form of sledge hammers pounding against the floor or rib, which can be easily detected when reviewing the daily signatures.

## 2.10 Components of a seismic monitoring system

### 2.10.1 Seismic transducers

A seismic transducer transforms ground motion, represented by displacement, velocity or acceleration, into a voltage. Figure 2.8 shows a basic diagram of a seismometer setup to monitor vertical ground motion, recreated from Havskov (2006). The diagram represents a mass suspended from a spring, with the mass being dampened by a dash pot in order to prevent excessive vertical motion near the natural frequency of the seismometer.

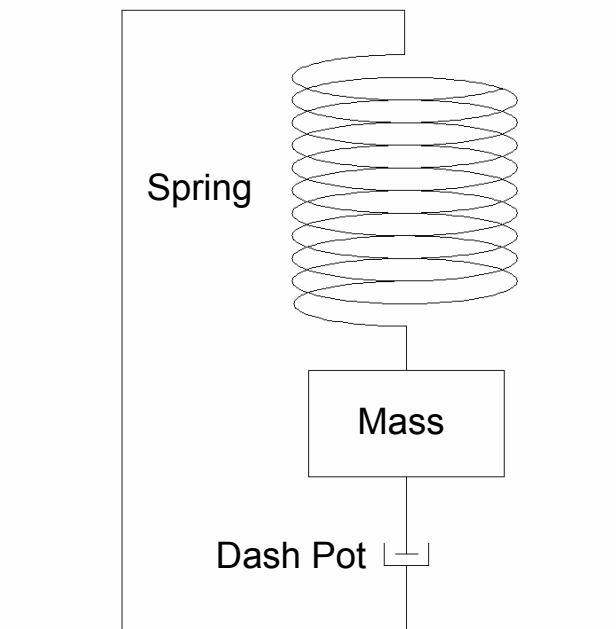


**Figure 2.8** – Simple diagram of a seismometer to monitor vertical ground motion (adapted from Havskov 2006).



The natural frequency of a seismometer is defined in Equation 2.10. If the frequency of the ground motion is similar to the natural frequency of the system, a larger relative motion will be recorded. Frequencies below the natural frequency of the system will result in a smaller relative motion recorded. The amplitude of how much larger and smaller the relative motions are will be dependent on the damping.

$$f_{natural} = \frac{1}{2\pi} \sqrt{k/m} \quad (2.10)$$

where:  $f_{natural}$  = natural frequency of seismometer,  
 $k$  = spring constant, and  
 $m$  = mass.

Sensors measuring different kinematic variables can make the same seismic signature appear different. This phenomenon is exemplified in Figure 2.9. The amplitude frequency response of a mechanical 4.5 Hz seismometer and 4.5 Hz velocity transducer is plotted. The specific instrument's response to displacement, velocity and acceleration are shown in each column from left to right, respectively. The x-axis represents frequency in Hz and both axes are plotted on a log scale. A damping factor of 0.7 was assumed for the example. The curves plotted were based on the expression for the displacement amplitude response,  $A_d(\omega)$ , shown in Equation 2.11 (Havskov 2006). Equation 2.11 can also be viewed as the relationship between the relative displacement of the instrument to the ground displacement.

$$A_d(\omega) = \frac{\omega^2}{\sqrt{(\omega_o^2 - \omega^2)^2 + 4h^2 \omega^2 \omega_o^2}} \quad (2.11)$$

where:  $\omega$  =  $2\pi f$  (frequency in Hz),  
 $\omega_o$  =  $2\pi f_{natural}$ , and  
 $h$  = damping factor.

Figure 2.9 shows that an instrument's response to a specific kinematic variable has two segments, with a change in response occurring at the instrument's natural frequency. Computing the relative displacement to ground displacement, velocity or acceleration can be related by adding or subtracting one unit of slope. This relationship can also correspond to a multiplication or division of frequency  $\omega$ , adjusted in Equation 2.11. An instrument used in the project measures the ground response in a different way. These seismometers measure a force proportional to acceleration necessary to keeping an internal mass stationary, however the force is then converted to velocity internally within the instrument.

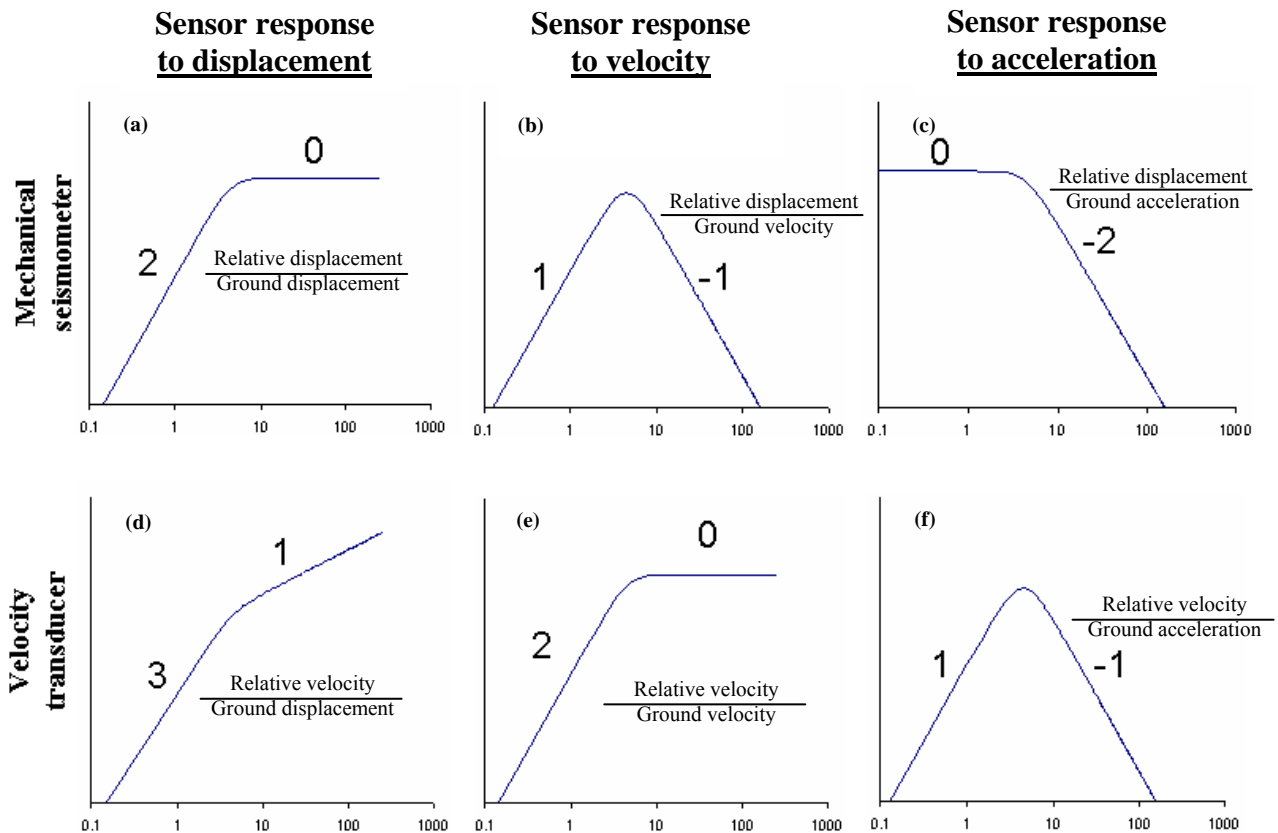


**Figure 2.9–** Amplitude frequency response of mechanical and velocity transducers to kinematic variables. The asymptotic slope of each curve segment is highlighted and changes at each instruments natural frequency. The ratios of relative to actual measurements are also shown beside each curve.

### 2.10.2 Analog to digital conversion

Analog signals collected by a geophone represent a continuous signature of ground motion. This signature must be converted to a series of representative numbers at discrete intervals before processing can occur. In order to do the conversion, the analog signal is continuously sampled at a constant time interval. This conversion is conducted by an analog to digital (A/D) converter (also referred to as a digitizer). The Nyquist criterion requires that the sampling frequency be at least twice the frequency of interest or information about the signal will be lost. For example, if signals up to 100 Hz are being monitored, the sampling frequency must be set at 200 samples per second or higher to obey the Nyquist criterion.

If the signal contains energy at frequencies greater than the Nyquist frequency, aliasing will occur. In order to illustrate the implications of aliasing in the time domain, consider the case of a single tone sine wave sampled as shown in Figure 2.10. In this example the sampling frequency, represented by  $f_s$ , is only slightly more than the analog input frequency  $f_a$ . In this situation, the Nyquist criterion has been violated. The pattern of the actual samples produces an aliased sine wave at a lower frequency equal to  $f_s - f_a$ . Therefore, by not using the appropriate sampling rate, the aliased signal recorded by the A/D converter is not representative of the analog input signal (Analog Devices 1994).

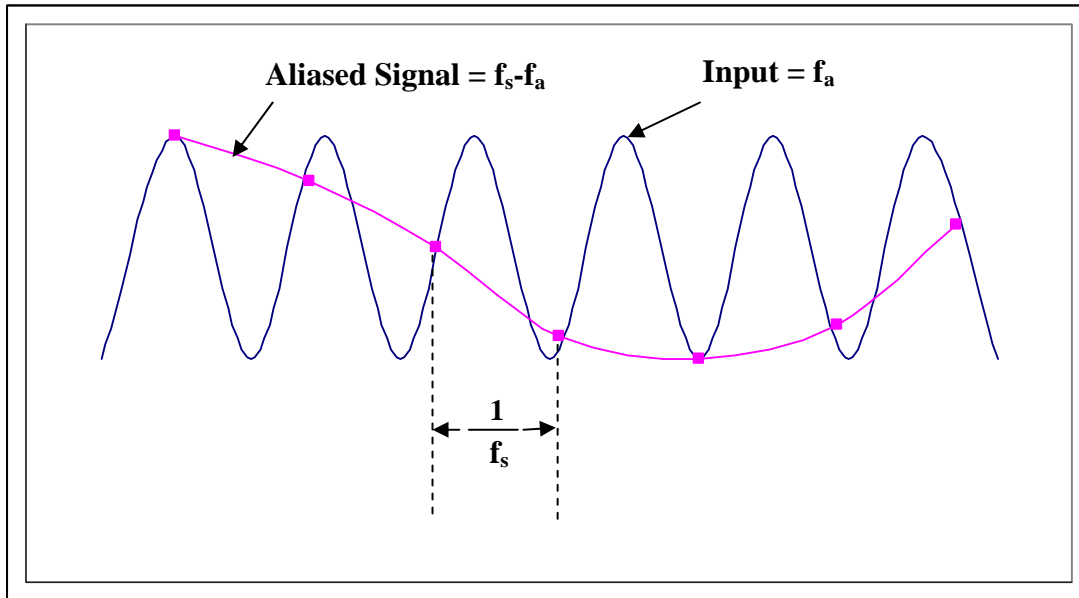


**Figure 2.10** – Example of an aliased signal which violates the Nyquist criterion (adapted from Analog Devices 1994).

The signal should be converted to digital form as close to the geophone as possible. By converting close to the analog source, the signal does not decay as it travels through the communication cables between the geophone and A/D converter. Once the signal is digitized, it can be sent to a computer for seismological processing, which includes visualization and interpretation of the seismic data, as discussed previously. Other key parameters of the A/D converter are the number of analog input channels and resolution of the data. The number of analog input channels will determine the number of sensors that can be used to acquire data per device. The number of bits in the A/D converter will determine the resolution. The number of digital codes for an A/D converter is described from the relation  $2^n$  where  $n$  is the number of bits. For example, if a measurement has a range of 250 psi and a precision to the nearest psi was required, an 8-bit A/D converter would be sufficient. An 8-bit A/D converter allows for 256 digital codes which is adequate for the requirement in the example given.

## **2.11 Review of past seismic studies on underground explosions**

In order to understand the signatures recorded at the Lake Lynn Experimental Mine, it is important to look at seismic research on underground explosions that has been conducted in the past. Seismic data collected from a methane explosion in an underground environment are scarce. However, a large amount of research has been published on other types of underground explosions such as quarry blasts or nuclear explosions. Literature on these findings is summarized in the following sections. First, the generation and description of body and surface waves for an explosive source is described. Factors which effect the generation of these waves include anisotropy, microfractures within the rock mass and confinement.

Next, the frequency content of underground explosions is studied. Two studies were summarized which provide information for body and surface wave frequency content. The frequency content was found to be dependent on factors such as distance from the source and stiffness of the rock. Next, moment magnitude and radiated seismic energy values were researched from past seismic recordings. By looking at previous data published for underground explosions, the estimates found at the Lake Lynn Experimental Mine could be compared and validated.

### ***2.11.1 Description of body and surface waves for an explosive source***

Studies in the past have shown that explosive sources produce a significant amount of shear energy if they are in anisotropic mediums. Because of a particular preferred orientation of the microstructure and bedding and cleavage planes, rocks behave in an anisotropic manner. Mandal and Toksoz (1991) conducted a study to show that placing an explosive source in an anisotropic medium produces an azimuthally dependent radiation pattern for P-, S- and Rayleigh

waves. The authors reviewed previous literature with explosion sources in anisotropic mediums and discovered that if the explosive source was contained in an anisotropic full space, it can generate a significant amount of shear wave energy where none would be generated in an isotropic medium. Also, the reflection at the free surface and conversion of seismic waves propagating throughout the medium was found to complicate the seismograms and their frequency dependence.

Studies on the reasons why S-waves are generated in anisotropic rock and not isotropic rock have been investigated. Kondrat'yev et al. (1984) conducted a study where the objective was to describe seismic waves caused by confined underground explosions in terms of a source model of the expanding center type. The confined underground explosions varied in size and were recorded at distances of 5.5 to 90 km. The explosions were detonated in strong rock beds described as being an area of complex geology. The authors reviewed two concepts explaining the generation of S-waves in underground explosions. The first is as the P-wave waves generated by the explosion propagate through the medium it changes to S-waves at non-uniformities. The other concept is that there is asymmetry in the explosion itself which causes P- and S-waves to both be created initially. The analysis showed better agreement with the hypothesis that the P-waves are converted to S-waves as they travel through the non-uniform medium.

Perret (1968) also studied how S-waves are generated from a nuclear explosion inside of a salt cavity. The study also shows an example of how much of the initial explosive energy is transferred into the rock. The recording instruments were placed within the salt cavity at ranges between 166 and 660 m. Shear waves were found to be the strongest in records of vertical motion at stations on the same elevation as the explosion. For horizontal seismograms at the

same elevation as the explosion, no shear waves could be identified. Above and below this elevation, shear waves were detectable in seismograms from both vertical and horizontal radial components, however they only accounted for 9 - 17% of the total seismic energy. The initial peak pressure loading on the roof and floor were considerably different, and this dissimilarity and diverse physical characteristics of the roof and floor were attributed to the low amplitude shear waves. Only about 0.02% of the total released energy by the explosion was propagated as seismic source energy.

The shape of the underground structure in which the explosion takes place has also been found to have an influence on the seismic waves. Gibson et al. (1996) studied the influence of cavity shape on the seismic radiation from an explosion source in isotropic (symmetric in all directions) and transversely isotropic (symmetric about an axis) media in the far-field. Two models using the indirect boundary-element method were involved in this study. The first model was an explosive point source, meaning a pressure field arrives instantaneously at each point on the cavity wall. In this model, the amplitude of the wave field was found to decay with increasing distance from the source. Both strong compressional and shear waves are generated and propagate into the far-field, with the compressional wave amplitude depending on direction of propagation. The second source model assumes that the explosion will instantaneously and uniformly pressurize the source cavity. The model was said to be a more realistic description of the explosion process. With this model, the explosion source location is not relevant. In this model, the shear wave was found to be largest for long, tunnel like cavities or short dislike cavities. The explosions conducted at the Lake Lynn Experimental Mine were in an area very similar to the description of a long, tunnel like cavity.

Another study, showing that S-waves are generated during a decoupled explosion, investigated shear waves generated by small-scale explosions in symmetric and asymmetric cavities in rock (Ahrens and Liu 1996). Since the experiments were conducted in a laboratory which produces wave profiles at higher frequencies, conventional seismic recording systems could not be used. The experiment used strain gauges to measure the incident compressional and shear wave amplitudes on the free surface of the rock along two perpendicular directions at one point. Two experiments were conducted during the study, which modeled a decoupled and tamped (coupled) explosion, on a limestone sample. The study found that the waves generated in the decoupled experiment generated higher frequencies. The efficiency of SV-wave generation from a tamped explosion was higher, due to a large plastic deformation near the cavity and development of a tensional fracture.

A final study was found that showed a similar scenario to the explosions conducted at the Lake Lynn Experimental Mine, where a disturbance happens in the atmosphere (in the case of LLEM, an explosion the middle of the entry decoupled with the limestone) and recording instruments on the free surface record the seismic waves. Thayer (1964) presented a thesis studying the ground motion caused by air explosions, sonic booms and thunder. The main finding in the study was that a pressure disturbance in the atmosphere, such as an explosion above the surface of the ground, can cause surface waves by an energy transfer across the air-ground interface. The explosions were conducted at a Navy test area and were shot on the ground or as high as ten feet above. The characteristics of the ground motions led the author to conclude that the type of wave was an air-coupled Rayleigh wave. The confirmation of the Rayleigh wave was conducted by finding the wave velocity and proving the wave had a retrograde particle motion. The particle motion was found to be retrograde by using a



hodograph, which is a point-by-point plot of the vector sums of the radial and vertical velocity components. Using the results from the air explosion data, the authors made predictions about what should be expected from a sonic boom or thunder. For a sonic boom (caused by jets breaking the sound barrier), they predicted a sharp air pulse should be expected and the waveform should contain three parts which include pre-sound ground motion, the direct wave and post-sound ground motion. For thunder, the predominant frequency should decrease with distance. Although the sonic booms did not occur near the ground, they were found to produce ground motion which suggested they were air-coupled Rayleigh waves. The thunder records showed a decrease in frequency with the low-frequency component, which was predicted and suggested that the motions recorded were air-couple Rayleigh waves. Johnston (1987) was cited earlier as saying air-coupled surface waves were generated with a pressure wave traveling at the speed of sound in air. The study was conducting using a similar source as a pressure disturbance in the air. A missile silo explosion was recorded by a seismic network, and the conclusions also stated that no traces of P- or S-waves were detected. The lack of P- and S-waves was attributed to most of the energy from the blast being channeled directly into the atmosphere.

### *2.11.2 Frequency content of body and surface waves for explosive sources*

The frequency content of seismic waves can help indicate the source or the type of seismic wave being recorded. Sharpe (1941) used a recording system to observe the elastic wave motion from an exploding charge ranging at distances from 15 to 300 ft. The study found that when a shot is fired in a hard rock, the motions near the source are of higher frequency when compared to when the shot is fired in a softer material. The study also suggested that the ground motion produced from the detonation of a charge is not a simple pulse. The motions were described as a long train of sinusoidal waves, which increases in both period and number of

cycles as the distance from the source increases. Based upon the reported results, it appears he was observing frequency dispersion as discussed in Section 2.5 about the characteristics of surface waves.

The frequency content of seismic waves has also been known to be dependent on the distance away from the source. Adushkin et al. (1990) described a monitoring method based on the observed dependence of maximum displacements in the Rayleigh surface wave on explosive strength and on distance to the epicenter during underground nuclear explosions. Surface waves were determined to be better suited for study because the displacement amplitude in the near seismic zone (defined as distances up to 300 km away from the epicenter) is greater compared to body waves. Also, the non-uniformities in the medium have a lesser degree of influence on surface waves because their periods exceeds the period of a body wave by several times. The frequency of the oscillations in the Rayleigh wave was found to be solely dependent on the distance from the epicenter and not based upon the power of the explosion or rock characteristics at the hypocenter of the source. Stump et al. (2001) found a similar conclusion when studying seismicity from mining explosions, ranging from surface coal cast blasting to hard rock fragmentation, for characterization of seismic and infrasound signals. The study did not find a relation between total explosive yield and peak amplitude from the seismograms. Also, a small percentage of the mining explosions were found to have infrasound signals, which can be attributed to the event size and propagation path effects.

### *2.11.3 Moment magnitude and radiated seismic energy studies from an explosive source*

Studies have been conducted in the past which have calculated moment magnitudes and radiated seismic energies of explosive sources using similar methods to this study. These values reported in the past will help for comparison with what is calculated from the experiments at the

Lake Lynn Experimental Mine. Iannacchione et al. (2005a) studied the seismic properties of blasts from nearby quarries. The blasts analyzed had explosive weights ranging from 658 – 26,053 kg. The moment magnitudes of these events ranged from 1.1 – 2.6 and radiated seismic energies ranged from  $3.1 \times 10^3$  to  $1.9 \times 10^6$  Joules. The estimates for moment magnitude and radiated seismic energy were based upon the P-wave portion of the seismic signature. Dewey (1998) conducted a study that applies earthquake detection and location methodologies to monitor mine explosions from both surface and underground operations. The explosions are both located and assigned magnitudes. During the study, 453 acknowledged explosions had a magnitude greater than or equal to 2. Most of the explosions stemmed from the central Appalachians of West Virginia and in the Rocky Mountain West from Wyoming southward. The located explosions and maps of their locations are located on the United States Geological Survey website under a catalogue called Routine Mining Seismicity in the United States. An example of data reported on the website is shown in Figure 2.11, which is a map of routine mining seismicity for the conterminous United States between May 1997 and March 2000. Mining-related seismic events are highlighted by red x's while earthquake-related events are highlighted by purple dots.

The amount of seismic energy transferred into the rock is also an important consideration to consider when studying the explosions at the Lake Lynn Experimental Mine. Hooper et al. (2006) studied the effects of confinement of chemical shots on surface wave data. Unconfined explosions were found to generate up to eight times less seismic energy than the equivalent confined explosions. This difference in energy and frequency content of the unconfined explosions caused an order of magnitude difference when compared to the confined

explosions. The amplitudes of the unconfined explosions were found to be two to four times smaller than the explosions that were fully confined.

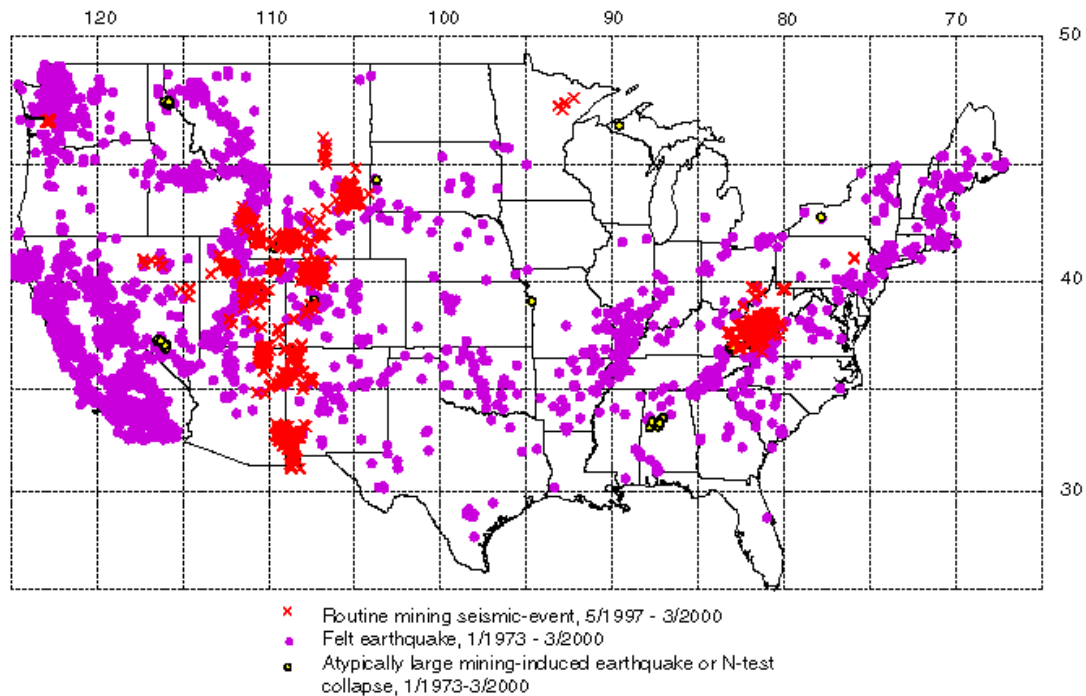


**Figure 2.11**– Map of routine mining seismicity for the conterminous United States between May 1997 and March 2000 (Dewey 1998).

#### 2.11.4 Mine seal response to methane and dust explosions

The experiments at the Lake Lynn Experimental Mine included mine seals, or structures representative of a seal, in the crosscuts. A previous study was found which studied the frequency response of mine seals in crosscuts during a methane and dust explosion. In the late 1990's, NIOSH, Tecrete Industries Pty. Ltd. and BHP Australia Coal cooperated in a research study to evaluate the strength characteristics and air leakage results of varying seal and stopping designs (Weiss et al., 1999). During some tests, seals were instrumented with accelerometers and the data was used to develop numerical models for future seal design. The seals that were

instrumented with accelerometers were located at crosscuts 1 – 4 between C- and B-Drifts at the Lake Lynn Experimental Mine. A detailed mine map and description of LLEM is shown in Section 3.1. The gas and dust explosions were ignited near the face of C-Drift. Since the report was focused more on how the seal designs survived or failed based upon the air leakage results, discussion on data from the accelerometers was very limited in the report conclusions. However, for mine shot #348 the report was able to make some conclusions based upon the data. The main conclusion from the data was that the stiffer seals (the seals that were thicker and/or had a smaller cross-sectional area) in general showed higher natural frequencies as indicated by the peaks in the Fourier transforms. The cross-sectional area was defined as the area of the face of the mine seal.

The full datasets obtained from LLEM personnel included records from mine shots #347, 348, 349, 350 and 351. Mine shot reports obtained for all the tests showed that for shots #350 and 351, all instrumentation was removed from behind the mine seal which included the accelerometers. Acceleration data from shot #349 was not available in the information that was obtained from the mine, although it was collected during the test. Therefore, the only tests which data were made available was for shots #347 and 348. The Fourier transforms from shots #347 and 348, from which the natural frequency of each seal can be determined, are shown in Figures 2.12 – 2.15. Table 2.2 provides the seal dimensions and natural frequencies as determined from the accelerometer data. The results from the Fourier transformations indicate that in general a stiffer seal (stiffness being indicated by a larger thickness and/or smaller cross-sectional area) produces a higher natural frequency. The hypothesis that was made from the initial test was proven by the same result from shot #347. The only anomalies in the dataset are very low frequencies observed for mine shot #348, as shown in Figure 2.15. It should be noted that during

shot #348, the mine seal in crosscut 4 was completely destroyed. This could be an explanation that the frequency spectrum for shot #348 does not match up as well with shot #347 because the accelerometer was probably damaged in the process.

**Table 2.2** – Seal size and associated natural frequencies obtained from LLEM Mine Shots #347 and 348.

Seal Name	Crosscut Size				Total Product Used (kg)	Natural Frequency (Hz)
	Thickness (m)	Width (m)	Height (m)	Area (m <sup>2</sup> )		
Plug seal 1	1.200	5.43	1.95	10.6	11,543	320-370
Meshblock seal 2	0.325	5.76	2.26	13.0	9,366	90-115
Meshblock seal 3	0.325	5.82	2.74	16.0	11,045	50-80
Meshblock seal 4	0.175	5.97	2.26	13.5	5,307	<20, 45-60

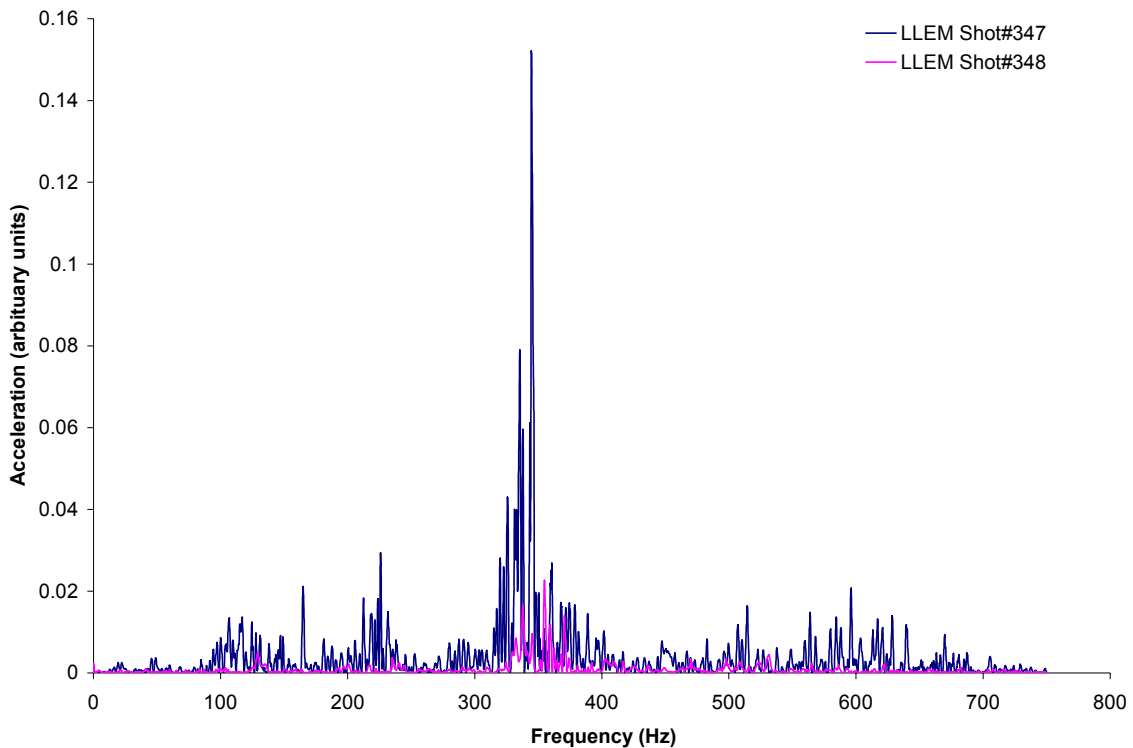


**Figure 2.12** – Fourier transform from the plug seal located in crosscut 1 during mine shots #347 and 348. The seal had a thickness of 1.2 m and total cross-sectional area of 10.6 m<sup>2</sup>. The peak frequencies occur at 320-370 Hz.

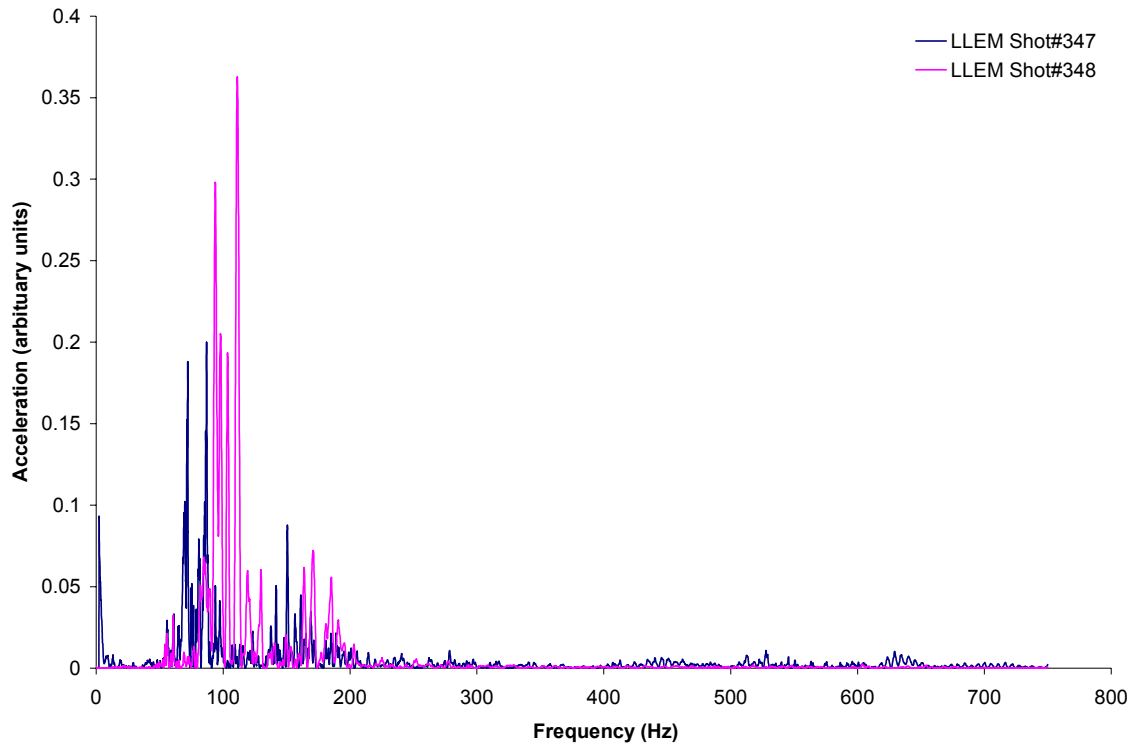


**Figure 2.13** – Fourier transform from the meshblock seal located in crosscut 2 during mine shots #347 and 348. The seal had a thickness of 0.325 m and total cross-sectional area of 13.0 m<sup>2</sup>. The peak frequencies occur at 90-115 Hz.

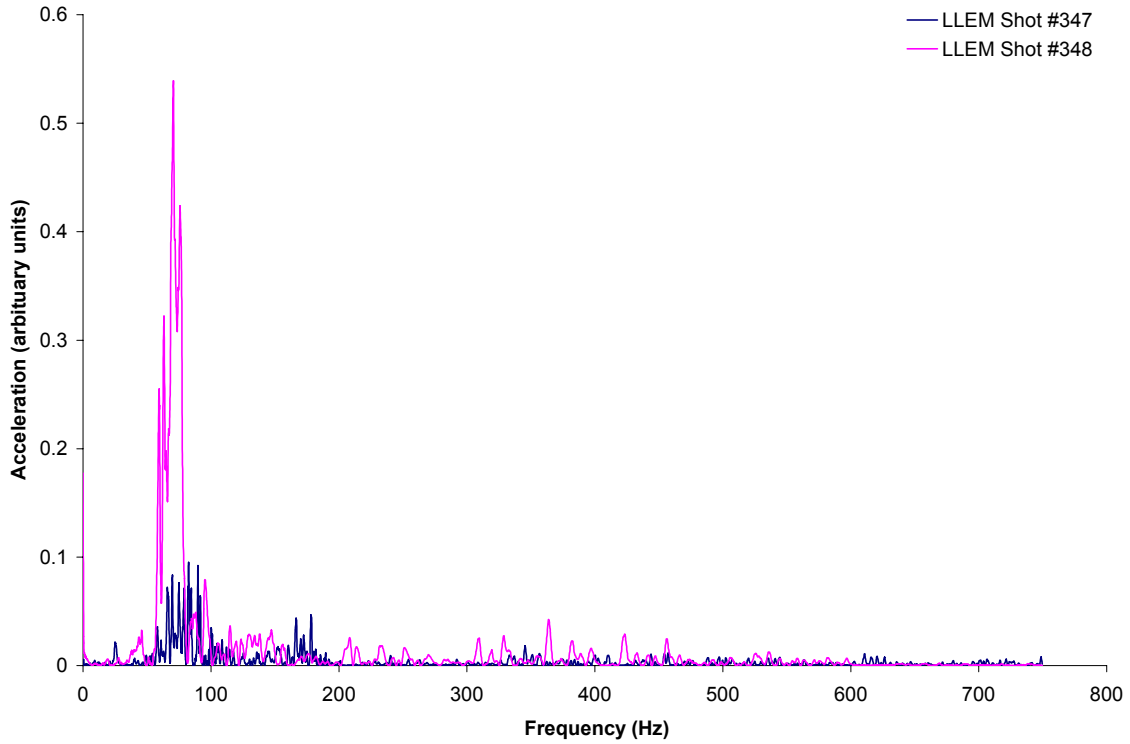


**Figure 2.14** – Fourier transform from the meshblock seal located in crosscut 3 during mine shots #347 and 348. The seal had a thickness of 0.325 m and total cross-sectional area of 16.0 m<sup>2</sup>. The peak frequencies occur at 50-80 Hz.

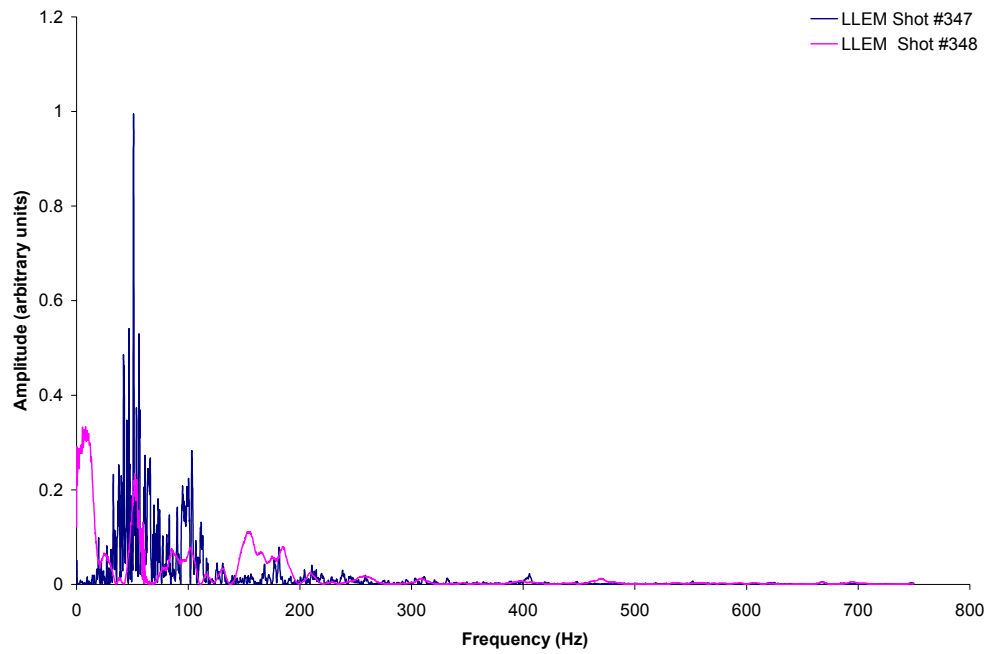


**Figure 2.15** – Fourier transform from the meshblock seal located in crosscut 4 during mine shots #347 and 348. The seal had a thickness of 0.175 m and total cross-sectional area of 13.5 m<sup>2</sup>. The seal failed during shot #348. The peak frequencies occur at 20 Hz and 45-60 Hz.



# Chapter 3 – Experimental Procedures

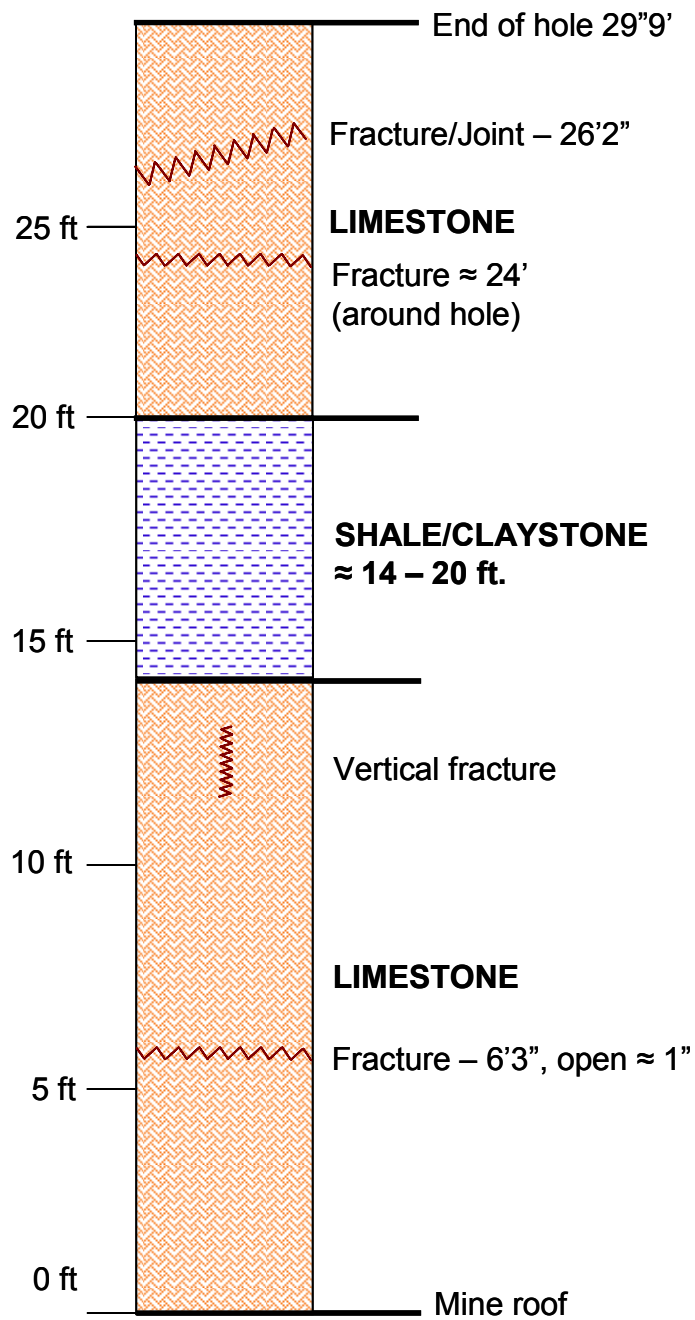
## 3.1 Lake Lynn Experimental Mine location and dimensions

The Lake Lynn Experimental Mine (LLEM) was the site chosen for the experiments conducted in the study. The Lake Lynn Experimental Mine is a full-scale, underground mining research facility on the site of a former limestone quarry. The facility is located approximately 96 km (60 miles) southeast of Pittsburgh, PA and 16 km (10 miles) northeast of Morgantown, WV, as indicated in Figure 3.1. Geologically, the mine is located in the Greenbrier limestone formation (Triebisch and Sapko 1990). A borehole drilled into the roof approximately 30 ft high in the old workings of the mine give indication to the different formations at the test site. The data from the borehole were obtained from the NIOSH engineers who conducted the borehole logs. The borehole logs analyzed in the old workings were confirmed by the NIOSH engineers to be approximately the same in the drift area where the explosions are ignited and most of the measurements were taken. From the surface of the roof to 14 ft above the mine is a fine-grained limestone. A shale/claystone formation located at 14 – 20 ft is present. Located at 20 – 29.75 ft, which is at the end of the observation hole, is a fine-grained limestone. A diagram of the results from the vertical borehole geology is reported in Figure 3.2.

Surface quarry and underground mining operations were conducted at the site in the 1950s and 1960s. The National Institute of Occupational Safety and Health's Pittsburgh Research Laboratory (NIOSH-PRL), formerly the U.S. Bureau of Mines, transformed the site to facilitate mining health and safety research studies by creating a simulated longwall layout adjacent to the old workings of the mine. Research conducted at the site has included large-scale studies on mine fires, explosions, performance of roof support products and seal design.

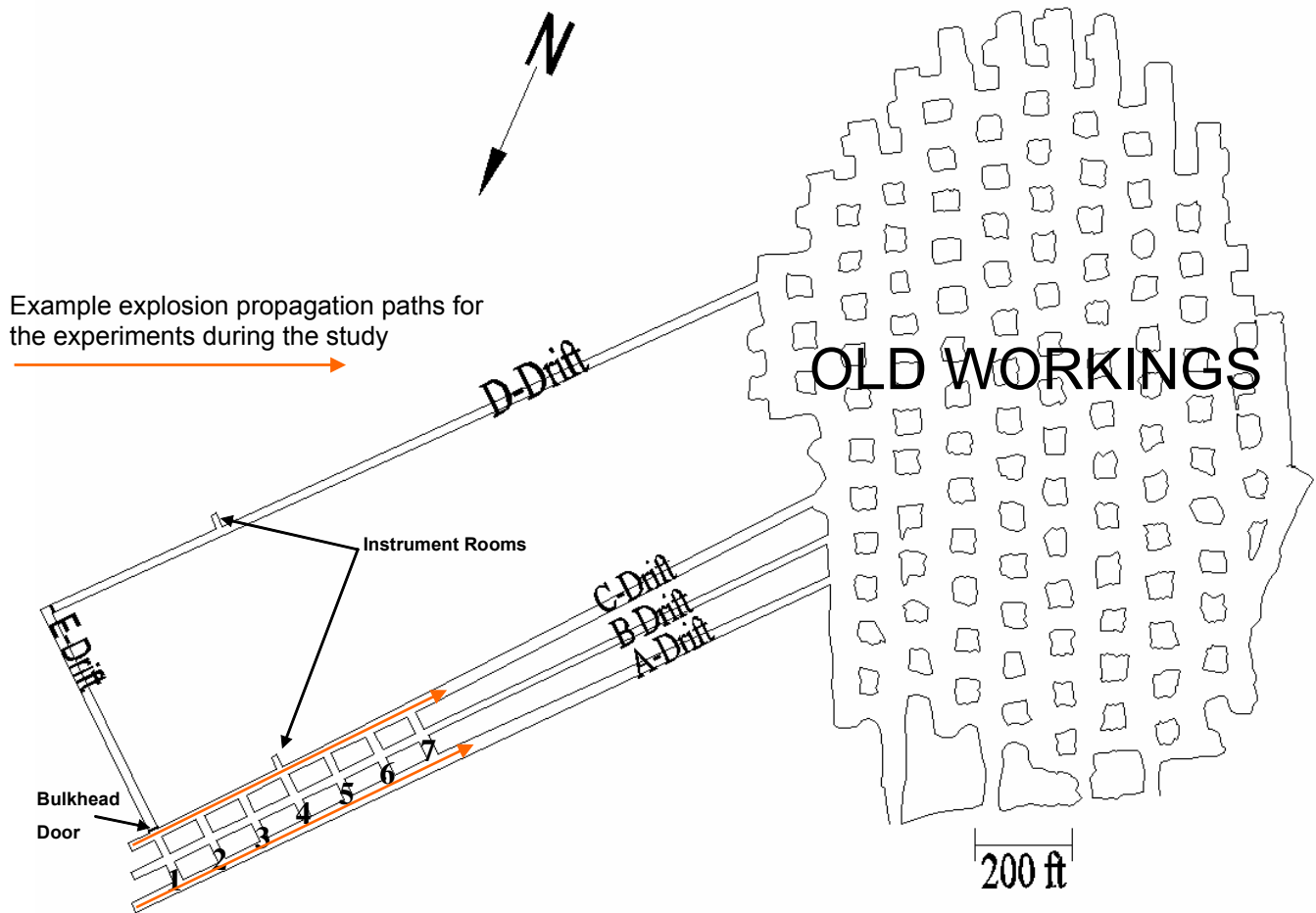


Figure 3.1 – Location of Lake Lynn Experimental Mine.



**Figure 3.2** – Vertical borehole geology of the old workings at the Lake Lynn Experimental Mine. The layers detected in the old workings were considered to be consistent with the geology of the drift area.

The mine layout is shown in Figure 3.3. The west side of the facility, known as the old workings, was mined when limestone was produced commercially from the site. This area of the research facility resembles a layout typical of an underground hard rock mine. The dimensions of entries in the old workings are 15.2 m (50 ft) wide by 9.1 m (30 ft) high. The east side of the facility contains mine drifts which were dimensioned to match configurations found in coal mines. The dimensions of these entries are 6.1 m (20 ft) wide by 2.0 m (6.5 ft) high. The size of the pillars in the simulated longwall gate roads is 24 x 12 m (80 x 40 ft). A-, B-, C- and D-Drifts are approximately 480 – 495 m (1,575 – 1,630 ft) long. E-Drift, which connects the longwall gate roads at the inby end, is 155 m (510 ft) long.



**Figure 3.3** – Lake Lynn Experimental Mine map. The crosscut numbering scheme, location of instrument rooms and bulkhead door, and explosion paths are indicated in the figure.

### 3.2 Features inside of the mine

A bulkhead door indicated on the mine map, Figure 3.3, at the intersection of E-Drift and C-Drift, and is shown in Figure 3.4 as partially opened across E-Drift. This 70-ton door, constructed in place with steel framework and reinforced concrete, was closed during explosion experiments. Instrumentation can be placed within E-Drift without being damaged from the explosion when the door is closed. The requirement of having the bulkhead door closed during experiments, allowed geophones to be placed within 10 m (33 ft) of the explosion source. This is the closest that the instrument could get to the source.

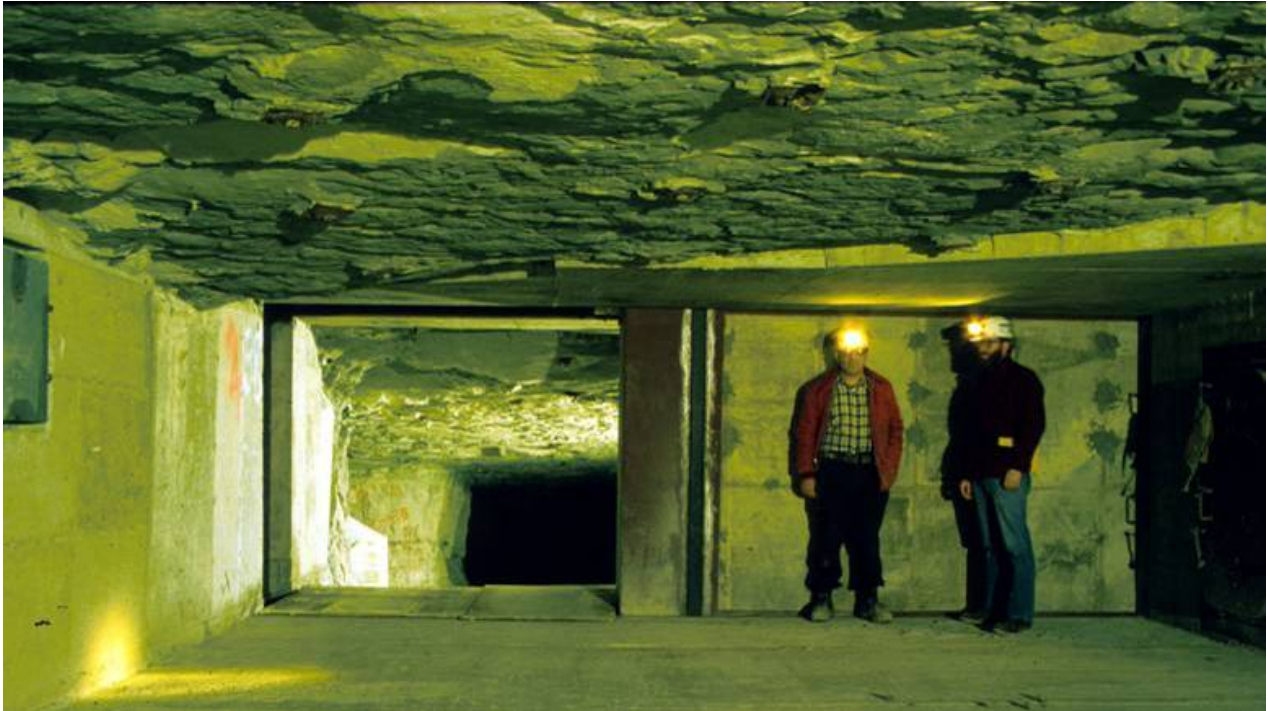


**Figure 3.4** – View of the bulkhead door partially closed in E-Drift.\*

Instrument rooms in the mine are located approximately three quarters of the way down C- and D-drifts. These rooms are protected from the entry via submarine-type doors. An instrument room viewed from the mine entry is shown in Figure 3.5. The instrument rooms provide a pre-wired network which allows instruments to communicate with equipment outside of the mine. The pre-wired network contains panels which have wire pairs that correspond to each other inside and outside of the mine. This is advantageous to the project because communication cable lengths of up to thousands of feet do not have to be strung and connected to the central computer outside of the mine since it is already in place. The panels inside and outside of the mine are shown in Figure 3.6.

---

\* Figure 3.4 was provided by Eric Weiss of the National Institute for Occupational Safety and Health, Pittsburgh Research Laboratory, Disaster Prevention and Response Branch.



**Figure 3.5** – View of the instrument room from C-Drift.\*



**Figure 3.6** – View of the panels inside (left) and outside (right) of the mine which contain corresponding wire terminals.

---

\* Figures 3.5 and 3.6 were provided by Eric Weiss of the National Institute for Occupational Safety and Health, Pittsburgh Research Laboratory, Disaster Prevention and Response Branch.



Located throughout the mine are stations referred to as data gathering (DG) stations and one is shown in Figure 3.7. Like the panels located inside of the instrumentation rooms, these stations allow instruments to be connected to the outside from many locations within the mine. The importance of the DG panel locations is the analog signal sent by the geophones can be digitized close by. Ideally, the signal should be digitized at the geophone location, as stated in Section 2.10.2, but often times that is unrealistic. Due to the accommodation of the stations throughout the mine, all geophones were located within a reasonable distance away from the digitizer for proper transmission of the analog signal.



**Figure 3.7** – Data gathering station located in one of the mine drifts.\*

---

\* Figure 3.7 was provided by Eric Weiss of the National Institute for Occupational Safety and Health, Pittsburgh Research Laboratory, Disaster Prevention and Response Branch.



### **3.3 Instrumentation used during the study**

#### *3.3.1 Seismic transducers*

For the study, geophones were chosen as the seismic transducer to record seismic waves emanating from the methane and gas explosions. Geophones are devices that convert ground motion to an electrical signal. An internal magnet surrounded by a coil produces an electrical signal output proportional to ground motion. Inside a mine, geophones are distributed around or throughout a volume of interest. In the case of the current study, the geophone locations surrounded the area of the gas and dust explosions at the Lake Lynn Experimental Mine. The geophones used in the study are model L-28 geophones manufactured by Sercel (formerly Mark Products). The geophones are triaxial and have a natural frequency of 4.5 Hz.

The geophone response curves provided by the manufacturer are shown in Figure 3.8. The response curve is the voltage response to ground velocity and the asymptotic slopes for each segment matches that shown from Figure 2.9(e). As mentioned previously, the damping factor effects the response of the geophone at its natural frequency. The effect of damping is illustrated by the response curve in Figure 3.8. If a damping factor much smaller than 1 is assumed, an exaggerated response at the geophones natural frequency of 4.5 Hz will occur. The flattest and most suitable frequency response is when a damping factor of 0.7 is assumed. For the calculations on data in the experiment, a damping factor of 0.7 was used, as highlighted by a darker line over Curve D in Figure 3.8. It should also be noted that the output provided by the manufacturer only includes responses up to 90 Hz. Although, the manufacturer doesn't provide responses for frequencies over 90 Hz, for this study it is assumed the response is constant but spurious responses could occur.

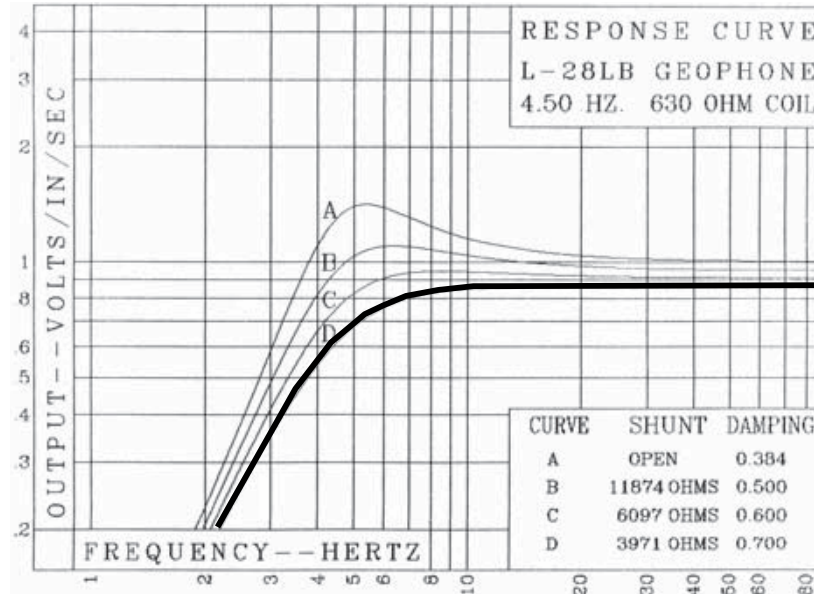
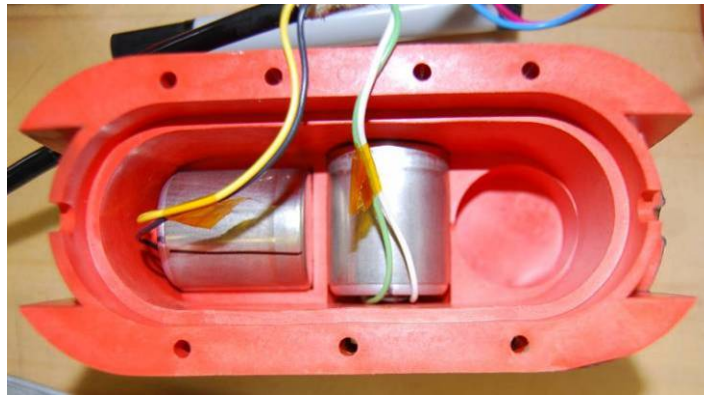


Figure 3.8 – Response curve of the Sercel L-28LB geophone (Sercel 2005).

Figure 3.9 shows a photograph of the L-28 geophones inside of a TDC II casing being installed on the mine roof inside of the Lake Lynn Experimental Mine. The three geophones are seated inside a casing in such a way that three different orientations provide the longitudinal, transverse and vertical directions, as shown in Figure 3.10. Figure 3.11 shows a photograph of the TDC II casing, provided by Sercel (formerly Mark Products). Wire pairs come out of the orange casing which relate to a geophone of a particular orientation. A level bubble is also provided on the casing to ensure proper alignment of the geophone on the rock surface.



**Figure 3.9** – Photograph of the geophone used in the study. In the photograph, the geophone is being installed at the test site.



**Figure 3.10** – Photograph demonstrating how the two horizontal components are seated inside of the TDC II casing.

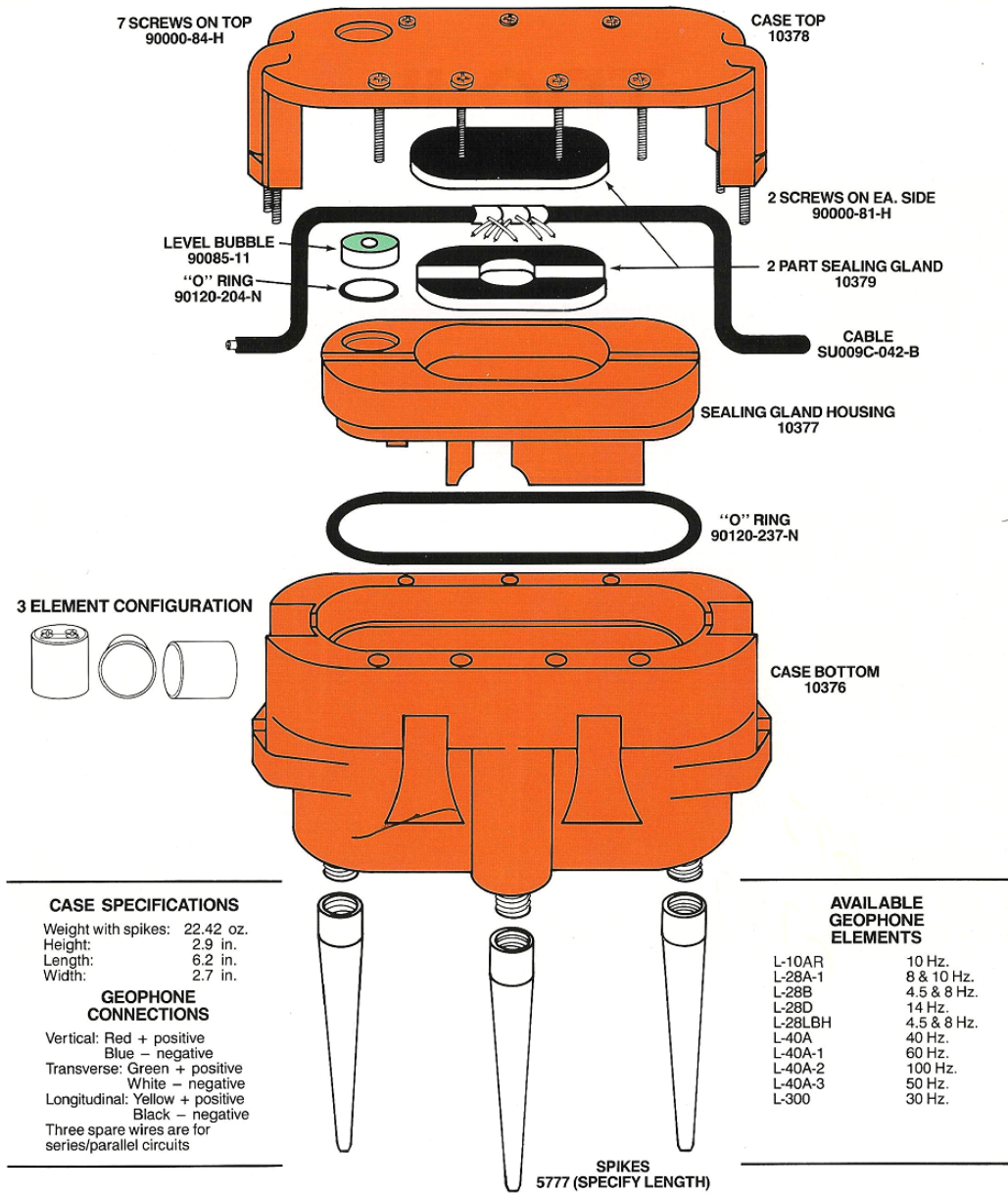
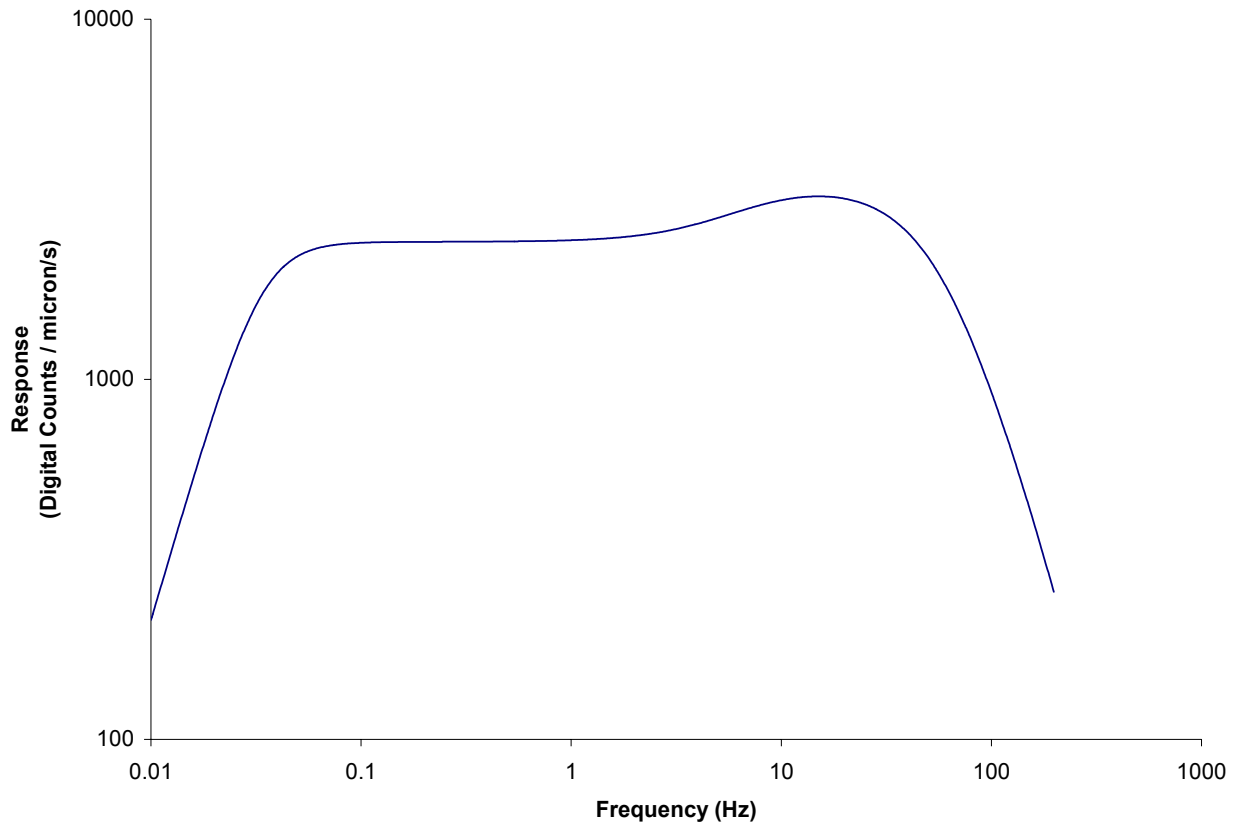


Figure 3.11 – Schematic of the TDC II casing (Sercel 2008).

Surface measurements were taken near the end of the study using Guralp CMG-6TD ultra-lightweight three-component digital output seismometer. The instrument was installed inside of a dug-out hole on the surface above the A-Drift ignition chamber. The instrument was set to sample at 500 samples per second and was oriented in the same manner as the geophones

installed inside of the mine. The response curve to velocity for the Guralp CMG-6TD, which was used to calculate the radiated seismic energy, is plotted in Figure 3.12.



**Figure 3.12** – Response to velocity for the Guralp CMG-6TD instrument installed on the surface above the mine.

### 3.3.2 Seismic monitoring system

An out-of-date seismic monitoring system, manufactured by ISS International Limited, used by NIOSH from another project, was refurbished and updated with new hardware and software. The system was installed within the existing structure of the Lake Lynn Experimental Mine. The A/D converters used in the study are called Microseismic (MS) boxes and Quake Seismometer (QS) boxes by the manufacturer. Both types of A/D converters have a sampling rate of 2,000 samples per second and contain six channels for input. The MS boxes have a 22-bit resolution (14-bit A/D with 8-bit gain) and the QS boxes have a 24-bit resolution.

Throughout the project, the seismic system utilized four MS boxes and four QS boxes. Licensing agreements allowed up to 30 channels to be connected to the system at one time. A maximum of 10 triaxial or 30 uniaxial geophones, or a combination of both, could be used at one time.

From the A/D converters, communication cable connects to a modem rack allowing the digitized signal to arrive at the processing computer. The modem rack provides up to sixteen A/D converters online with the system via DB-9 connector ports. Line drivers between the A/D converter and modem rack help send the RS232 communication signal. A serial hub takes the sixteen ports from the modem rack and converts them into a single 100/10 LAN cable connected to the data acquisition computer.

The seismic monitoring system is a trigger-based system, in contrast to a real-time continuous monitoring system. This system only records and saves data based upon two or more geophones being triggered by an event. For normal operation, a significant amount of ground movement, exceeding preset threshold values, must occur and be detected by at least two geophones for the event to be recorded. This setup ensures that the data being sent back from a single geophone is not electrical noise or another form of unwanted data. The number of triggering geophones and sensitivity values can be set by the user. For the tests at LLEM, the threshold values were set to the most sensitive that the system allows and the number of triggering geophones was set to two. The mine environment is very quiet before an explosion and the time of the event is known, so making the system very sensitive is beneficial in obtaining valuable data.

### *3.3.3 Calibration of the seismic monitoring system*

Before important variables such as the seismically-recorded moment magnitude and radiated seismic energy can be calculated for an event captured by the seismic monitoring system, the number of digital counts for a one volt input signal as a function of frequency needed to be determined. Once the number of digital counts for a one volt signal, defined as the digitizer constant  $C$ , the total system response to ground displacement and velocity can be defined.

The first attempt to determine the digitizer constant was made during the week of May 7<sup>th</sup> – 11<sup>th</sup>, 2007. The seismic monitoring system was installed at the Virginia Tech Seismological Observatory (VTSO) located in Blacksburg, Virginia. The objective was to record an event by both the ISS system and VTSO recording stations and compare the responses to determine the needed variable. The initial calibration attempt included only a QS box and a triaxial geophone. The triaxial geophone was set on a pier inside of the observatory, which was oriented in a North-South direction. Once the system was functioning, it was left to monitor until the next day. During this time period it was expected that blasts from nearby quarries would trigger both systems. Two blasts from local quarries were triggered by the VTSO recording station. These events did not trigger ISS seismic system, although the sensitivity settings of the system were set to the most sensitive setting that the system allows. It was hypothesized that these events did not trigger the ISS system because they were too small in amplitude and did not exceed the background noise. Since the ISS system is trigger-based as described in Section 3.3.2, a continuous stream of data could not be analyzed in an attempt to find the blast through filtering.

As a result, the plan was to produce an event close by the observatory so that both systems could be triggered. To produce this event, a hammer tap on the pier where the

geophones were placed was used to create seismic waves. Hammer taps on the pier were in the North-South, East-West and vertical orientations. The seismic activity caused both systems to trigger and capture the events. However, the instruments at the VTSO do not record frequencies above 50 Hz. Hammer taps on the pier generated high-frequency activity, but not much low-frequency content. In order to determine the constant  $C$ , a both low and high frequencies must be analyzed. Therefore, the second attempt to determine the response of the ISS system was unsuccessful because a full range of frequency content could not be compared between both systems.

After unsuccessful attempts to determine the total system response from seismic events, a more direct, “calibration-type” approach was employed using a waveform generator to create a sinusoidal wave of a specific frequency at a specific voltage. Therefore, if the peak-to-peak amplitude of a 2-V signal was generated, the number of counts per volt would be the maximum amplitude recorded for each period in the waveform. The response to each calibration frequency, between 50 –1,000 Hz at 50 Hz intervals, was digitized by both the MS and QS boxes and plotted. The results are shown in Figure 3.12. Sine waves input to the digitizer by the signal generator were checked by an oscilloscope to maintain a constant 2-V signal and by a multimeter for validation of the frequency value. The calibration points of each specific frequency are represented by dots on Figure 3.13.



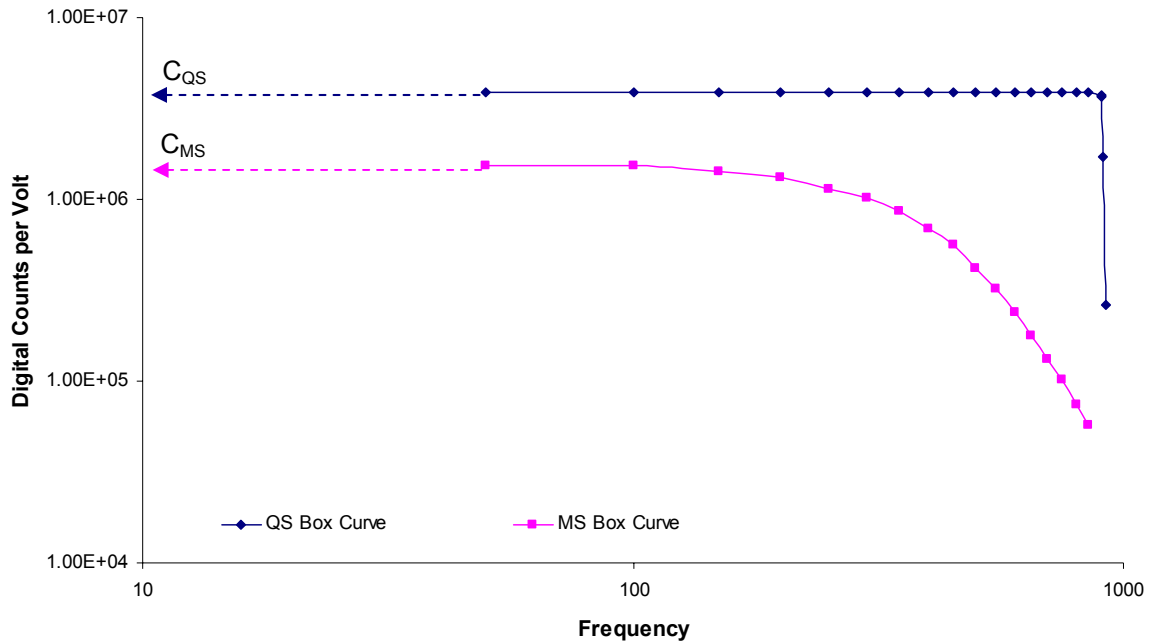


Figure 3.13 – Calibration results for both MS and QS boxes.

From the calibration results, the digitizer constant,  $C$ , is indicated in Figure 3.13 for each digitizer. The digitizer constant is the where the constant response (flat part of each curve) intersects the y-axis. The values of the digitizer constant are  $1.54e10^6$  counts/volt for the MS box and  $3.85e10^6$  counts/volt for the QS box. The responses of the anti-aliasing filters for each digitizer are also observed in Figure 3.12. The QS box has a constant response at both low and high frequencies. The sudden change in high-frequency response of the curve is due to the anti-aliasing filter near the Nyquist frequency of 1,000 Hz. This response was to be expected since the A/D converter samples at 2,000 samples per second, as described in Section 2.10.2.

The results for the MS box show a constant response at low frequencies up to approximately 100 Hz. The loss in amplitude at higher frequencies is due to an anti-aliasing low-pass filter built into the MS box. The amplitude response at higher frequencies can be modeled based upon the calibration response. The amplitude response of the low-pass filter,  $G(\omega)$ , was derived and is shown in Equation 3.1. The corner frequency of the filter was found to

be around 250 Hz. The resulting filter response is plotted in Figure 3.14. Based upon Equation 3.1, the response is constant up to approximately 100 Hz with a response value constant at 1. After this, the response changes as a result of the anti-aliasing filter inside the MS box.

$$G(\omega) = \frac{1}{1 + \left(\frac{\omega}{\omega_c}\right)^3} \quad (3.1)$$

where:  $\omega = 2\pi f$ ,  $f$  = frequency in Hz, and  
 $\omega_c = 2\pi f_{corner}$ ,  $f_{corner}$  = frequency in Hz.

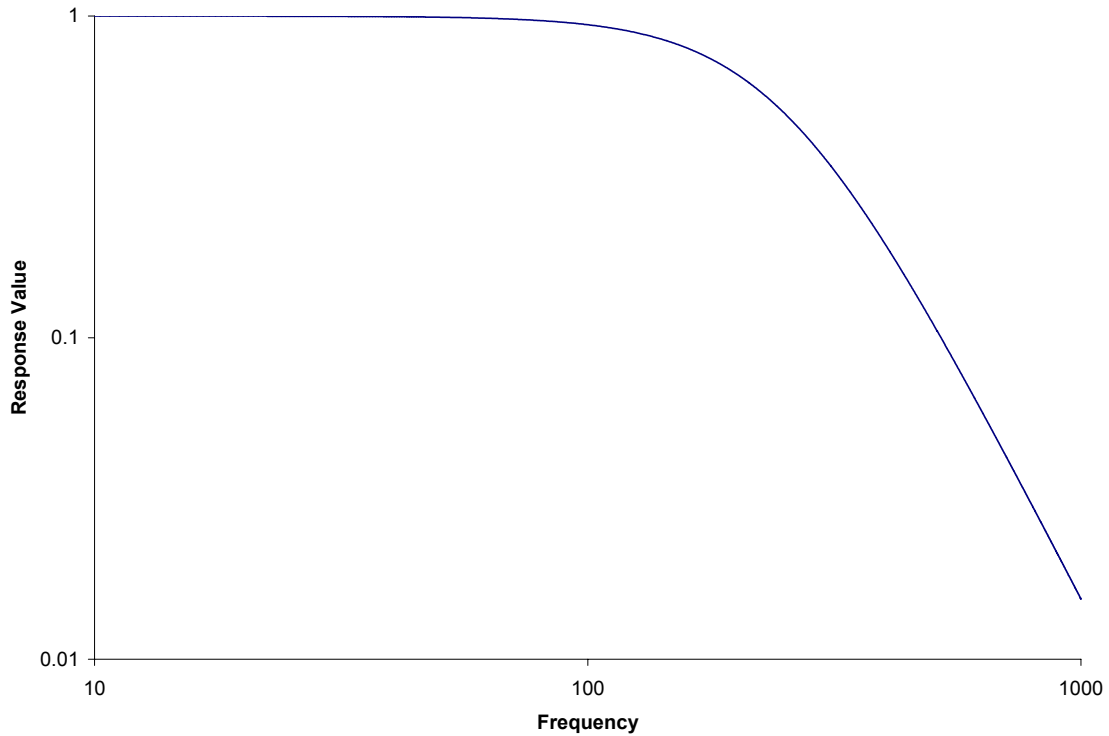


**Figure 3.14** – Filter response,  $G(\omega)$ , for MS box.

Now that the number of digital counts for a one volt signal has been identified for each digitizer, the full system amplitude response can be derived based upon the calibration results

and specification sheets of the geophones provided by the manufacturer. The system amplitude response to ground displacement and velocity are needed for moment magnitude and radiated seismic energy calculations. The instrument response of the geophone was derived using a single degree of freedom damped spring-mass system model (Aki and Richards 2002) and the Sercel geophone product sheet (Sercel 2005). The full system amplitude response, which incorporates corrections for both the geophone and A/D converter, to ground displacement,  $d(\omega)$ , is defined and shown in Equation 3.2. The response is in units of digital counts per meter. The plot of the response is shown in Figure 3.15.

$$d(\omega) = \left( \frac{EC\omega^3 \left( \frac{R_s}{R_t} \right)}{\sqrt{(\omega_o^2 - \omega^2)^2 + (2h\omega_o\omega)^2}} \right) G(\omega) \quad (3.2)$$

- where:  $E$  = geophone electrodynamic constant (volts/m/s),  
 $C$  = digitizer constant, determined from sinusoidal input test (digital counts/volt),  
 $\omega$  =  $2\pi f$  (frequency in Hz),  
 $R_s$  = shunt resistance for a given damping (ohms),  
 $R_t$  = total circuit damping (ohms),  
 $\omega_o$  =  $2\pi f_{natural}$  (natural frequency in Hz), and  
 $h$  = geophone damping.

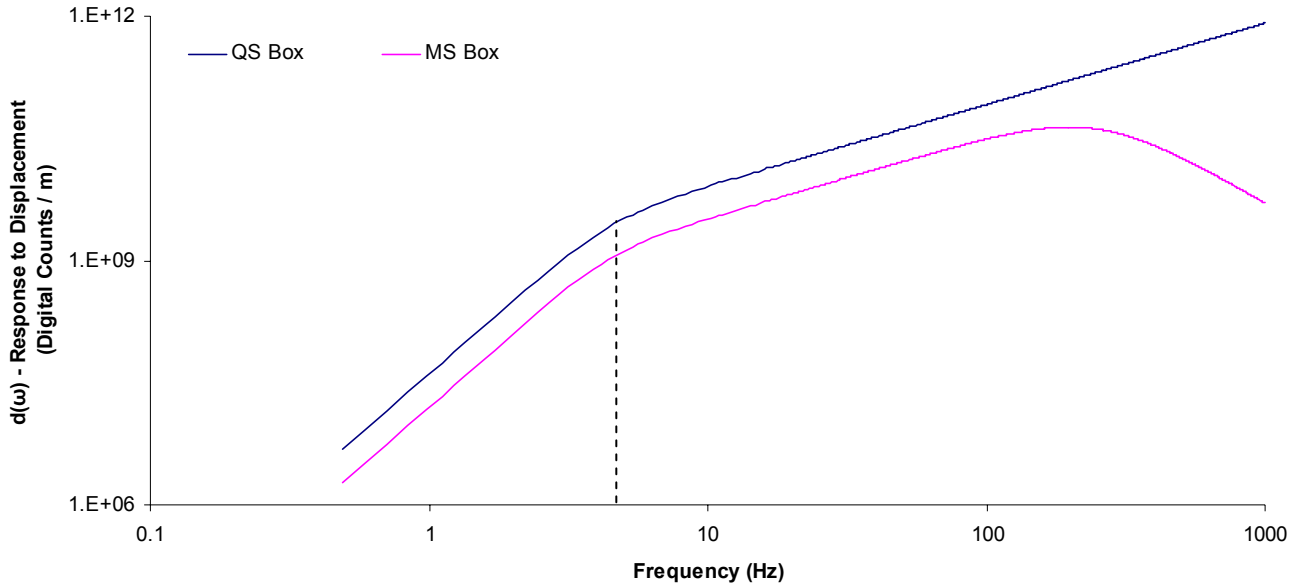


**Figure 3.15** – Complete system amplitude response to ground displacement,  $d(\omega)$ . The natural frequency of the geophone is highlighted by the dotted line at 4.5 Hz.

The log-log plot in figure above shows that above the geophone natural frequency of 4.5 Hz, the slope of the response line is equal to one. Below the natural frequency of the geophone, the slope is equal to three. This response behavior is expected for an amplitude response to ground displacement using a velocity transducer, using the example given in Figure 2.9(d). At frequencies above 100 Hz for the MS box, the response changes because of the anti-aliasing low pass filter. This response behavior is expected and similar to what was reported during the calibration tests.

The system amplitude response to ground velocity,  $v(\omega)$ , is defined in Equation 3.3 and plotted in Figure 3.16. Equation 3.3 is adjusted slightly from Equation 3.2, with the difference being a division by frequency to turn  $\omega^3$  into  $\omega^2$  in the numerator, as described in Section 2.10.1. The asymptotic slope below the natural frequency has a value of two and a value of zero after, agreeing with what was described in Figure 2.9(e). For the MS box, the response changes near 100 Hz due to the anti-aliasing filter.

$$v(\omega) = \left( \frac{EC\omega^2 \left( \frac{R_s}{R_t} \right)}{\sqrt{(\omega_o^2 - \omega^2)^2 + (2h\omega_o\omega)^2}} \right) G(\omega) \quad (3.3)$$

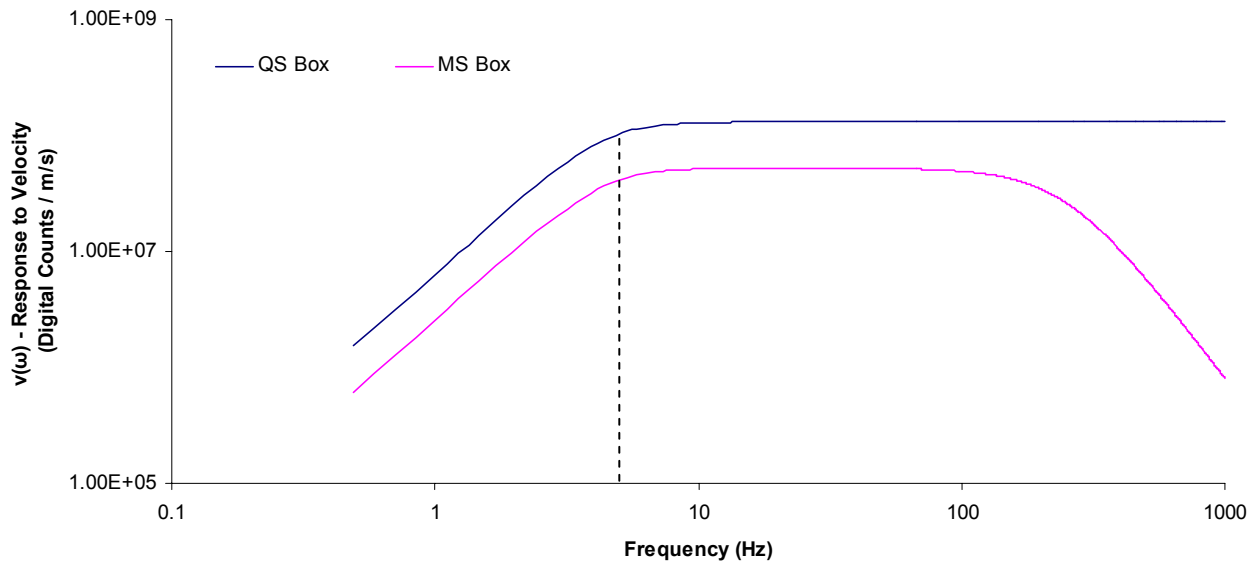


**Figure 3.16** – Complete system amplitude response to ground velocity,  $V(\omega)$ . The natural frequency of the geophone is highlighted by the dotted line at 4.5 Hz.

The geophone cables used during the calibration process were not the specific cables used in the mining environment during the study. However, both cables used during the calibration and in the mine were the same type. The length of geophone cable used in the mine was well under the limits the manufacturer’s recommendation, so it is assumed that the responses to displacement and velocity would be the same if the cables from the mine were used.

### **3.4 Data collection at the Lake Lynn Experimental Mine**

#### *3.4.1 – Geophone locations*

The methane and dust explosions conducted at the Lake Lynn Experimental Mine were ignited at the inby end of A- or C-drift. The chosen locations of the geophones attempted to “surround” the explosion at various distances. The locations of both uniaxial and triaxial geophones are indicated on the mine map in Figure 3.17. Also shown in the figure is location of rock drop tests, which is later described in Section 3.4.4. Over the time interval of the experiment, nine triaxial and three uniaxial geophones were utilized. Geophone 7 is not listed on the mine map because it is a “dummy” geophone used for testing purposes. For each test monitored at LLEM, not all geophones were present. The geophone placement was proactive as the study progressed. Additional geophones were added to the existing array in specific locations as a response to new findings in the data.

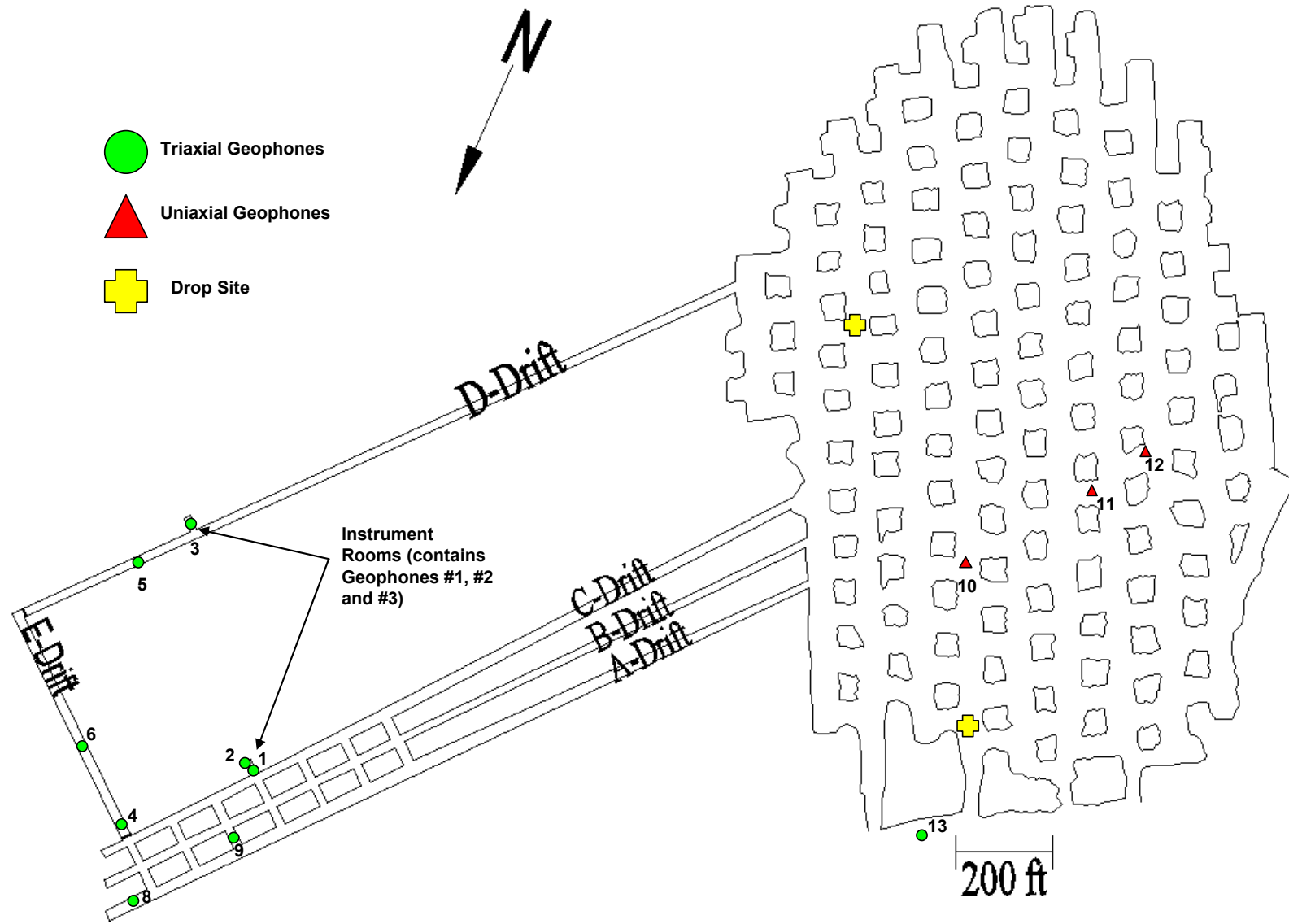
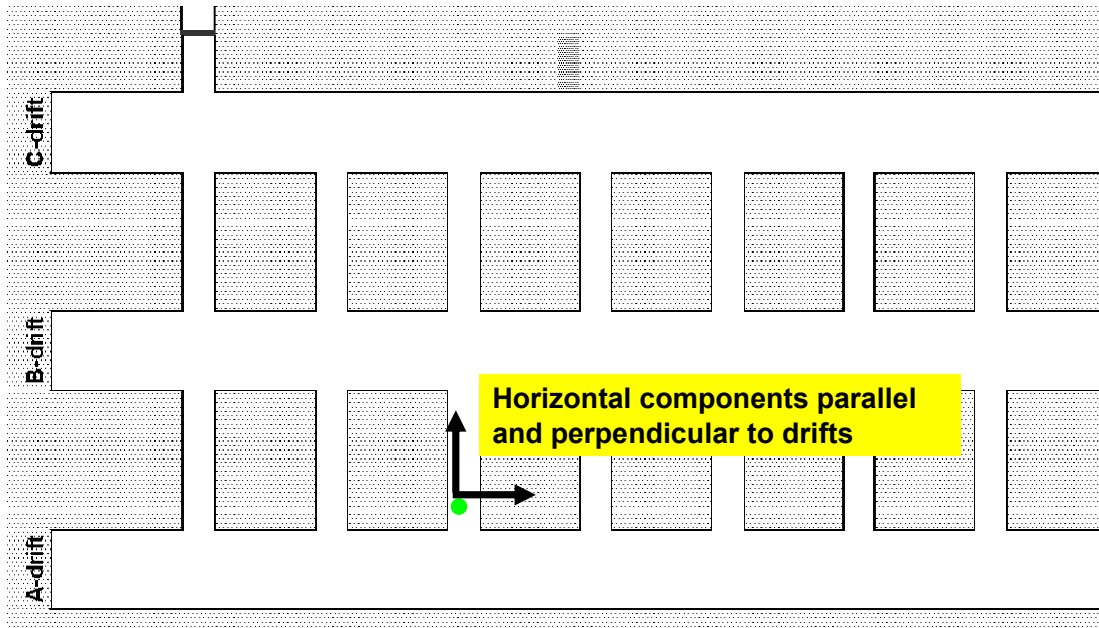


Figure 3.17 – Geophone and rock drop test site location map.



**Figure 3.18** – Horizontal geophone orientations inside of Lake Lynn Experiment Mine. One horizontal component was oriented parallel to the drift and the other horizontal component was oriented perpendicular to the drift.

Figure 3.18 shows the way the horizontal components inside of the triaxial geophone were oriented. The component labeled as East-West was oriented parallel to the mine drifts (Channel 1) and the component labeled North-South was oriented perpendicular to the mine drifts and parallel to the crosscuts between pillars (Channel 2). Channel 3 of the triaxial geophones was the vertical component. Table 3.1 is a summary of when the geophones were installed. Geophones 1, 2, 3 and 4 were installed initially to test the system. Geophones 5, 6, 8 and 9 were installed to monitor tests containing seals in C-Drift. The objective of these locations was to surround the explosion. Geophones 8 and 9 had to be removed in December 2007 due to explosions being conducted in A-Drift. Geophones 10, 11 and 12 were installed in the old workings of the mine as an attempt to monitor the sinkhole. Geophone 13 was installed outside of the mine to collect data far away from the source.



**Table 3.1** – Summary of installation dates for geophones.

<b>Geophone Number</b>	<b>Installation Date</b>
1	Aug-06
2	Aug-06
3	Aug-06
4	Aug-06
5	Oct-06
6	Oct-06
8	Oct-06
9	Oct-06
10	Feb-07
11	Feb-07
12	Feb-07
13	Feb-08

### *3.4.2 – Methane and dust explosions as a seismic source\**

The explosions conducted at the Lake Lynn Experimental Mine can be located in A-, B-, C- or D-Drifts. A typical explosion consists of natural gas ( $\approx 98\%$  methane) injected into an ignition chamber at the face of the drift. Figure 3.19 is a photograph of one of the ignition chambers at LLEM. A plastic diaphragm is draped across the entry to contain the methane in the ignition chamber. A photograph of a partially closed plastic diaphragm is shown in Figure 3.20. An electric fan with an explosion-proof motor housing mixes the natural gas with the air to result in an approximate 9.5% methane-air concentration. The flammable natural gas-air volume was ignited using a triple-point ignition source. This ignition source consists of three sets of two 100-J electric matches that are equally spaced at mid-height across the closed end of the drift and ignited at the same time. Five barrels filled with water, located near the outby end of the ignition chamber, act as turbulence generators to achieve a projected pressure pulse. To increase the explosion pressure, either the ignition chamber is lengthened or pulverized coal dust is

---

\* Mine shots #503 – 524 were conducted for purposes other than this study. Mine shots #503 – 507 are referenced in Cashdollar et al. (2007) and Gates et al. (2007). Mine shots #508 and 509 are referenced in Weiss et al. (2008a). Mine shots #510 and 519 are referenced in Weiss et al. (2008b). Mine shots #523 and 524 are referenced in Millero (2008). Mine shots #513, 514, 516 – 18, 520 – 522 are not yet published however the work was completed by Ken Cashdollar, Eric Weiss and Sam Harteis as part of the mine explosion program for NIOSH, Pittsburgh Research Laboratory's Disaster Prevention and Response Branch.

suspended on shelves from the mine roof starting just outside of the ignition chamber. A photograph of explosive coal dust and rock dust being suspended from the mine roof and placed on the floor, as shown in Figure 3.21.



**Figure 3.19** – Ignition chamber located at the end of C-Drift.\*



**Figure 3.20** – Plastic diaphragm used to contain the methane within the ignition chamber.

---

\* Figures 3.19 and 3.20 were provided by Eric Weiss of the National Institute for Occupational Safety and Health, Pittsburgh Research Laboratory, Disaster Prevention and Response Branch.



**Figure 3.21** – Example of the coal and rock dust being suspended from the mine roof and placed on the mine floor.\*

Appendix A provides a comprehensive summary of the experimental designs of the explosions conducted at the Lake Lynn Experimental Mine. The summary of each mine shot includes the date the test was conducted, if there was a seal in the entry and if that seal was destroyed, a mine map of the experimental design, a summary of the seals, structures or stoppings involved and also a table summarizing the pressures that were recorded at those seals, structures or stoppings. Mine shots conducted between August 4, 2006 and April 12, 2007 were in the C-Drift entry. Mine shots conducted between December 11, 2007 and May 21, 2008 were conducted in the A-Drift entry.

---

\* Figure 3.21 was provided by Eric Weiss of the National Institute for Occupational Safety and Health, Pittsburgh Research Laboratory, Disaster Prevention and Response Branch.

### 3.4.3 – Cast boosters as a seismic source\*

Austin Powder 1-lb cast boosters were used as a seismic source in A-Drift at the Lake Lynn Experimental Mine to investigate the response of a ventilation control structure, mainly to see if the predominant frequencies of the structure could be excited and detected. According to the supervisor at LLEM, this structure does not meet the regulatory requirements to be called a mine seal. The structure was constructed from solid concrete blocks with nominal dimensions of 6-in x 8-in x 16-in with compressive strengths of 1,330 to 1,780 psi (9-12 MPa) (based upon full block testing conducted by other researchers at NIOSH). Type-S mortar was used to in all horizontal and vertical block joints and at the block-rib, block-floor, and block-roof interfaces (no wood wedges were used). The main wall of the structure is 16 in thick with a center interlocked pilaster 16-in wide by 24-in deep (as measured from A- to B-Drift). Normally, the pilaster would extend into A-drift but other experiments required the seals be flush with the A-Drift rib line. Steel angles (6-in by 6-in by 0.5-in thick) were anchored to the floor on both sides of the structure and on the B-Drift side ribs (normally the rib angle is also used on the A-drift side) using 1-in diameter by 9-in long anchor bolts (Hilti Kwik Bolt III) on a maximum of 18-in spacings. The structure at crosscut 1 also has the blast-resistant door between the center pilaster and the inby rib, which will stiffen the structure. The structures located between crosscuts 2-5 were essentially the same, minus the blast resistant door. The structures in crosscut 2 and 3 have extra steel angle reinforcement (along the mine roof and vertical angle halfway between the center pilaster and the inby/outby rib) on the B-drift side. The geophone was attached to the seal located at crosscut 1 between the center pilaster and the outby crosscut rib. During these tests, crosscuts 6 and 7 were open. Figure 3.22 shows a picture of the structure located at crosscut 1

---

\*The series of cast booster detonations, mine shots #528 – 540, were conducted exclusively for this study.

from the B-Drift side. The center pilaster, blast resistant door and geophone can be viewed in the figure. The geophone is circled and was located midway between the floor/roof and center pilaster/outby rib.

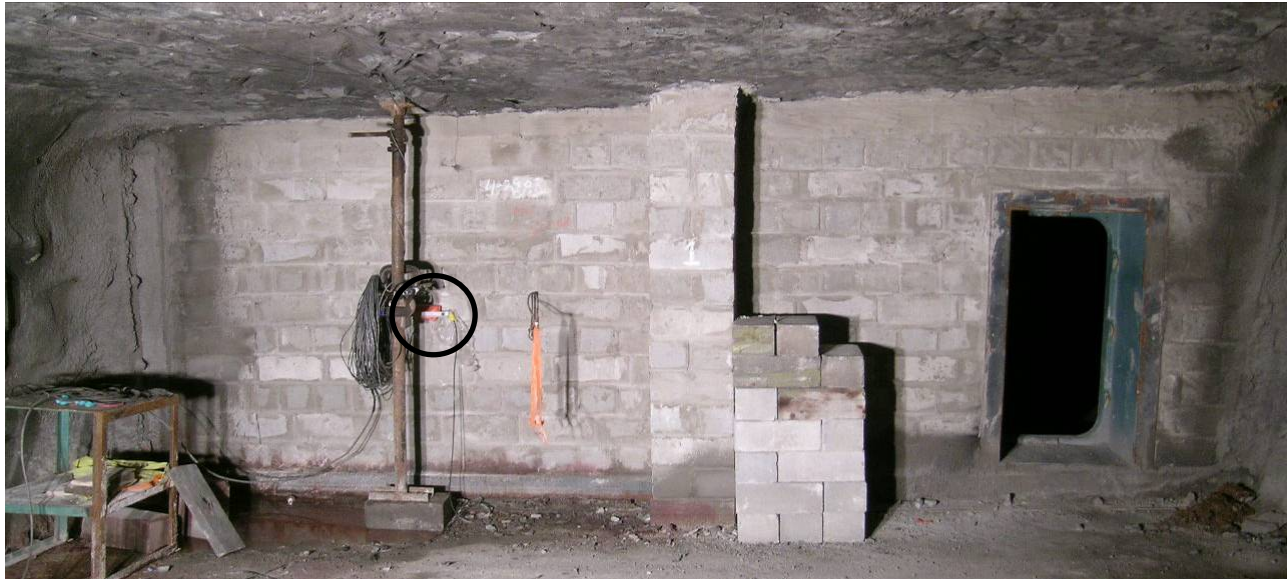


**Figure 3.22** – Photograph of the structure located at crosscut 1 as viewed from B-Drift. The geophone location is circled in the figure. The post in front of the seal and geophone location contained instrumentation used for a different study by the mine staff.<sup>\*</sup>

---

<sup>\*</sup> Figure 3.22 was provided by Eric Weiss of the National Institute for Occupational Safety and Health, Pittsburgh Research Laboratory, Disaster Prevention and Response Branch.

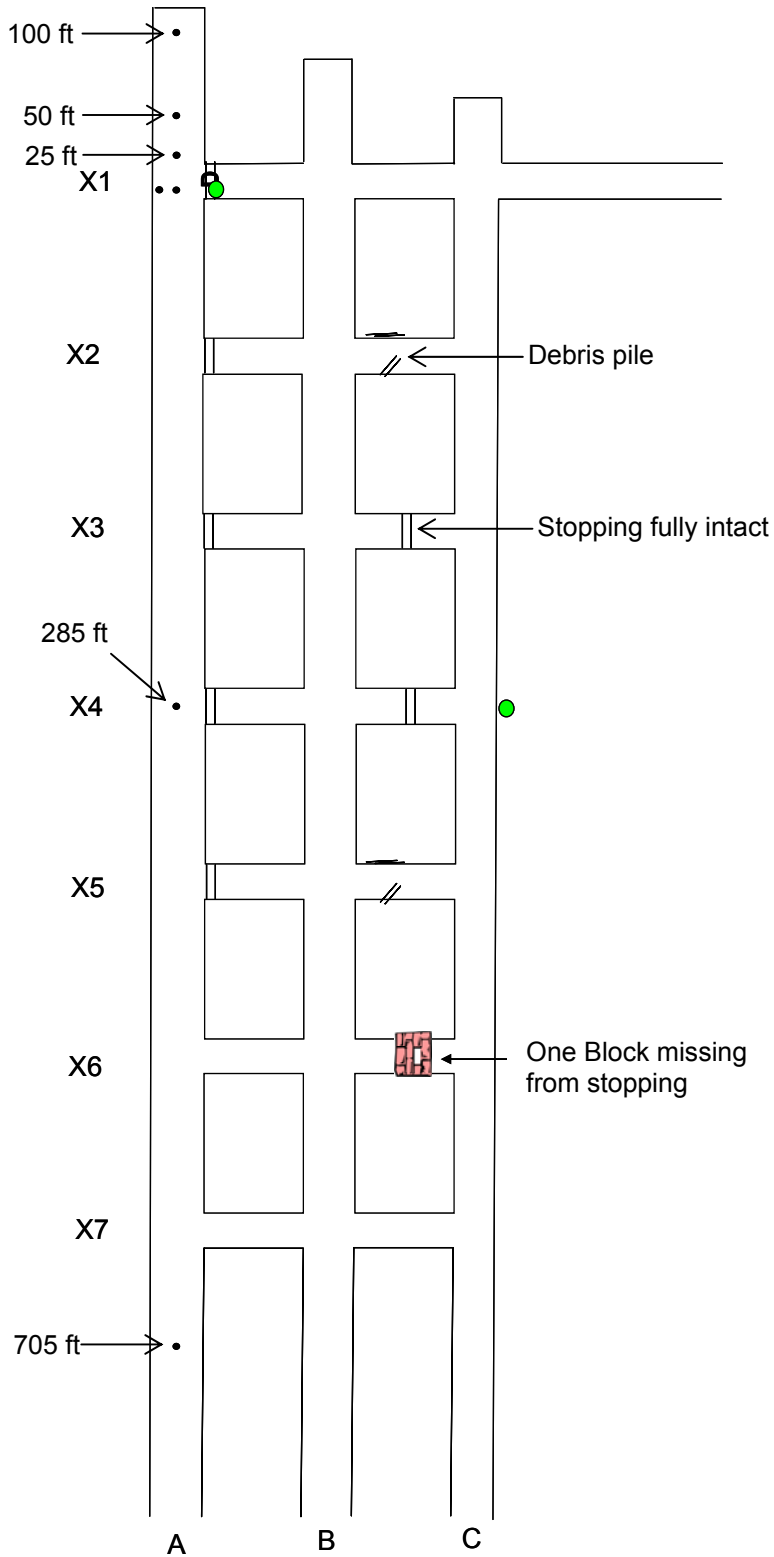


**Figure 3.23** – Map of the experimental design for the booster detonation experiments. The black dots in A-Drift show the booster detonation locations. The structures are shown in crosscuts X1-X5 between A- and B-Drifts. In the crosscuts between B- and C-Drifts are stoppings, some of which are debris piles as indicated by broken lines. The closest geophones during these tests were on the structure in crosscut 1 and the C-Drift instrument room as indicated by the green dots.

Experiments included cast boosters detonated directly in front of the crosscut 1 structure and cast boosters detonated inby and outby the structure to create a “sweeping by” pressure, similar to what would be created during a methane and dust explosion. A mine map of the experimental design is shown in Figure 3.23 and the cast booster locations are represented by black dots. Directly in front of the structure at crosscut 1, tests were conducted at 10 and 20 ft away. Inby the structure at crosscut 1, tests were conducted at 25, 50 and 100 ft away. Outby the structure at crosscut 1, tests were conducted at approximately 285 and 705 ft away. The geophones are shown as green dots and located at the crosscut 1 structure and C-Drift instrument room. Geophones were also located in D- and E-Drifts up to 250 m away, however they can not be shown within the limits of the figure.

#### *3.4.4 – Rock drops tests as a seismic source*

Rock drop tests were conducted inside of the mine to help obtain P- and S-wave velocities necessary for analysis. The locations of the drop sites are indicated by the yellow crosses on the mine map in Figure 3.17. At both sites, the limestone floor was exposed and was free of debris. It should be noted that the limestone floor in the old workings and the limestone roof in the entry area of the mine (where most of the geophones which monitored the methane and dust explosions are located) are different limestone formations. The reason the velocities in the old workings were used for the rock drop tests, is because the floor in the longwall gallery entries area is cement. In order to drop rocks onto limestone to produce significant seismic energy, the old workings had to be used.

Rocks of various sizes were dropped from a height of 3.2 m (10.6 ft). Also dropped during the experiment were a 725-kg (1,600 lb) concrete block and a 1,429-kg (3,150 lb) block of steel. Seven drop tests are included for this study. During the drop tests, only Geophones 10,



11 and 12 close to the drop sites in the old workings registered the events. The results from the seven drop tests are reported in Table 3.2. An earlier study showed that both P- and S-waves are generated during drop tests (Iannacchione et al. 2005a). The P- and S-wave arrival time difference was minimal for each drop and the sampling rate was insufficient to resolve the S-wave arrival. Also, the vertical component sensor is not optimal for observing S-wave arrivals. Therefore, the S-wave was determined from the P-wave arrival time. The S-wave velocity was calculated by dividing the P-wave velocity by  $\sqrt{3}$ , as described in Section 2.6 earlier. The P- and S-wave velocities used for analysis were 4,511 m/s (14,800 ft/sec) and 2,604 m/s (8,545 ft/sec). These values are in the same velocity range as another limestone formation in Pennsylvania (Iannacchione et al. 2005a). The results were taken to represent seismic wave velocities for the entire mine.

**Table 3.2** – Summary of P- and S-wave velocities collected during the rock drop tests.

<b>Test</b>	<b>P-Wave Velocity m/s (ft/s)</b>	<b>S-Wave Velocity m/s (ft/s)</b>
1	3,677 (12,063)	2,123 (6,965)
2	4,760 (15,617)	2,748 (9,016)
3	4,252 (13,950)	2,455 (8,054)
4	4,511 (14,800)	2,604 (8,545)
5	4,111 (13,488)	2,373 (7,787)
6	6,380 (20,932)	3,683 (12,085)
7	4,577 (15,016)	2,643 (8,670)
<b>Mean</b>	4,609 (15,124)	2,661 (8,732)
<b>Standard Deviation</b>	858 (2,814)	495 (1,625)
<b>Median</b>	4,511 (14,800)	2,604 (8,545)

### 3.5 Seismic data analysis procedures

#### 3.5.1 Transforming the data for analysis

When the event is imported into a spreadsheet created during the study for seismic calculations, the waveform data are in units of m/s. The system response corrections setup in



Section 3.3.3 requires the waveform data to be in the raw units of digital counts. Using the sensitivity, coil resistance, shunt resistance, the number of bits of resolution and A/D range found in the settings for the geophone and A/D converter a gain factor can be calculated. By dividing the waveform data imported into the spreadsheet by the gain factor, the data is converted to units of digital counts. For the MS box and QS box, the gain factors were  $1.75e-8$  and  $8.762e-9$ , respectively. This is an important step because the data can be analyzed in its most raw format and all assumptions from here can be controlled.

Next, a Fourier transformation is conducted on the data. The software used to conduct the transformations had a limit of 4096 points. By using 4096 points, most of the signature plus background noise can be encompassed in the transformation. A Fourier transformation of just the background noise is also conducted at this time. A sample waveform with its Fourier transformation sample intervals, indicated by red lines, is shown in Figure 3.24.

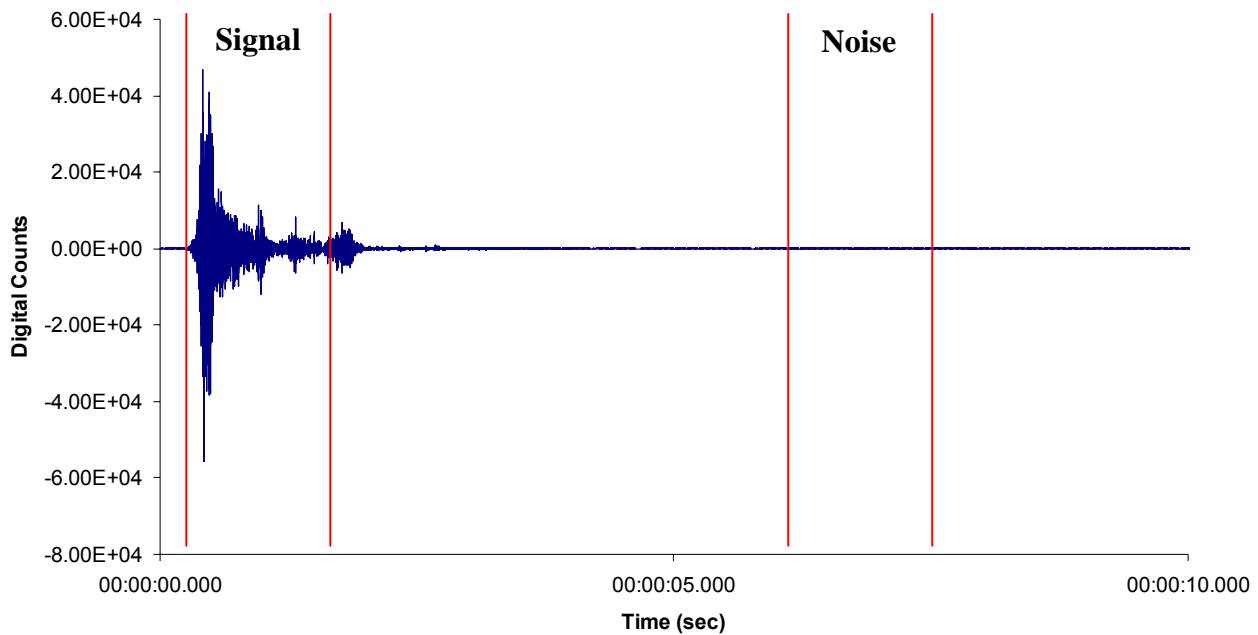


**Figure 3.24** –Fourier transformation windows selected for the signal and background noise.

The waveform (vertical component) is from the C-Drift instrument room for mine shot #507. The full seismic signature was not included in the signal interval. The Fourier transformations were limited to 4096 points, so in some cases, parts of the signature were left out. Once the Fourier transformation is conducted on the data, it is in the frequency domain and in units of digital counts per Hz. This transformed data set is defined as  $S(\omega)$ . An example of the transformed data from the signal interval in the frequency domain is shown in Figure 3.25.

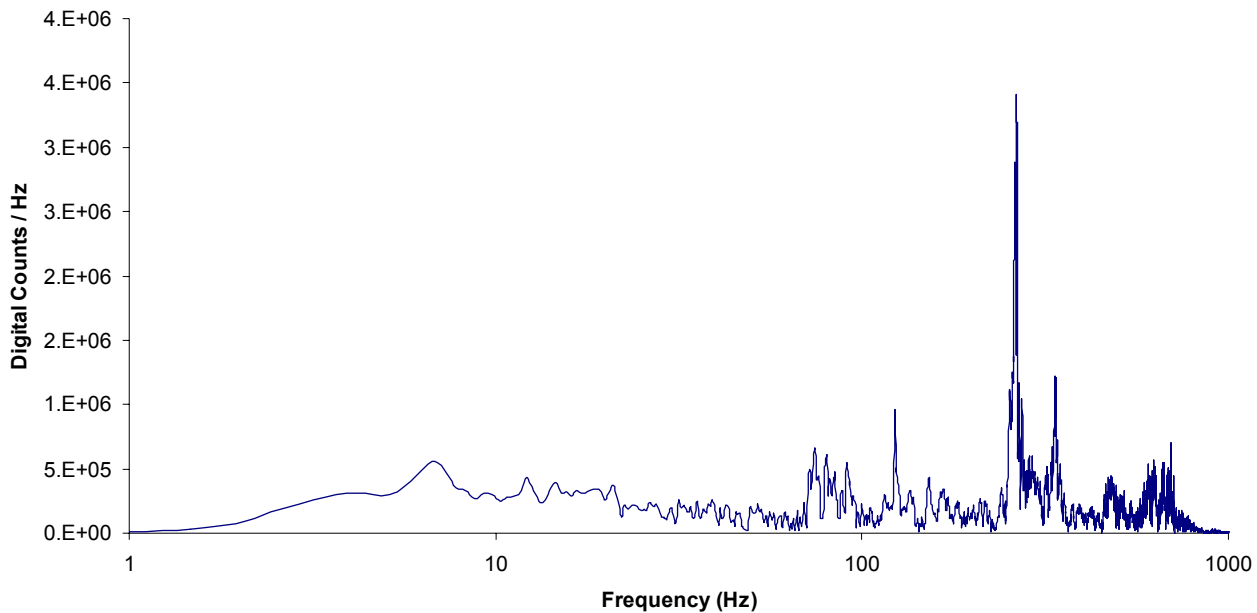


**Figure 3.25** – Example of the data observed in the frequency domain after a Fourier transformation.

### 3.5.2 Spectral analysis of the data

Once the data is in the frequency domain, spectral analysis techniques can be conducted which yield results such as moment magnitude and radiated seismic energy of the event. When the data are in the frequency domain, instrument correction is performed by division of  $d(\omega)$ , which was defined earlier in Equation 3.2. The result is  $D(\omega)$ , which is the Fourier amplitude spectrum of ground displacement in units of m/Hz, as shown in Equation 3.4.

$$D(\omega) = \frac{S(\omega)}{d(\omega)} \quad (3.4)$$

Using the dataset from Figures 3.24 and 3.25, an example of the Fourier amplitude spectrum for ground displacement is plotted and shown in Figure 3.26. The signal is represented by the blue line and the background noise is represented by the pink line. The data end at 1000 Hz because of the Nyquist criterion, as described in Section 2.10.2.

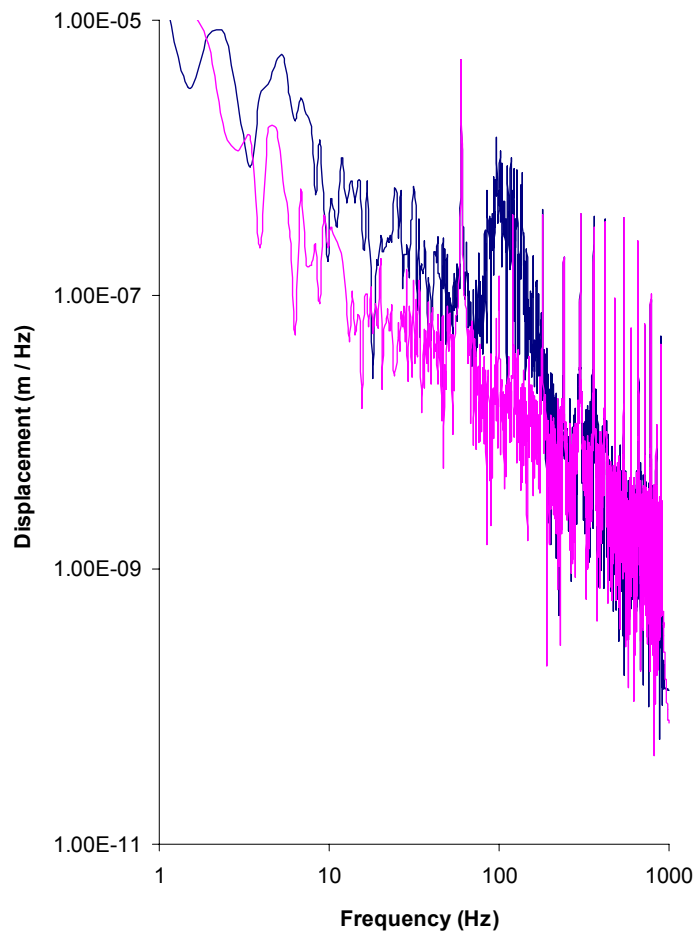


**Figure 3.26** – Example of the Fourier amplitude spectrum of ground displacement,  $D(\omega)$ . The blue line represents the signature from the event and the pink line represents the background noise.

The dataset can also be divided by the instrument correction  $v(\omega)$  which was defined earlier in Equation 3.3. The result is  $V(\omega)$ , which is the Fourier amplitude spectrum of ground velocity in units of m/s / Hz, as shown in Equation 3.5. The plot of the Fourier amplitude spectrum of ground velocity is shown in Figure 3.27.

$$V(\omega) = \frac{S(\omega)}{v(\omega)} \quad (3.5)$$

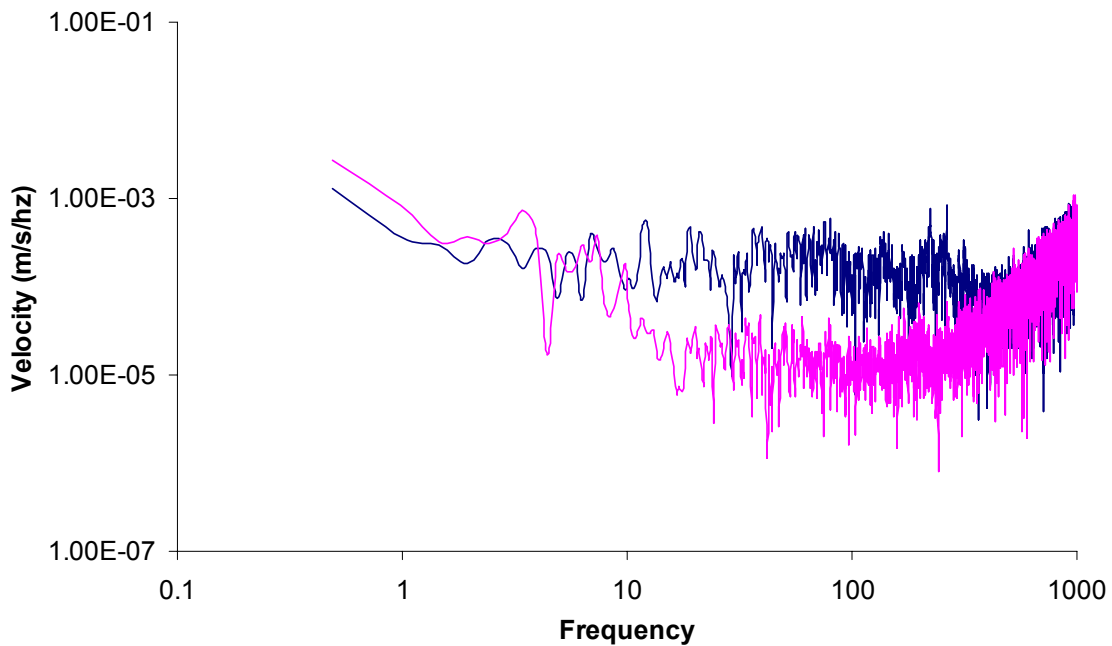


**Figure 3.27** – Example of the Fourier amplitude spectrum of ground velocity,  $V(\omega)$ . The blue line represents the signature from the event and the pink line represents the background noise.

### 3.5.3 Moment magnitude and radiated seismic energy calculations using the displacement and velocity spectra

The equation for moment magnitude, Equation 2.8 in Section 2.7.3, states that one of the variables needed is  $\Omega_0$ , the low-frequency spectral plateau observed in the Fourier displacement amplitude spectrum. The Brune model for displacement spectra, Equation 2.8 in Section 2.7.2,

can be plotted and superimposed over the Fourier amplitude spectrum of ground displacement to aid in determining  $\Omega_0$ . An example is shown in Figure 3.28. The green curve represents the Brune model and where the flat asymptote crosses the y-axis is the value of  $\Omega_0$ . To obtain this value, recall that two inputs for the Brune displacement curve are the corner frequency and  $\Omega_0$ . These two values are estimated from the spectrum of ground displacement and adjusted until they fit the data.

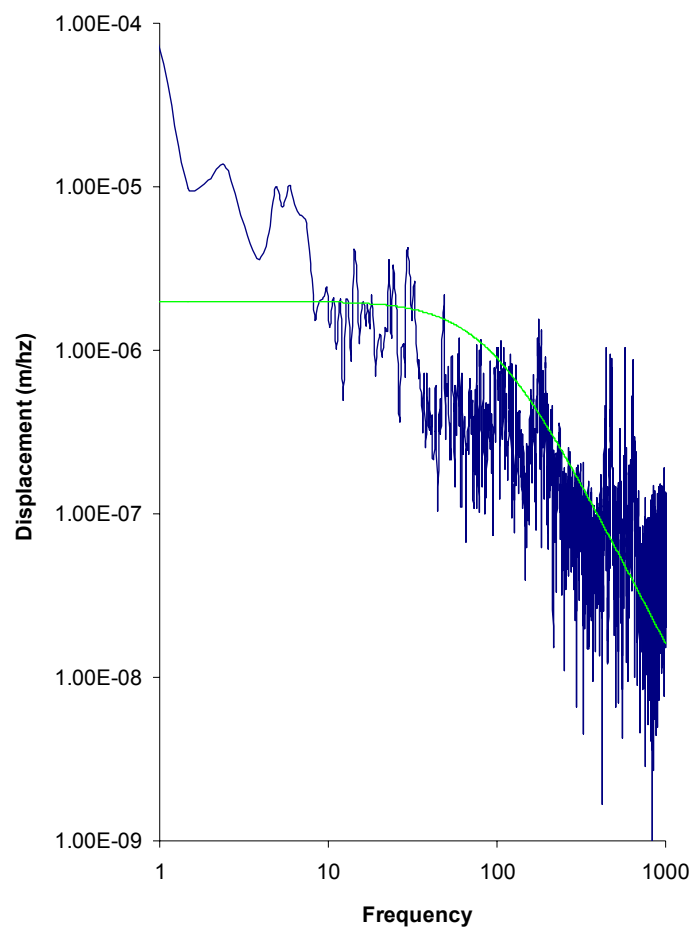


**Figure 3.28** – Example of the Brune model superimposed on the Fourier amplitude spectrum of ground displacement to help determine  $\Omega_0$ .

The equation for radiated seismic energy, Equation 2.9 in Section 2.7.3, states that one of the variables needed is  $I$ , the integral of square velocity in the Fourier amplitude spectrum of ground velocity. The method on how to find this value was similar to the analysis from Iannacchione et al. 2005a and an example is shown in Figure 3.29.

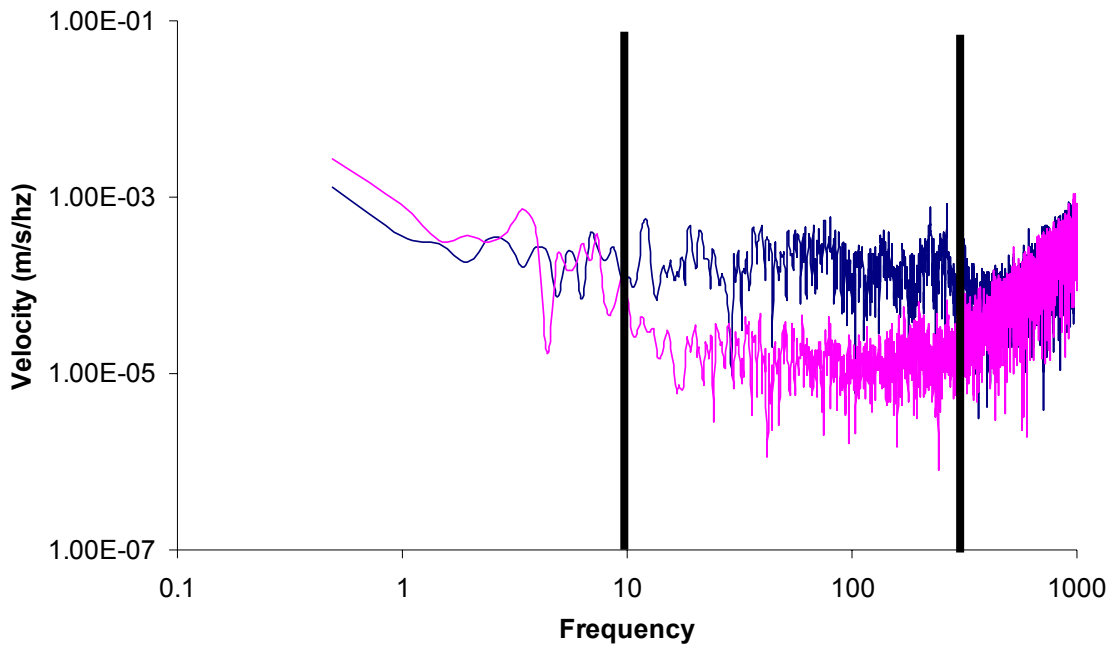


**Figure 3.29** – Example of Fourier amplitude spectrum of ground velocity to help determine the radiated seismic energy. The blue line represents the signature from the event and the pink line represents the background noise.

The area between blue and pink curves, within specified frequency limits, squared represents the integral of squared velocity needed for calculating the radiated seismic energy. On the left side of Figure 3.28, the two curves “follow” each other and are somewhat merged together. Between 0.5 and 10 Hz, they are separated; however, still have very similar trends. On the right side of the figure, they are completely merged together. When the signals are merged together like this, it means that the signal-to-noise ratio is very low and the energy from that

specific frequency has approximately the same amount of energy in both the signature and background noise. The area between the two thick black lines is the area used to calculate the integral of squared velocity. In this specific example, the frequency interval is approximately 10 – 300 Hz. It can be observed in this frequency interval that the signals are not merged together and do not follow similar trends. A signal-to-noise ratio criterion of at least 3 was also taken into consideration when calculating the energy.

In some instances, the frequency window chosen was more difficult to determine than the previous example, as indicated in Figure 3.30. In this example, since the signal exceedingly rises out of the background noise, the two curves are never merged together. It should be noted that the same window for both the signature and the background noise was used in the Fourier transformation. If the full frequency range is used for the energy estimation, the total radiated seismic energy for this example would be 5,758 MJ. This energy estimation value is approximately eight times more than the initial energy included in the explosion. In Section 2.11 in the literature review, it was shown that uncoupled explosions have less than 1% of the initial energy transferred into the rock as seismic waves. Because more energy is estimated seismically than what was initially present, the estimation is considered inaccurate.

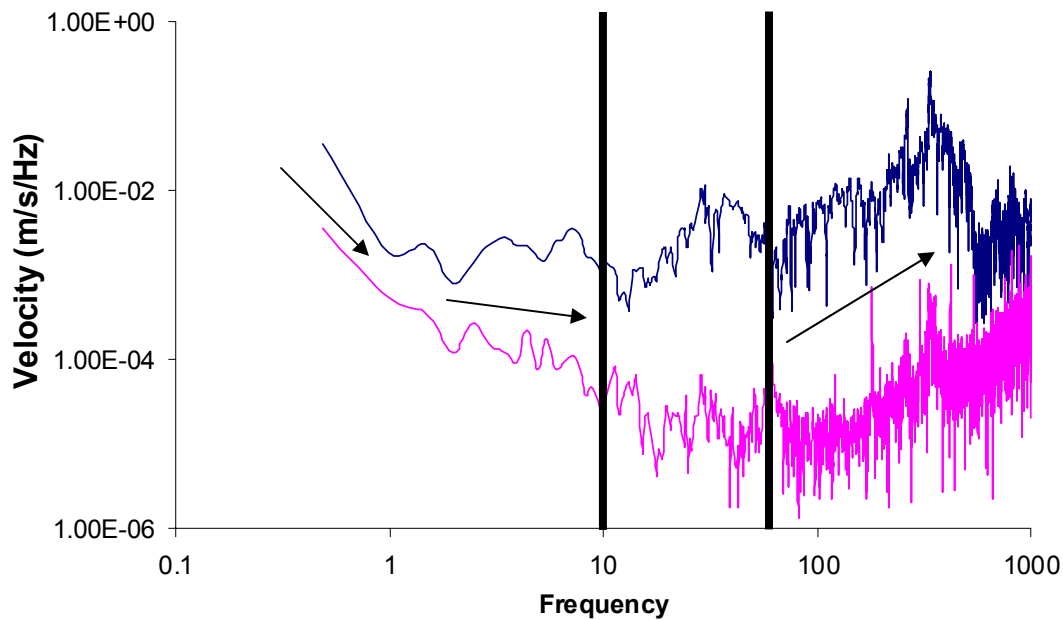


**Figure 3.30** – Example of the Fourier amplitude spectrum of ground velocity to help determine the radiated seismic energy. In this example the frequency intervals to include in the calculation is more difficult to determine. The blue line represents the signature from the event and the pink line represents the background noise.

If Figure 3.30 is looked at closely, it can be observed that the two curves “follow” each other despite not being merged at lower and higher frequencies. These areas are indicated by arrows. However, between 10 – 70 Hz the two curves seem to spread apart. If this area is used for the energy calculation, the radiated seismic energy is approximately 3 MJ which is 0.4% of the initial total energy. This agrees with what was stated in the literature review. Another reference, Aki (2002), states that the seismic efficiency is at most a few percent when referring to the energy released by earthquake faulting. The explosions conducted the mine are not effectively coupled with the rock, meaning energy efficiencies of less than 1% are expected. Therefore when looking at the ground velocity spectra, if the signal and background curves appeared to follow each other, the energy observed in that frequency range was not taken into consideration.



### 3.6 Determination of the size of the explosion

In the objective statement in Section 1.2, one of the major goals of the project is to relate the seismic assessments to the size of the explosion. For this study, the size of the explosion is defined as the peak pressure generated in the cavity of the experiment. Pressure measurements, sampled at 1,500 samples per second, were obtained from the staff at the Lake Lynn Experimental Mine and were not on the same time scale as the seismic measurements. An example of a pressure-time curve is plotted in Figure 3.31. The peak pressure generated for this example is around 55 psi, which would be considered the size of the explosion. The full set of pressure-time curves obtained during this study for the explosions are reported in Appendix B.

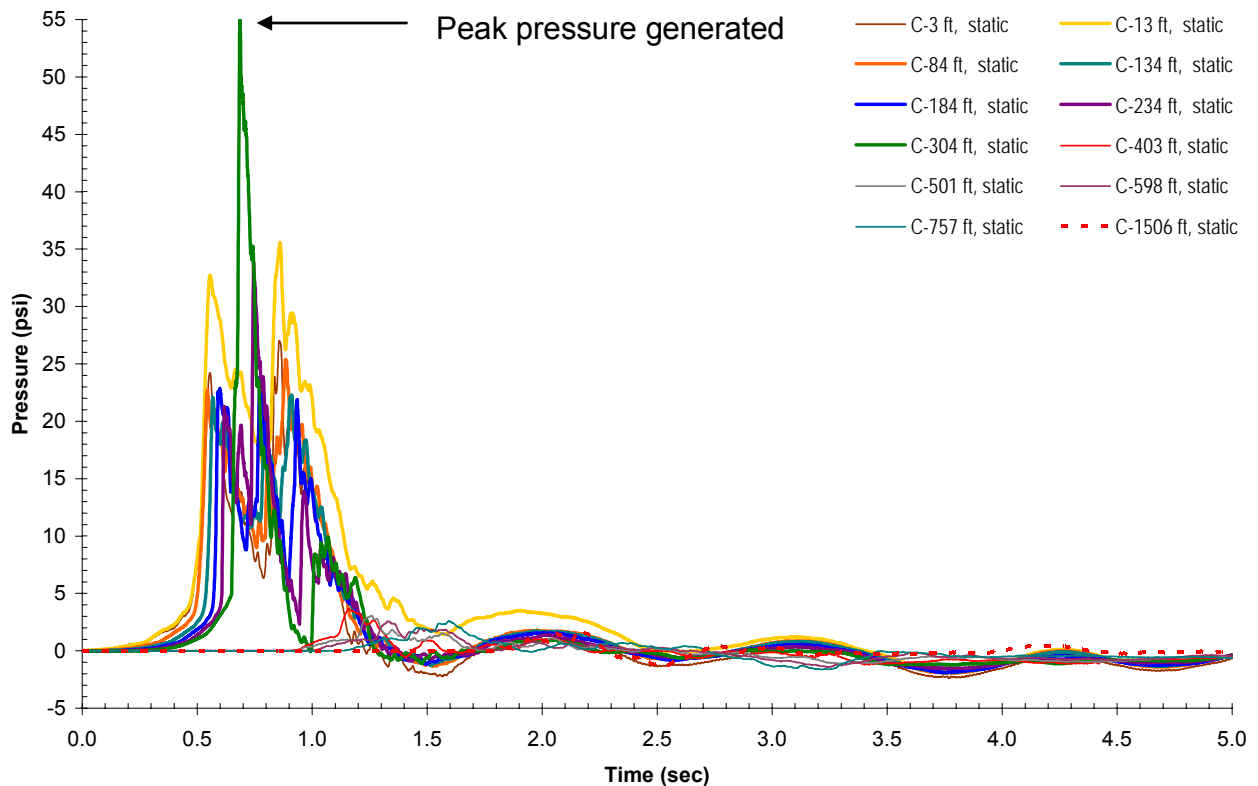
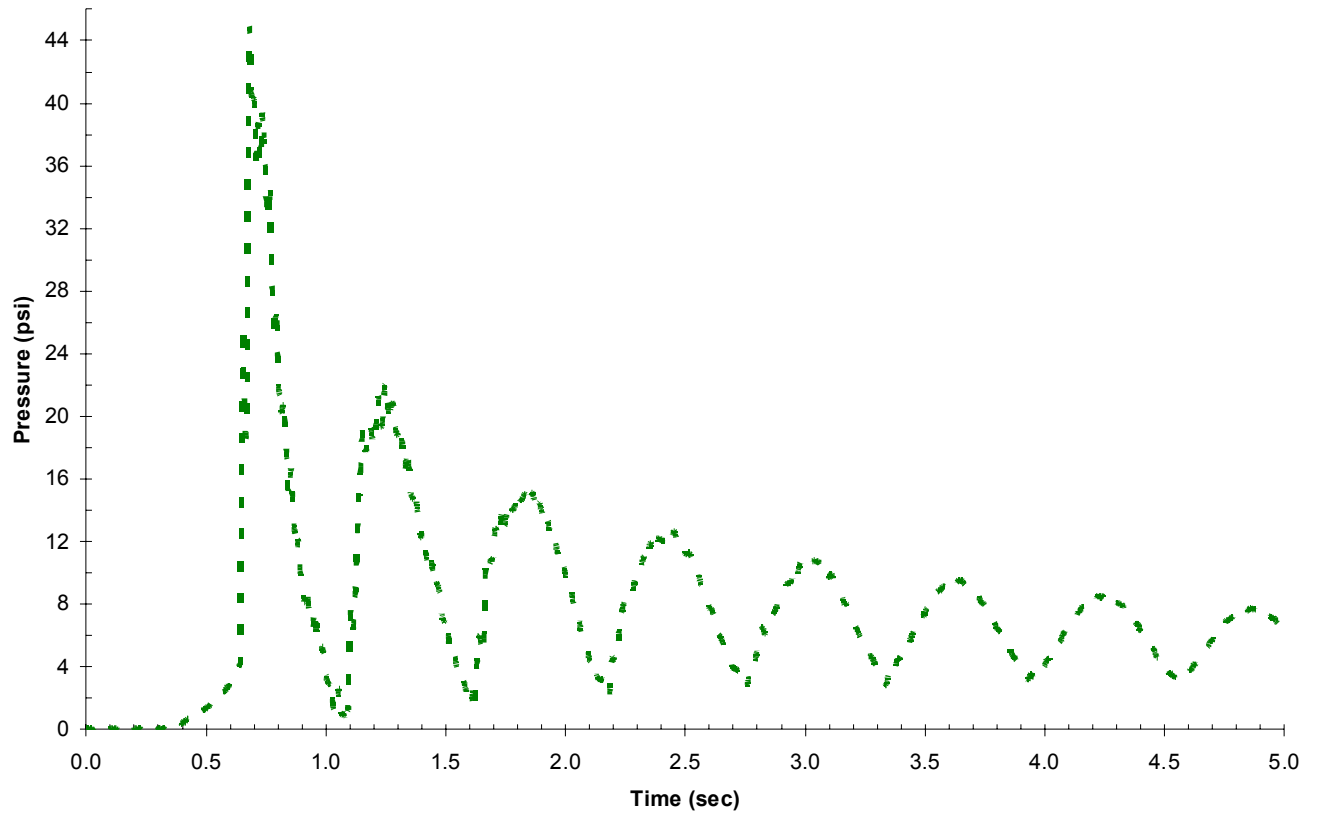


Figure 3.31 – Example of pressure-time curves used to obtain the size of the explosion, as defined by the peak pressure generated.

In Figure 3.31, the legend indicates that measurements are taken at different intervals along the drift. For example, C-3 ft indicates that the measurement was taken in C-Drift 3 ft away from the mine face at the wall of the drift. Measurements taken at the wall are considered to be the sweeping quasi-static (omnidirectional) pressure and measurements taken head-on are considered to be the total explosion pressure (combination of omnidirectional and dynamic/wind pressures). The peak pressure generated during the experiments were found to be dependent on factors such as the mine geometry, seal locations and combination of the methane-air concentrations and amount of coal dust used to boost the explosion. When the explosion was confined within a sealed area, the pressure-time curves had characteristics which were significantly different and example is plotted in Figure 3.32. In this specific example, an oscillation with a period of approximately 0.6 seconds is observed. A similar oscillation can be observed for all the explosions that are confined to the sealed area, as shown in Figures B.1, B.2, B.6 and B.18. These pressure histories are significantly different than the expected plot reported in Figure 2.4. The addition of the seal causes the pressure wave oscillations, due to the reflected waves within the confined area, and the suck-back phenomena is not be observed. A detailed comparison of this observation to the seismic data is reported in Section 6.6.



**Figure 3.32** – Example of a pressure-time curve for the confined explosions, which shows an oscillating pressure pulse.

# Chapter 4 – Amplitude, Attenuation and Duration of the Seismic Signatures

In Chapter 4, the amplitude, attenuation and duration of the seismic signatures are studied. The amplitude is studied in order to determine if the maximum ground velocity from each experiment can be correlated to the size of the explosion. From the maximum amplitude measured at different distances away from the source for a single event, the attenuation of the seismic signature is calculated. Finally, the duration of the seismic signatures are investigated to determine if the impact of the varying experiment designs can be observed.

## 4.1 Amplitude analysis of the seismic signatures

### 4.1.1 Method of analysis

The maximum amplitudes from the seismic signatures were studied to investigate relationships between the different explosive sizes and to evaluate the attenuation of the seismic signatures. The maximum seismic wave amplitudes were converted into units of m/s from the original digital counts. The size of the explosion was found using the peak pressure generated for each mine shot determined from the pressure-time curves documented in Appendix B. The maximum ground velocity, or amplitude, is referenced as the peak particle velocity, not the velocity of the seismic wave traveling through the medium. The maximum ground velocity versus peak pressure generated by the explosion plots were made for each component for each triaxial geophone. An example is shown in Figure 4.1.

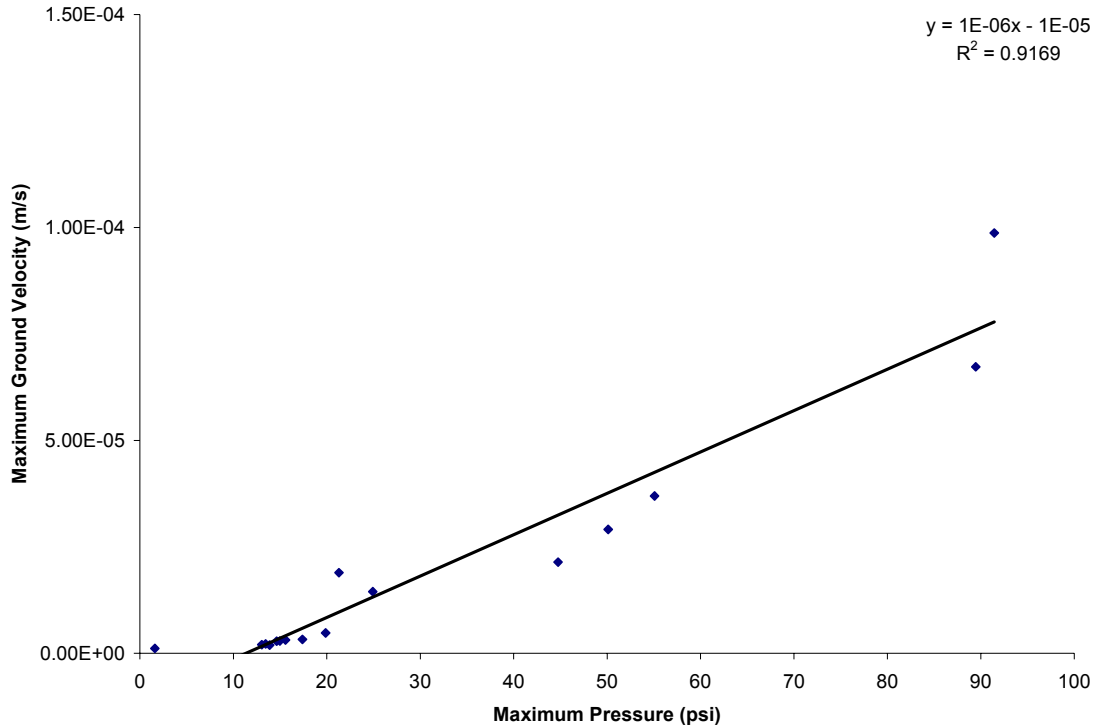


Figure 4.1 – Plot of maximum ground velocity versus maximum pressure for Geophone 5 (Channel 1).

#### 4.1.2 Results from mine shots #503-524 and discussion

Mine shots #503 – 524 were the methane and coal dust explosions monitored during the study and the specific experimental designs are described in Appendix A. The complete set of plots for maximum ground velocity versus peak pressure generated by the explosion are reported in Appendix C. Close to the source, Geophones 1, 2, 8 and 9 (Figure 3.17) appear to show a large amplitude measurement for mine shot #507, which generated a relatively small pressure of 21 psi. Geophones 1 and 2, although not directly exposed to the explosion, were affected by the pressure wave “sweeping by” the C-Drift instrument room. These geophone locations are shown in relation to the C-Drift entry in Figure 3.17, which indicates that Geophones 1 and 2 were located approximately 3 m (10 ft) from the pressure wave sweeping by that location. If mine shot #507 is kept in the ground velocity-pressure relationship curves from these two geophones,

Geophone 1 shows a poor relationship (Figure C.1) and Geophone 2 shows a good relationship (Figure C.3). At first, it was assumed that the relationship was logarithmic since the regression lines fit these data better. If the data point from mine shot #507 is removed from the plot and the regression line is made linear, the data show a better correlation between amplitude and pressure (Figures C.2 and C.4). Therefore it was assumed that the maximum ground velocity from mine shot #507 for these two geophones was more related to the experimental design since the pressure wave swept by the geophones 3 m (10 ft) away.

Geophones 8 and 9, located in A-Drift, were actually exposed to the pressure wave which caused an exaggerated amplitude. The pressure wave itself is hypothesized to come into contact with the geophones due to the extremely high amplitudes. Since some of the crosscuts were open between A-, B- and C-Drifts, the explosive pressure wave was allowed to travel into and towards the faces of A- and B-Drifts (see the mine shot #507 experimental design in Appendix A). Once the data points for mine shot #507 were removed from the plots for these geophones, a better discernible correlation between amplitude and pressure could be made (Figures C.9 – C.12). The data from the geophones located in E-Drift (Geophones 4 and 6) showed similar correlations as what had been observed from A- and C-Drifts. Geophone 4 lacked data points from a wide range of peak pressures generated by the explosion because it was initially located in a cement block attached to the roof. An impedance mismatch between the cement block and limestone roof caused a loss of energy in the seismic waves. The plots for Geophone 4 only include data from when the instrument was located on the limestone roof. Far away from the source, a linear correlation between ground velocity and size of the explosion could be observed from the geophones in D-Drift (Figures C.5 and C.7).

Since most of the trends observed from Appendix C showed similar correlations, a linear relationship between the amplitude of the seismic signature and size of the explosion was observed. Shown in Table 4.1 are the slope and offsets obtained from the data. The data are reported for each component of each geophone included in the analysis and are averaged. A trend was observed from the coefficients that geophones near the source were better correlated together compared to the data from geophones far away. The average coefficients of the geophones located between 0 – 150 meters and 150 – 250 meters were grouped together in the table in the final column.

**Table 4.1** – Slope and offsets which relate the ground velocity to maximum pressure during methane and dust explosions. Different average coefficients were observed for data in ranges between 0-150 meters and 150-250 meters.

		Channel	Slope	Offset	Average for Each Component		Average Near vs. Far	
					Slope	Offset	Slope	Offset
Between 0-150 meters	Geophone #1	1	4.21E-05	-5.38E-04	3.42E-05	-4.16E-04	2.50E-05	-4.72E-04
		2	3.55E-05	-3.75E-04				
		3	2.51E-05	-3.36E-04				
	Geophone #2	1	3.09E-05	-4.16E-04	2.46E-05	-3.11E-04		
		2	2.06E-05	-2.29E-04				
		3	2.22E-05	-2.87E-04				
	Geophone #4	1	4.04E-06	-4.88E-05	1.36E-05	-1.81E-04		
		2	1.87E-05	-2.53E-04				
		3	1.79E-05	-2.41E-04				
	Geophone #6	1	4.08E-05	-7.07E-04	4.51E-05	-8.35E-04		
		2	5.02E-05	-9.41E-04				
		3	4.43E-05	-8.57E-04				
	Geophone #8	1	5.29E-06	-1.34E-04	1.09E-05	-3.27E-04		
		2	1.41E-05	-4.97E-04				
		3	1.33E-05	-3.49E-04				
Geophone #9	1	2.62E-05	-9.58E-04	2.20E-05	-7.63E-04			
	2	2.64E-05	-9.82E-04					
	3	1.33E-05	-3.49E-04					
Between 150-250 meters	Geophone #3	1	9.72E-07	-1.10E-05	7.49E-07	-8.17E-06	5.56E-07	-3.33E-06
		2	6.69E-07	-9.78E-06				
		3	6.07E-07	-3.72E-06				
	Geophone #5	1	1.79E-07	2.23E-06	3.63E-07	1.51E-06		
		2	4.69E-07	3.05E-06				
		3	4.40E-07	-7.57E-07				

Using the data from Figure 4.1, scaling relationships created between the maximum seismic velocity amplitude and the size of the explosion (Equations 4.1 and 4.2). It should be

noted that the variables are switched in Equations 4.1 and 4.2 so the amplitude becomes the independent variable.

For distances between 0-150 meters:

$$P_{\max} = 40000(A_{\max}) + 20 \quad (4.1)$$

For distances between 150-250 meters:

$$P_{\max} = 1798500(A_{\max}) + 6 \quad (4.2)$$

where:  $P_{\max}$  = Maximum pressure from the explosion (psi), and  
 $A_{\max}$  = maximum amplitude observed in the seismic signature (m/s).

It is noted that Equation 4.1 will not calculate a pressure value under 20 psi and Equation 4.2 will not calculate a pressure value under 6 psi. The data from which these equations were derived from included pressures generated under these two values, making them unrepresentative of the observations. In order to develop a better relationship, the regression lines in the velocity-pressure curves from Appendix C were forced to intersect at the origin. For the recalculation of the relationship between ground velocity and maximum pressure, the data from Geophone 4 were not included because of the poor correlation coefficient. The new dataset is reported in Table 4.2 and the charts are re-plotted in Appendix C. The standard deviation is included in the table to help determine range of calculated pressure values. Equations 4.3 and 4.4 are the new relationships derived from the data in Table 4.2.



**Table 4.2** – Recalculated slopes which relate the ground velocity to maximum pressure during methane and dust explosions. Different average coefficients were observed for data in ranges between 0-150 meters and 150-250 meters.

		Channel	Slope	Average for Each Component Slope	Average Near vs. Far Slope	Standard Deviation
<b>Between 0-150 meters</b>	Geophone #1	1	3.48E-05	2.86E-05	1.98E-05	1.04E-05
		2	3.04E-05			
		3	2.05E-05			
	Geophone #2	1	2.32E-05	1.89E-05		
		2	1.64E-05			
		3	1.69E-05			
	Geophone #4	1	-	-		
		2	-			
		3	-			
	Geophone #6	1	2.97E-05	3.20E-05		
		2	3.53E-05			
		3	3.09E-05			
	Geophone #8	1	3.64E-06	6.88E-06		
		2	8.02E-06			
		3	8.99E-06			
Geophone #9	1	1.45E-05	1.26E-05			
	2	1.44E-05				
	3	8.99E-06				
<b>Between 150-250 meters</b>	Geophone #3	1	7.67E-07	6.09E-07	5.06E-07	1.64E-07
		2	5.23E-07			
		3	5.36E-07			
	Geophone #5	1	2.63E-07	4.03E-07		
		2	5.20E-07			
		3	4.27E-07			

For distances between 0-150 meters:

$$P_{\max} = 50600(A_{\max}) \quad (4.3)$$

For distances between 150-250 meters:

$$P_{\max} = 1798500(A_{\max}) \quad (4.4)$$

To demonstrate the estimation of a maximum pressure generated during a mine explosion, assume a signature was recorded by a geophone located 50 m from the source. If the signature had had a maximum ground velocity of 4.35e-05 m/s, which is a velocity within the ranges of values reported in the dataset, the estimated maximum pressure for that explosion would be between 1.5 – 5 psi. If the receiver was further from the source in the 150 – 250 m

range, the estimated maximum pressure would be in the range of 65 – 128 psi. Despite this being a large range of values, it is determined from the limited evaluations over 150 m, and at the very least gives an initial estimation from data which included many different types of experimental designs. Another fact to keep in mind is that these explosions are largely decoupled from the limestone. Comparing the amplitude of a methane explosion at LLEM to an amplitude from a quarry blast would not be expected to provide a comparison of the overall source size because one is coupled with the rock and one is not.

#### *4.1.3 Results of from the cast booster experiments and discussion*

The cast booster experiments were investigated in order to observe the standard deviations of the seismic velocity amplitudes. Since the cast boosters contained equal initial energy, it is assumed that the source should repeatedly generate the same amplitude if the source to receiver location is constant. The amplitudes from Geophone 5 are reported for this investigation. The cast boosters blasted midway down A-Drift (Figure 3.23) were not included, because the distance from the source to receiver changed too dramatically (causing the amplitude to fluctuate too dramatically for the analysis). The results are reported in Table 4.3. The columns labeled 1, 2 and 3 refer to Channels 1, 2 and 3 of the triaxial geophone. The results show that there is some variability within the amplitude that is observed, which was expected. The variability is most likely due to the smaller changes in distance between the booster test locations (maximum difference of 30.5 m) near the A-Drift face and the fact that the seismic waves are traveling through an anisotropic medium.

**Table 4.3** – Amplitude of ground velocities collected by Geophone 5 for the boosters set off near the A-Drift face.

	Amplitude of Ground Velocity (m/s)		
	1	2	3
	4.67E-06	7.19E-06	8.58E-06
	8.68E-06	5.80E-06	5.42E-06
	3.98E-06	5.69E-06	5.92E-06
	5.13E-06	7.81E-06	7.22E-06
	4.84E-06	6.04E-06	8.06E-06
	3.35E-06	5.62E-06	6.62E-06
	4.10E-06	4.75E-06	6.10E-06
	4.04E-06	5.21E-06	7.80E-06
	4.60E-06	7.70E-06	7.54E-06
Average	4.82E-06	6.20E-06	7.03E-06
Standard Deviation	1.54E-06	1.10E-06	1.07E-06

## 4.2 Attenuation of the seismic signatures

### 4.2.1 Method of analysis

In the previous section, the amplitude of the seismic signature was studied separately at near versus far distances. In order to relate the data together, the attenuation of the seismic signatures were studied to see how much the amplitude decays as the seismic wave travels through the limestone. The attenuation was calculated in terms of decibels, which compares the ratios of amplitudes observed at different locations within the mine. The formula used to calculate the decibels is shown in Equation 4.5.

$$dB = 20 \log \left( \frac{V_1}{V_2} \right) \quad (4.5)$$

where:  $V_1$  = Measured input (volts), and  
 $V_2$  = Reference input (volts).

Equation 4.5 calculates the decibels by using a ratio of two voltages. Since amplitude is linearly related to the voltage from the geophone, a ratio of measured and reference amplitude values are used in the decibel calculation instead of volts. The measured input is the measured amplitude at different distances away from the source. The reference input would be related to an initial amplitude observed at zero distance away from the source of the explosion. Since a geophone was never present at the location of the source, this parameter had to be estimated from the seismic data for each explosion. An example is shown for mine shot #506 in Figure 4.2. For this example, the y-axis is on a logarithmic scale. The amplitude of ground velocity was observed to decrease exponentially with distance. The reference input,  $V_1$ , can be estimated at 0.053 m/s based upon where the regression line crosses the y-axis.

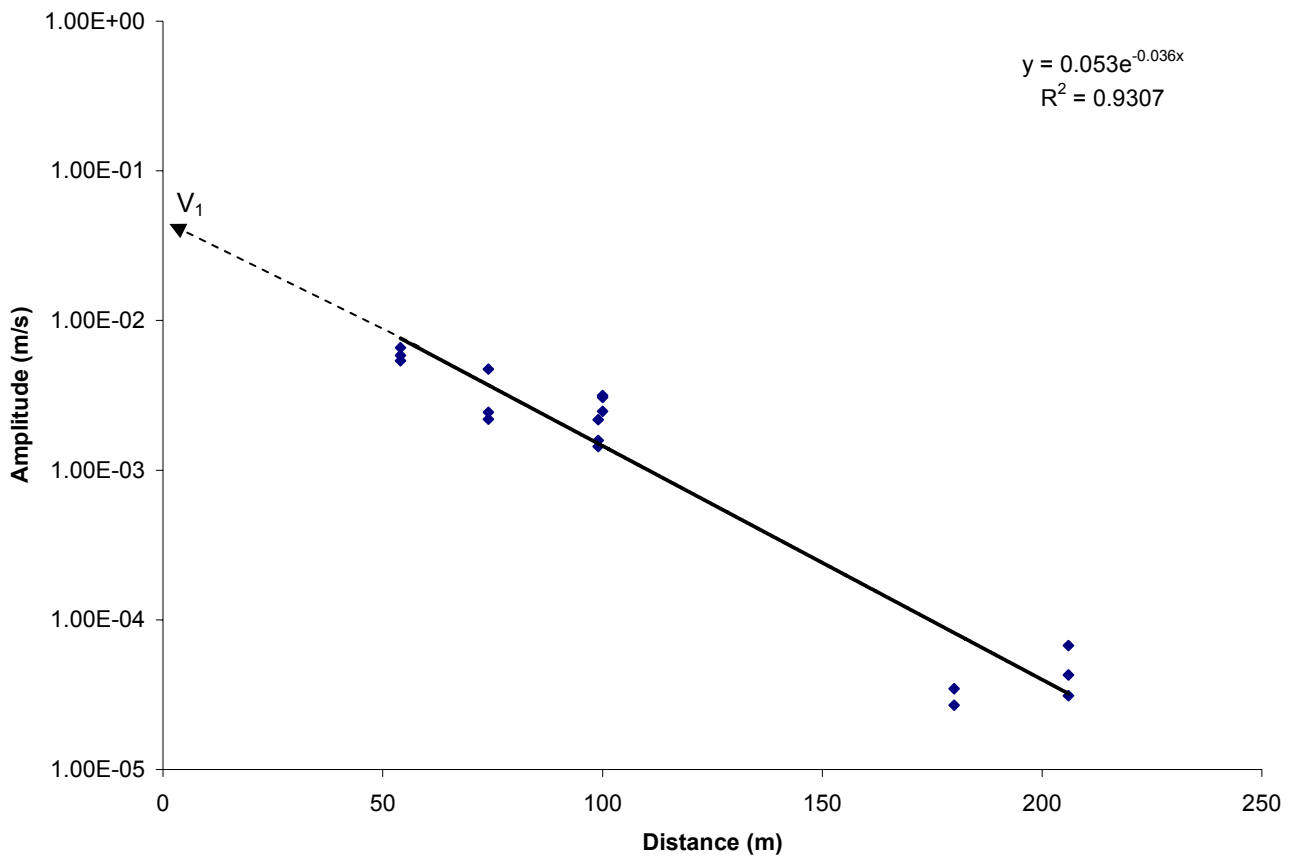
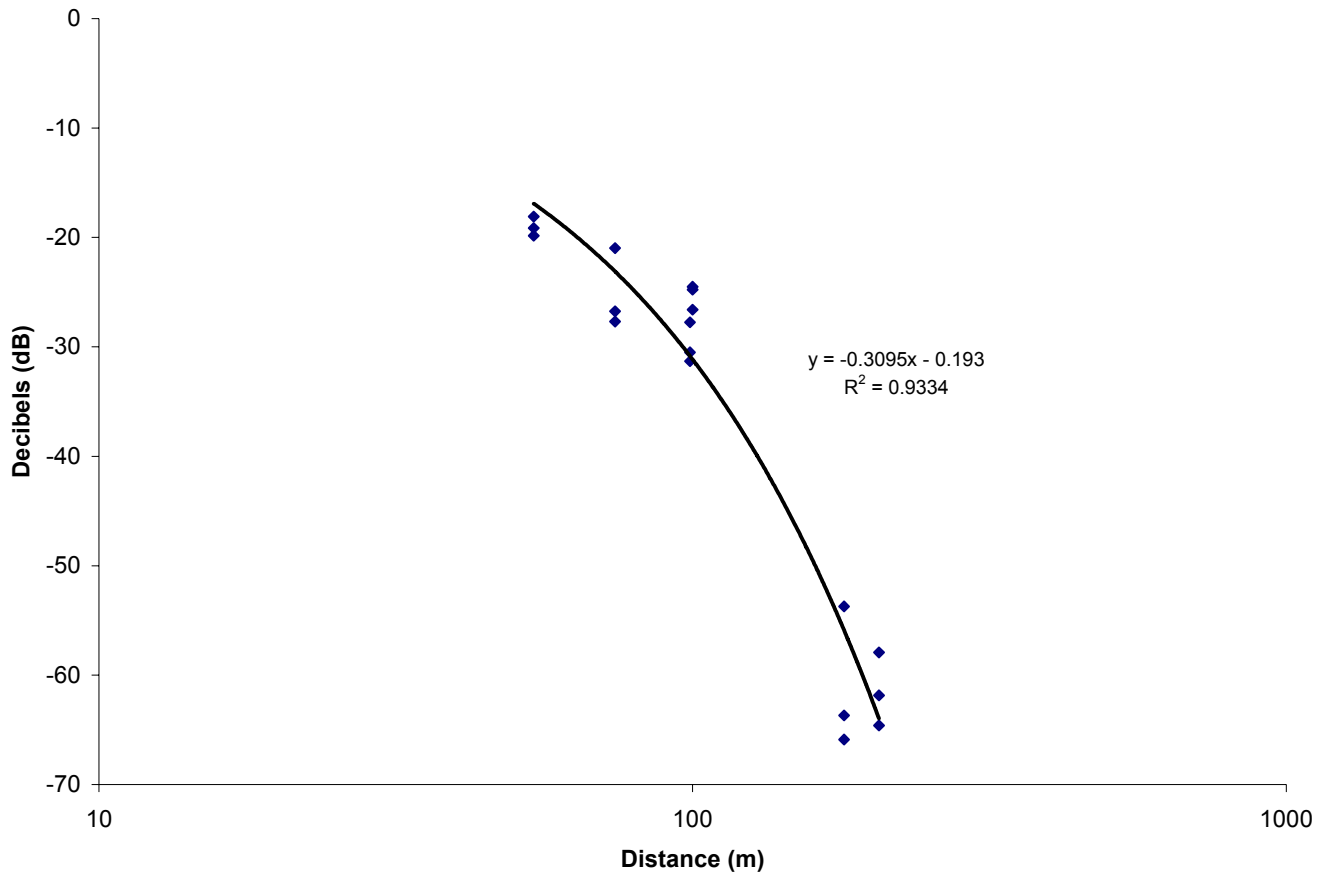


Figure 4.2 – Plot of amplitude versus distance for mine shot #506.

The reference inputs were calculated for each mine shot are reported in Appendix D. For each of these examples, the y-axis is on a logarithmic scale. Once the reference powers are calculated for each mine shot, the attenuation for each mine shot was calculated based on Equation 4.5 and plotted. An example demonstrating the attenuation of the amplitude for mine shot #506 is plotted in Figure 4.3. For this example, the x-axis is on a logarithmic scale. For each geophone location, three points are included for each of the triaxial components.



**Figure 4.3** – Plot of attenuation for mine shot #506.

A 6 dB loss results in a 50% change in amplitude. Figure 4.3 shows that there is an approximate loss of 0.3 dB for each meter away from the source. This means that for the example given, the amplitude is reduced by 0.965 (or 96.5% of the original amplitude) for every

meter using standard decibel and voltage loss relationships. To validate this method using data from mine shot #506, geophones in the C-Drift and D-Drift instrument rooms were analyzed. In the C-Drift instrument room, Geophone 2 recorded an amplitude value of  $3.16 \times 10^{-3}$  m/s. Using the attenuation factor calculated previously, Geophone 3 in D-Drift, located 106 m further away, should expect an amplitude loss by a factor of 0.009 ( $0.965 / 106$  m), resulting to a value of  $2.88 \times 10^{-5}$  m/s. Although the estimation is not perfect, the actual measured value was found to be  $3.12 \times 10^{-5}$ , which is in the same approximate range.

#### *4.2.2 Results and discussion from mine shots #503-524*

The attenuation curves for the other mine shots are reported in Appendix D. For each of these examples, the x-axis is on a logarithmic scale. Table 4.4 shows a summary of the values obtained for the reference input values and attenuation factors for each mine shot. The maximum pressure from that particular mine shot is also given. The data for mine shot #507 appeared to have an exaggerated response, as discussed in Section 4.1. The data from mine shot #507 is given in Table 4.4 however the values were not included in the statistical summary.

**Table 4.4** – Amplitude of ground velocities collected by Geophone 5 for the boosters set off near the A-Drift face.

	<b>Max Pressure (psi)</b>	<b>V<sub>1</sub> (m/s)</b>	<b>Attenuation Factor</b>
Mine Shot #503	17.40	1.16E-04	-0.1515
Mine Shot #504	19.88	1.49E-03	-0.2386
Mine Shot #505	55.08	1.28E-01	-0.3814
Mine Shot #506	89.47	5.30E-02	-0.3095
Mine Shot #507	21.31	3.00E-01	-0.4323
Mine Shot #508	50.12	1.07E-03	-0.2087
Mine Shot #509	91.45	1.52E-03	-0.0844
Mine Shot #510	14.63	5.39E-04	-0.1928
Mine Shot #513	13.87	2.44E-04	-0.1677
Mine Shot #514	14.98	9.89E-04	-0.2110
Mine Shot #516	13.03	2.65E-04	-0.1668
Mine Shot #517	13.45	1.55E-04	-0.1369
Mine Shot #518	13.28	9.38E-05	-0.1142
Mine Shot #519	24.92	8.90E-04	-0.1611
Mine Shot #520	15.58	5.18E-03	-0.2731
		Average	-0.1998
		Standard Deviation	0.0798

No correlation could be made based upon the size of the explosion or experimental design to the attenuation factors observed. The lowest attenuation factor was observed for mine shot #509, which was the largest explosion in terms of maximum pressure generated. The highest attenuation factor was observed for mine shot #505 which was also one of the largest explosions. The average attenuation factor was -0.20 dB/m with a standard deviation of 0.080. For each shot, it appears that the amplitude of ground velocity attenuates very quickly. This would be consistent with why the shots were never observed on the Mt. Chateau regional seismic network, 10 miles away, and also why mine shots #510 – 524 were never observed in the old workings or by Geophone 13 which was located on a limestone outcrop outside of the mine.

Although attempts were made to get beyond the near-field environment and monitor the explosions from further distances, this was not a possibility since the signal attenuated into the

background noise. The geophones in the old workings were made part of the system shortly after mine shot #506. The two shots they were triggered on were for mine shots #508 and 509, where both explosions generated pressures close to or over 50 psi. The largest explosions created at the mine, which generated peak pressures of 90 psi, were never observed on the regional seismic network 10 miles away. Although the large explosions are quite destructive, they were unable to be seismically observed at far distances due to the combination of the attenuation of seismic waves and the source being decoupled from the limestone.

### **4.3 Duration of the seismic signatures**

#### *4.3.1 Method of analysis*

The overall duration of the mine shots helps give insight on how the experimental design may affect the seismic signatures observed at different locations. For example, when a mine seal is in the path of the explosion, if a signature is significantly longer in duration than when the mine seal is not there, then it can be said the seal had a significant affect on the signature. A program written in LabVIEW was used to estimate the durations. The code and description of the program is shown in Appendix E. The time frame of the seismic signature was defined by the window between the first arrival and when the signature was believed to drop back into the background noise. Due to the complexity of the seismic signatures, the method of analysis was conducted in a qualitative manner. In some cases, this was hard to observe and bandstop filters applied to the noisy waveforms in an attempt to evaluate the signature further. Also, in some cases reflections of the pressure wave hitting the mine face or mine structures or the suck-back phenomena were observed. These events were not included in the duration calculation as just the seismic activity from the explosion was of interest. In cases where the explosions and reflections were merged together and inseparable, the full duration was reported. Although the objective of



the study was to observe the seismicity from methane and dust explosions, a more in depth speculation of reflections and other types of secondary events is shown in Appendix F. The following analyzes the average durations of signatures observed by geophones close and far away from the methane and dust explosions. The discussion is broken into sections differentiated by the mine shots.

#### *4.3.2 Results and discussion for mine shots #506 – 509*

Although data were collected for mine shots #503 – 505, the digitizers at the time were only programmed to collect a limited amount of data. The duration of the signatures that were collected for these three shots was questionable since it is unknown if the full signature was captured. Therefore, for the mine shots conducted in C-Drift, only four experiments were available for duration analysis. These shots included two experiments where a mine seal in the path of the explosion failed (mine shot #506 and 509), an experiment where a mine seal was in the path of the explosion but it did not fail (mine shot #508) and an experiment where nothing was in the path of the explosion (mine shot #507).

For Geophone 1 and 2, located approximately 100 meters away from the source in the C-Drift instrument room, data were not available for mine shot #508. The average durations are reported in Table 4.5. The averages were taken between the two geophones on all three components. Table 4.5 also indicates whether a seal was in the propagation path of the pressure wave and if it was destroyed. Table 4.5 shows that when a mine seal is in the path of a pressure wave, a longer duration is recorded and the structure has a direct effect on the seismic signature. The longer duration was attributed to the destruction of the mine seal and impacts against the roof and rib. The standard deviations indicate that the differences in the average durations are statistically significant. Representative signatures from the data reported in Table 4.5 are plotted

in Figures 4.4 and 4.5. The signatures are for mine shots #507 and 509 and are from Geophone 2 located on the C-Drift roof.

**Table 4.5** – Average durations from Geophones 1 and 2 for mine shots #505 – 509.

	<b>Mine Seal</b>	<b>Average Duration (sec)</b>	<b>Standard Deviation (sec)</b>
<b>Mine Shot #506</b>	Yes - Destroyed	3.10	0.21
<b>Mine Shot #507</b>	No	1.86	0.25
<b>Mine Shot #509</b>	Yes - Destroyed	3.95	0.23

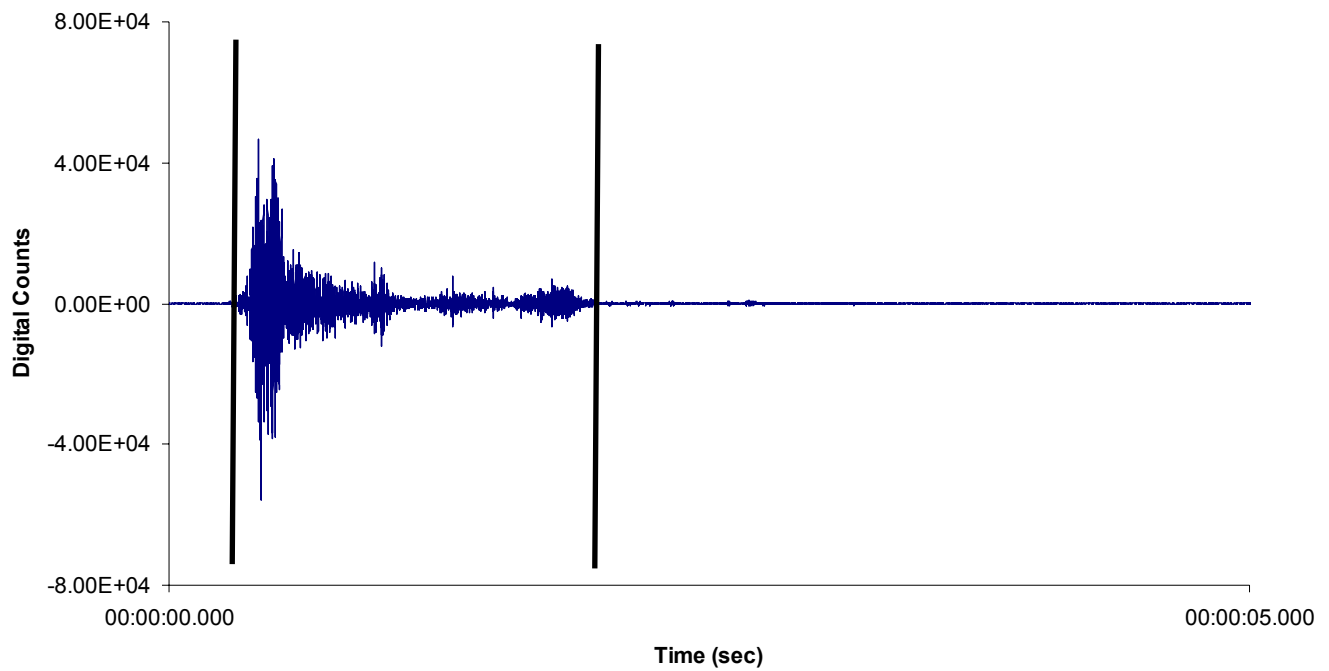


**Figure 4.4** – Representative waveform from Geophone 2 for mine shot #507. The two lines indicate the interval which determined the duration.

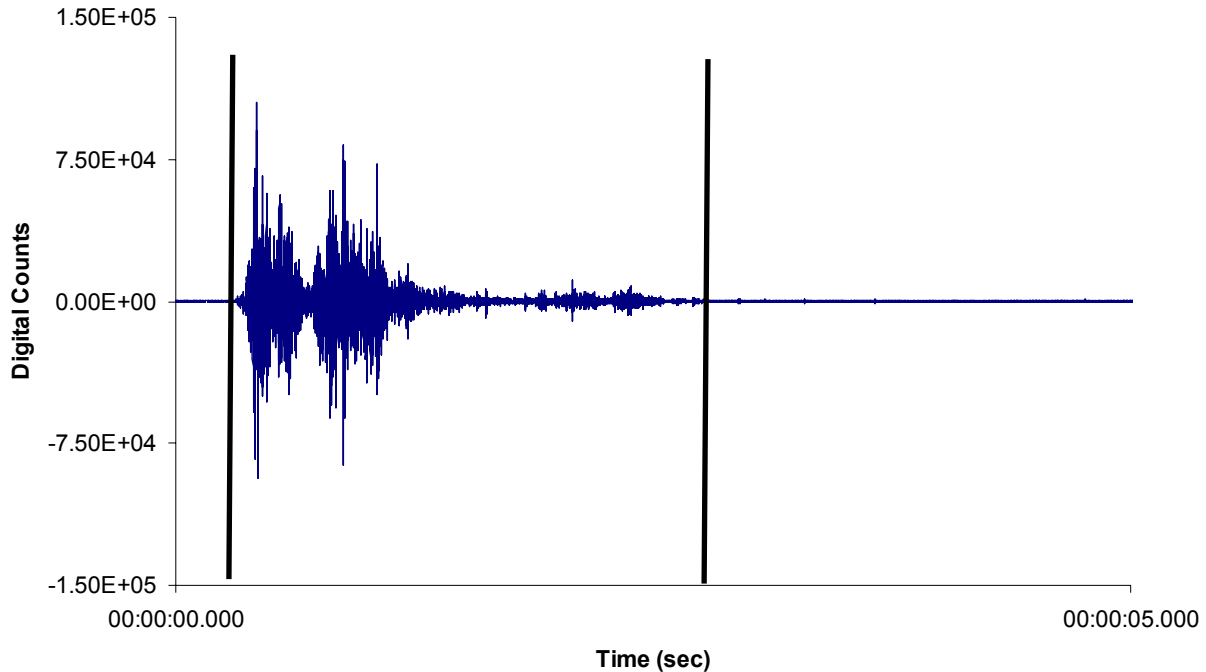


**Figure 4.5** – Representative waveform from Geophone 2 for mine shot #509. The two lines indicate the interval which determined the duration.

The average durations for Geophones 3 and 5, located between 108 – 206 meters away from the source in D-Drift are reported in Table 4.6. The same conclusions, as before, are observed where a longer duration can be observed when a structure is in the path of the mine explosion. The duration is observed to be longest when the explosion is confined within the sealed area. In this scenario, the pressure pulse is reflected repeatedly between the structure and mine face. Representative signatures from the data reported in Table 4.6 are plotted in Figures 4.6 – 4.8. The signatures are for mine shots #507, 508 and 509 and are from Geophone 3 located in the D-Drift instrument room. Since these geophones are representative of the full dataset, the indicated durations are slightly different than the indicated averages seen in Table 4.6. Not enough data were available from E-Drift to calculate significant averages.

**Table 4.6** – Average durations from Geophones 3 and 5 for mine shots #505 – 509.

	Mine Seal	Average Duration (sec)	Standard Deviation (sec)
Mine Shot #506	Yes - Destroyed	3.56	0.13
Mine Shot #507	No	2.26	0.14
Mine Shot #508	Yes	4.22	0.14
Mine Shot #509	Yes - Destroyed	3.50	0.08

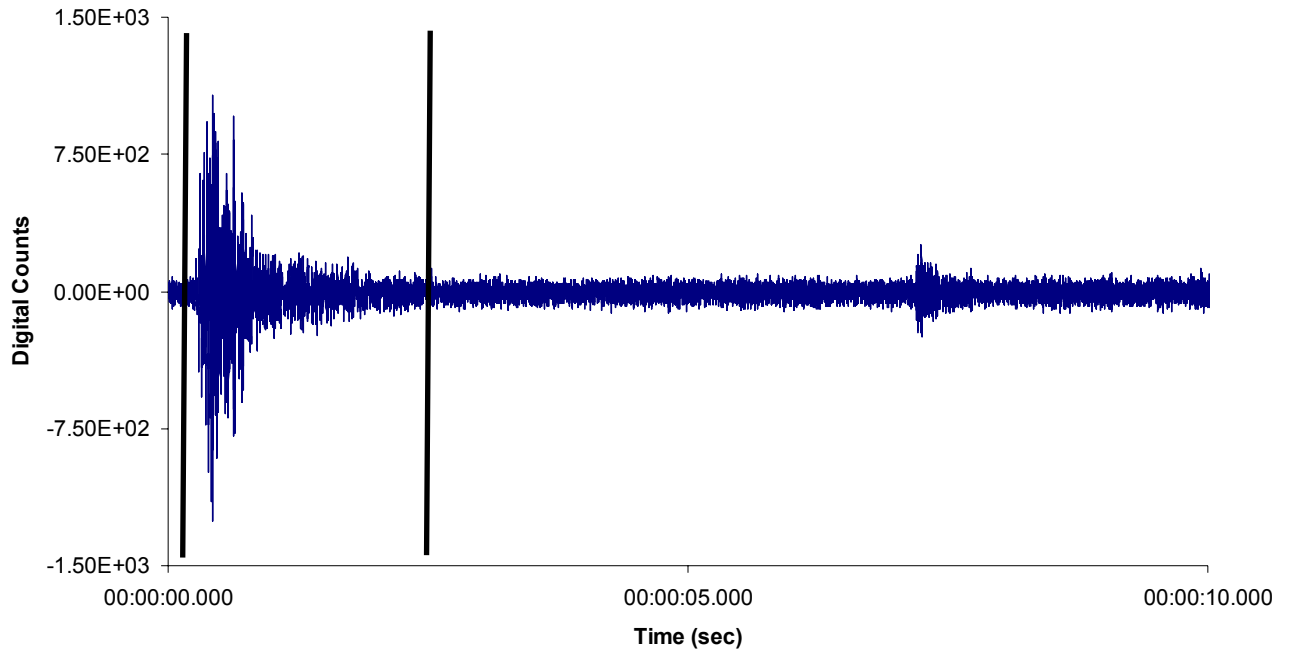


**Figure 4.6** – Representative waveform from Geophone 3 for mine shot #507. The two lines indicate the interval which determined the duration. Past the right indicator, an event occurs at approximately 8.3 seconds. This event is believed to be the “suck-back” of the pressure wave to the mine face which was expected for the experimental design in mine shot #507, as described in more detail in Section 2.4 and in Appendix F.

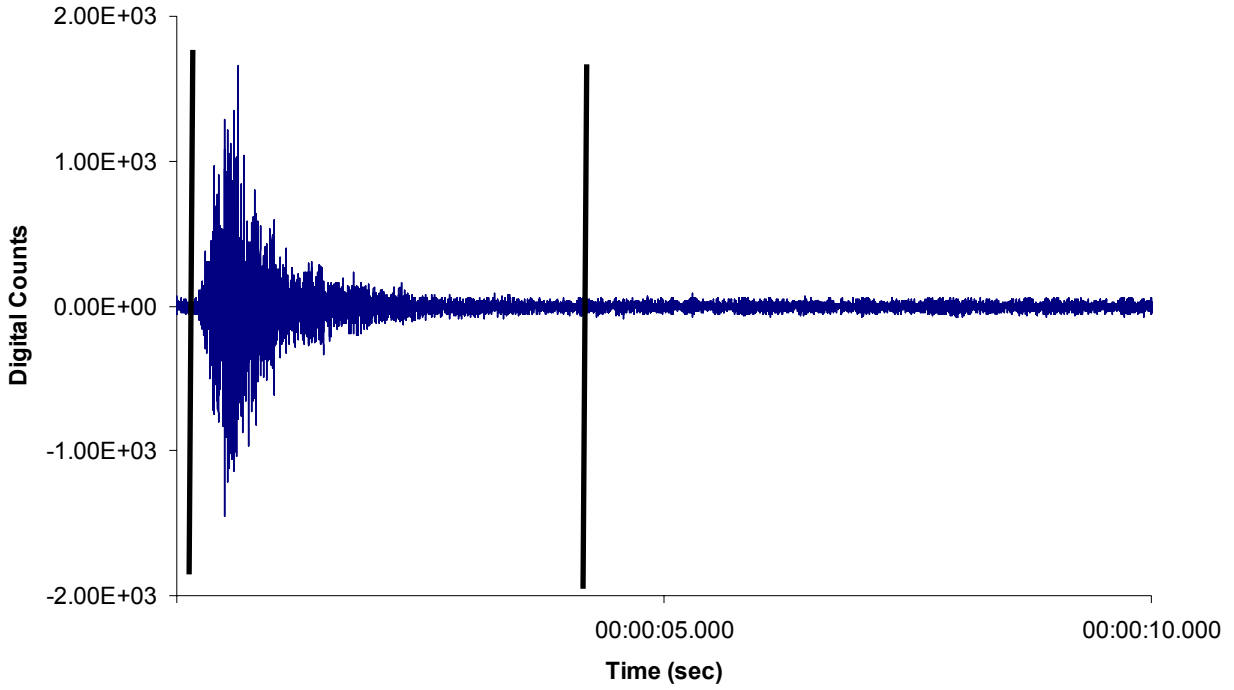


**Figure 4.7** – Representative waveform from Geophone 3 for mine shot #508. The two lines indicate the interval which determined the duration. The interval was believed to represent a long duration because of the confinement of the pressure wave, which is described in more detail in Section 6.6.

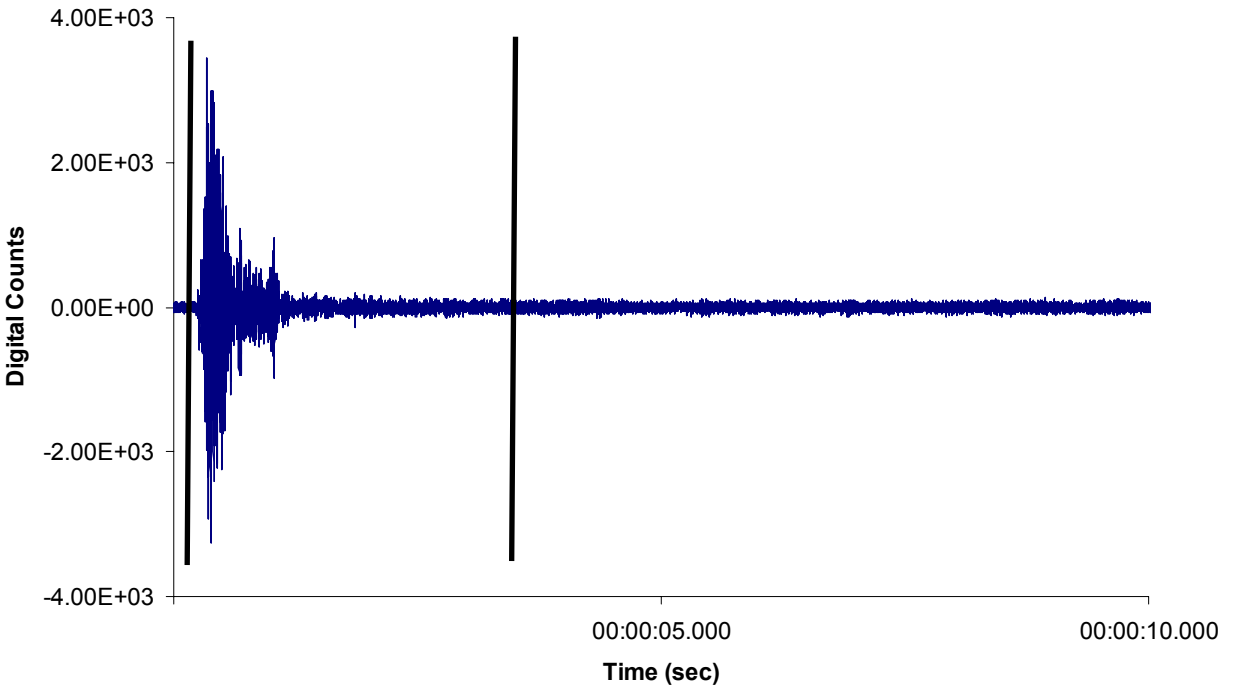


**Figure 4.8** – Representative waveform from Geophone 3 for mine shot #509. The two lines indicate the interval which determined the duration. Smaller events representing debris impacts are believed to be observed within the time interval indicated.

#### 4.3.3 Results and discussion for mine shots #510 – 519 and 521

Mine Shots #510 – 519 and 521 were conducted in A-Drift and no seals were in the propagation path of the pressure wave caused by the explosion. Representative waveforms from these shots are plotted in Appendix F. The experimental designs for these mine shots can be defined as an isolated system, meaning that structures in crosscuts between A- and B-Drifts caused the propagation path of the explosion to remain completely in A-Drift. Figure 4.9 is a simplified schematic of the experimental design demonstrating the propagation path for the explosion. As indicated in the figure, structures (dotted blue rectangles) and stoppings (dotted green rectangles) between A- and B-Drifts cause the pressure wave to be isolated within A-Drift.

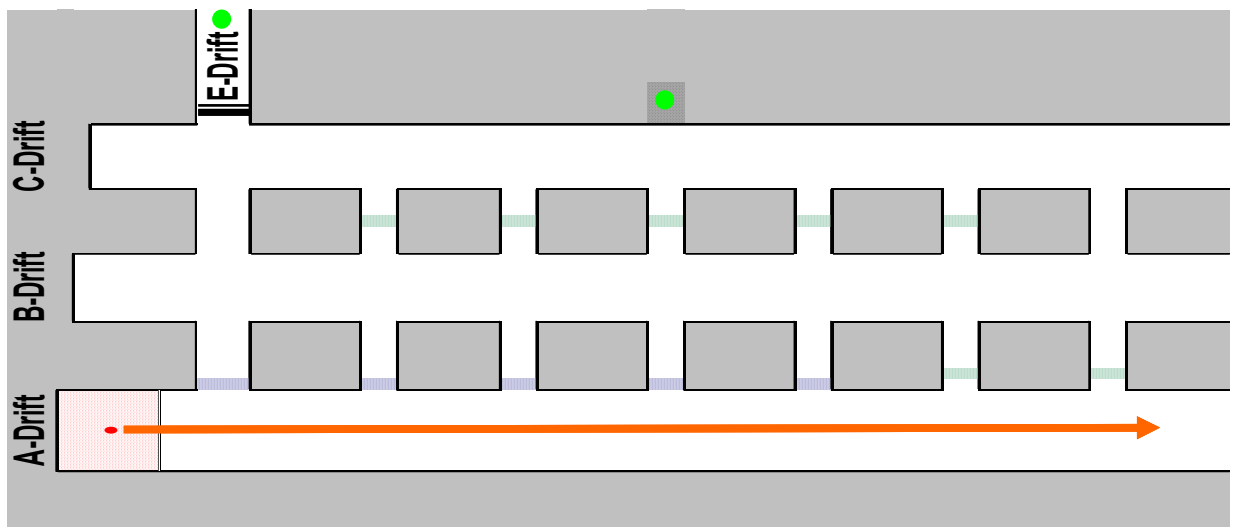


**Figure 4.9** – Simplified schematic of the experimental design for mine shots #510 – 519 and 521. The design indicates that that propagation path of the pressure wave is isolated within A-Drift. The green dots indicate the geophone locations within the bounds of the figure.

For mine shots #510 – 524, three geophones were located within 120 m, which were the closest geophones to the source. These instruments were Geophone 2, 4 and 6. Table 4.7 shows the average durations between these geophones and their standard deviation. The only outlier appears to be mine shot #519, which showed a duration estimate approximately twice as long as

the other mine shots. The reason why this duration appeared to be much larger is that the initial amount of fuel was significantly larger compared to the other shots and no limestone dust was used to dampen the explosion. The subsequent peak pressures generated for these two explosions were much larger than the others.

**Table 4.7** – Average durations from the closer geophones during mine shots #510– 519.

	<b>Mine Seal</b>	<b>Average Duration (sec)</b>	<b>Standard Deviation (sec)</b>
Mine Shot #510	No	1.92	0.17
Mine Shot #513	No	1.52	0.44
Mine Shot #514	No	2.02	0.10
Mine Shot #516	No	2.09	0.04
Mine Shot #517	No	1.91	0.05
Mine Shot #518	No	1.41	0.30
Mine Shot #519	No	4.55	0.12

Geophones located further away, specifically Geophones 3 and 5 located in D-Drift, showed durations which were in the same range, as reported in Table 4.8. These geophones, which are further beyond the near-field environment, are not affected by factors such as a large initial air-coupled surface wave associated with a larger explosion. Mine shot #521, which was not able to be observed on the closer geophones, showed the shortest duration of any methane and dust explosion with an average duration of 0.61 seconds. This explosion was very weak, in comparison to the others, as indicated by its maximum pressure value of approximately 2 psi, as reported in Figure B.16 in Appendix B.

**Table 4.8** – Average durations from the far away geophones during mine shots #510– 519 and 521.

	Mine Seal	Average Duration (sec)	Standard Deviation (sec)
Mine Shot #510	No	2.20	0.09
Mine Shot #513	No	1.93	0.05
Mine Shot #514	No	2.25	0.05
Mine Shot #516	No	2.06	0.08
Mine Shot #517	No	2.09	0.10
Mine Shot #518	No	1.85	0.10
Mine Shot #519	No	2.29	0.10
Mine Shot #521	No	0.61	0.01

#### 4.3.4 Results and discussion for mine shots #520 and 522

Mine shots #520 and 522 were experimentally different than the previously described tests conducted in A-Drift. During these shots, the stoppings at crosscuts X6 and X7 between A- and B-Drifts were removed, allowing the pressure wave of the explosion to propagate into B- and C-Drifts. A schematic of this experimental design is shown in Figure 4.10, with arrows indicating possible paths that the pressure wave could take.

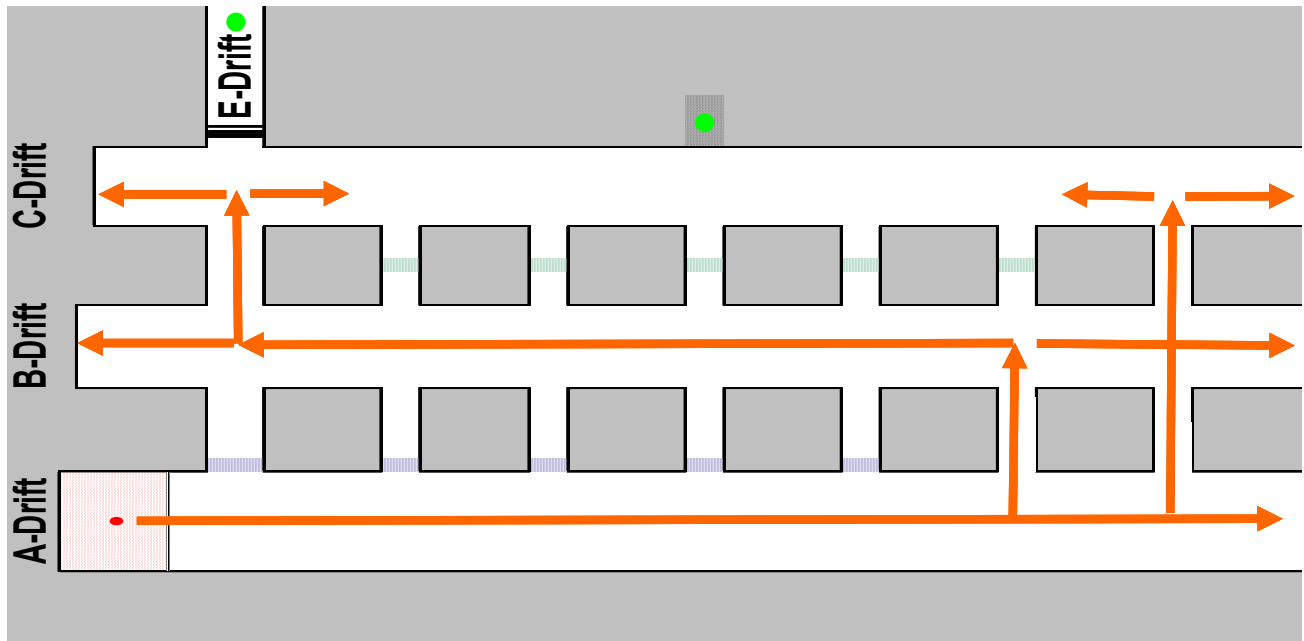


**Figure 4.10** – Schematic of the experimental design for mine shots #520 and 522. The design indicates that that propagation path of the pressure wave was allowed to enter into B- and C-Drifts. The green dots indicate the geophone locations within the bounds of the figure.



The experimental design causes a more complex scenario than the previous experiments conducted in A-Drift. The signatures observed from the closer geophones, located in the C-Drift instrument room and E-Drift, appeared to be affected by interactions of the pressure wave entering into the B- and C-Drifts. Table 4.9 indicates the average duration of the signatures observed from these geophones for the two mine shots. These durations are significantly longer than what was previously observed. The seismicity of the methane and dust explosion could not be differentiated from the seismicity of the pressure wave interacting with the ribs and mine structures as it entered into B- and C-Drifts. An example of the complexity of the signature can be viewed in Figure 4.11. Not enough data were available to compile significant findings for the further away geophones in D-Drift.

**Table 4.9** – Average durations for the closer geophones during mine shots #520 and 522.

	<b>Mine Seal</b>	<b>Average Duration (sec)</b>	<b>Standard Deviation (sec)</b>
Mine Shot #520	No	3.72	0.25
Mine Shot #522	No	5.41	0.32

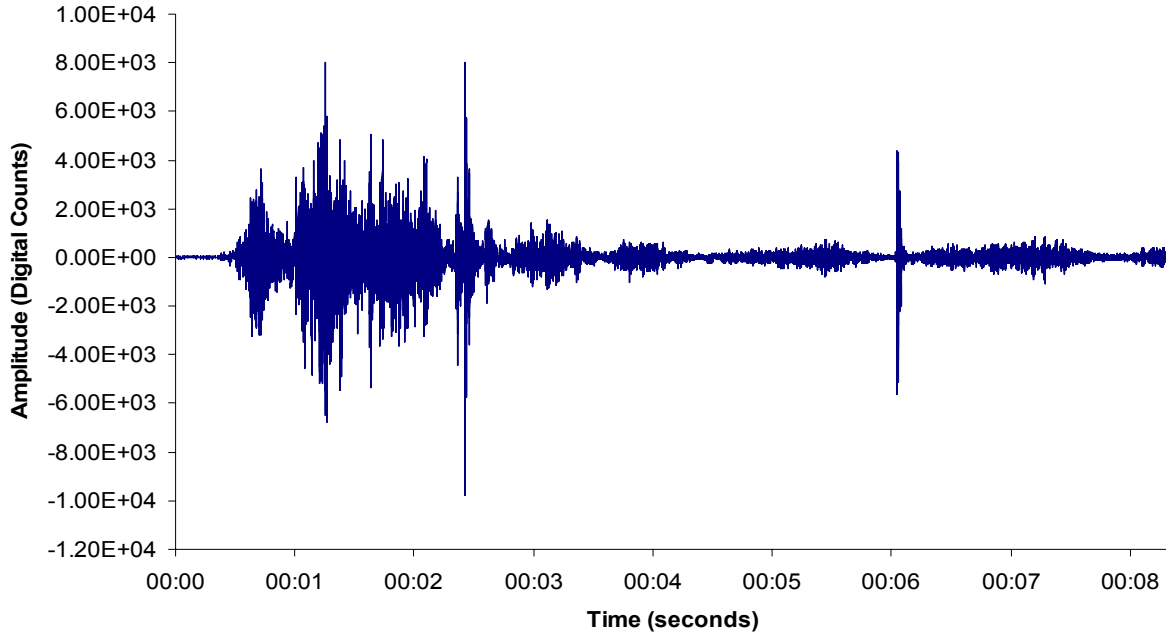


**Figure 4.11** – Example of a seismic signature collected during mine shot #522 by Geophone 2. The signature appears to contain multiple reflections as a result of the pressure wave from the methane and dust explosion entering into B- and C-Drifts.

Mine shots #523 and 524 were the only experiments conducted in A-Drift where a seal was in the direct path of the pressure wave. In both cases, the seal was able to withstand the pressure wave. Seismic data from the ISS system was only available from the geophones located far away from the source in D-Drift. Compared to the durations observed for tests without seals, the effect of the seal placement in the middle of the entry appears to have a direct effect on the duration of the seismic signature (Table 4.10). In Chapter 6, a more in depth study between the geophones in the mine and surface instrument outside the mine compares the durations of the low-frequency content.

**Table 4.10** – Average durations for the closer geophones during mine shots #523 and 524.

	<b>Mine Seal</b>	<b>Average Duration (sec)</b>	<b>Standard Deviation (sec)</b>
Mine Shot #523	Yes	3.62	0.26
Mine Shot #524	Yes	3.08	0.03

# Chapter 5 – Velocity Analysis of the Seismic Signatures

In Chapter 5, the apparent velocities of the seismic waves arriving at geophones located at different distances were studied. By investigating the first break in the signatures for each geophone, more understanding of the types of seismic waves generated initially during the methane and dust explosions is made.

## 5.1 Method of analysis

The first arrivals of the signatures from each test collected at LLEM were analyzed. As explained in Section 3.2.2, the seismic system is trigger-based and requires ground movement exceeding certain pre-set threshold values in order to start recording data. Also, a limitation is each geophone requires its own trigger in order to record an event. This means that if one geophone is triggered, the other geophones will not automatically start sending data back to the central computer. Since each geophone requires its own individual trigger to record data, the signatures contained in a particular event have different initial starting times. For example, the time 12:34:56.3032 on one signature is the same on another signature, but in a different location on the x-axis since the time zeroes are not the same. The initial trigger times for each signature can be used as a “first arrival” time. This is assumed to be correct because the system saves the time that ground movement exceeded the threshold at a particular geophone, therefore representing the time of the first arrival. The only problem with this method is a geophone located at a different location could have a first arrival which represents a different phase of the

signature (i.e. surface wave versus P-wave). This is a limitation of the instrumentation used and cannot be avoided.

In order to associate all the trigger times from different geophones for a single event, a reference time is created and made to occur before the time of the first trigger. The arrival times are then calculated from the reference point and trigger time for each geophone. Although the first geophone might have an invalid arrival time of 1.4 seconds after the event was generated, the difference in arrival times between each successive geophone will be correct. For each event, the arrival time and distance away from the source was plotted against each other. A regression line through the data points was plotted and the slope represents the apparent seismic wave velocity. An example of one of these plots is shown Figure 5.1. In Figure 5.1, it is shown that the average velocity of the seismic wave, based upon the first break of each signature from mine shot #508, is 2,769 m/s (9,085 ft/sec) with a correlation coefficient value of 0.98.

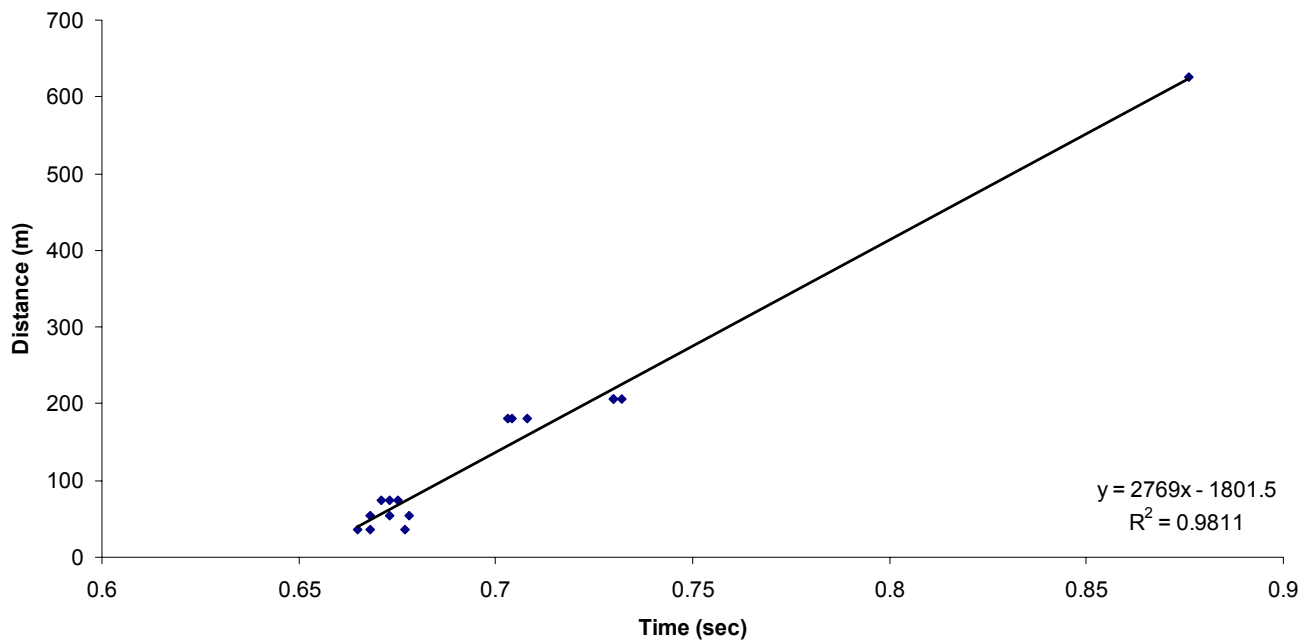


Figure 5.1 – Distance-time plot for mine shot #508.

Whether or not seals were included in the experiment does not matter for these calculations since only the first break of the waveform was being studied. The first break is always assumed to represent the seismic energy emanating from the initial ignition of the explosion. The only problem with the assumption is if during experiments where there is a mine seal in the entry, the initial explosion does not produce seismic energy. In this scenario, the first break in the signature could represent interactions of the explosive pressure wave and mine seal which seems unlikely. Based upon tests without mine seals in the entry, it was found that the initial explosion produces significant seismic energy that can be recorded by the geophone and the assumption is valid.

Since the geophones are very close to the source for this study compared to standard seismic assessments made kilometers away, the phases of the seismic signature, in most cases, did not have adequate time to separate. This means that if the P-, S- and surface waves are all present in the seismic signature being analyzed, they are only separated by time intervals under one second and in some cases by only milliseconds. Very few measurements were able to be made far away from the source (over 600 m); however, in one instance where measurements were taken far away, a distinct separation between two phases in the signature can be viewed Figure 5.2.

The two phases are believed to be the seismic energy due to the explosion and the acoustic air blast represented by an air-coupled Rayleigh wave, respectively. In order to further establish the phases of these two arrivals, the velocities based upon the arrival times were evaluated. Knowing the seismic velocities determined from the drop tests and difference in arrival times between the two phase arrivals, a velocity can be found for the second arrival. The velocity of the second phase arrival was found to be approximately 320 m/s (1,050 ft/sec),

consistent with the speed of sound of air. The speed of sound in air is a function of temperature, which for the mine (at 55° F) would be approximately 340 m/s (1,100 ft/sec), sufficiently close to validate the second phase as the acoustic air blast. It is expected that much closer to the ignition of the explosions, the waveforms are likely to represent a combination of the acoustic and seismic energy; however, the clear distinction, as shown in Figure 5.2, won't be observed. Other considerations such as the influence of the raypath on the detected phases were not taken into account during this analysis. It was assumed that the seismic activity detected at the geophones included raypaths that traveled strictly through the limestone, meaning the shale/claystone layer 14 ft into the roof was not considered to affect the signatures. Thus, the detected seismic velocities found during the study were considered apparent velocity measurements.

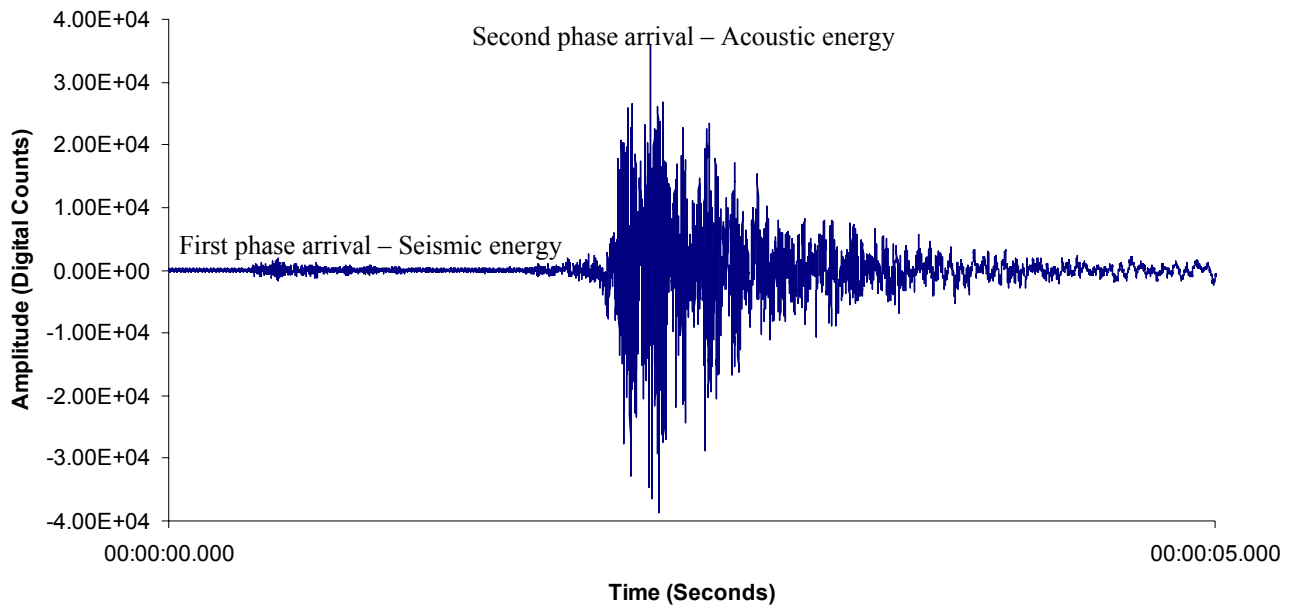


**Figure 5.2** – Waveform from far away geophone which shows two distinct phase arrivals.

## 5.2 Results and discussion from mine shots #503 – 524

The distance-time plots for the other methane and dust explosions (mine shots #505 – 520) are reported in Appendix G. Distance-time plots were created for mine shots which had a minimum of three geophones triggered. During some mine shots, Geophone 4 was located on a cement block attached to the mine roof. Since the seismic wave had to cross a boundary layer from the rock into the cement block, the geophone was triggered late. Data points from Geophone 4 were removed from the distance-time plots during these mine shots. With all the average apparent velocities found, a histogram was created to see the highest frequency of values as shown in Figure 5.3. The histogram represents bimodal distribution. It can be observed that the main distributions are centered at 475 m/s and 2,430 m/s. The bins for the generation of the histogram were setup at 500 m/s intervals. Based the bimodal distribution in the histogram, it appears that for some tests the first arrival represents a surface wave and in other cases the first arrival represents a body wave.

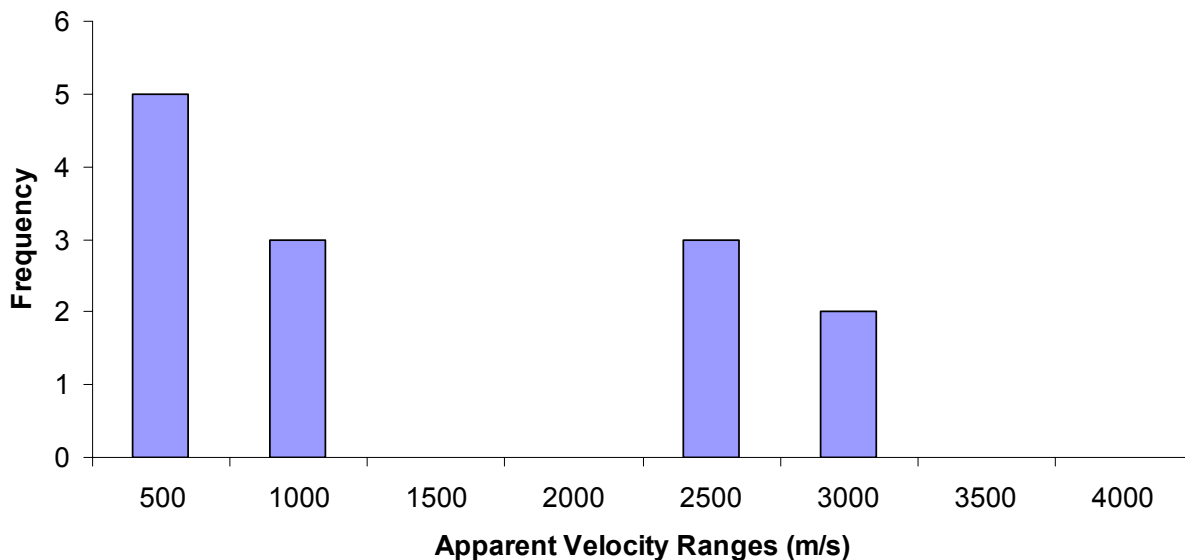


Figure 5.3 – Histogram of apparent average velocities based upon arrival times calculated from the mine shots.

In order to study the reason for different average velocities, the experimental design parameters of the explosions were evaluated, as shown in Table 5.1. It was believed that the size of the explosion had an impact on the types of seismic waves recorded, as suggested in the literature review when Johnston (1987) reported that some seismic records can lack P- and S-waves because most of the seismic energy will be dissipated in the atmosphere and not transferred into the ground. The initial energy of each explosion is shown in column in Table 5.1. The initial energy is defined as the amount of methane gas and coal dust for each experiment converted to an equivalent measure of energy. A more complete discussion on how the initial energy was calculated is reported at the beginning of Chapter 7. A plot of seismic wave velocity versus initial energy is shown in Figure 5.4.

**Table 5.1** – Summary of initial energy, pressure from inside of the ignition chamber and the resulting average apparent velocities based upon the first arrival in the signature found for mine shots #505-520.

<b>Shot #</b>	<b>Initial Energy (MJ)</b>	<b>Pressure (psi)</b>	<b>Velocity (m/s)</b>	<b>Velocity (ft/s)</b>
505	710	32.46	2,102	6,896
506	799	46.12	2,725	8,939
507	710	26.10	2,475	8,120
508	710	21.78	2,769	9,085
509	1525	44.40	2,073	6,801
510	511	14.00	688	2,258
513	511	13.58	286	940
514	511	14.18	413	1,354
516	511	12.74	341	1,120
517	511	13.08	368	1,208
518	511	12.99	337	1,107
519	1085	23.69	825	2,706
520	511	14.71	552	1,810
<b>AVG</b>			1,227	4,026
<b>STDev</b>			1,018	3,339



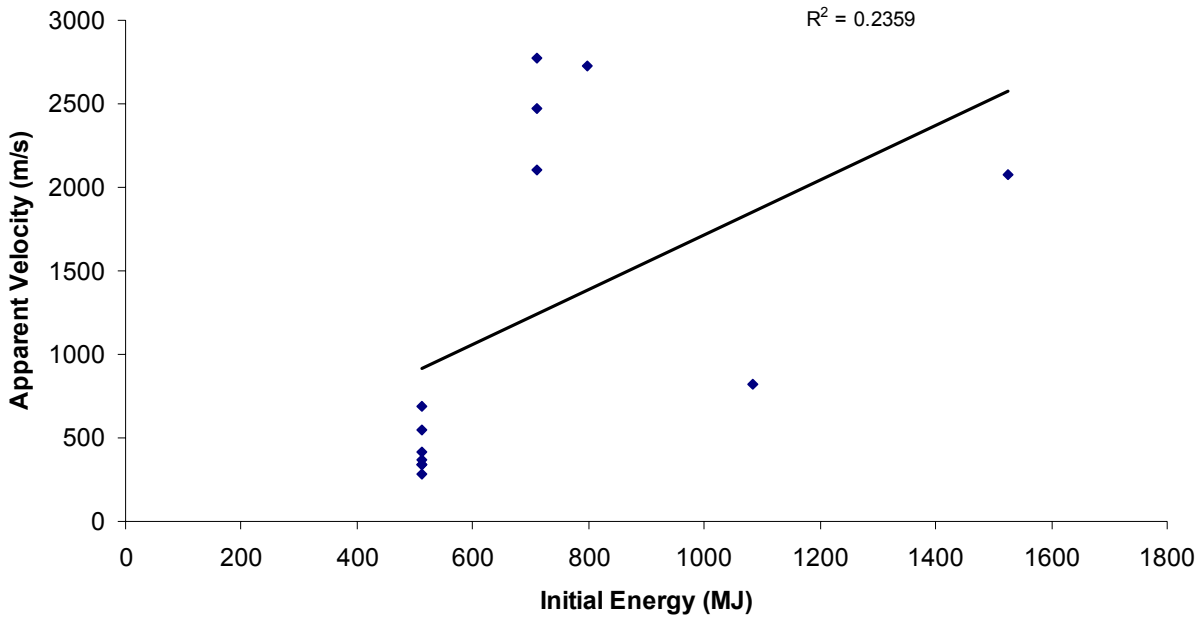


**Figure 5.4** – Plot of apparent seismic wave velocity versus initial energy for mine shots #505-520.

An overall trend cannot be made from the results in Figure 5.4. The coal dust added to the explosive energy outside of the initial ignition zone, the initial pressure expansion inside of the ignition zone caused the initial seismic waves to be produced during each test. Another factor which cannot be attributed in the initial energy is the placement of the electric matches which is a significant characteristic that determines the size of the explosion. With the same amount of methane gas, matches sparked closer to the mine face will result in a slightly larger explosion because it is more confined compared to the case where the matches are sparked in the middle of the ignition zone. If the apparent seismic velocity versus the amount of initial methane were to be plotted, the results would not be completely representative of the size of the explosion (similar to Figure 5.4).

A pressure transducer was located inside of the ignition chamber (for both series of mine shots conducted in A- and C-Drifts), to measure the initial pressure generated by the methane explosion. The advantage of using the maximum pressure from inside the ignition chamber is

that it does not take into account the coal dust outside of the chamber and the values are affected by the placement of the electrical matches. Therefore, the initial size of the explosion, in terms of peak pressure generated, is not affected by the mine seal or enhancement by the coal dust. The values of initial pressures inside of the ignition chamber are reported in Table 5.1. In some cases, the maximum pressure measured from the pressure transducer in the ignition chamber was considered questionable from the mine supervisor. In these cases, the next closest pressure transducer down the drift was used.

A plot of apparent seismic wave velocity versus pressure from inside of the ignition zone is shown in Figure 5.5. The surface wave velocity value is shown as a red line. The surface wave velocity can be similar to the speed of sound in air for an air-coupled Raleigh wave, as discussed in the literature review. The speed of sound in air is a function of temperature, which for the mine (at 55° F) would be approximately 340 m/s (1,100 ft/sec). The S-wave velocity range was obtained from the rock drop tests discussion in Section 3.4.4. The standard deviation calculated from the rock drop test, as reported in Table 3.2, defined the bounds of the S-wave velocity range.

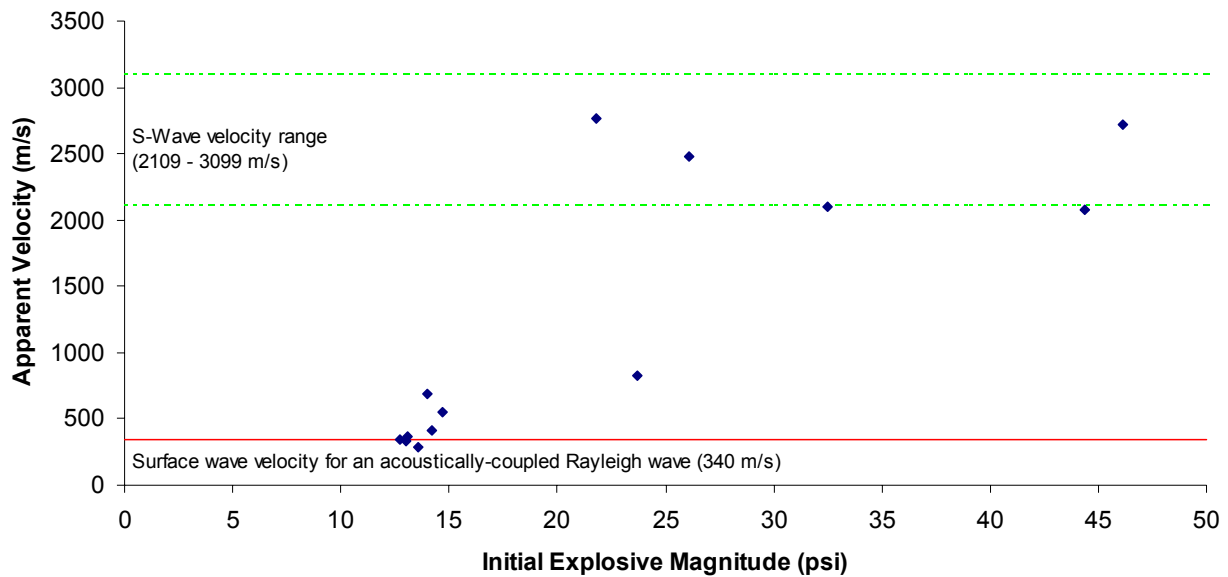


**Figure 5.5** – Plot of apparent seismic wave velocity versus pressure from inside the ignition zone for mine shots #505-520.

It is interpreted from Figure 5.5 that both body waves and surface waves were generated by the methane and dust explosions, however certain factors affect what wave types were observed by the geophones. A trend can be observed from Figure 5.5 where, for the most part, acoustically-coupled Rayleigh waves were observed for explosions produced under 20 psi and S-waves were obtained for explosions produced above 20 psi. With this observation, it appears that the size of the explosion affects the first seismic wave type detected at the geophones. With the larger explosions above 20 psi, the initial pressure wave transmitted a large enough S-wave to be captured by geophones at different distances away from the source instead of having this energy dissipated into the atmosphere or attenuated into the background noise. The smaller explosions, below 20 psi, had a consistent average velocity close to the speed of sound. This observation also indicates that the size of the explosion influences the efficient transmission of different seismic waves into the rock.

There is one outlier in Figure 5.5 which is the data point represented by mine shot #519. For this test an average seismic wave velocity of 825 m/s (2,706 ft/sec) was observed for an explosion having an initial pressure of 23.69 psi. This particular velocity is in between the average value for the surface wave and S-wave velocity. Therefore, it was speculated that another factor, which affects the types of waves observed, is responsible for this disparity. Mine shots #507 and 508 had initial pressures in the same range as mine shot #519; however, #519 had average values in the S-wave velocity range. Mine shots #507 and 508 were much closer to the geophones than #519. Therefore, it may be possible that all types of seismic waves are produced for each explosion but some are not observed because they were too small in amplitude to rise above the background noise.

Particle motion diagrams were looked into to verify the speculation that an air-coupled Rayleigh wave was observed in cases where the apparent velocity indicated only surface waves moving at the speed of sound in air were detected. A sample particle motion diagram can be seen in Figure 5.6 taken from mine shot #518. The particle motion indicates a retrograde motion, as discussed in Section 2.5 as a characteristic of the surface wave. The motion is slightly skewed because the receiver was not in direct line with the source. Similar results were seen from the other mine shots where the surface wave was determined from the apparent velocities.

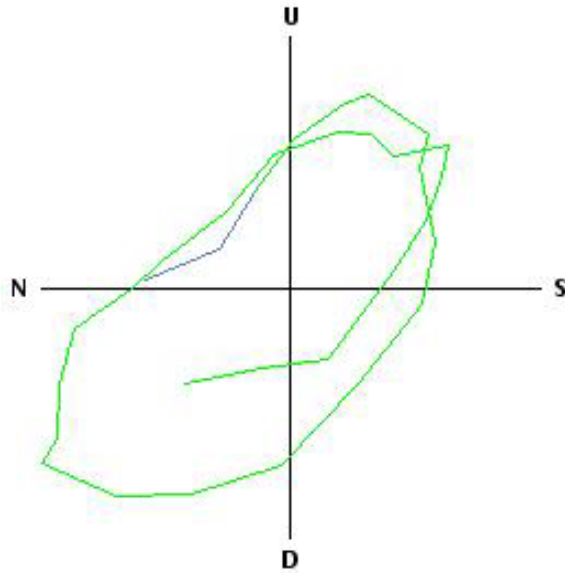


**Figure 5.6** – Sample particle motion diagram for mine shot #518.

### **5.3 Results and discussion from mine shots #528 – 540**

The average apparent velocities observed from the cast booster detonations supports the hypothesis that all types of seismic waves can be produced initially; however, the distance from the source is a significant factor determining the type of seismic wave first observed. The advantage of studying this dataset is the same sized cast booster was used for each test and the testing location for each shot varied. Therefore, the distance between the source and receiver was constantly changing as the size of the source remained the same. Table 5.2 shows the average velocities found from the cast booster experiments. The final two cast booster experiments (mine shots #539 and 540) were not included in the results because only two geophones were triggered. The distance-time plots which were used to find the average velocities are shown in Appendix G. A visual plot of average velocity versus mine shot number is reported in Figure 5.7.

**Table 5.2** – Summary of average apparent velocities based upon the first arrival in the signature found for the cast booster experiments (mine shots #528-538).

Shot #	Velocity (m/s)	Velocity (ft/s)
528	2,258	7,406
529	2,252	7,390
530	2,877	9,439
531	4,223	13,855
532	3,462	11,359
533	2,333	7,655
534	2,676	8,780
535	2,515	8,251
536	2,194	7,199
537	2,697	8,850
538	2,885	9,466
<b>AVG</b>	2,761	9,059
<b>STDev</b>	612	2,008

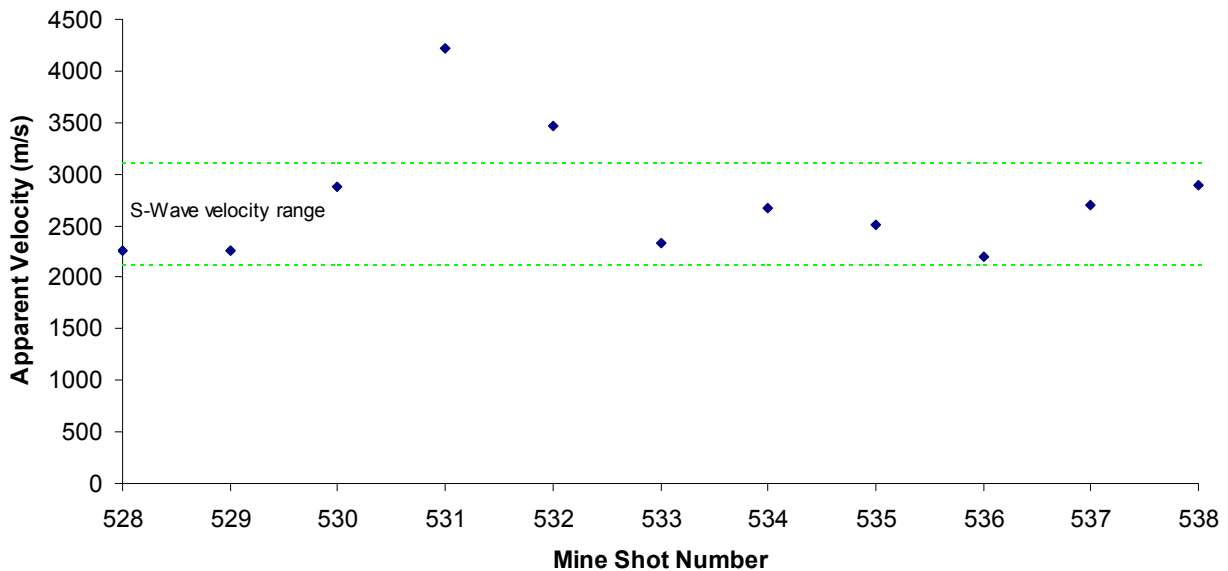


**Figure 5.7** – Plot of apparent seismic wave velocity for the cast booster experiments (mine shots #528-538).

Except for two of the cast booster tests, all the data were within the range of the S-wave velocity. If these two tests were removed from Table 5.2, the average velocity is found to be 2,521 m/s (8,271 m/s) with a standard deviation of 273 m/s (879 ft/sec). This velocity range is similar to the results reported in the rock drop tests summarized in Table 3.2, meaning the two

limestone formations (floor of the old workings versus roof of the entries) have comparable seismic velocity values for P- and S-waves, an assumption which was made earlier.

The two cast booster detonations which yielded seismic velocities outside of the S-wave velocity range were mine shots #531 and 532. The location of these two mine shots were the closest experiments to Geophone 2 with a source to receiver distance of 42 m (138 ft). It is believed that Geophone 2 was able to capture a very small amplitude signal in the waveform associated with the P-wave arrival. An example of this arrival is shown in Figure 5.8, which had to be magnified heavily to see the first break. The other geophones, which did not see the arrival of the P-wave because it attenuated quickly, captured the S-wave as the first arrival. Therefore, the average apparent seismic velocity for mine shots #531 and 532 was found in between expected values of the P- and S-waves, which makes sense because different phases were captured between the close versus further away geophones. However, it must be kept in mind that these are apparent velocity measurements made based off of the first breaks in the waveforms. Due to the proximity of the receiver to the source, the signatures are very complex since the geophones capture a variety of phase arrivals that cannot be separated apart.

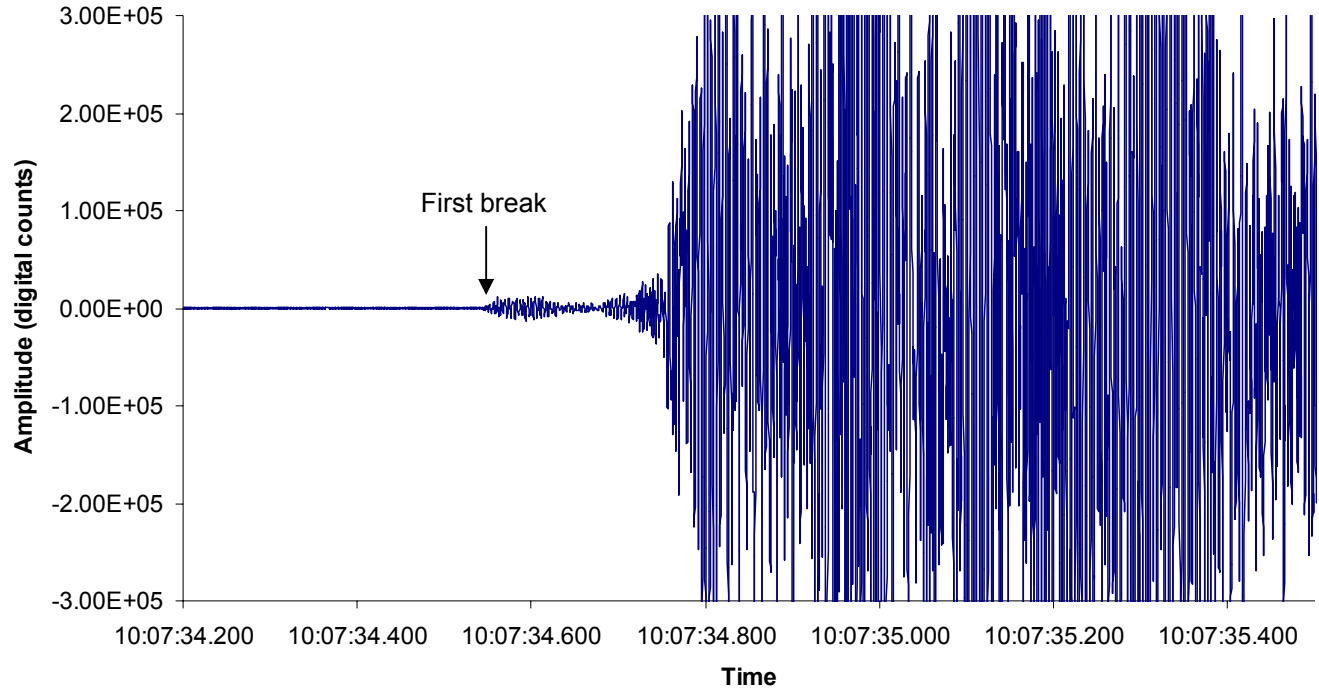


**Figure 5.8** – Waveform from Geophone 2 (vertical component) for mine shot #531 which shows the first break in the signature believed to be the arrival of the P-wave according to the apparent velocity calculated. The signature had to be zoomed significantly to observe the arrival.

For comparison, an example of the first break during an experiment where the average seismic velocity found was well within the S-wave velocity is shown in Figure 5.9. The P-wave during these experiments, although captured in two instances where the source is close to the receiver, is believed to be generated however very weak and attenuated quickly. These results show that it is possible P- and S-waves are generated during the explosion tests, however they are initially weak and never rise out of the background noise or attenuate into the background noise before they reach the receiver.



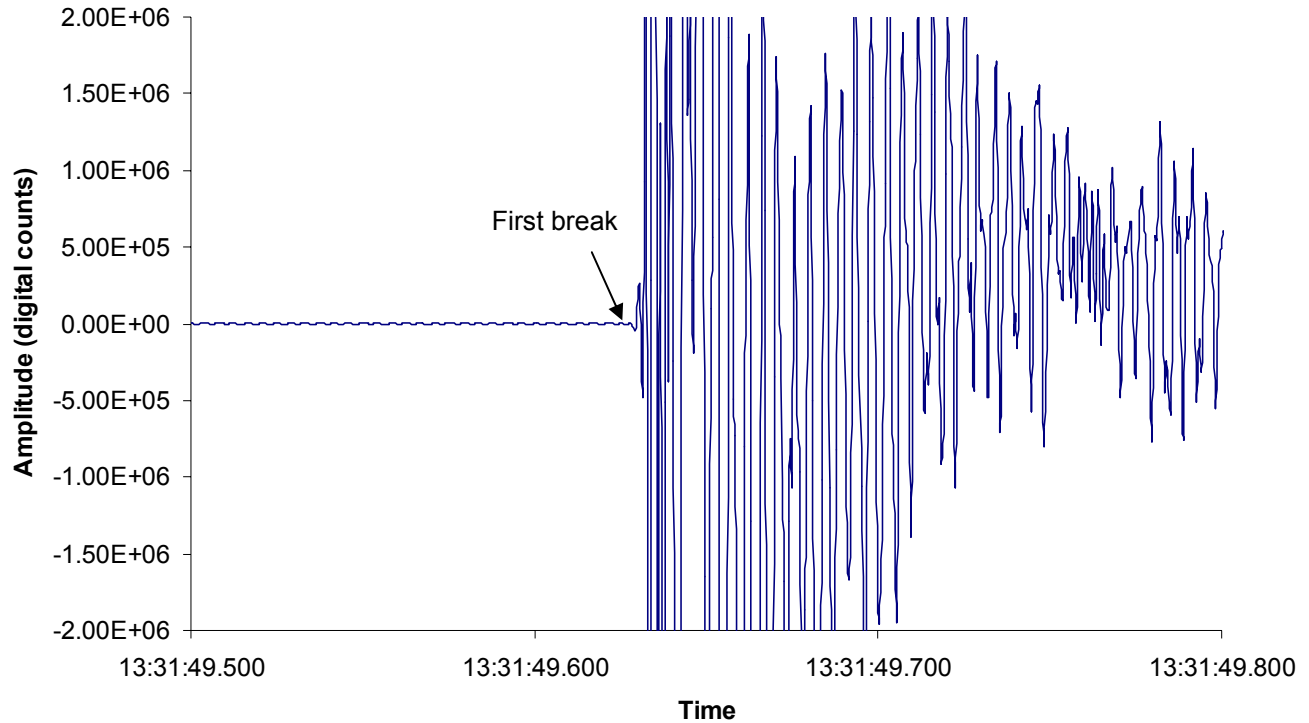


**Figure 5.9** – Waveform from Geophone 2 (vertical component) for mine shot #528 which shows the first break in the signature believed to be the arrival of the S-wave according to the apparent velocity calculated.

While most of the correlation coefficients for the distance-time plots had values above 0.95, a final comment should be mentioned on the plots with poor correlation coefficients. An example of this is shown in Figure G.15 (reported in Appendix G) for mine shot #530 which had a correlation coefficient of 0.51. In these cases, the poor fits are associated with noisy data where the first breaks in the seismic signature were not as easy to observe. An example of this is shown in Figure 5.10, which is a signature from Geophone 3 from mine shot #530. It can be observed that there is no clean first break for this signature, unlike the signature shown in Figure 5.9. The arrows in the signature indicate the first breaks which were considered to be the arrival time of the seismic wave while analyzing the signature. Arrival times were picked in a consistent manner, using similar features which stood out when trying to observe them in noisy data. In Figure 5.10, the red arrow indicates the arrival time which was used in the data analysis.

If several picks could be made that were within a very small time interval, similar features observed from signatures assisted in making the eventual pick. In these scenarios, the picks were never adjusted to obtain a better correlation coefficient value. Despite some poor fits in the distance-time plots, the slope in the trend line still resulted in a reasonable calculated seismic wave velocity.

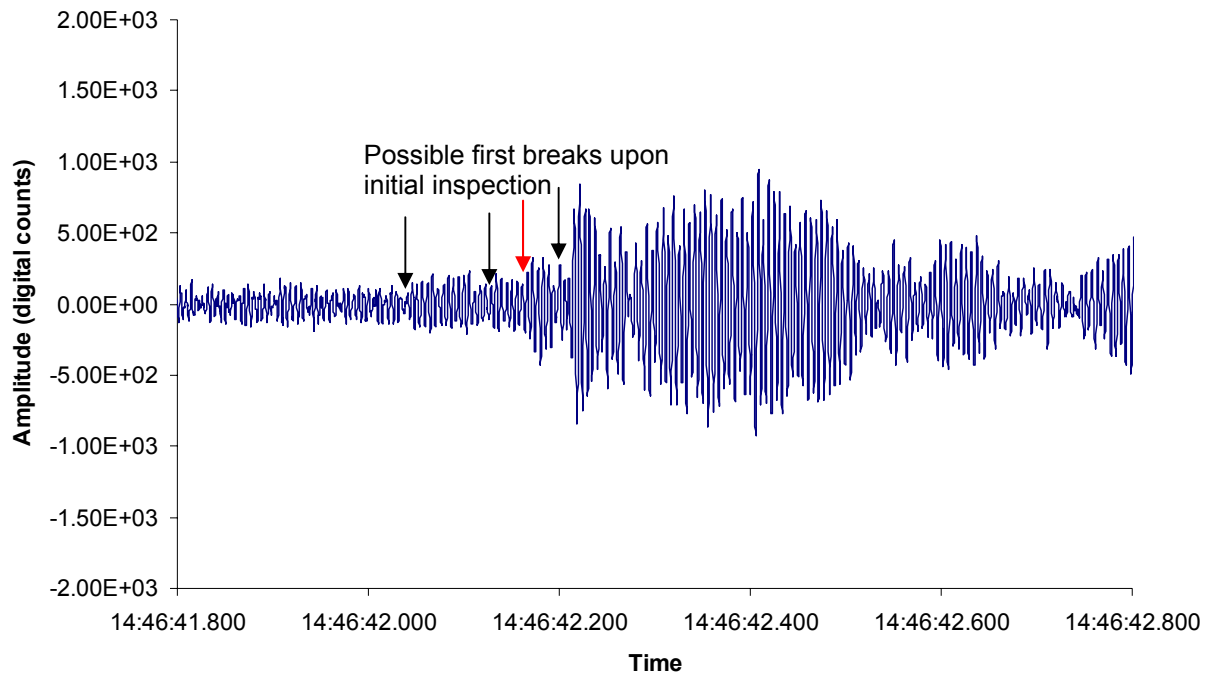


**Figure 5.10** – Waveform from Geophone 3 (horizontal component perpendicular to the drifts) for mine shot #530 which shows an instance where the first break of the signature was difficult to observe. The black arrows indicate the assumptions on where the arrival of the seismic wave is located. The red arrow indicates the location where the arrival time was eventually picked.

# Chapter 6 – Frequency Analysis of the Seismic Signatures

The dominant frequencies of a seismic signature can give information on the seismic source. In Chapter 6, the frequency content of the seismic signatures is analyzed in order to determine the impact of the varying experimental designs. Results from the determination of the natural frequency of a mine structure and the impact of the confinement of an explosion are also presented.

## 6.1 – Method of analysis

In order to study the frequency content of the signatures collected during the study, the LabVIEW program, described in Appendix E, was utilized. The program can create an FFT over the whole signature, or a selected part of the signature. An example FFT is shown in Figure 6.1 from Geophone 3 and mine shot #507. It can be observed that very low-frequency is detected below 50 Hz and a dominant frequency spike can be detected between 170 – 180 Hz. All the signatures were analyzed in this method and dominant frequencies were noted to observe any differences between the different mine explosions. In cases of noisy data, a background noise window was analyzed and compared with the event window of the seismic signature. Signal levels from noise were also noted.

First, analysis was conducted on mine shots #528 – 540, which were the series of cast booster detonations. An analysis of the geophone attached to a mine structure in a crosscut is presented and followed by an analysis of the frequencies observed from the other geophones monitoring the cast booster detonations. After determination of the potential frequency ranges

that are associated with a mine structure, frequency content is analyzed for mine shots #507 – 524 to search for any correlation with the varying experimental designs associated with the tests. A final section presents a significant finding from the evaluation of low-frequency signal from the explosions that were confined within a sealed area. It should be noted that certain frequencies are reported outside of the geophone’s range provided by the manufacturer (Section 3.3.1). It was assumed that the response after 90 Hz for the geophone was constant.

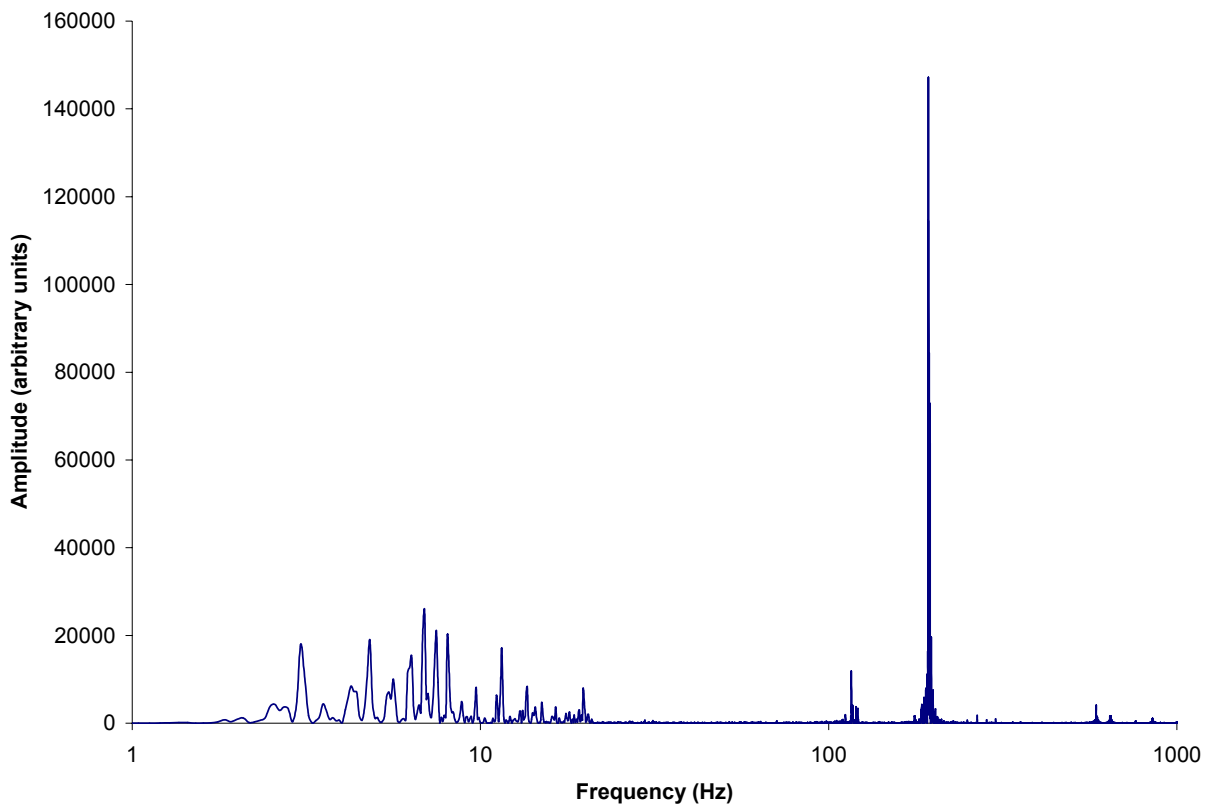


Figure 6.1 – Sample FFT from Geophone 3 during mine shot #507.

## 6.2 – Results and discussion from the analysis of a mine structure during mine shots #528 – 540

Cast boosters were used as a seismic source in A-Drift to provide some degree of control in the experiments to facilitate assessing the impact of the seal response on the seismic

signatures. A geophone was attached to a mine structure located in crosscut 1 between A- and B-Drifts. The cast boosters were detonated at different locations within A-Drift. A more detailed review of the experimental design and the structure is reported in Section 3.4.3.

Figure 6.2 shows the frequency response of the structure when a cast booster was detonated approximately 100 ft down the entry from the structure near the A-Drift face (mine shot #530). Channel 2, is oriented perpendicular to drift and the structure, should see most vibration on this channel since it is “fixed” in the orientations of Channel 1 and 3.

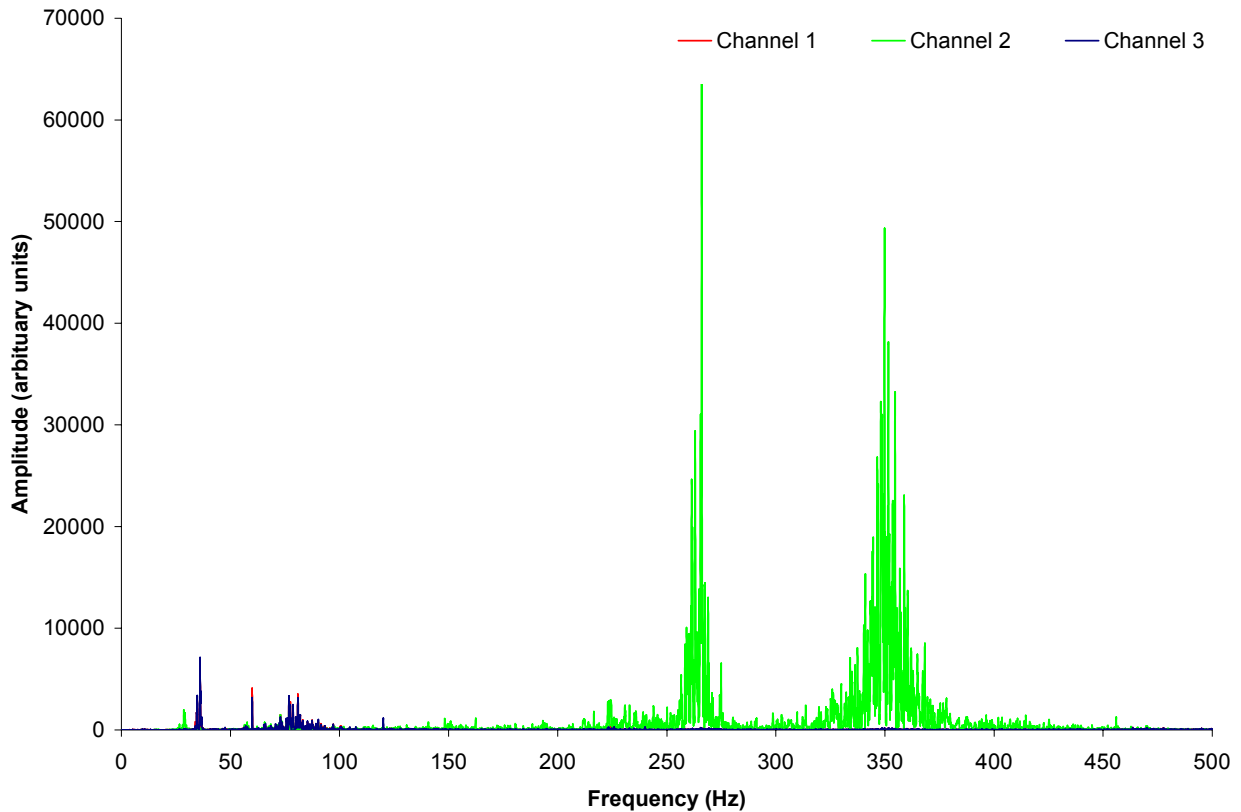


**Figure 6.2** – FFT from the geophone attached to a mine structure during mine shot #530.

The cast booster detonation excited two dominant frequencies within the structure, which are centered around 265 and 350 Hz. The exact ranges are between 255 – 275 Hz and

340 – 375 Hz. Trials were completed at distances of 50 ft and 25 ft inby the structure and the same frequencies were excited. Next, data obtained from cast boosters detonated directly in front of the structure were analyzed. Figures 6.3 and 6.4 shows the frequency response of the structure when a cast booster is set off 10 ft (mine shot #529) and 20 ft (mine shot #533) directly in front of the structure.

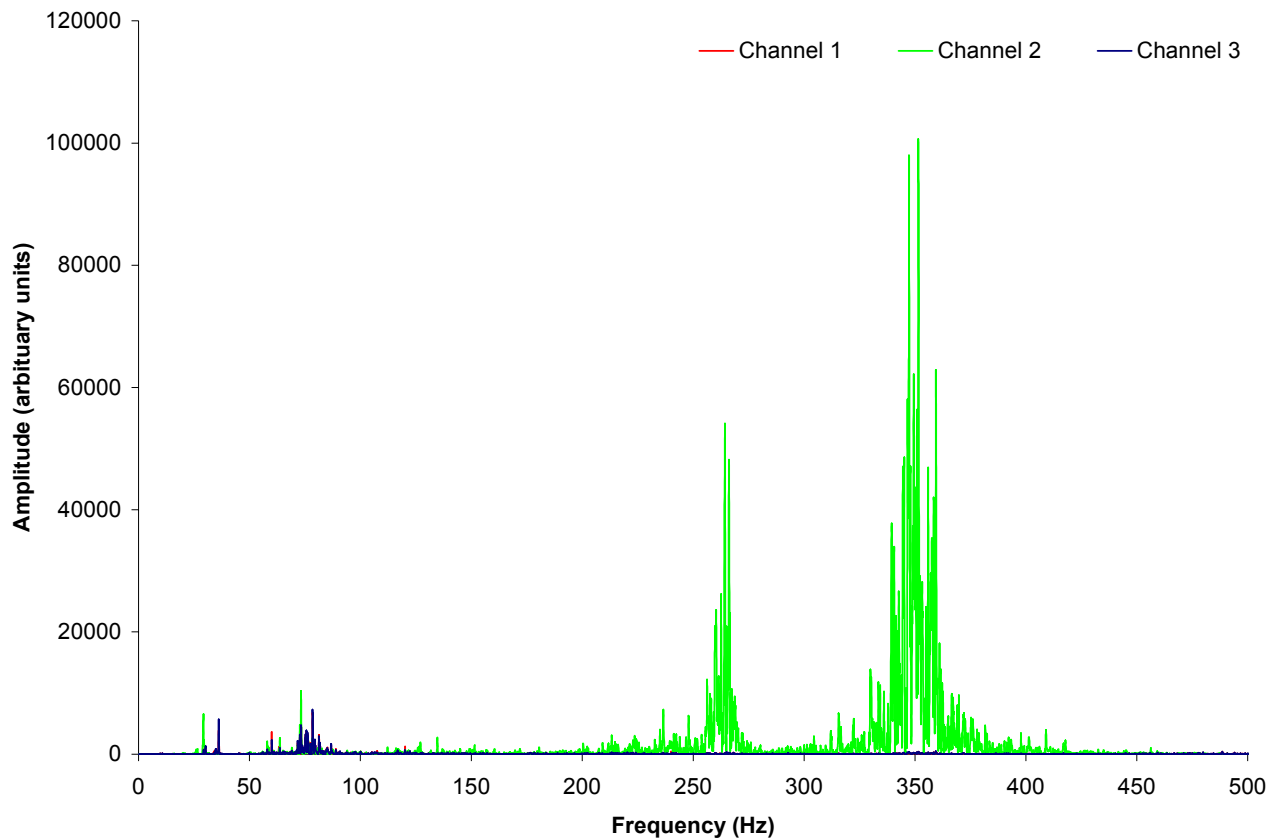


**Figure 6.3** – FFT from the geophone attached to a mine structure during mine shot #529.

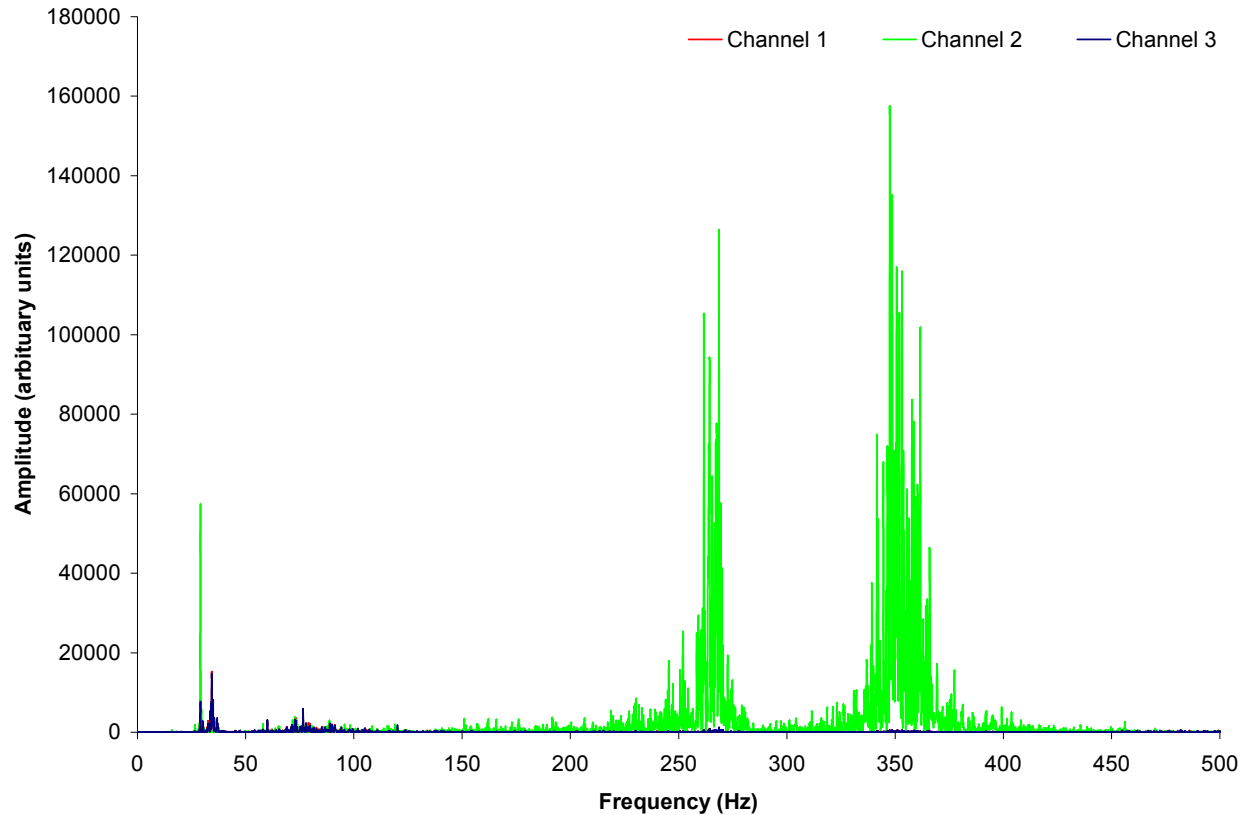


**Figure 6.4** – FFT from the geophone attached to a mine structure during mine shot #533.

When the cast boosters were detonated approximately 10 ft away from the mine structure, peak frequencies centered around 265 and 350 Hz can be observed again. When the detonation location is 10 ft in front of the seal, a 30 Hz spike can be observed in the signature. The frequency spike can be observed on the other FFT's, however is more predominant for a closer proximity to the structure. The last set of detonation locations were very far away from the structure at distances of 285 ft and 705 ft outby crosscut 1. An FFT is shown in Figure 6.5 for mine shot #540, when the detonation location was 705 ft outby the mine seal.

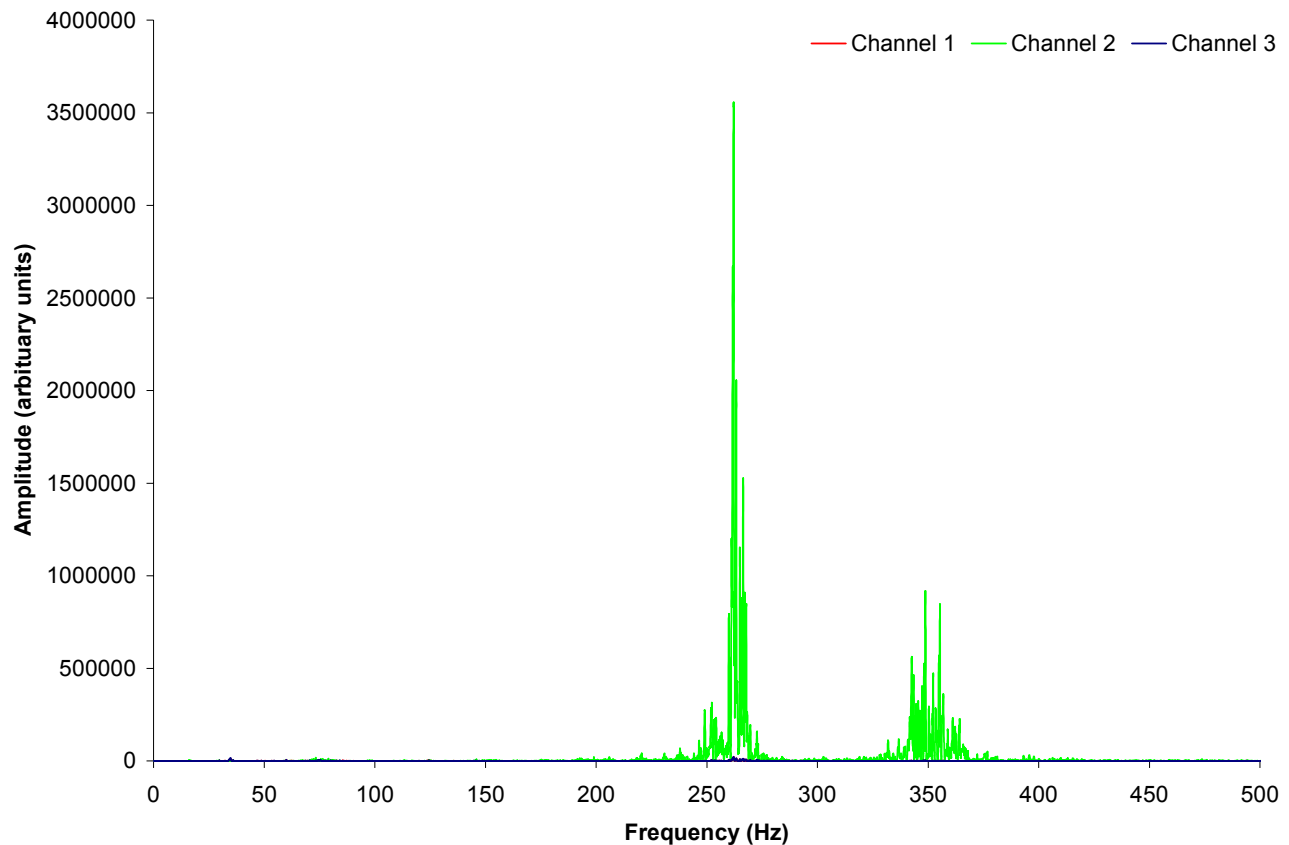


**Figure 6.5** – FFT from the geophone attached to a mine structure during mine shot #540.

When the detonation location was down the drift far away from the mine seal, the peak frequencies centered around 265 and 350 Hz were still observed. However, as expected, a dominant peak frequency around 30 Hz was not observed since the cast booster was located much further away than before.

The frequency ranges of 255 – 275 Hz and 340 – 375 Hz are associated with the structure since they occur repeatedly on the geophone component corresponding to the seal orientation that is not fixed. The source location within A-Drift does not appear to have an effect on exciting these dominant frequencies, except that closer to the source a 30 Hz frequency is observed. Due to the structure being composed of three main parts, including solid concrete



blocks, a center pilaster and a blast resistant door, it is possible that two natural frequencies could be excited.

### **6.3 – Results and discussion from mine shots #528 – 540**

Geophone 2 and 5 monitored the cast booster detonations and were located in the C-Drift instrument room and in the D-Drift entry, respectively. The objective was to see if the dominant frequencies from the mine structure can be observed on geophones from distances away from the structure.

An FFT generated from the signatures at Geophone 2 is shown in Figure 6.6. The example given in Figure 6.6 represents the data obtained from mine shot #534 when the cast booster was detonated 10 ft directly in front of the mine seal. A broad range of peak frequencies was observed up 150 Hz. A dominant frequency range between 210 – 235 Hz was detected, which is close to and could be associated with one of the peak frequencies excited by the structure. If this peak frequency does represent the vibration of the mine structures, it would be a combination of all the structures located between crosscuts 1 – 5, since they are essentially the same design. No frequency peak can be observed around 350 Hz, which was the other peak frequency detected during the structure analysis. A peak frequency occurs around 60 Hz, which is attributed to electrical noise in the system. The FFT's generated from Geophone 2 for the other cast booster detonations showed very similar results.

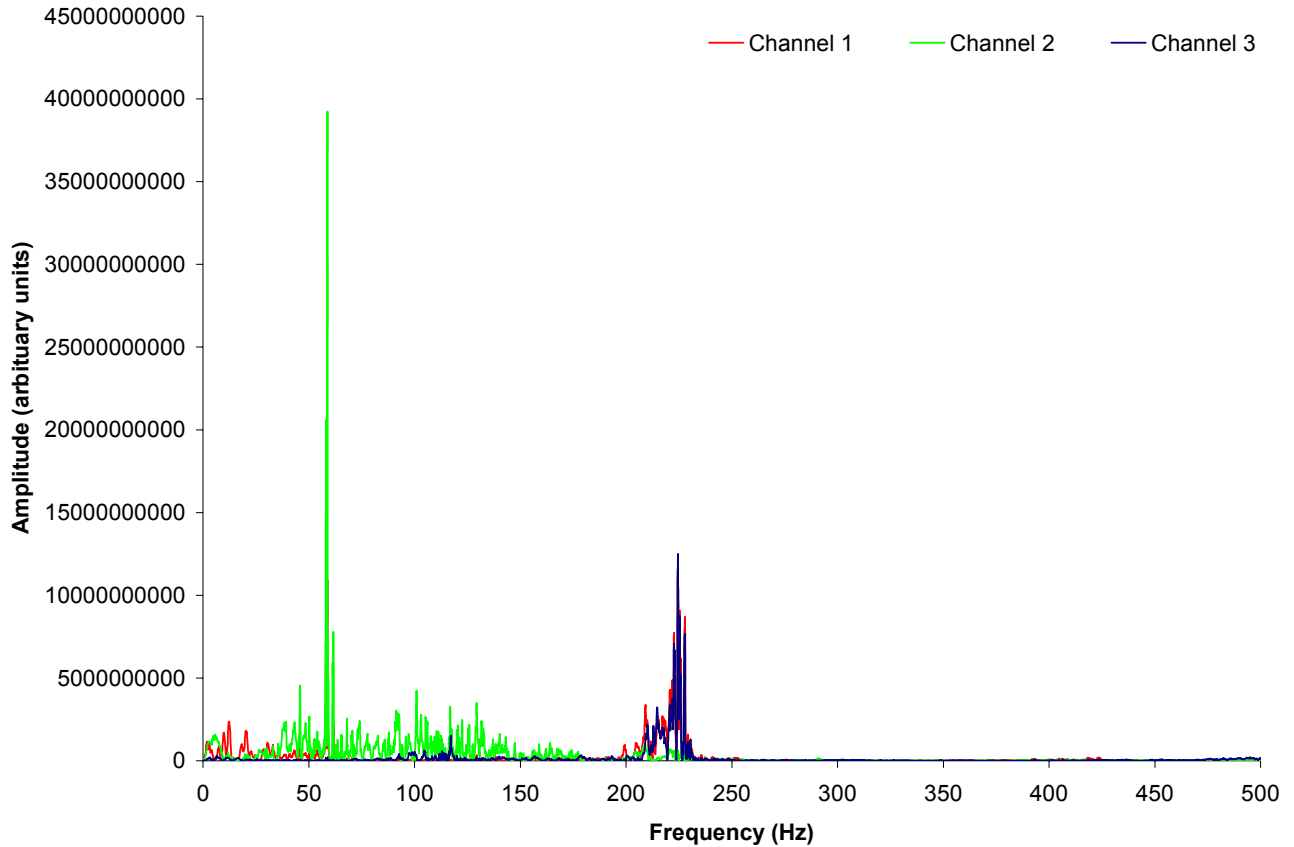


**Figure 6.6** – FFT from the Geophone 2 during mine shot #534.

An FFT generated for the signatures from Geophone 5 is shown in Figure 6.7. The example given in Figure 6.7 also represents data taken from mine shot #534. A frequency range can be detected between 100-150 Hz. Dominant frequencies in this range were observed at Geophone 2. Another dominant frequency range can be observed between 230 – 250 Hz. Although it does not match perfectly with what was observed at Geophone 2 or the mine seal, it still appears to be within a range significantly close to the structure response. Frequency spikes can also be observed throughout the waveform, which either occurs at frequency multiples of 60 Hz and are attributed to electrical noise in the system or are considered spurious responses. The FFT’s generated from Geophone 5 for mine shots #528 – 540 showed very similar results.

The frequency results from these mine shots appeared to be repeatable at each monitoring location.

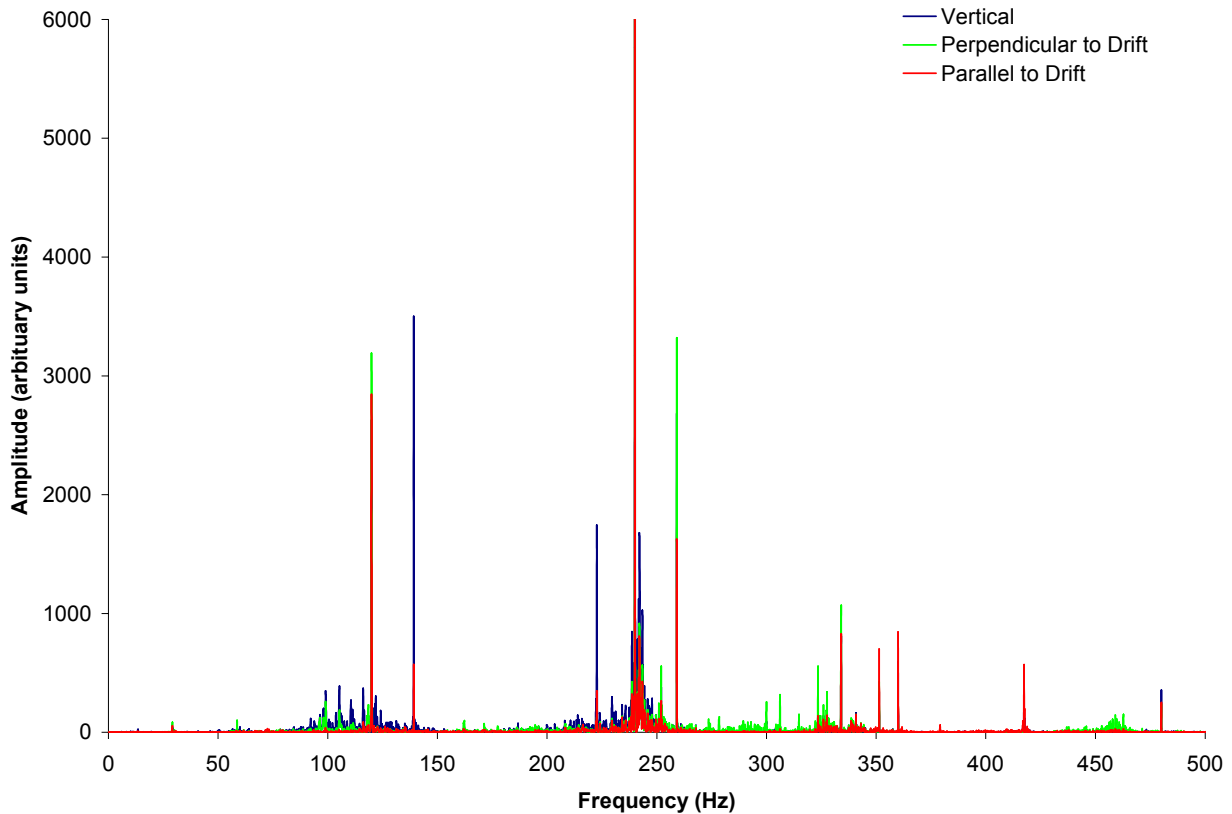
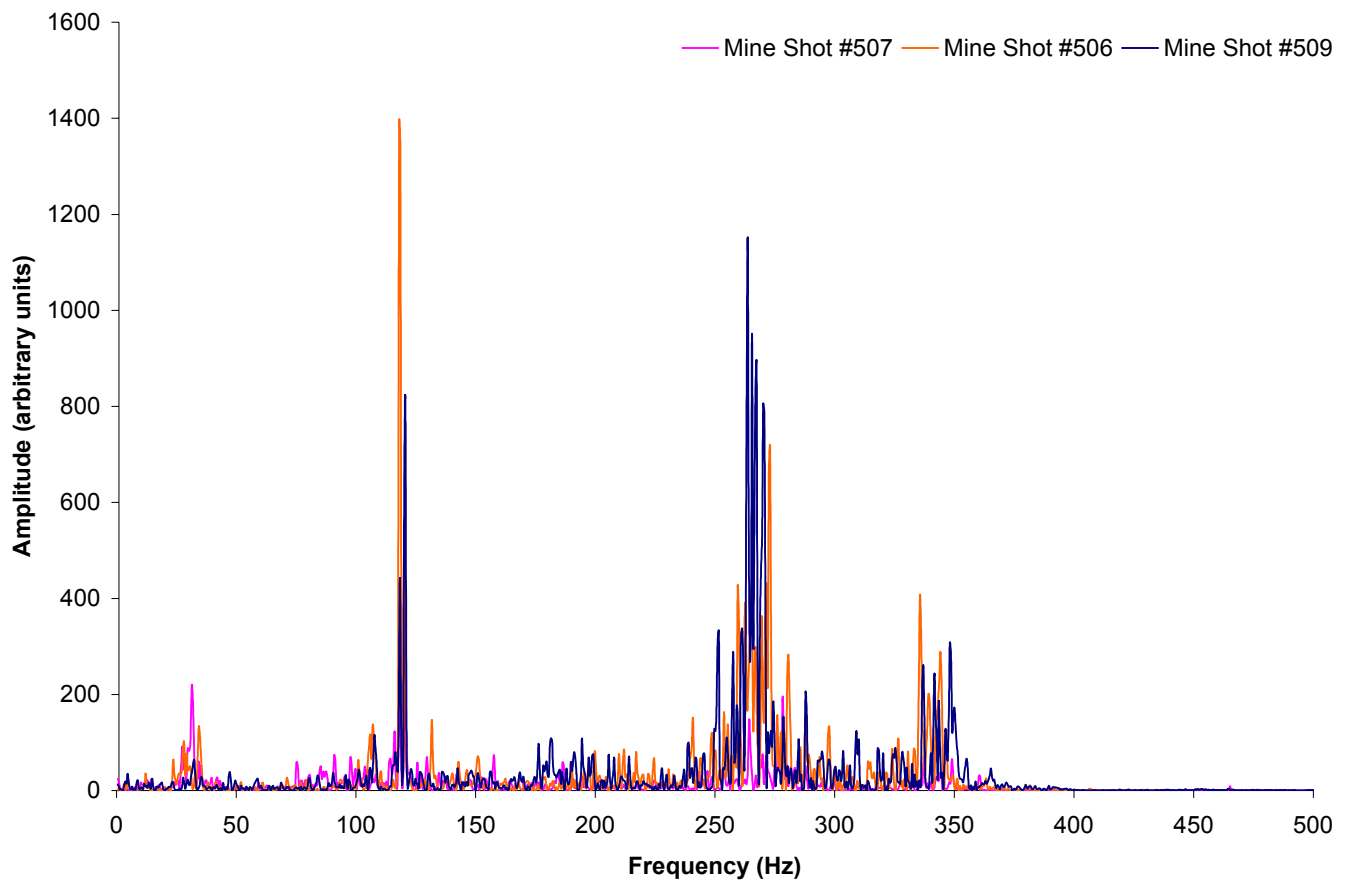


Figure 6.7 – FFT from the Geophone 5 during mine shot #534.

#### 6.4 – Results and discussion from mine shots #503 – 524 for the D-Drift geophones

When analyzing the frequency content for the methane and dust explosions, the data were clustered in groups based upon the location of the receivers. The instruments from D-Drift were analyzed separately since they were able to monitor a larger number of experiments and were considered to be most in the far-field. For mine shots #503 – 509, only one test did not have a seal in the path of the pressure wave, which was mine shot #507. The geophones located in D-Drift consistently observed higher frequencies above 300 Hz for the seven mine shots where a seal was in the path of the pressure wave. An example FFT is shown in Figure 6.8 that compares

the frequency content from mine shots #506, 507 and 509 obtained by Geophone 3. It can be observed that with mine shots #506 and 509, which contained a seal in the entry that was destroyed, higher frequencies are more prominent. The higher frequencies are in the same range that was observed for the dominant frequencies of the mine structure responses. At lower frequencies, especially at 30 Hz, the scales are the same for all three mine shots. A spike around 120 Hz is attributed to electrical noise.



**Figure 6.8** – FFT comparison from Geophone 3 during mine shot #506, 507 and 509.

Data were collected in D-Drift for mine shots #505 and 508, which was a scenario where the pressure wave was confined to a sealed area. It can be observed from these transformations that large amounts of low-frequency content are as predominant as the higher frequencies. For

mine shot #505 the higher frequency range was between 250 – 300 Hz. Mine shot #508 did not see an expected higher frequency range over 250 Hz, except for between 470 – 480 Hz. Although these two experiments contained the explosion within a sealed area, the seal in the entry was structurally different.

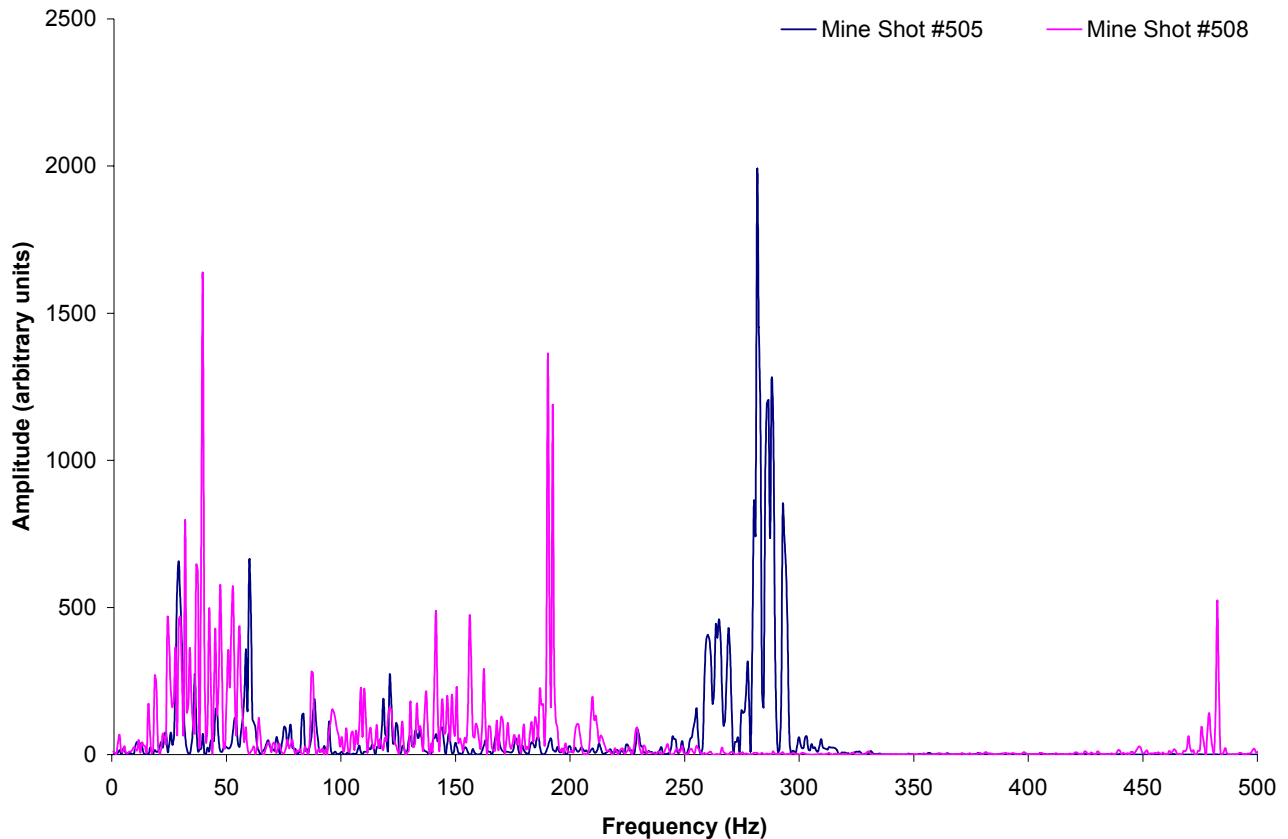
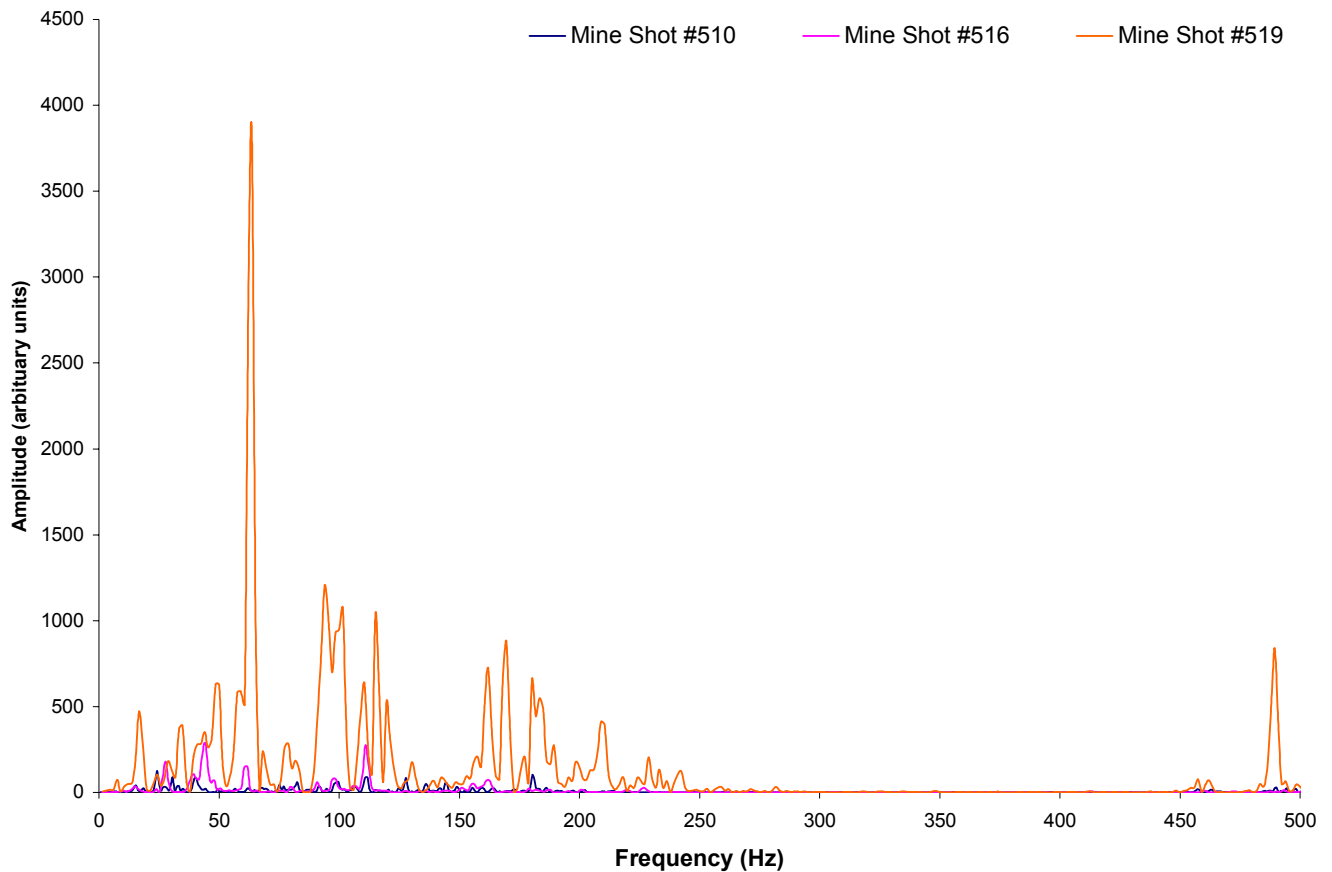


Figure 6.9 – FFT comparison from Geophone 3 during mine shot #505 and 508.

Mine shots #510 – 522 showed frequencies up to 200 Hz, however no frequency content was observed between 250 – 350 Hz. These experiments did not include a containment seal in the experimental design. Example FFT's from three of these tests are shown in Figure 6.10 for comparison. Comparing these results to when a mine seal was in the C-Drift entry, it appears that the addition of a mine seal does cause a change in frequency content which can be observed.

For the mine shots when a seal was in the C-Drift entry, specific spikes were centered on higher frequencies. For the tests with no seal in the A-Drift entry, a broader range of frequencies up to 250 Hz is observed. One final FFT from D-Drift gives an example of when a seal was placed in the path of a pressure wave in A-Drift during mine shot #524 and is shown in Figure 6.11. A dominant frequency range can be detected between 175 – 185 Hz. The seal tested during mine shot #524 was structurally different than what was tested in the previous experiments.



**Figure 6.10** – FFT comparison from Geophone 3 during mine shot #510, 516 and 519.

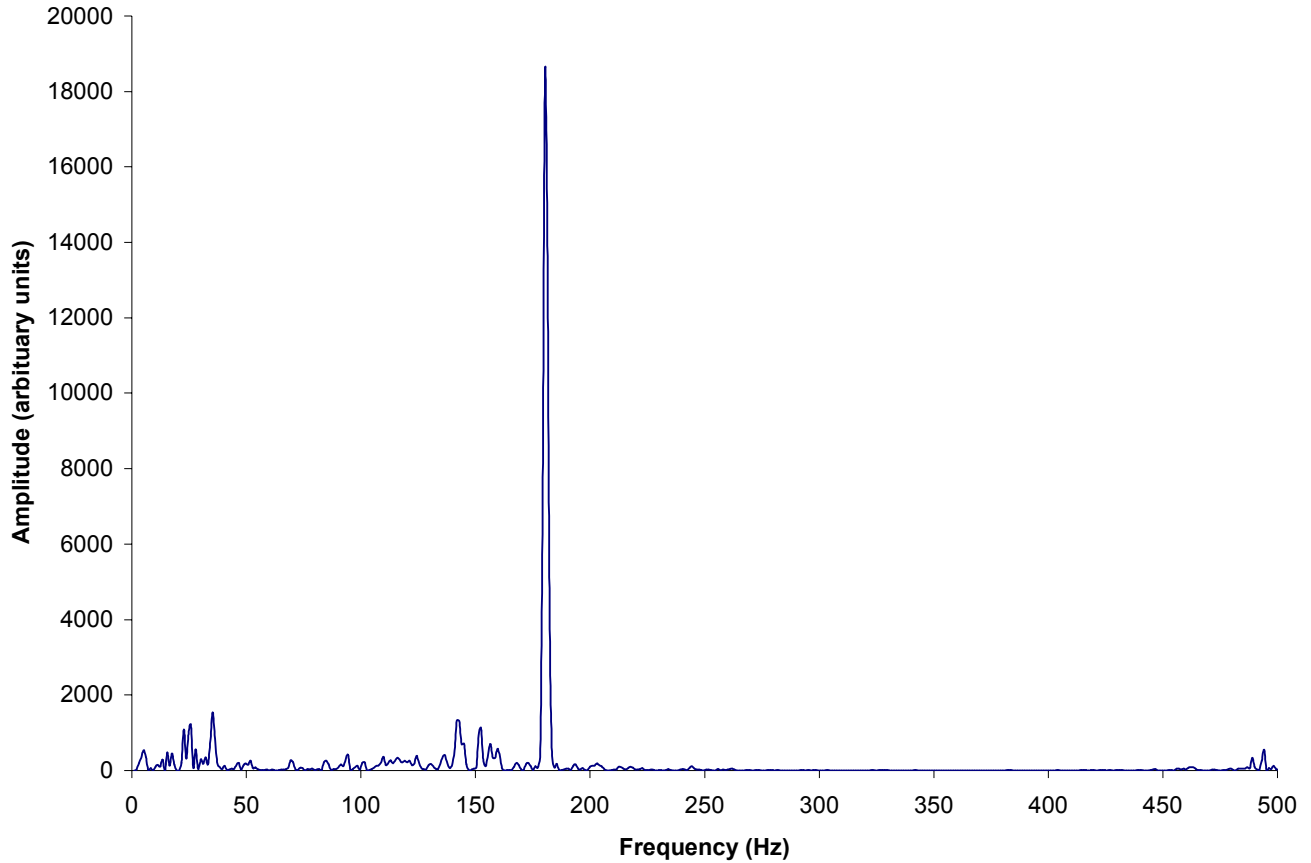


Figure 6.11 – FFT comparison from Geophone 3 during mine shot #524.

## 6.5 – Results and discussion from mine shots #503 – 524 for the other geophones

The dominant frequency ranges, observed from the two geophones in the C-Drift instrument room during mine shots #503 – 509, are summarized in Table 6.1. The method of finding the dominant frequencies was the same as the geophones in D-Drift; however, they are summarized in a table for better presentation. Geophone 1 is anchored onto the C-Drift instrument room’s floor, which is concrete and not limestone. The two geophones were not able to monitor during mine shot #508. Table 6.1 indicates that no real difference can be noted from the different experiment designs for mine shots #503 – 509, even though varying experimental designs are involved. When the explosions are conducted in A-Drift, the only frequencies

detected over 250 Hz are on the vertical channel. Although not reported, data obtained from E-Drift show, for the most part, identical frequencies as reported in Table 6.1. The instruments located in C- and E-Drifts were all within 150 m of the seismic source. Therefore, close to the source no distinction between the frequency content to the experimental designs can be made.



**Table 6.1** – Summary of dominant frequency ranges detected from Geophone 1 and 2 during mine shots 503 – 524.

	C-Drift Floor			C-Drift Roof		
	1	2	3	1	2	3
Mine Shot #503	150-250 350-360	25-35 150-200	150-250 350-360	250-275 320-360	250-300 320-360	250-300 320-360
Mine Shot #504	320-360	25-35 150-250	150-250 350-360	250-300 320-360	250-300 320-360	250-300 320-360
Mine Shot #505	240-250 260-270	400-430	230-250	250-275 320-360	240-280 320-360	240-280 320-360
Mine Shot #506	235-260	400-450	235-260	260-275 325-350	260-275 325-350	260-275 325-350
Mine Shot #507	200-250 375	375 400-420	120-130 200-250 375	250-275 325-350	250-275 325-350	250-275 325-350
Mine Shot #508	-	-	-	-	-	-
Mine Shot #509	220-240 260	375-425	230-240	260 320-380	360-280 320-340	360-280 320-340
Mine Shot #510	-	-	-	0-150 225-275	0-100 225-275	400-450
Mine Shot #513	-	-	-	200-250	200-250	375-425
Mine Shot #514	-	-	-	200-250	200-250	400-450
Mine Shot #516	-	-	-	0-250	225-275	400-450
Mine Shot #517	-	-	-	0-250	0-275	400-450
Mine Shot #518	-	-	-	0-250	0-250	0-200 400-450
Mine Shot #519	-	-	-	0-250	0-275	0-200 400-450
Mine Shot #520	-	-	-	0-250	0-275	0-300 400-450
Mine Shot #521	-	-	-	-	-	-
Mine Shot #522	-	-	-	0-250	200-300	350-450

## 6.6 – Observation of low-frequency content during confined explosions in a sealed area

The frequency content obtained from the Guralp instrument located on the surface above the mine over A-Drift, during mine shots #523 and 524, showed only frequencies 50 Hz and

below. However the sampling rate for this instrument was 500 samples per second and following the Nyquist theorem means only frequencies 250 Hz and below could be observed.

An interesting observation was made while studying the waveforms when a lowpass filter set at 15 Hz was applied to the signature. The lowpass filtered waveform, obtained from the LabVIEW program created for the study, is plotted in Figure 6.12. After the initial explosion, the signature contains a repeatable period at 0.61 seconds lasting for approximately 15 seconds. This activity can be attributed to the pressure wave confined within the sealed area. The same period can be detected in the pressure-time curve in Figure B.18. The period could be observed for the Guralp instrument inside of the mine, as shown in Figure 6.13. During mine shot #524 the same period could be observed on the Guralp instruments in and out of the mine.

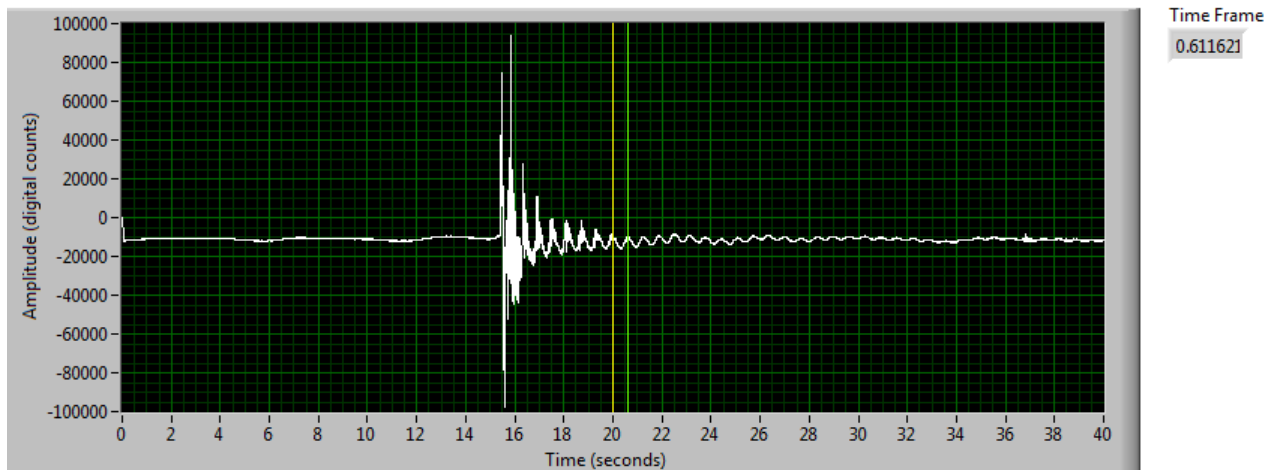


**Figure 6.12** – Filtered waveform from the Guralp surface geophone during mine shot #523.

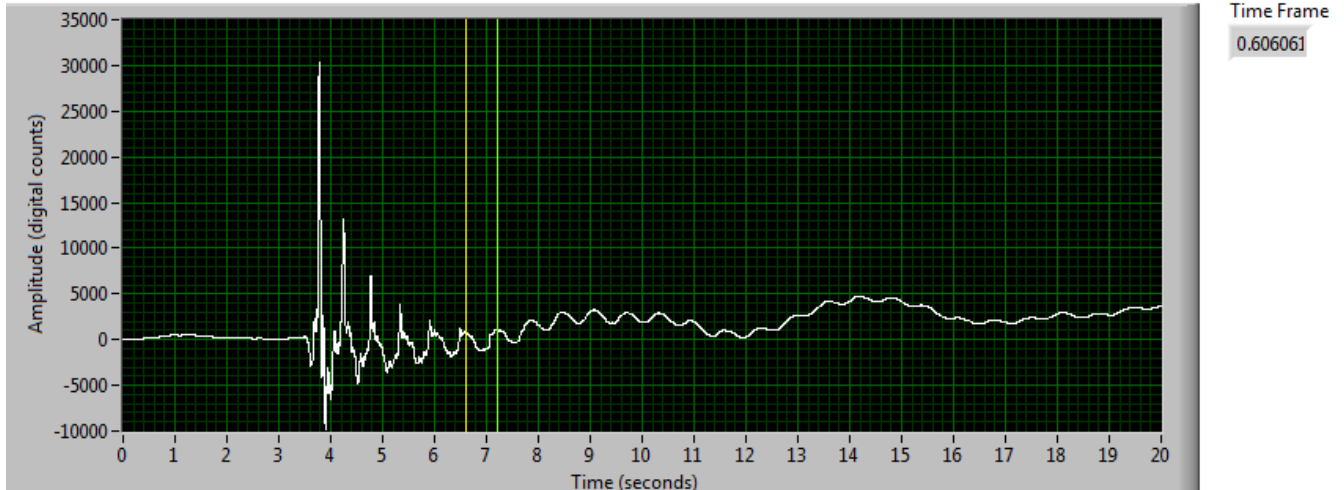


**Figure 6.13** – Filtered waveform from the Guralp in-mine geophone during mine shot #523.

Next, it was investigated whether this period could be observed on the geophones connected to the ISS seismic system. Figure 6.14 is an example displaying a signature collected by Geophone 3 in D-Drift from mine shot #524. Although the observation is not as clear on the Guralp geophones, the period could be detected for a geophone on the ISS seismic system. In order to see if this period could be detected on tests with an explosion that was not confined, the signatures from Geophone 6 were studied, as shown in Figure 6.15.

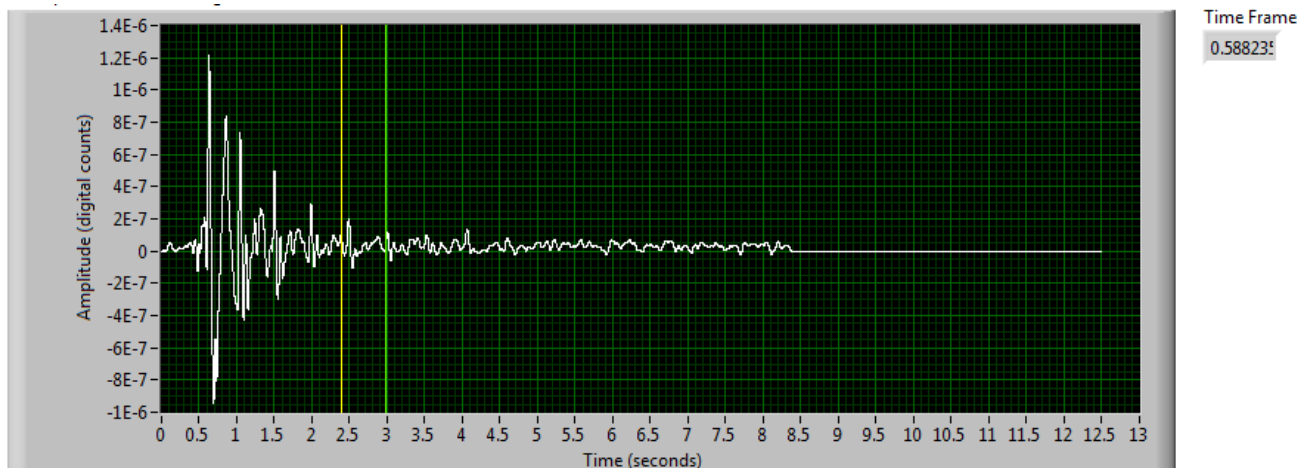


**Figure 6.14** – Filtered waveform from Geophone 3 during mine shot #524.

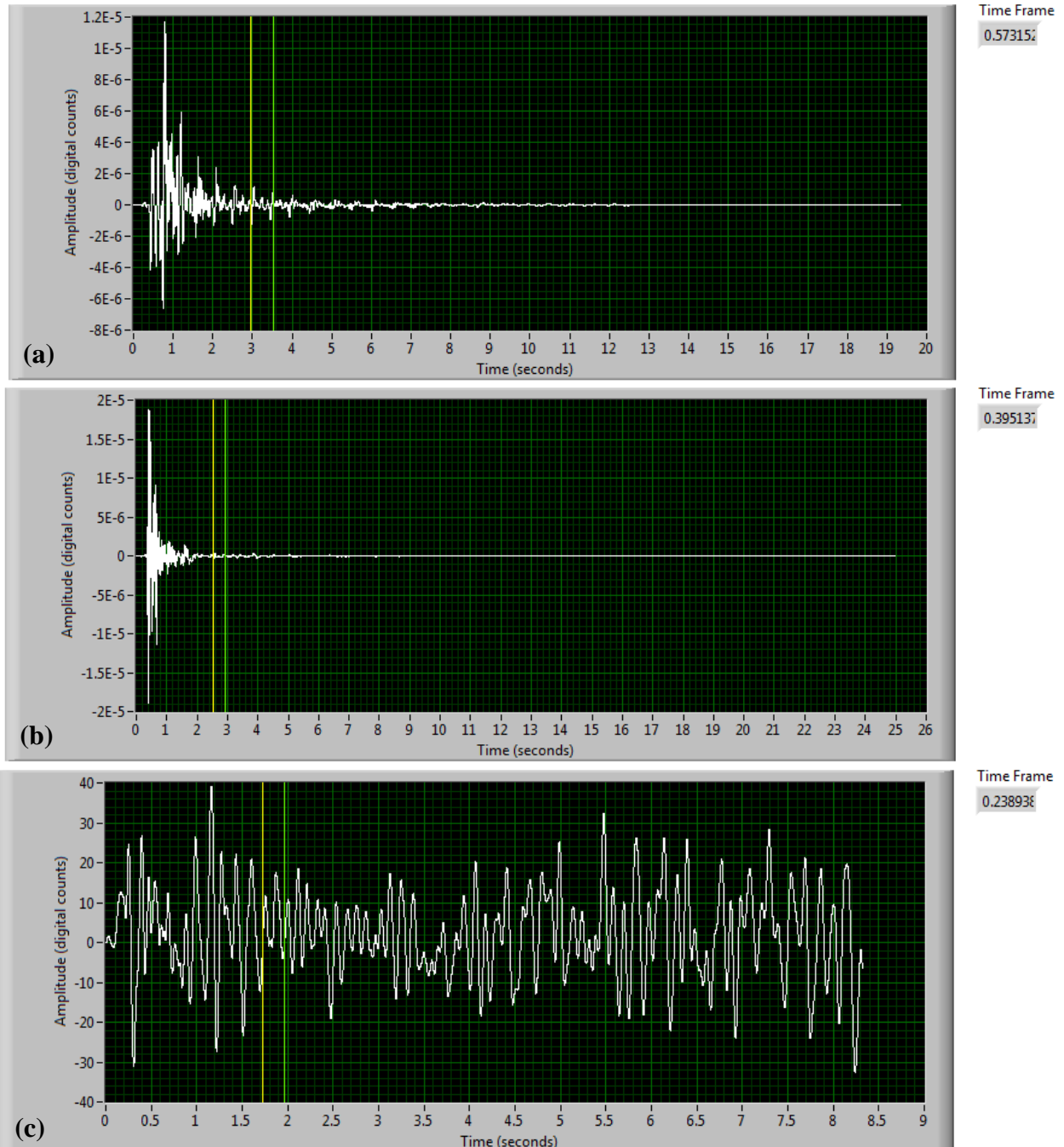


**Figure 6.15** – Filtered waveforms from Geophone 6 during three mine shots: (a) a seal in the entry that did not fail, (b) a seal in the entry that did fail and (c) and explosion with no seal in the entry.

The results in Figure 6.15 show that the period could be observed when the explosion was confined within a sealed area. Figure 6.15(a) represents a filtered waveform from mine shot

#508. The pressure-time curve for this mine shot is plotted in Figure B.6, which shows the same approximate period as observed in Figure 6.15(a). Figure 6.15(b) represents a filtered waveform from mine shot #509, where a seal was completely destroyed. Seismic data less than 15 Hz were observed for this signature, however a constant period after the initial explosion can not be observed. The pressure-time curve for this explosion, Figure B.7, shows no evidence of a period similar to the previous example as well. Figure 6.15(c) represents a filtered waveform from mine shot #520, where there was no seal in the path of the pressure wave. The seismic data less than 15 Hz for this signature appears to be noise. The pressure-time curve for mine shot #520, Figure B.15, also shows no evidence of a period after the initial explosion.

A significant finding from this analysis is that when the explosion is confined, a period of the same value can be detected on both the pressure-time curves and filtered seismic signatures. The Guralp instrumentation showed this period lasting for up to 15 seconds after the explosion. It is believed the specific time period is caused by the explosive pressure wave striking the mine seal or mine face multiple times as it reflects back and forth in the sealed area. The mine seal is located approximately 375 ft away from the source location where the explosion ignites, as reported in the mine shot experimental design in Figure A.18. If the explosive pressure wave were to travel twice this distance, because it is being reflected back, the distance becomes 750 ft. If the pressure wave travels at 1,100 ft/sec as observed previously, the pressure wave should come in contact with either the mine seal or mine face approximately every 0.68 seconds which is significantly close to the period observed.

# **Chapter 7 – Radiated Seismic Energy and Moment Magnitude Estimates from the Seismic Signatures**

In Chapter 7, the radiated seismic energy and moment magnitude estimates from the seismic signatures are presented. These estimates are compared in the following sections to investigate whether the varying experimental designs have an effect on the values. Finally, it is investigated whether a relationship between the radiated seismic energy, which incorporates many of the previously analyzed seismic variables, to the size of the explosion exists.

## **7.1 – Method of analysis**

The calibration of the seismic system helped develop the formulas and methods used for calculating the moment magnitude and energy estimates for the mine shots. The method of analysis for calculating these estimates are reported in Section 3.5.3. A tabulated summary of the energy and moment magnitude results from mine shots #503 – 524 can be viewed in Appendix H. The initial estimated energy from the source is also summarized in the tables documented in Appendix H. These estimates of the initial energy contained in the explosion are based upon the amount of coal dust and methane gas reported in the mine shot summaries in Appendix A. The combustion properties of methane were needed to provide a factor which related the volume of methane to an energy value. For methane, the heat of combustion was found to be 50 MJ/kg (Gexcon 2006). Consultation with experienced engineers at NIOSH, who have extensively studied methane explosions, remarked that the same factor could be used with the estimation of the amount of energy contained within the coal dust. For mine shots

#510 – 524, when the coal dust was mixed with rock dust to create a rock dust concentration, the amount of coal dust is not considered in the initial energy estimation because the rock-dust concentration considerably weakens the explosion. The calculations were all based upon the unfiltered seismic signatures. The radiated seismic energy estimations are considered to be relative values between the different experiments and not the absolute values. For this study, there were too many unknowns for the estimations to be considered anything but relative values.

## **7.2 – Results and discussion on the radiated seismic energy and moment magnitude estimates**

### *7.2.1 Estimated energy as a percentage of the original energy*

The final column in the tables in Appendix H show the percentage of the estimated seismic energy of the explosions compared to the initial explosive energy from the experimental design. In the literature review, it was stated that the amount of seismic energy estimated is typically less than 1% of the original energy of the source. The high energy estimates from the geophones, in most cases, could be attributed to a seal failure. If the results from Geophone 3 are looked at in Table H.3, it can be observed that for the two explosions where a mine seal failed (mine shot #506 and 509), the percentage of energy detected at the geophone is over 1%. Mine shot #505 also contained a seal that failed but at the time the geophones were only able to record a portion of the event so there was a low energy estimate.

In some cases, a large over-estimate of the seismic energy was calculated from the geophones located closer to the source. For example, in Table H.6, the estimate of seismic energy for mine shot #506 from Geophone 6 is 110% of the original energy. This geophone appeared to have recorded seismic energy from a source other than the initial explosion, possibly associated with the seal failure or the massive bulkhead door at the intersection of C- and

E-Drifts. Geophones close to the source could have also been affected by the acoustic air blast. For example during mine shot #507, which was a simple methane explosion with no seal in the entry, the geophone on the cement floor in the C-Drift instrument room recorded 8% of the initial seismic energy. The geophone on the roof in the same location appeared to not be as heavily affected by the air blast passing by the instrument room, as it only recorded 0.52% of the initial energy.

### *7.2.2 Radiated seismic energy estimates versus moment magnitude from the geophones located over 150 m*

The geophones located in D-Drift (Geophones 3 and 5) were analyzed to see if any relationships between moment magnitude and radiated seismic energy from the explosion could be made. These are the geophones which recorded the most data far away from the source. Figure 7.1 displays the relationship between moment magnitude and radiated seismic energy if all the mine shots are included. Figure 7.2 displays the relationship between moment magnitude and radiated seismic energy for the mine shots without seals in the entry and Figure 7.3 displays the relationship between moment magnitude and radiated seismic energy for mine shots only with a seal in the entry. Figure 7.3 show that when just seals in the entry are studied, a correlation between moment magnitude and radiated seismic energy is less obvious. It is believed that addition of a seal in the entry has a direct effect on the moment magnitude and radiated seismic energy calculations. It appears that in some cases, a lower moment magnitude is associated with a higher radiated seismic energy and vice versa making the analysis of these estimates complex. The higher energy associated with a lower moment magnitude is possibly due to the additional seal and rock impacts against the rib, causing more scatter anticipated by secondary sources associated with the seal failure.



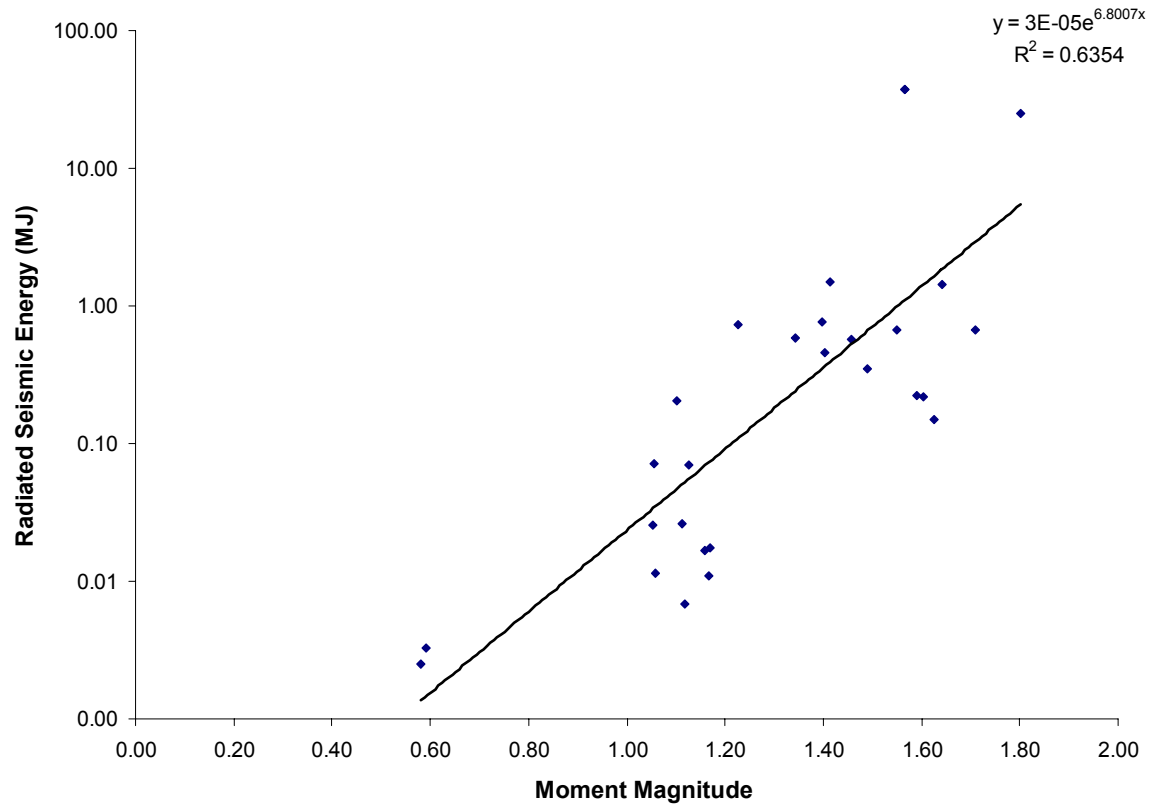


**Figure 7.1** – Radiated seismic energy versus moment magnitude estimates made over 150 m away from the seismic source for all the tests.

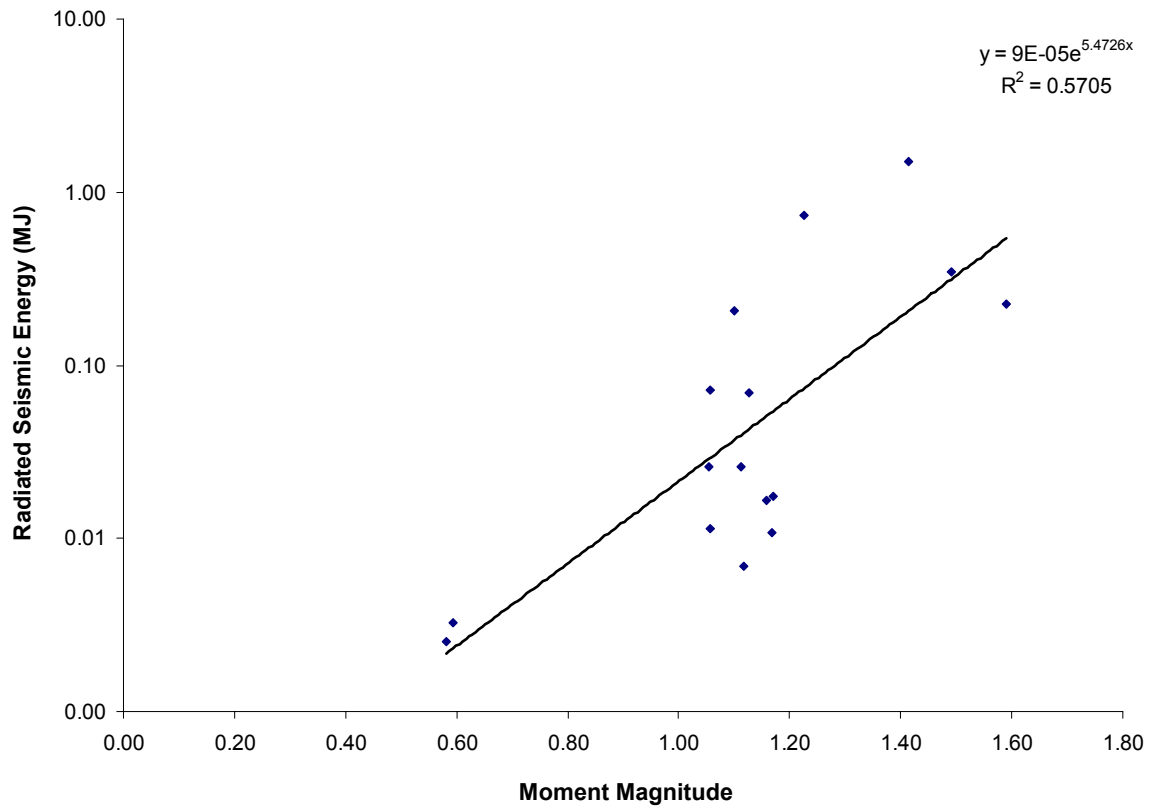


**Figure 7.2** – Radiated seismic energy versus moment magnitude estimates made over 150 m away from the seismic source for just tests with no seal in the entry.

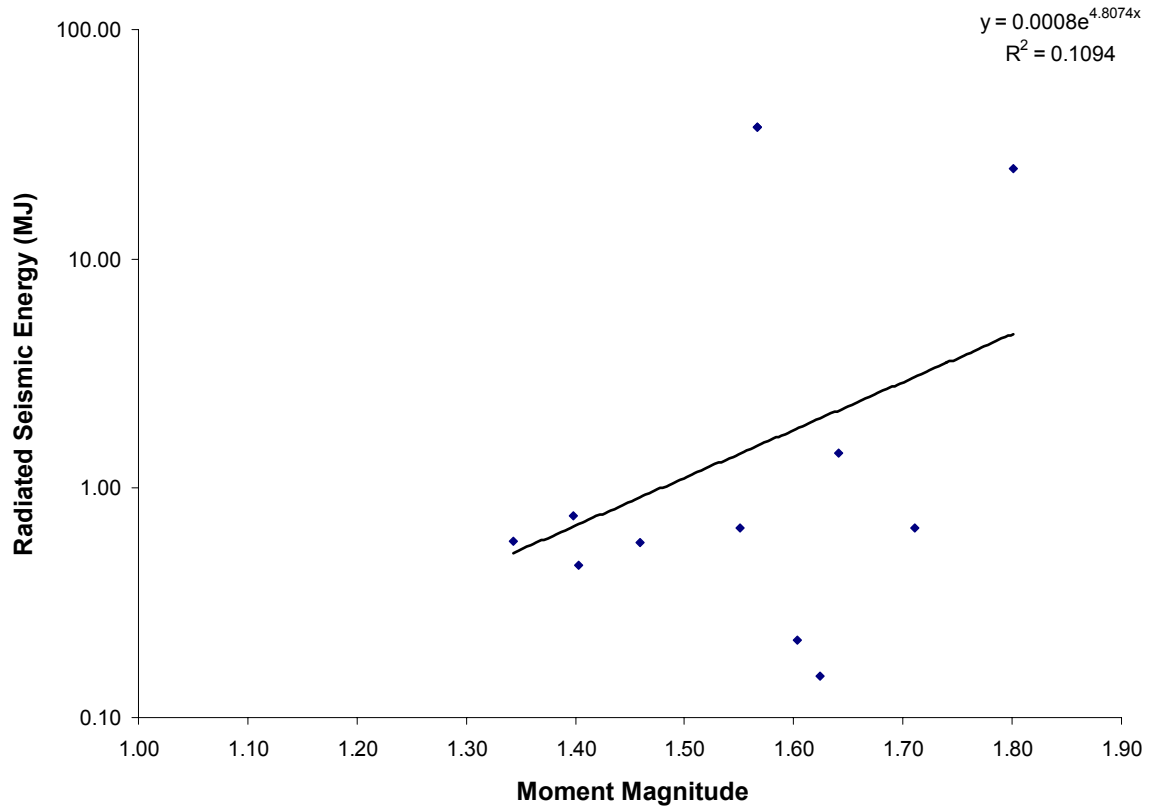


**Figure 7.3** – Radiated seismic energy versus moment magnitude estimates made over 150 m away from the seismic source for just tests with a seal in the entry.

### 7.2.3 Radiated seismic energy estimates versus moment magnitude from the geophones located under 150 m

The geophones located in the C-Drift instrument room (Geophones 1 and 2) and E-Drift (Geophones 4 and 6) were analyzed to see if any relationships between moment magnitude and radiated seismic energy from the explosion could be made. The geophones located in A-Drift were not included in the analysis because they are directly exposed during most of the mine shots. Figure 7.4 displays the relationship between moment magnitude and radiated seismic energy if all the mine shots are included. Figure 7.5 displays the relationship between moment magnitude and radiated seismic energy for the mine shots without seals in the entry and Figure 7.7 displays the relationship between moment magnitude and radiated seismic energy for mine

shots only with a seal in the entry. These charts show a much better correlation between moment magnitude and radiated seismic energy than the instruments located further away from the source.

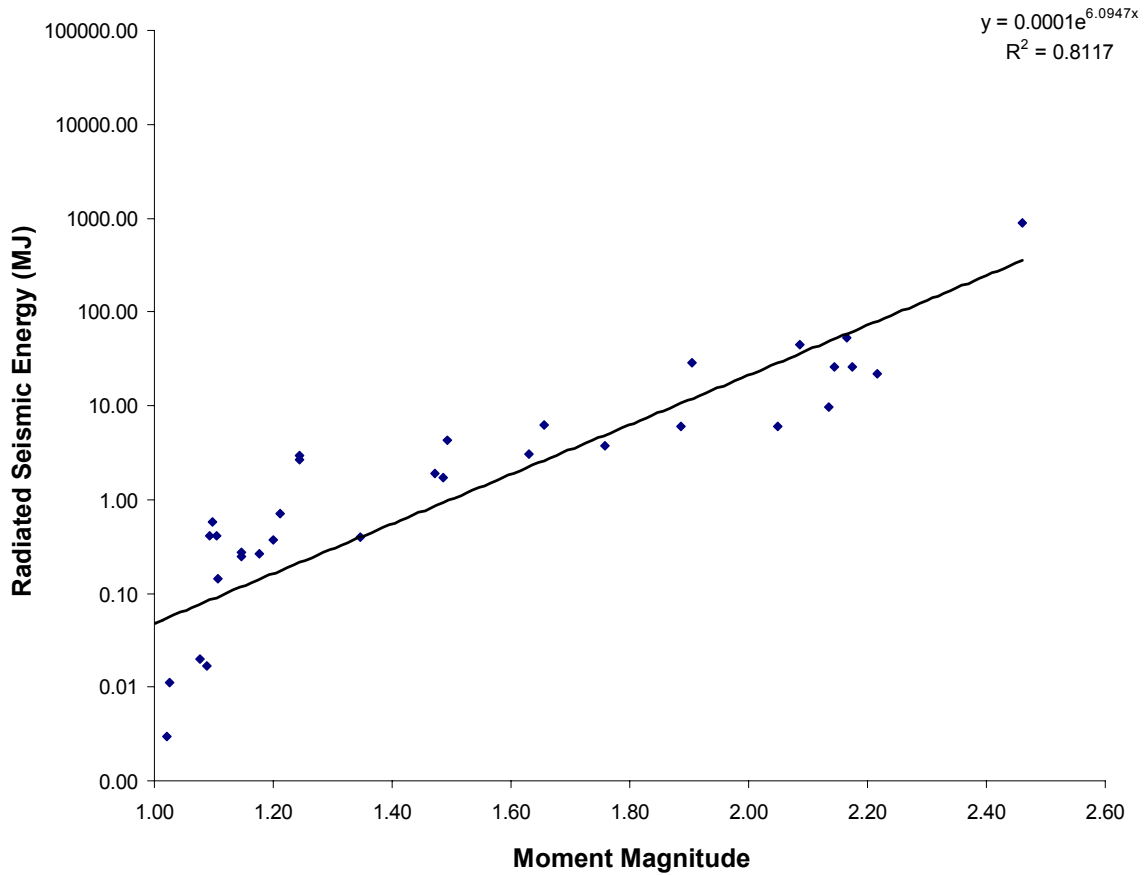


**Figure 7.4** – Radiated seismic energy versus moment magnitude estimates made less than 150 m away from the seismic source for all the tests.

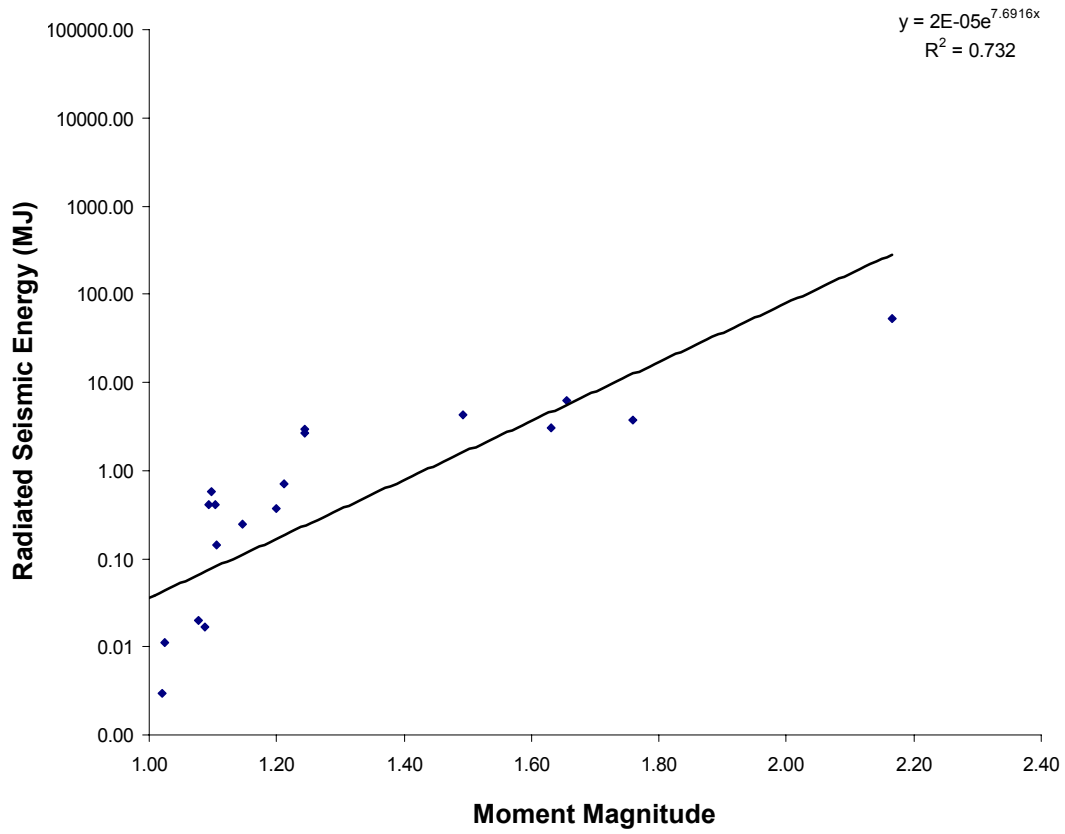


**Figure 7.5** – Radiated seismic energy versus moment magnitude estimates made less than 150 m away from the seismic source for just tests with no seal in the entry.

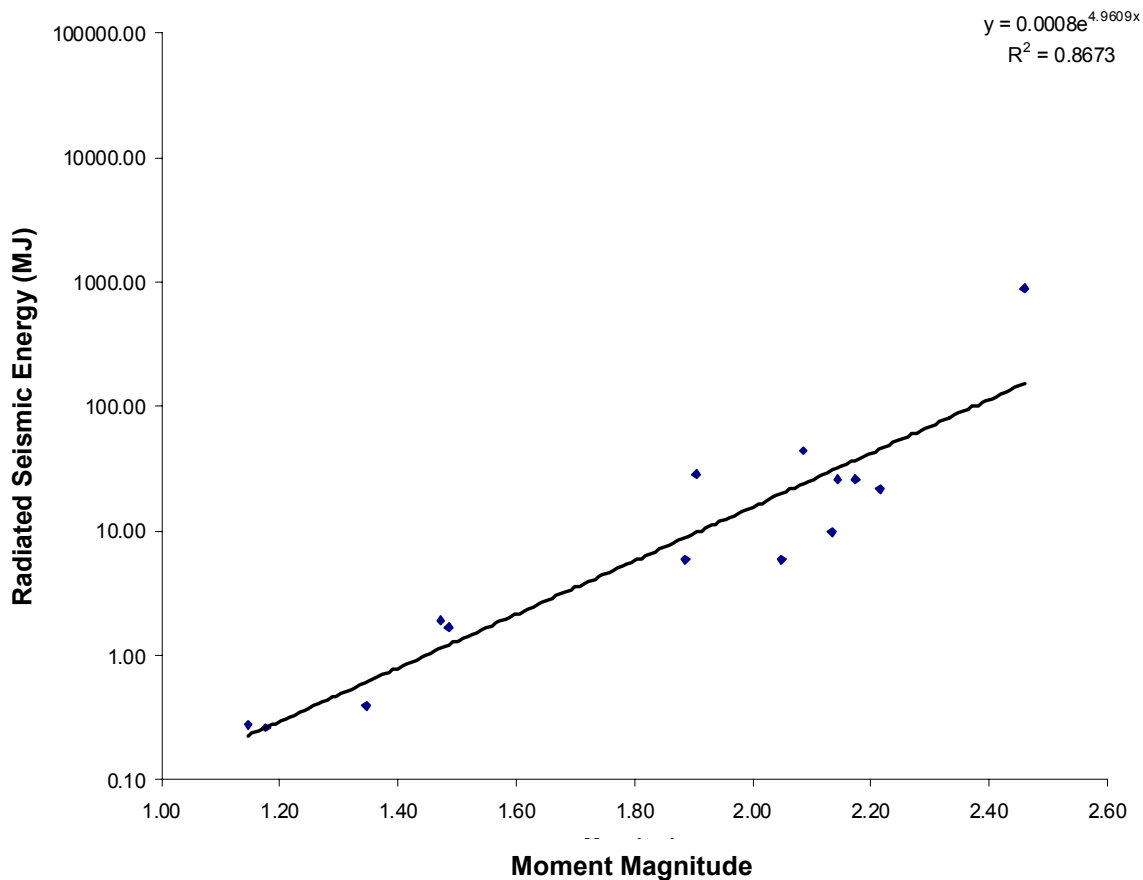


**Figure 7.6** – Radiated seismic energy versus moment magnitude estimates made less than 150 m away from the seismic source for just tests with a seal in the entry.

An assumption on why Figures 7.4 – 7.6 show a better correlation can be related to the larger ranges in radiated seismic energy observed due to being closer to the source. The geophones close to the source recorded seismic activity that the geophones far away from the source do not. The geophones closer are possibly more affected by the seals in the crosscuts. The attenuation calculations proved that the amplitude of the seismic signatures attenuate very quickly. Some of the energy associated with high-frequency content could attenuate before it is observed by the far away geophones.

### **7.3 – Relationship between the radiated seismic energy and size of the explosion**

The analysis that was conducted on the data and reported in Chapters 4 – 6 include items such as amplitude, duration and frequency content. The radiated seismic energy estimate for each set of seismic waveforms, as calculated by Equation 2.9 on page 22, takes these parameters into account by considering the integral of squared velocity. The radiated seismic energy equation is also derived from physical characteristics of the environment such as the medium density and the seismic wave velocity. Since this single value takes into account the significant parameters observed during this study, a relationship between radiated seismic energy and size of the explosion was derived. By doing this, the size of the explosion, defined as the peak pressure generated, can be estimated using the seismic observations. First, a linear relationship between these variables was considered, as shown in Figure 7.7. The plotted data points are representative of all the explosions with at least three triggered geophones and the relative radiated seismic energy estimates are averaged from the geophones.

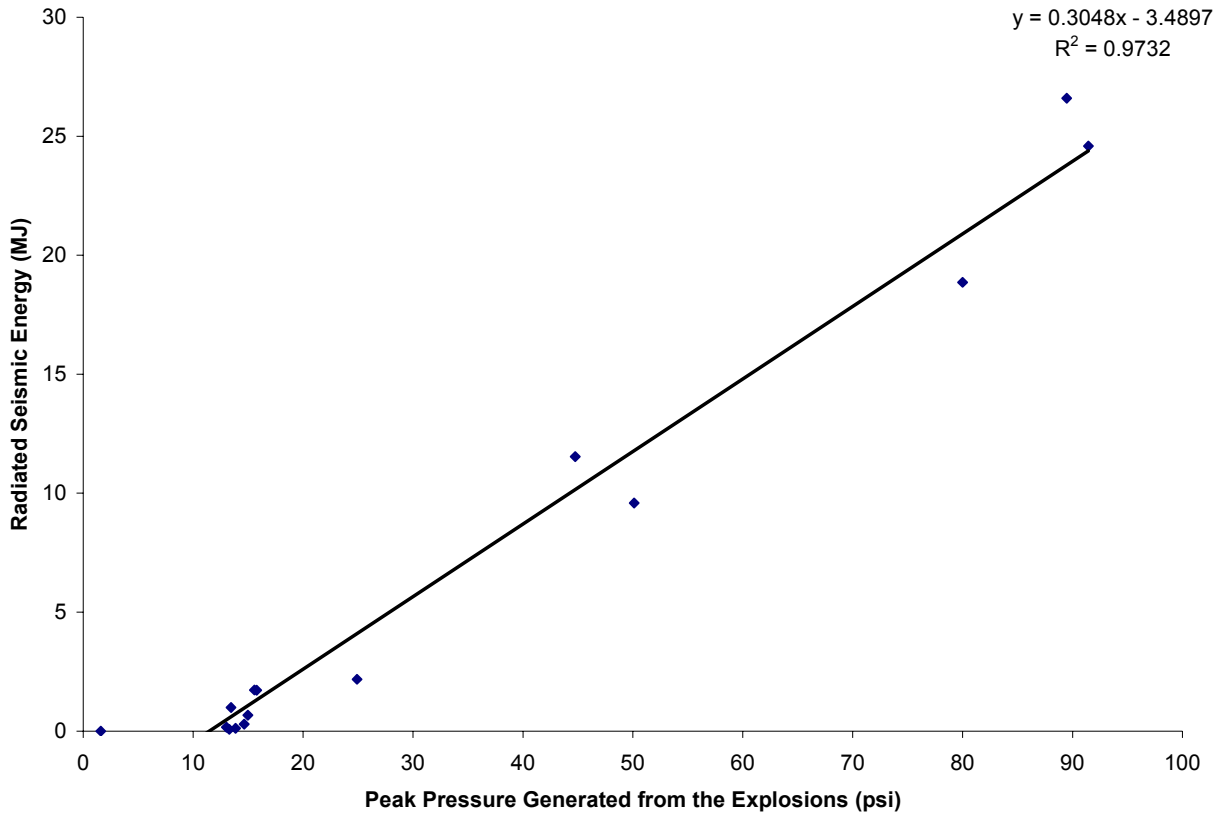


**Figure 7.7** – Linear relationship of the radiated seismic energy versus size of the explosion for all the mine shots observed.

Although a good correlation coefficient of 0.97 is calculated from the linear regression line, the problem with this relationship is that explosions below 10 psi will be associated with a negative energy value. Figure 7.8 contains the same dataset but a power trend line is used to correlate the radiated seismic energy and size of the explosion. Although the correlation coefficient is less than the previous chart, the curve is a better representation of the data.



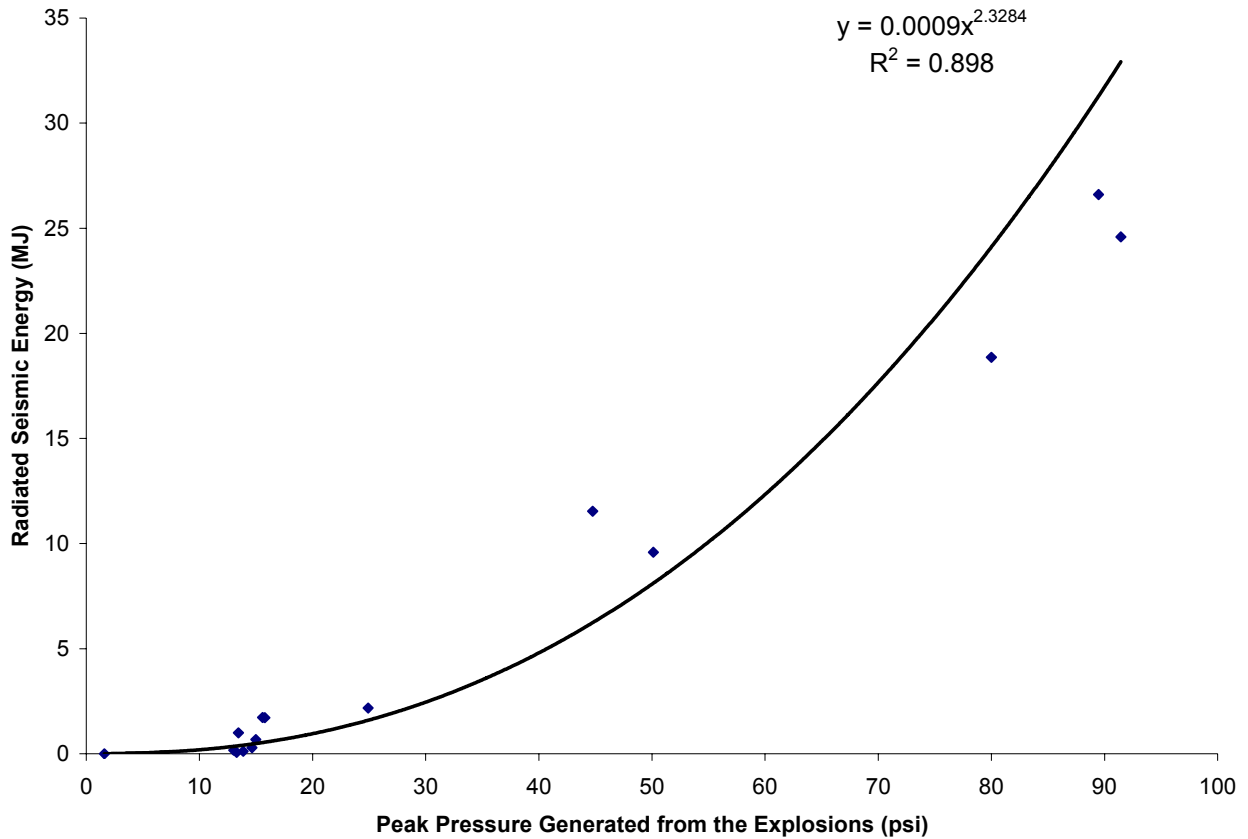


**Figure 7.8** – Power relationship of the radiated seismic energy versus size of the explosion for all the mine shots observed.

In order to estimate the size of the explosion based upon an estimated radiated seismic energy, the relationship in Equation 7.1 was derived from the trend in Figure 7.8.

$$P = \left( \frac{E_s}{0.0009} \right)^{\frac{1}{2.33}} \quad (7.1)$$

where: P = Peak pressure of the explosion (psi), and  
 E<sub>s</sub> = radiated seismic energy (MJ).

A more detailed relationship of the estimated energy and the size of the explosion, which integrates both Equations 7.1 and 2.9, is reported in Equation 7.2. Two important considerations to take into account about Equation 7.2 are the relationship is based upon relative radiated

seismic energy estimations (as oppose to the absolute values) and the scaling differences between the Lake Lynn Experimental Mine and an actual active mine. The volumetric difference between the drifts at LLEM versus a sealed off area in a mine is vastly different. An explosion occurring at an underground mine would contain more energy compared to an explosion of the same size occurring at the test facility where the measurements were made.

$$P = \left( \frac{4\pi\rho c R^2 (I_1 + I_2 + I_3)}{0.0009} \right)^{\frac{1}{2.33}} \quad (7.2)$$

where: P = Size of the explosion (psi), and  
 $\rho$  = density of the rock at the source (kg/m<sup>3</sup>),  
R = distance from source to receiver (m),  
c = P- or S-wave velocity (m/s), and  
I = integral of squared velocity for a geophone orientation (m<sup>2</sup>/s<sup>2</sup>/Hz).

## Chapter 8 – Conclusions and Recommendations for Future Research

Seismic signatures emanating from controlled methane and dust explosions at the Lake Lynn Experimental mine were studied. The objective was to analyze and characterize these signatures at different distances within the mine. A total of nineteen explosions were monitored over the course of the study. The explosions were experimentally different from each other in terms of the placement of explosion-containment seals and blast pressures generated by the fuel creating the explosion. An additional twelve experiments were conducted, which involved a series of 1-lb cast boosters detonated within the entries of the longwall gallery section of the mine. The objective of these experiments was to provide some degree of control in the experiments to facilitate assessing the impact of the seal response on the seismic signatures.

A seismic system was installed at the mine and geophones were mounted on the mine roof or floor in ranges of 10 – 700 m away from the source. However, most of the seismic signatures were only observed between 10 – 250 m away from the source. Calibration of the seismic system was performed through the analysis provided by a sophisticated program written in Microsoft Excel, using Visual Basic for Applications (VBA), to estimate the moment magnitude and radiated seismic energy. The program also estimated the seismic moment and corner frequency by fitting a Brune model to the seismic data. A program written in LabVIEW was utilized to help create frequency spectrums, apply various forms of filters to the seismic data, and determine the duration of the seismic signatures.

An assessment of the seismic data is more easily understood by comparing the signatures from the closer geophones (0 – 150 m away from the source) to the far away geophones (150 – 250 m away from the source). By analyzing the data in this method, it can be understood how the seismic signatures change with distance. It was also easier in some cases to interpret of the results if the explosions conducted from two different parts of the mine were compared separately. Since the experimental designs were different for most of the experiments, separating out the source location in some cases allowed control over unknown variables such as site effects. The following conclusions can be made from the analysis of the seismic signatures:

- The degree of decoupling of the methane explosion to the limestone believed to be a significant factor in the transfer of energy into the rock. The methane explosion is ignited in an open space and the transfer of the energy occurs as the expanding pressure wave interacts with the surrounding rock. This is very different from other types of seismic sources such as an earthquake or a roof fracturing in an underground mine where the source is direct rock-on-rock contact. Therefore, the transfer of seismic energy from methane explosions into the rock is significantly less than other mining-related mechanisms that create seismic energy.
- A linear relationship was found between the amplitude of the seismic signature and size of the explosion. The size of the explosion is defined as the peak pressure generated and determined from the pressure-time curves measured for each explosion by the mine's operation staff. A relationship was generated for the close (0 – 150 m away) and far (150 – 250 m away) geophones that could estimate the maximum pressure from the amplitude.

- No correlation could be made between the experimental designs to the attenuation factors between the different mine shots. The average attenuation factor between all the mine shots was -0.20 dB/m. Various attempts were made throughout the course of the study to observe seismic activity with geophones installed 250 m away and through a regional seismic network station 16 km away. The observed attenuation of the signatures validated why the signatures could not be observed at these distances.
- During the mine shots conducted in C-Drift, the duration of the seismic signatures was shortest for experiments with no seals in the path of the pressure wave and longest for experiments where a seal blocked the direct path of the explosive pressure wave. For the experiments where the explosion is confined within the sealed area, a seismic detection instrument on the surface of the mine detected seismic signals for up to 15 seconds. The weakest explosion from all the tests, which had a maximum pressure generated of 2 psi, had an average seismic activity duration of 0.61 seconds. The containment geometry also played a role in the duration of the seismic signatures when open crosscuts allow the explosion to travel into different parts of the mine. The signatures from these scenarios had multiple events which were related to the explosive pressure wave entering into the new area and interacting with the rib or face.
- An assessment on the seismic wave type was made using apparent velocity measurements. Body waves and surface waves were believed to be generated from all of the explosions. However, the size of the explosion was a significant factor in what wave type was observed at the geophone. For large explosions (approximately 25 psi and over), the average seismic

wave had a velocity in the S-wave range. For explosions under 25 psi, the seismic waves had an average velocity related to the surface wave. For the cast booster detonations, which were coupled better with the surrounding limestone rock, a very small amplitude arrival could be observed, which proved to be the P-wave, however this was only observed when the test locations were close to the receiver. The P- or S-waves that were not observed in the weaker explosions were believed to be attenuated into the background noise before they reached the receiver.

- The cast booster detonations were able to excite two frequencies in a mine ventilation control structure located in a crosscut. These two frequency ranges were between 255 – 275 Hz and 340 – 375 Hz. The frequency range 255 – 275 Hz was observed on the geophones attached to the mine roof at multiple locations in the mine. Seismic data obtained from a previous study was analyzed and it was found that stiffer structures have higher natural frequencies. Since every explosion had mine seals or stoppings in the crosscuts, the frequency spectrums observed from the explosions were believed to contain some component from these structures.
- The type of ventilation control structure (i.e. seal or stopping) being tested had an impact on the types of seismic frequencies that were observed. When the seal fails, higher frequencies were observed which could be attributed to the rock impacts. The literature review indicated that rock drop tests produced frequencies up to 400 Hz. For the geophones further away, when the explosion is confined within the sealed area, frequencies 50 Hz and below were dominant in the frequency spectrum. When a different seal structure was placed in the path

of a pressure wave, the dominant frequency was observed at 175 Hz. When the explosion causes the mine seal to fail, frequencies around 350 Hz were observed, which were not observed with the other experimental designs. The spectrum observed when there was no seal located in the path of the pressure wave was similar to that when the seal failed, however no dominant frequency was detected at the 350 Hz level.

- Close to the source (0 – 150 m), it was difficult to observe differences in frequency content between the different types of experimental designs.
- The smallest moment magnitude was found to be approximately 0.6 for a 2-psi explosion. The largest moment magnitude was found to be around 2.0 for a 90-psi explosion. Close to the source, the relationship between moment magnitude and radiated seismic energy could be correlated very well. Far away from the source, the correlation could not be made as well. The poor correlation could have been due to the attenuation of higher frequencies as the distance increased.
- For most of the explosions, the amount of seismic energy observed was less than 1% of the original energy. However, in cases where the seal failed, the seismic energy was as much as 5% of the original energy. The higher percentage could be attributed to the added impacts of the debris from the failed seal striking the surrounding rock.
- The radiated seismic energy estimates calculated for each experiment was considered to be relative values. A power relationship was determined which related the radiated seismic

energy to the size of the explosion, as defined by the peak pressure generated. The radiated seismic energy estimate takes into account the seismic observations for each experiment while the size of the explosion is a function of the experimental design. A detailed version of the relationship from Chapter 7 is shown again.

$$P = \left( \frac{4\pi\rho c R^2 (I_1 + I_2 + I_3)}{0.0009} \right)^{\frac{1}{2.33}}$$

where:  $P$  = Size of the explosion (psi), and  
 $\rho$  = density of the rock at the source ( $\text{kg/m}^3$ ),  
 $R$  = distance from source to receiver (m),  
 $c$  = P- or S-wave velocity (m/s), and  
 $I$  = integral of squared velocity for a geophone orientation ( $\text{m}^2/\text{s}^2/\text{Hz}$ ).

Based upon these results, it is concluded that a combination of the observations is needed to begin to differentiate the seismic activity results from the varying test set ups conducted in the mine explosion test program. The factors that most affect the seismic signatures were the mine geometry, size of the methane and dust explosion, stiffness of the mine seal and location of the seal, whether it is in the crosscut or mine entry.

While these results contribute to the advancement of the science by analyzing a type of mining-induced seismicity where measurements have not been made before, more could be learned if the experimental limitations explained in the introduction were not in place. Because of financial barriers, the geophones used in the project were only able to be anchored onto the surface of the mine roof. If boreholes could be drilled through the rock from the surface and geophones properly grouted in the limestone, it is believed that a better observation of P- and S-waves could have been made. This would allow for better moment magnitude and radiated seismic energy assessments to be made and the lack of surface waves could potentially make the FFT charts less complex. An attempt was made to grout three geophones into a 20-ft borehole



drilled into the mine roof from the mine entry underground, however difficulties arose regarding the installation of the geophones and reliable data were never able to be collected. The single, surface-mounted instrument above the mine was only available for two of the tests. This instrument, along with another, was planned to be installed on the surface from the beginning of the project, however they were not available until the end of the project. It is believed that instruments on the surface would provide signatures more closely related to the signature collected during the Sago mine explosion (a surface mounted instrument collecting data outside of the mining environment) and should be used in the future at different locations.

The signatures analyzed during the study were difficult to evaluate because of the complexity of the seismic signature due to the large number of experimental variables. An example of this is the mine supervisor indicated that it is possible as the pressure wave moves into each crosscut, it is reflected to the other side of the crosscut, is reflected again, and so on. If control was allowed over the experimental variables, it is felt that additional significant findings could have been observed. The final recommendation is to simplify the experimental design so that unobstructed methane explosions of different sizes could be examined independent of seal structures and crosscuts. Once this effort is completed, a series of controlled explosions at varying sizes, with a controlled explosion-containment structure could be evaluated. Following this, explosion-containment structures that are structurally different could be evaluated to see the effect in the seismic signatures. However, such a study is well beyond the scope of this project, would require several years to complete and is currently not part of the NIOSH agenda for the LLEM facility.

# References

- Adushkin, V. V., V. I. Kulikov, F. F. Safonov and A. A. Solomonov (1990). "Method for determining power of underground explosion from seismic wave parameters in near seismic zone." *Physics of the Solid Earth*, **26**(12), 1002-1009.
- Analog Devices (1994). "Analog-Digital Conversion Handbook." Prentice Hall.
- Ahrens, T. J. and C. Liu (1996). Shear wave generation from contained explosions. Scientific report, Contract F1962B-95-C-0115; Project 5101: California Institute of Technology, Seismological Laboratory 252-21, Pasadena, CA, United States
- Aki, K. (1968). Seismic displacements near a fault. *Journal of Geophysical Research*, **73**(16), 5359-5376.
- Aki, K. and P.G. Richards (2002). Quantitative Seismology. Second Edition, ed. J. Ellis. Sausalito, CA: University Science Books.
- Armstrong, B. H. (1969). Acoustic emission prior to rockbursts and earthquakes. *Bulletin of the Seismological Society of America*, **59**(3), 1259-1279.
- Blake, W., and D. G. F. Hedley (2003). "Chapter 12 - Cambell Mine - Red Lake, Ontario." In: *Rockbursts – Case Studies from North American Hard-Rock Mines*. Littleton, Colorado: Society for Mining, Metallurgy and Exploration, Inc. (SME).
- Boatwright, J. and J. B. Fletcher (1984). The partition of radiated seismic energy between P and S Waves. *Bulletin of the Seismological Society of America*, **74**, 361-376.
- Bolstad, D. D. (1990). "Keynote lecture: Rock burst control research by the US Bureau of Mines." In: *Rockbursts and Seismicity in Mines - Proceedings of the 2nd International Symposium on Rockbursts and Seismicity in Mines*. Ed. C. Fairhurst. Minneapolis: A.A. Balkema. 371-75.
- Bolt, B. A. (1982). Inside the Earth. San Francisco, CA: Freeman.
- Boore, D. M. and J. Boatwright (1984). Average body-wave radiation coefficients. *Bulletin of the Seismological Society of America*, **74**, 1615-1621.
- Brune, J. N. (1970). "Tectonic stress and the spectra of seismic shear waves from earthquakes." *Journal of Geophysical Research*, **75**: 4997-5009.
- Brune, J. N. (1971). "Correction." *Journal of Geophysical Research*, **76**: 5002.
- Cashdollar, K. L., E. S. Weiss, T. G. Montgomery and J. E. Going (2006). "Post-Explosion Observations of Experimental Mine and Laboratory Coal Dust Explosions." In: *Proceedings of the Sixth International Symposium on Hazards, Prevention, and Mitigation of Industrial Explosions (Halifax, NS, Canada, Aug. 27 - Sept. 1, 2006)*, 662-675.

- Cashdollar, K. L., Weiss, E. S., Harteis, S. P., Sapko, M. J. (2007). Experimental Study of the Effect of LLEM Explosions on Various Seals and Other Structures and Objects. NIOSH Briefing Report to the Mine Safety and Health Administration and the West Virginia Office of Miners' Health, Safety, and Training, March 2007.
- Chapman, M. C. (2006), "Appendix CC - Results from Analysis of Seismic Data for the January 2, 2006, event near Sago, WV," Virginia Polytechnic Institute and State University: Blacksburg, VA. <http://www.msha.gov/Fatals/2006/Sago/sagoreport.asp>
- Checca, E. L. and D.R. Zuchelli (1995). "Lightning strikes and mine explosions." In: Wala, A. M., ed. *Proceedings of the Seventh U.S. Mine Ventilation Symposium*. Lexington, K.Y.: University of Kentucky, 245-250.
- Dewey, J. W. (1998). "Explosion and impact event analyses and monitoring." *Seismological Research Letters*, **69**(2), 176. <http://neic.usgs.gov/neis/mineblast/>
- Dolar, D. R., T. E. Marshall, T. M. Barczak and T. P. Mucho (2003). "Stability of Underground Openings Adjacent to the Sink Hole at the NIOSH Lake Lynn Research Laboratory." *2003 SME Annual Meeting, Feb 24-26, preprint 03-154*, Society for Mining, Metallurgy, and Exploration, Cincinnati, Ohio.
- Funk, C., G. Aswegen, and B. Brown (1997). "Visualisation of seismicity." In: *Rockbursts and Seismicity in Mines - Proceedings of the 4th International Symposium on Rockbursts and Seismicity in Mines*. Eds. S.J. Gibowicz and S. Lasocki. Kraków, Poland: A.A. Balkema. 81-87.
- Gates, R. A., R. L. Phillips, J. E. Urosek, C. R. Stephan, R. T. Stoltz, D. J. Swentosky, et al. (2007). Report of investigation, fatal underground coal mine explosion, January 2, 2006. Sago Mine, Wolf Run Mining Company, Tallmansville, Upshur County, West Virginia, I.D. No. 46-08791. Arlington, VA: U.S. Department of Labor, Mine Safety and Health Administration.
- Gexcon (2006). "Chapter 4 – Combustion Properties of Fuel-Air Mixtures." *Gas Explosion Handbook*. <http://www.gexcon.com>. 6/30/2006.
- Gibson, R. L. Jr., M. N. Toksöz, and W. Dong (1996). "Seismic radiation from explosively loaded cavities in isotropic and transversely isotropic media." *Bulletin of the Seismological Society of America*, **86**(6), 1910-1924.
- Gibowicz, S. (1963). "Magnitude and energy of subterranean shocks in Upper Silesia." *Studia Geophys. Geod.*, **7**, 1-19.
- Grammar, J. Jr. (1818) "An account of the coal mines in the vicinity of Richmand, Virginia." *American Journal of Science*, **1**, 125-130.
- Hanks, T. and H. Kanamori (1979). "A moment magnitude scale." *Journal of Geophysical Research*, **84**(B5), 2348-2350.
- Havskov J. and G. Alguacil (2006). *Instrumentation in Earthquake Seismology*. The Netherlands: Springer.

- Hooper, H., J. Bonner and M. Leidig (2006). "Effects of confinement on short-period surface waves: observations from a new dataset." *Bulletin of the Seismological Society of America*, **96**(2), 697-712.
- Humphrey, H. B. (1960). Historical summary of coal-mine explosions in the United States, 1810-1958. *Bureau of Mines Bulletin No. 586*.
- Iannacchione, A. T., T. Batchler and T. E. Marshall (2004). "Mapping hazards with microseismic technology to anticipate roof falls – a case study." In: Proceedings of the 23rd International Conference on Ground Control in Mining, August 3-5, 2004. Morgantown, WV: West Virginia University, 327-333.
- Iannacchione, A. T., L. M. Burke and M. C. Chapman (2005a). "Characterizing roof fall signatures from underground mines." In: *Proceedings of the Sixth International Symposium on Rockburst and Seismicity in Mines (Perth, Australia, March 9-11, 2005)*. Nedlands, Australia: Australian Centre for Geomechanics, 619-629.
- Iannacchione, A. T., G. S. Esterhuizen, T. S. Bajpayee, P. L. Swanson and M. C. Chapman (2005b). "Characteristics of mining-induced seismicity associated with roof falls and roof caving events." In: *Proceedings of the 40th U.S. Rock Mechanics Symposium*, Anchorage, AK.
- Iannacchione, A. T., T. S. Bajpayee and J. Edwards (2005c). "Forecasting roof falls with monitoring technologies – a look at the Moonee Colliery experience." In: *Proceedings of the 24th International Conference on Ground Control in Mining*, Morgantown, West Virginia, August 2-4, 2005.
- Johnston, A. C (1987). "Air blast recognition and location using regional seismographic networks". *Bulletin of Seismological Society of America*, **77**(4), 1446-1456.
- Kattenbraker, S. R. (2002). Explosion at Big Ridge Mine Portal #2, February 1, 2002. Memorandum of July 2, 2002, for the record from Steven R. Kattenbraker: U.S. Department of Labor, Mine Safety and Health Administration.
- Kearey, P., M. Brooks and I. Hill (2002). *An Introduction to Geophysical Exploration*, Third Ed., Blackwell Science, London.
- Kondrat'yev, Yu. V., S. K. Daragan, Ye. I. Lyuke and V. Ye. Peregontseva (1984). "The spectra of longitudinal and converted seismic waves as a function of underground explosion energy." *Physics of the Solid Earth*, **20**(4), 262-268.
- Leighton, F. J. (1984). "Microseismic monitoring and warning of rockbursts." In *Rockbursts and Seismicity in Mines* (N.C. Gay and E.H. Wainwright, eds.), Symp. Ser. No. 6, pg. 287-295, S. Afr. Inst. Min. Metal., Johannesburg.
- Light, T. E., R. C. Herndon, A. R. Guley Jr., G. L. Cook, M. A. Odum, R. M. Bates Jr., et al. (2007). Report of investigation, fatal underground coal mine explosion, May 20, 2006. Darby Mine No. 1, Kentucky Darby L.L.C., Holmes Mill, Harlan County, Kentucky, I.D. No. 15-18185. Arlington, VA: U.S. Department of Labor, Mine Safety and Health Administration.
- Mandal, B. and M. N. Toksoz (1991). "Effects of an explosive source in an anisotropic medium." *Geophysical Monograph*, **65**, 261-268.

- Mendecki, A. J. (1997). "Keynote lecture: Principles of monitoring seismic rock mass response to mining." In: *Rockbursts and Seismicity in Mines - Proceedings of the 4th International Symposium on Rockbursts and Seismicity in Mines*. Eds. S. J. Gibowicz and S. Lasocki. Kraków, Poland: A.A. Balkema. 69-80.
- Millero, E. R. Jr. (2008). "Strengthening an Existing 20-psi Mine Seal with PPG's Polyurea Coated Retrofit." Contract report for NIOSH BAA: 2007-N-09921.
- Mitchell, D. W. (1971). Explosion-proof bulkheads: present practices. *RI 7581, NTIS No. PB 205 507*. Pittsburgh, PA: U.S. Department of the Interior, Bureau of Mines.
- MSHA (2007). Accident, illness and injury and employment self-extracting files (part 50 data), 1975-2006. Denver, CO: U.S. Department of Labor, Mine Safety and Health Administration, Office of Injury and Employment Information. [<http://www.msha.gov/STATS/PART50/p50y2k/p50y2k.HTM>]. Date accessed: July 2007.
- Nagy, J. (1981). The explosion hazard in mining. *IR 1119*. Pittsburgh, PA: U.S. Department of Labor, Mine Safety and Health Administration.
- Perret, W. R. (1968). "Shear waves from a nuclear explosion in a salt cavity." *Bulletin of the Seismological Society of America*, **58**(6), 2043-2051.
- Rice, G. S., L. M. Jones, W. L. Egy and H. P. Greenwald (1922). Coal-dust explosion tests in the experimental mine, 1913-1918, inclusive. *Bureau of Mines Bulletin No. 167*.
- Rice, G. S., H. P. Greenwald, H. C. Howarth and S. Arins (1931). Concrete stoppings in coal mines for resisting explosions: detailed tests of typical stoppings and strength of coal as a buttress. *Bureau of Mines Bulletin No. 345*.
- Richmond, J. K., G. C. Price, M. J. Sapko and E. M. Kawenski. Historical summary of coal mine explosions in the United States, 1959-81. *IC 8909*. Pittsburgh, PA: U.S. Department of Labor, Bureau of Mines.
- Ross, E. Jr. and M. J. Schultz (1996). Report of investigation (underground coal mine). Noninjury coal mine explosion. Mine No. 1 (I.D. No. 46007273), Oasis Contracting, Inc., Quinland, Boone County, West Virginia, May 15, 1996 and June 22, 1996: U.S. Department of Labor, Mine Safety and Health Administration.
- Rutherford, J. W., R. J. Painter, J. E. Urosek, C. R. Stephan and W. A. Dupree Jr. (1993). Report of investigation, underground coal mine explosion, Blacksville No 1. Mine, I.D. No. 46-01867. Consolidation Coal Company, Blacksville, Monongalia County, West Virginia, March 19, 1992. Arlington, VA: U.S. Department of Labor, Mine Safety and Health Administration.
- Sapko, M. J., E. S. Weiss, K. L. Cashdollar and I. A. Zlochower (2000). "Experimental Mine and Laboratory Dust Explosion Research at NIOSH." *Journal of Loss Prevention in the Process Industries*, **13**(3), 229-242.
- Scott, D. S. and C. R. Stephan (1997). Accident investigation report (underground coal mine). Non-injury methane explosion. Oak Grove Mine (I.D. No. 01-00851), U.S. Steel Mining Company L.L.C., Adger, Jefferson County, Alabama, July 9, 1997. Birmingham, AL: U.S. Department of Labor, Mine Safety and Health Administration.
- Sercel (2005). L-28 Digital Grade Geophone. <ftp://ftp.sercel.com/pdf/brochures/GeophonesHydrophones.pdf>.
- Sercel (2008). Mark Products TDC-II case brochure. <http://www.sercel.com/>.

- Sharpe, J. A. (1941). "The production of elastic waves by explosion pressures, II, results of observations near an exploding charge." *Geophysics*, **7**(3), 311-321.
- Šílený, J., V. Vavryčuk, C. Baker, et al. (1997). "Determination of source parameters from noisy waveforms: Inversion of displacement seismograms versus accelerograms." In: *Rockbursts and Seismicity in Mines - Proceedings of the 4th International Symposium on Rockbursts and Seismicity in Mines*. Eds. S.J. Gibowicz and S. Lasocki. Kraków, Poland: A.A. Balkema. 95-100.
- Smith, A. T. (1993). "Discrimination of explosions from simultaneous mining blasts." *Bulletin of the Seismological Society of America*, **83**(1), 160-179.
- South, J. S. (1987). Report of investigation (underground coal mine). Non-injury methane explosion. Roadfork No. 1 mine (I.D. 15-10753), Sidney Coal Company, Incorporated, Sidney, Pike County, Kentucky, Discovered: October 7, 1986: U.S. Department of Labor, Mine Safety and Health Administration.
- Smith, A. T. (1993). "Discrimination of Explosions from Simultaneous Mining Blasts." *Bulletin of the Seismological Society of America*. **83**(1), 160-179.
- Stump, B., C. Hayward, C. Hetzer and R. Zhou (2000). "Utilization of seismic and infrasound signals for characterizing mining explosions." In: *Proceedings of the 23rd Seismic Research Review on Worldwide Monitoring of Nuclear Explosions*, 2– 5 October 2001, Jackson, Wyoming.
- Swanson, P., B. Kenner and T. Krahenbuhl (2002). "Seismic Event Data Acquisition and Processing: Distribution and Coordination Across PC-Based Networks." In: *Application of Computers and Operations Research in the Mineral Industry: Proceedings of the 30th International Symposium* S. Bandopadhyay ed., Society Of Mineral Metallurgy, and Exploration.
- Sumpter, J. E., M. J. Hudak, M. G. Kalich, L.E. Cook, W. A. Dupree Jr. and M. J. Schultz (1996). Report of investigation (underground coal mine). Noninjury coal mine explosion. Gay No. 50 mine (ID No. 46-01816), U.S. Steel Mining Company, Inc., Pineville, Wyoming County, West Virginia, between June 9-16, 1995. Mount Hope, WV: U.S. Department of Labor, Mine Safety and Health Administration.
- Thayer, D. D (1964). Ground motion caused by explosions, sonic booms, and thunder. Thesis, New Mexico Institute of Mining and Technology, Master of Science.
- Triebisch, G. and M. J. Sapko (1990), "Lake Lynn Laboratory: A State-of-the-Art Mining Research Facility." In: *Proceedings of the International Symposium on Unique Underground Structures*, 2:75-1 - 75-21.
- Watteyne, V., C. Meissner and A. Desborough (1908). The prevention of mine explosions: report and recommendations, with letter of transmittal by James Rudolph Garfield, Secretary of the Interior. Bulletin 369, Washington D.C.: Department of the Interior, United States Geological Survey.
- Weiss, E. S., Cashdollar, K. L., Mutton, I. V., Kohli, D. R. and Slivensky, W. A. (1999). Evaluation of Reinforced Cementitious Seals. *Publication No. 99-136*, Pittsburgh, PA: U.S. Department of Health and Human Services, Public Health Service, Centers for Disease Control and Prevention, National Institute for Occupational Safety and Health, DHHS(NIOSH) Publication No. 99-136, Report of Investigations 9647.

- Weiss, E. S., and Harteis, S. P. (2008a). Strengthening Existing 20-psi Mine Ventilation Seals With Carbon Fiber-Reinforced Polymer Reinforcement. *Publication No. 2008-106*, Pittsburgh, PA: U.S. Department of Health and Human Services, Public Health Service, Centers for Disease Control and Prevention, National Institute for Occupational Safety and Health, DHHS(NIOSH) Publication No. 2008-106, Report of Investigations 9673.
- Weiss, E. S., Cashdollar, K. L., Harteis, S. P., Shemon, G. J., Beiter, D. A. and Urosek, J. E. (2008b). Explosion Effects on Mine Ventilation Stoppings. *Publication No. 2009-102*, Pittsburgh, PA: U.S. Department of Health and Human Services, Public Health Service, Centers for Disease Control and Prevention, National Institute for Occupational Safety and Health, DHHS(NIOSH) Publication No. 2009-102, Report of Investigations 9676.
- Yang, X., B. W. Stump and W. S. Phillips (1998). "Source mechanism of an explosively induced mine collapse." *Bulletin of the Seismological Society of America*, **88**(3), 843-854.
- Zipf, R. K., M. J. Sapko and J. F. Brune (2007). Explosion pressure design criteria for new seals in U.S. coal mines. *Publication No. 2007-144, Information Circular 9500*: Pittsburgh, PA: Department of Health and Human Services, Public Health Service, Centers for Disease Control and Prevention, National Institute for Occupational Safety and Health.

# Appendix A:

## Mine Shot Plans and Mine Structure Descriptions<sup>\*</sup>

---

<sup>\*</sup> Mine shot plan summaries and experimental designs provided by National Institute for Occupational Safety and Health, Pittsburgh Research Laboratory, Disaster Prevention and Response Branch. Mine shots #503 – 507 are referenced in Cashdallar et al. (2007) and Gates et al. (2007). Mine shots #508 and 509 are referenced in Weiss et al. (2008a). Mine shots #510 and 519 are referenced in Weiss et al. (2008b). Mine shots #523 and 524 are referenced in Millero (2008). Mine shots #513, 514, 516 – 18, 520 – 522 are not yet published however the work was completed by Ken Cashdollar, Eric Weiss and Sam Harteis as part of the mine explosion program for NIOSH, Pittsburgh Research Laboratory's Disaster Prevention and Response Branch.



# Lake Lynn Experimental Mine Shot #503

**Mine Shot Date:** August 4, 2006

**Description of Mine Shot:** Methane explosion against a seal in C-drift. Approximately 9.5% gas up to C-47 (661 ft<sup>3</sup> natural gas) was used and ignited at C-35 using triple point ignition (two matches twisted together at each of the three locations) which is equally spaced across the entry 1 ft off the floor at C-35. Five water-filled barrels were spaced equally across the entry at C-40 to act as turbulence generators. Two shelves were suspended from the mine roof at C-44 which contained 4 pounds (100 g/m<sup>3</sup> coal concentration) of PPC dust on each shelf (total PPC of 8 pounds).

**Seal in the path of explosion:** Yes

**Seal failure due to explosion:** No

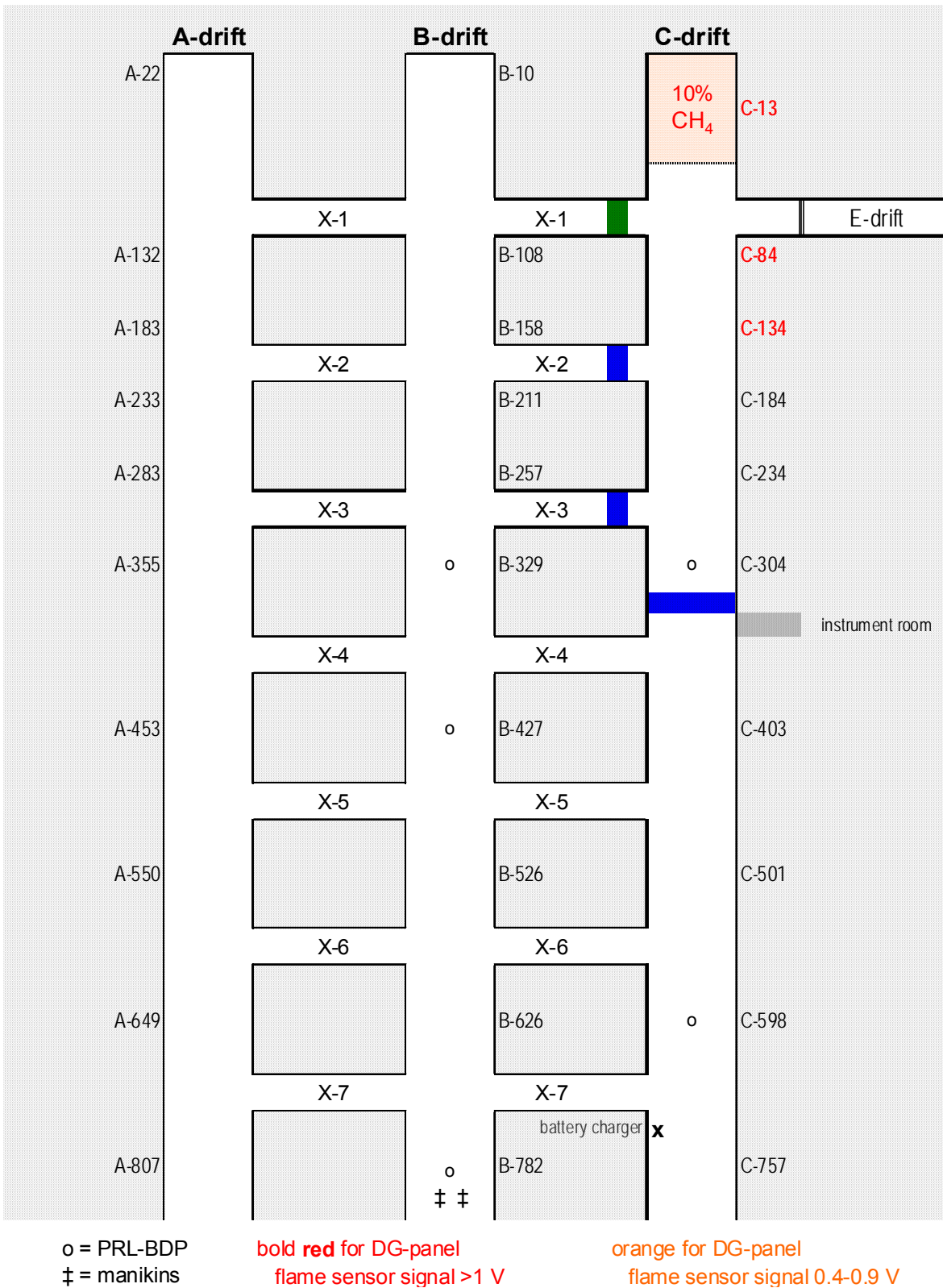


Figure A.1 – Experimental design for mine shot #503.

**Seal Notes (colors coordinate with seal locations in Figure A.1):**

- A standard-type, solid-concrete-block seal (with pilaster) is located at X1 between B- and C-drifts. Quikrete’s BlocBond (1225-51) was used as mortar.
- A properly constructed 40” thick low-strength cellular concrete seal block seal is located at X2 between B- and C-Drifts; staggered joints, fully mortared joints (BlocBond), no hitching.
- A Sago 40” thick low-strength cellular concrete seal block seal is located at X3.
- A Sago 40” thick low-strength cellular concrete seal block seal was located across C-drift between crosscuts 3 & 4 (~C-320).

**Table A.1 – Maximum pressures observed at the seals during mine shot #503.**

<b>C-Drift Pressure &amp; Break-Wire Data at Seals</b>							
Seal	Seal Pressures				LVDT		Break Time
	Wall Static Pressures			Deflection			
	kPa, NI	psi, NI	psi, KS	in	mm	sec	
X-1 BC 59 ft 18 m	H				--	--	--
	V		~15	~14.5			
		seal survived					
X-2 BC 156 ft 130½ m	H	92	13.3	13.4	0.01	0.3	--
	V		13.6				
		seal survived					
X-3 BC 256 ft 78 m	H	108	15.7	15.7	0.04	1.0	--
	V	109	15.8				
		seal survived					
C-drift 321 ft 98 m	rib	119	17.2	17.2	0.04	1.0	--
	H	118	17.2	17.2			
	V	117	17.0		seal survived		

# Lake Lynn Experimental Mine Shot #504

**Mine Shot Date:** August 16, 2006

**Description of Mine Shot:** Methane explosion against a seal in C-Drift. Approximately 9.5% gas up to C-47 (661 ft<sup>3</sup> natural gas) was used and ignited at C-28.5 using triple point ignition (two matches twisted together at each of the three locations) which is equally spaced across the entry 1 ft off the floor at C-35. Five water-filled barrels were spaced equally across the entry at C-40 to act as turbulence generators. Two shelves were suspended from the mine roof at C-44 which contained 4 pounds (100 g/m<sup>3</sup> coal concentration) of PPC dust on each shelf (total PPC of 8 pounds).

**Seal in the path of explosion:** Yes

**Seal failure due to explosion:** No

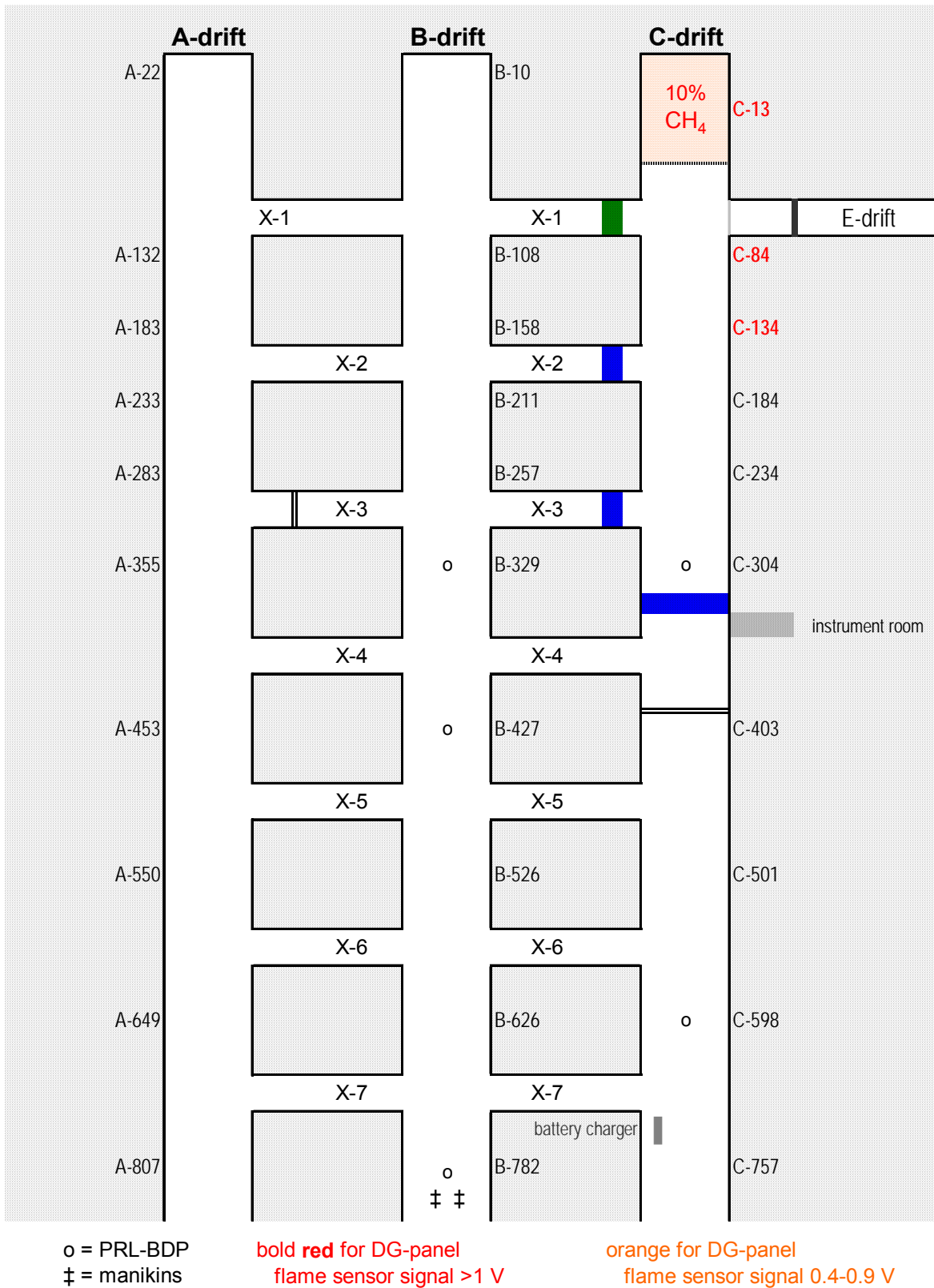


Figure A.2 – Experimental design for mine shot #504.

**Seal Notes (colors coordinate with seal locations in Figure A.2):**

- A standard-type, solid-concrete-block seal (with pilaster) is located at X1 between B- and C-drifts. Quikrete’s BlocBond (1225-51) was used as mortar.
- A properly constructed 40” thick low-strength cellular concrete seal block seal is located at X2 between B- and C-Drifts; staggered joints, fully mortared joints (BlocBond), no hitching.
- A Sago 40” thick low-strength cellular concrete seal block seal is located at X3.
- A Sago 40” thick low-strength cellular concrete seal block seal was located across C-drift between crosscuts 3 & 4 (~C-320).
- A dry-stacked, hollow-concrete-block (3-cell block) stopping was located in crosscut 3 between A- and B-drifts and across C-drift between crosscuts 4 and 5. Quikrete B-bond was used to coat both sides of each stopping.

**Table A.2 – Maximum pressures observed at the seals during mine shot #504.**

<b>C-Drift Pressure, LVDT, &amp; Break-Wire Data at Seals</b>							
Seal		Seal Pressures			LVDT		Break
		Wall Static Pressures			Deflection		Time,
		kPa, NI	psi, NI	psi, KS	in	mm	sec
<b>X-1 BC</b>							
59 ft			~16½	~16½	--	--	
18 m		<i>seal survived</i>					
<b>X-2 BC</b>	<i>H</i>	103	14.9	14.9	0.01	0.4	--
156 ft			15.3				
130½ m		<i>seal survived</i>					
<b>X-3 BC</b>	<i>H</i>	126	18.2	18.2	0.09	2.2	--
256 ft	<i>V</i>	126	18.2	18.2			
78 m			18.0				
		<i>seal survived</i>					
<b>C-drift</b>	<i>rib</i>	142	20.5	20.5	0.07	1.7	--
321 ft	<i>H</i>	142	20.6	20.6			
98 m	<i>V</i>	140	20.4	20.4			
		<i>seal survived</i>					

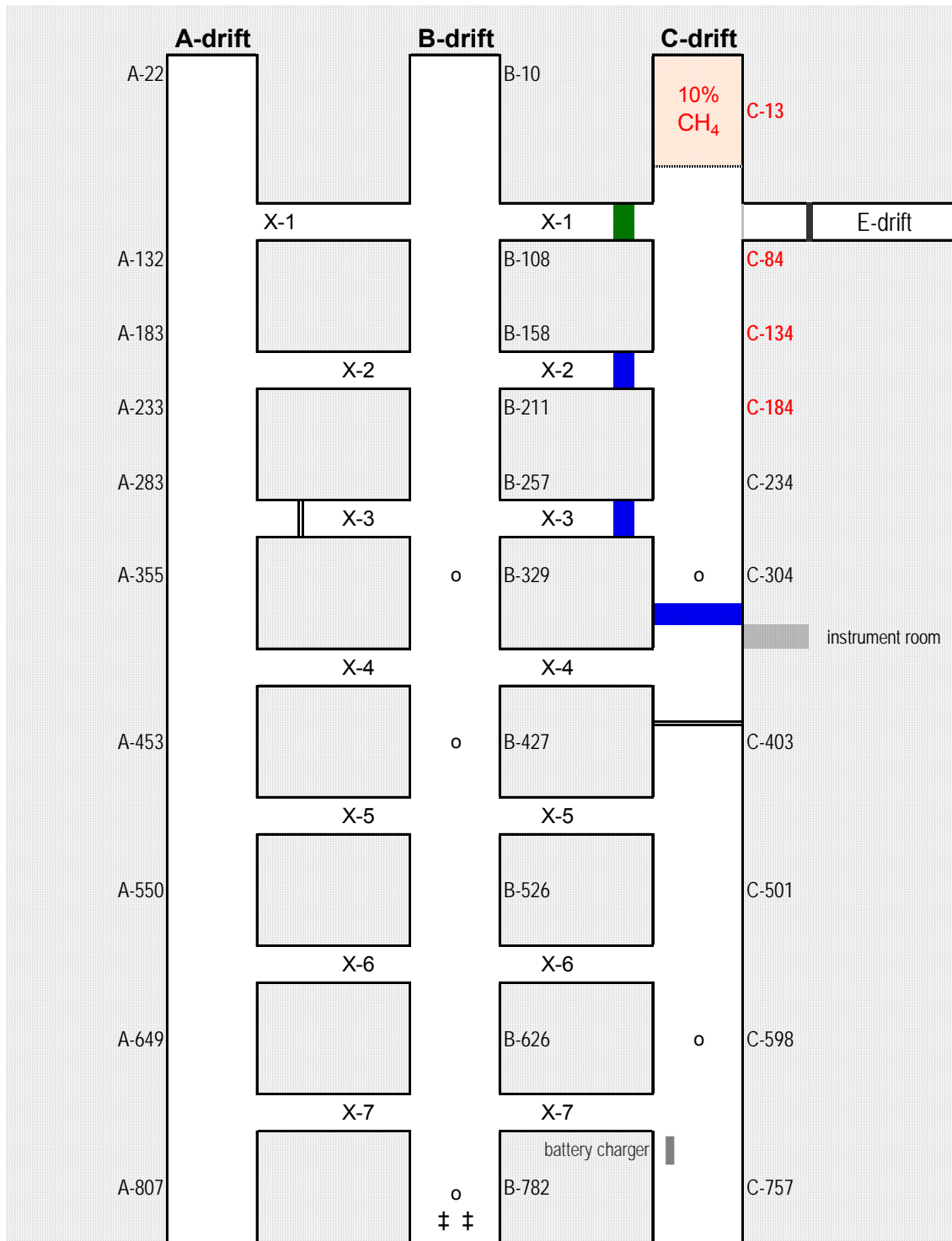
# Lake Lynn Experimental Mine Shot #505

**Mine Shot Date:** August 23, 2006

**Description of Mine Shot:** Methane explosion against a seal in C-drift. Approximately 9.5% gas up to C-47 (661 ft<sup>3</sup> natural gas) was used and ignited at the face using triple point ignition (two matches twisted together at each of the three locations) which is equally spaced across the entry 1 ft off the floor at C-35. Five water-filled barrels were spaced equally across the entry at C-40 to act as turbulence generators. Two shelves were suspended from the mine roof at C-44 which contained 4 pounds (100 g/m<sup>3</sup> coal concentration) of PPC dust on each shelf (total PPC of 8 pounds).

**Seal in the path of explosion:** Yes

**Seal failure due to explosion:** Yes



o = PRL-BDP  
 ‡ = manikins

**bold red** for DG-panel  
 flame sensor signal >1 V

orange for DG-panel  
 flame sensor signal 0.4-0.9 V

**Figure A.3** – Experimental design for mine shot #505.



**Seal Notes (colors coordinate with seal locations in Figure A.3):**

- A standard-type, solid-concrete-block seal (with pilaster) is located at X1 between B- and C-drifts. Quikrete’s BlocBond (1225-51) was used as mortar.
- A properly constructed 40” thick low-strength cellular concrete seal block seal is located at X2 between B- and C-Drifts; staggered joints, fully mortared joints (BlocBond), no hitching.
- A Sago 40” thick low-strength cellular concrete seal block seal is located at X3.
- A Sago 40” thick low-strength cellular concrete seal block seal was located across C-drift between crosscuts 3 & 4 (~C-320).
- A dry-stacked, hollow-concrete-block (3-cell block) stopping was located in crosscut 3 between A- and B-drifts and across C-drift between crosscuts 4 and 5. Quikrete B-bond was used to coat both sides of each stopping.

**Table A.3 – Maximum pressures observed at the seals during mine shot #505.**

<b>C-Drift Pressure &amp; Break-Wire Data at Seals</b>							
Seal	Stopping	Seal Pressures			LVDT		Break
		Wall Static Pressures			Deflection		Time,
		kPa, NI	psi, NI	psi, KS	in	mm	sec
X-1 BC							
59 ft			~25½	~25	--	--	
18 m		<i>seal survived</i>					
X-2 BC	H	178	??	25.8	0.03	0.6	--
156 ft			23				
130½ m		<i>seal survived</i>					
X-3 BC	H	239	34.7	33.1	>6	>150	0.753
256 ft	V	226	32.8	32.8			0.743
78 m			-41				
		<i>seal destroyed, debris to far wall of A-drift (~108 ft)</i>					
X-3 AB	H	28	4.0	4.0			2.17
		<i>stopping partially destroyed, debris to A-drift wall</i>					
C-drift	rib	407	59.1	58.9	>6	>150	
320 ft	H	391	56.6	55.7			0.685
98 m	V	373	54.1	54.1			0.677
		<i>seal destroyed, debris traveled ~556 ft</i>					
C-drift	H	86	12.4	12.4			1.092
384 ft		<i>stopping destroyed, debris traveled ~460 ft</i>					

# Lake Lynn Experimental Mine Shot #506

**Mine Shot Date:** October 19, 2006

**Description of Mine Shot:** Methane explosion against a seal in C-drift. Approximately 9.5% gas up to C-71 (1,265 ft<sup>3</sup> natural gas) was used and ignited at the face using triple point ignition (two matches twisted together at each of the three locations) which is equally spaced across the entry 1 ft off the floor at C-35. Five water-filled barrels were spaced equally across the entry at C-40 to act as turbulence generators.

**Seal in the path of explosion:** Yes

**Seal failure due to explosion:** Yes

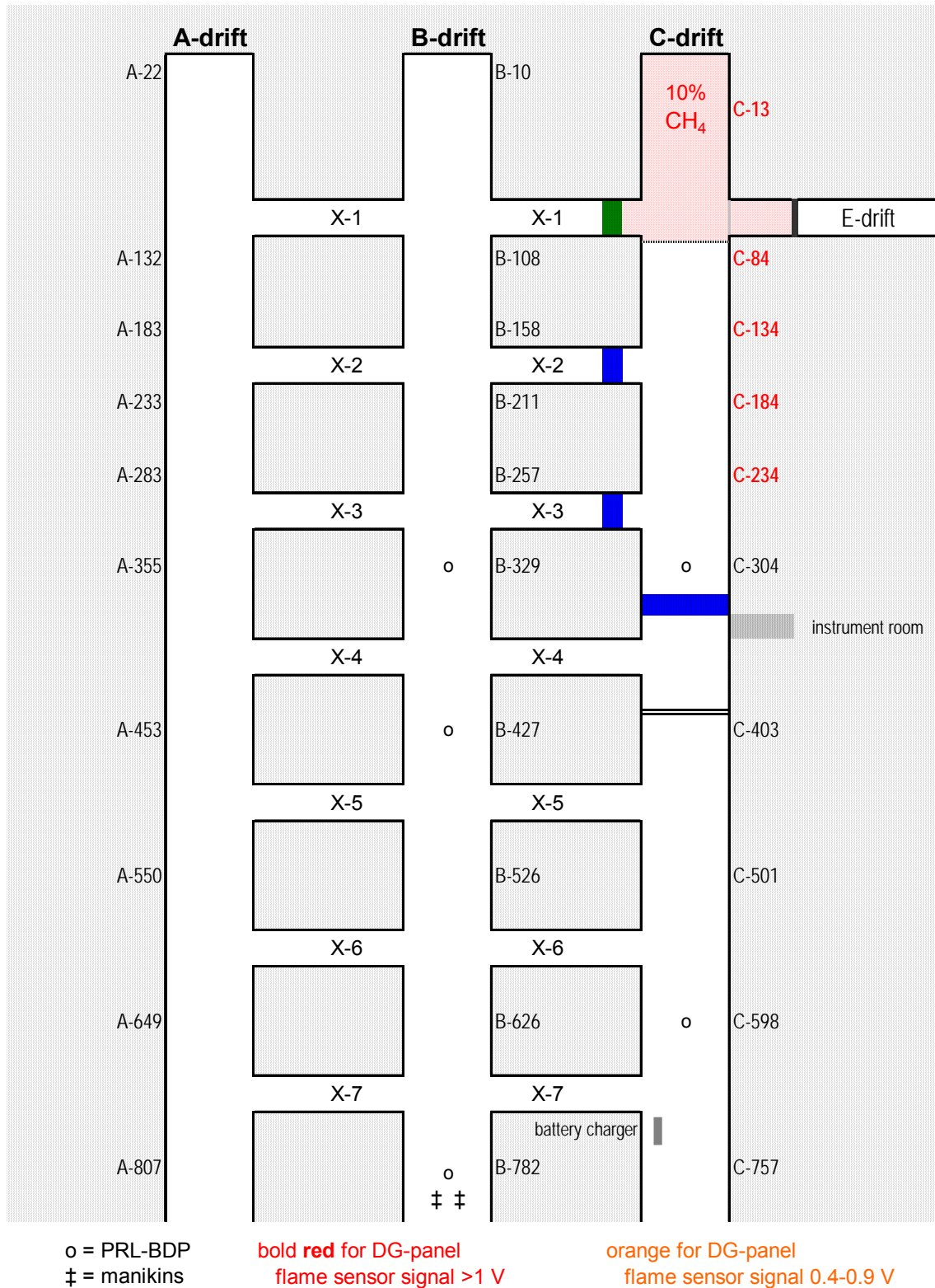


Figure A.4 – Experimental design for mine shot #506.

**Seal Notes (colors coordinate with seal locations in Figure A.4):**

- A standard-type, solid-concrete-block seal (with pilaster) was located at X1 between B- and C-drifts. Quikrete’s BlocBond (1225-51) was used as mortar.
- A properly constructed 40” thick low-strength cellular concrete seal block seal was located at X2 between B- and C-Drifts; staggered joints, fully mortared joints (BlocBond), no hitching.
- A standard solid-concrete-block seal (w/pilaster) was located in crosscut 3 between B- and C-drifts with Type S mortar and B-bond face coatings applied.
- A Sago 40” thick low-strength cellular concrete seal block seal was located across C-drift between crosscuts 3 & 4 (~C-320).
- A dry-stacked, hollow-concrete-block (3-cell block) stopping was located in crosscut 3 between A- and B-drifts and across C-drift between crosscuts 4 and 5. Quikrete B-bond was used to coat both sides of each stopping.

**Table A.4 – Maximum pressures observed at the seals during mine shot #506.**

<b>C-Drift Pressure &amp; Break-Wire Data at Seals</b>							
Seal or Stopping Location		Seal Pressures			LVDT		Break
		Wall Static Pressures			Deflection		Time,
		kPa, NI	psi, NI	psi, KS	in	mm	sec
X-1 BC	H		36.7				
59 ft			~37	~37	--	--	--
18 m		<i>seal survived</i>					
X-2 BC	V,i	253	36.7	36.4	0.06	1.6	--
	H,c	349	50.7	49.2			
156 ft	V,o	437	63.3	60.6			
130 1/2 m		<i>seal survived</i>					
X-3 BC	H	337	48.8	48.4	0.14	3.6	--
256 ft	V						--
78 m							
		<i>seal survived</i>					
C-drift	rib	684	99.2	99.3	>6	>150	
	H, embedded	637	92.3	92.6			
320 ft	H	629	91.1	89.0			0.578
98 m	V	622	90.1	89.2			0.575
		<i>seal destroyed, Omega block debris traveled ~917 ft, piece of BlocBond traveled ~1168 ft</i>					
C-drift	H	52	7.5	7.6			0.790
384 ft		<i>stopping destroyed, debris traveled ~748 ft</i>					

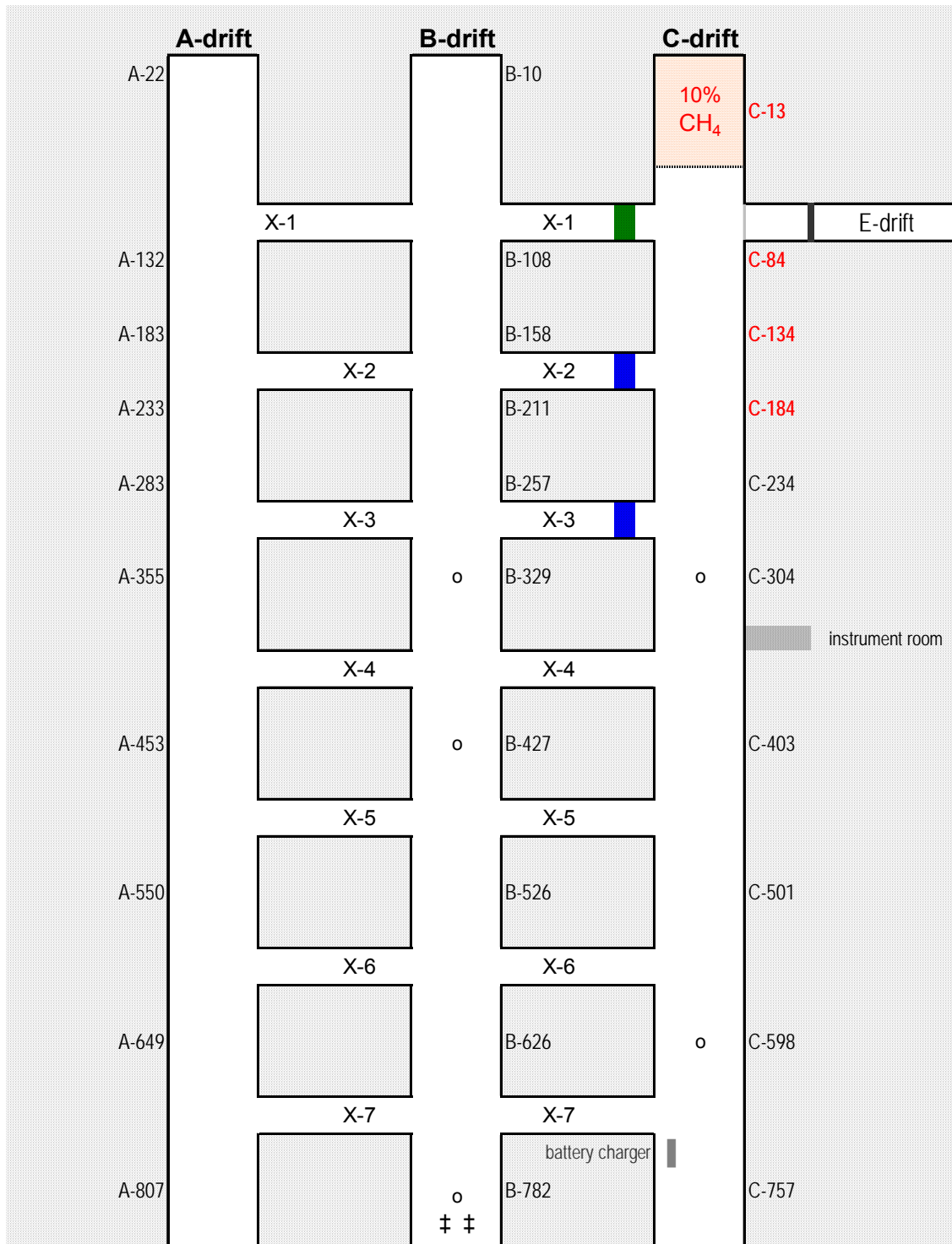
# Lake Lynn Experimental Mine Shot #507

**Mine Shot Date:** November 1, 2006

**Description of Mine Shot:** Methane explosion in C-Drift. Approximately 9.5% gas up to C-47 (1,265 ft<sup>3</sup> natural gas) was used and ignited at the face using triple point ignition (two matches twisted together at each of the three locations) which is equally spaced across the entry 1 ft off the floor at C-35. Five water-filled barrels were spaced equally across the entry at C-40 to act as turbulence generators. Two shelves were suspended from the mine roof at C-44 which contained 4 pounds (100 g/m<sup>3</sup> coal concentration) of PPC dust on each shelf (total PPC of 8 pounds).

**Seal in the path of explosion:** No

**Seal failure due to explosion:** No



o = PRL-BDP  
 ‡ = manikins

**bold red** for DG-panel  
 flame sensor signal >1 V

orange for DG-panel  
 flame sensor signal 0.4-0.9 V

Figure A.5 – Experimental design for mine shot #507.

**Seal Notes (colors coordinate with seal locations in Figure A.5):**

- A standard-type, solid-concrete-block seal (with pilaster) was located at X1 between B- and C-drifts. Quikrete's BlocBond (1225-51) was used as mortar.
- A properly constructed 40" thick low-strength cellular concrete seal block seal was located at X2 between B- and C-Drifts; staggered joints, fully mortared joints (BlocBond), no hitching.
- A standard solid-concrete-block seal (w/pilaster) was located in crosscut 3 between B- and C-drifts with Type S mortar and B-bond face coatings applied.
- A Sago 40" thick low-strength cellular concrete seal block seal was located across C-drift between crosscuts 3 & 4 (~C-320).
- A dry-stacked, hollow-concrete-block (3-cell block) stopping was located in crosscut 3 between A- and B-drifts and across C-drift between crosscuts 4 and 5. Quikrete B-bond was used to coat both sides of each stopping.

A tabulated summary of the pressure data measured at the mine seals was unavailable for mine shot #507, however a pressure-time curve for this experiment is plotted in Figure B.5 in Appendix B.

# Lake Lynn Experimental Mine Shot #508

**Mine Shot Date:** April 10, 2007

**Description of Mine Shot:** Methane explosion against a seal in C-drift. Approximately 9.5% gas up to C-47 (661 ft<sup>3</sup> natural gas) was used and ignited at the face using triple point ignition (two matches twisted together at each of the three locations) which is equally spaced across the entry 1 ft off the floor at C-35. Five water-filled barrels were spaced equally across the entry at C-40 to act as turbulence generators. Two shelves were suspended from the mine roof at C-44 which contained 4 pounds (100 g/m<sup>3</sup> coal concentration) of PPC dust on each shelf (total PPC of 8 pounds).

**Seal in the path of explosion:** Yes

**Seal failure due to explosion:** No



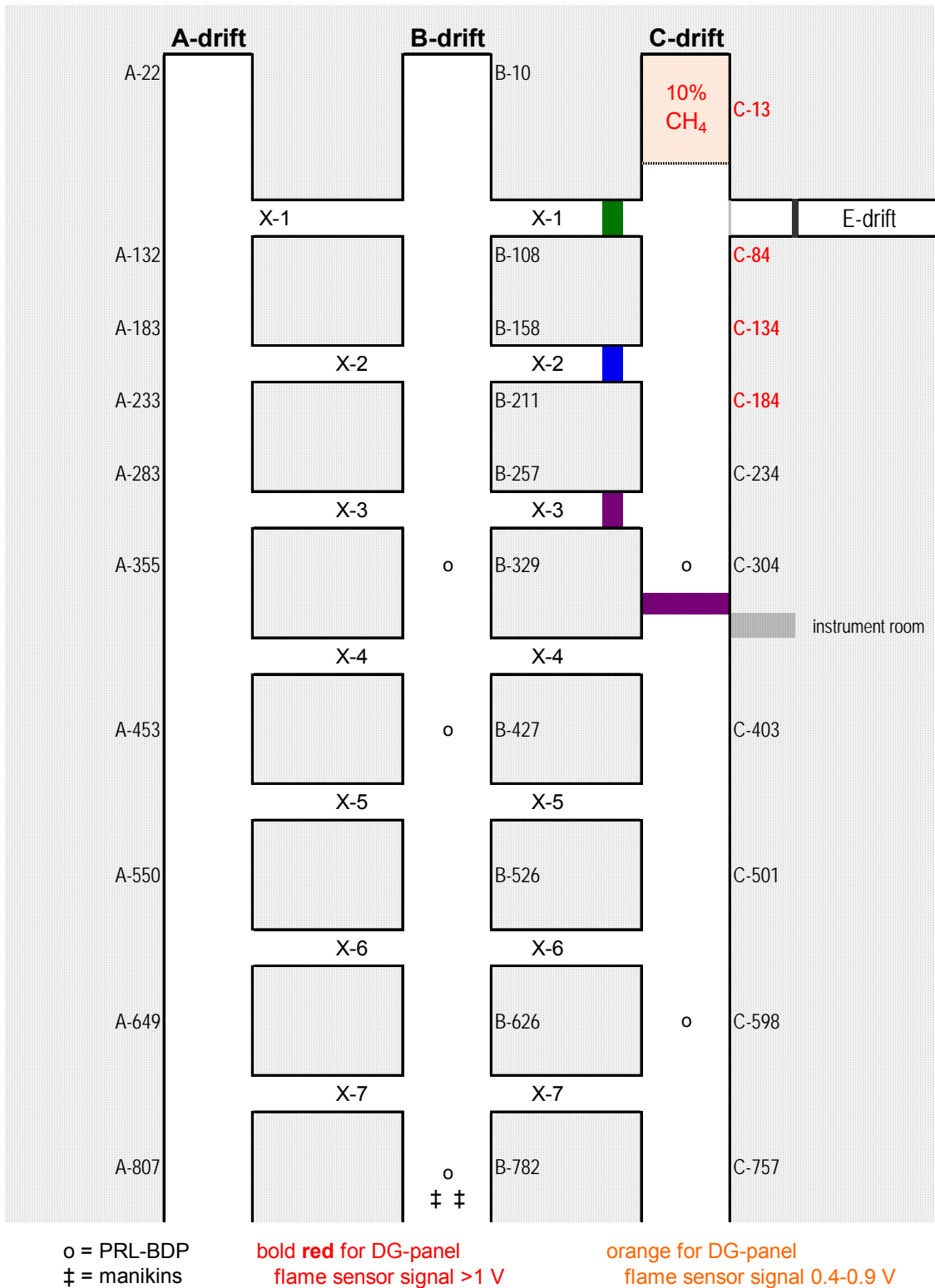


Figure A.6 – Experimental design for mine shot #508.

**Seal Notes (colors coordinate with seal locations in Figure A.6):**

- A standard-type, solid-concrete-block seal (with pilaster) was located at X1 between B- and C-drifts. Quikrete’s BlocBond (1225-51) was used as mortar.
- A properly constructed 40” thick low-strength cellular concrete seal block seal was located at X2 between B- and C-Drifts; staggered joints, fully mortared joints (BlocBond), no hitching. To ensure the seal that this seal did not fail a 6-in x 6-in x 0.5-in thick steel angle was anchored (using 1-in diameter Hilti Kwik Bolt III) across the roof and floor on the B-drift side of the seal.
- A 24-in thick low-strength cellular concrete seal block seal (with a 48-in by 48-in interlocked center pilaster and keyed to the ribs and floor with 6-in x 6-in x 0.5-in thick steel angle) was located in crosscut 3.
- A 4-ft thick pumpable cementitious seal using material with a 150- to 200-psi average compressive strength was located across C-drift between crosscuts 3 & 4 (~C-320-ft).

**Table A.5 – Maximum pressures observed at the seals during mine shot #508.**

<b>C-Drift Pressure &amp; Break-Wire Data at Seals</b>							
Seal or Stopping Location		Seal Pressures			LVDT		Break
		Wall Static Pressures			Deflection		Time,
		kPa, NI	psi, NI	psi, KS	in	mm	sec
<b>X-1 BC</b>							
59 ft		201	29.1	29.0	--	--	
18 m		<i>seal survived</i>					
<b>X-2 BC</b>	<i>I</i>	167	24.2	24.5	--	--	--
156 ft	<i>C</i>	182	26.4	26.9			
130 ½ m	<i>O</i>	210	30.4	30.2			
		<i>seal survived</i>					
<b>X-3 BC</b>	<i>I</i>	343	49.8	48.1	0.05	1.3	
256 ft	<i>C</i>	250	36.3	36.0	0.03	0.8	
78 m	<i>em</i>	228	33.0	32.3			
	<i>O</i>	265	38.4	38.6	0.04	1.0	
		<i>seal survived</i>					
<b>C-drift</b>	<i>rib</i>	408	59.1	58.6	0.60	15.2	
320 ft	<i>em</i>	357	51.7	51.6			
98 m	<i>H</i>	418	60.6	59.2	0.61	15.5	
	<i>V</i>	396	57.4	57.6			
		<i>seal survived</i>					

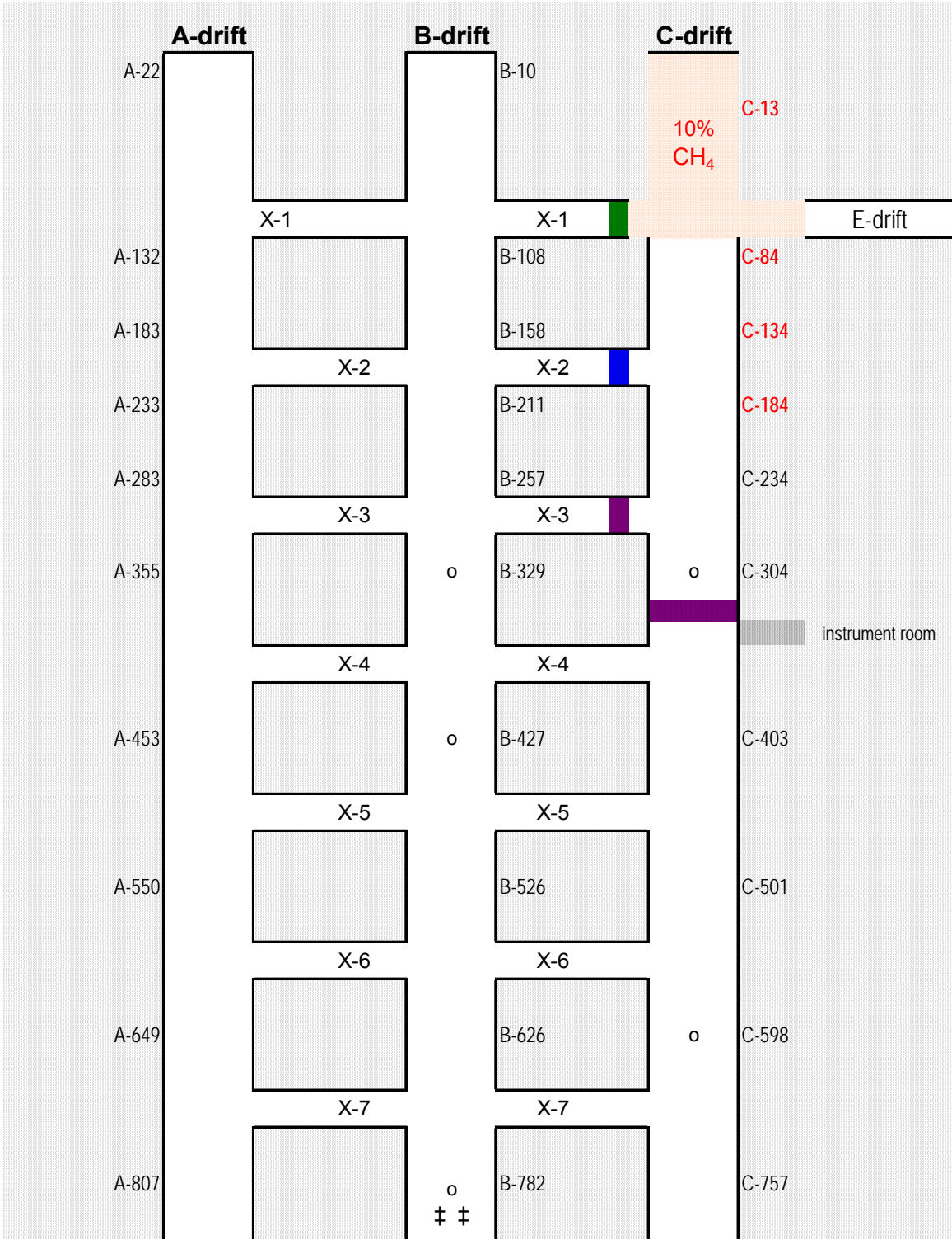
# Lake Lynn Experimental Mine Shot #509

**Mine Shot Date:** April 12, 2007

**Description of Mine Shot:** Methane explosion against a seal in C-drift. Approximately 9.5% gas up to C-71 (1,265 ft<sup>3</sup> natural gas) was used and ignited at the face using triple point ignition (two matches twisted together at each of the three locations) which is equally spaced across the entry 1 ft off the floor at C-35. Five water-filled barrels were spaced equally across the entry at C-40 to act as turbulence generators. Two shelves were suspended from the mine roof at C-77, C-87, C-97, and C-107 which contained 4 pounds (100 g/m<sup>3</sup> coal concentration) of PPC dust on each shelf (total PPC of 32 pounds).

**Seal in the path of explosion:** Yes

**Seal failure due to explosion:** Yes



o = PRL-BDP  
 ‡ = manikins

**bold red** for DG-panel  
 flame sensor signal >1 V

orange for DG-panel  
 flame sensor signal 0.4-0.9 V

Figure A.7 – Experimental design for mine shot #509.

**Seal Notes (colors coordinate with seal locations in Figure A.7):**

- A standard-type, solid-concrete-block seal (with pilaster) was located at X1 between B- and C-drifts. Quikrete's BlocBond (1225-51) was used as mortar.
- A properly constructed 40" thick low-strength cellular concrete seal block seal was located at X2 between B- and C-Drifts; staggered joints, fully mortared joints (BlocBond), no hitching. To ensure the seal that this seal did not fail a 6-in x 6-in x 0.5-in thick steel angle was anchored (using 1-in diameter Hilti Kwik Bolt III) across the roof and floor on the B-drift side of the seal.
- A 24-in thick low-strength cellular concrete seal block seal (with a 48-in by 48-in interlocked center pilaster and keyed to the ribs and floor with 6-in x 6-in x 0.5-in thick steel angle) was located in crosscut 3.
- A 4-ft thick pumpable cementitious seal using material with a 150- to 200-psi average compressive strength was located across C-drift between crosscuts 3 & 4 (~C-320-ft).

A tabulated summary of the pressure data measured at the mine seals was unavailable for mine shot #507, however a pressure-time curve for this experiment is plotted in Figure B.7 in Appendix B.

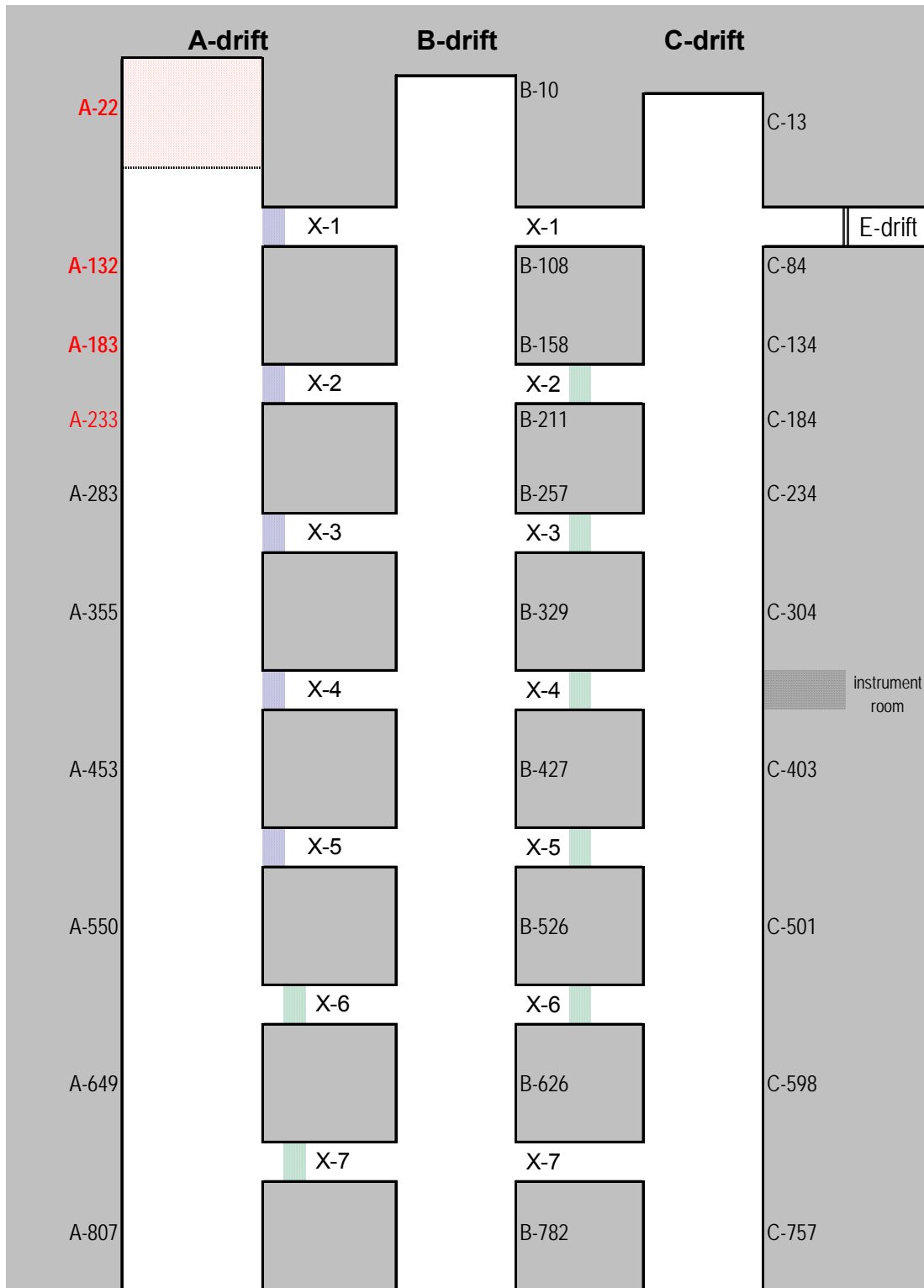
# Lake Lynn Experimental Mine Shot #510

**Mine Shot Date:** December 11, 2007

**Description of Mine Shot:** Methane explosion in A-Drift. Approximately 10% gas up to A-40 (530 ft<sup>3</sup> natural gas) was used and ignited at the face using a single point ignition (two matches twisted together at a center point of the face at mid-height).

**Seal in the path of explosion:** No

**Seal failure due to explosion:** No



**bold red for DG-panel**      orange for DG-panel  
 flame sensor signal >1 V      flame sensor signal 0.4-0.9 V

Figure A.8 – Experimental design for mine shot #510.

**Seal Notes (colors coordinate with seal locations in Figure A.8):**

- Standard-type, 16-in thick solid concrete block seals (w/32-in x 16-in center pilaster and Type S mortar) were located in crosscuts 1-5 between A- and B-Drifts. Each of these seals have been constructed as close as possible to the A-Drift rib-line. The seal in crosscut 1 had a blast-resistant door located between the center pilaster and the inby crosscut rib.
- An 8-in thick solid concrete block stopping with fully mortared (Type S) joints was constructed in crosscut 6 between A- and B-Drifts. A 6-in thick mortared solid-concrete-block stopping was constructed in crosscut 7. These stoppings were located approximately 10 ft into the crosscut as measured from the A-Drift rib-line and both were coated on the A-Drift side.
- Regular stoppings were located in crosscuts 2-5 between B- and C-Drifts.

**Table A.6 – Maximum pressures observed at the stoppings during mine shot #510.**

<b>Pressure, LVDT, &amp; Break-Wire Data at Stoppings</b>						
Stopping Location	Stopping Pressures &			LVDT		Break Time, sec
	Wall Pressures			Deflection		
	kPa, NI	psi, NI	psi, KS	in	mm	
<b>X-6 AB</b>	100	14.5	14.6	0.3	7	--
600 ft	75	11				
183 m	<i>stopping survived</i>					
<b>X-7 AB</b>	93	13.5	12.8	0.5	13	--
699 ft	73	11				
213 m	<i>stopping survived</i>					



# Lake Lynn Experimental Mine Shot #513

**Mine Shot Date:** January 15, 2008

**Description of Mine Shot:** Methane explosion in A-Drift with 80% rock dust concentration mix. Approximately 10% gas up to A-40 (530 ft<sup>3</sup> natural gas) was used and ignited at the face using a single point ignition (two matches twisted together at a center point of the face at mid-height). The dust zone extended from A-40 to A-340 (300 ft zone) and 480 lbs of PPC dust was mixed with 1,920 lbs of rock dust to provide an 80% rock dust concentration (81.5% total incombustible content). Pittsburgh pulverized coal (PPC) dust is approximately 80% minus 200 mesh. Total mix of the rock dust and coal dust was 2,400 lbs. Approximately 50% of the dust mixture was loaded on the roof shelves and the remainder on the mine floor.

**Seal in the path of explosion:** No

**Seal failure due to explosion:** No

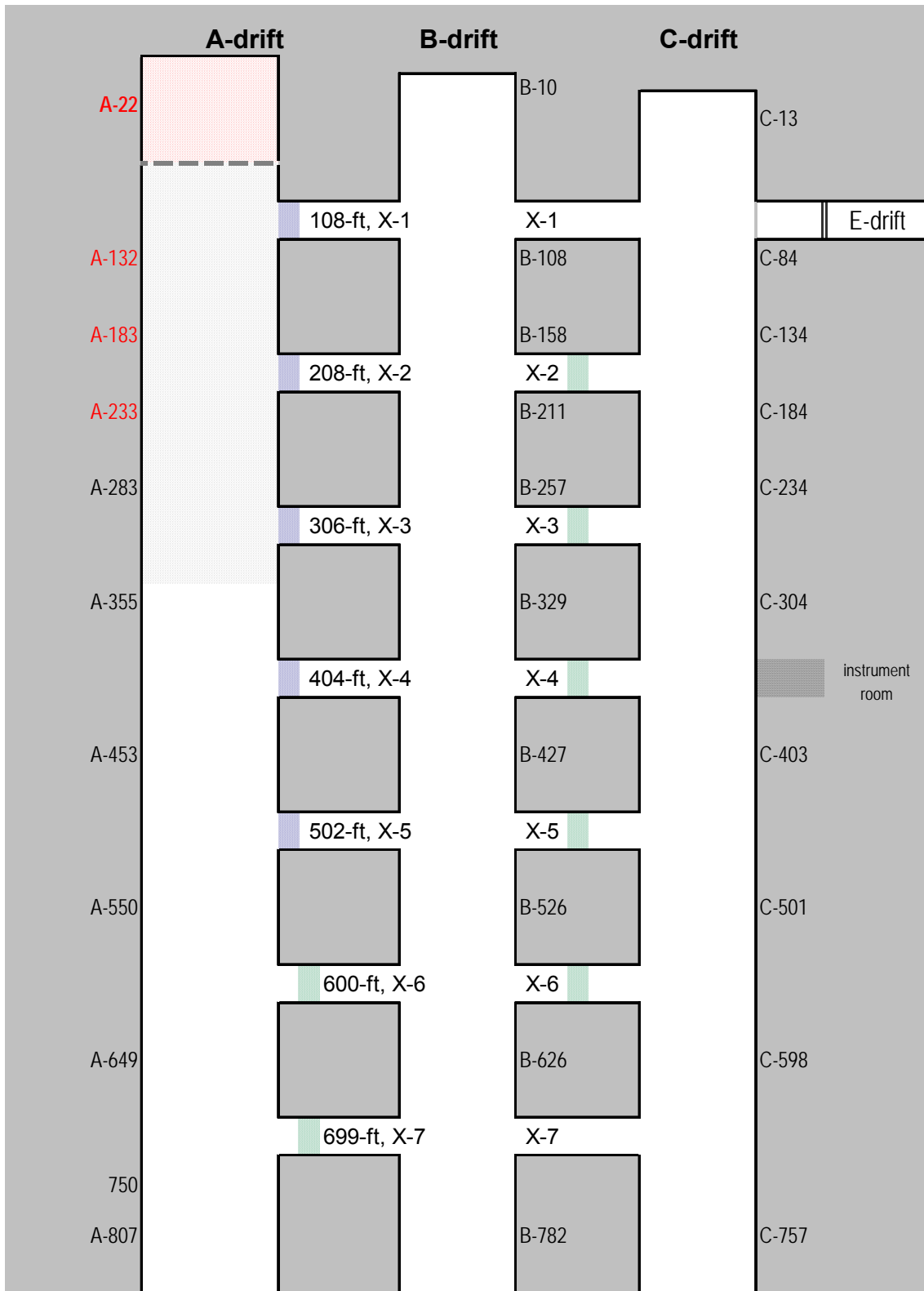


Figure A.9 – Experimental design for mine shot #513.

**Seal Notes (colors coordinate with seal locations in Figure A.9):**

- Standard-type, 16-in thick solid concrete block seals (w/32-in x 16-in center pilaster and Type S mortar) were located in crosscuts 1-5 between A- and B-Drifts. Each of these seals have been constructed as close as possible to the A-Drift rib-line. The seal in crosscut 1 had a blast-resistant door located between the center pilaster and the inby crosscut rib.
- An 8-in thick solid concrete block stopping with fully mortared (Type S) joints was constructed in crosscut 6 between A- and B-Drifts. A 6-in thick mortared solid-concrete-block stopping was constructed in crosscut 7. These stoppings were located approximately 10 ft into the crosscut as measured from the A-Drift rib-line and both were coated on the A-Drift side.
- Regular stoppings were located in crosscuts 2-5 between B- and C-Drifts.

**Table A.7 – Maximum pressures observed at the stoppings during mine shot #513.**

<b>Pressure, LVDT, &amp; Break-Wire Data at Stoppings</b>						
Stopping	Stopping Pressures & Wall Pressures			LVDT Deflection		Break Time,
	kPa, NI	psi, NI	psi, KS	in	mm	sec
	<b>X-6 AB</b>	66	9.5	9.6	--	
600 ft	56	8				
183 m	<i>stopping survived</i>					
<b>X-7 AB</b>	65	9.4	9.1	0.47	12	--
699 ft	57	8				
213 m	<i>stopping survived</i>					

# Lake Lynn Experimental Mine Shot #514

**Mine Shot Date:** January 23, 2008

**Description of Mine Shot:** Methane explosion in A-Drift with 64% rock dust concentration mix. Approximately 10% gas up to A-40 (530 ft<sup>3</sup> natural gas) was used and ignited at the face using a single point ignition (two matches twisted together at a center point of the face at mid-height). The dust zone extended from A-40 to A-340 (300 ft zone) and 451 lbs of coarse coal dust, 29 lbs of PPC dust was mixed with 853 lbs of rock dust to provide a 64% rock dust concentration (81.5% total incombustible content). Pittsburgh pulverized coal (PPC) dust is approximately 80% minus 200 mesh. Total mix of the rock dust and coal dust was 1,333 lbs. Approximately 50% of the dust mixture was loaded on the roof shelves and the remainder on the mine floor.

**Seal in the path of explosion:** No

**Seal failure due to explosion:** No

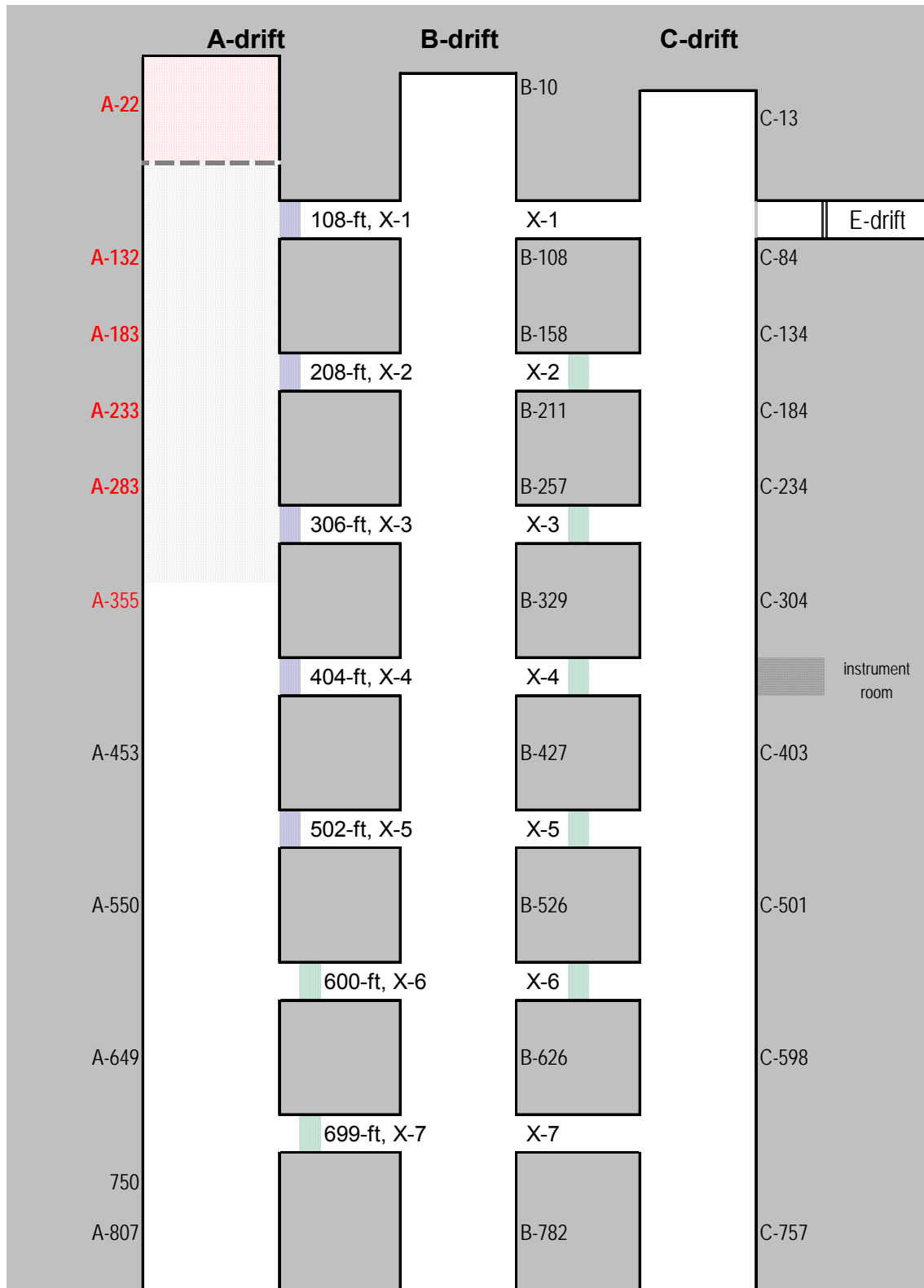


Figure A.10 – Experimental design for mine shot #514.

**Seal Notes (colors coordinate with seal locations in Figure A.10):**

- Standard-type, 16-in thick solid concrete block seals (w/32-in x 16-in center pilaster and Type S mortar) were located in crosscuts 1-5 between A- and B-Drifts. Each of these seals have been constructed as close as possible to the A-Drift rib-line. The seal in crosscut 1 had a blast-resistant door located between the center pilaster and the inby crosscut rib.
- An 8-in thick solid concrete block stopping with fully mortared (Type S) joints was constructed in crosscut 6 between A- and B-Drifts. A 6-in thick mortared solid-concrete-block stopping was constructed in crosscut 7. These stoppings were located approximately 10 ft into the crosscut as measured from the A-Drift rib-line and both were coated on the A-Drift side.
- Regular stoppings were located in crosscuts 2-5 between B- and C-Drifts.

**Table A.8 – Maximum pressures observed at the stoppings during mine shot #514.**

<b>Pressure, LVDT, &amp; Break-Wire Data at Stoppings</b>						
Stopping	Stopping Pressures &			LVDT		Break
	Wall Pressures			Deflection		Time,
	kPa, NI	psi, NI	psi, KS	in	mm	sec
<b>X-6 AB</b>	94	13.6	12.3	0.32	8	--
600 ft	66	10				
183 m	<i>stopping survived</i>					
<b>X-7 AB</b>	75	10.8	11.2	0.54	14	--
699 ft	63	9				
213 m	<i>stopping survived</i>					

# Lake Lynn Experimental Mine Shot #516

**Mine Shot Date:** February 6, 2008

**Description of Mine Shot:** Methane explosion in A-Drift with 69% rock dust concentration mix. Approximately 10% gas up to A-40 (530 ft<sup>3</sup> natural gas) was used and ignited at the face using a single point ignition (two matches twisted together at a center point of the face at mid-height). The dust zone extended from A-40 to A-340 (300 ft zone) and 451 lbs of coarse coal dust and 29 lbs of PPC dust was mixed with 1,068 lbs of rock dust to provide a 69% rock dust concentration (71.5% total incombustible content). Pittsburgh pulverized coal (PPC) dust is approximately 80% minus 200 mesh. Total mix of the rock dust and coal dust was 1,548 lbs. Approximately 50% of the dust mixture was loaded on the roof shelves and the remainder on the mine floor.

**Seal in the path of explosion:** No

**Seal failure due to explosion:** No

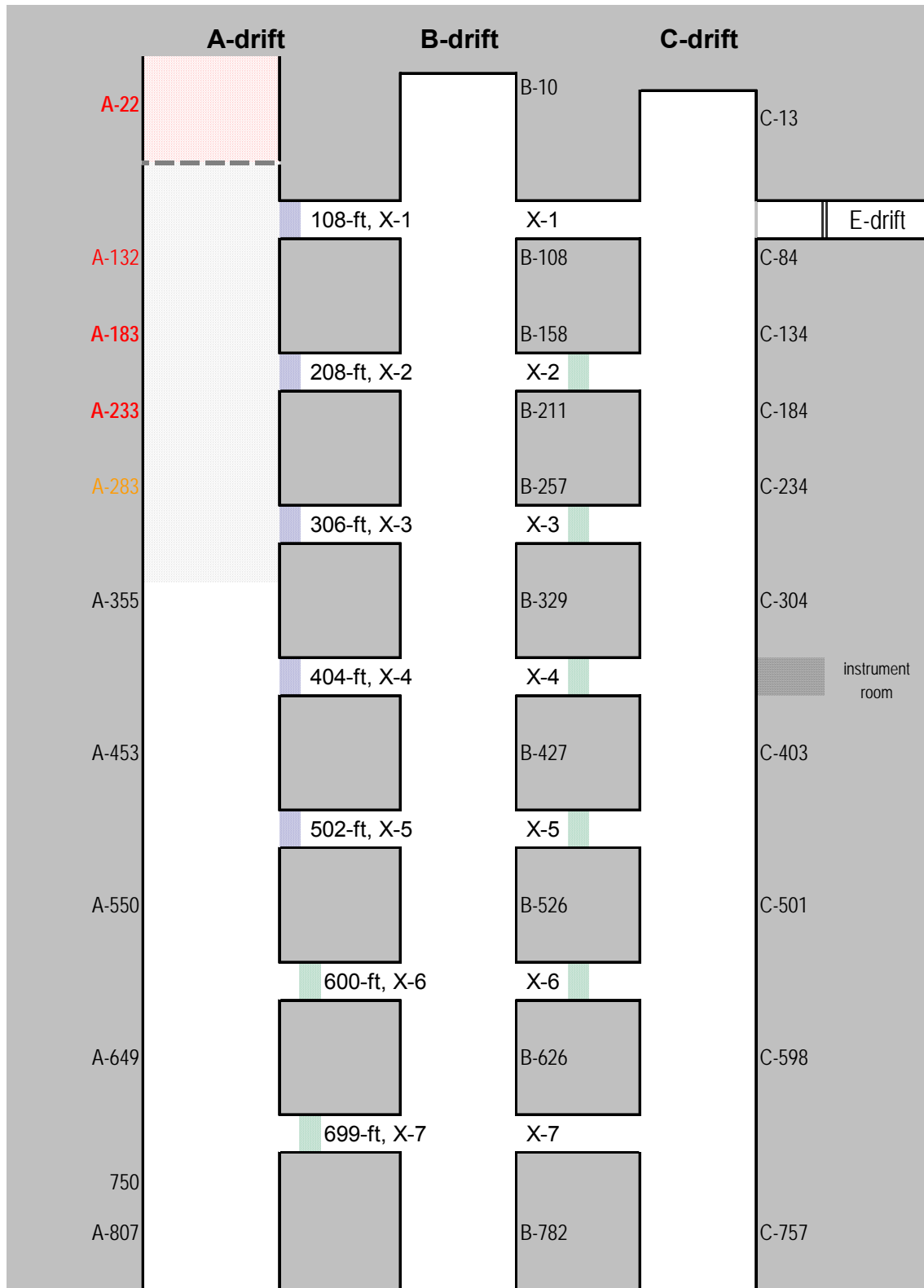


Figure A.11 – Experimental design for mine shot #516.



**Seal Notes (colors coordinate with seal locations in Figure A.11):**

- Standard-type, 16-in thick solid concrete block seals (w/32-in x 16-in center pilaster and Type S mortar) were located in crosscuts 1-5 between A- and B-Drifts. Each of these seals have been constructed as close as possible to the A-Drift rib-line. The seal in crosscut 1 had a blast-resistant door located between the center pilaster and the inby crosscut rib.
- An 8-in thick solid concrete block stopping with fully mortared (Type S) joints was constructed in crosscut 6 between A- and B-Drifts. A 6-in thick mortared solid-concrete-block stopping was constructed in crosscut 7. These stoppings were located approximately 10 ft into the crosscut as measured from the A-Drift rib-line and both were coated on the A-Drift side.
- Regular stoppings were located in crosscuts 2-5 between B- and C-Drifts.

**Table A.9 – Maximum pressures observed at the stoppings during mine shot #516.**

<b>Pressure, LVDT, &amp; Break-Wire Data at Stoppings</b>						
Stopping	Stopping Pressures & Wall Pressures			LVDT Deflection		Break Time,
	kPa, NI	psi, NI	psi, KS	in	mm	sec
	<b>X-6 AB</b>	85	12.4	11.5	0.26	7
600 ft	55	8				
183 m	<i>stopping survived - no damage</i>					
<b>X-7 AB</b>	69	10.0	10.2	0.67	17	--
699 ft	52	8				
213 m	<i>stopping survived - small horizontal crack at mid-height</i>					

# Lake Lynn Experimental Mine Shot #517

**Mine Shot Date:** February 13, 2008

**Description of Mine Shot:** Methane explosion in A-Drift with 71.7% rock dust concentration mix. Approximately 10% gas up to A-40 (530 ft<sup>3</sup> natural gas) was used and ignited at the face using a single point ignition (two matches twisted together at a center point of the face at mid-height). The dust zone extended from A-40 to A-340 (300 ft zone) and 297.6 lbs of coarse coal dust and 182.4 lb of PPC dust mixed was mixed with 1,216 lbs of rock dust to provide a 71.7% rock dust concentration (74% total incombustible content). Pittsburgh pulverized coal (PPC) dust is approximately 80% minus 200 mesh. Total mix of the rock dust and coal dust was 1,696 lbs. Approximately 50% of the dust mixture was loaded on the roof shelves and the remainder on the mine floor.

**Seal in the path of explosion:** No

**Seal failure due to explosion:** No

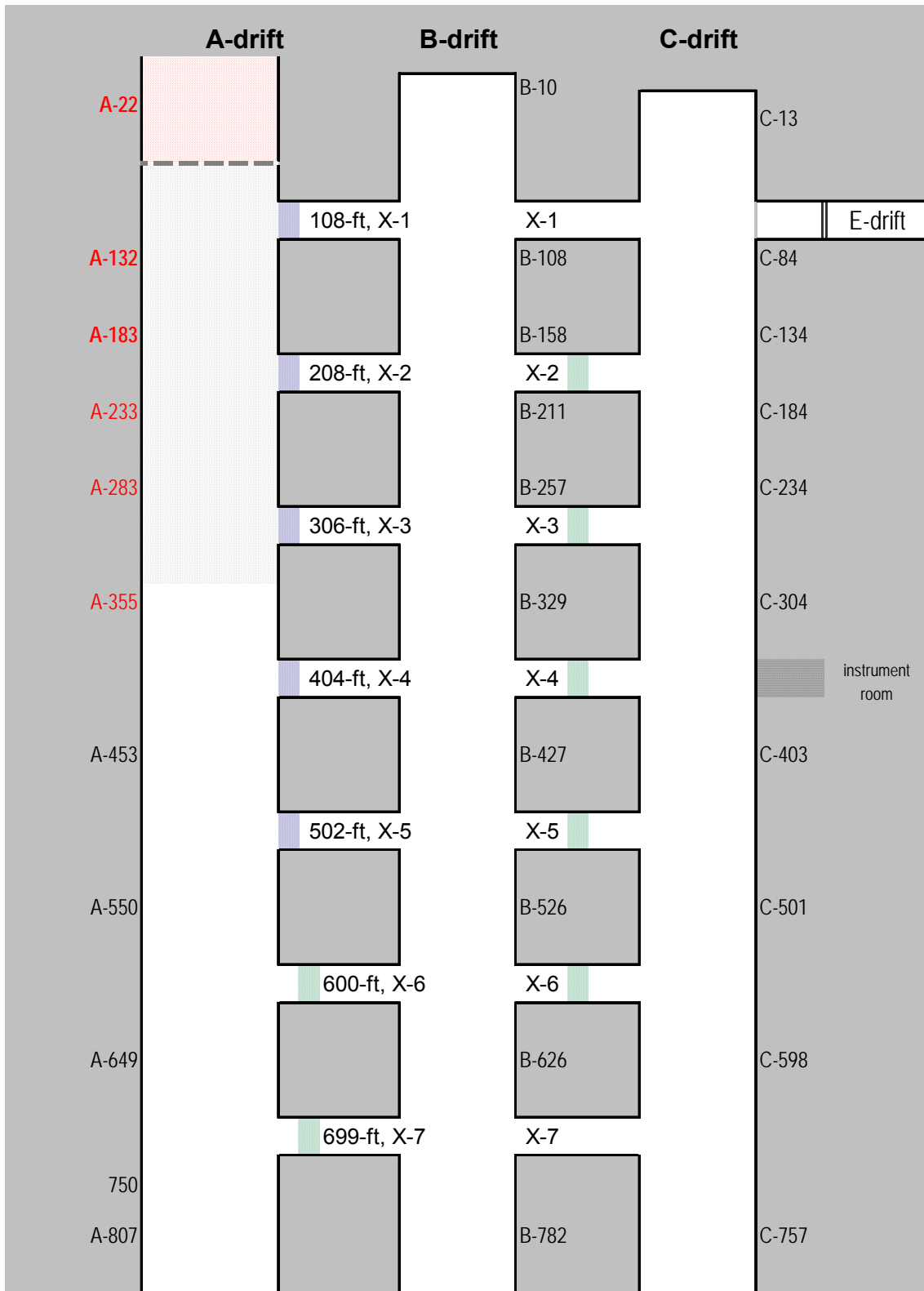


Figure A.12 – Experimental design for mine shot #517.

**Seal Notes (colors coordinate with seal locations in Figure A.12):**

- Standard-type, 16-in thick solid concrete block seals (w/32-in x 16-in center pilaster and Type S mortar) were located in crosscuts 1-5 between A- and B-Drifts. Each of these seals have been constructed as close as possible to the A-Drift rib-line. The seal in crosscut 1 had a blast-resistant door located between the center pilaster and the inby crosscut rib.
- An 8-in thick solid concrete block stopping with fully mortared (Type S) joints was constructed in crosscut 6 between A- and B-Drifts. A 6-in thick mortared solid-concrete-block stopping was constructed in crosscut 7. These stoppings were located approximately 10 ft into the crosscut as measured from the A-Drift rib-line and both were coated on the A-Drift side.
- Regular stoppings were located in crosscuts 2-5 between B- and C-Drifts.

**Table A.10 – Maximum pressures observed at the stoppings during mine shot #517.**

<b>Pressure, LVDT, &amp; Break-Wire Data at Stoppings</b>						
Stopping	Stopping Pressures & Wall Pressures			LVDT Deflection		Break Time,
	kPa, NI	psi, NI	psi, KS	in	mm	sec
<b>X-6 AB</b>	86	12.5	11.6	0.32	8	--
600 ft	56	8				
183 m	<i>stopping survived - no damage</i>					
<b>X-7 AB</b>	73	10.6	10.4	0.72	18	--
699 ft	54	8				
213 m	<i>stopping survived - small horizontal crack at mid-height after #516</i>					

# Lake Lynn Experimental Mine Shot #518

**Mine Shot Date:** February 27, 2008

**Description of Mine Shot:** Methane explosion in A-Drift with 74.4% rock dust concentration mix. Approximately 10% gas up to A-40 (530 ft<sup>3</sup> natural gas) was used and ignited at the face using a single point ignition (two matches twisted together at a center point of the face at mid-height). The dust zone extended from A-40 to A-340 (300 ft zone) and 278.4 lbs of coarse coal dust and 201.6 lb of PPC dust mixed was mixed with 1,395 lbs of rock dust to provide a 74.4% rock dust concentration (74% total incombustible content). Pittsburgh pulverized coal (PPC) dust is approximately 80% minus 200 mesh. Total mix of the rock dust and coal dust was 1,875 lbs. Approximately 50% of the dust mixture was loaded on the roof shelves and the remainder on the mine floor.

**Seal in the path of explosion:** No

**Seal failure due to explosion:** No

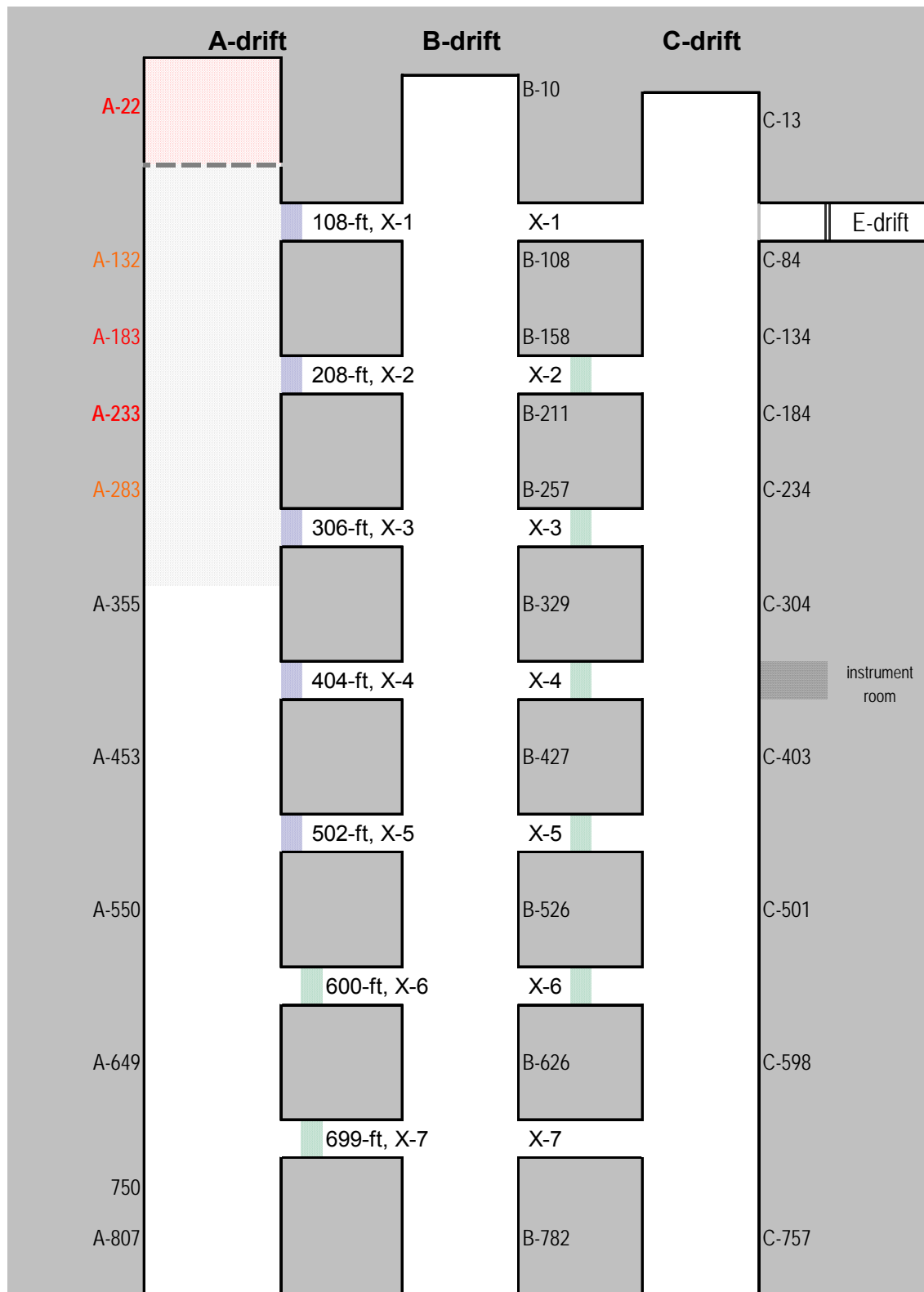


Figure A.13 – Experimental design for mine shot #518.

**Seal Notes (colors coordinate with seal locations in Figure A.13):**

- Standard-type, 16-in thick solid concrete block seals (w/32-in x 16-in center pilaster and Type S mortar) were located in crosscuts 1-5 between A- and B-Drifts. Each of these seals have been constructed as close as possible to the A-Drift rib-line. The seal in crosscut 1 had a blast-resistant door located between the center pilaster and the inby crosscut rib.
- An 8-in thick solid concrete block stopping with fully mortared (Type S) joints was constructed in crosscut 6 between A- and B-Drifts. A 6-in thick mortared solid-concrete-block stopping was constructed in crosscut 7. These stoppings were located approximately 10 ft into the crosscut as measured from the A-Drift rib-line and both were coated on the A-Drift side.
- Regular stoppings were located in crosscuts 2-5 between B- and C-Drifts.

**Table A.11 – Maximum pressures observed at the stoppings during mine shot #518.**

<b>Pressure, LVDT, &amp; Break-Wire Data at Stoppings</b>						
Stopping	Stopping Pressures &			LVDT		Break
	Wall Pressures			Deflection		Time,
	kPa, NI	psi, NI	psi, KS	in	mm	sec
<b>X-6 AB</b>	76	11.0	10.7	0.31	8	--
600 ft	56	8				
183 m	<i>stopping survived - no damage</i>					
<b>X-7 AB</b>	71	10.3	10.4	0.73	19	--
699 ft	57	8				
213 m	<i>stopping survived - small horizontal crack at mid-height after #516</i>					

# Lake Lynn Experimental Mine Shot #519

**Mine Shot Date:** March 3, 2008

**Description of Mine Shot:** Methane explosion in A-Drift. Approximately 10% gas up to A-85 (1,100 ft<sup>3</sup> natural gas) was used and ignited at the face using a single point ignition (two matches twisted together at a center point of the face at mid-height).

**Seal in the path of explosion:** No

**Seal failure due to explosion:** No, however the stopping in crosscut 7 between A and B-Drifts was destroyed.



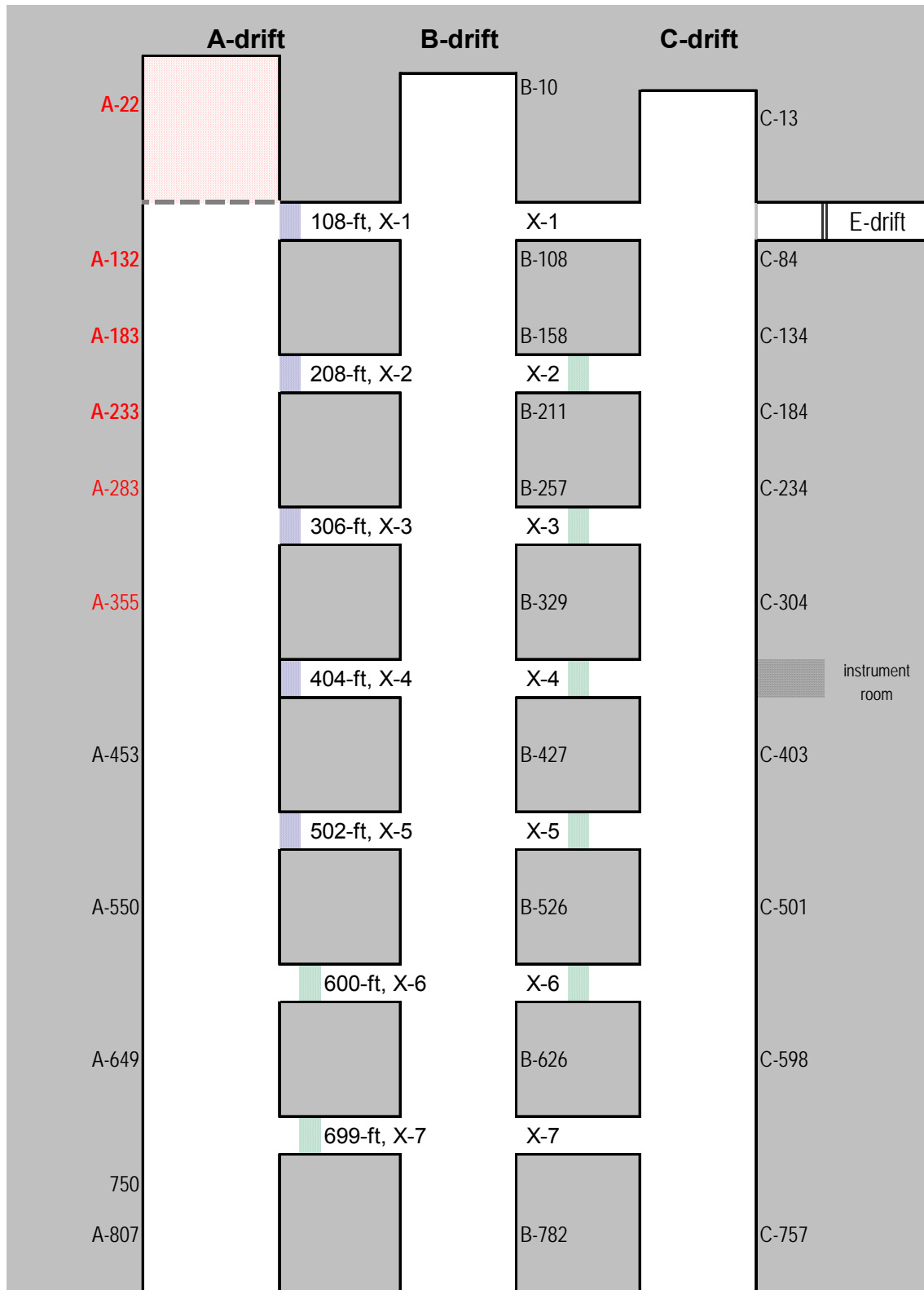


Figure A.14 – Experimental design for mine shot #519.

**Seal Notes (colors coordinate with seal locations in Figure A.14):**

- Standard-type, 16-in thick solid concrete block seals (w/32-in x 16-in center pilaster and Type S mortar) were located in crosscuts 1-5 between A- and B-Drifts. Each of these seals have been constructed as close as possible to the A-Drift rib-line. The seal in crosscut 1 had a blast-resistant door located between the center pilaster and the inby crosscut rib.
- An 8-in thick solid concrete block stopping with fully mortared (Type S) joints was constructed in crosscut 6 between A- and B-Drifts. A 6-in thick mortared solid-concrete-block stopping was constructed in crosscut 7. These stoppings were located approximately 10 ft into the crosscut as measured from the A-Drift rib-line and both were coated on the A-Drift side.
- Regular stoppings were located in crosscuts 2-5 between B- and C-Drifts.

**Table A.12 – Maximum pressures observed at the stoppings during mine shot #519.**

<b>Pressure, LVDT, &amp; Break-Wire Data at Stoppings</b>						
Stopping	Stopping Pressures & Wall Pressures			LVDT Deflection		Break Time,
	kPa, NI	psi, NI	psi, KS	in	mm	sec
	<b>X-6 AB</b>	185	26.8	25.2	1.03	26
600 ft	134	19				
183 m	<i>stopping survived, horizontal crack at mid-height, some blocks slightly displaced</i>					
<b>X-7 AB</b>	174	25.3	24.2	>3	>75	V=1.223
699 ft	130	19	H=1.232			
213 m	<i>stopping was destroyed - debris blown to C-drift</i>					

# Lake Lynn Experimental Mine Shot #520

**Mine Shot Date:** March 12, 2008

**Description of Mine Shot:** Methane explosion in A-Drift with 68.5% rock dust concentration mix. Approximately 10% gas up to A-40 (1,100 ft<sup>3</sup> natural gas) was used and ignited at the face using a single point ignition (two matches twisted together at a center point of the face at mid-height). The dust zone extended from A-40 to A-340 (300 ft zone) and 278.4 lbs of coarse coal dust and 201.6 lb of PPC dust mixed was mixed with 1,044 lbs of rock dust to provide a 68.5% rock dust concentration (71% total incombustible content). Pittsburgh pulverized coal (PPC) dust is approximately 80% minus 200 mesh. Total mix of the rock dust and coal dust was 1,524 lbs. Approximately 50% of the dust mixture was loaded on the roof shelves and the remainder on the mine floor.

**Seal in the path of explosion:** No

**Seal failure due to explosion:** No

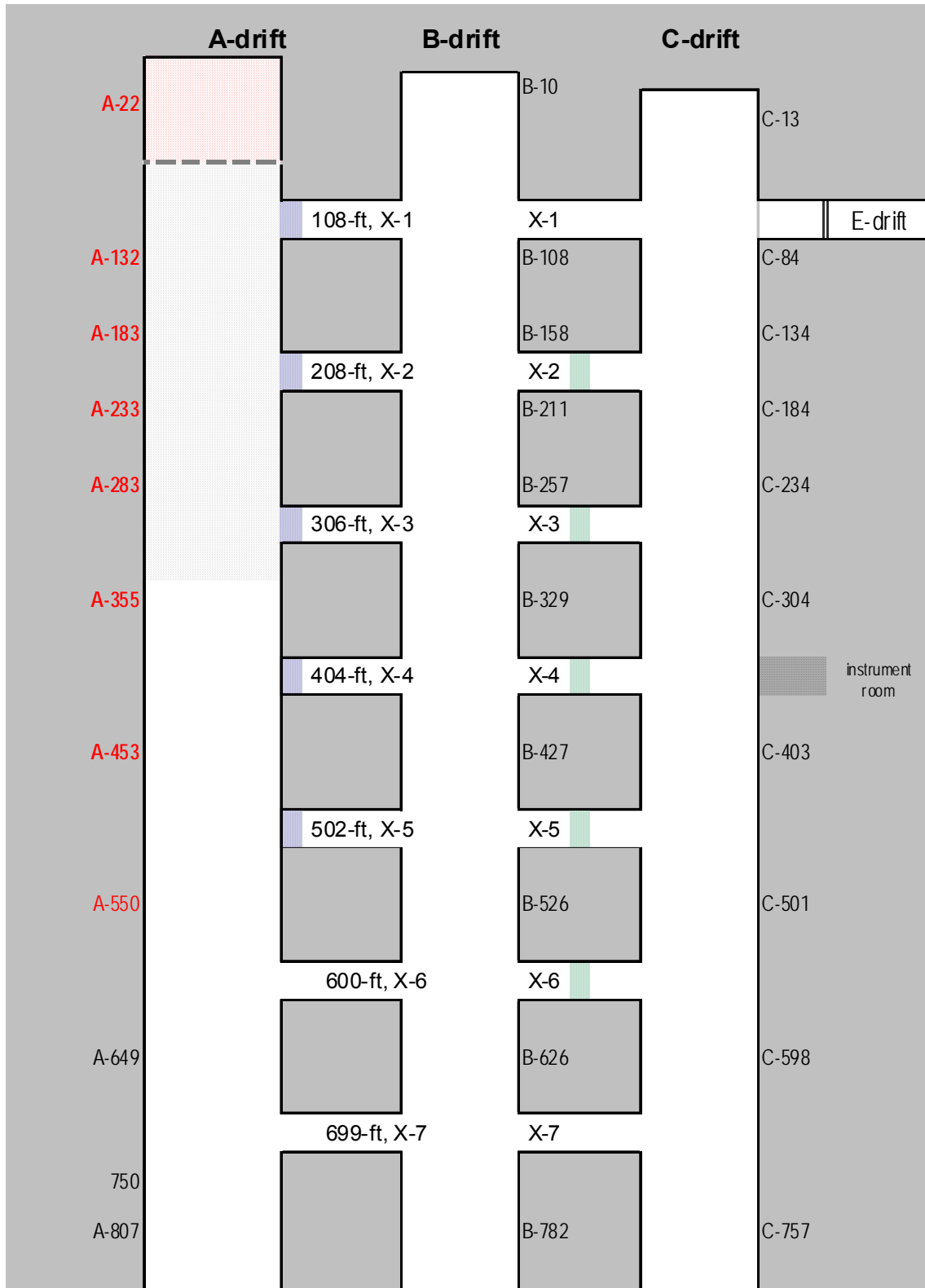


Figure A.15 – Experimental design for mine shot #520.

**Seal Notes (colors coordinate with seal locations in Figure A.15):**

- Standard-type, 16-in thick solid concrete block seals (w/32-in x 16-in center pilaster and Type S mortar) were located in crosscuts 1-5 between A- and B-Drifts. Each of these seals have been constructed as close as possible to the A-Drift rib-line. The seal in crosscut 1 had a blast-resistant door located between the center pilaster and the inby crosscut rib.
- Regular stoppings were located in crosscuts 2-5 between B- and C-Drifts.

**Table A.13 – Maximum pressures observed at the stoppings during mine shot #520.**

<b>Pressure, LVDT, &amp; Break-Wire Data at Stoppings</b>						
Stopping	Stopping Pressures & Wall Pressures			LVDT Deflection		Break Time,
	kPa, NI	psi, NI	psi, KS	in	mm	sec
	<b>X-6 AB</b>	57	8.3	7.5		
600 ft	54	8				
183 m	<i>no stopping present - open crosscut</i>					
<b>X-7 AB</b>	39	5.6	5.3			--
699 ft	43	6				
213 m	<i>no stopping present - open crosscut</i>					

# Lake Lynn Experimental Mine Shot #521

**Mine Shot Date:** March 24, 2008

**Description of Mine Shot:** Methane explosion in A-Drift. Approximately 8.5% gas up to A-40 (490 ft<sup>3</sup> natural gas) was used and ignited at A-39.5 using a single point ignition (two matches twisted together at a center point of the face at mid-height).

**Seal in the path of explosion:** No

**Seal failure due to explosion:** No, however the stoppings in crosscuts 6 and 7 between A- and B-Drifts failed.

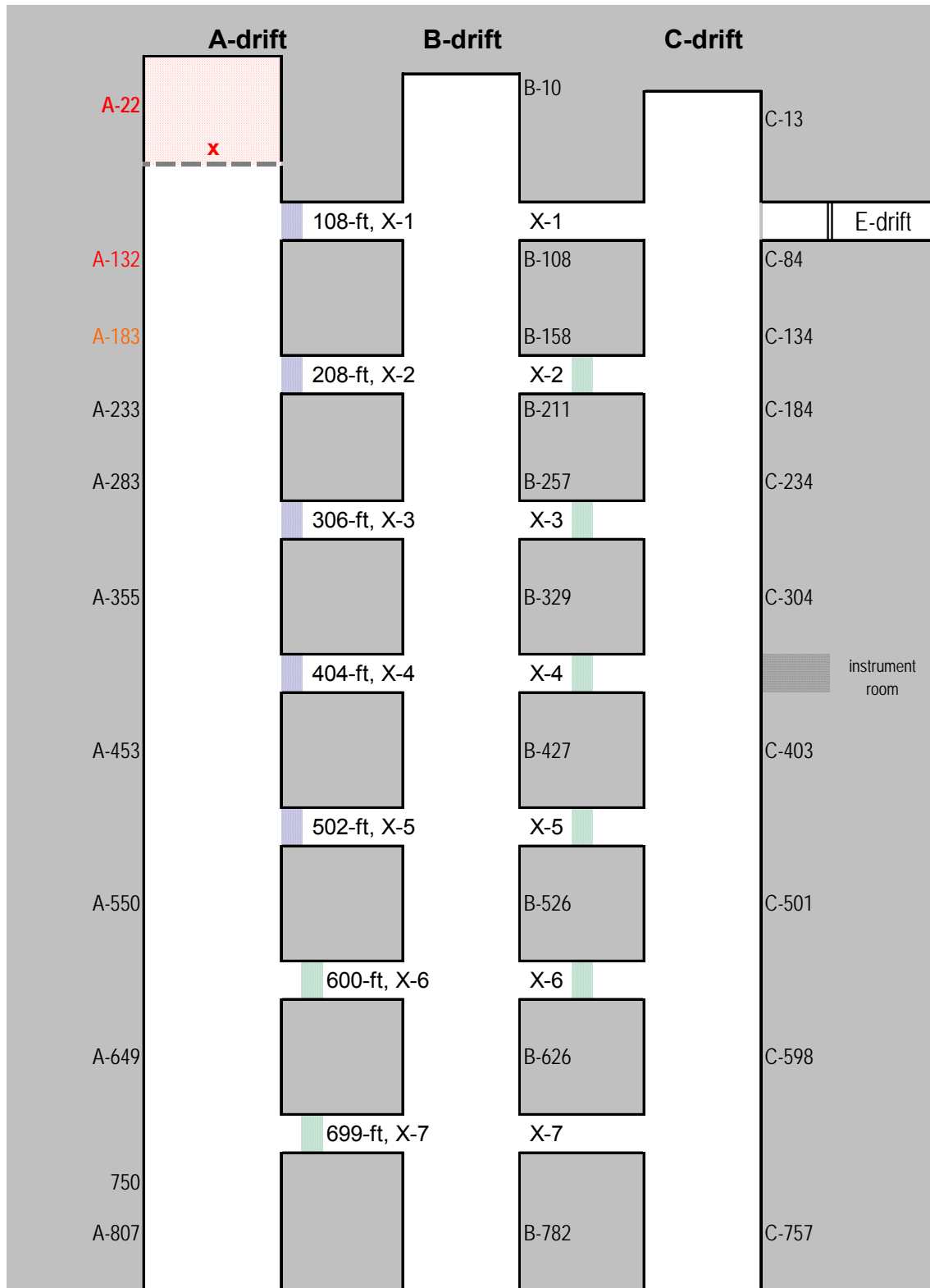


Figure A.16 – Experimental design for mine shot #521.

**Seal Notes (colors coordinate with seal locations in Figure A.16):**

- Standard-type, 16-in thick solid concrete block seals (w/32-in x 16-in center pilaster and Type S mortar) were located in crosscuts 1-5 between A- and B-Drifts. Each of these seals have been constructed as close as possible to the A-Drift rib-line. The seal in crosscut 1 had a blast-resistant door located between the center pilaster and the inby crosscut rib.
- A 16-in thick dry-stacked low-density block stopping was located in crosscut 6 between A- and B-Drifts. An 8-in thick dry-stacked low-density block stopping was located in crosscut 7 between A- and B-Drifts. The stoppings were located approximately 10 ft into the crosscut as measured from the A-drift rib-line and both had a 0.25-in thick full-face coating of Quikrete BlocBond on the A-drift face and only along the perimeter on the B-drift side.
- Regular stoppings were located in crosscuts 2-5 between B- and C-Drifts.

**Table A.14 – Maximum pressures observed at the stoppings during mine shot #521.**

<b>Pressure, LVDT, &amp; Break-Wire Data at Stoppings</b>						
Stopping	Stopping Pressures &			LVDT		Break
	Wall Pressures			Deflection		Time,
	kPa, NI	psi, NI	psi, KS	in	mm	sec
<b>X-6 AB</b>	9	1.2	1.2	>3 negative		V = 2.63    H = 2.77
600 ft	8	1.2				
183 m	<i>stopping survived the initial pressure pulse and failed on reverse pressure</i>					
<b>X-7 AB</b>	8	1.1	1.1	>3		V = 1.425    H = 1.425
699 ft	8	1.2				
213 m	<i>stopping failed on initial pressure pulse, blocks knocked toward B-drift</i>					



# Lake Lynn Experimental Mine Shot #522

**Mine Shot Date:** March 26, 2008

**Description of Mine Shot:** Methane explosion in A-Drift with 74.4% rock dust concentration mix. Approximately 10% gas up to A-40 (530 ft<sup>3</sup> natural gas) was used and ignited at the face using a single point ignition (two matches twisted together at a center point of the face at mid-height). The dust zone extended from A-40 to A-340 (300 ft zone) and 278.4 lbs of coarse coal dust and 201.6 lb of PPC dust mixed was mixed with 1,395 lbs of rock dust to provide a 74.4% rock dust concentration (76.4% total incombustible content). Pittsburgh pulverized coal (PPC) dust is approximately 80% minus 200 mesh. Total mix of the rock dust and coal dust was 1,875 lbs. Approximately 50% of the dust mixture was loaded on the roof shelves and the remainder on the mine floor.

**Seal in the path of explosion:** No

**Seal failure due to explosion:** No

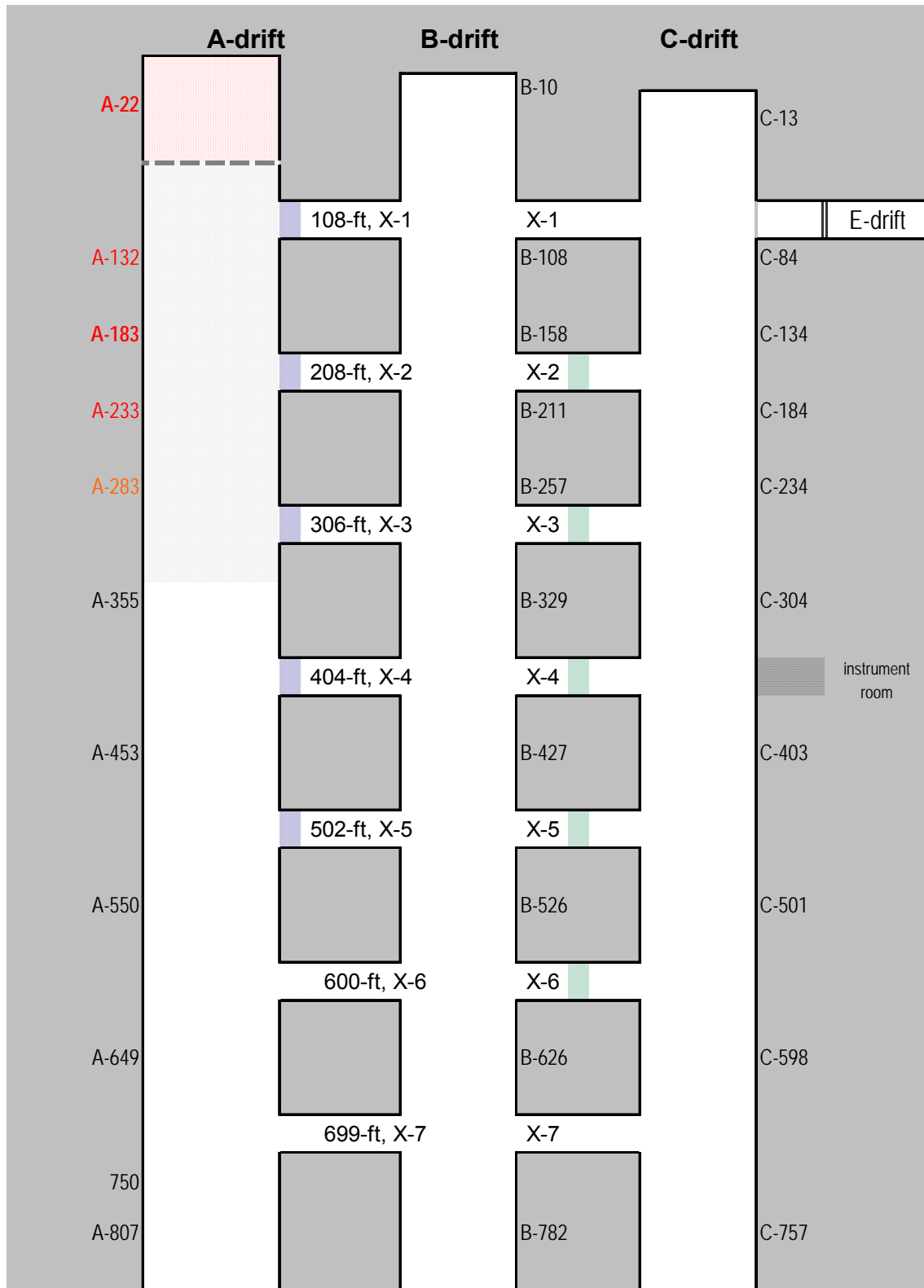


Figure A.17 – Experimental design for mine shot #522.

**Seal Notes (colors coordinate with seal locations in Figure A.17):**

- Standard-type, 16-in thick solid concrete block seals (w/32-in x 16-in center pilaster and Type S mortar) were located in crosscuts 1-5 between A- and B-Drifts. Each of these seals have been constructed as close as possible to the A-Drift rib-line. The seal in crosscut 1 had a blast-resistant door located between the center pilaster and the inby crosscut rib.
- Regular stoppings were located in crosscuts 2-5 between B- and C-Drifts.

**Table A.15 – Maximum pressures observed at the stoppings during mine shot #522.**

<b>Pressure, LVDT, &amp; Break-Wire Data at Stoppings</b>						
Stopping	Stopping Pressures &			LVDT		Break
				Deflection		Time,
	kPa, NI	psi, NI	psi, KS	in	mm	sec
<b>X-6 AB</b>	49	7.1				--
600 ft						
183 m	<i>no stopping present</i>					
<b>X-7 AB</b>	36	5.2				--
699 ft						
213 m	<i>no stopping present</i>					

# Lake Lynn Experimental Mine Shot #523

**Mine Shot Date:** May 14, 2008

**Description of Mine Shot:** Methane explosion against a seal in the A-Drift. Approximately 10% gas up to A-50 (695 ft<sup>3</sup> natural gas) was used and ignited at the face using a triple point ignition (two matches twisted together equally spaced at mid-height across the closed end face). Five water-filled barrels were each spaced equally across the entry at A-25 and A-45 to act as turbulence generators.

**Seal in the path of explosion:** Yes

**Seal failure due to explosion:** No

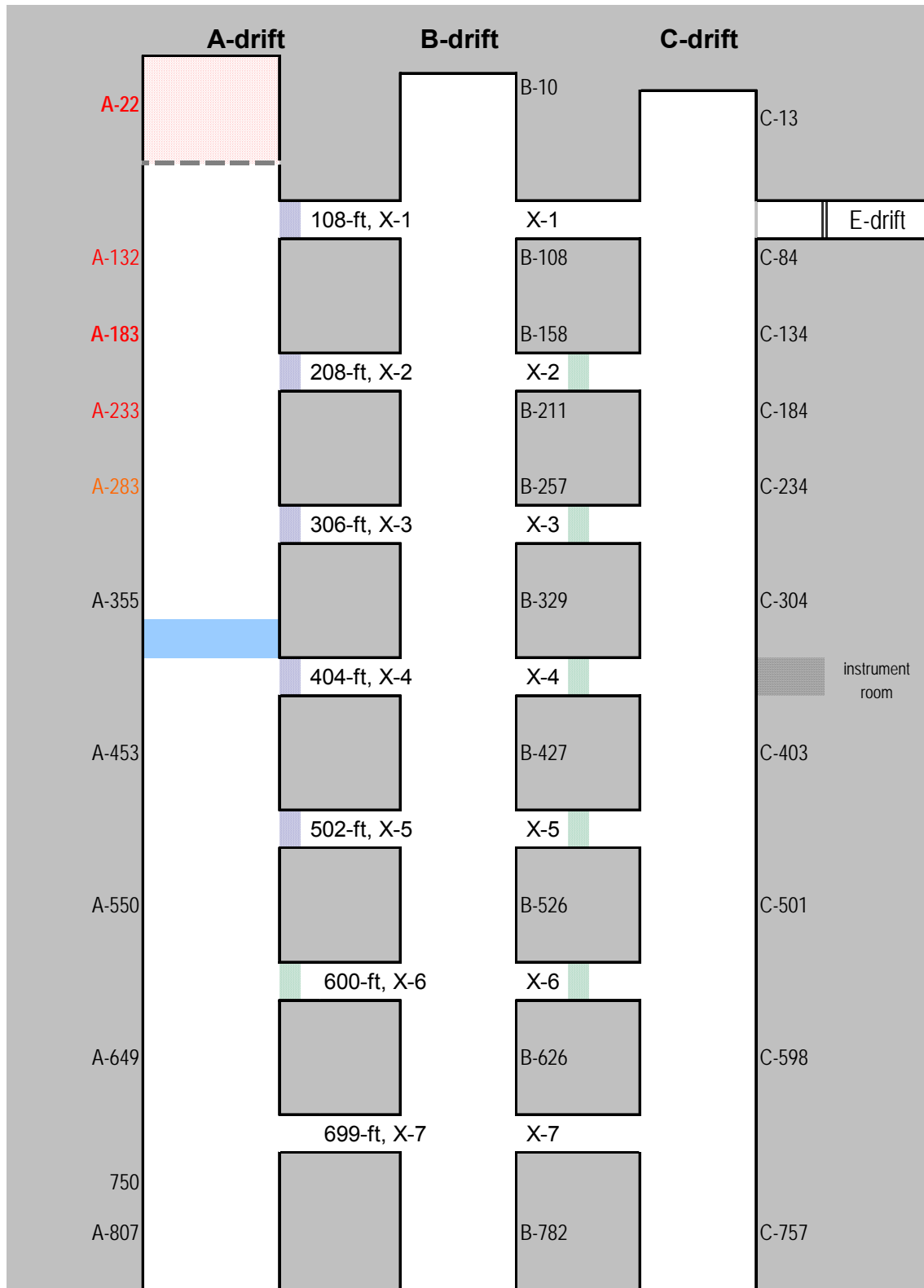


Figure A.18 – Experimental design for mine shot #523.

**Seal Notes (colors coordinate with seal locations in Figure A.18):**

- Standard-type, 16-in thick solid concrete block seals (w/32-in x 16-in center pilaster and Type S mortar) were located in crosscuts 1-5 between A- and B-Drifts. Each of these seals have been constructed as close as possible to the A-Drift rib-line. The seal in crosscut 1 had a blast-resistant door located between the center pilaster and the inby crosscut rib.
- An alternative type seal with 8-in by 8-in by 16-in dry-stacked solid-concrete block walls with a 16-in wide Sealok-120 polyurethane and aggregate core was installed at A-375. A retrofit wall using 8-in solid-concrete-blocks with Roclok-70 adhesive between block joints was installed approximately 8-in outby the seal and the 8-in gap was filled with 10 lb density Sealok-120 polyurethane foam, followed by an 0.125-in thick spray-applied coating of the polyurea to the outby face of the block wall with a 2-ft overlap to the floor, roof, and ribs. A fire-resistant latex coating was then applied with paint rollers over the polyurea.
- A 16-in thick wet-laid Low-strength cellular concrete seal block stopping with a 48-in by 48-in pilaster was located in crosscut 6, approximately 10-ft into the crosscut.
- Regular stoppings were located in crosscuts 2-5 between B- and C-Drifts.

A tabulated summary of the pressure data measured at the mine seals or stoppings was unavailable for mine shot #523. The pressure-time curve for this experiment was also unavailable however the mine supervisor approximated the maximum pressure at approximately 40 psi.

# Lake Lynn Experimental Mine Shot #524

**Mine Shot Date:** May 21, 2008

**Description of Mine Shot:** Methane explosion against a seal in the A-Drift. Approximately 10% gas up to A-85 (1,100 ft<sup>3</sup> natural gas) was used and ignited at A-20 using a triple point ignition (two matches twisted together equally spaced at 1-ft off the floor). Five water-filled barrels were each spaced equally across the entry at A-25 and A-45 to act as turbulence generators.

**Seal in the path of explosion:** Yes

**Seal failure due to explosion:** No

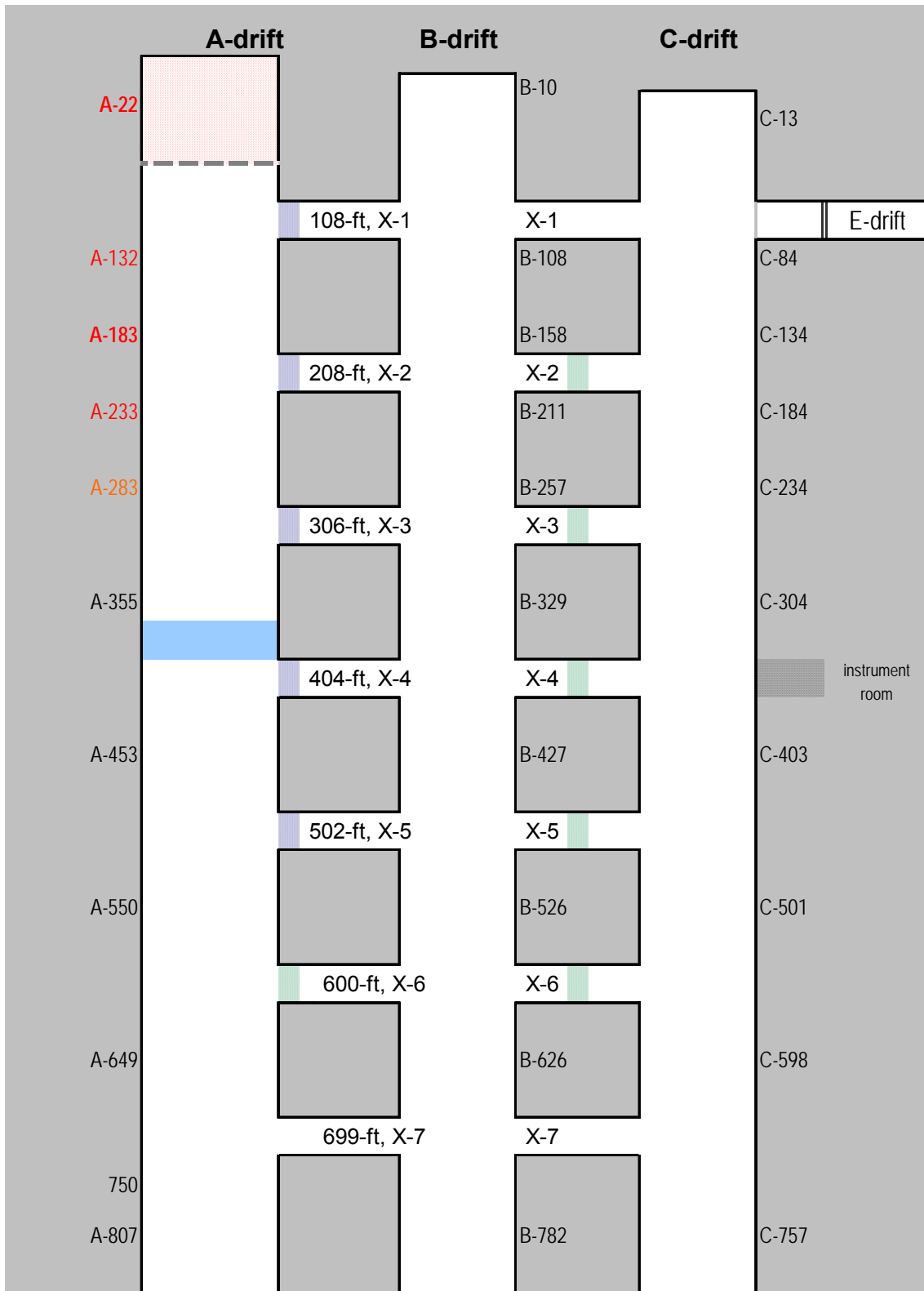


Figure A.19 – Experimental design for mine shot #524.



**Seal Notes (colors coordinate with seal locations in Figure A.19):**

- Standard-type, 16-in thick solid concrete block seals (w/32-in x 16-in center pilaster and Type S mortar) were located in crosscuts 1-5 between A- and B-Drifts. Each of these seals have been constructed as close as possible to the A-Drift rib-line. The seal in crosscut 1 had a blast-resistant door located between the center pilaster and the inby crosscut rib.
- An alternative type seal with 8-in by 8-in by 16-in dry-stacked solid-concrete block walls with a 16-in wide Sealok-120 polyurethane and aggregate core was installed at A-375. A retrofit wall using 8-in solid-concrete-blocks with Roclok-70 adhesive between block joints was installed approximately 8-in outby the seal and the 8-in gap was filled with 10 lb density Sealok-120 polyurethane foam, followed by an 0.125-in thick spray-applied coating of the polyurea to the outby face of the block wall with a 2-ft overlap to the floor, roof, and ribs. A fire-resistant latex coating was then applied with paint rollers over the polyurea.
- A 16-in thick wet-laid Low-strength cellular concrete seal block stopping with a 48-in by 48-in pilaster was located in crosscut 6, approximately 10-ft into the crosscut.
- Regular stoppings were located in crosscuts 2-5 between B- and C-Drifts.

A tabulated summary of the pressure data measured at the mine seals or stoppings and the pressure-time curves were unavailable for mine shot #524. The pressure-time curve for this experiment was also unavailable however the mine supervisor approximated the maximum pressure at approximately 80 psi.

# Appendix B:

## Pressure-Time Curves for Mine Shots\*

---

\* Data for pressure-time curves provided by National Institute for Occupational Safety and Health, Pittsburgh Research Laboratory, Disaster Prevention and Response Branch. Mine shots #503 – 507 are referenced in Cashdollar et al. (2007) and Gates et al. (2007). Mine shots #508 and 509 are referenced in Weiss et al. (2008a). Mine shots #510 and 519 are referenced in Weiss et al. (2008b). Mine shots #523 and 524 are referenced in Millero (2008). Mine shots #513, 514, 516 – 18, 520 – 522 are not yet published however the work was completed by Ken Cashdollar, Eric Weiss and Sam Harteis as part of the mine explosion program for NIOSH, Pittsburgh Research Laboratory's Disaster Prevention and Response Branch.

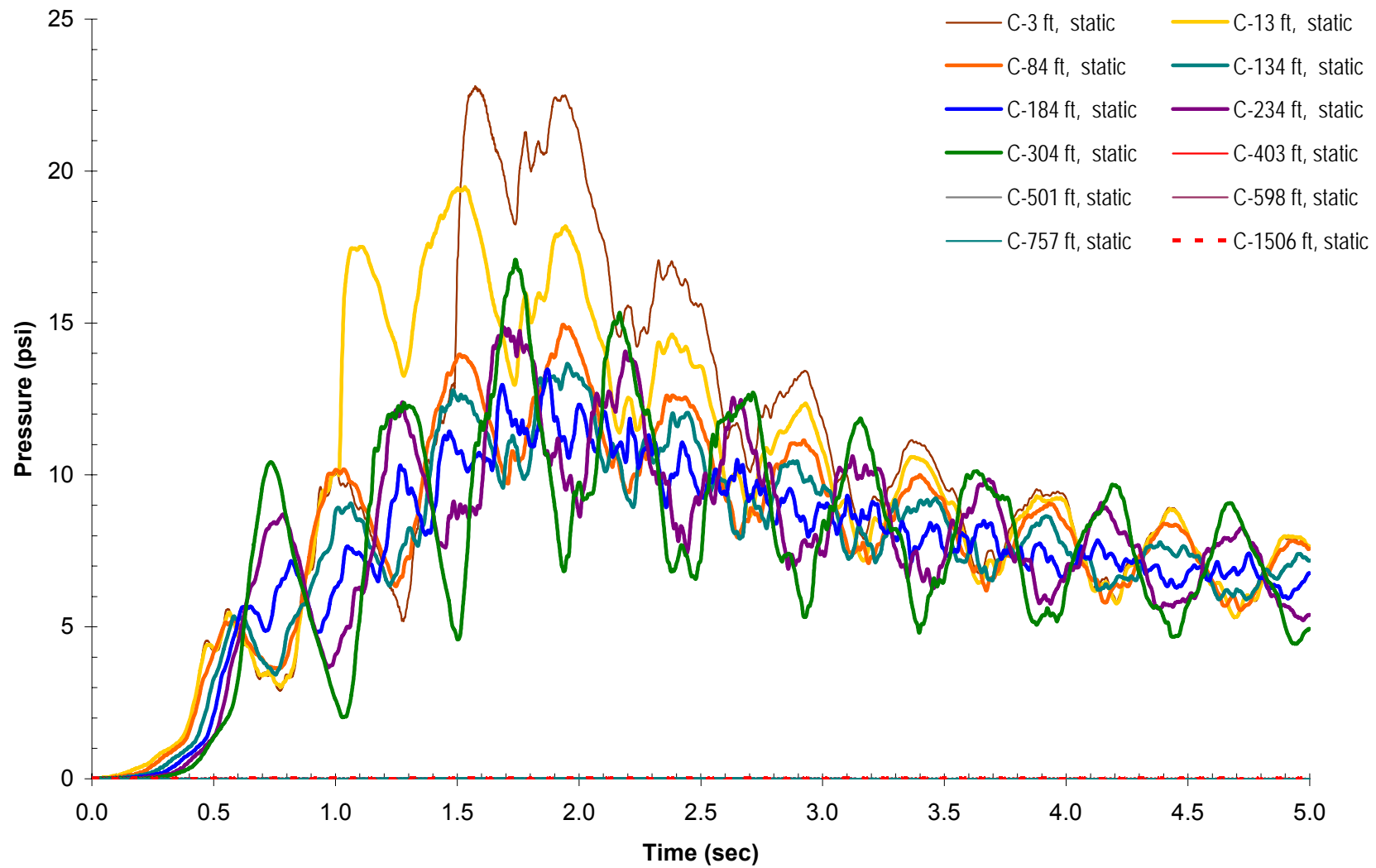


Figure B.1 – Pressure-time curve for mine shot #503.

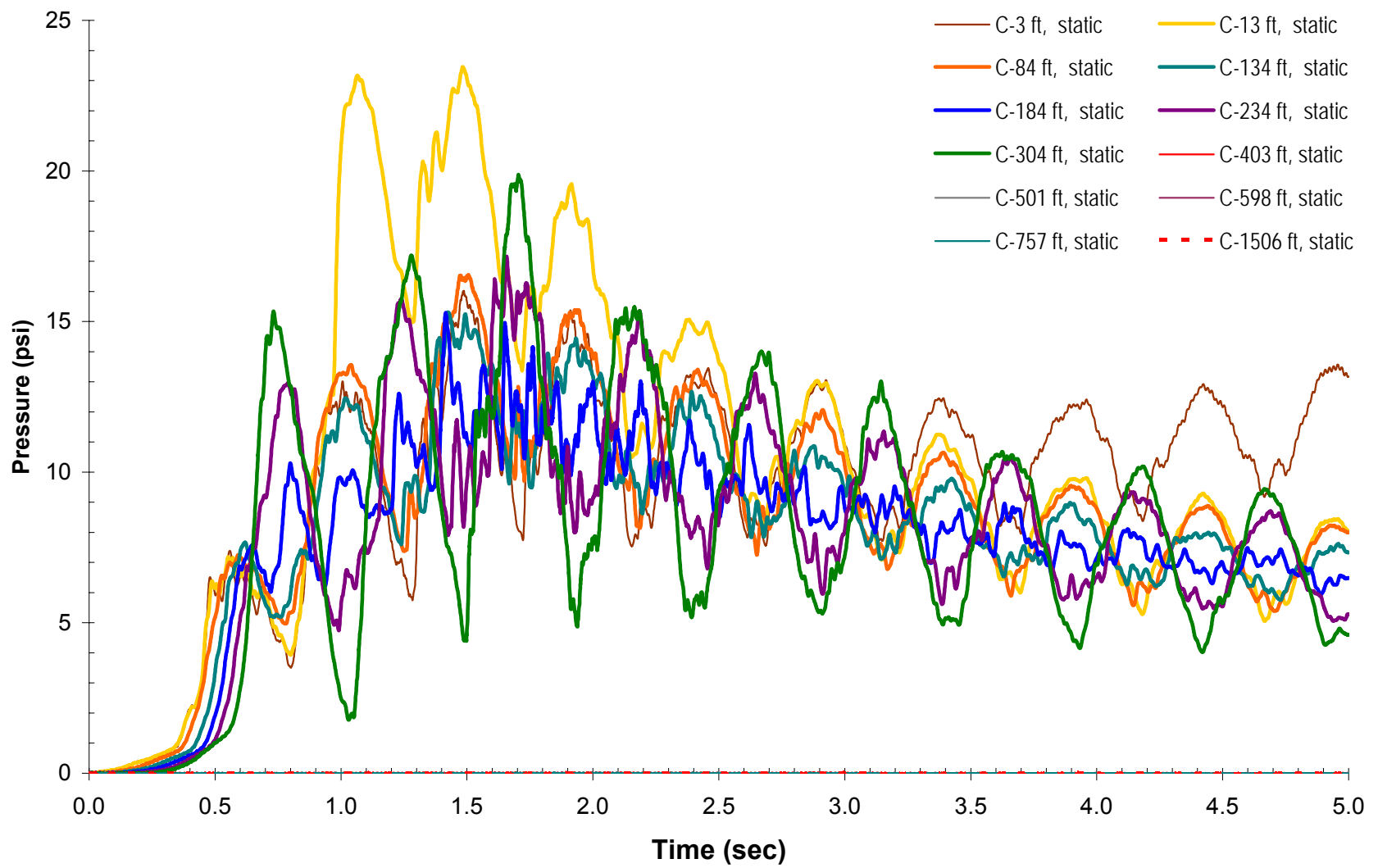


Figure B.2 – Pressure-time curve for mine shot #504.

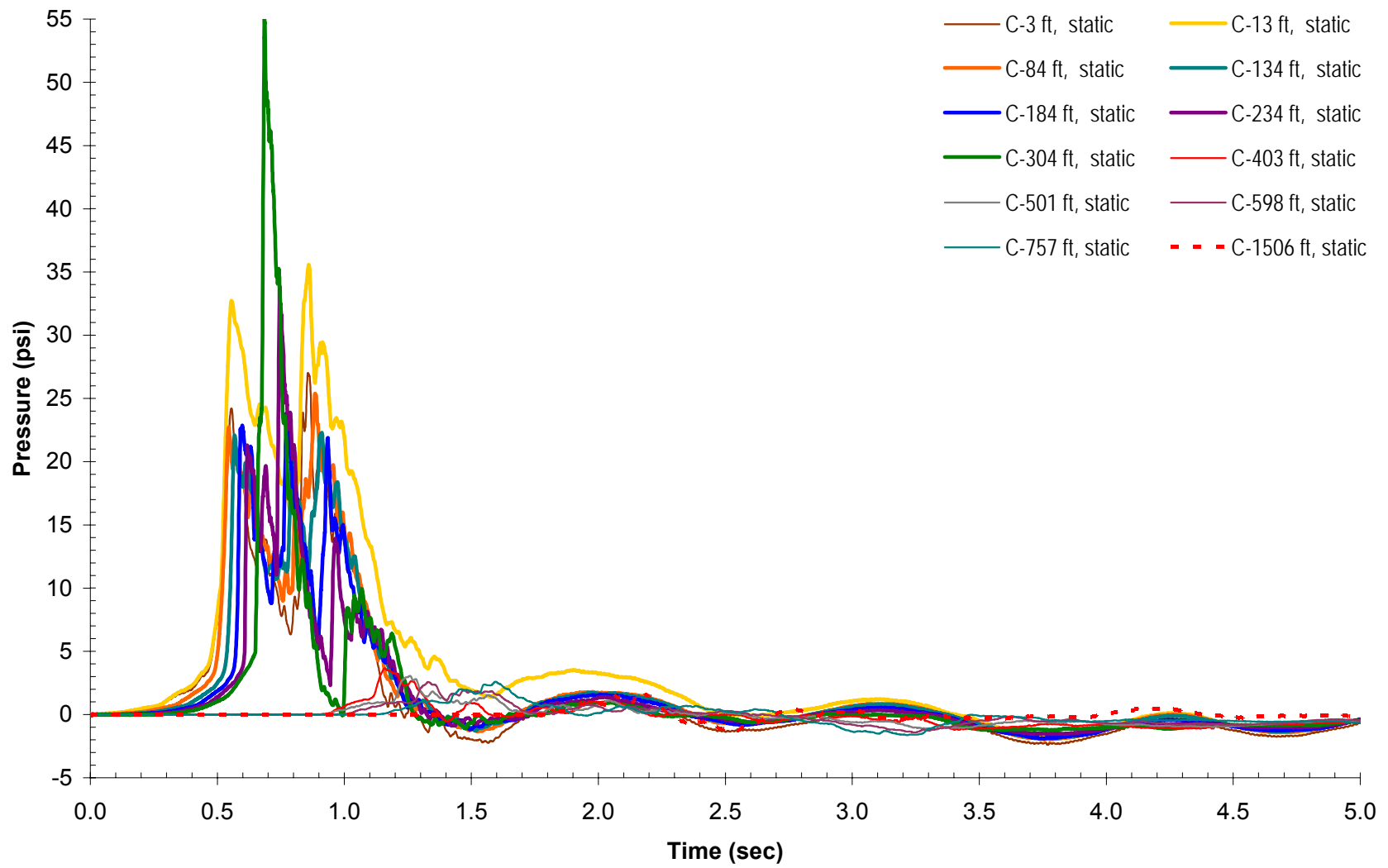


Figure B.3 – Pressure-time curve for mine shot #505.

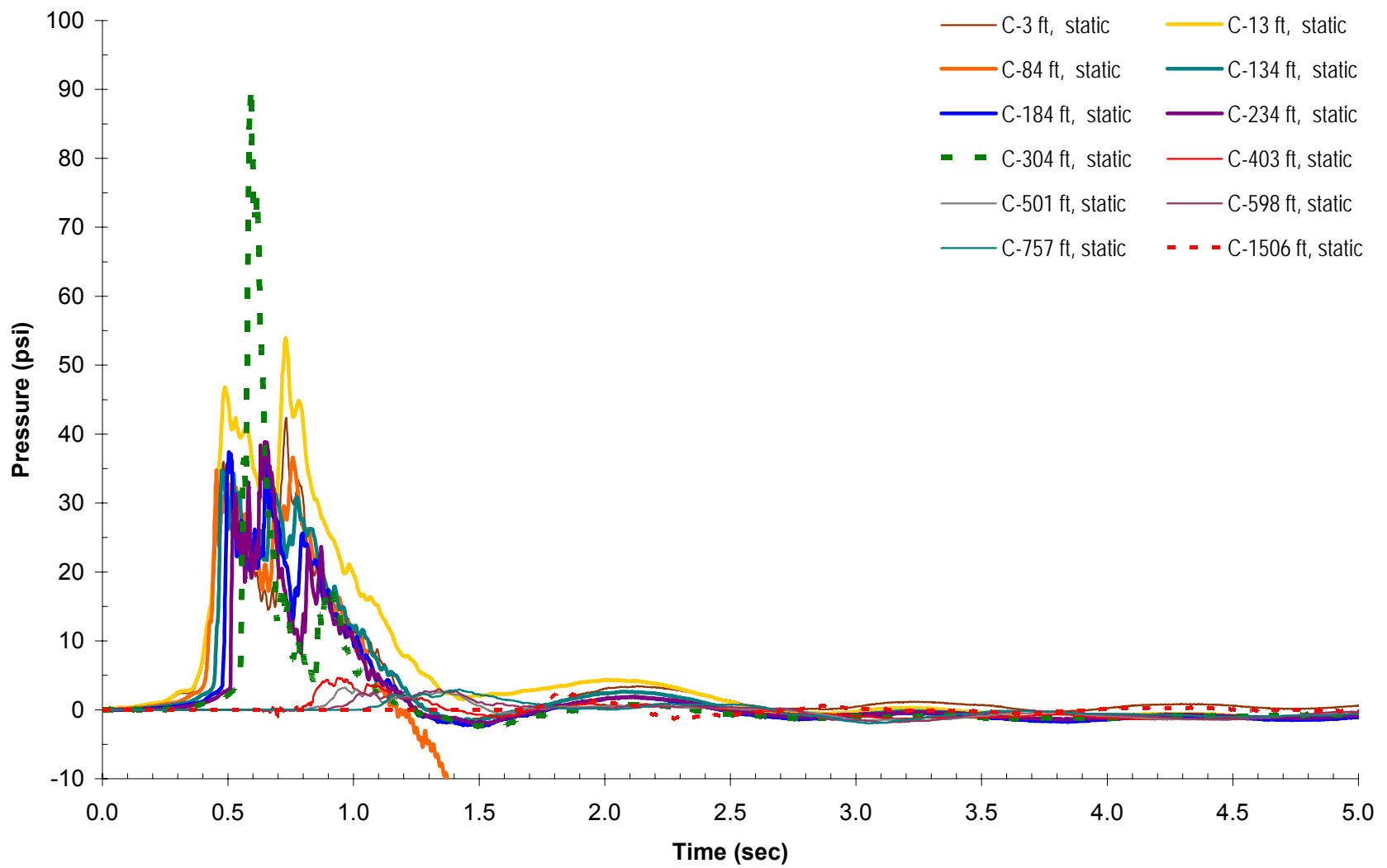


Figure B.4 – Pressure-time curve for mine shot #506.

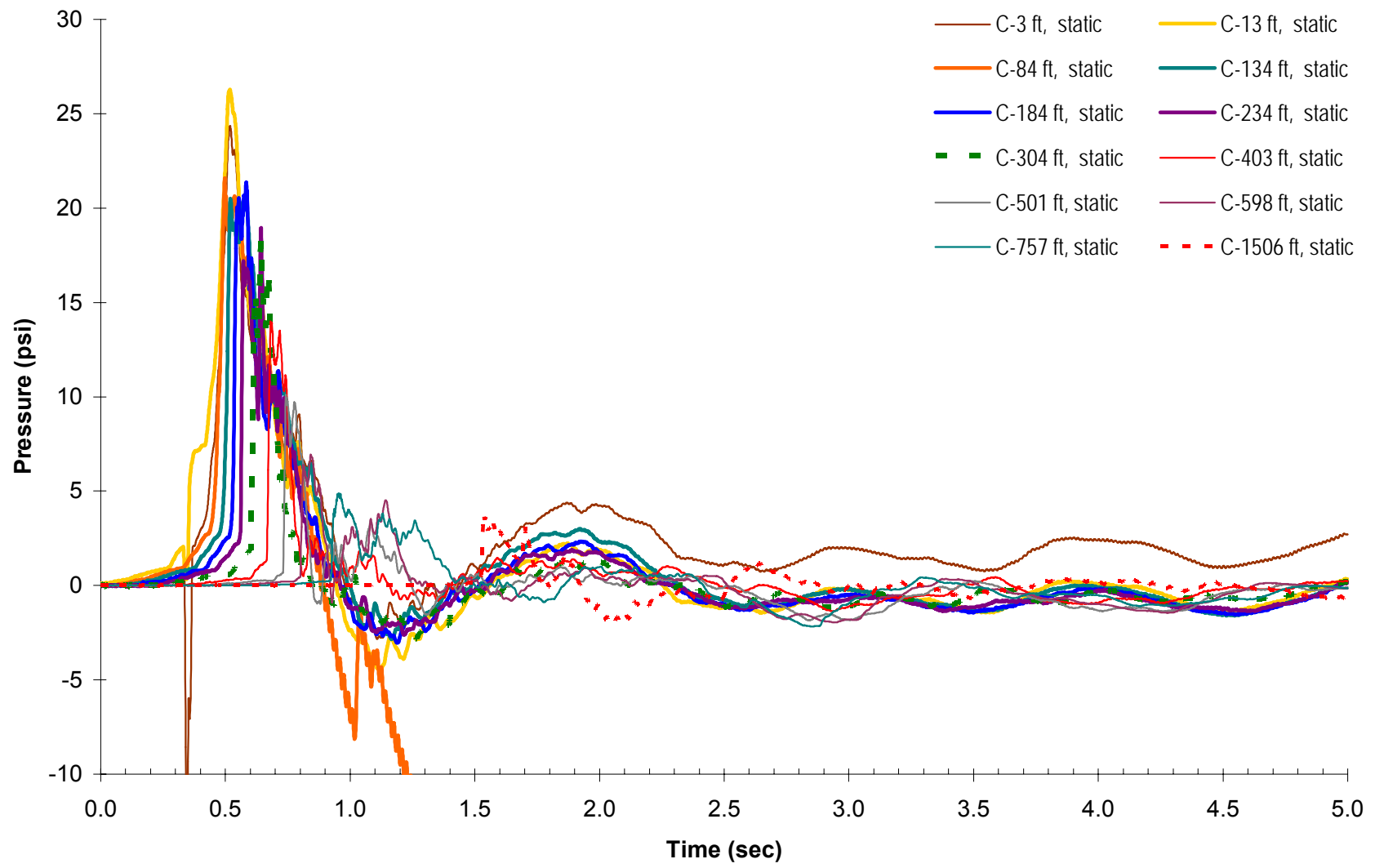


Figure B.5 – Pressure-time curve for mine shot #507.

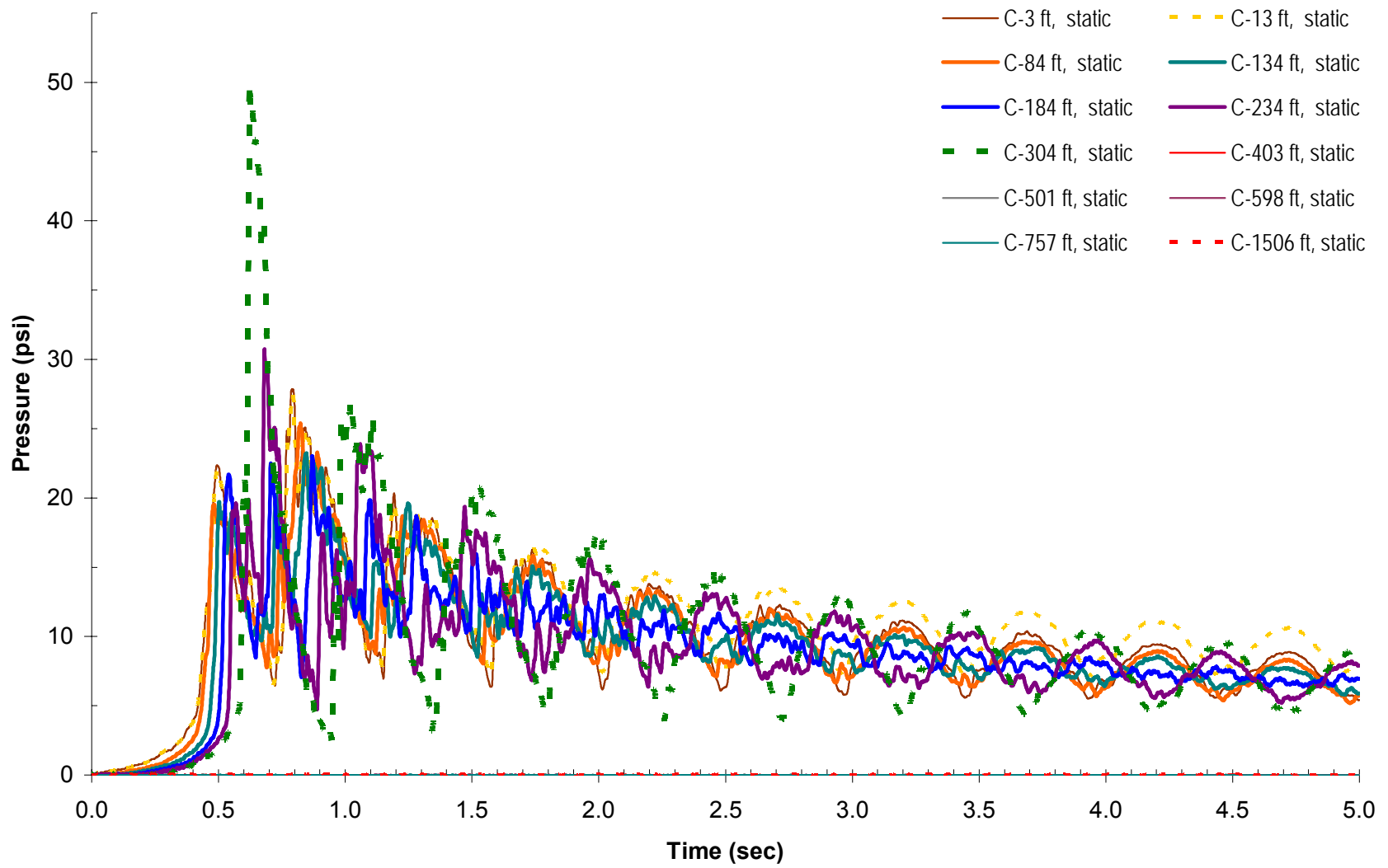


Figure B.6 – Pressure-time curve for mine shot #508.



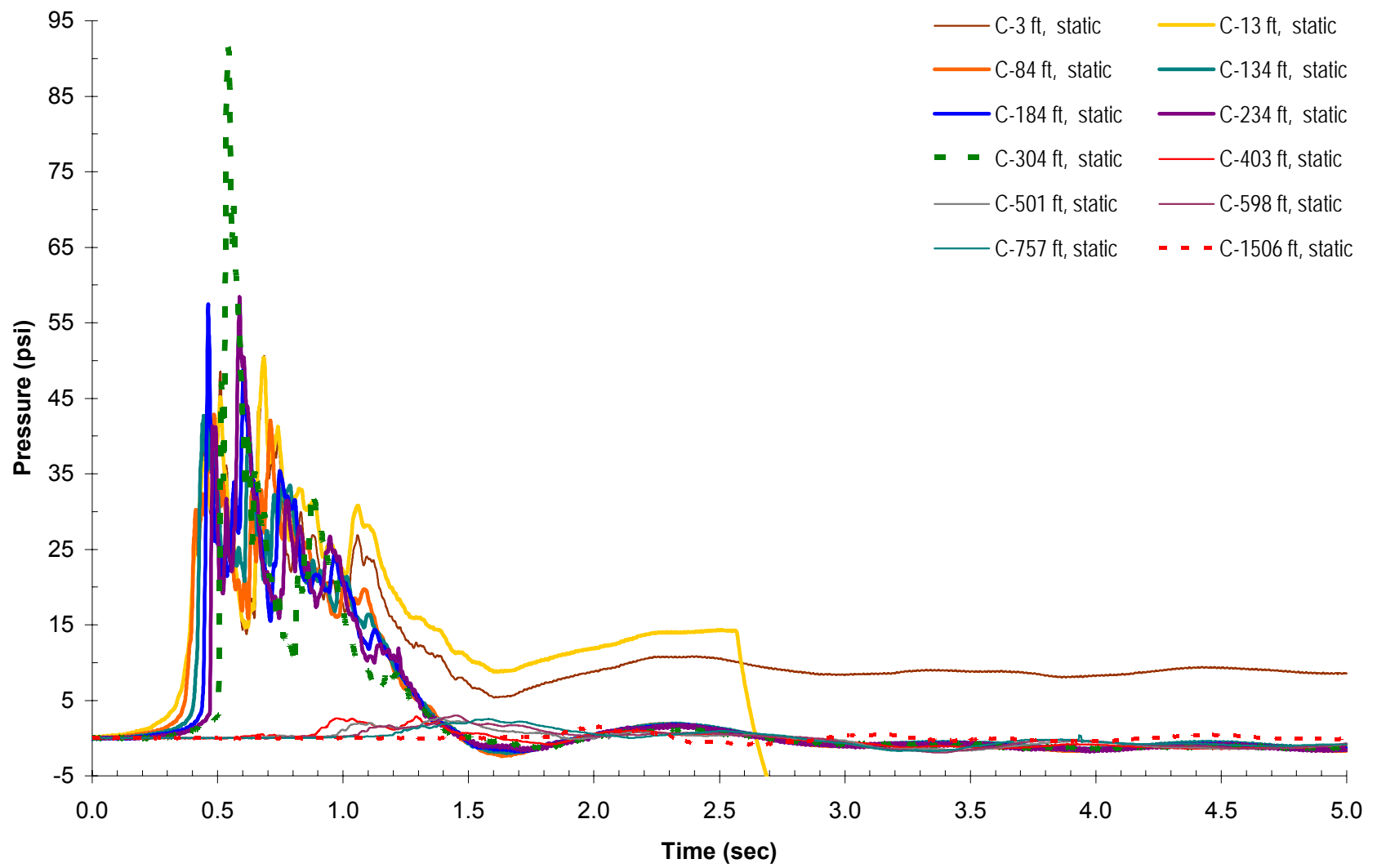


Figure B.7 – Pressure-time curve for mine shot #509.

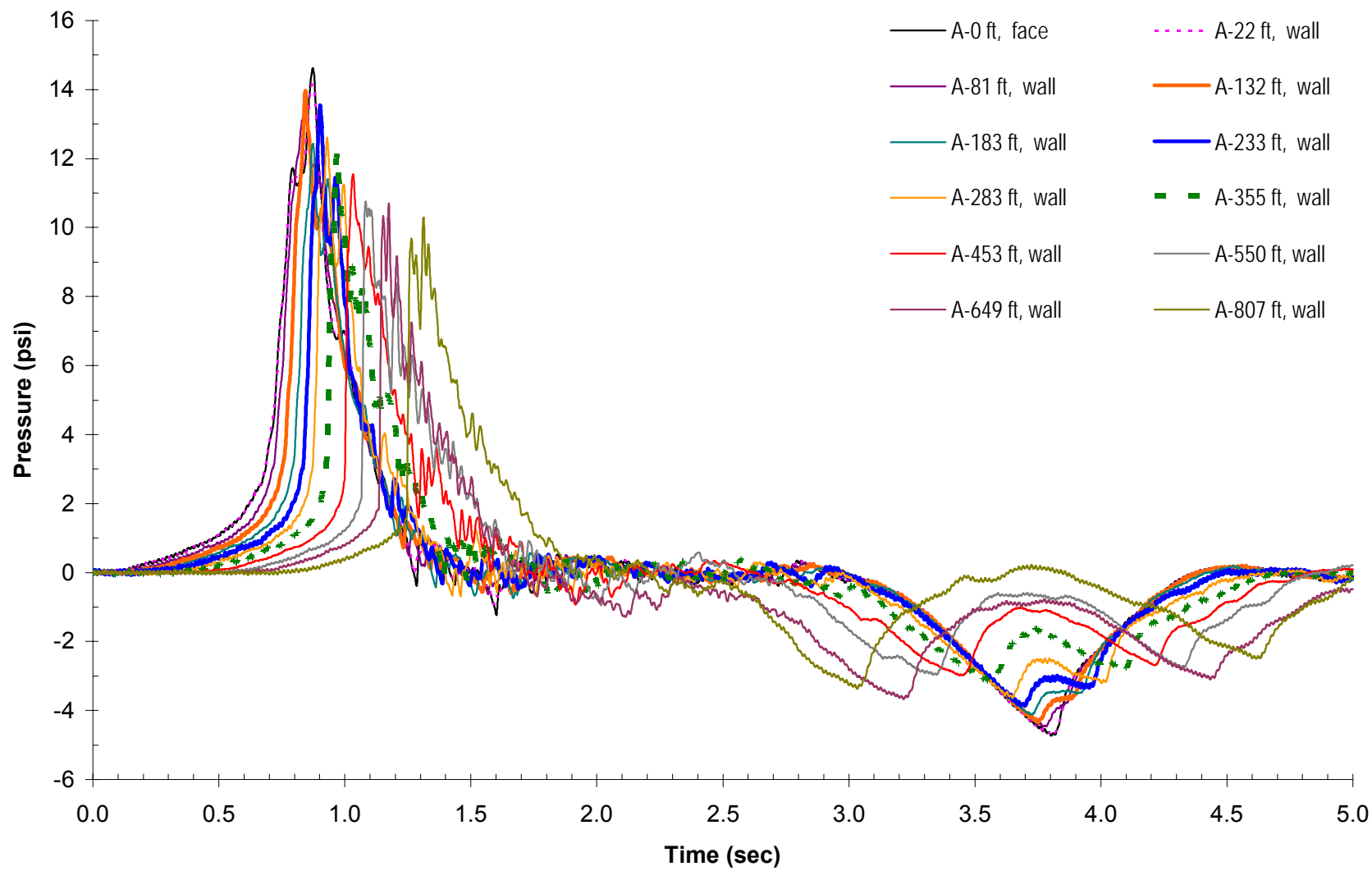


Figure B.8 – Pressure-time curve for mine shot #510.

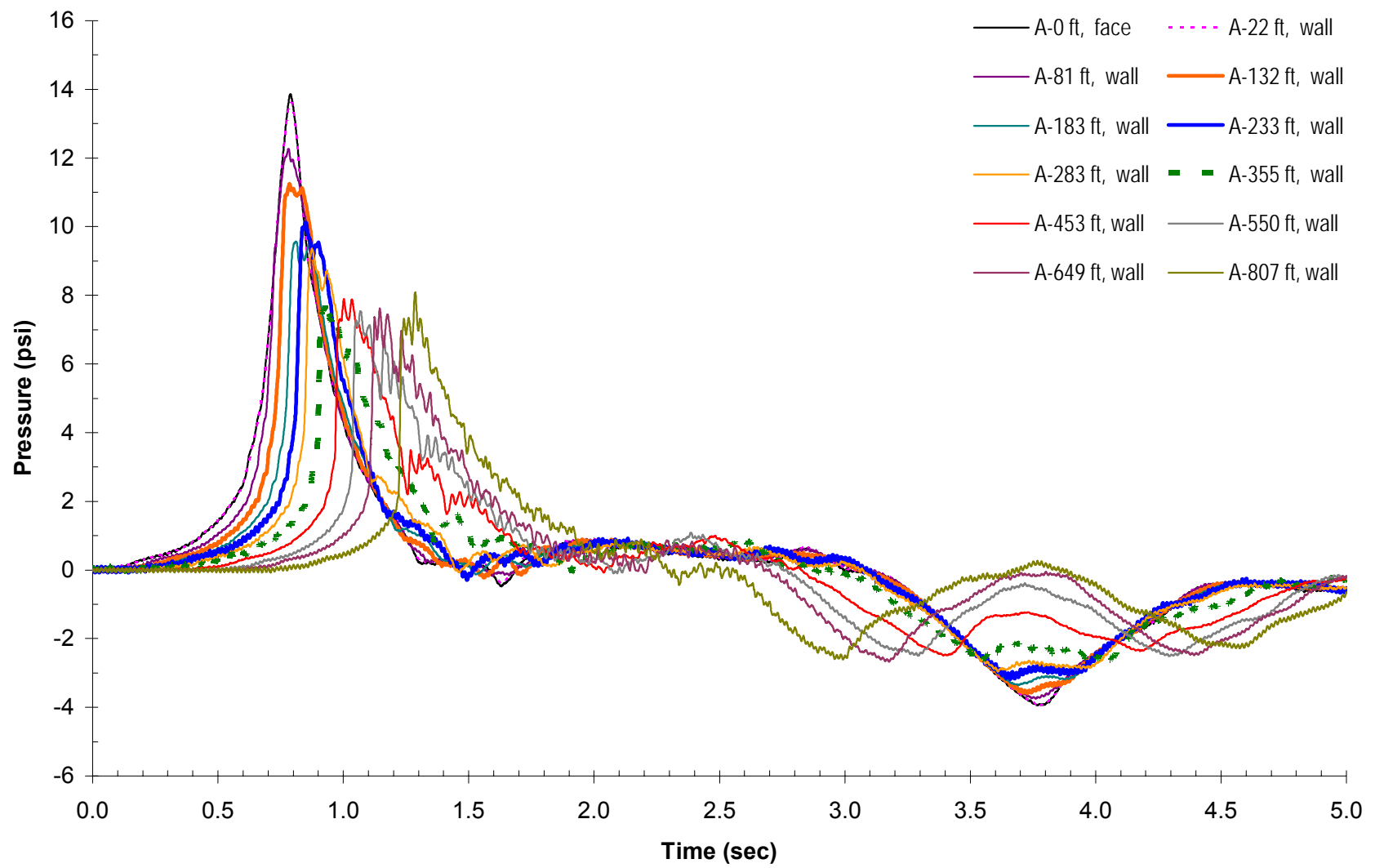


Figure B.9 – Pressure-time curve for mine shot #513.

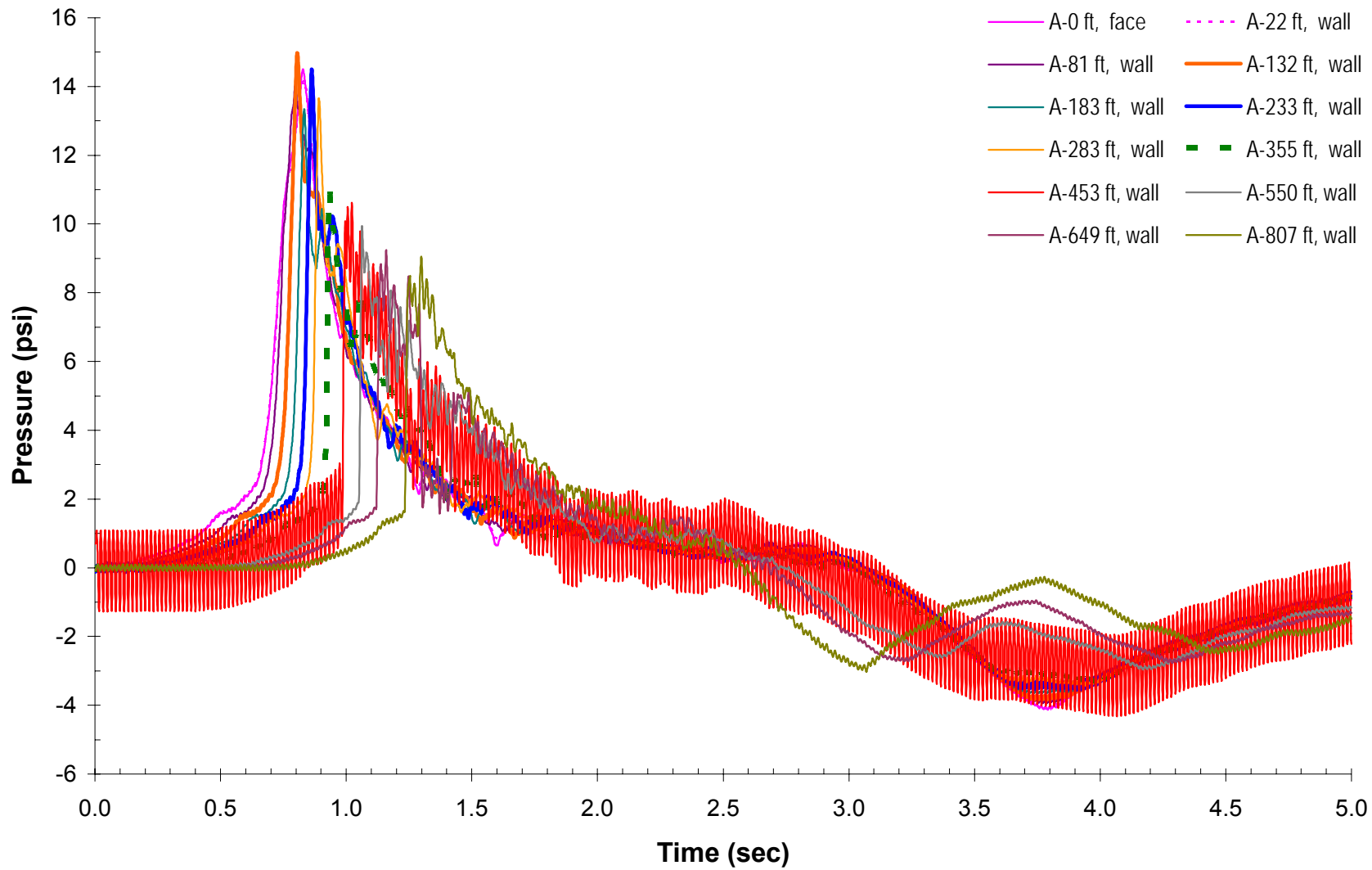


Figure B.10 – Pressure-time curve for mine shot #514.

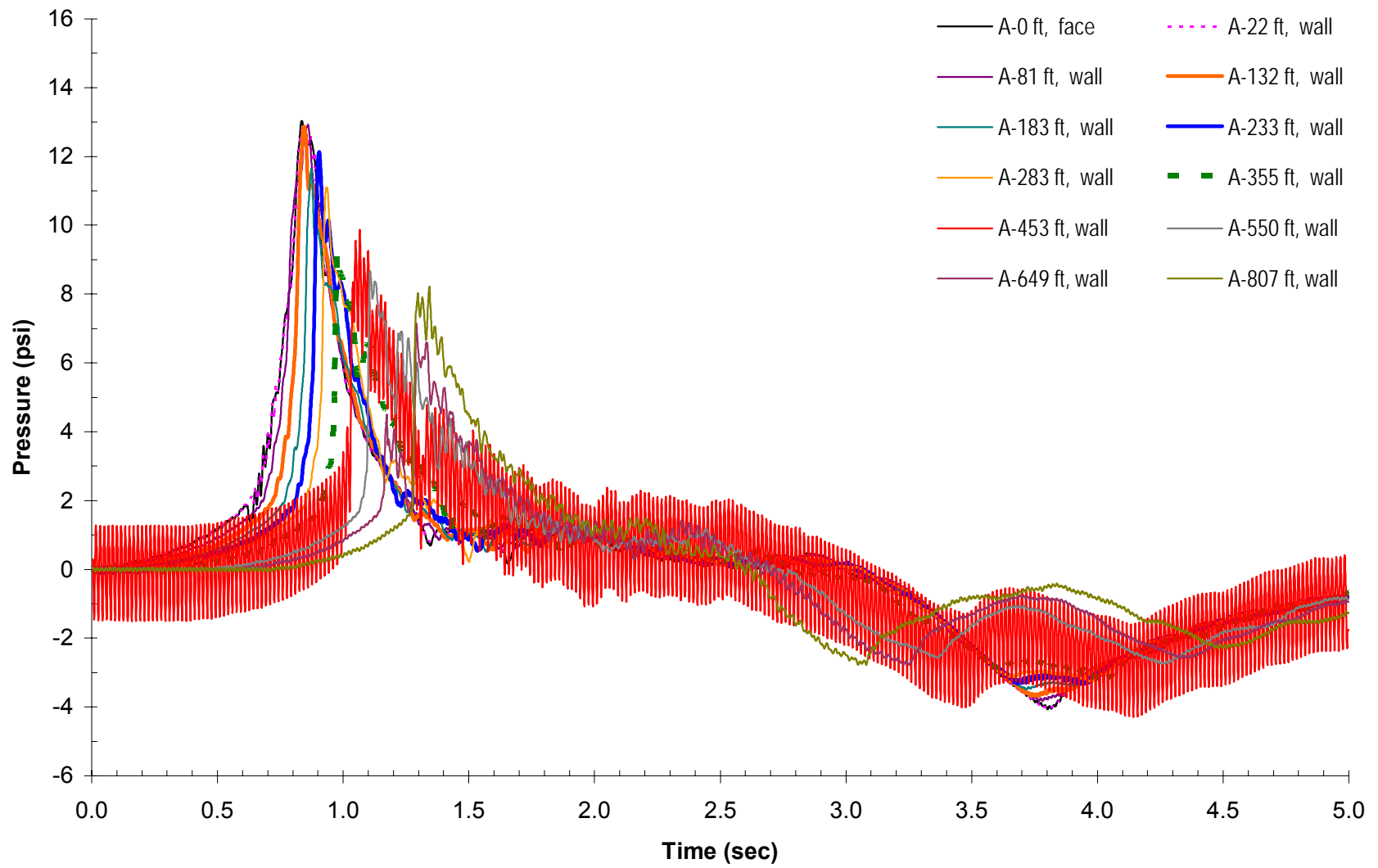


Figure B.11 – Pressure-time curve for mine shot #516.

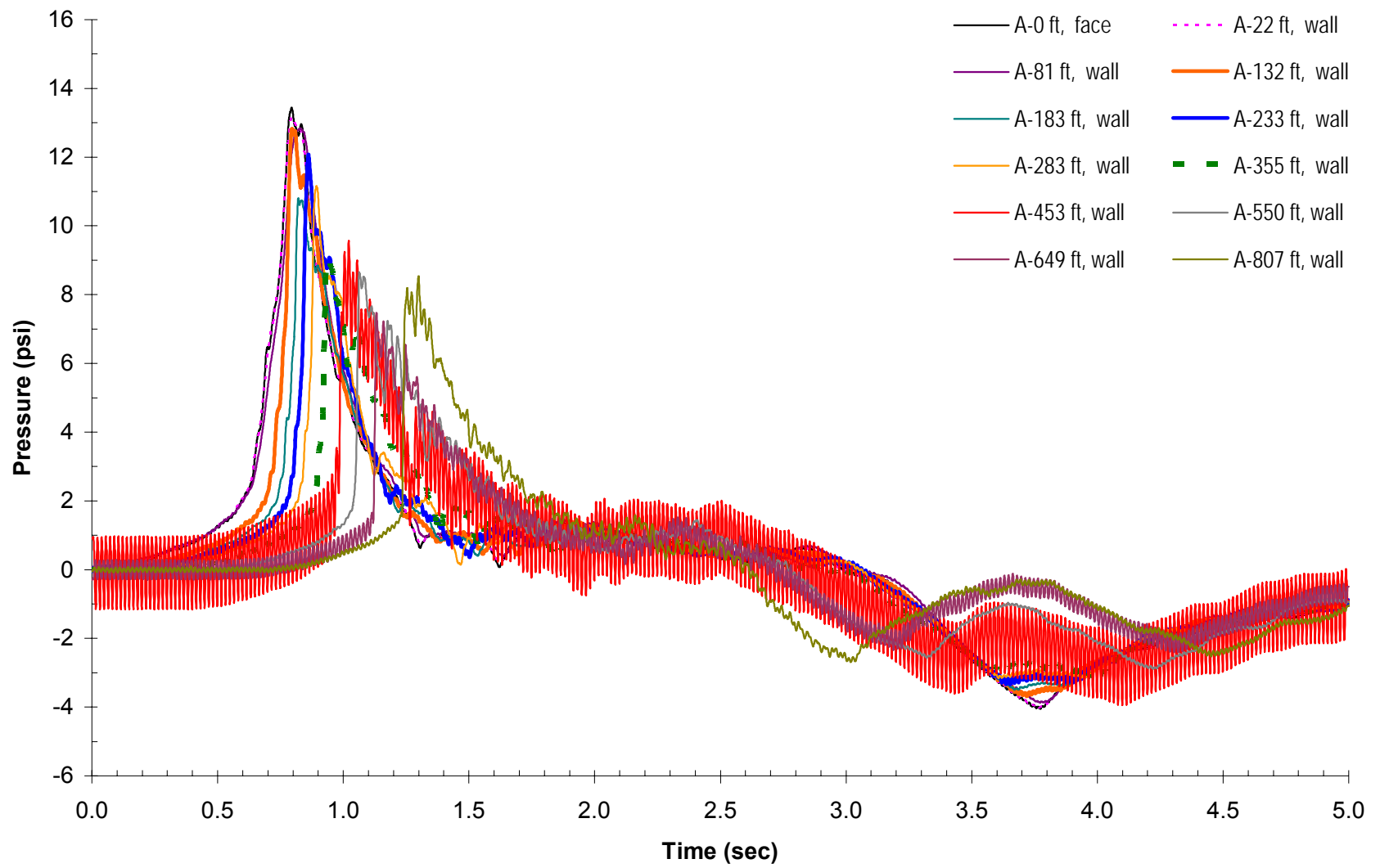


Figure B.12 – Pressure-time curve for mine shot #517.

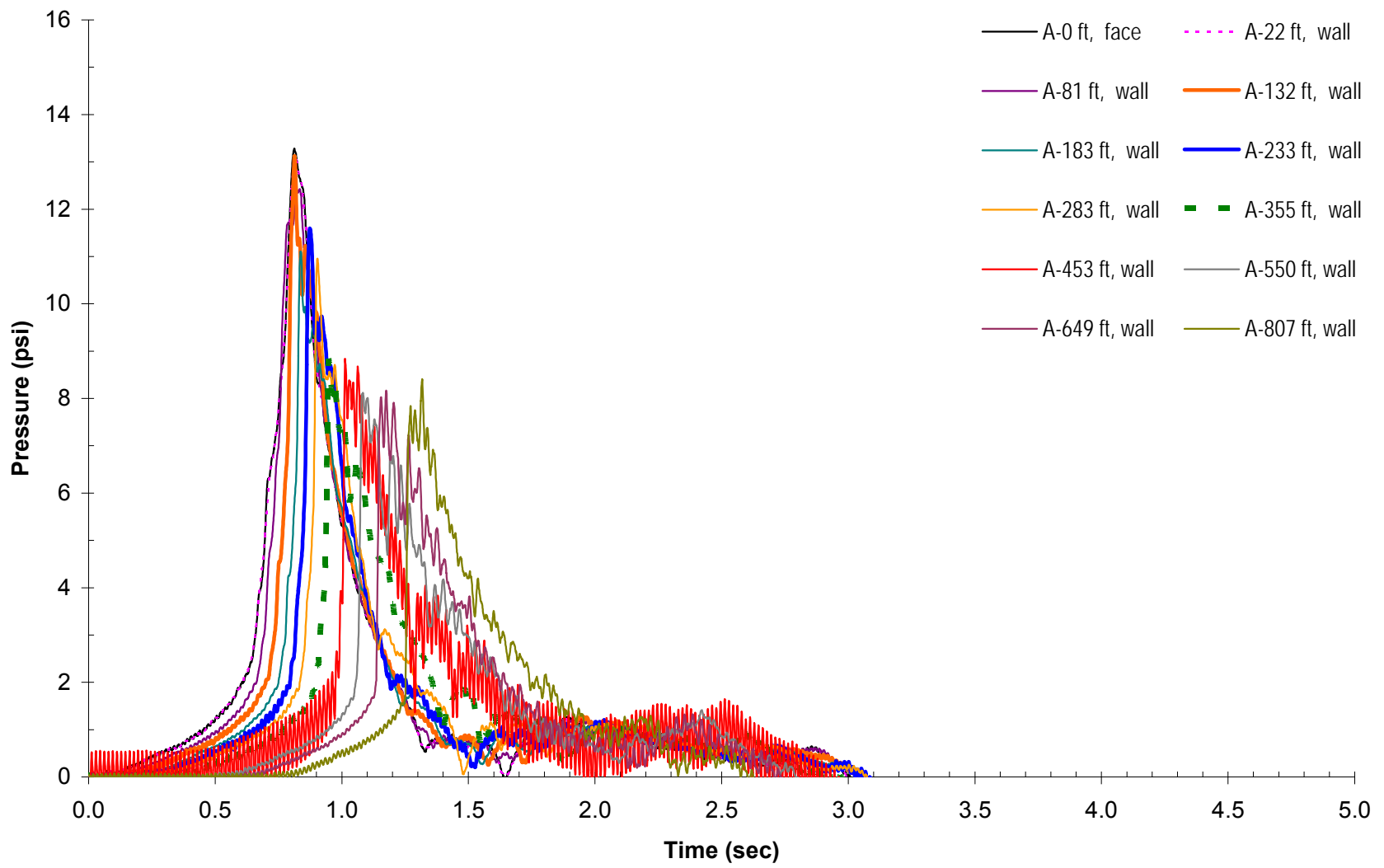


Figure B.13 – Pressure-time curve for mine shot #518.

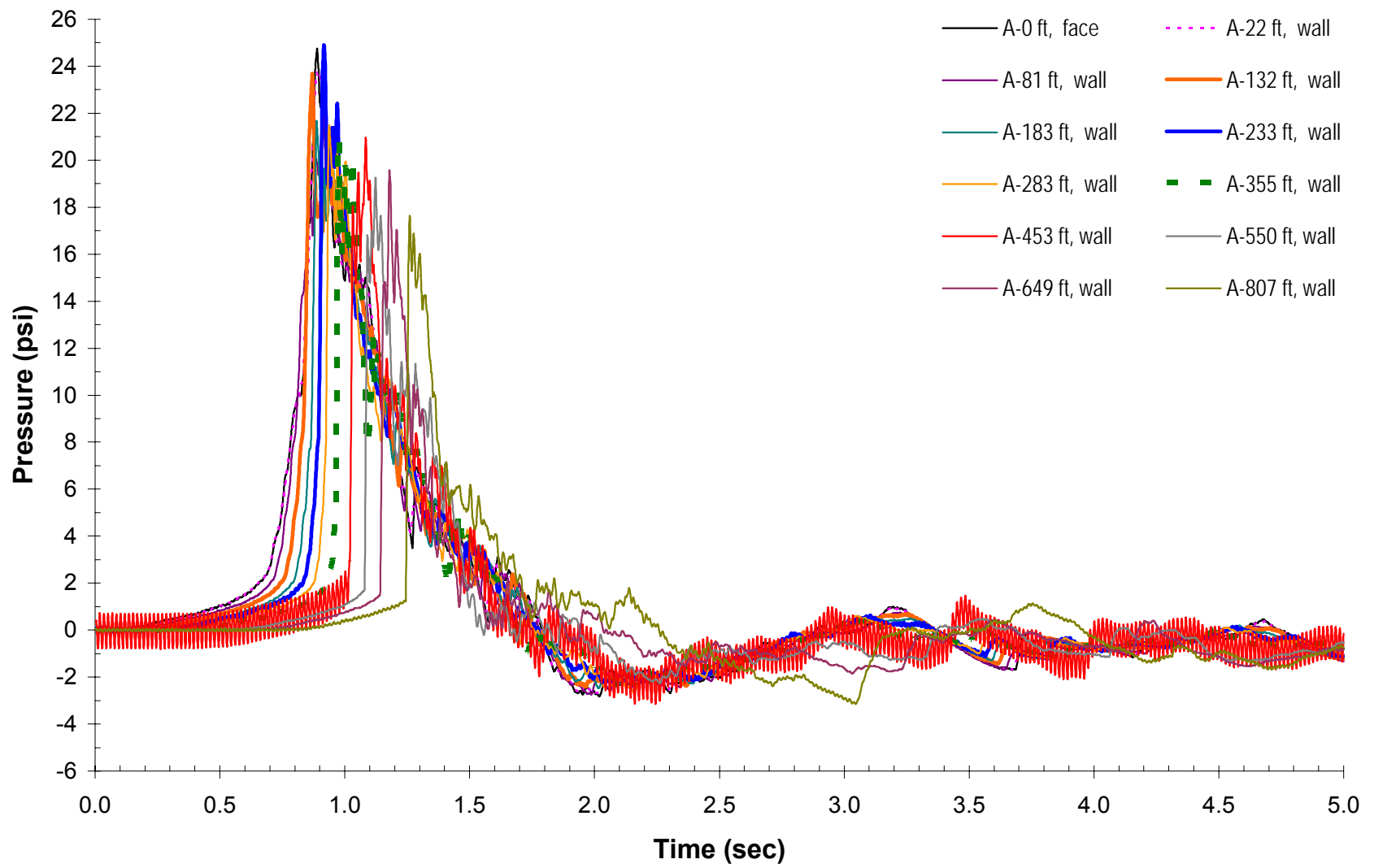


Figure B.14 – Pressure-time curve for mine shot #519.



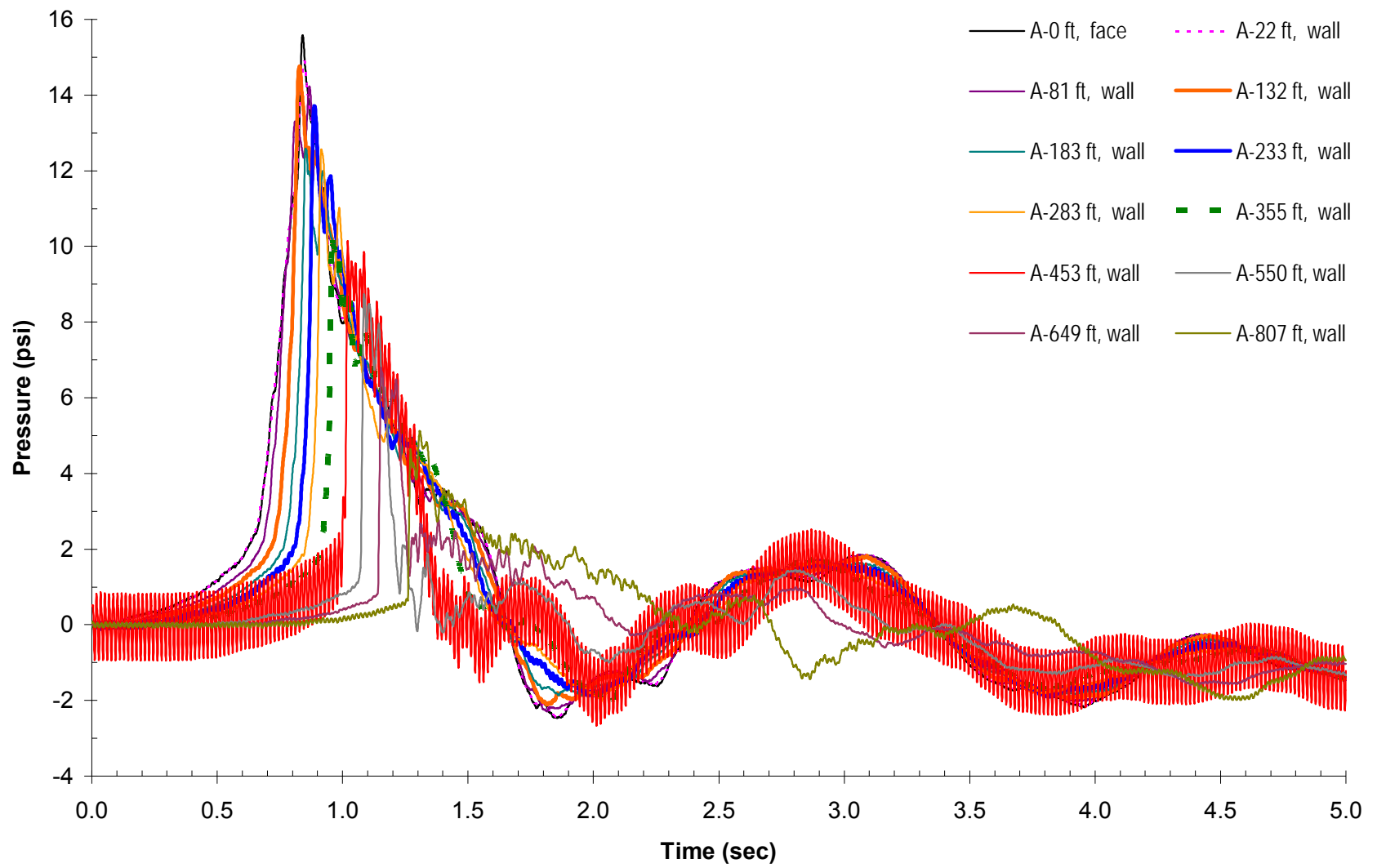


Figure B.15 – Pressure-time curve for mine shot #520.

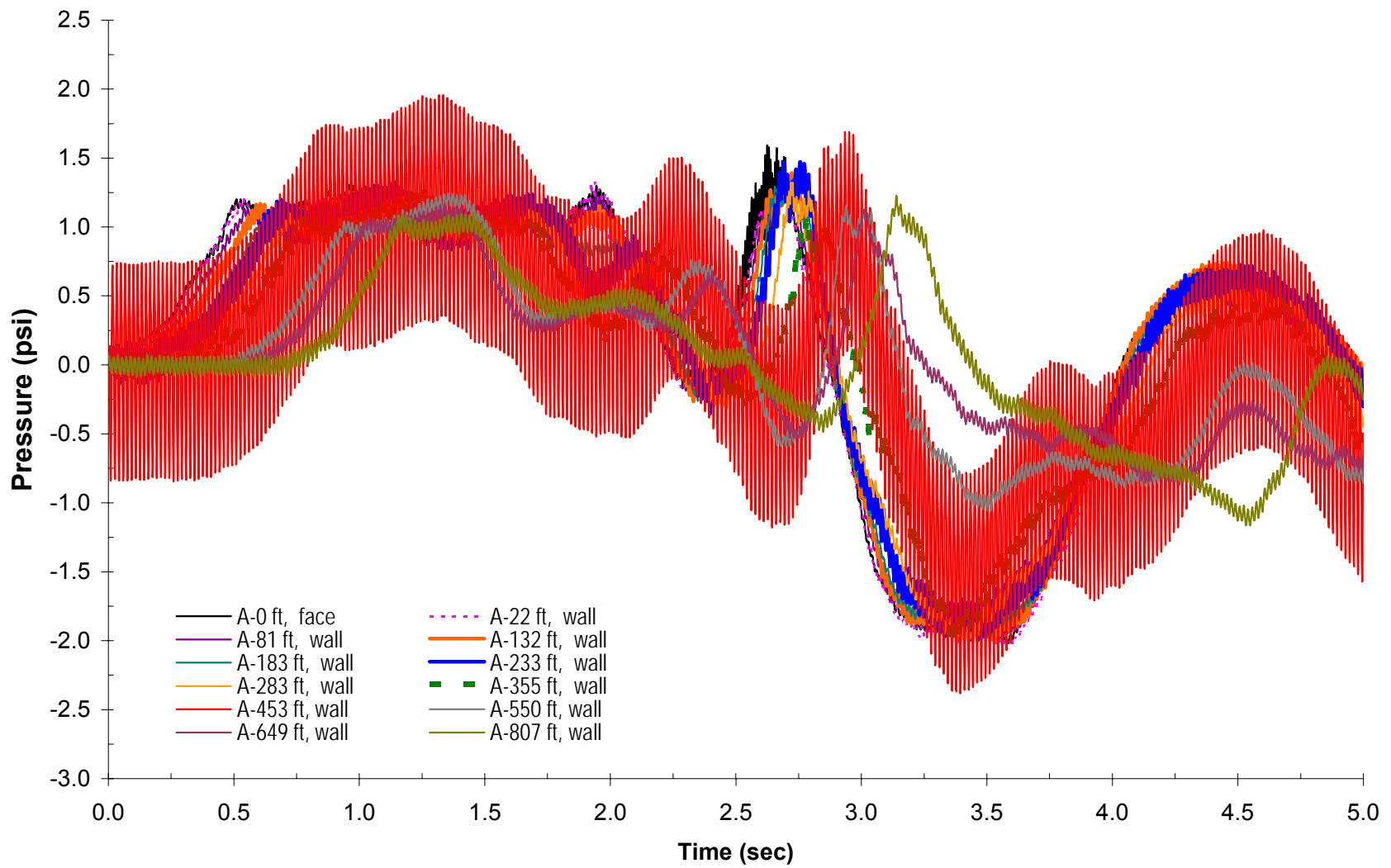


Figure B.16 – Pressure-time curve for mine shot #521.

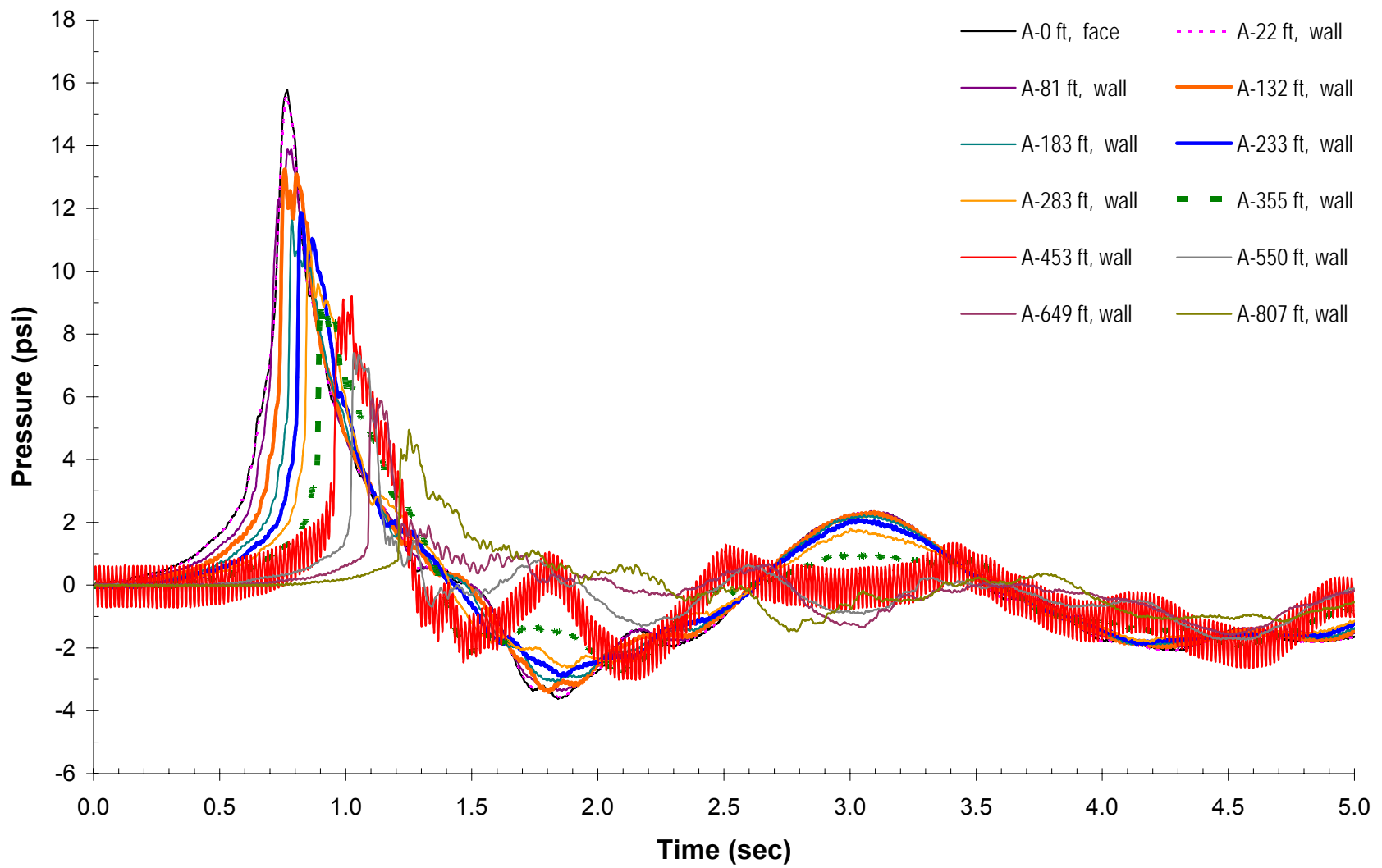


Figure B.17 – Pressure-time curve for mine shot #522.

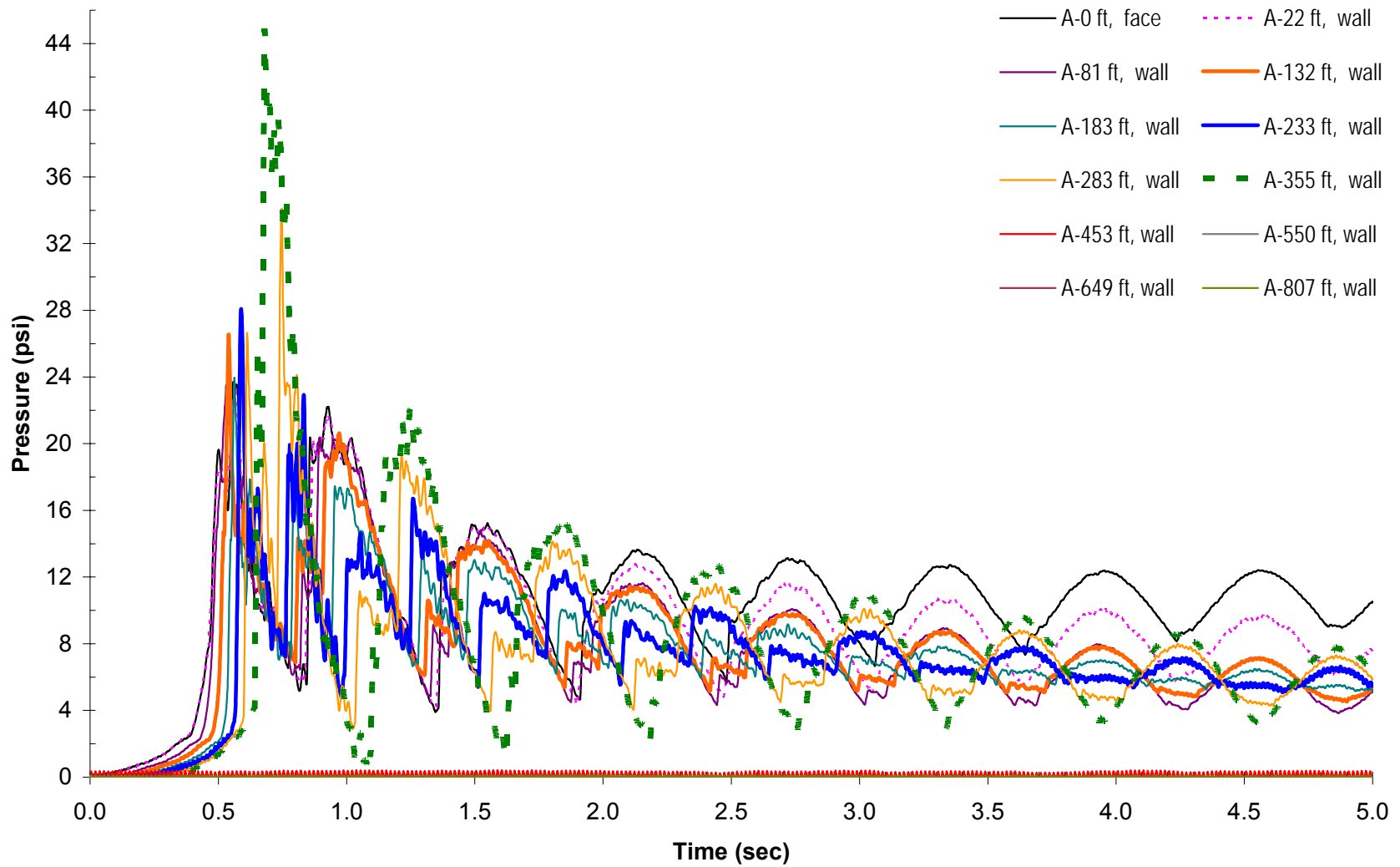
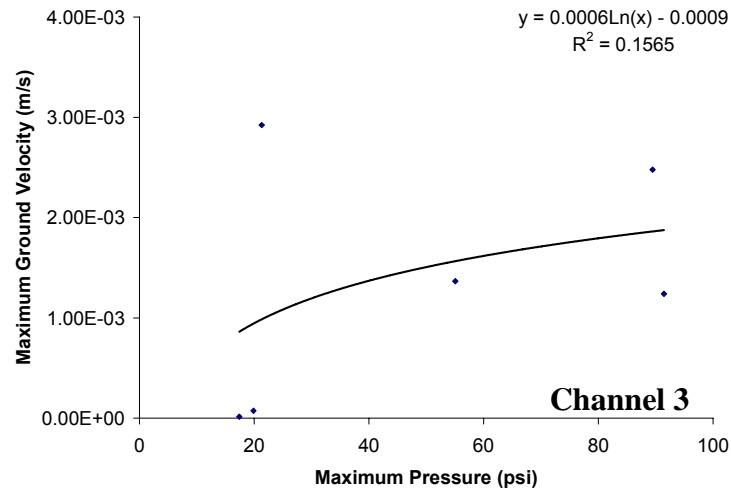
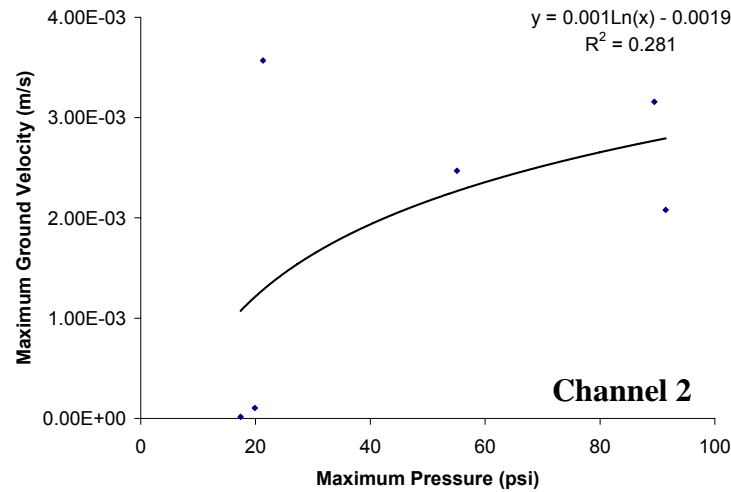
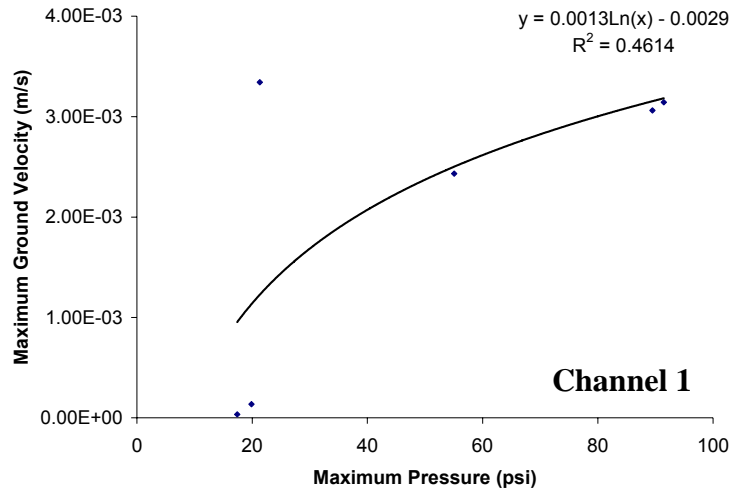


Figure B.18 – Pressure-time curve for mine shot #523.

A pressure-time curve was unavailable for Mine Shot #524. Maximum pressure was approximated at 80 psi by verbal communication with the mine supervisor.

# **Appendix C:**

## **Maximum Ground Velocity (Amplitude) – Peak Pressure Plots**



**Figure C.1** – Maximum ground velocity versus maximum pressure for Geophone 1 (C-Drift instrument room floor). Mine shot #507, which generated a pressure of 21 psi, appears to be an outlier.

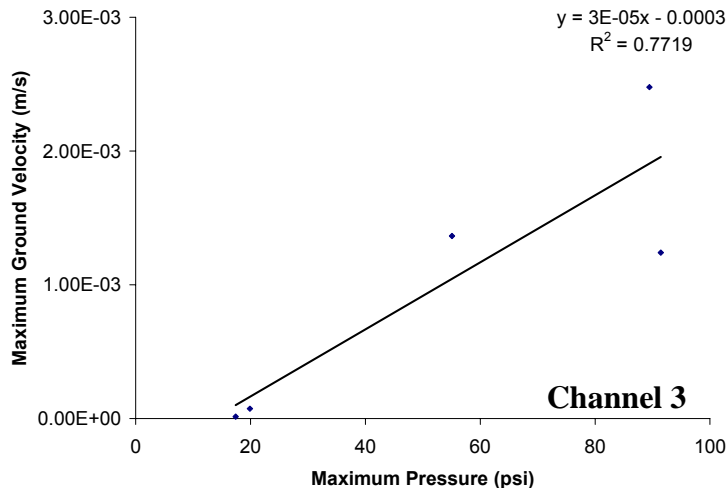
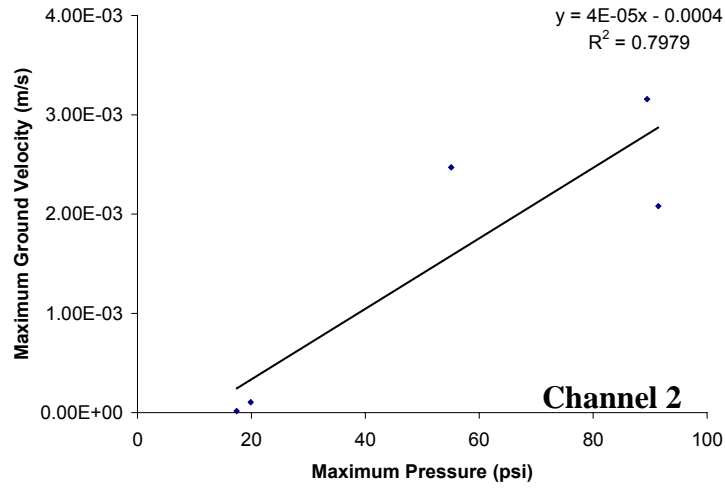
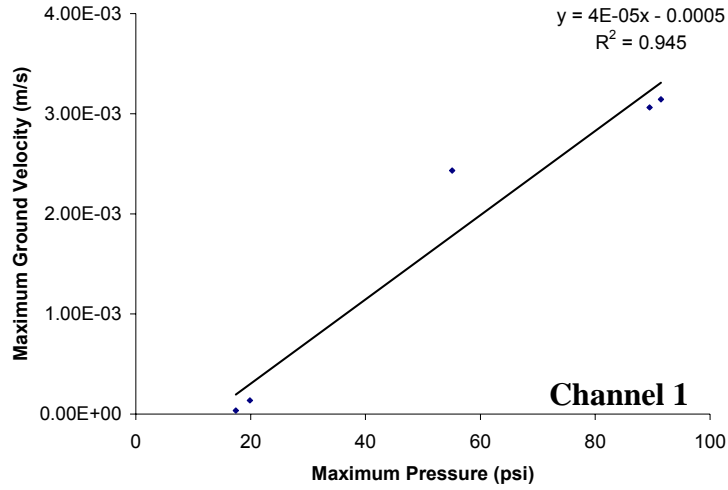


**Figure C.2** – Maximum ground velocity versus maximum pressure for Geophone 1 (C-Drift instrument room floor). The plots have removed mine shot #507 from the dataset which results in better overall trends when compared to Figure C.1.

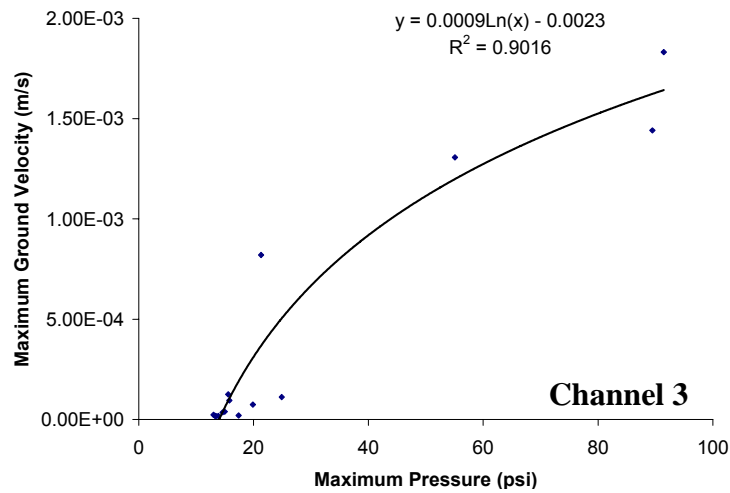
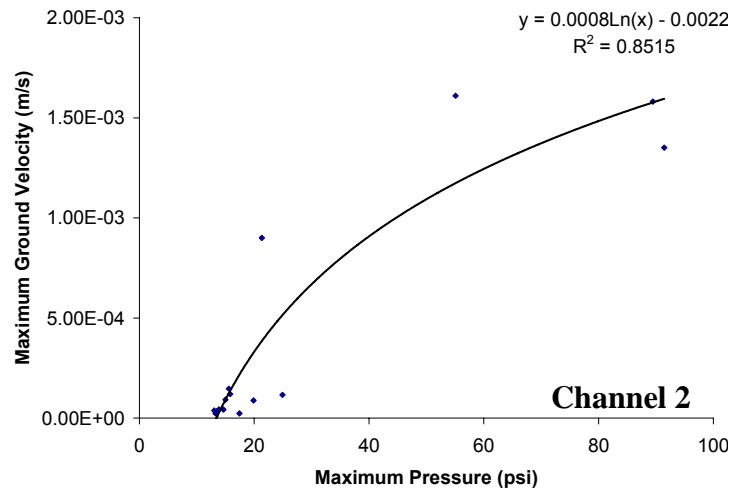
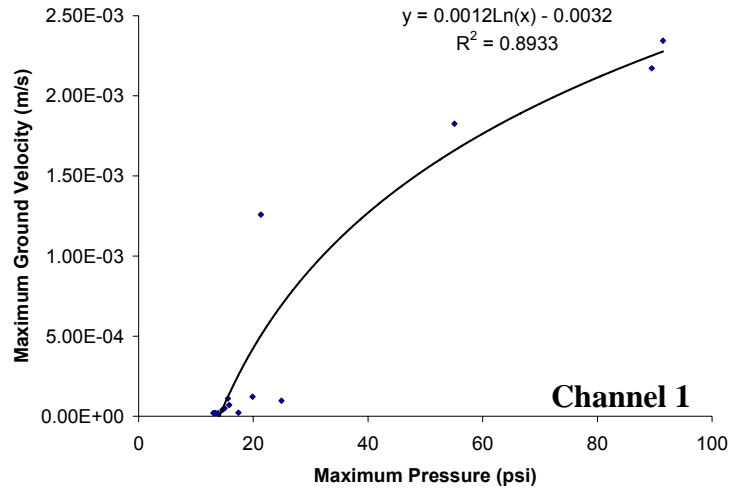


**Figure C.3** – Maximum ground velocity versus maximum pressure for Geophone 2 (C-Drift instrument room roof). Mine shot #507, which generated a pressure of 21 psi, appears to be an outlier.



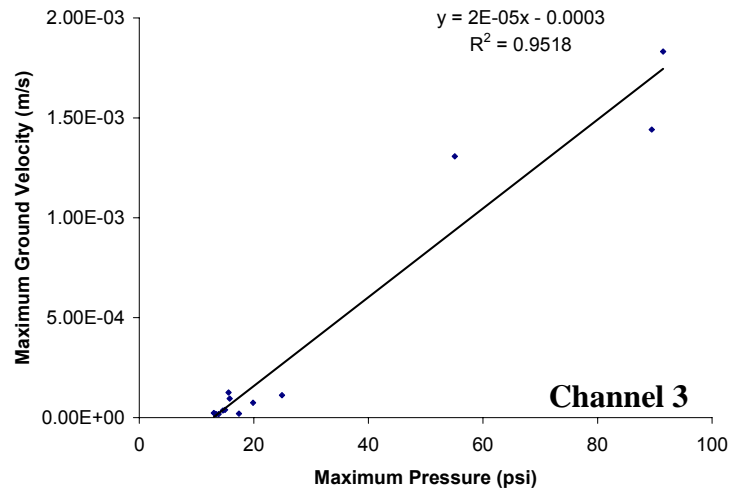
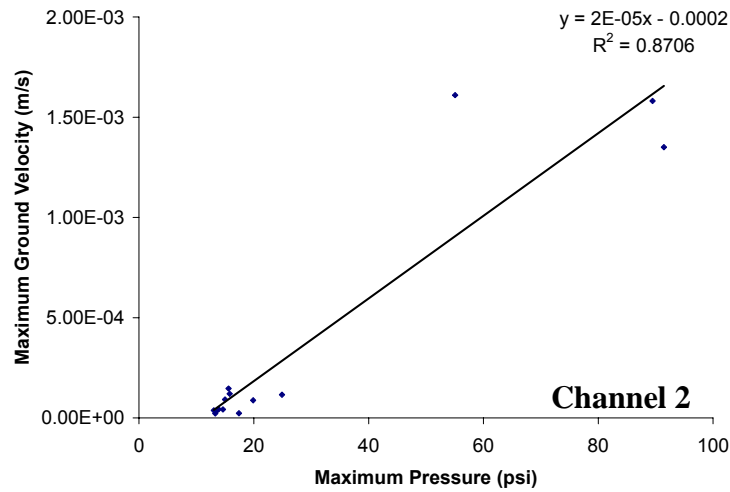
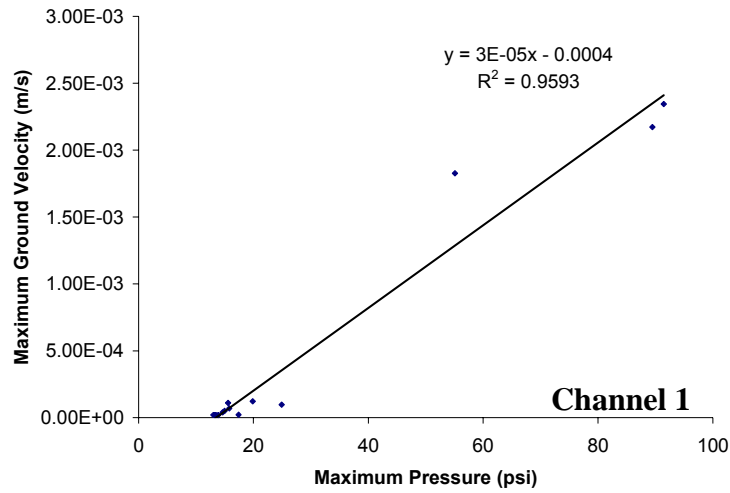


**Figure C.4** – Maximum ground velocity versus maximum pressure for Geophone 2 (C-Drift instrument room roof). The plots have removed mine shot #507 from the dataset which results in better overall trends when compared to Figure C.3.

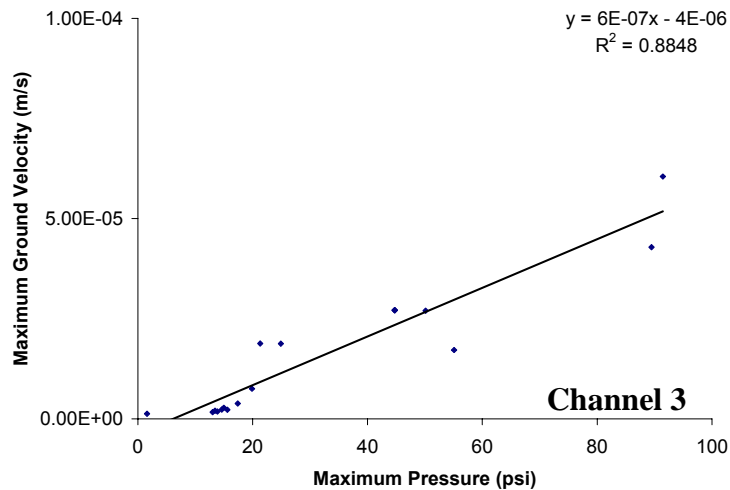
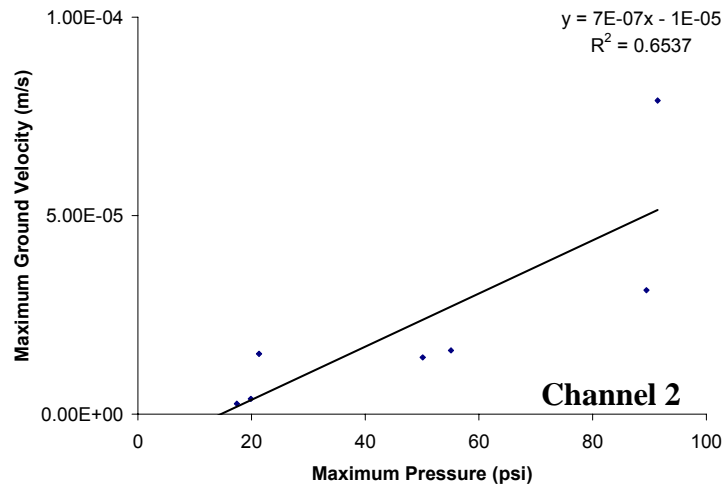
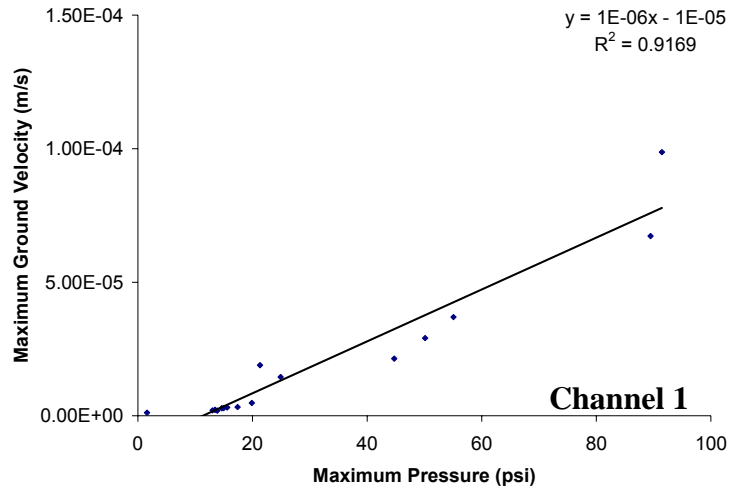


**Figure C.5** – Maximum ground velocity versus maximum pressure for Geophone 3 (D-Drift instrument room). The data from Channel 2 were considered questionable for some tests due to digitizer and/or geophone malfunction, which resulted in not as many data points for that plot.

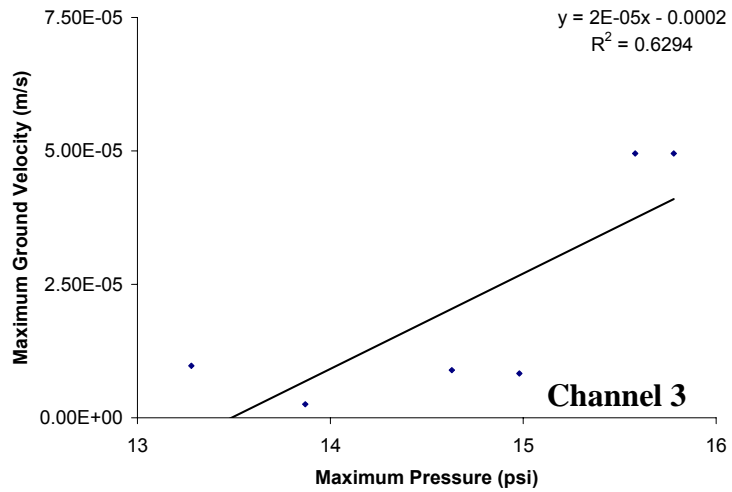
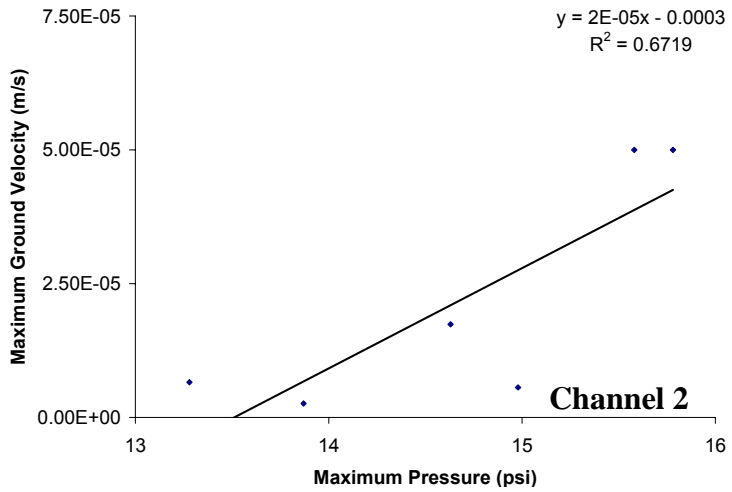
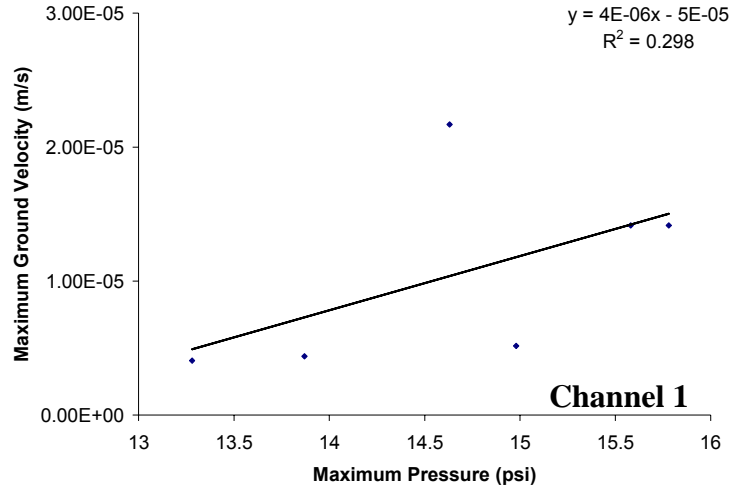


**Figure C.6** – Maximum ground velocity versus maximum pressure for Geophone 4 (E-Drift entry near bulkhead door). Data were only available from this location for a very small range of maximum explosive pressures.

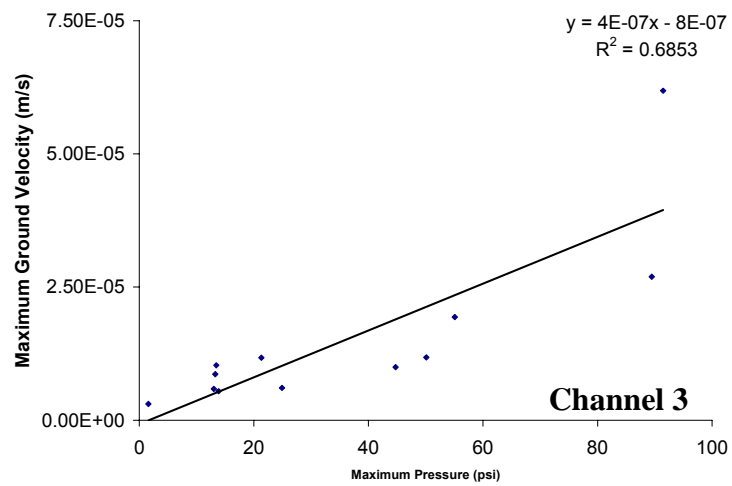
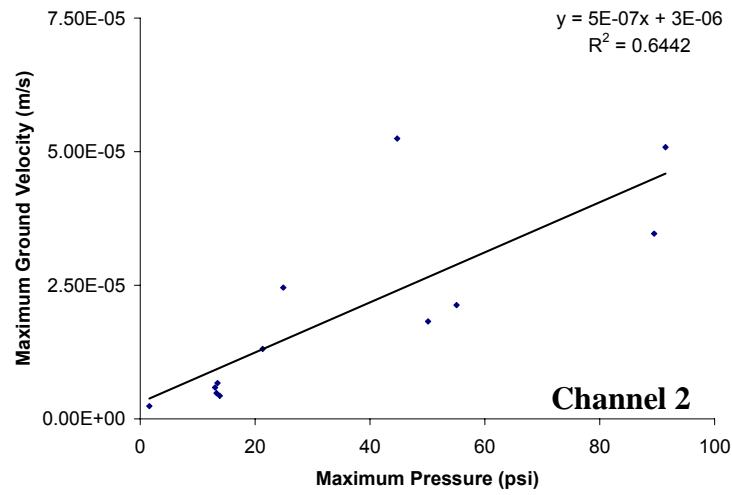
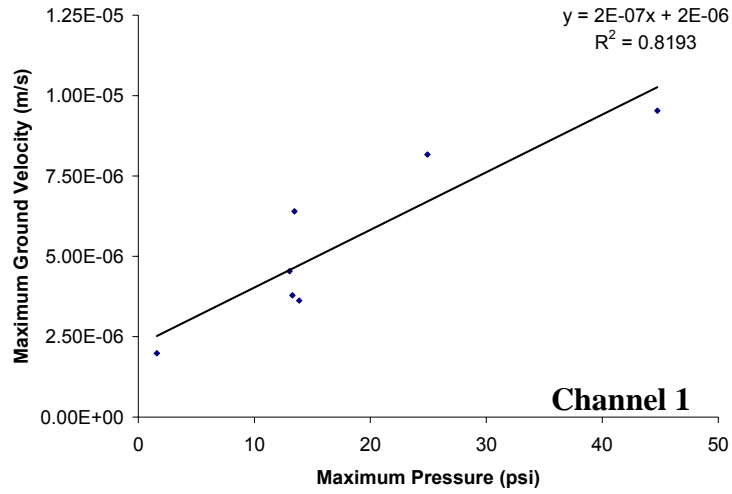


**Figure C.7** – Maximum ground velocity versus maximum pressure for Geophone 5 (D-Drift entry). The data from Channel 1 were considered questionable due to digitizer and/or geophone malfunction, which resulted in not as many data points for that plot.

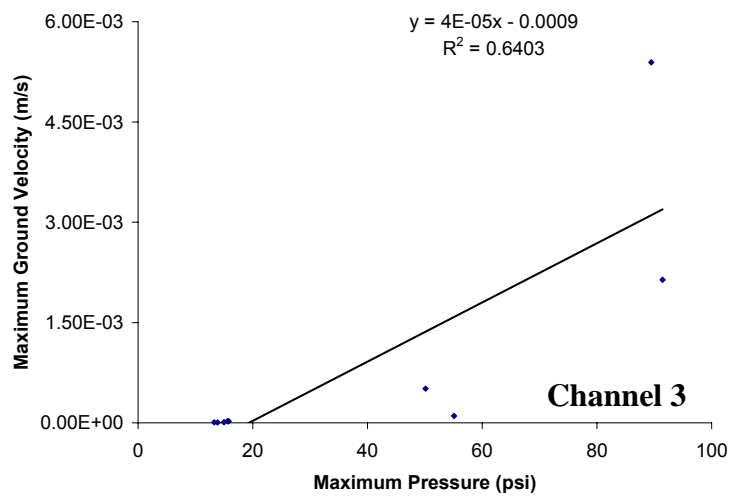
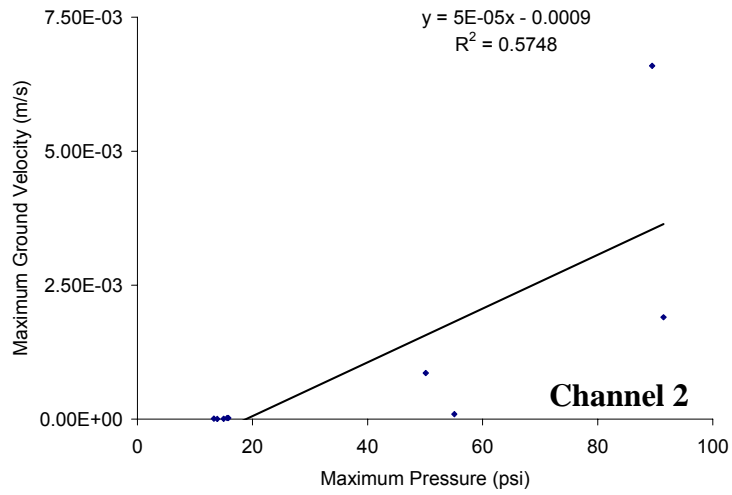
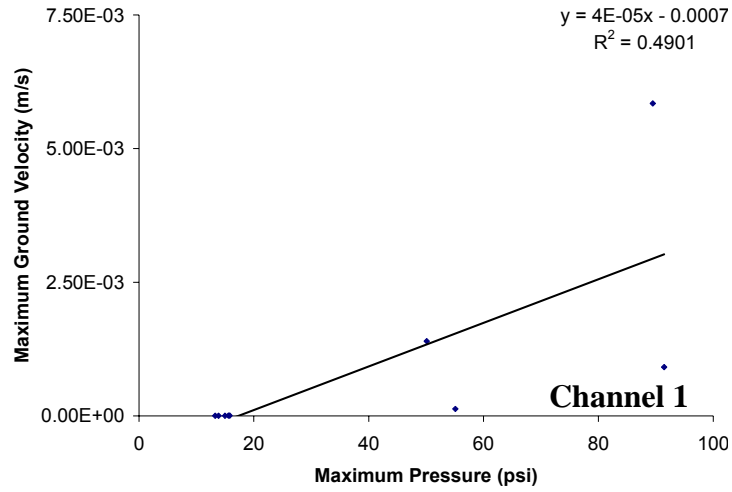


**Figure C.8** – Maximum ground velocity versus maximum pressure for Geophone 6 (E-Drift middle of entry).

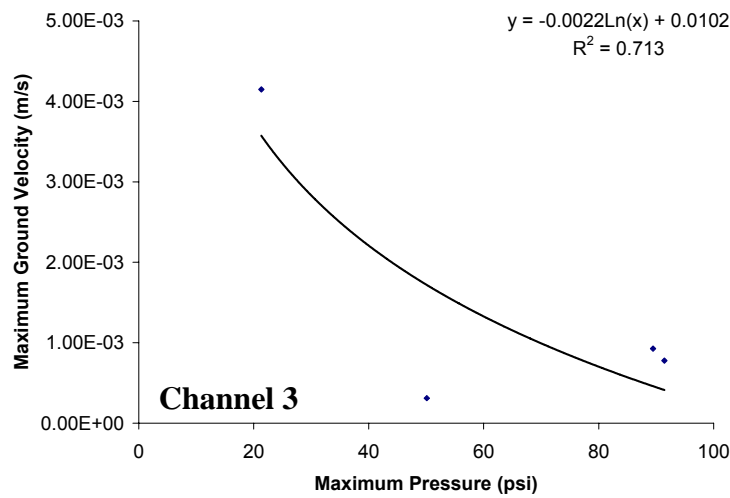
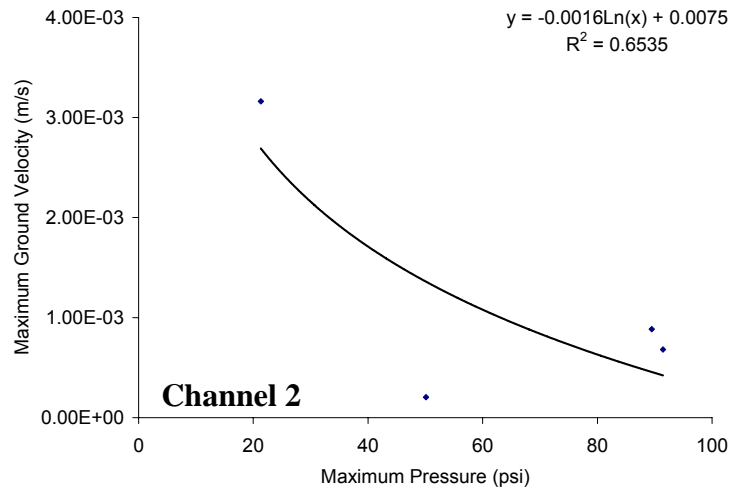
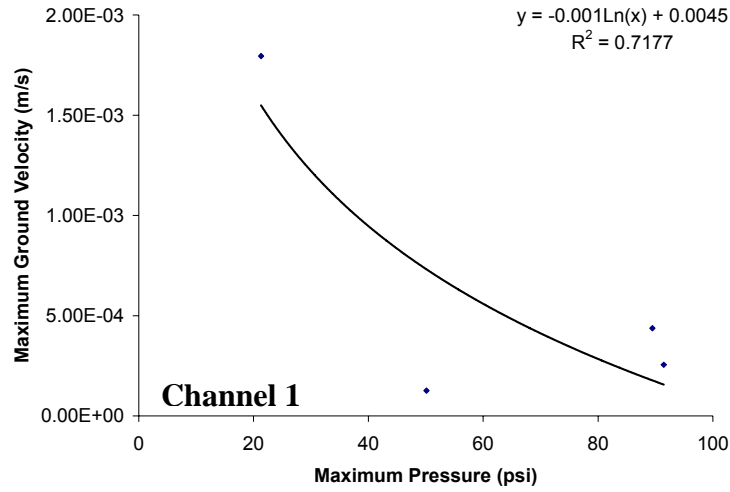


**Figure C.9** – Maximum ground velocity versus maximum pressure for Geophone 8 (A-Drift face). Mine shot #507, which generated a pressure of 21 psi, appears to be an outlier.

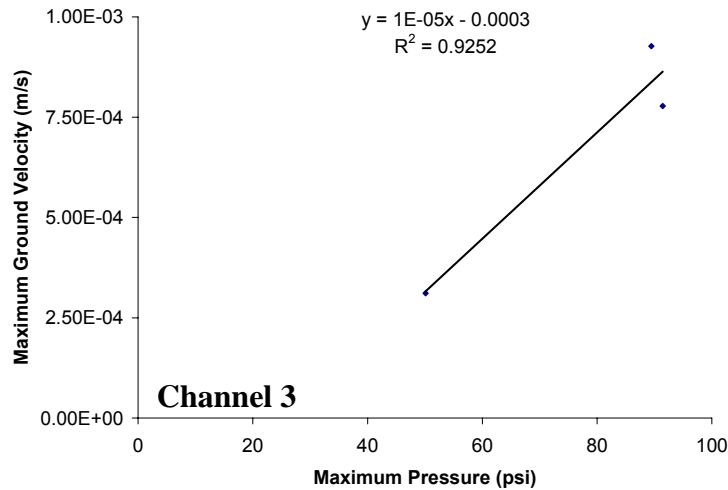
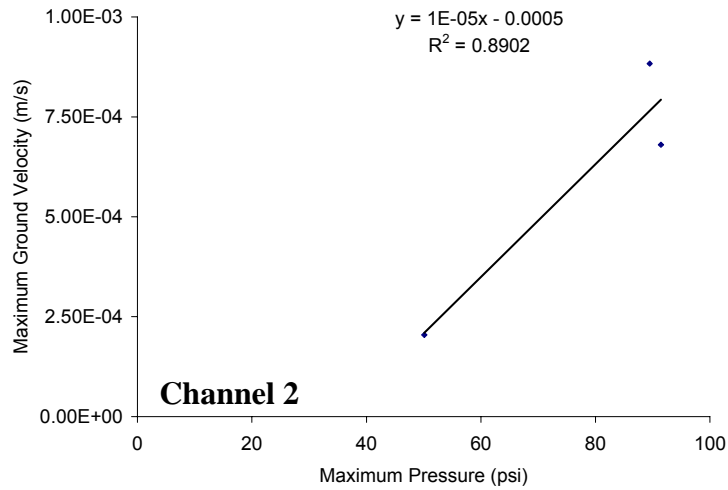
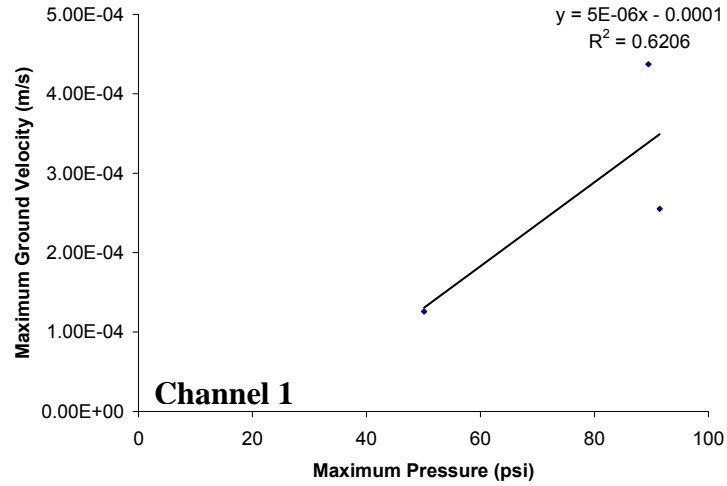


**Figure C.10** – Maximum ground velocity versus maximum pressure for Geophone 8 (A-Drift face). The plots have removed mine shot #507 from the dataset which results in similar trends as the other datasets, although only three tests were recorded from this location.

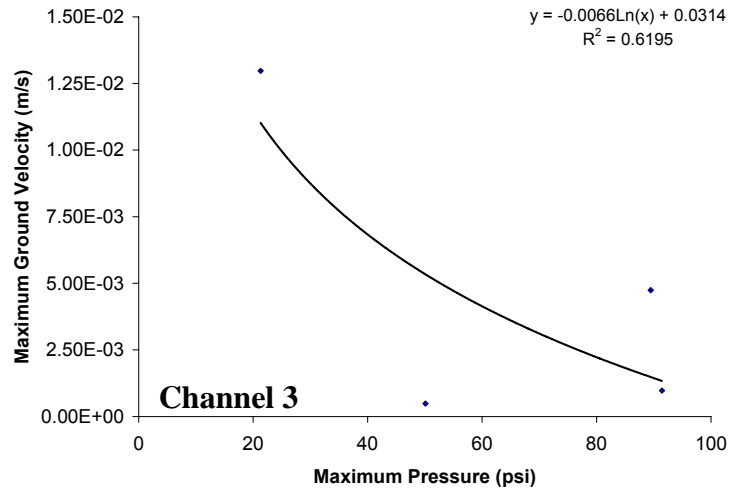
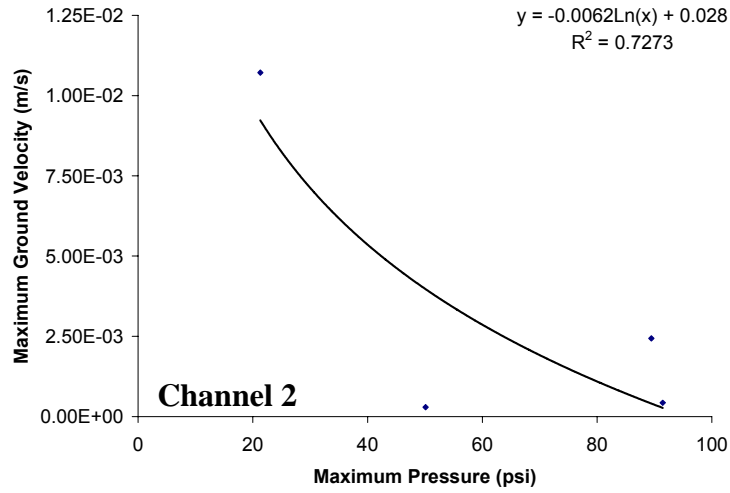
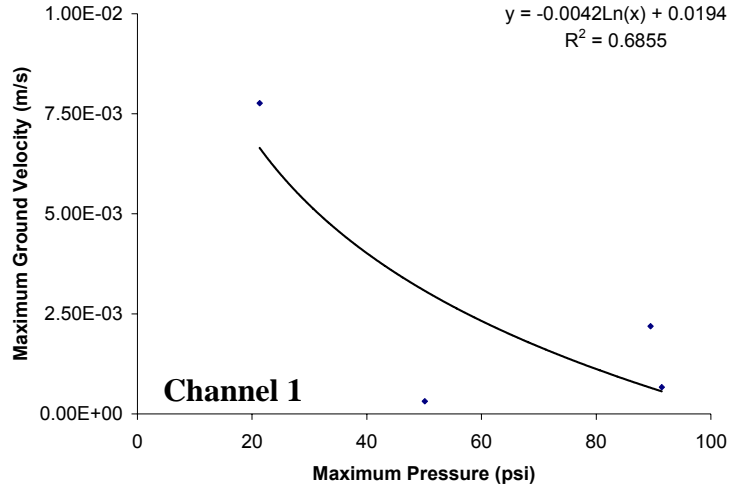


**Figure C.11** – Maximum ground velocity versus maximum pressure for Geophone 9 (A-Drift crosscut). Mine shot #507, which generated a pressure of 21 psi, appears to be an outlier.



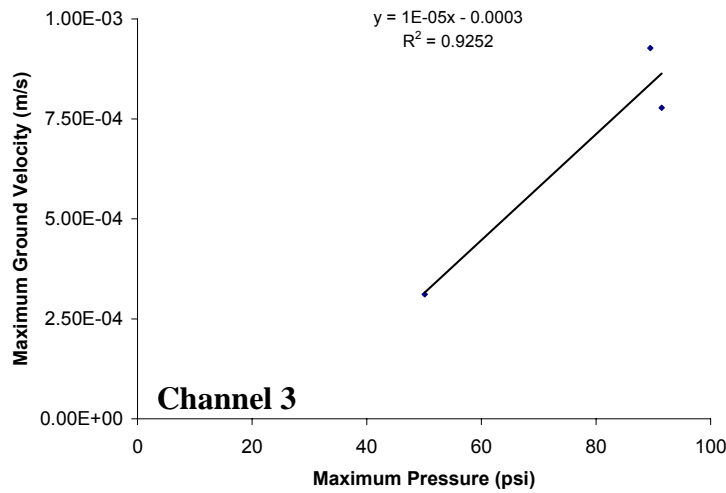
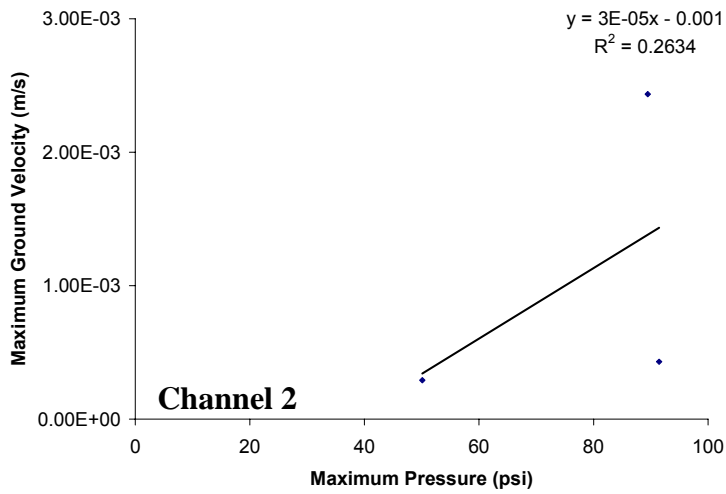
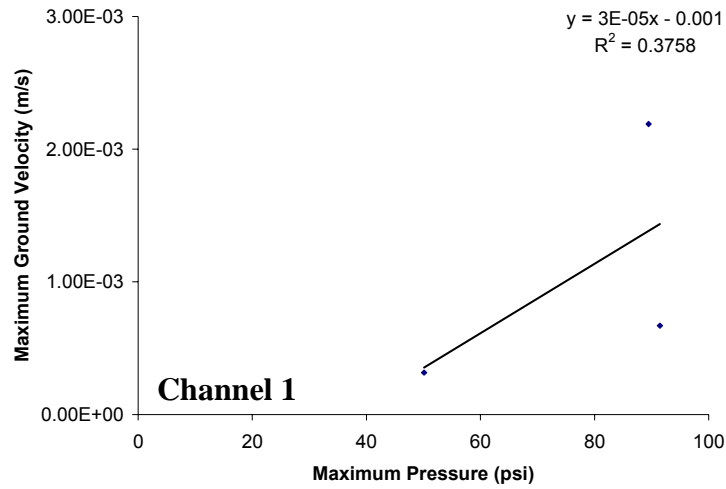


**Figure C.12** – Maximum ground velocity versus maximum pressure for Geophone 9 (A-Drift crosscut). The plots have removed mine shot #507 from the dataset which results in similar trends as the other datasets, although only three tests were recorded from this location.

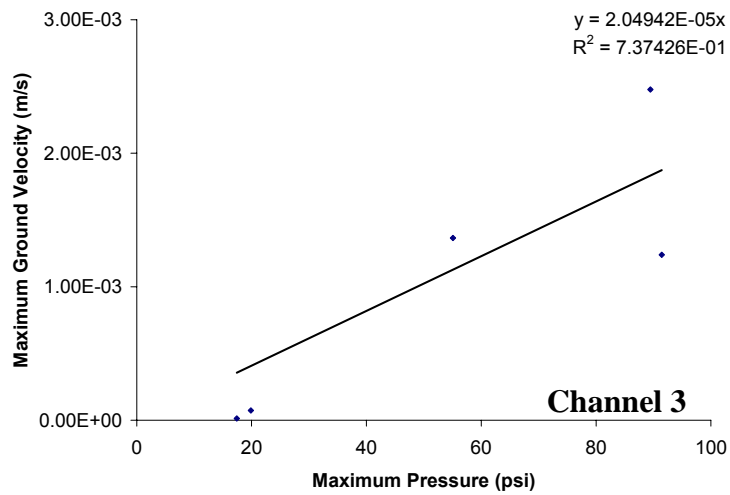
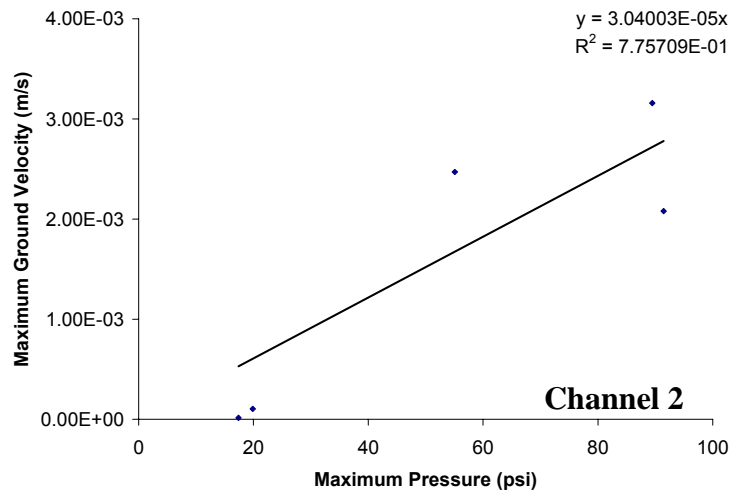
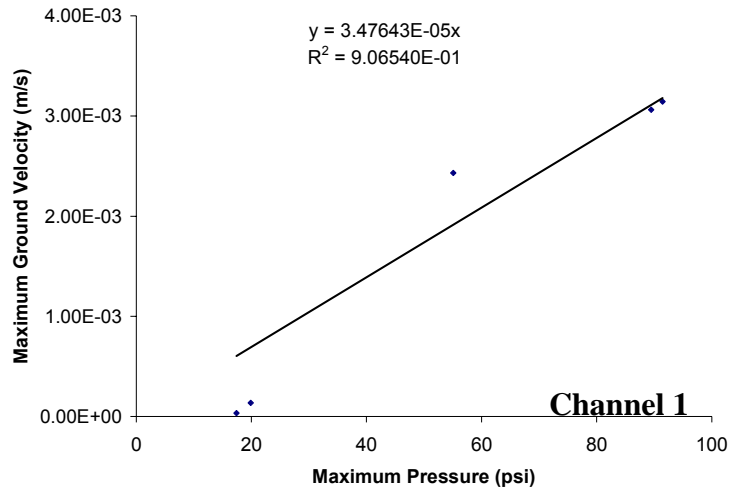


Figure C.13 – Maximum ground velocity versus maximum pressure for Geophone 1 (C-Drift instrument room floor) recalculated to allow the regression line to intersect the origin.

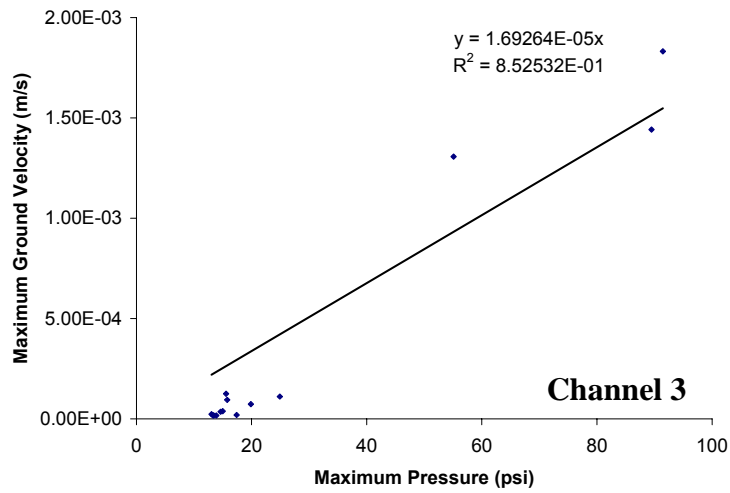
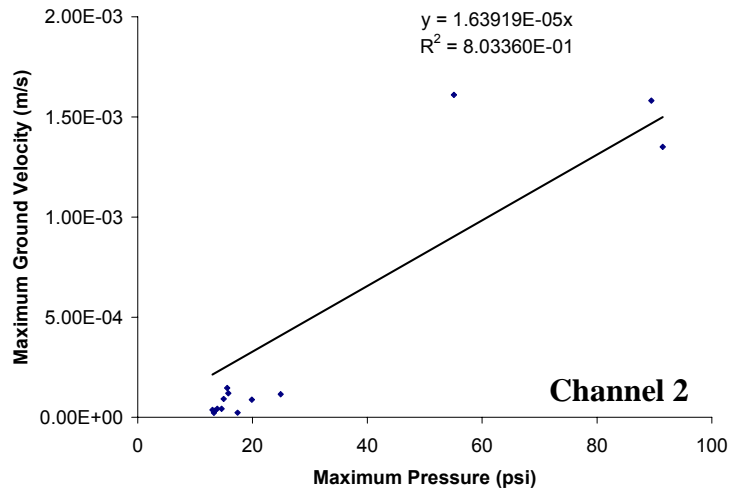
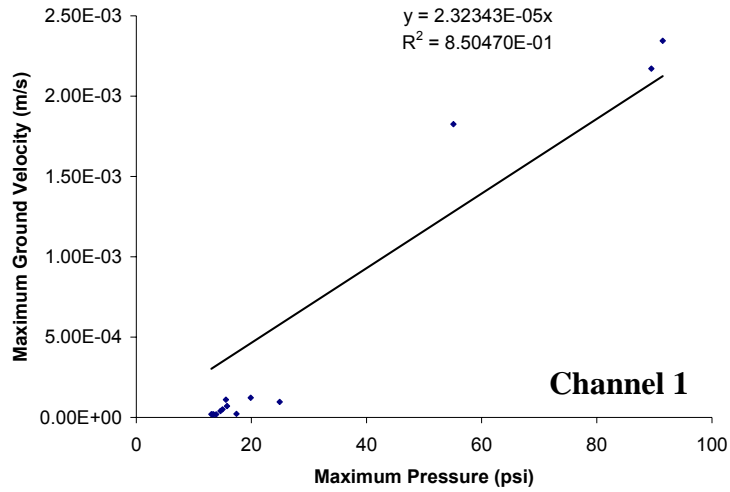


Figure C.14 – Maximum ground velocity versus maximum pressure for Geophone 2 (C-Drift instrument room roof) recalculated to allow the regression line to intersect the origin.

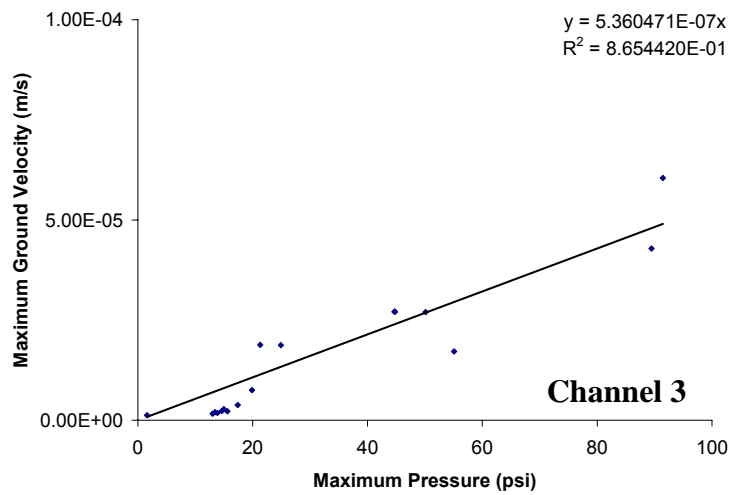
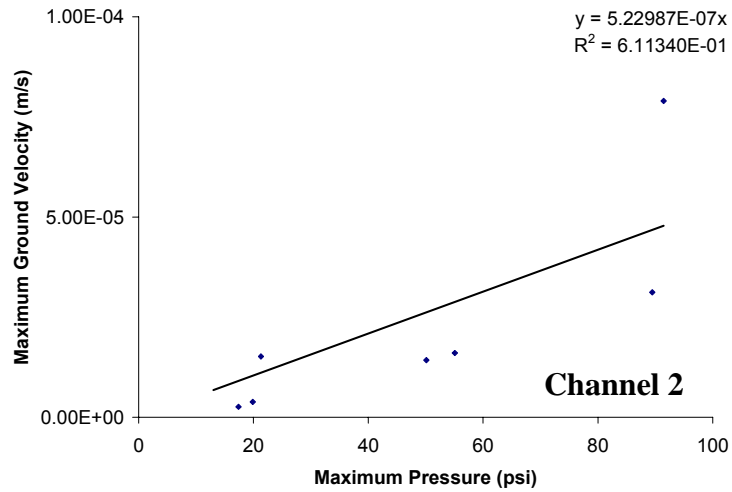
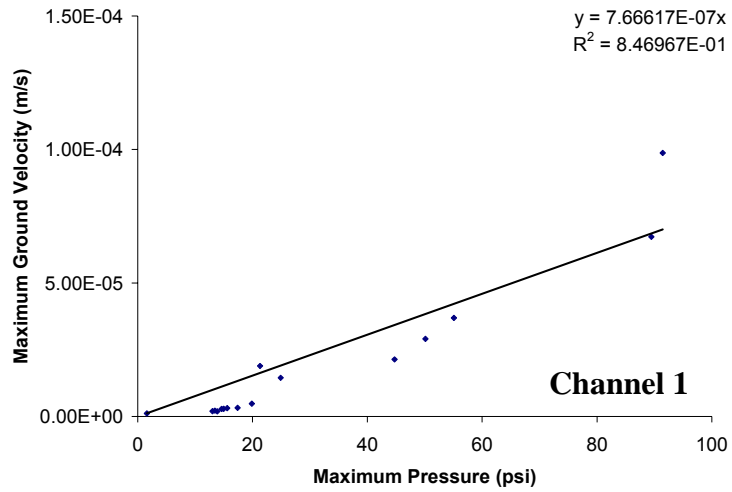


Figure C.15 – Maximum ground velocity versus maximum pressure for Geophone 3 (D-Drift instrument room) recalculated to allow the regression line to intersect the origin.

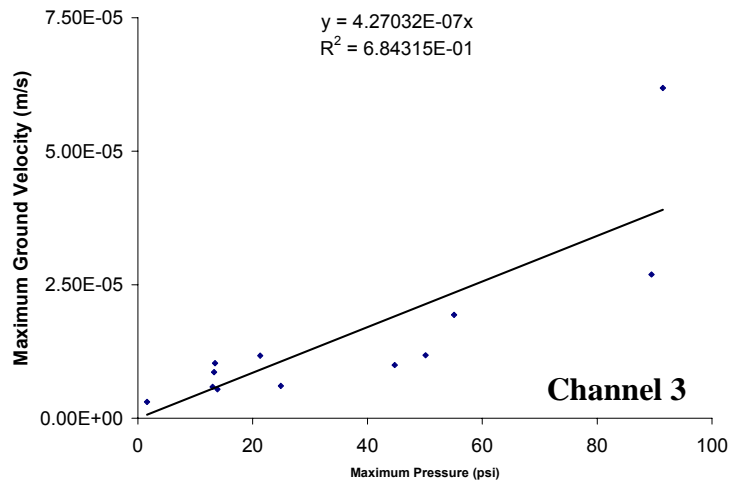
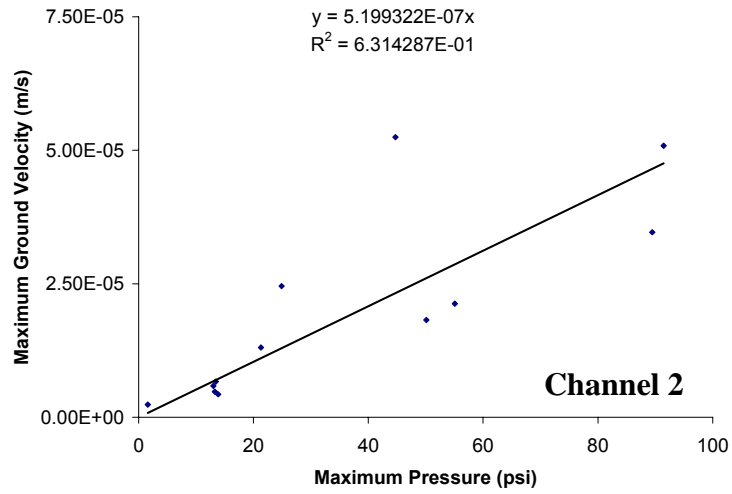
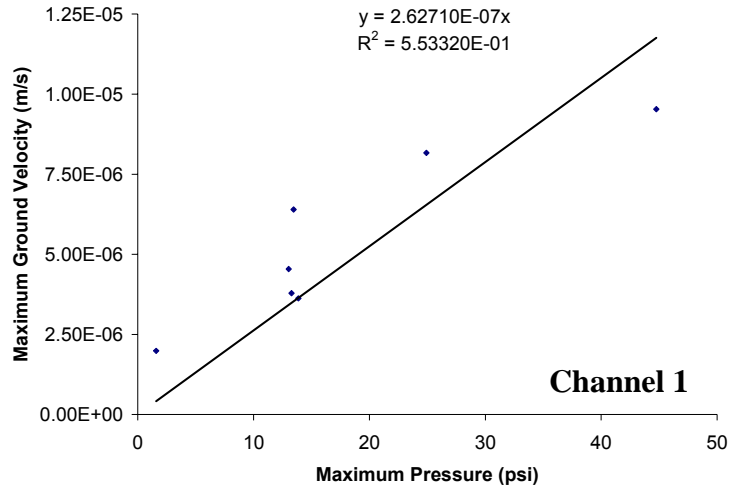


Figure C.16 – Maximum ground velocity versus maximum pressure for Geophone 5 (D-Drift entry) recalculated to allow the regression line to intersect the origin.

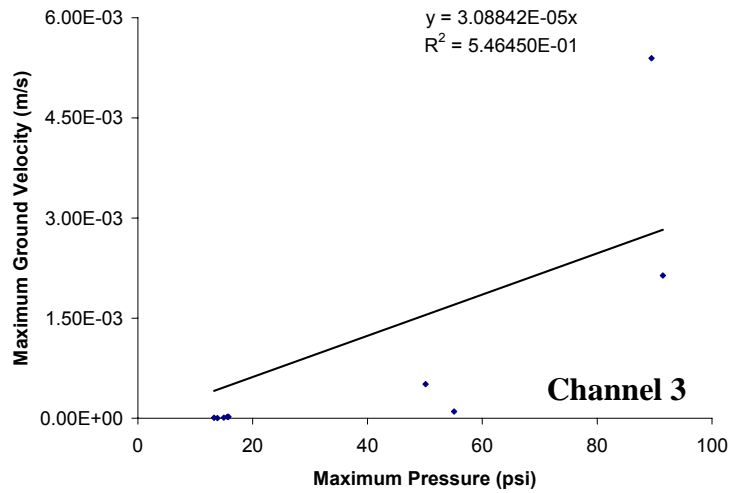
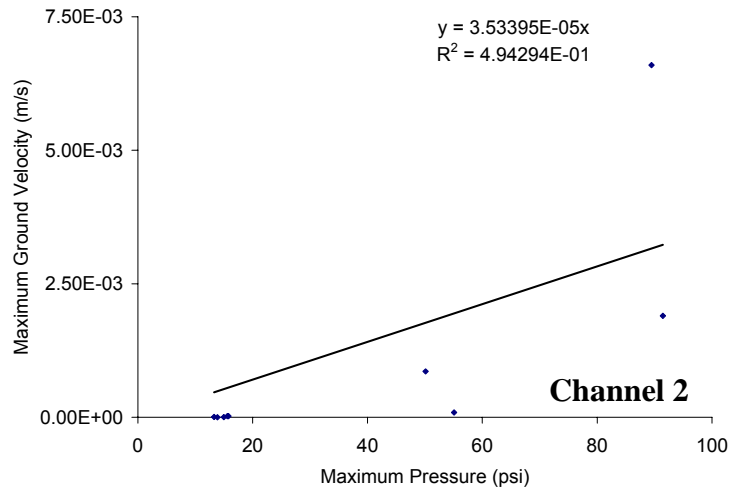
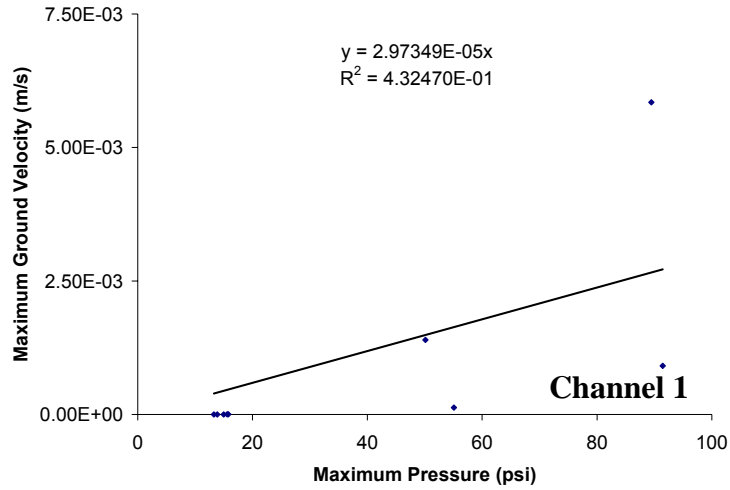
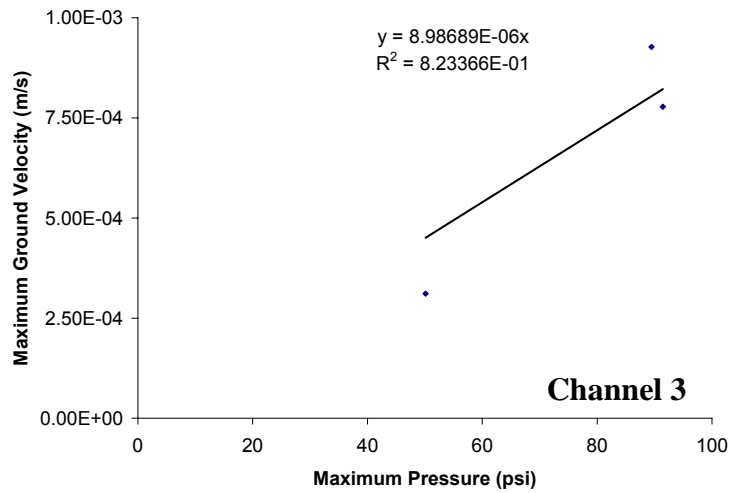
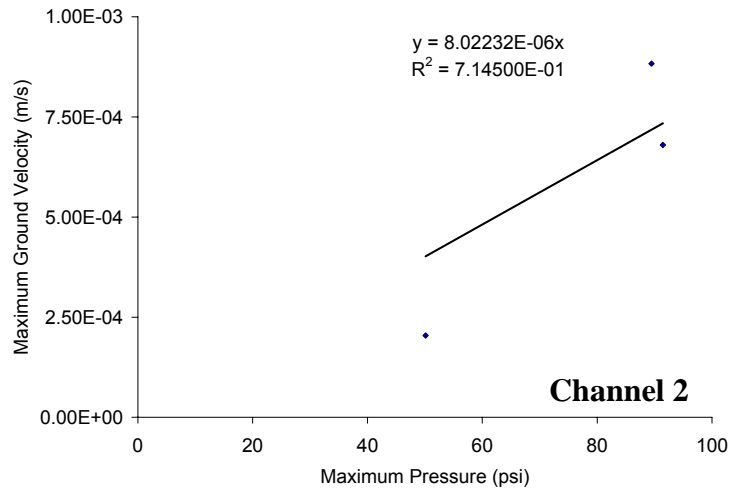
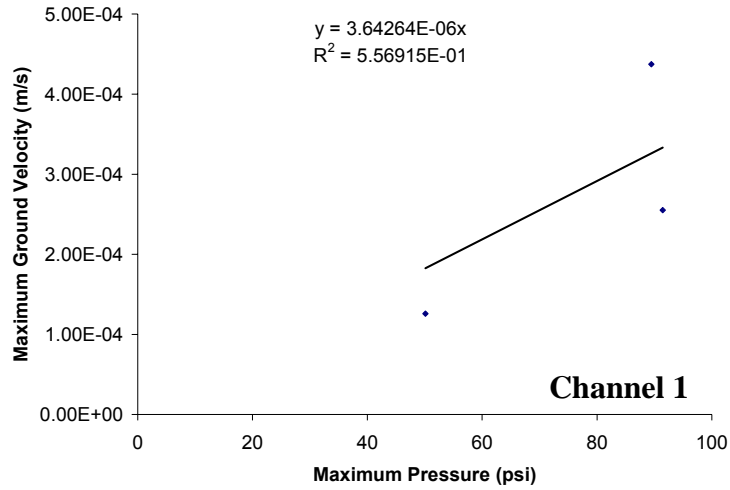
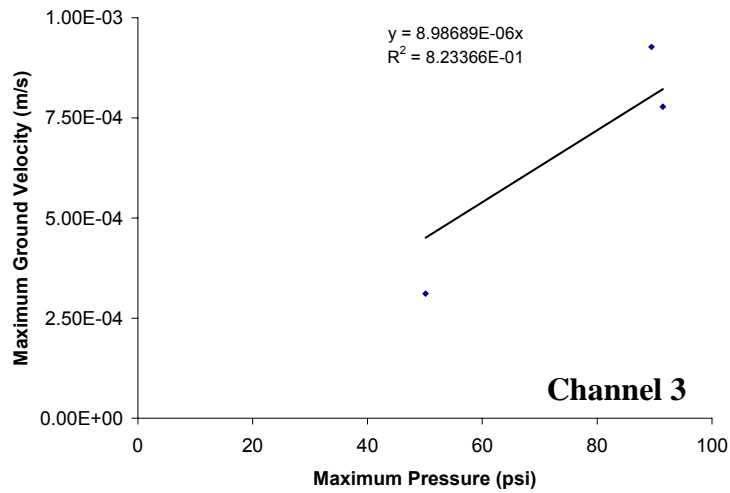
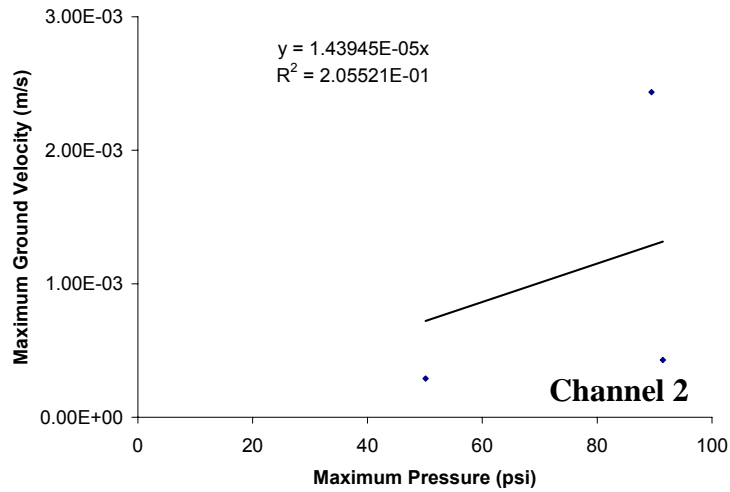
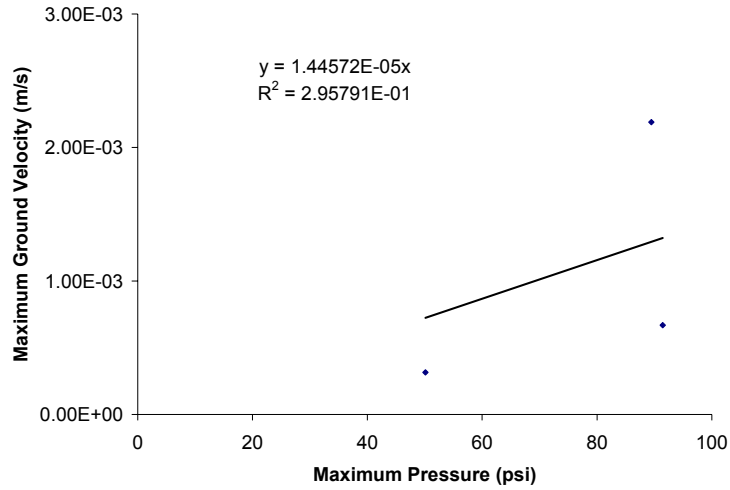


Figure C.17 – Maximum ground velocity versus maximum pressure for Geophone 6 (E-Drift middle of entry) recalculated to allow the regression line to intersect the origin.



**Figure C.18** – Maximum ground velocity versus maximum pressure for Geophone 8 (A-Drift face) recalculated to allow the regression line to intersect the origin.



**Figure C.19** – Maximum ground velocity versus maximum pressure for Geophone 9 (A-Drift crosscut) recalculated to allow the regression line to intersect the origin.



# **Appendix D:**

## **Attenuation Curves for the Mine Shots**

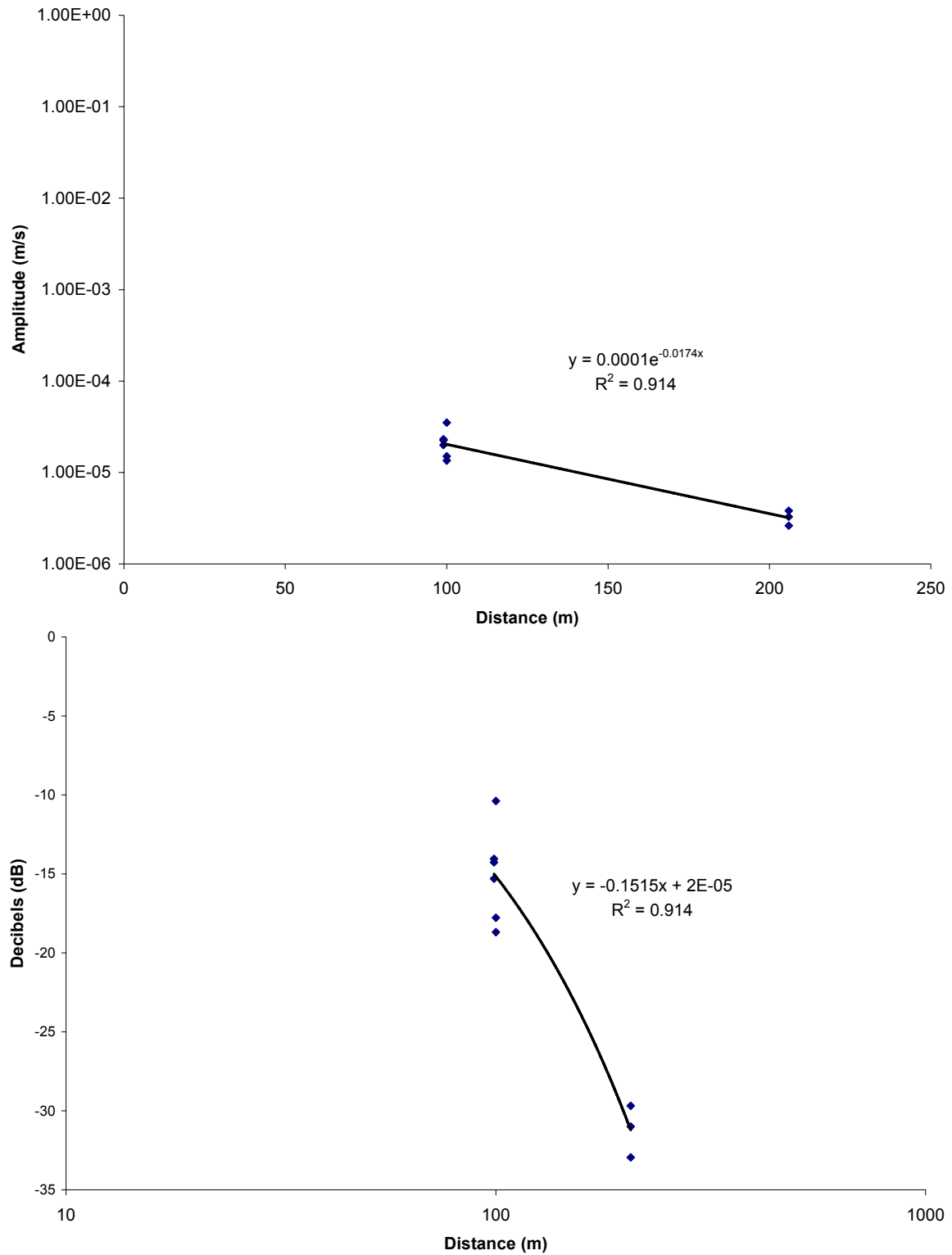


Figure D.1 – Amplitude versus distance plot (top) with resulting attenuation plot (bottom) for mine shot #503.

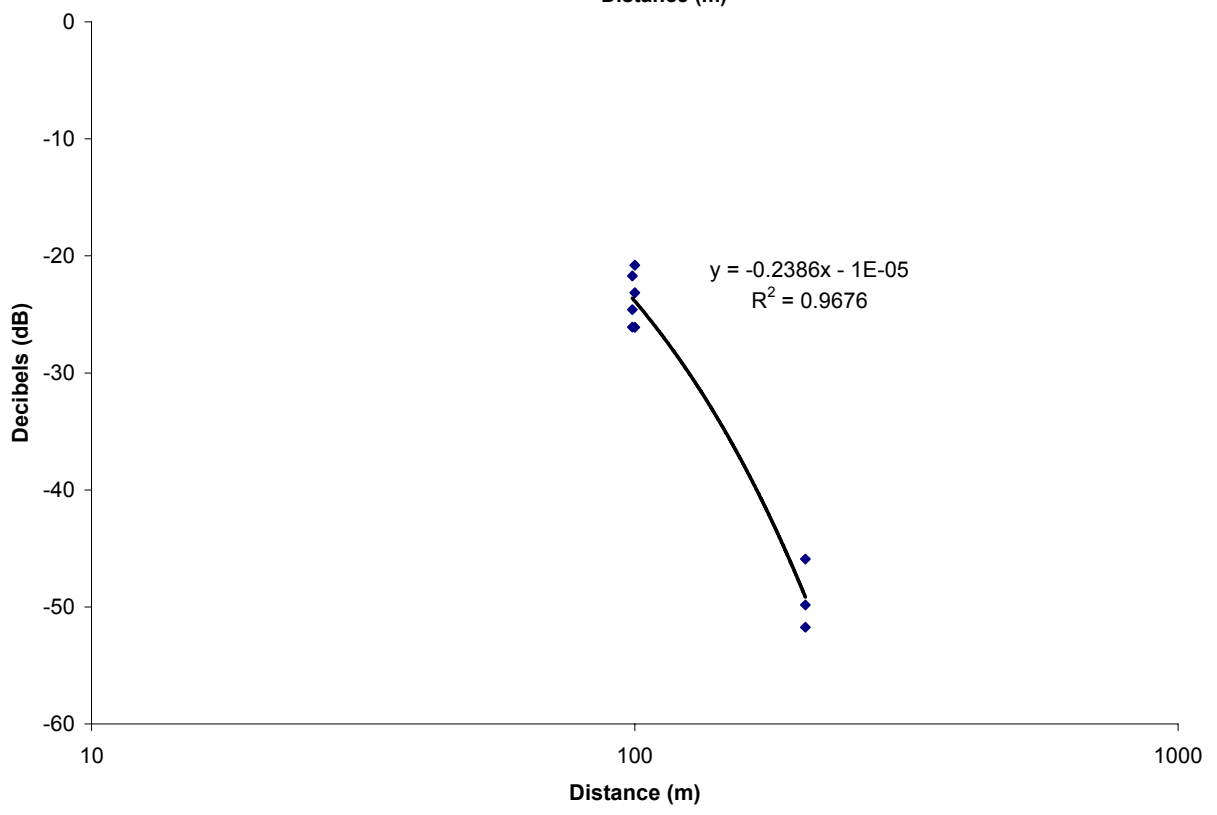
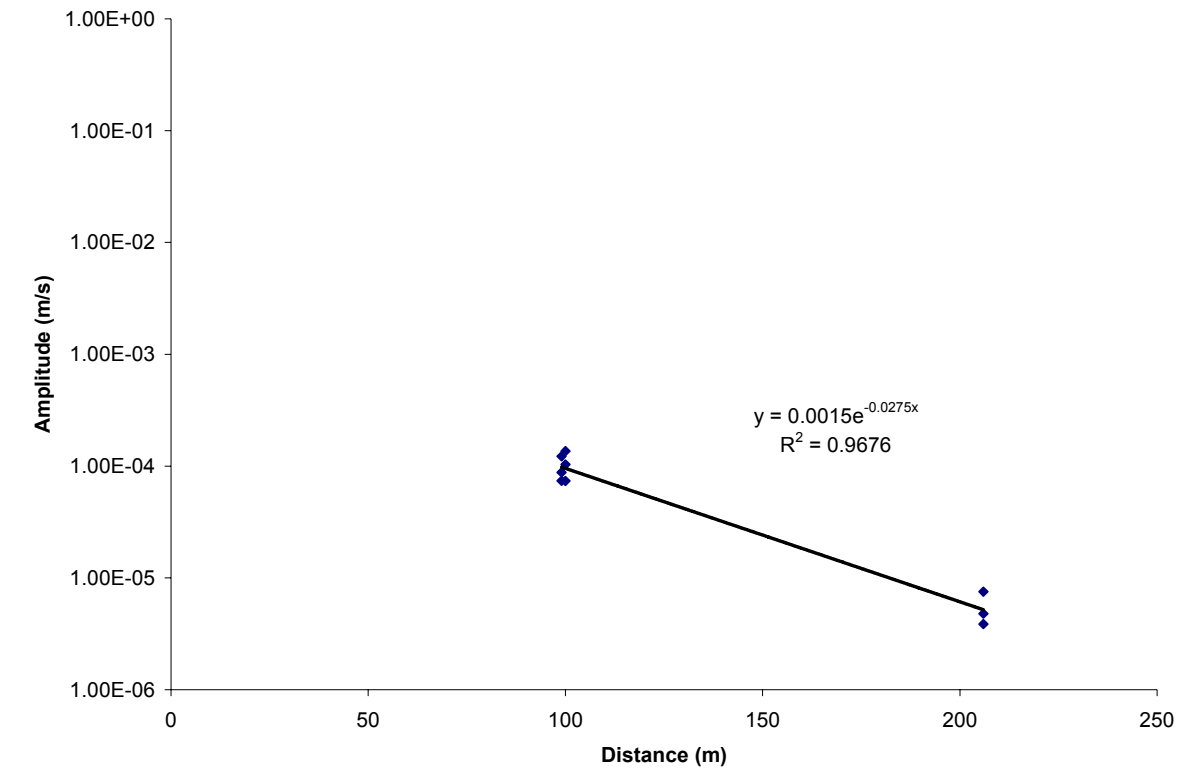


Figure D.2 – Amplitude versus distance plot (top) with resulting attenuation plot (bottom) for mine shot #504.

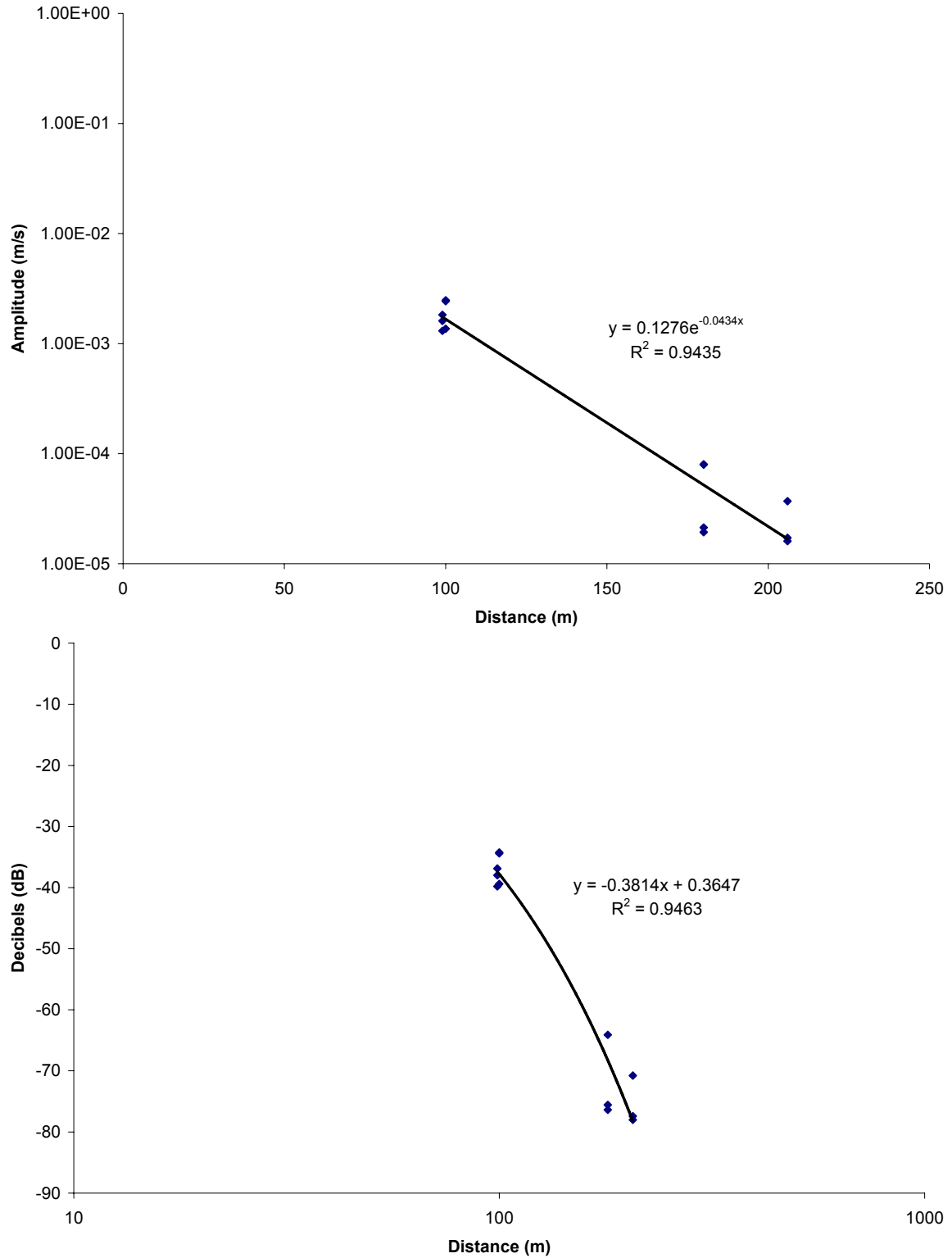


Figure D.3 – Amplitude versus distance plot (top) with resulting attenuation plot (bottom) for mine shot #505.

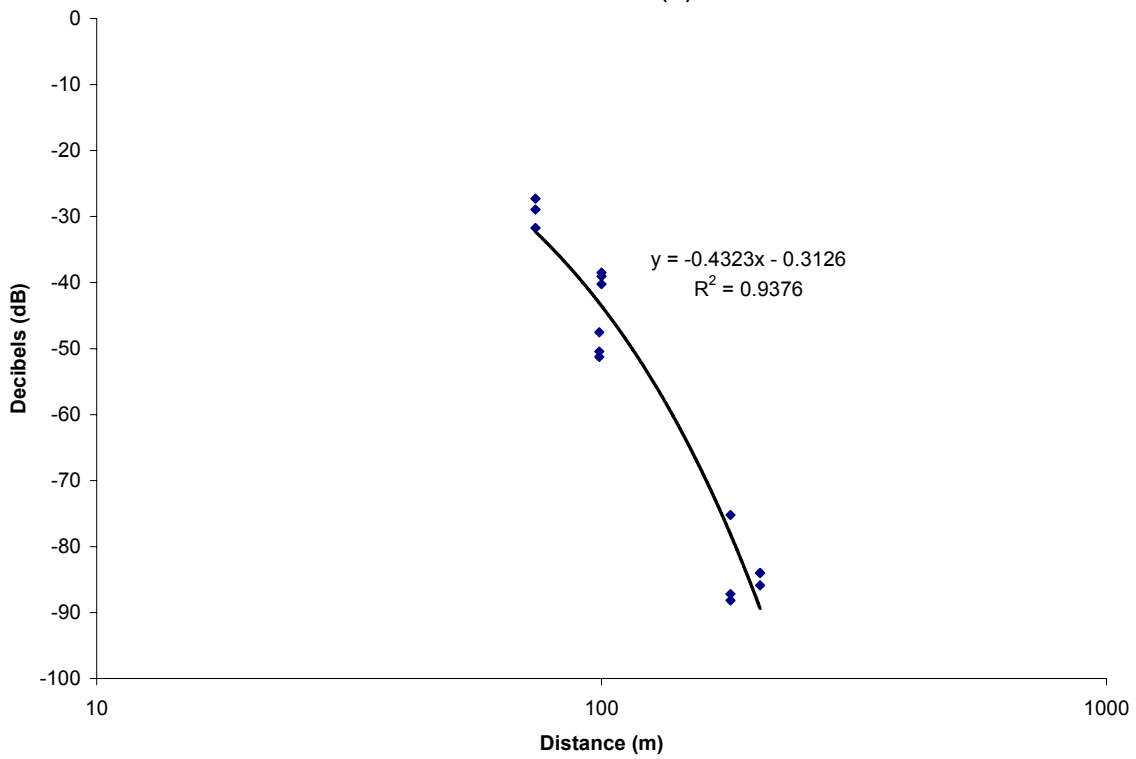
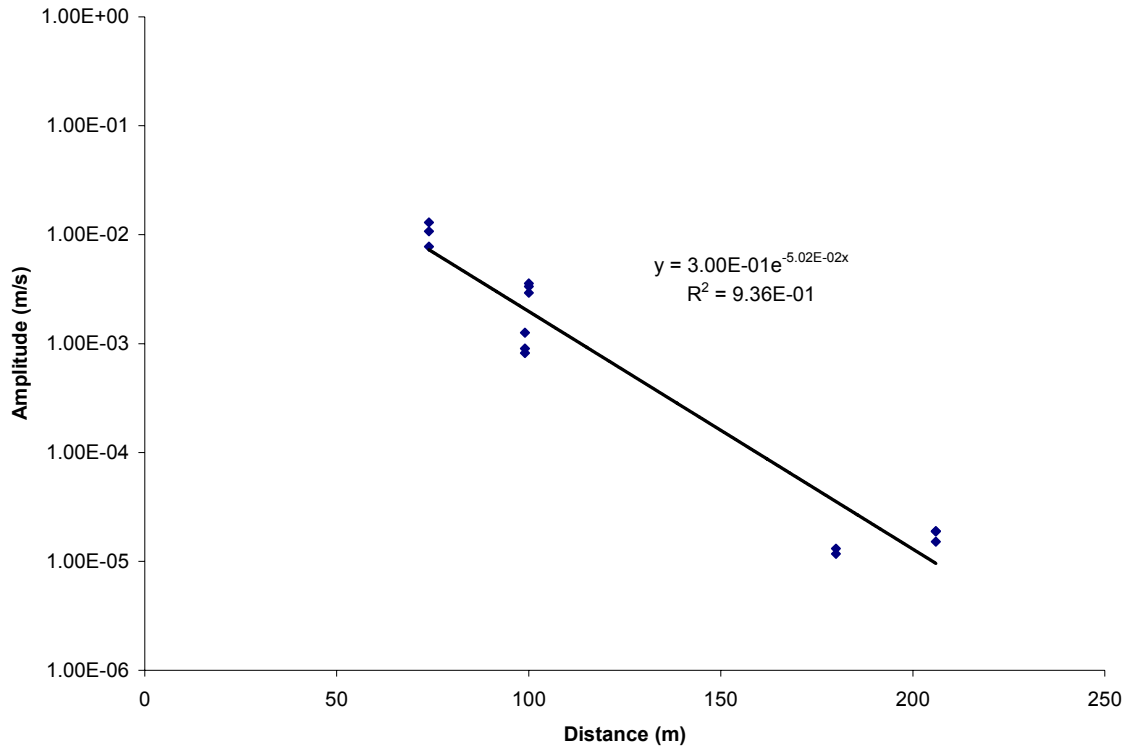


Figure D.4 – Amplitude versus distance plot (top) with resulting attenuation plot (bottom) for mine shot #507.

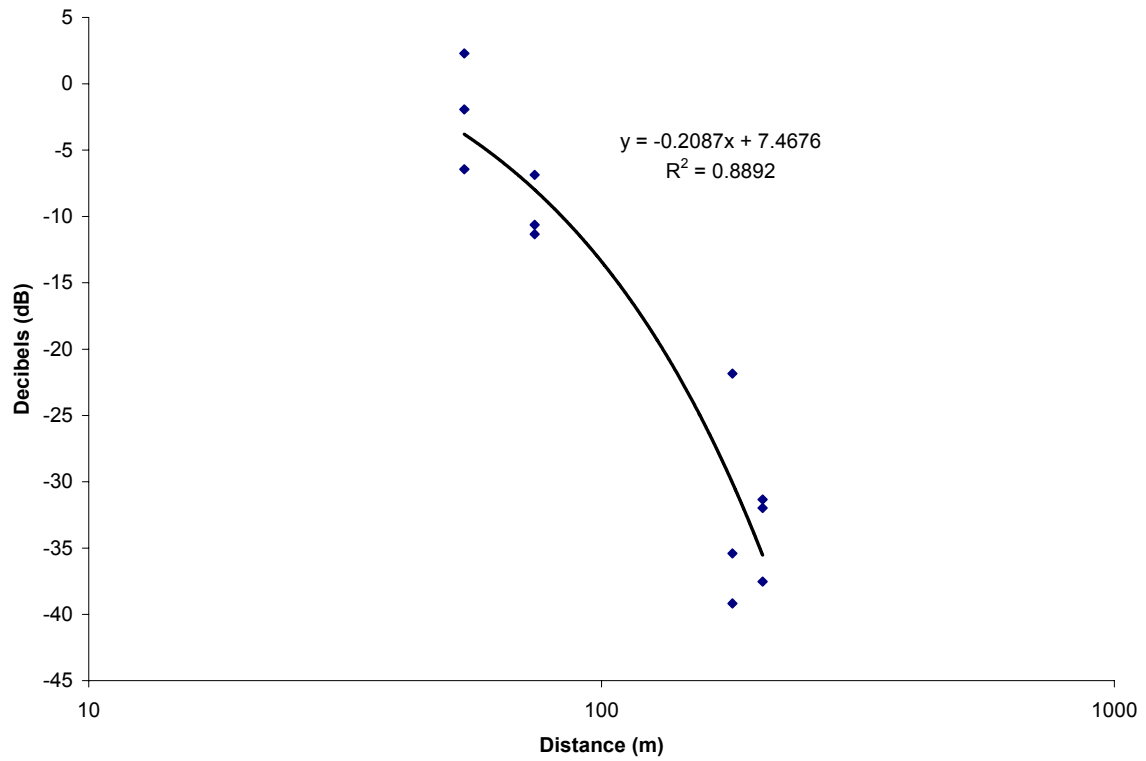
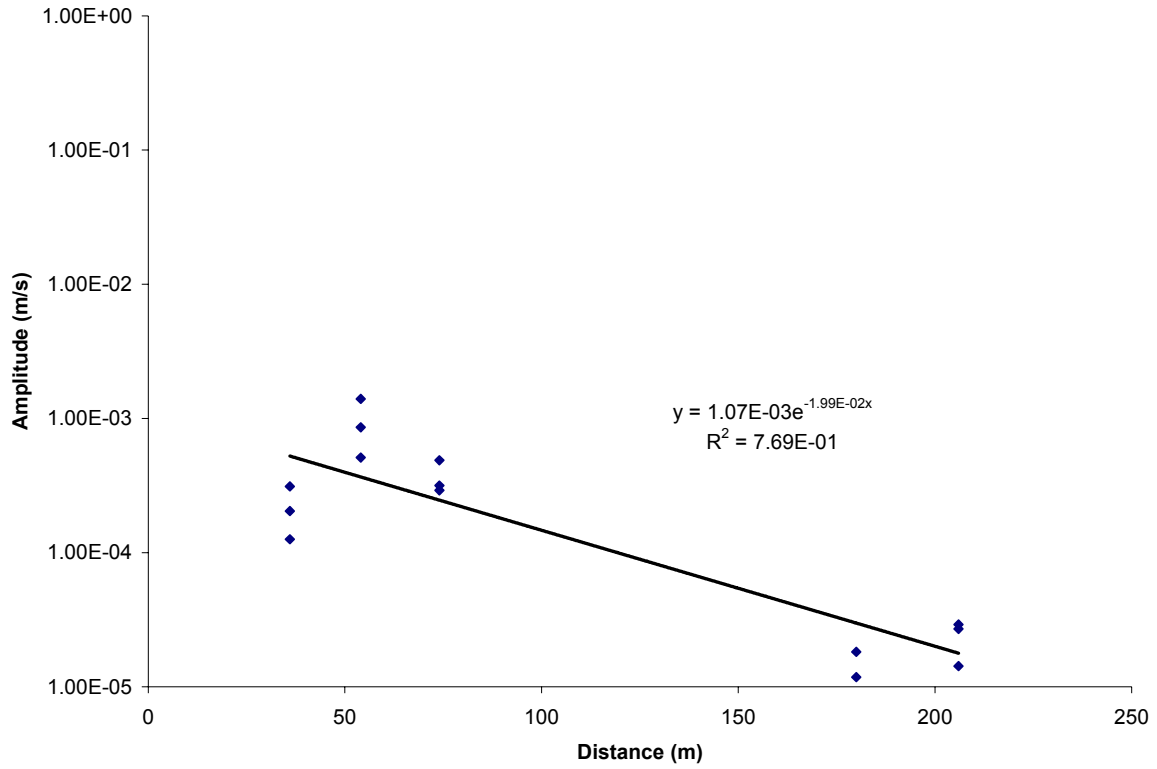


Figure D.5 – Amplitude versus distance plot (top) with resulting attenuation plot (bottom) for mine shot #508.

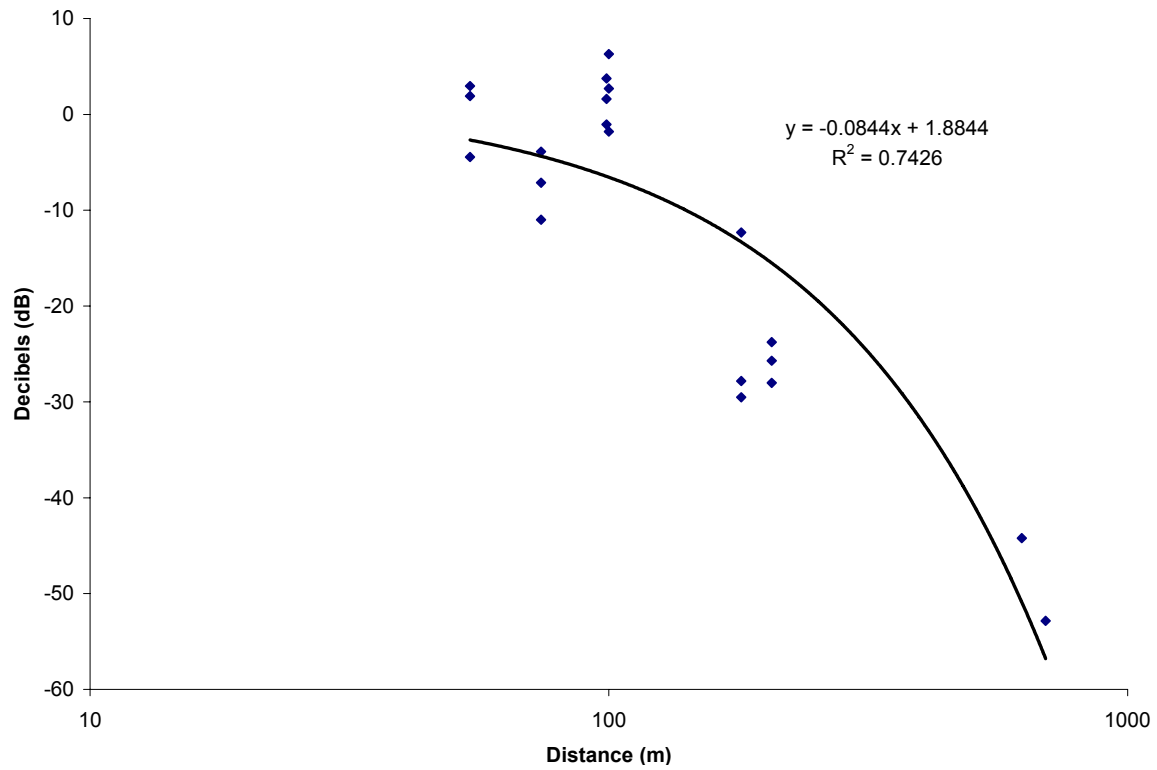
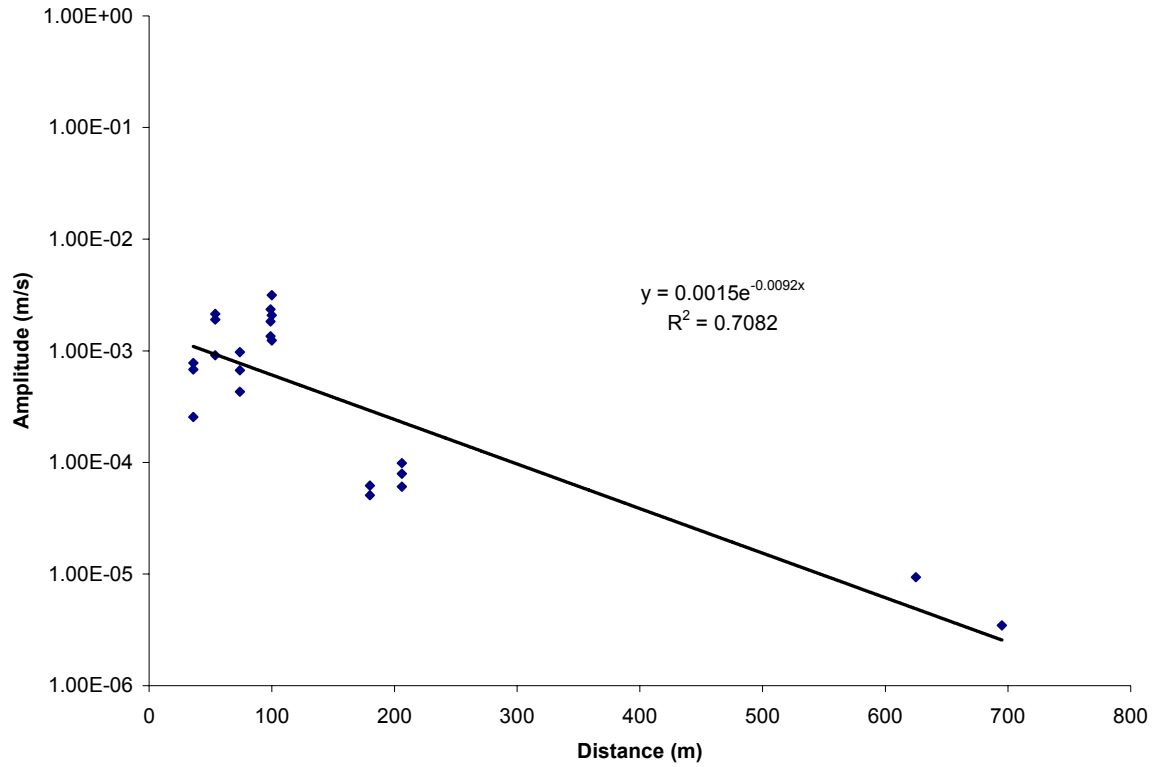


Figure D.6 – Amplitude versus distance plot (top) with resulting attenuation plot (bottom) for mine shot #509.

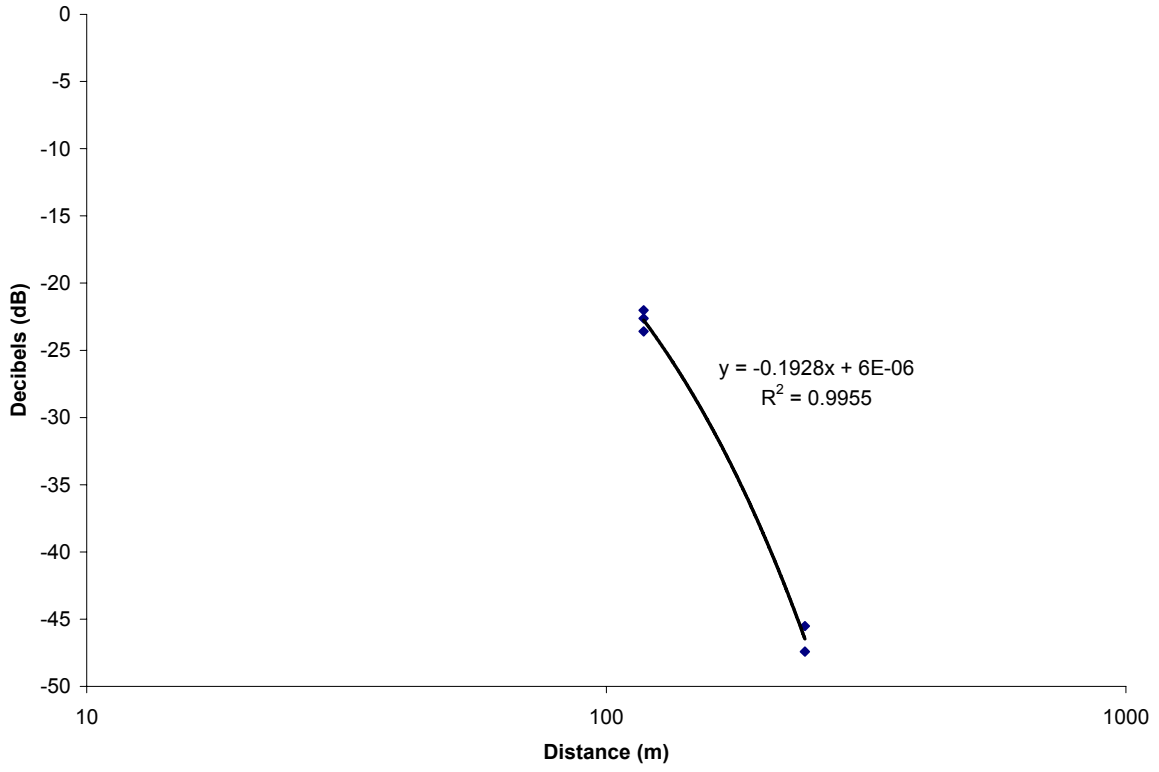
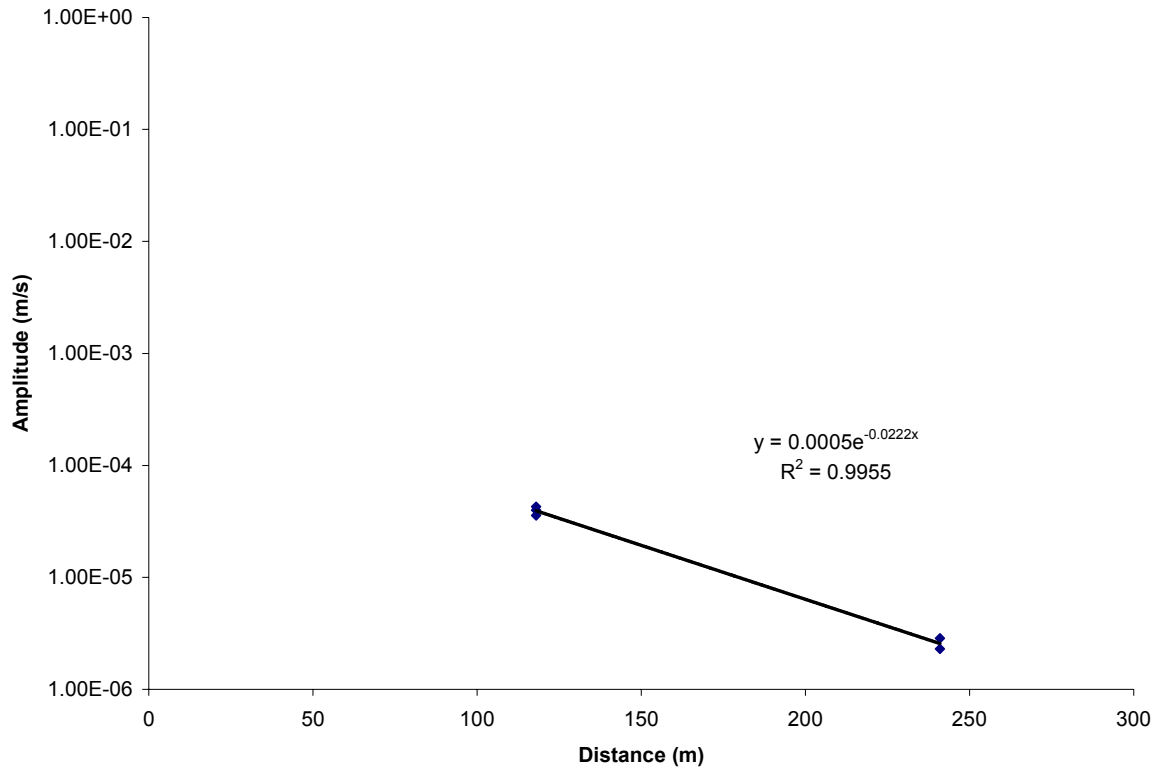


Figure D.7 – Amplitude versus distance plot (top) with resulting attenuation plot (bottom) for mine shot #510.



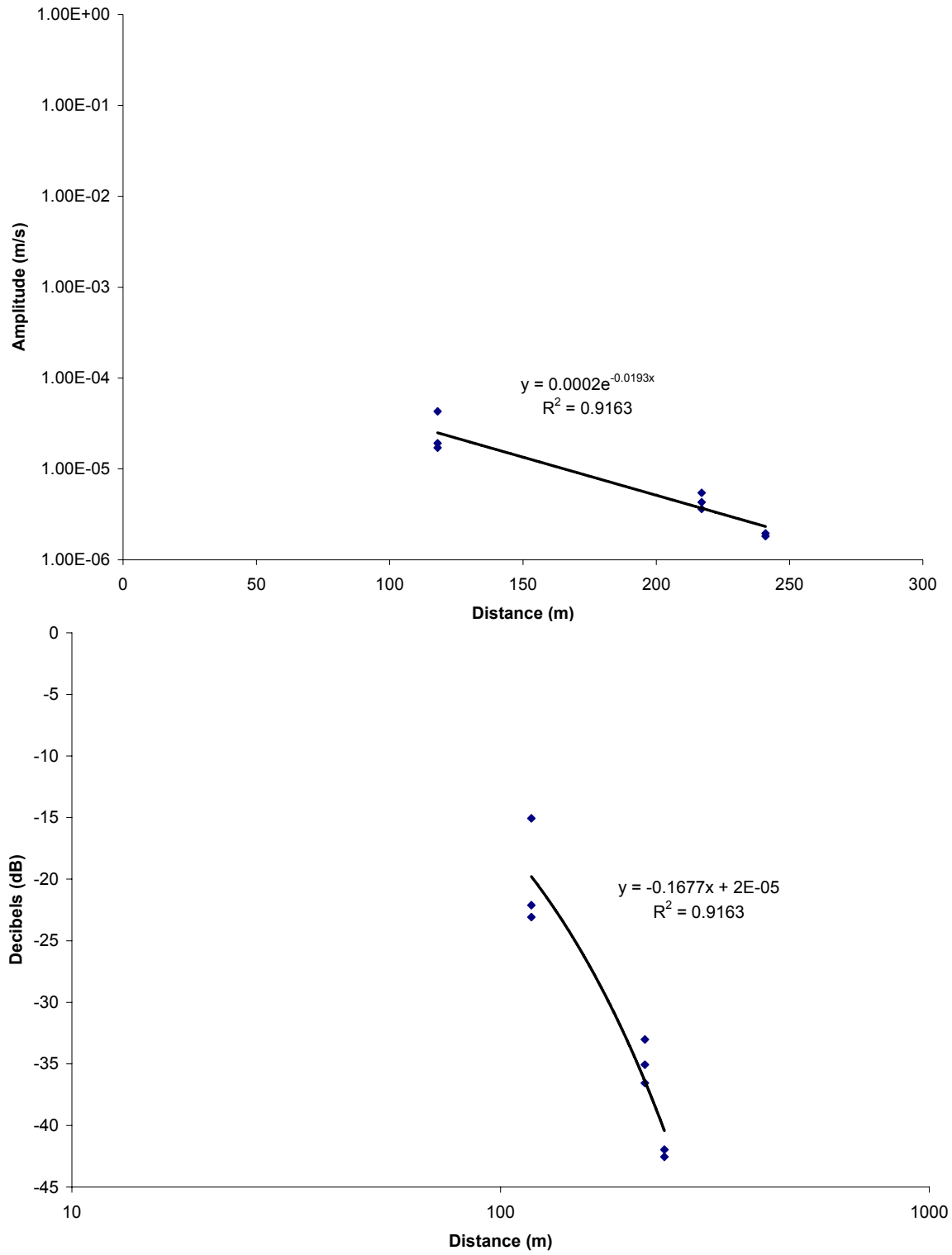


Figure D.8 – Amplitude versus distance plot (top) with resulting attenuation plot (bottom) for mine shot #513.

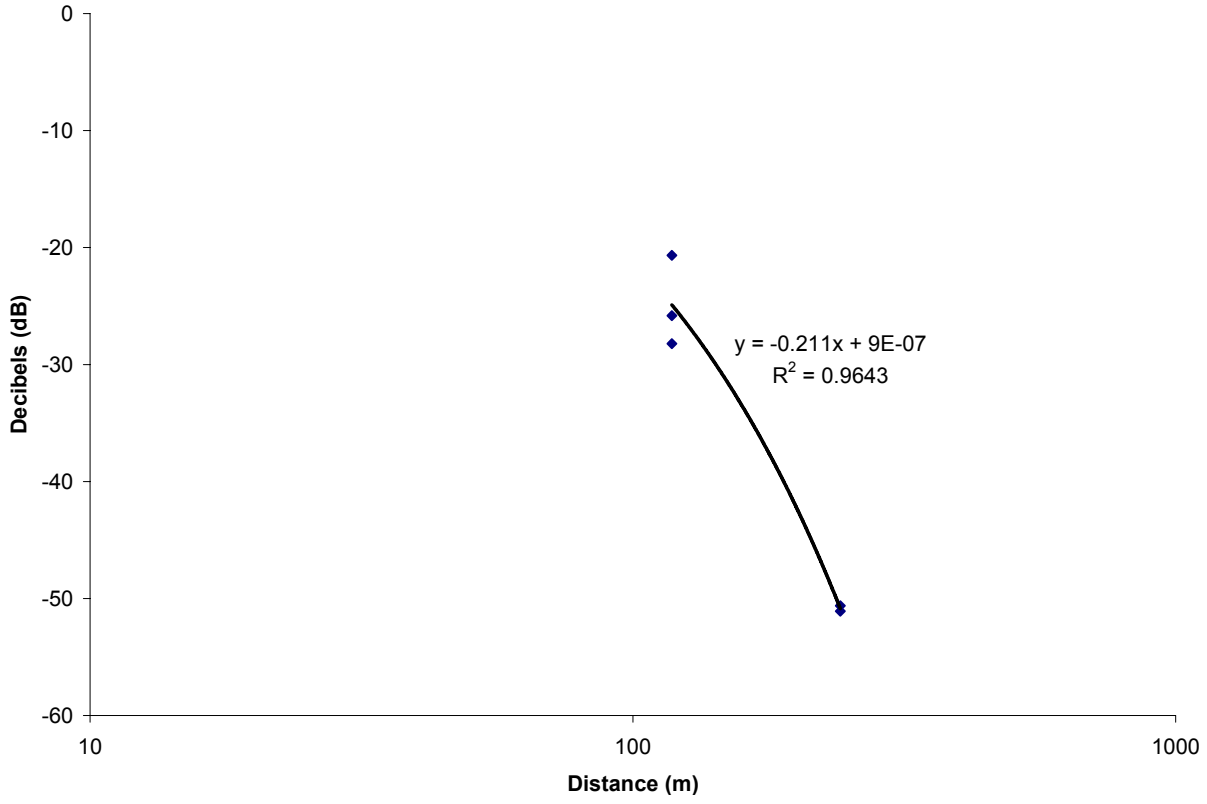
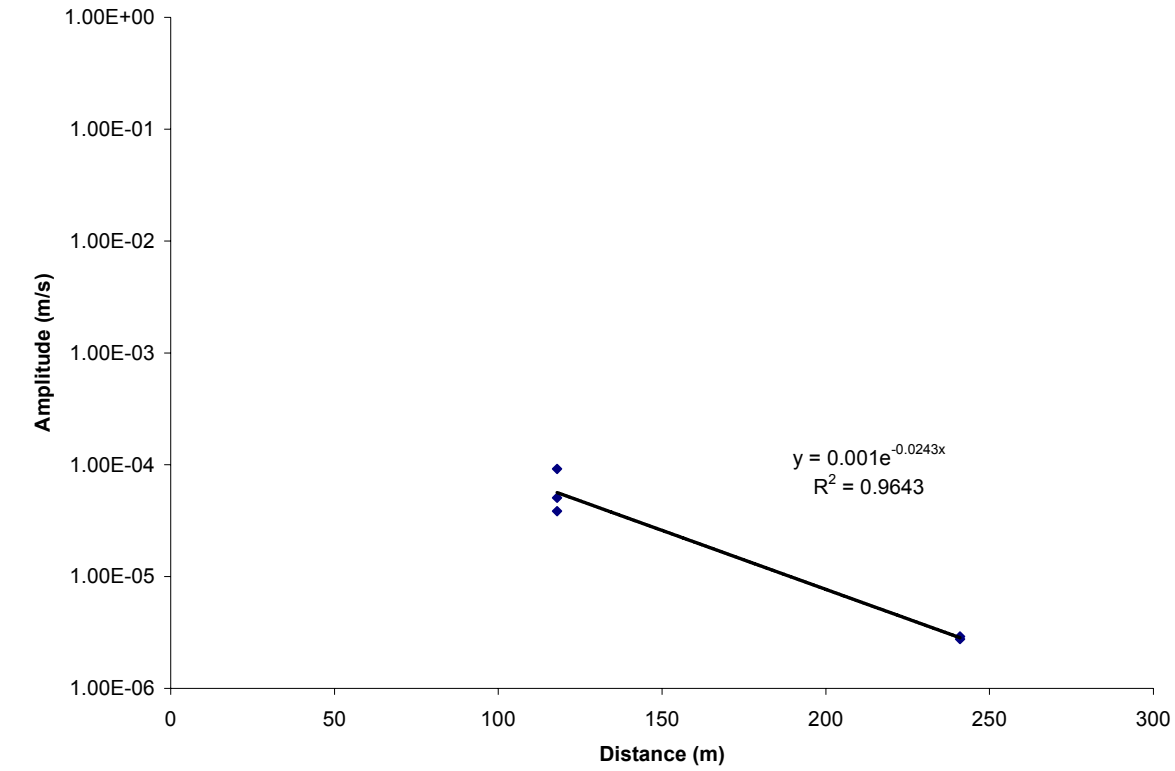


Figure D.9 – Amplitude versus distance plot (top) with resulting attenuation plot (bottom) for mine shot #514.

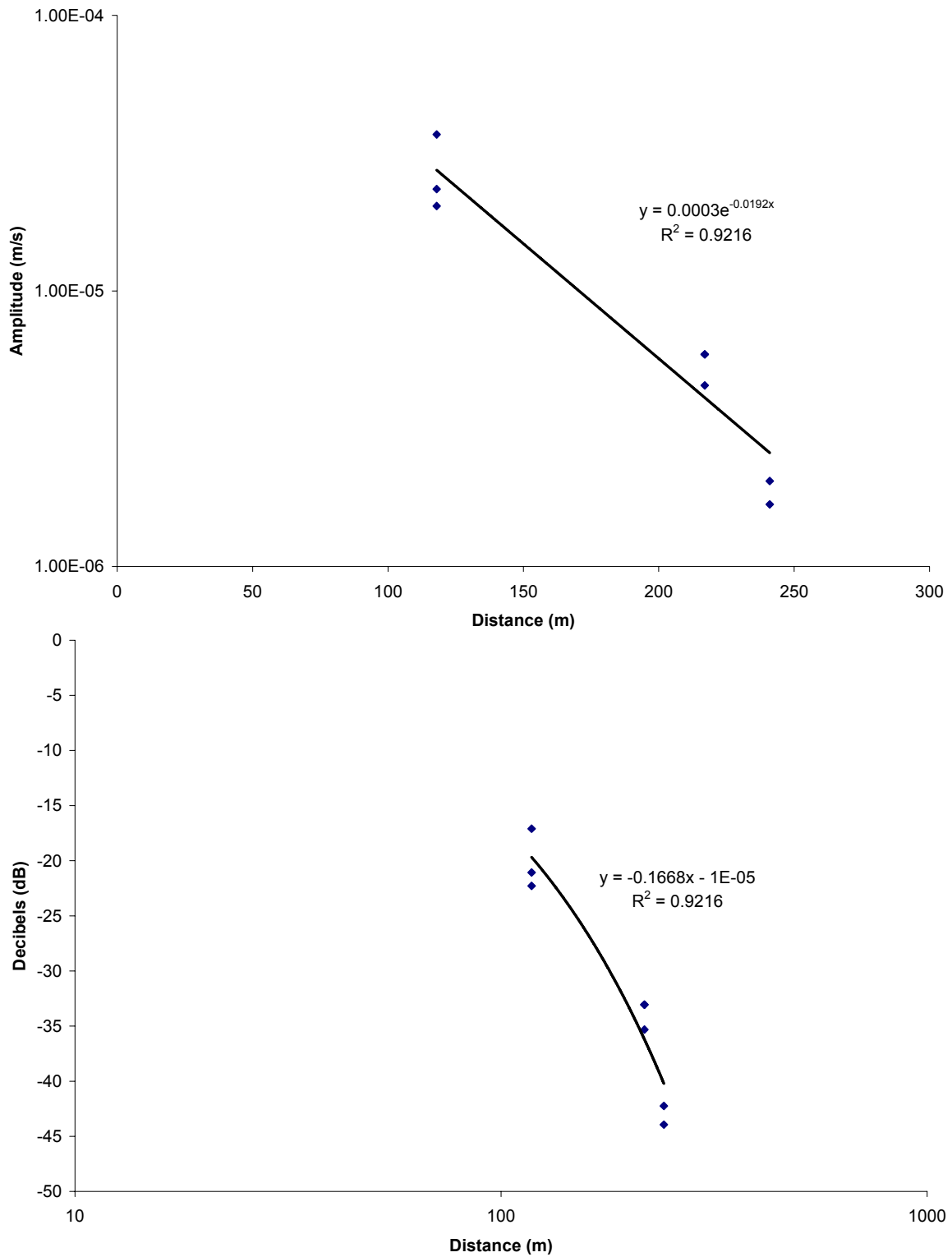


Figure D.10 – Amplitude versus distance plot (top) with resulting attenuation plot (bottom) for mine shot #516.

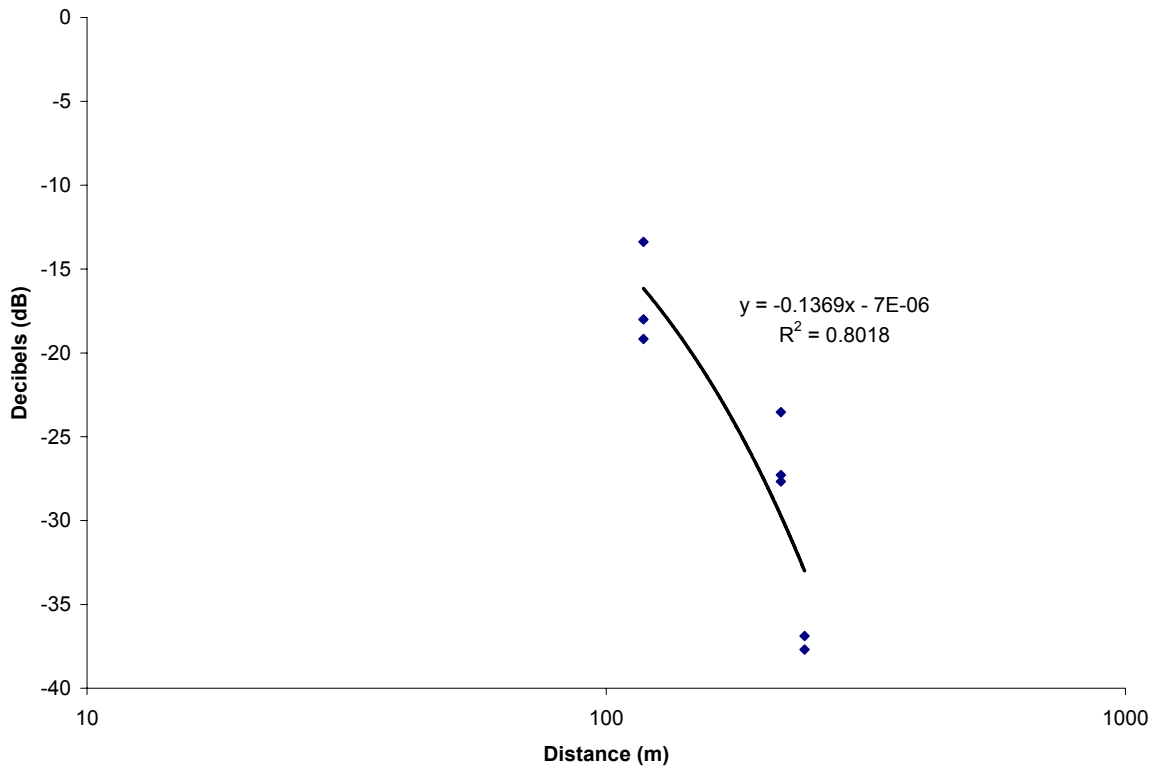
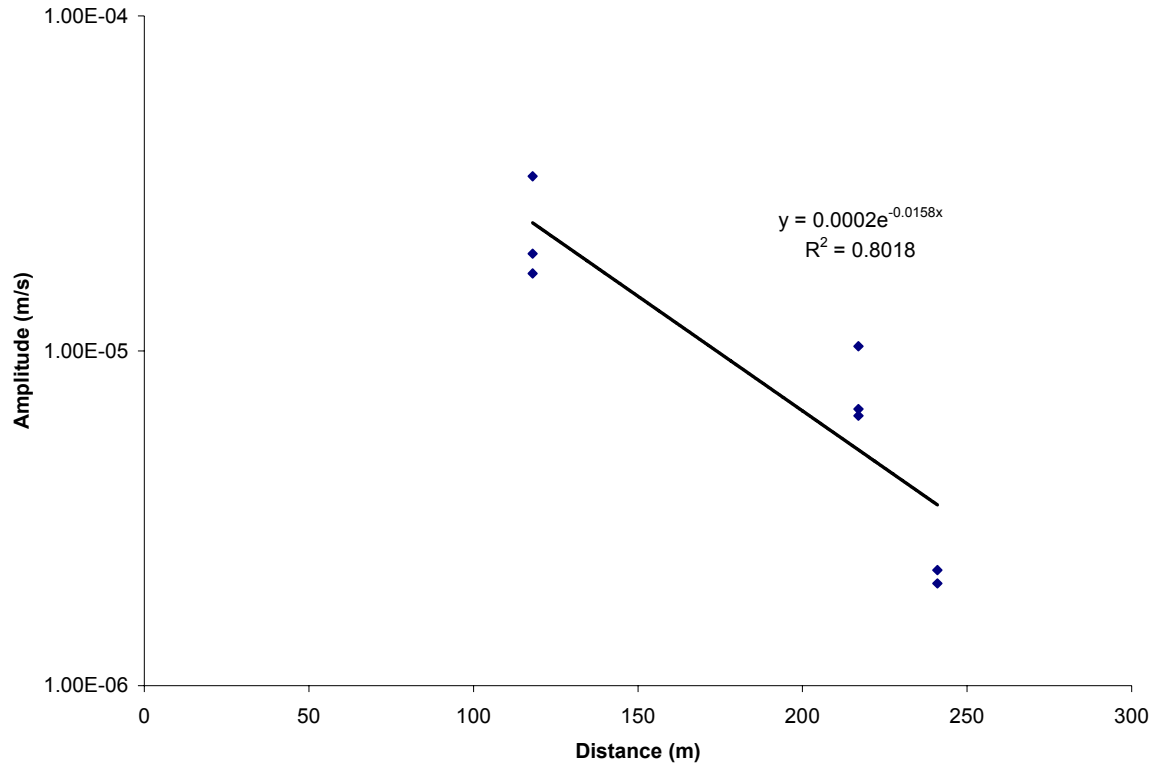


Figure D.11 – Amplitude versus distance plot (top) with resulting attenuation plot (bottom) for mine shot #517.

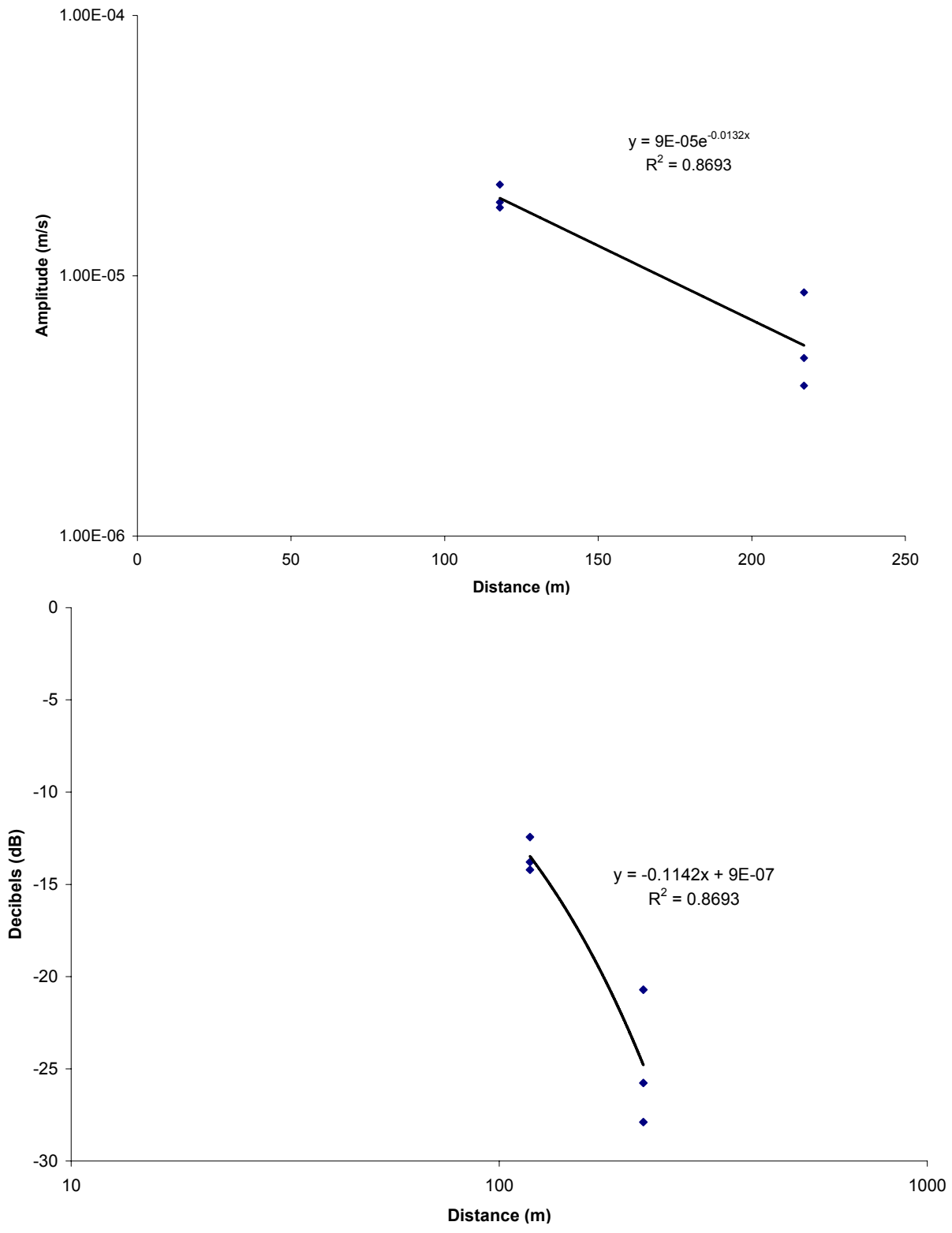


Figure D.12 – Amplitude versus distance plot (top) with resulting attenuation plot (bottom) for mine shot #518.

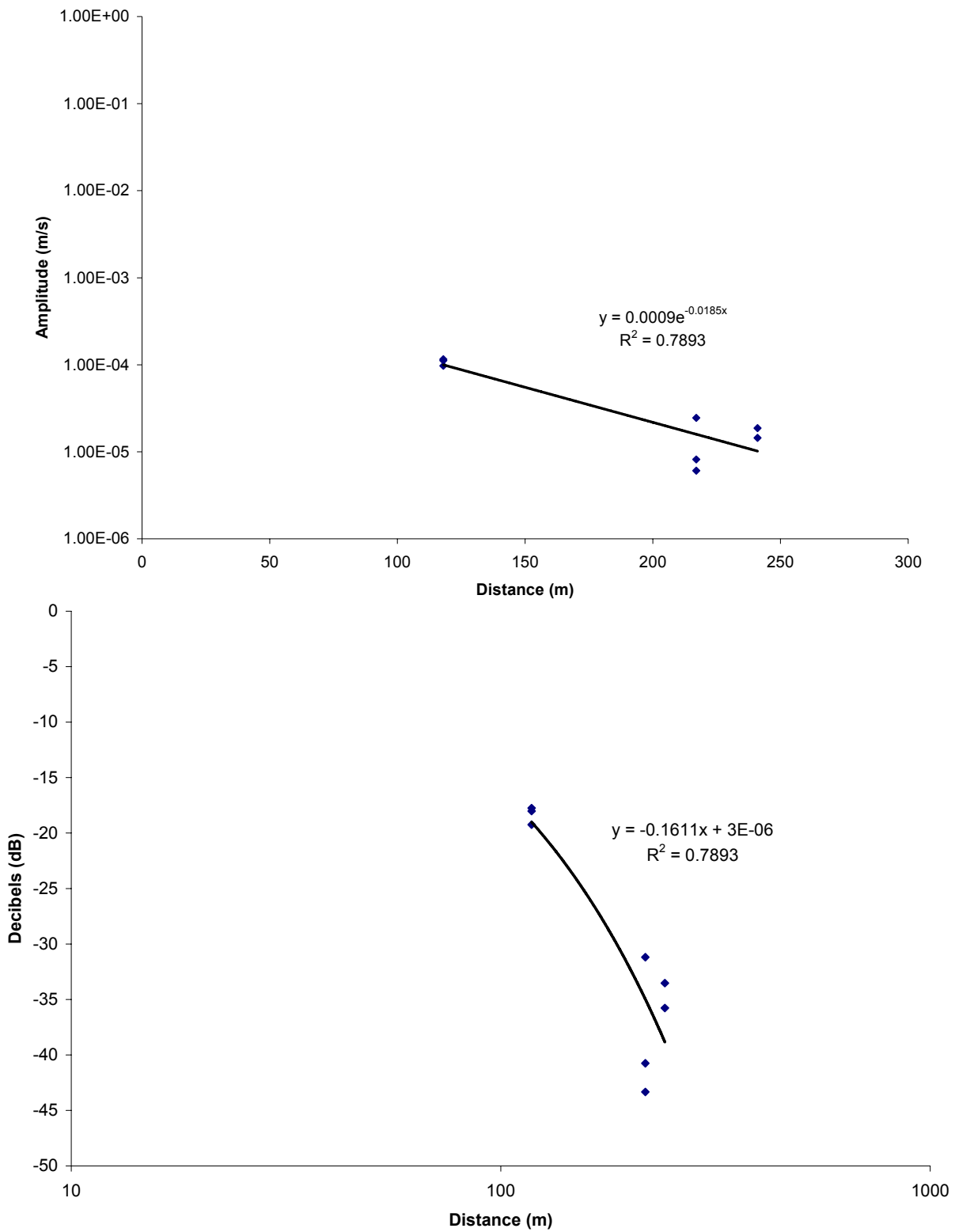
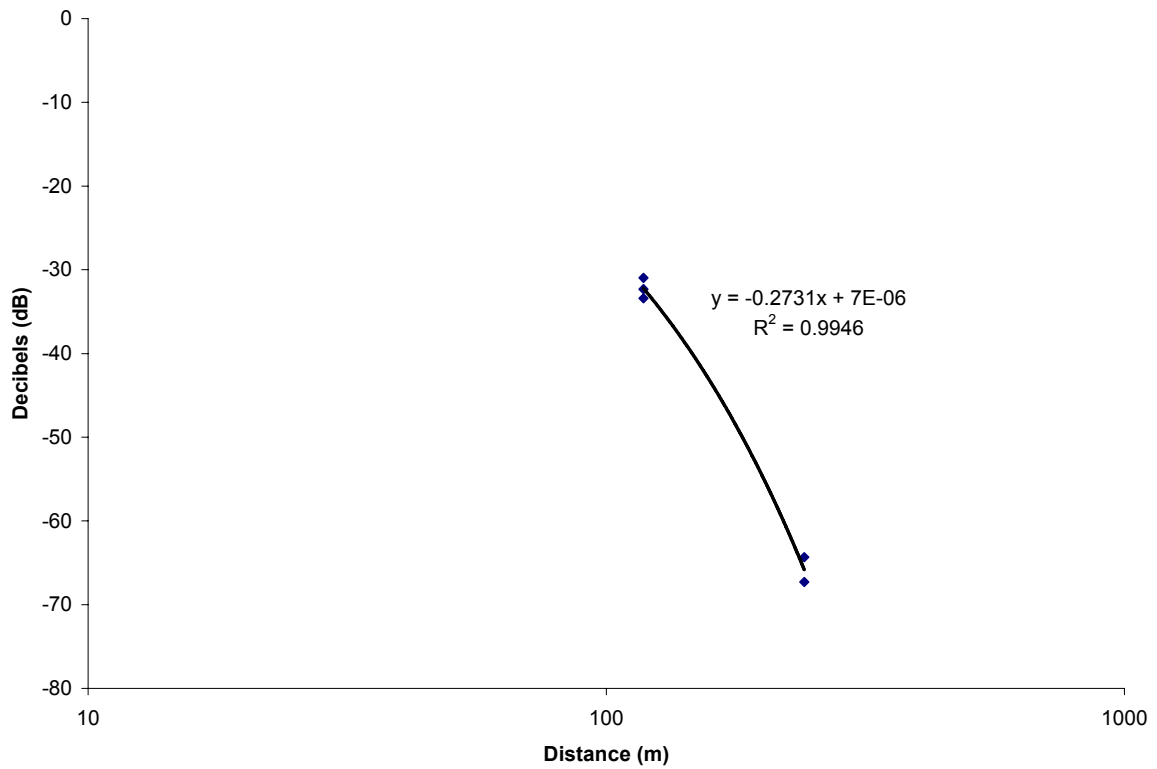
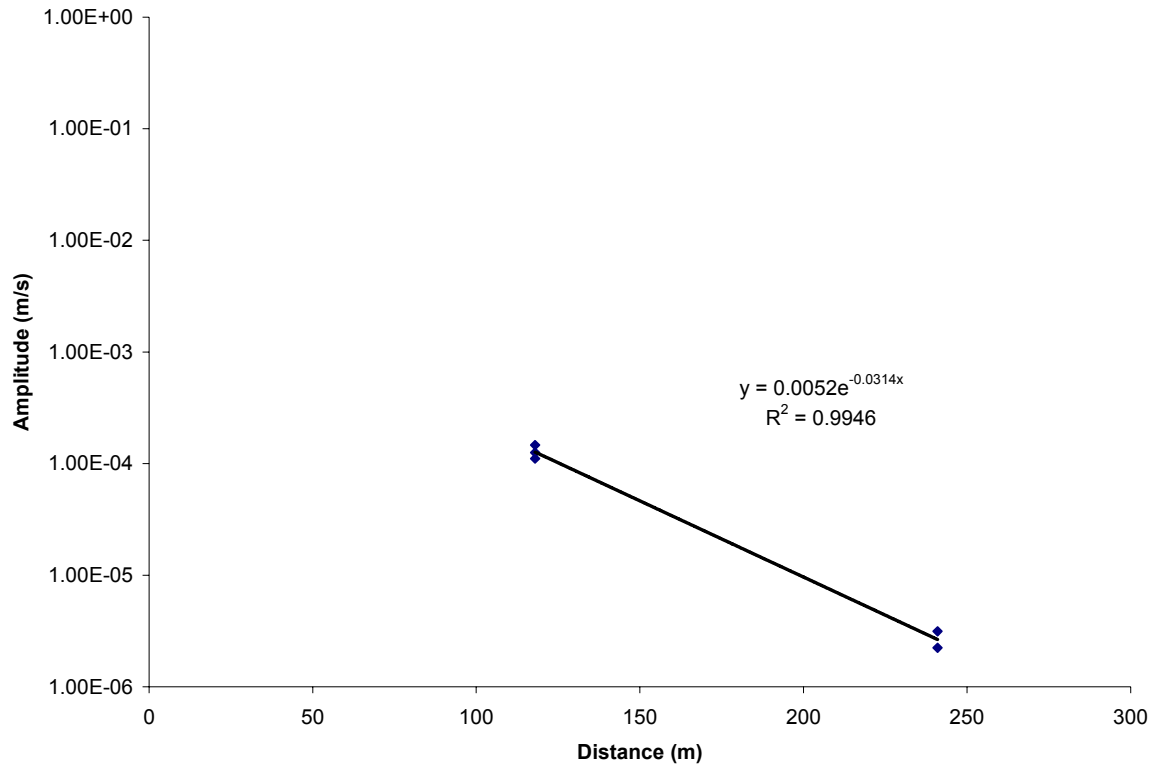


Figure D.13 – Amplitude versus distance plot (top) with resulting attenuation plot (bottom) for mine shot #519.



**Figure D.14** – Amplitude versus distance plot (top) with resulting attenuation plot (bottom) for mine shot #520.

# **Appendix E:**

**LabVIEW Program Used for Analysis of the  
Seismic Signatures**



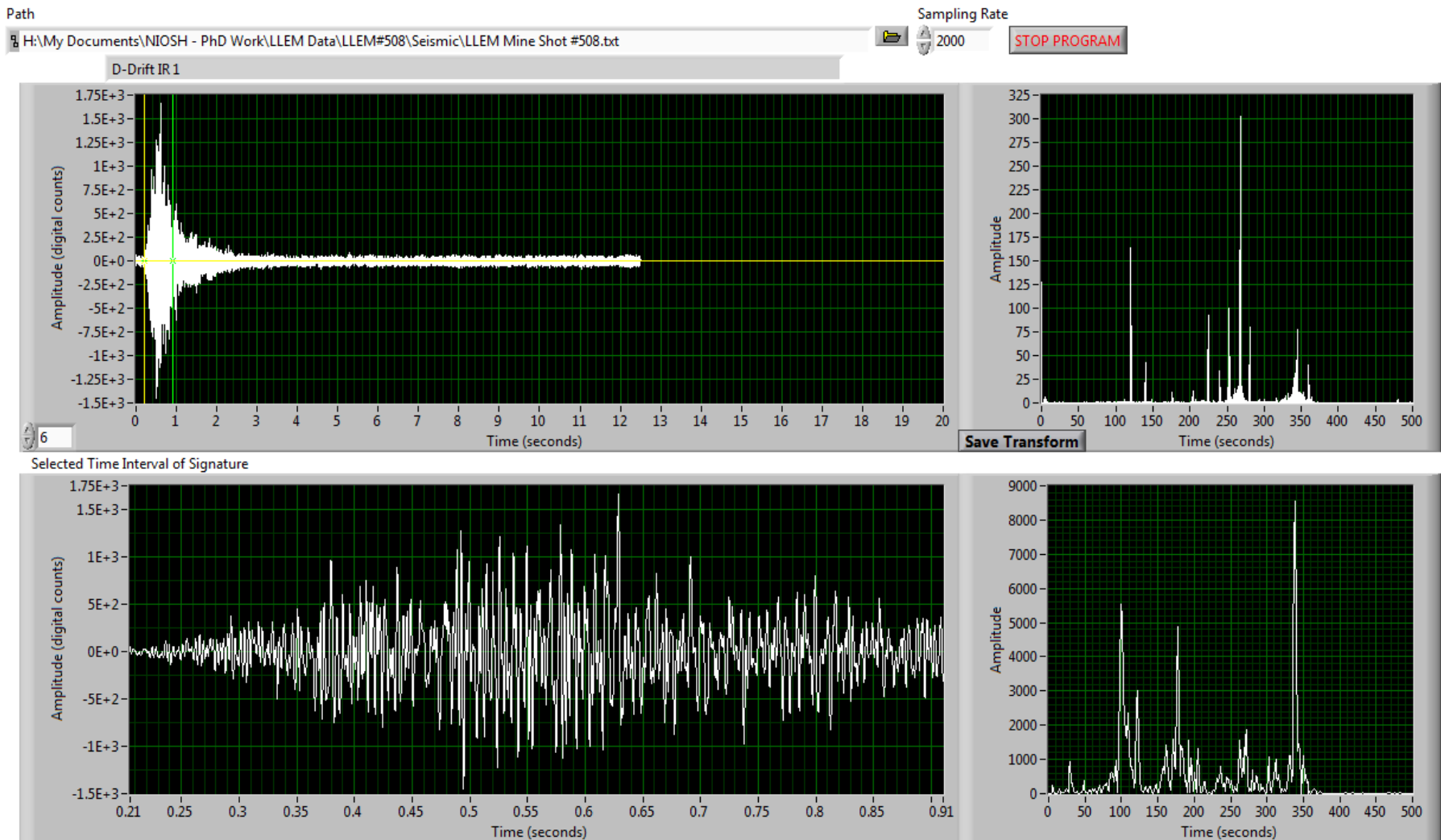


**Figure E.1** – Screenshot demonstrating the main purpose of the program. A .txt file containing columns of seismic data, with a header displaying location of the geophone, is loading into the path box. The sampling rate is set in order to properly display the frequencies. The top waveform chart displays the full signature with its FFT on the side. A yellow and green vertical line allows the selection of a window in the signature. The selected window is then displayed on the bottom waveform chart with its FFT on the side. The transform of either FFT can be saved (depending on background code). The window also shows the time frame selected (not shown in the screenshot) which was helpful in determining the durations of the seismic signatures. The name of the saved FFT file is programmed to be the name of the input file + name of the geophone location. Another waveform chart (not shown) displays a filtered waveform (low-pass, high-pass, band-pass or band-stop optional) from the original signal based upon program code.

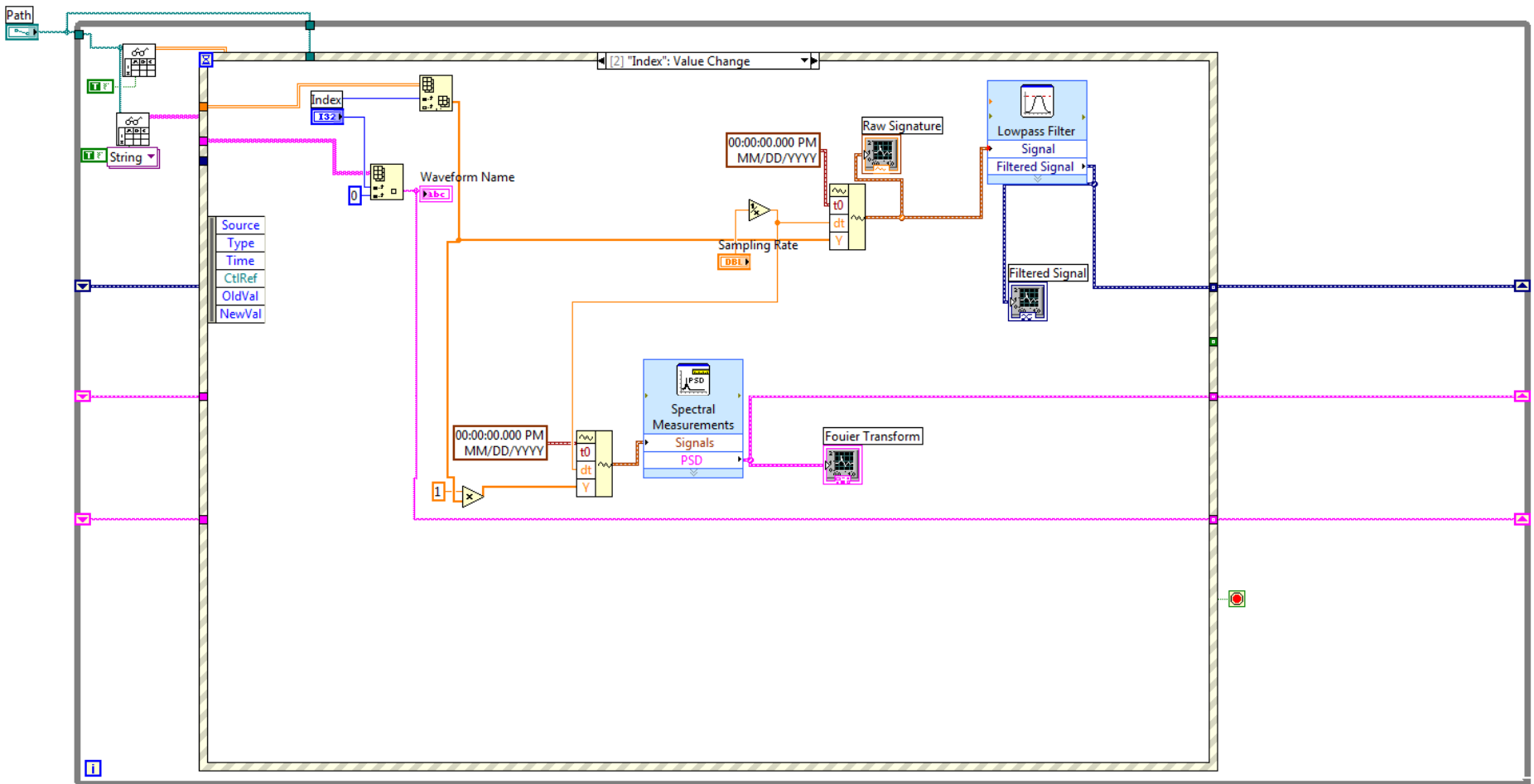


**Figure E.2** – Screenshot displaying the code which displays a seismic signature when a different column is selected from the data. The data is passed to an FFT calculation and also passed through a lowpass filter. The lowpass filter icon can be double clicked on and for a selection of a different frequency range type of filter.

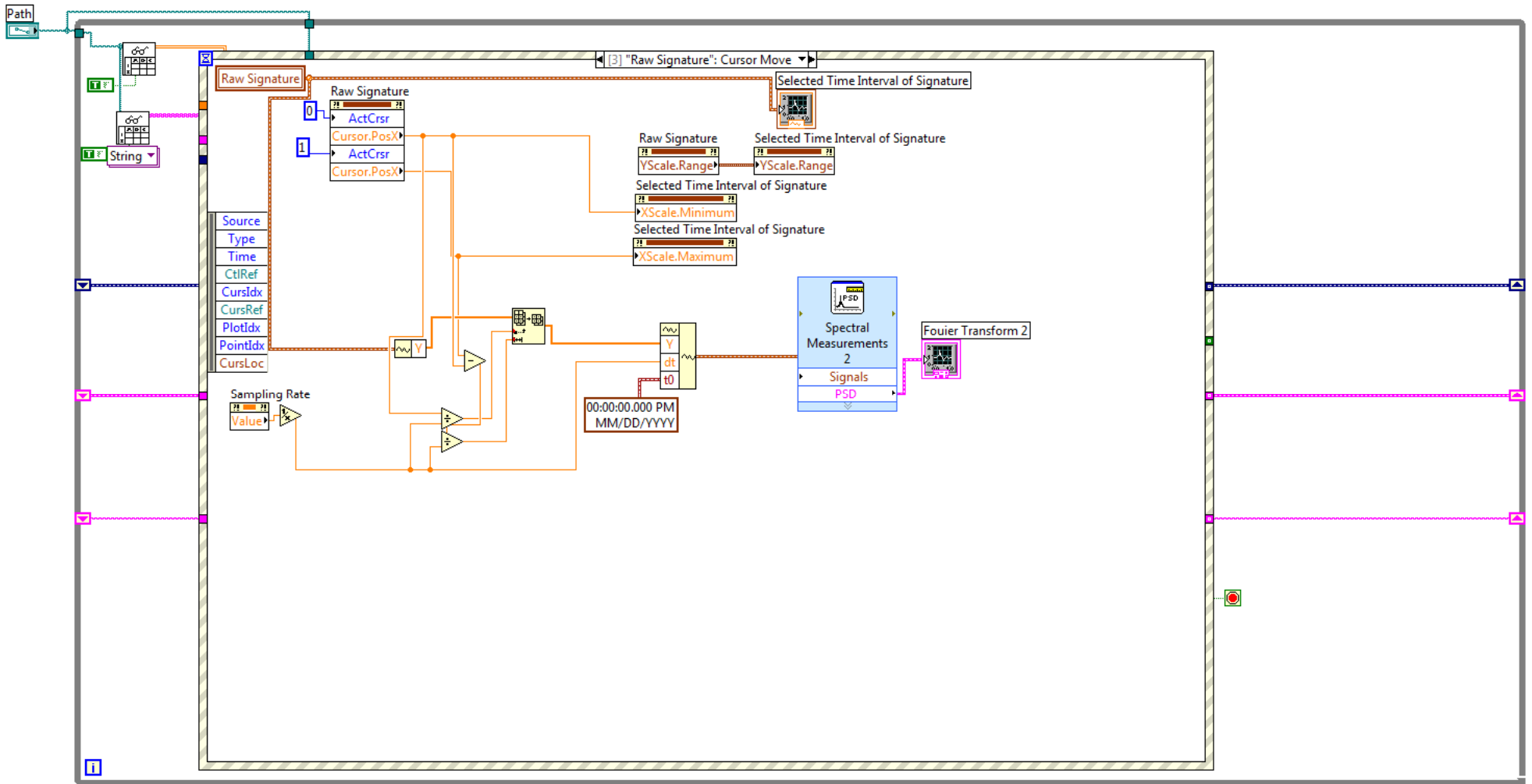


**Figure E.3** – Screenshot displaying the code for selection of two vertical lines which form a time window around the seismic signature. The selected portion of the signature is then sent to a waveform chart and an FFT calculation.

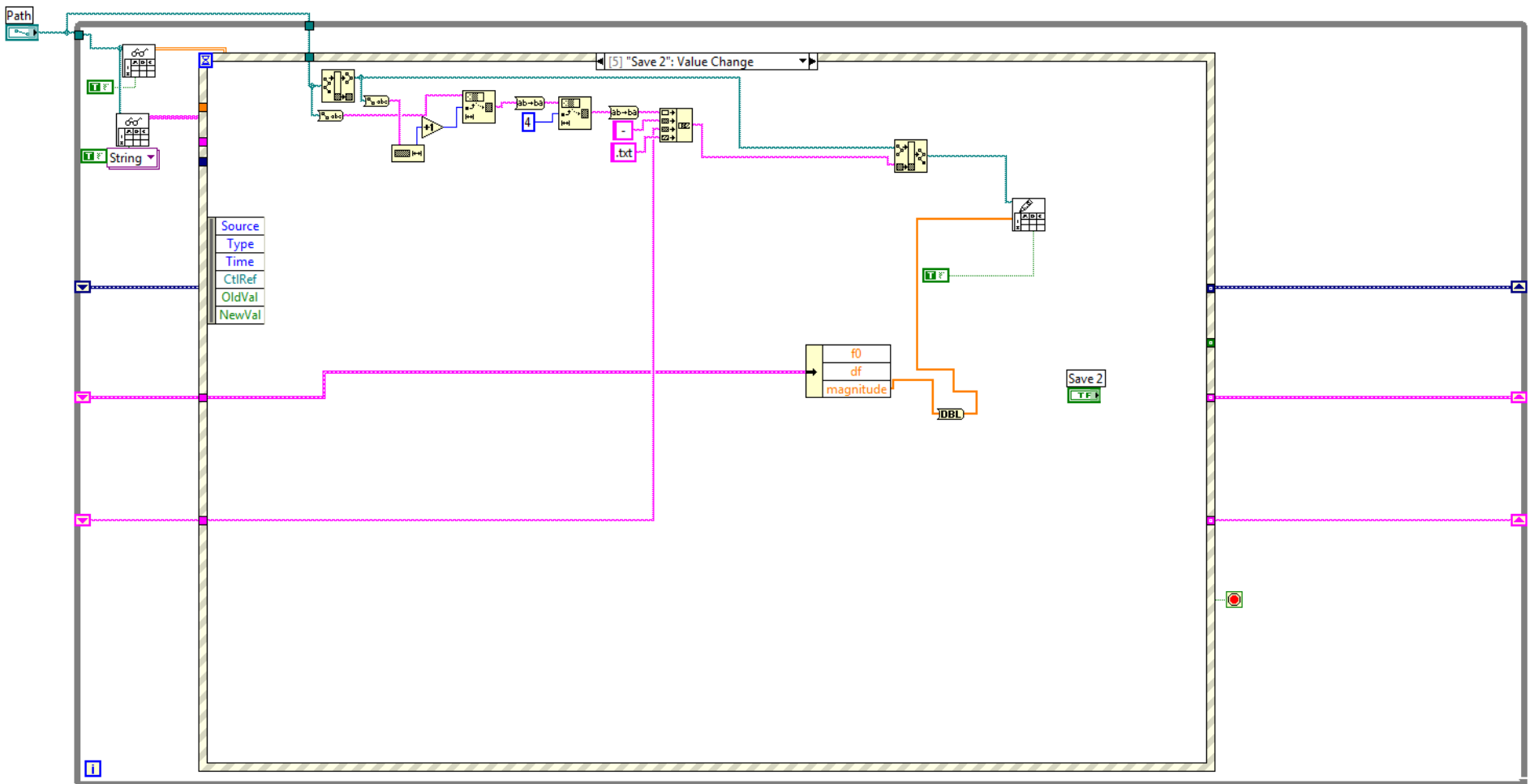


Figure E.4 – Screenshot displaying the code which formats the name of the .txt file which is saved from the FFT.

# **Appendix F:**

**Analysis of Secondary Events Collected During  
Mine Shots #510-522**

During the proposal defense held on June 19, 2008, a figure was presented which showed a seismic signature from an explosion. The explosion was from a series of experiments, taking place in A-Drift, researching the effect of different rock and coal dust concentrations (mine shots #510-522). The seismic signature is presented in Figure F.1. This waveform was collected from Geophone 2, which is located in the C-Drift instrument room. Figure F.1 displays events labeled as the “initial explosion” and a number of secondary events called “interactions with seals.” These secondary events are unique because:

- These types of distinguishable secondary events were not observed by Geophone 2 during any explosion conducted in C-Drift (mine shots #504-509).
- The secondary events were not observed on other geophones monitoring the same experiment.
- The amplitudes of the secondary events are on the same scale or larger than the initial explosion however much smaller in duration.

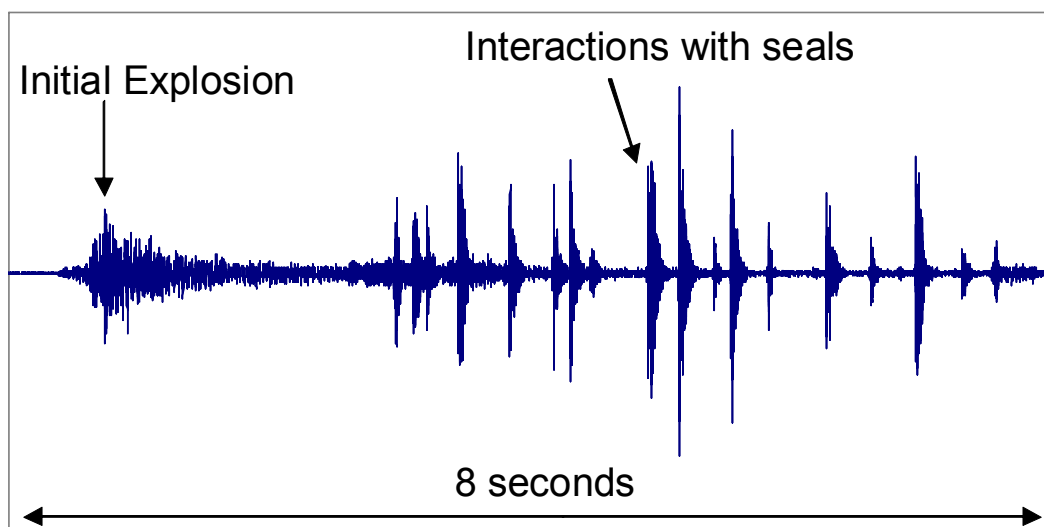


**Figure F.1** – Seismic signature from Geophone 2 collected during mine shot #517 which was presented during the defense proposal.

The question asked was “Are these secondary events actually the interactions of the pressure wave with the mine structures in the crosscuts or could other objects/structures in the area be the seismic source?” Analysis discussed in the dissertation proposal supported the speculation that the secondary events were emanating from the structures as they were interacting with the pressure wave. However, these results in the proposal were very preliminary and not substantial in terms of being able to prove the speculation. It was later found that these events had more to do with the chains and shelves used to hang the rock dust than the structures in the crosscuts. The following analysis shows an in-depth analysis supporting the speculation.

A baseline gas explosion was conducted in A-Drift (no rock or coal dust was used) as mine shot #510. The seismic signature captured during this shot from Geophone 2 is plotted in Figure F.2. This waveform does not contain secondary events as observed in Figure F.1 however a significant event detected just before three seconds occurs. To explain this, the pressure data obtained from the A-Drift face is shown in Figure F.3.

The data from Figure F.3 show two distinctive changes in pressure which begin approximately 2.4 seconds apart from each other. These changes in pressure would represent the ignition of the explosion at the face and the suck-back phenomena that was reported in Figure 2.4. This “suck-back” characteristic is only observed when the explosion is isolated in A-Drift and there is no seal in the entry. On the seismic signature plotted in Figure F.2, the two distinctive events are approximately 2.1 seconds apart which is seemingly close enough to be correlated to the suck-back wave interacting with the mine face. On the seismic waveforms, two more distinct events can be detected, especially on the red waveform. The two events occur at intervals of 2.1 seconds and 1.8 seconds. It is speculated that these two events are the suck-back waves interacting with the mine face for a third and fourth time.

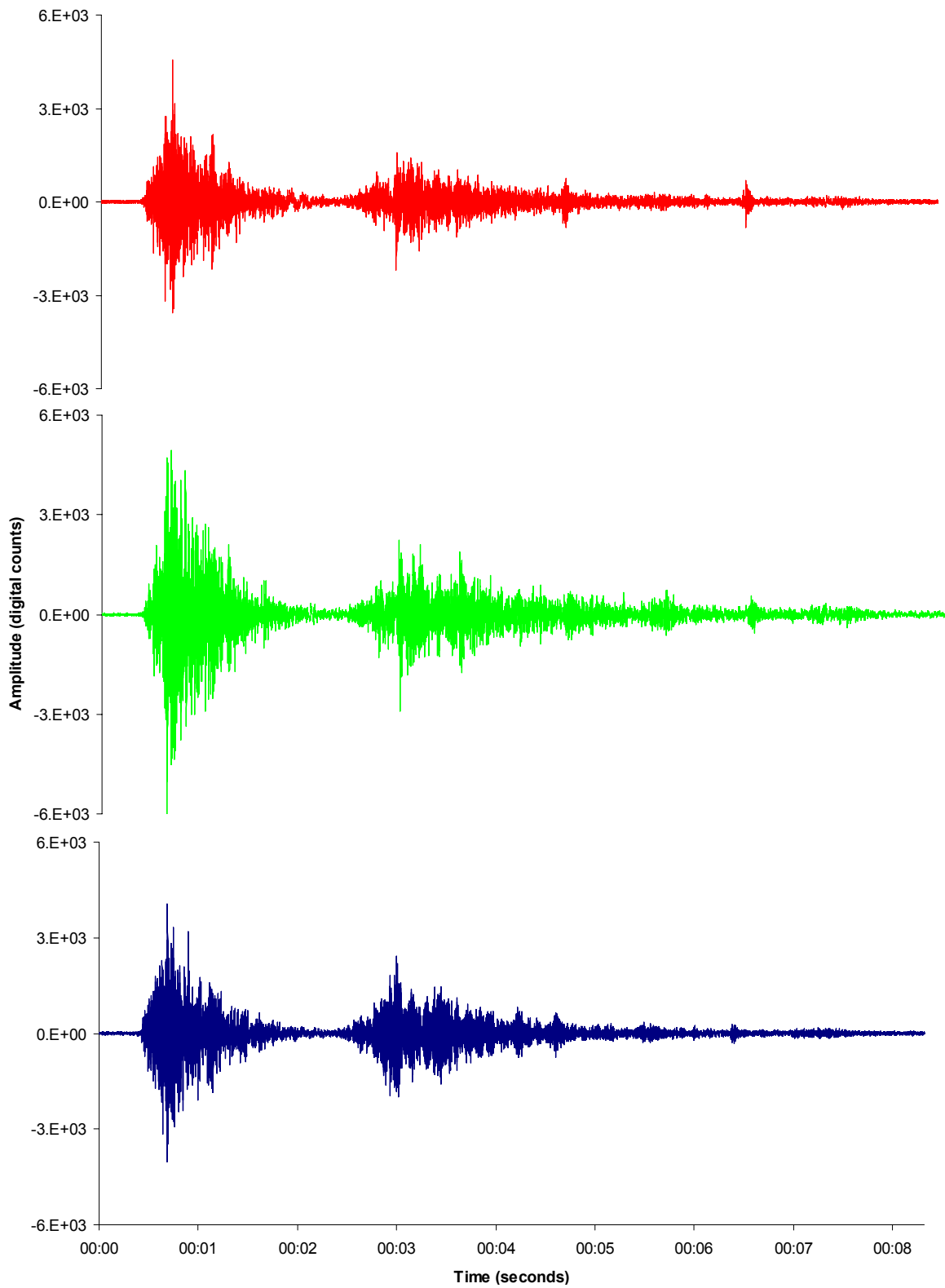


**Figure F.2** – Seismic signature from Geophone 2 collected during mine shot #510. The red waveform represents the horizontal component parallel to the mine drifts, green waveform represents the horizontal component perpendicular to the drifts and the blue waveform represents the vertical component.



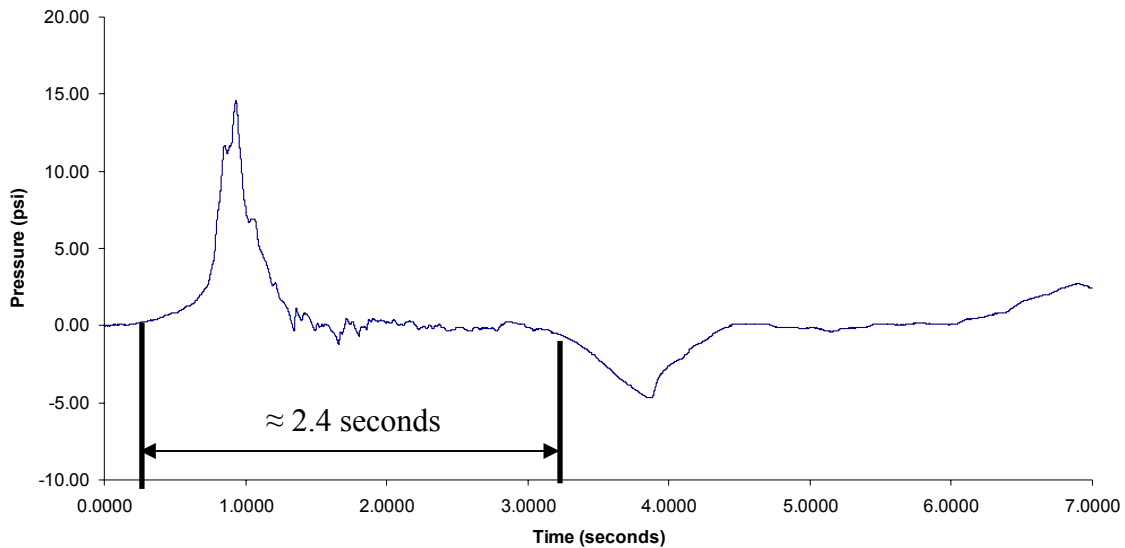


**Figure F.3** – Pressure data obtained from the LLEM monitoring system at the A-Drift face for mine shot #510.

A similar test was conducted, mine shot #519, where methane was ignited and no rock or coal dust was present in the drifts. mine shot #519 used 1,100 ft<sup>3</sup> of natural gas as an initial amount of fuel whereas mine shot #510 used 530 ft<sup>3</sup> of natural gas. The signatures obtained from Geophone 2 are plotted in Figures F.4 – F.6 with the waveforms from mine shot #510 superimposed for scale comparison. Also, the pressure-time curve from mine shot #519 is plotted in Figure F.7 with the data mine shot #510 superimposed for scale comparison.

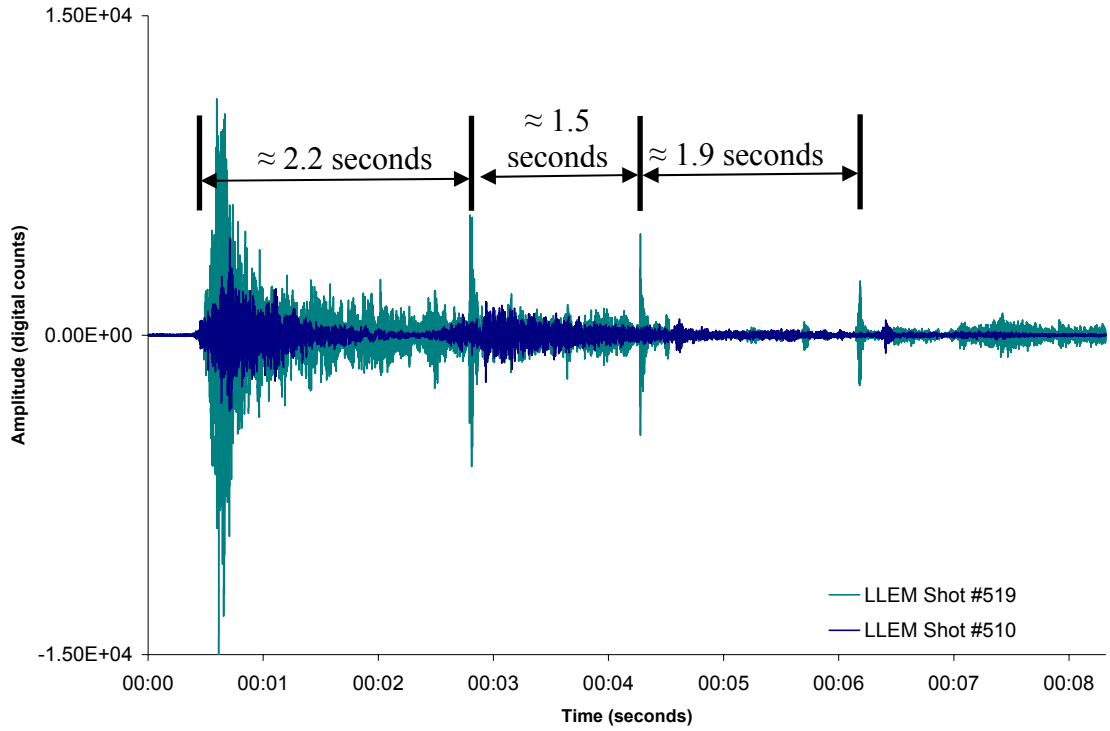


**Figure F.4** – Seismic signature from Geophone 2 collected during mine shot #510 and 519. These waveforms represent the horizontal component parallel to the mine drifts of the geophone.

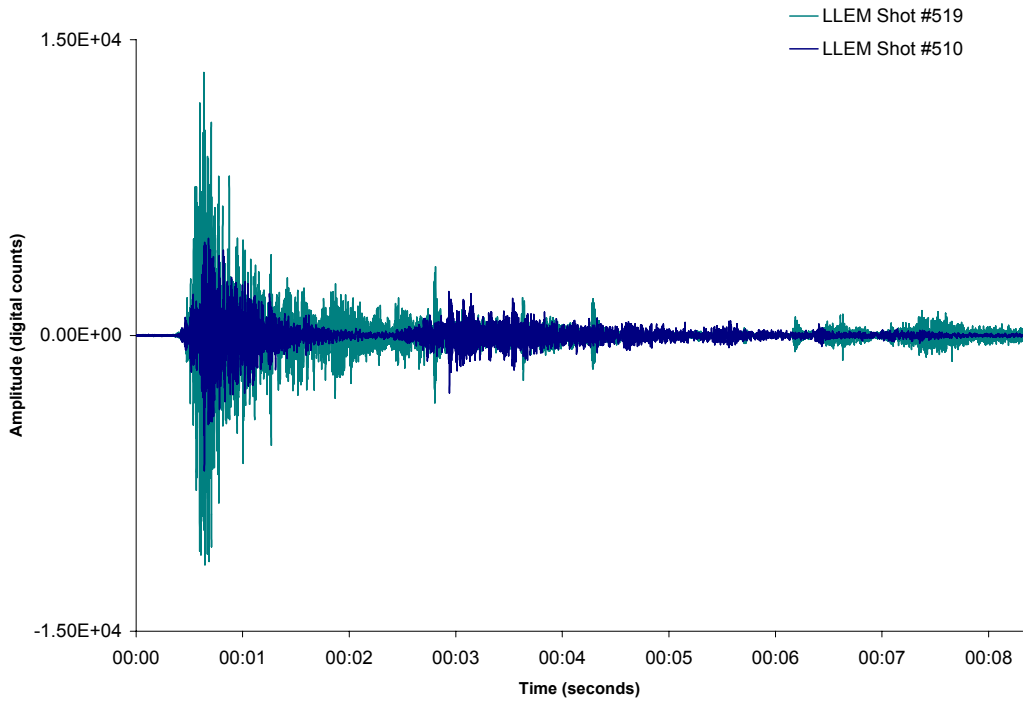


**Figure F.5** – Seismic signature from Geophone 2 collected during mine shot #510 and 519. These waveforms represent the horizontal component perpendicular to the mine drifts of the geophone.

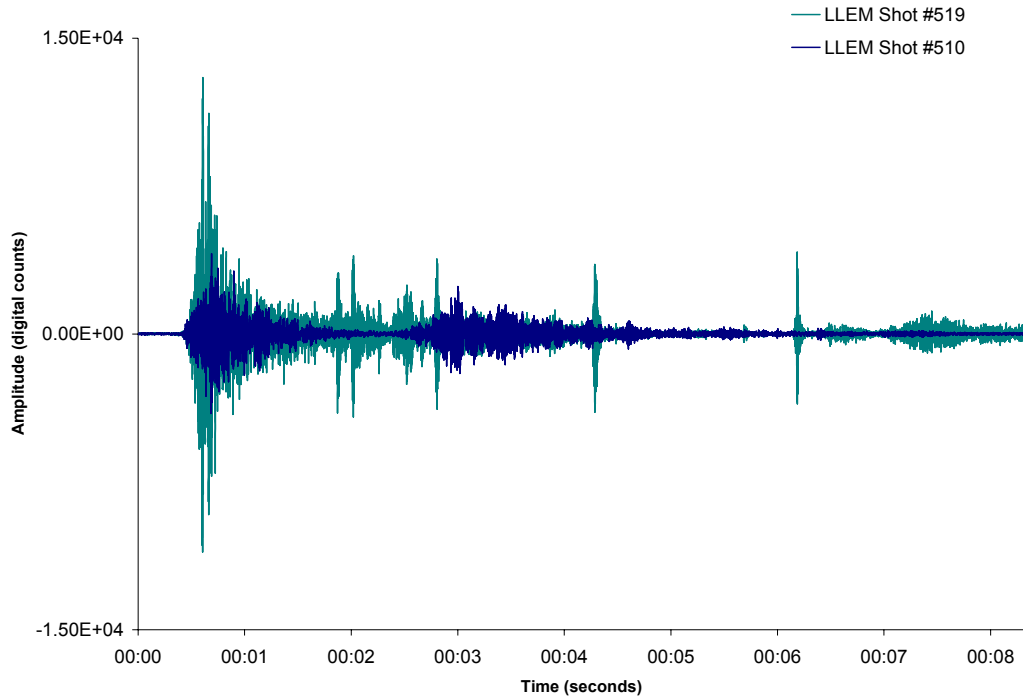


**Figure F.6** – Seismic signature from Geophone 2 collected during mine shot #510 and 519. These waveforms represent the vertical component of the geophone.

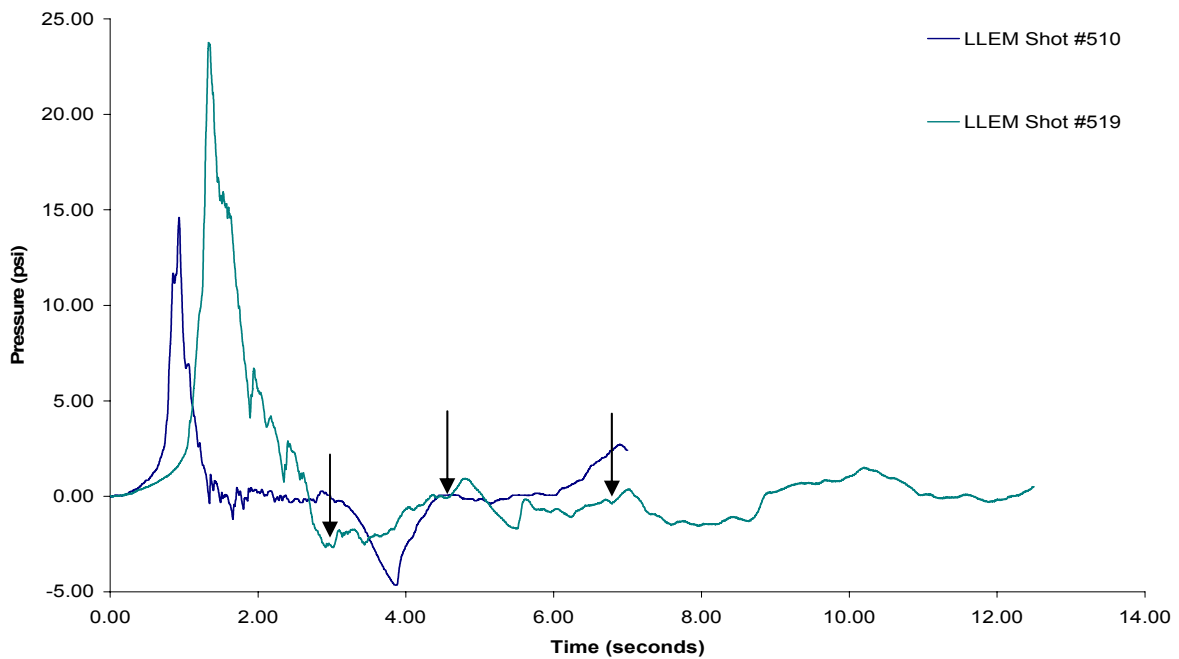


**Figure F.7** – Pressure data obtained from the LLEM monitoring system at the A-Drift face for mine shot #519 with the data from shot #510 superimposed for comparison. The arrows indicate peaks correlated to peaks in the seismic signature plotted in Figure F.4.

Plotted in Figure F.7 is a much larger pressure pulse for mine shot #519, which is attributed to the larger amount of initial fuel. This correlation can also be observed in the seismic data from Figures F.4 – F.6. There is much larger seismic amplitude for shot #519 when compared to shot #510. The first peaks of both pressure-time curves in Figure F.7 do not occur at the same time because shot #519 is ignited 45 ft more outby than shot #510 and the pressure transducer is located at the face in both cases. Figures F.4 – F.5 show spikes in the seismic signature after the initial explosion and the time differences in these spikes are highlighted in Figure F.4. These time intervals found in the seismic data plotted onto Figure F.7 as arrows. These arrows were able to be correlated to small negative peaks in pressure followed by a positive peak, similar observations were in Figure F.3 which correlated to the pressure wave coming back to the face. Based on these correlations, it is assumed that the secondary events detected during mine shots #510 and 519 are related to the pressure wave interacting with the A-Drift face multiple times.

Next, explosions were monitored at LLEM with varying rock and coal dust concentrations. Out of the eight shots monitored during this series of experiments, five showed a number of “secondary events” in the waveforms from Geophone 2, similar to the events detected Figure F.1. These experiments are shots #513, 514, 516, 517 and 518. The signatures are shown in Appendix B as Figures F.8 – F.10.

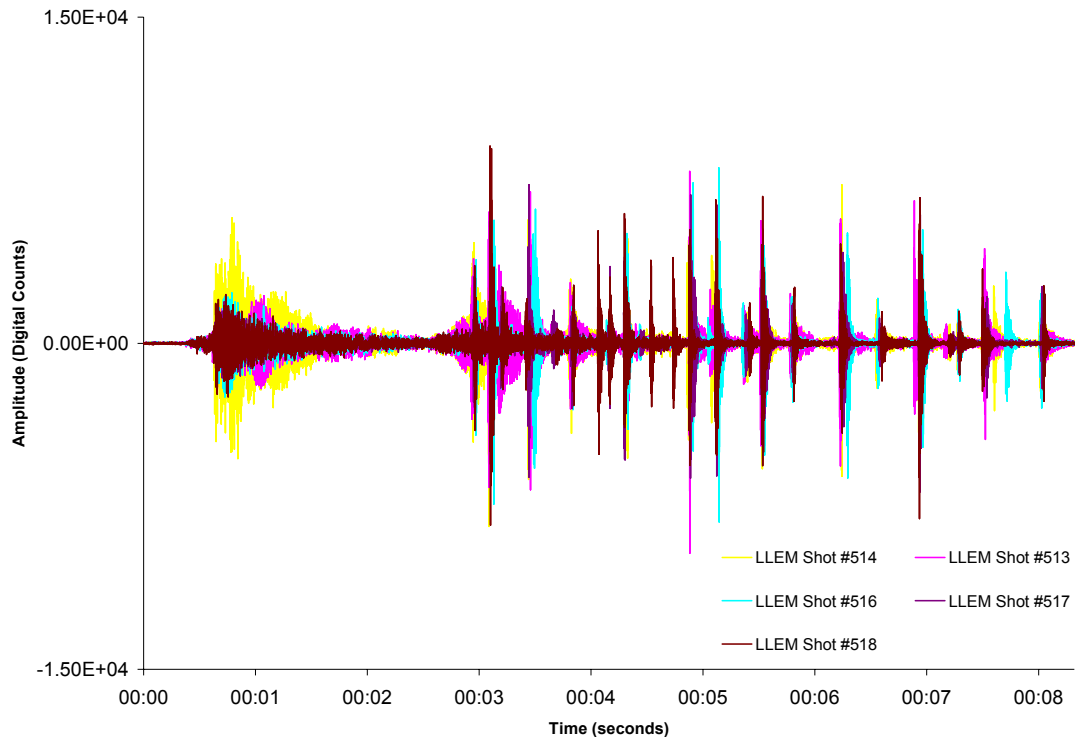


**Figure F.8** – Seismic signature from Geophone 2 collected during mine shots which showed significant secondary events. These waveforms represent the horizontal component parallel to the mine drifts of the geophone.

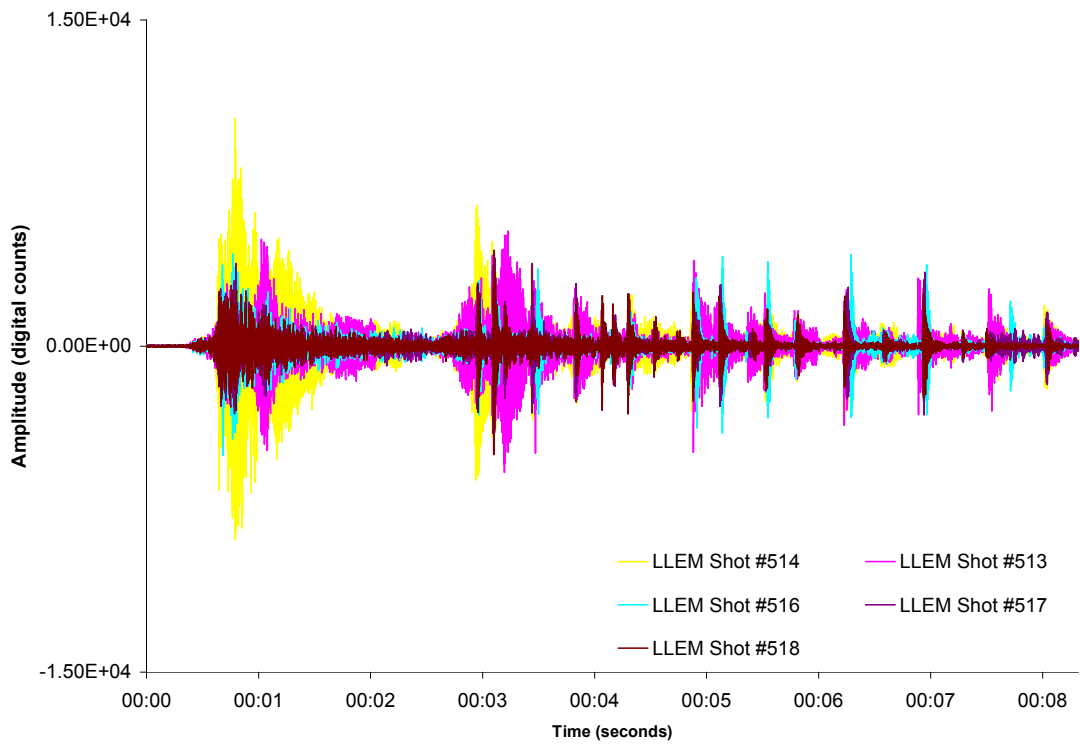


**Figure F.9** – Seismic signature from Geophone 2 collected during mine shots which showed significant secondary events. These waveforms represent the horizontal component perpendicular to the mine drifts of the geophone.

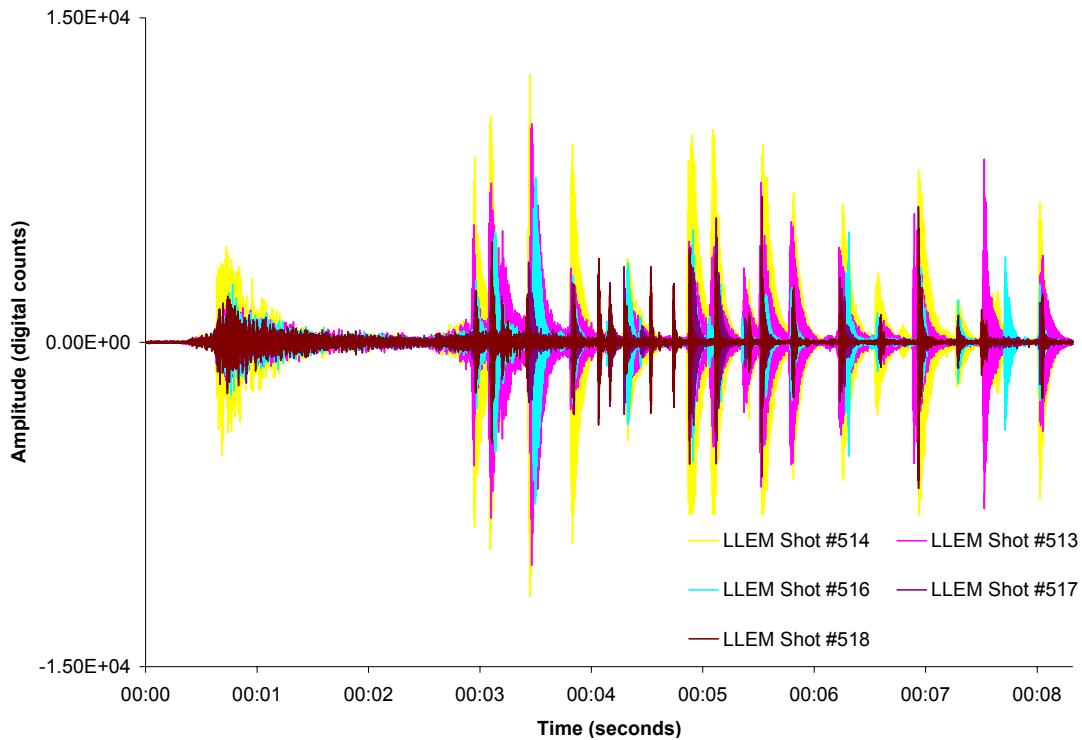


**Figure F.10** – Seismic signature from Geophone 2 collected during mine shots which showed significant secondary events. These waveforms represent vertical component of the geophone.

The spikes of the secondary events appear to occur at approximately the same time between different shots. On average, the spikes of each event occur in intervals of 320 milliseconds with a standard deviation of 134 milliseconds (each spike was taken into consideration for this calculation, including ones that were significantly smaller). The pressure-time curves for all the data, taken at the A-Drift face, are plotted on a single graph and shown in Figure F.11. It can be observed that around approximately three seconds, when the secondary events begin to happen in the seismic data, no significant correlation can be made to the pressure-time curves. In fact, for all the pressure-time curves, despite significant differences in the seismic signatures between Figures F.4 – F.6 and F.8 – F.10, they look very similar. The pressure-time data was also sampled at 1,000 samples/sec, which is a suitable sampling rate to see periods of 320 milliseconds. Although not shown in the report, pressure measurements were

taken throughout the entry in A-Drift and no pressure-time curve showed significant secondary events which could correspond to the seismic data.

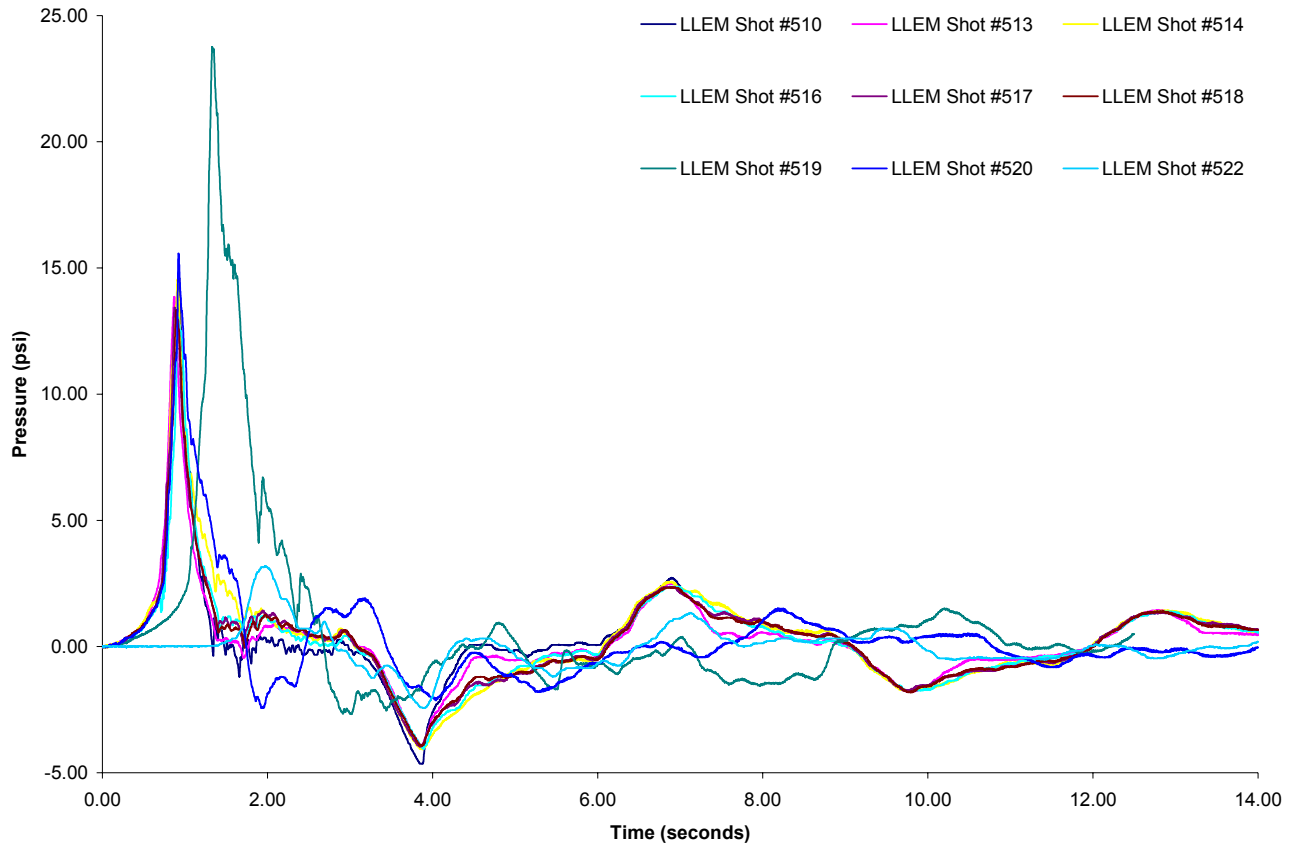


Figure F.11 – Pressure data obtained from the LLEM monitoring system at the A-Drift face for mine shots #510 - 519.

Preparation instructions for all the explosions were obtained from the mine supervisor to investigate other differences between mine shots #510 and 519 versus the experiments which showed a significant amount of secondary events. During the defense proposal, a comment was brought up that anything in the entry could be a source of seismic activity. During mine shots #513, 514, 516, 517 and 518 it was reported that shelves were hung by chains anchored onto the roof, which contained the rock/coal dust concentrations, were placed close to the roof as shown in Figure F.12.



**Figure F.12** – Photograph of the mine shelves and chains used in the series of mine shots with different rock and coal dust concentrations.

The dust shelves shown in Figure F.12 were in a zone starting 40 ft away from the mine face (directly outside of the ignition zone) and extending to 340 ft away. Depending on the mine shot, rows of either two or three shelves were placed apart at intervals of 10 ft, resulting in either 60 or 90 total shelves to be used. With this amount of dust shelves being used, up to 270 chains would be anchored to the mine roof. The dust shelves are approximately 8-in wide by 1.5-in thick by 8-ft long and made from expanded polystyrene. These shelves weigh between 0.7 – 0.8 lbs and break up when the pressure wave hits them. The shelf pieces not consumed by the flame are in the range of 6 – 12 in long and scattered down the entry. Mine personnel stated that these pieces could be a source of seismic activity, however by that point they are in the form of a soft Styrofoam.

---

\* Figure F.12 was provided by Eric Weiss of the National Institute for Occupational Safety and Health, Pittsburgh Research Laboratory, Disaster Prevention and Response Branch.



The chains which were anchored to the roof were then looked into as a possible seismic source. Mine personnel commented that chains most definitely impact the roof when the pressure wave hits them. These chains are in a fixed position between each test. Assuming the chains are the source of the secondary events, it would make sense why the spikes of these events occur at the same time between different shots since they are the same chains in the same position. If the source is assumed to be the debris from the dust shelves being thrown down the entry, it makes more sense that the spikes would occur at different times in the seismic signature since it is a random process. These secondary event signatures are also very high-frequency (approximately 400 Hz) and very short in duration, similar to hammer taps that have been observed in the past used to help check the functionality of the system. It makes sense that smacking a chain against the rock would create the same type of seismic signature as a hammer tap since they are both metal objects impacting the mine roof.

One of the limitations of the seismic system used in this study is that it cannot obtain and store a continuous signature. A change in ground movement has to trigger the system and then based upon parameters setup by the user it will record for a certain amount of time. The system has been setup to record the maximum amount of data at 2,000 samples per second with no decimation of the signal, which allows only approximately 8.3 seconds data to be captured for a single trigger. It is possible more secondary events occurred after 8.3 seconds and are not shown in the signature due to the limitations of the digitizers.

In the introduction, it was stated that secondary events were never observed when mine explosions were conducted in C-Drift during mine shots #503 – 509. The experimental designs for these shots contained only two dust shelves for all but one shot where eight shelves were used. These shelves were at locations of 44 ft, 77 ft, 97 ft and 107 ft away from the C-Drift face.

When only two shelves were used, they were located at 44 ft, which was directly outside of the ignition zone. If three chains are used per shelf, the amount of chains for these experiments would be very small compared to the shots where 270 chains were used. It could be possible the chains holding the few final row shelves during the tests conducted in A-Drift were the source of the seismic activity. Geophone 2 is directly in line with crosscut 4, which is located 404 ft away from the face. The final row of shelves was approximately midway between crosscuts 3 and 4. If this is the case, it would explain why the signatures were not detected on the explosions conducted in C-Drift and also why the signatures were not observed on the D-Drift or E-Drift geophones during mine shots #510 – 522.

The two remaining shots, mine shot #520 and 522 showed secondary events in the seismic signatures however they are not as abundant like previously observed. These signatures can be detected Figures F.13 – F.15. However, the peaks of the secondary events in the signatures from these two shots (especially between 2.5 and 4 seconds) occur at intervals which cannot be directly correlated to the pressure-time curves unlike the straight gas shots.

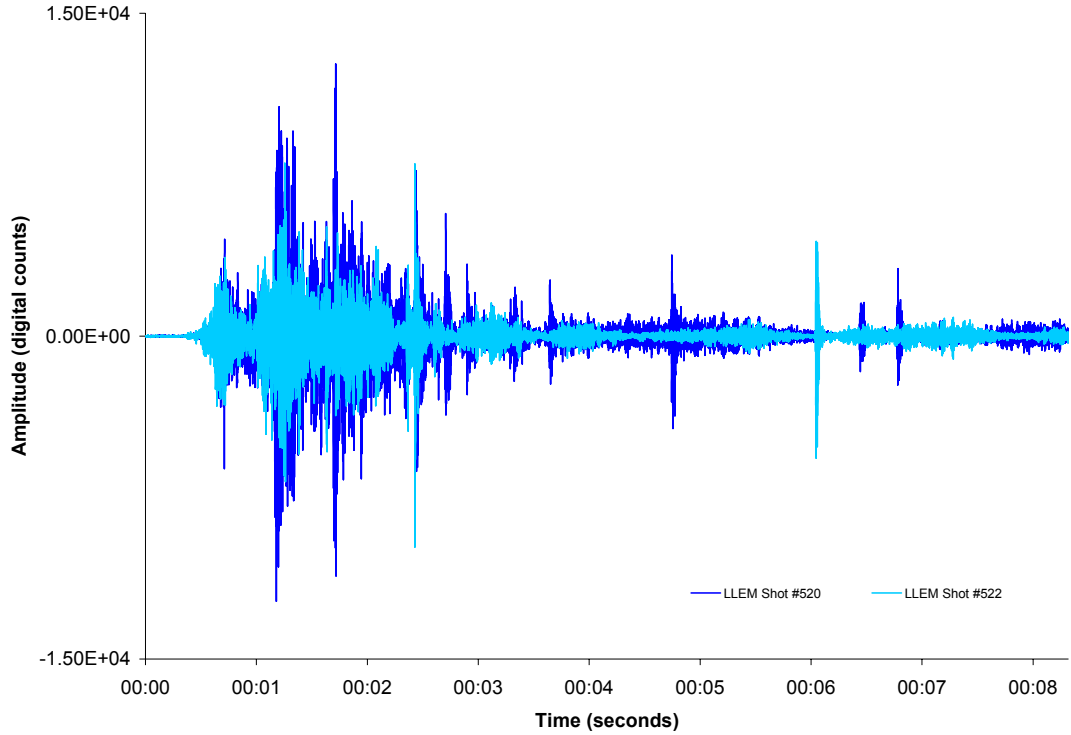


**Figure F.13** – Seismic signature from Geophone 2 collected during mine shots which showed some secondary events. These waveforms represent the horizontal component parallel to the mine drifts of the geophone.

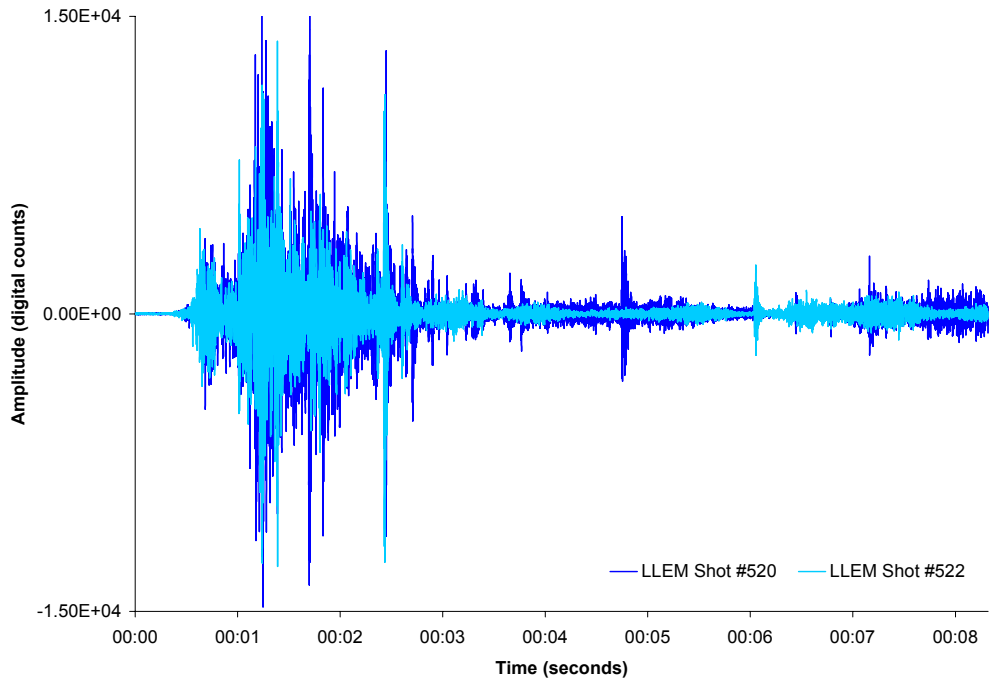


**Figure F.14** – Seismic signature from Geophone 2 collected during mine shots which showed some secondary events. These waveforms represent the horizontal component perpendicular to the mine drifts of the geophone.

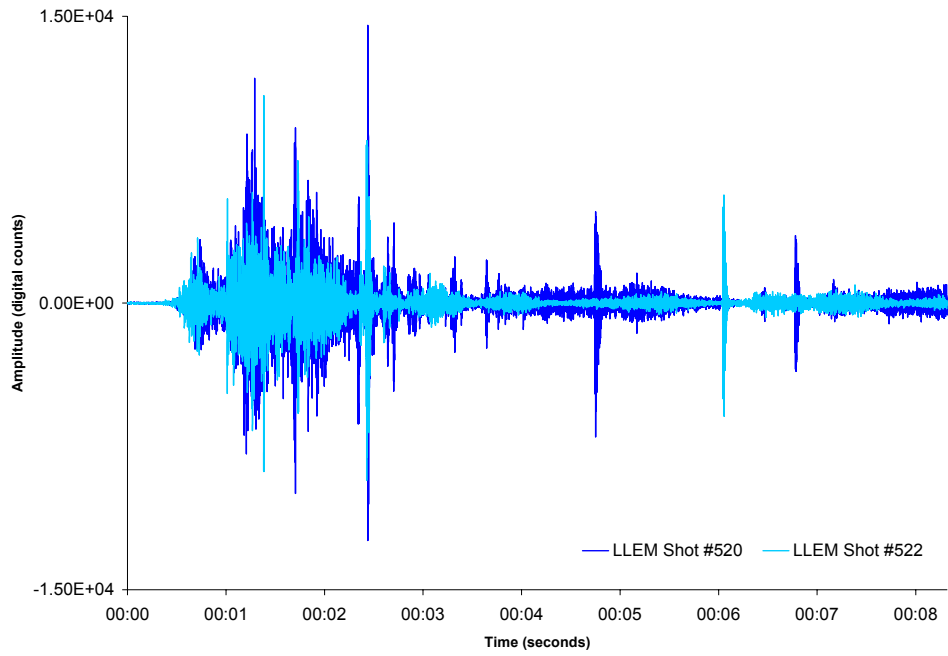


**Figure F.15** – Seismic signature from Geophone 2 collected during mine shots which showed some secondary events. These waveforms represent the vertical component of the geophone.

Both of these shots contained 90 shelves located at the same locations and intervals as before. The difference between these two shots and the previous shots which did show significant secondary events is that the stoppings in crosscut 6 and crosscut 7 were removed. These stoppings were present for the gas shots which produced no secondary events in the seismic signature, so the stoppings can be disproved as a possible source for the secondary events. The reason believed that there are not as many secondary events is that the pressure wave heading back towards the face is not as strong as the previous tests. The system is no longer isolated and much of the pressure wave is dissipated into B- and C-Drifts. The mine supervisor confirmed that the pressure wave can be significantly dissipated into B- and C-Drifts even with only two of the crosscuts opened based upon previous experience. Some of the spikes in the signature are possibly related to the pressure wave entering the drifts and interacting with the mine faces in B- and C-Drifts.

The following study has disproved the speculation that the secondary events observed during these shots are related to the mine structures in the crosscuts. The secondary events are more related to the chains and shelves used to hang the rock dust. It was also shown that when the system is no longer isolated and the pressure wave is allowed to enter into the other drifts, the signature can become very complex.

# **Appendix G:**

## **Distance-Time Plots for Velocity Calculations**

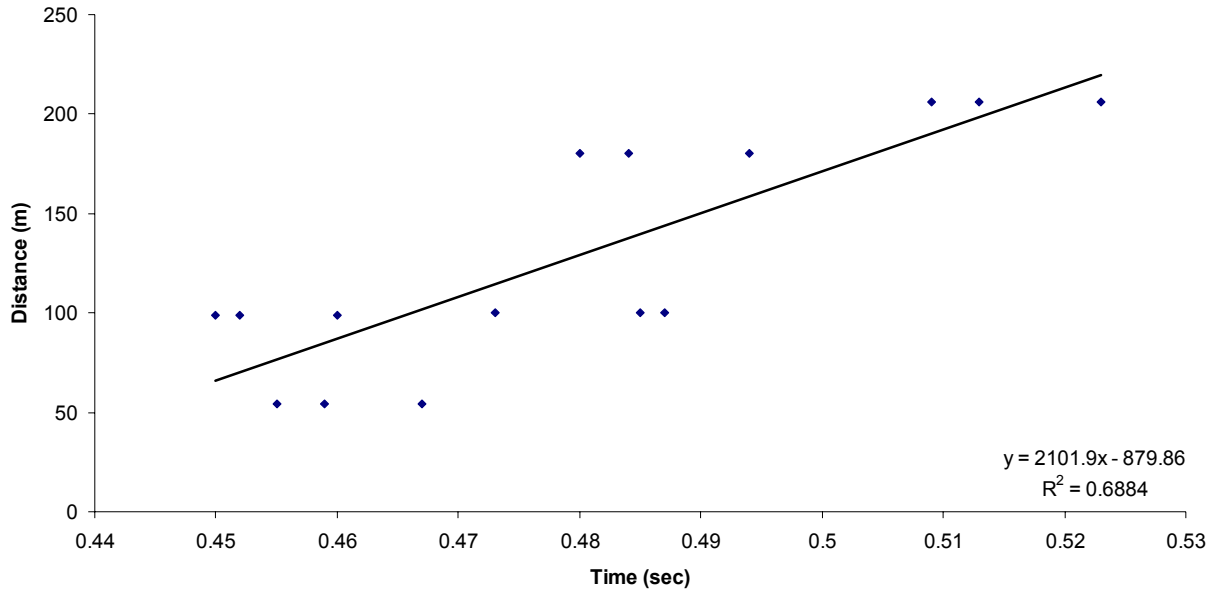


Figure G.1 – Distance-time plot for mine shot #505.

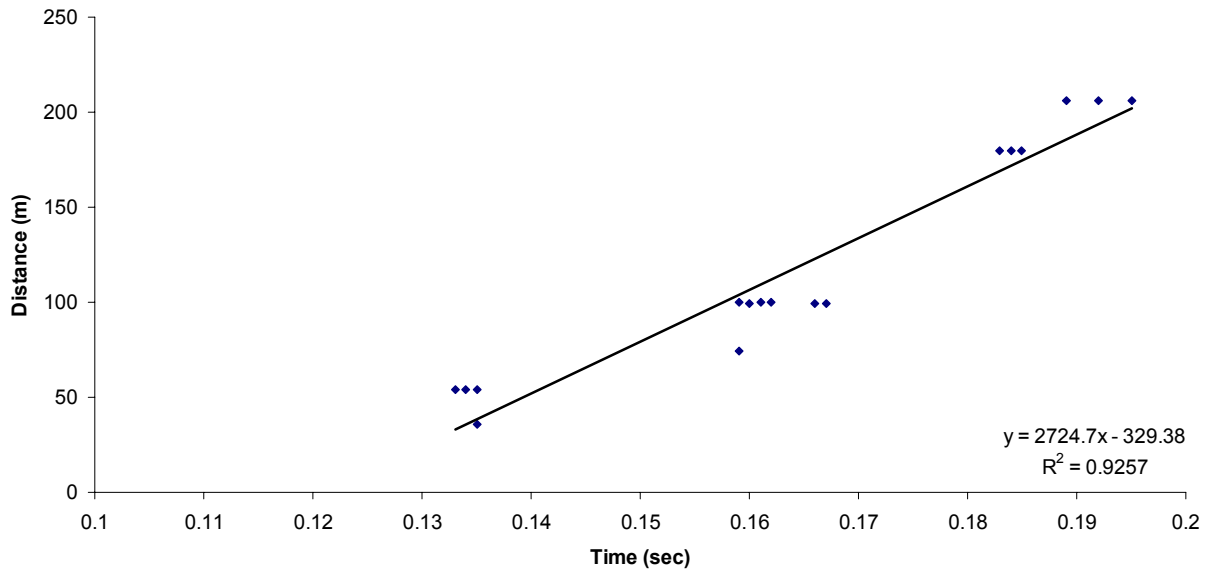


Figure G.2 – Distance-time plot for mine shot #506.

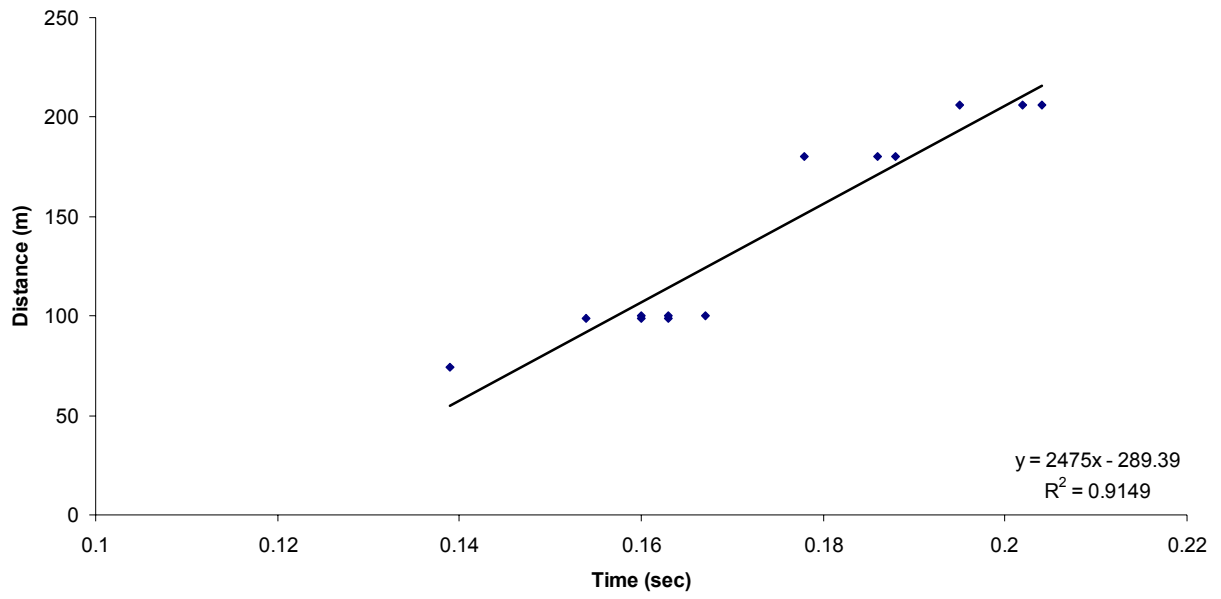


Figure G.3 – Distance-time plot for mine shot #507.

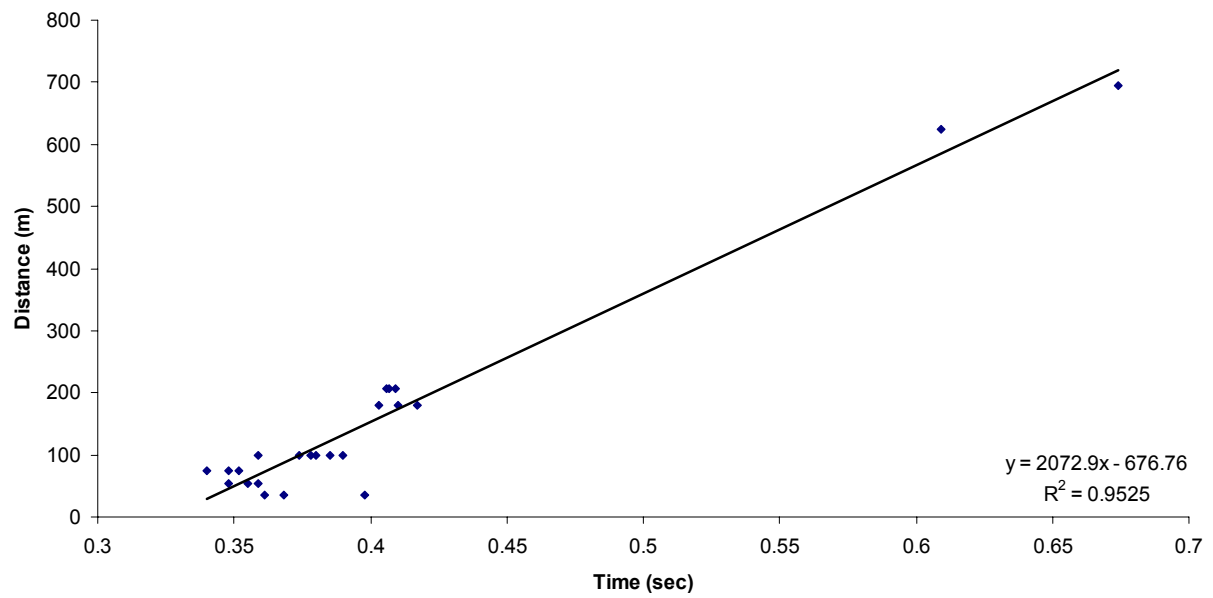


Figure G.4 – Distance-time plot for mine shot #509.



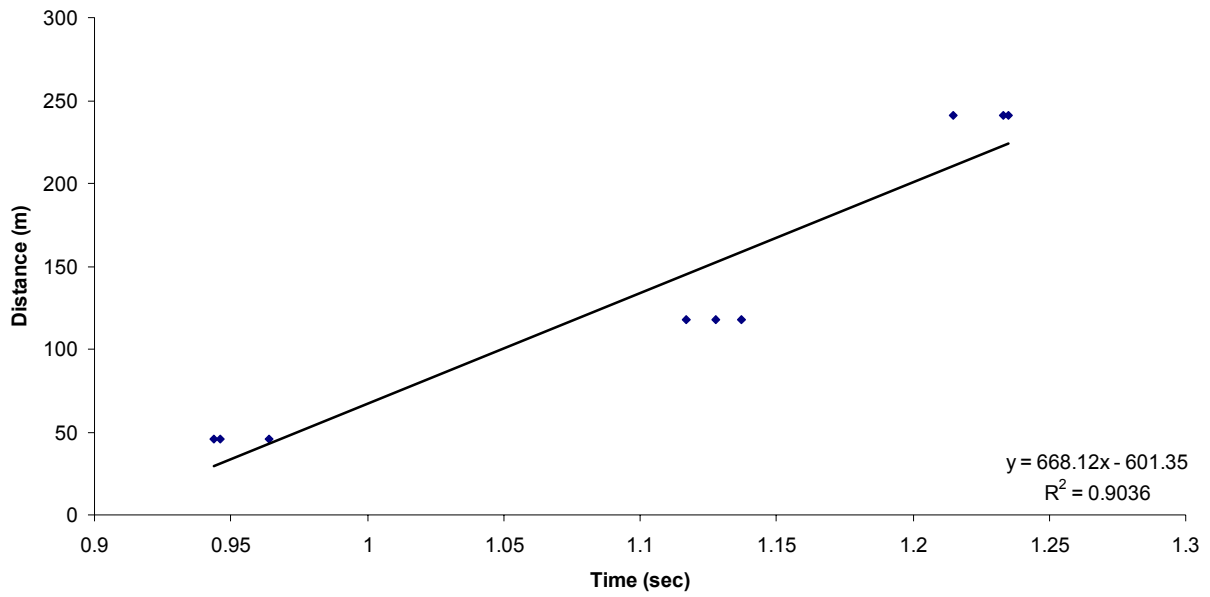


Figure G.5 – Distance-time plot for mine shot #510.

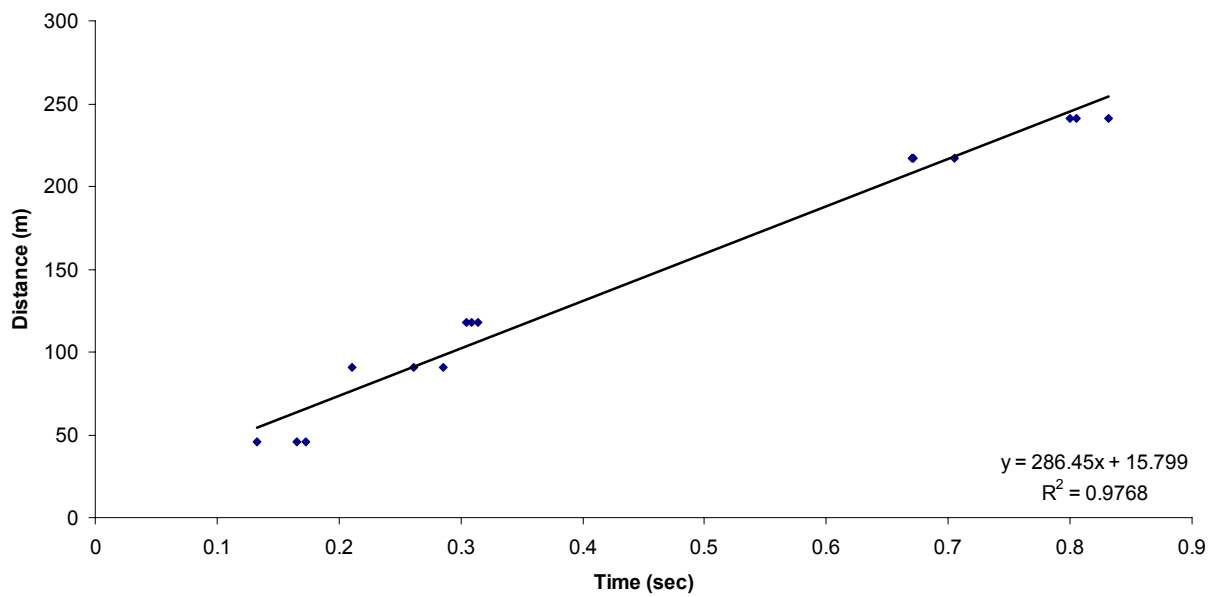


Figure G.6 – Distance-time plot for mine shot #513.

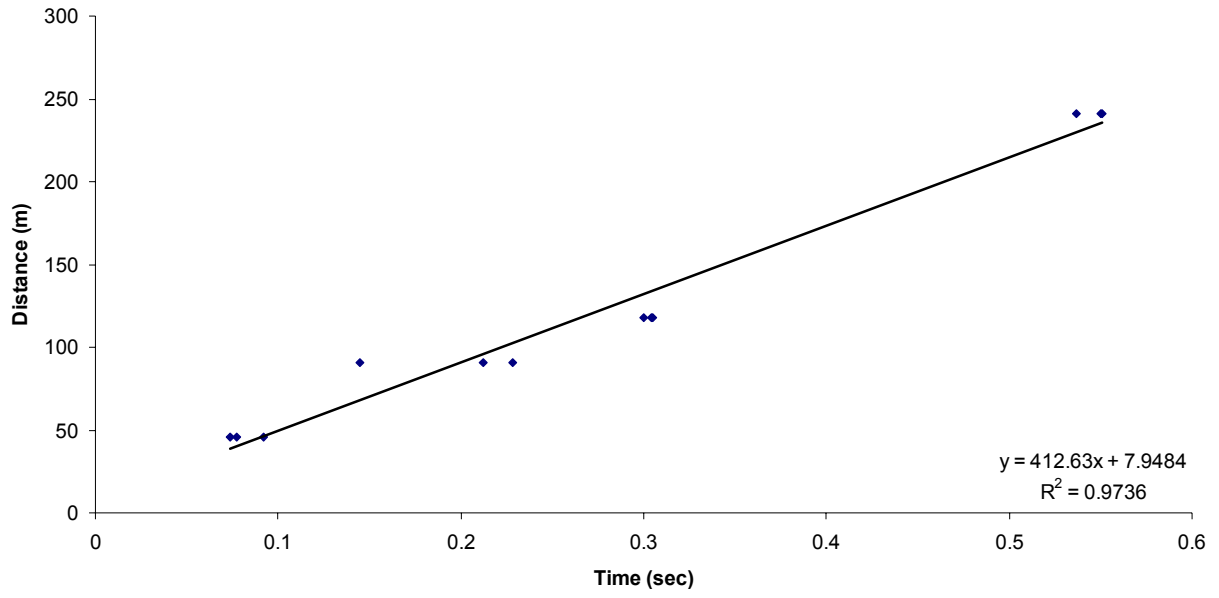


Figure G.7 – Distance-time plot for mine shot #514.

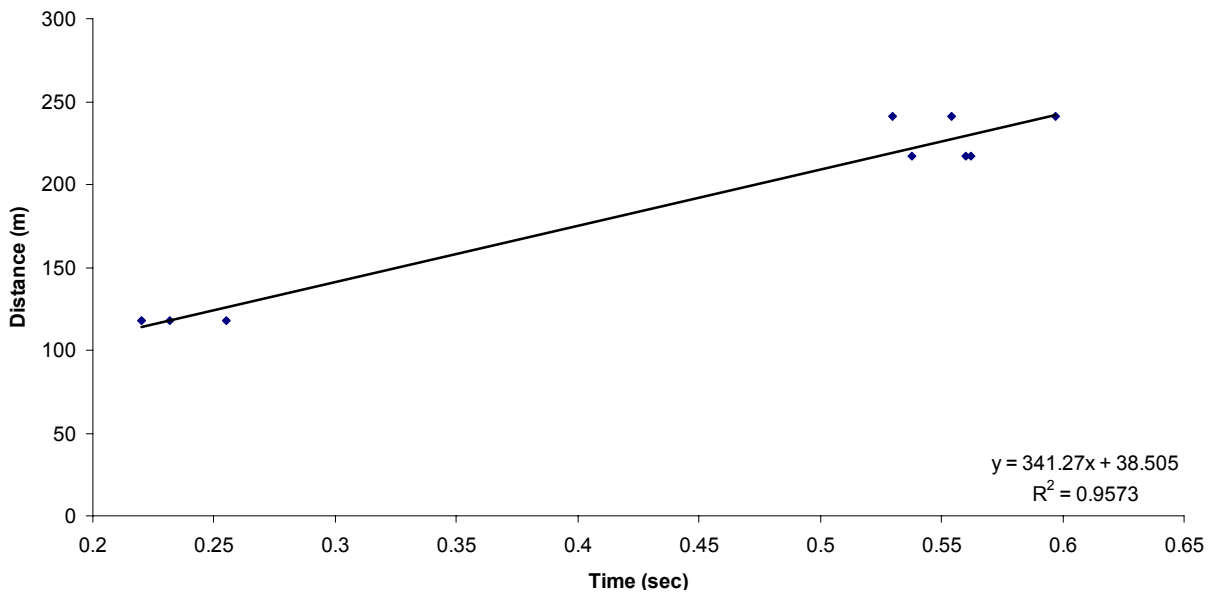


Figure G.8 – Distance-time plot for mine shot #516.

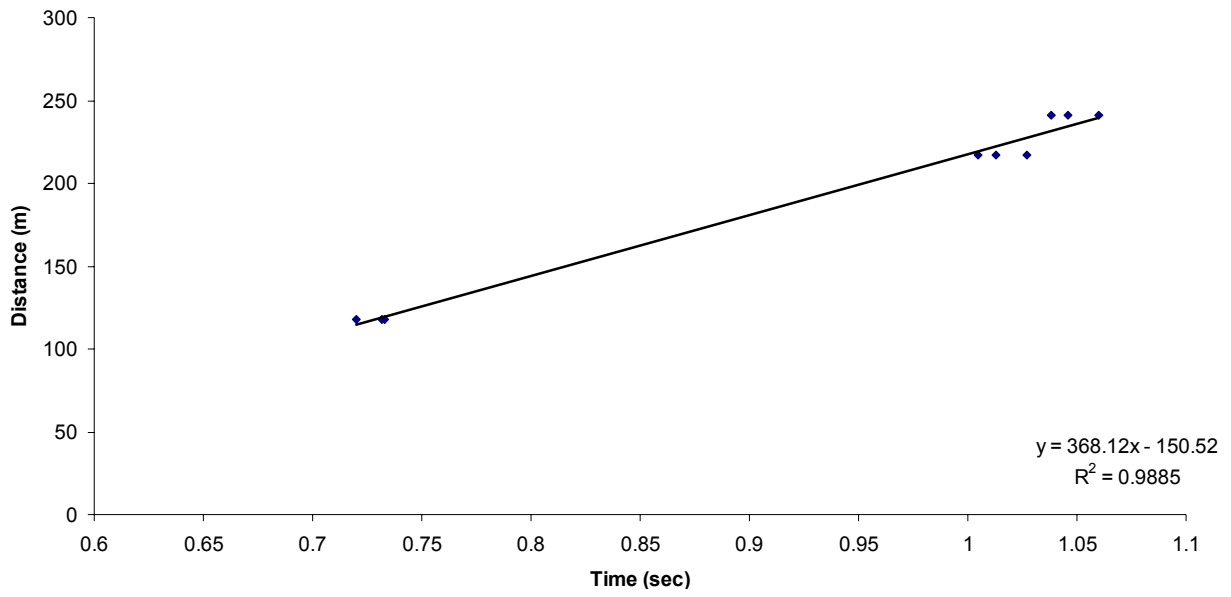


Figure G.9 – Distance-time plot for mine shot #517.

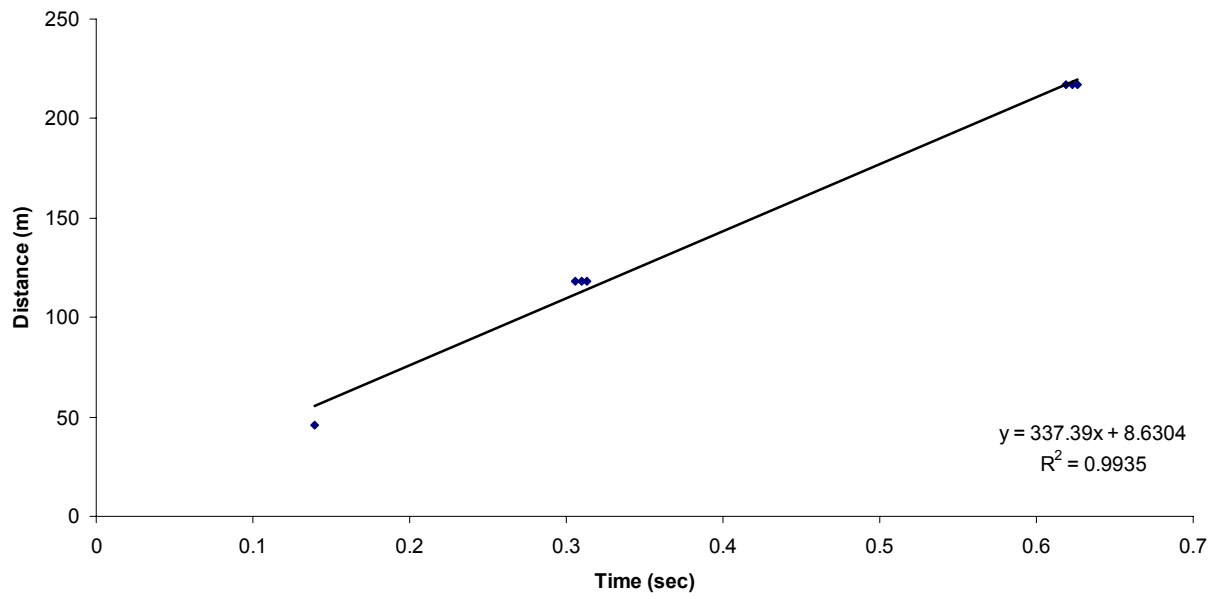


Figure G.10 – Distance-time plot for mine shot #518.

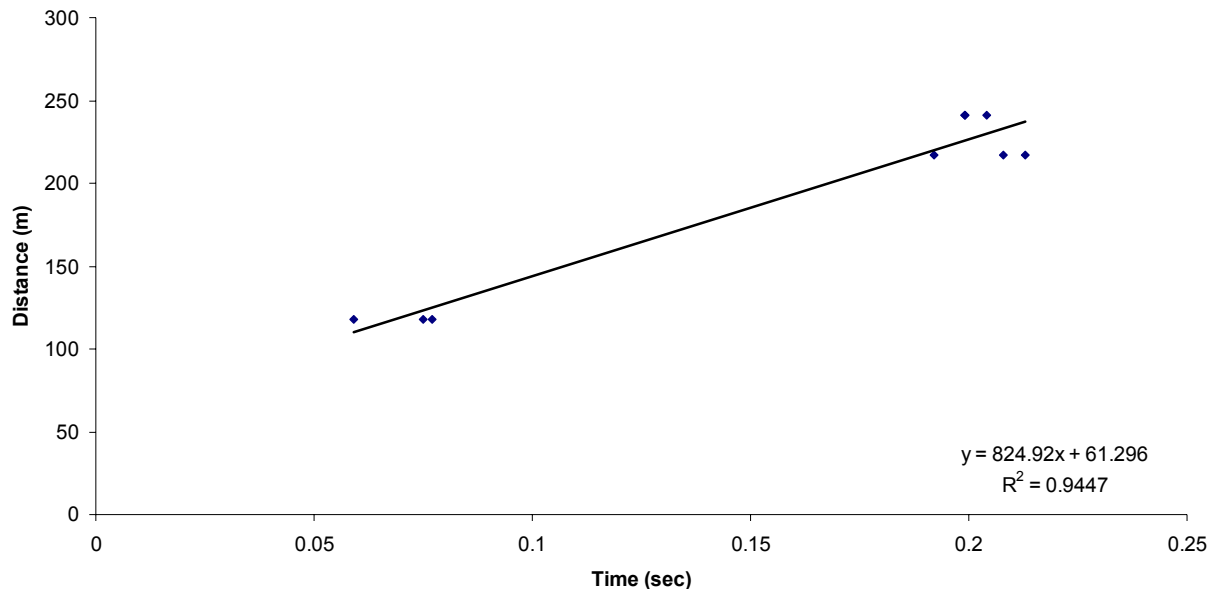


Figure G.11 – Distance-time plot for mine shot #519.

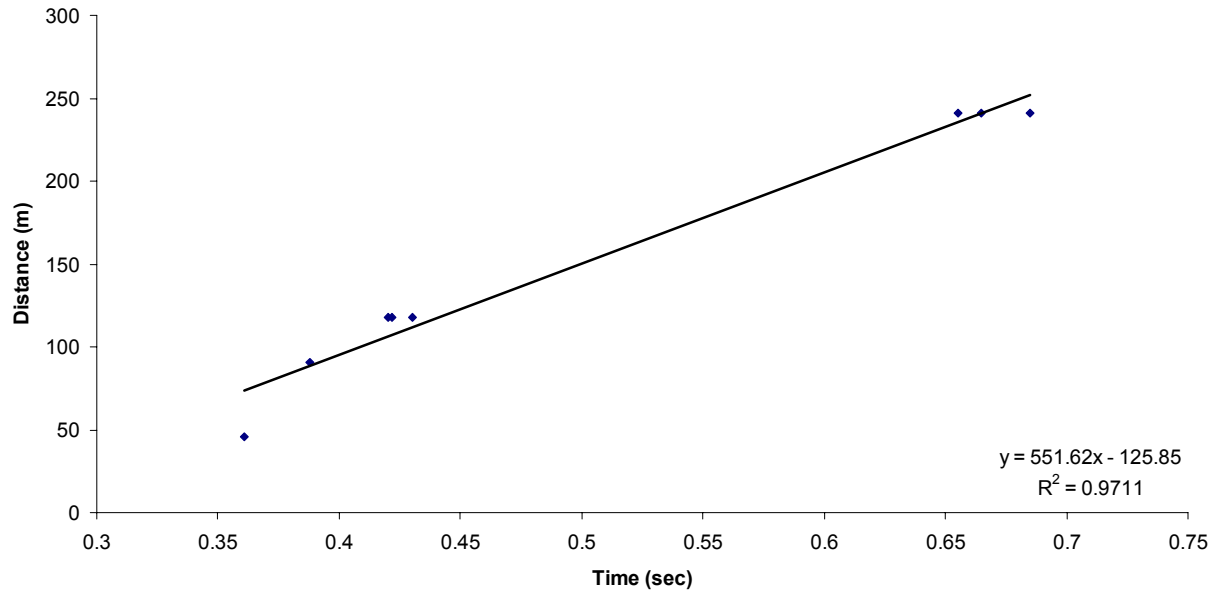


Figure G.12 – Distance-time plot for mine shot #520.

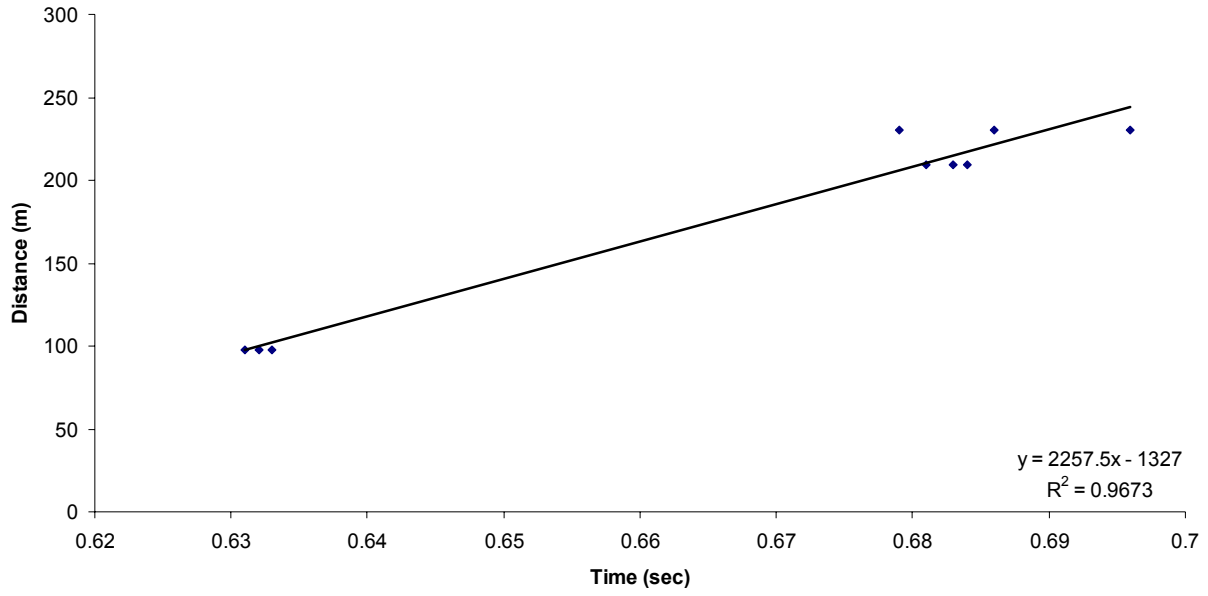


Figure G.13 – Distance-time plot for mine shot #528.

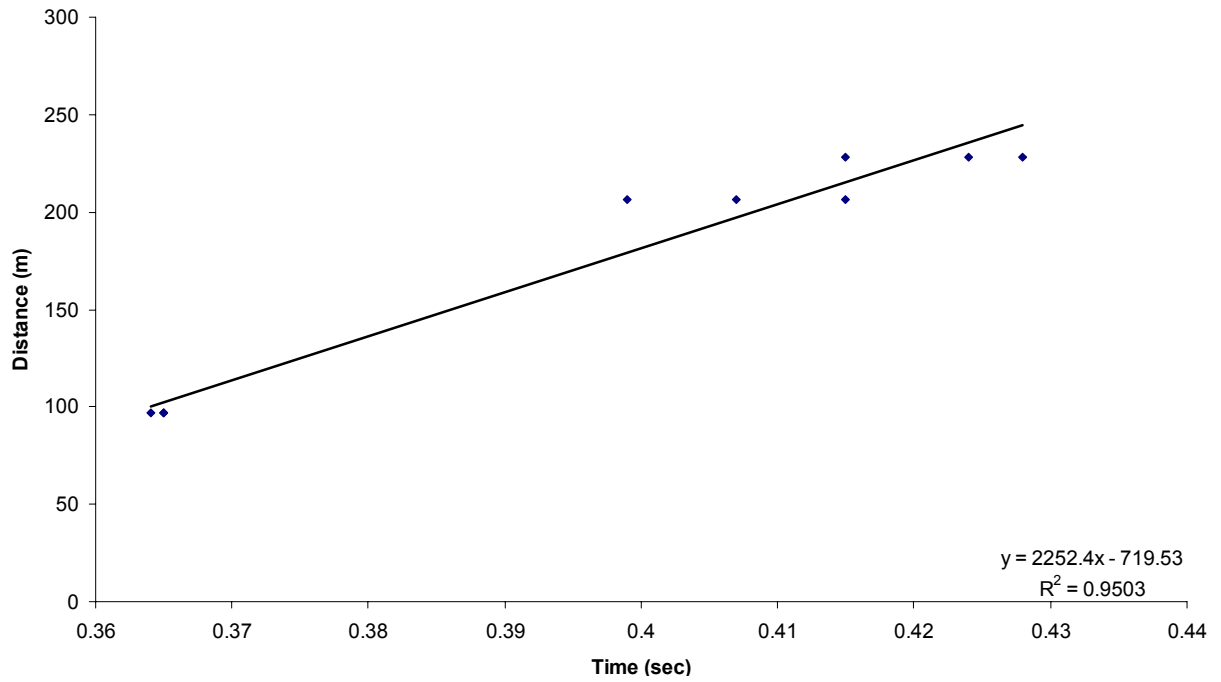


Figure G.14 – Distance-time plot for mine shot #529.

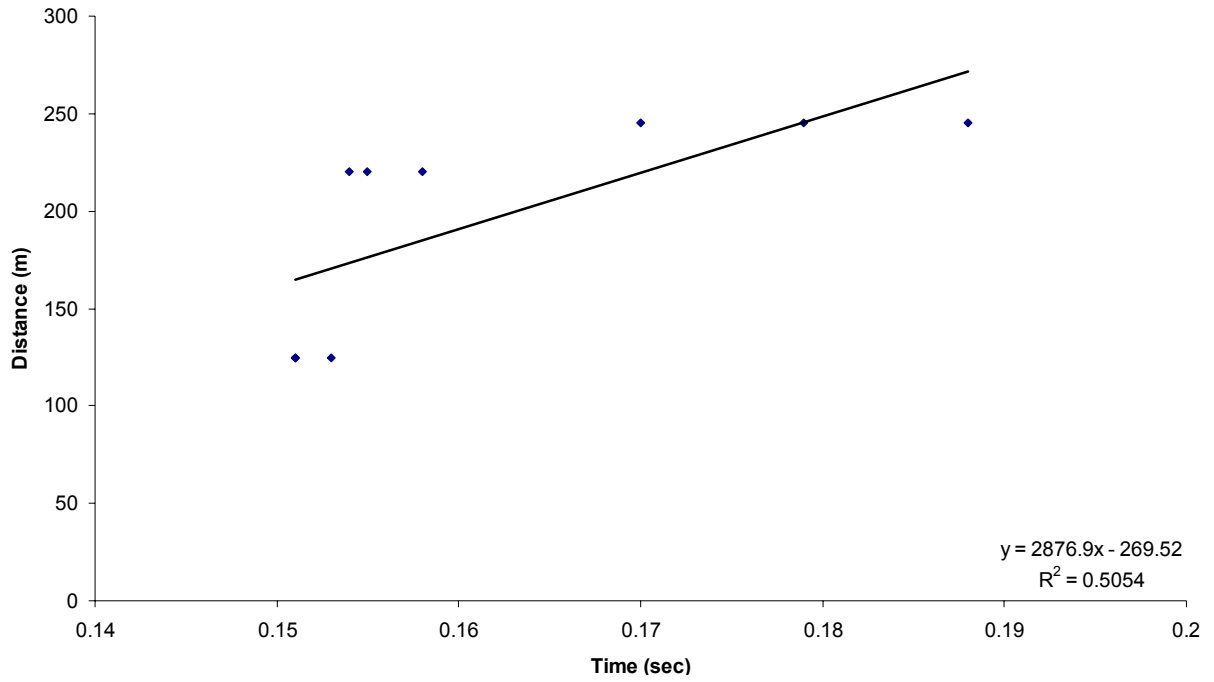


Figure G.15 – Distance-time plot for mine shot #530.

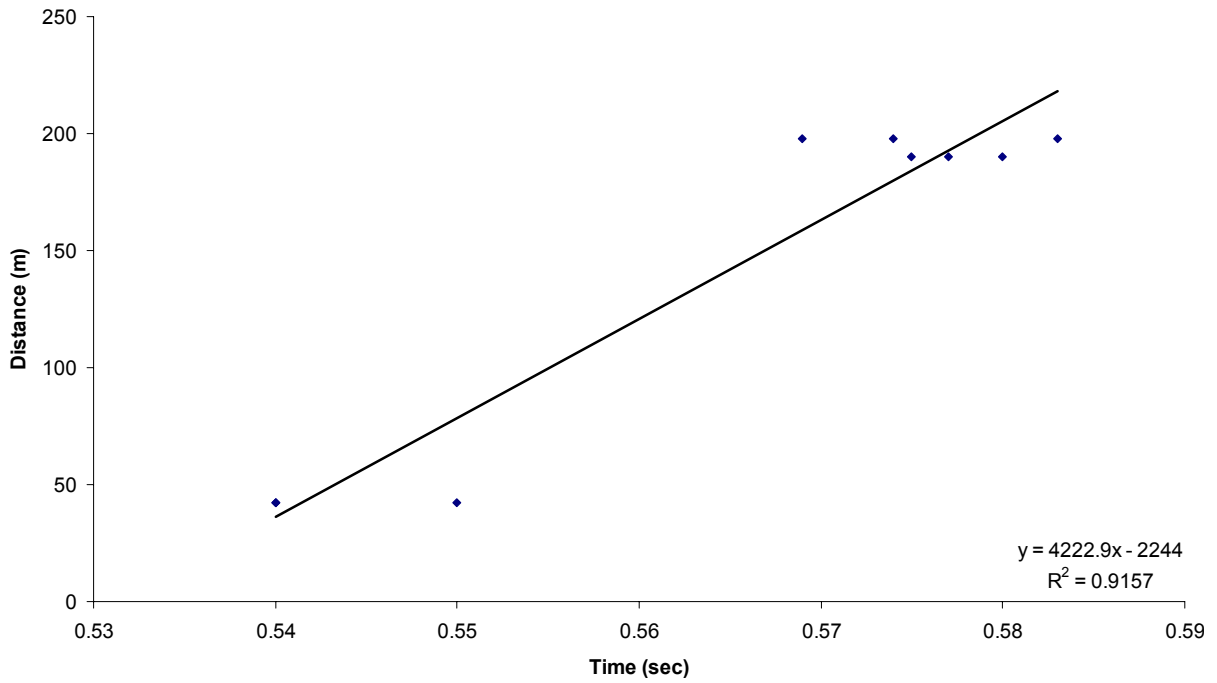


Figure G.16 – Distance-time plot for mine shot #531.

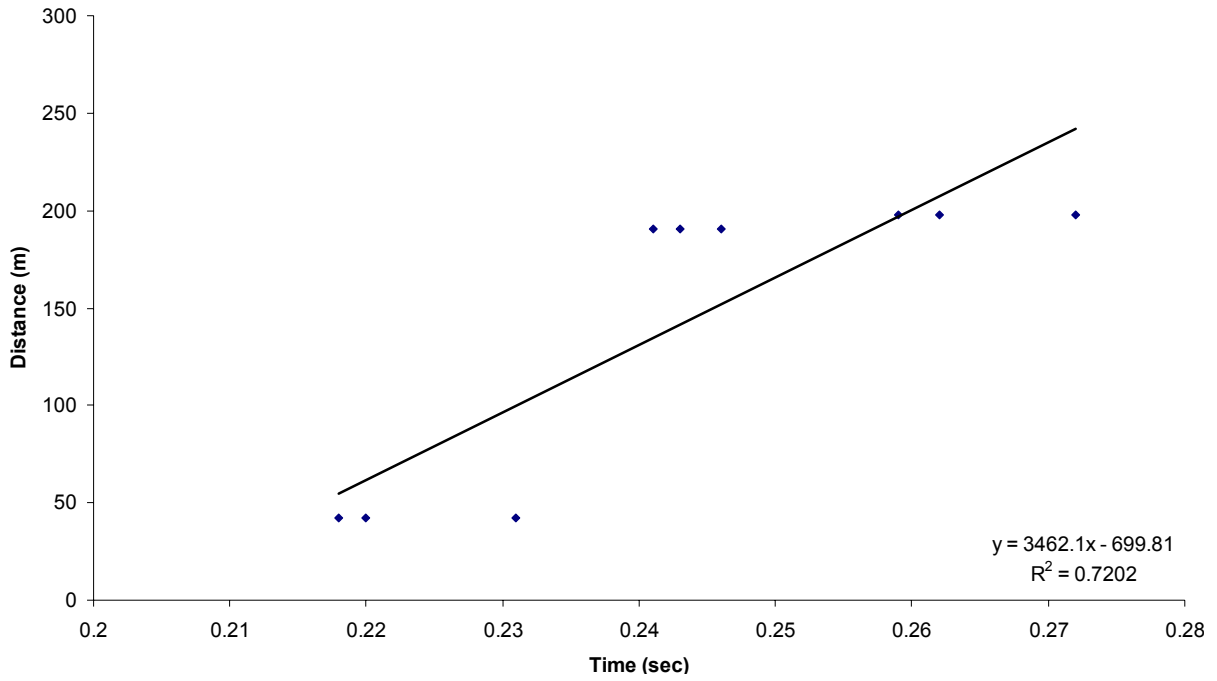


Figure G.17 – Distance-time plot for mine shot #532.

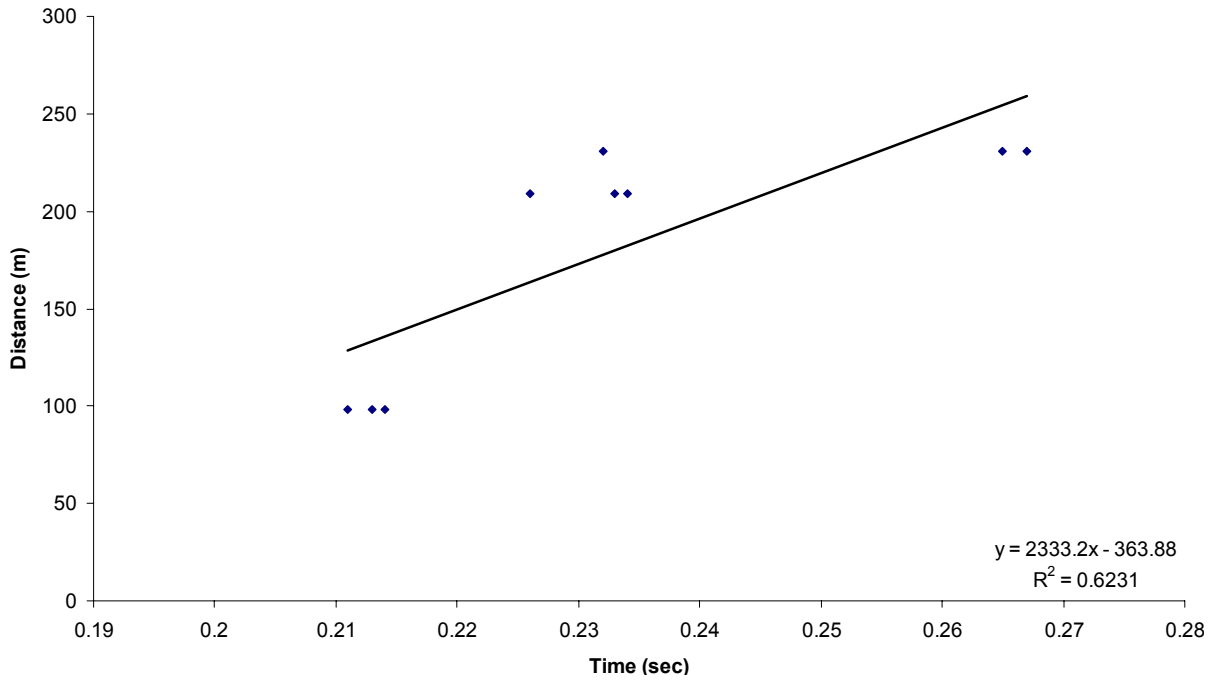


Figure G.18 – Distance-time plot for mine shot #533.

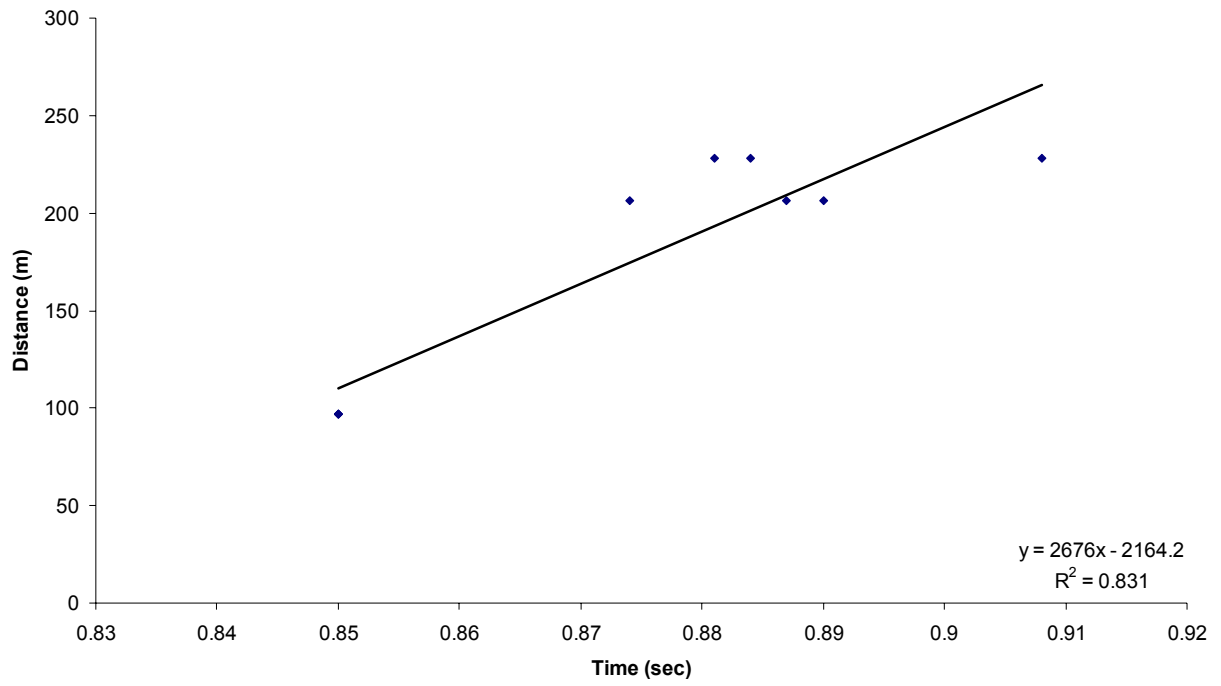


Figure G.19 – Distance-time plot for mine shot #534.

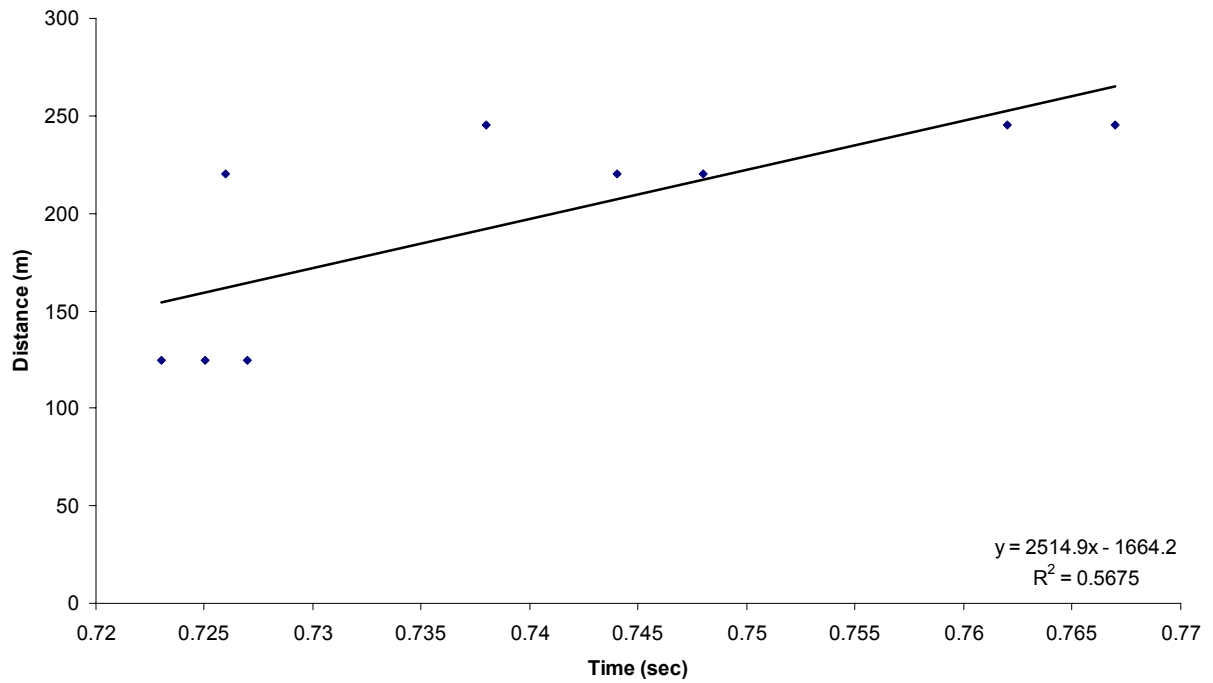


Figure G.20 – Distance-time plot for mine shot #535.



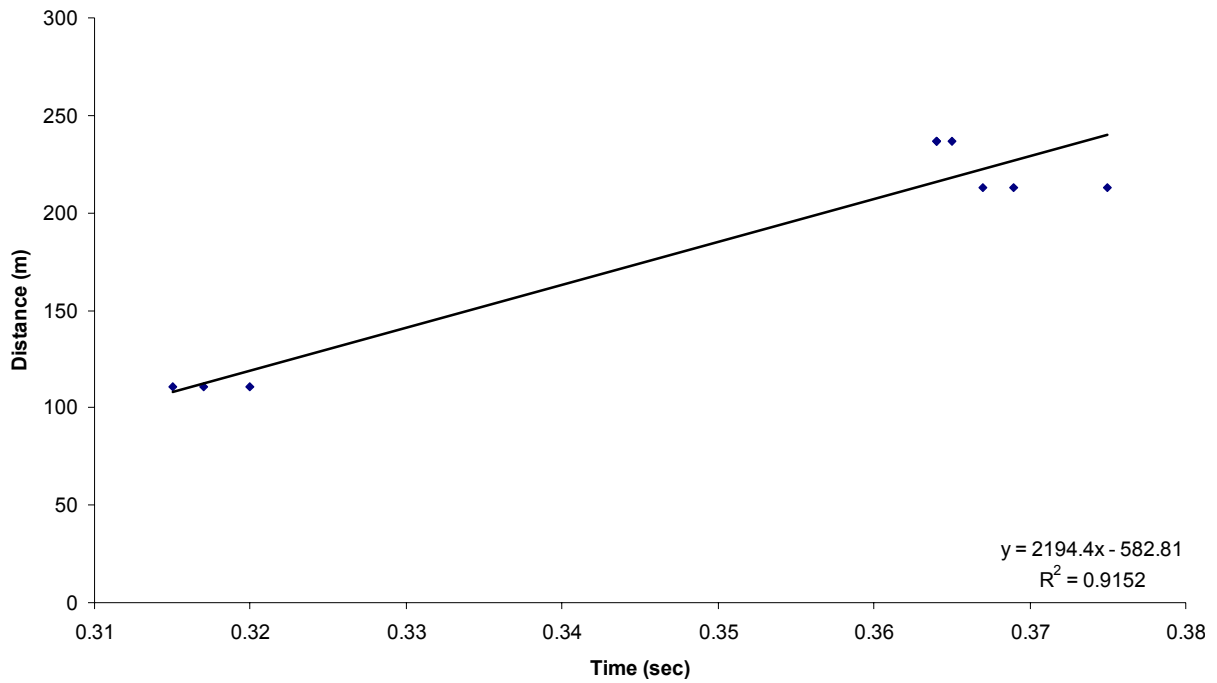


Figure G.21 – Distance-time plot for mine shot #536.

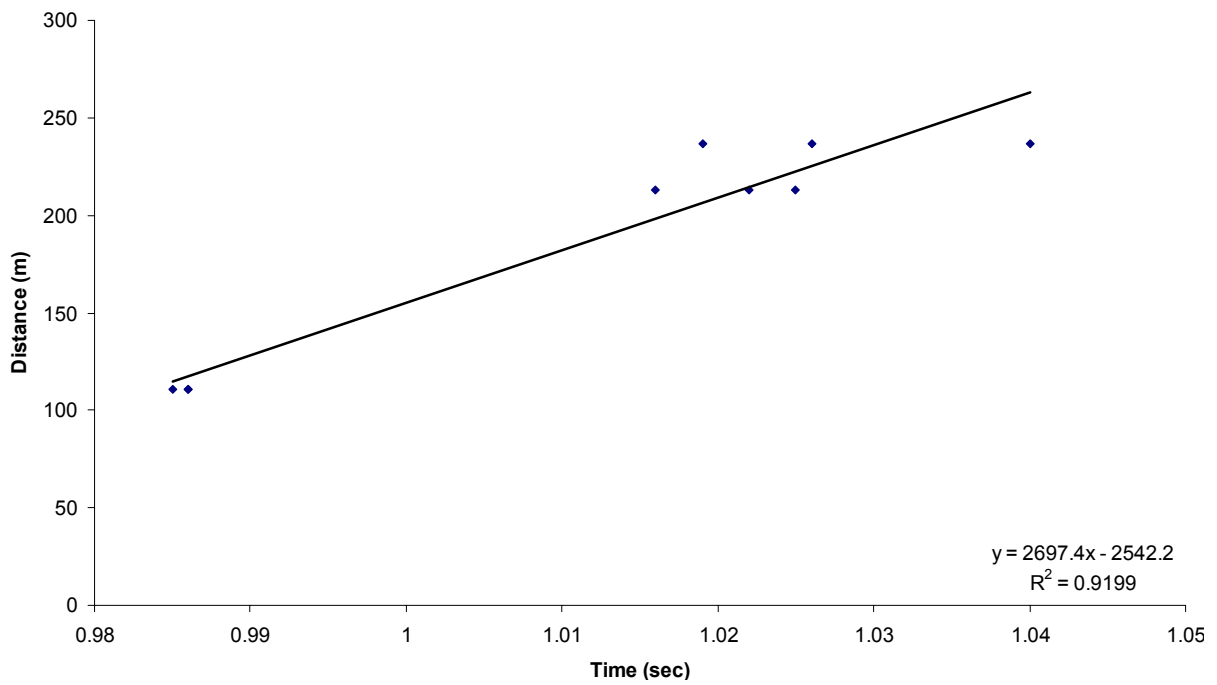
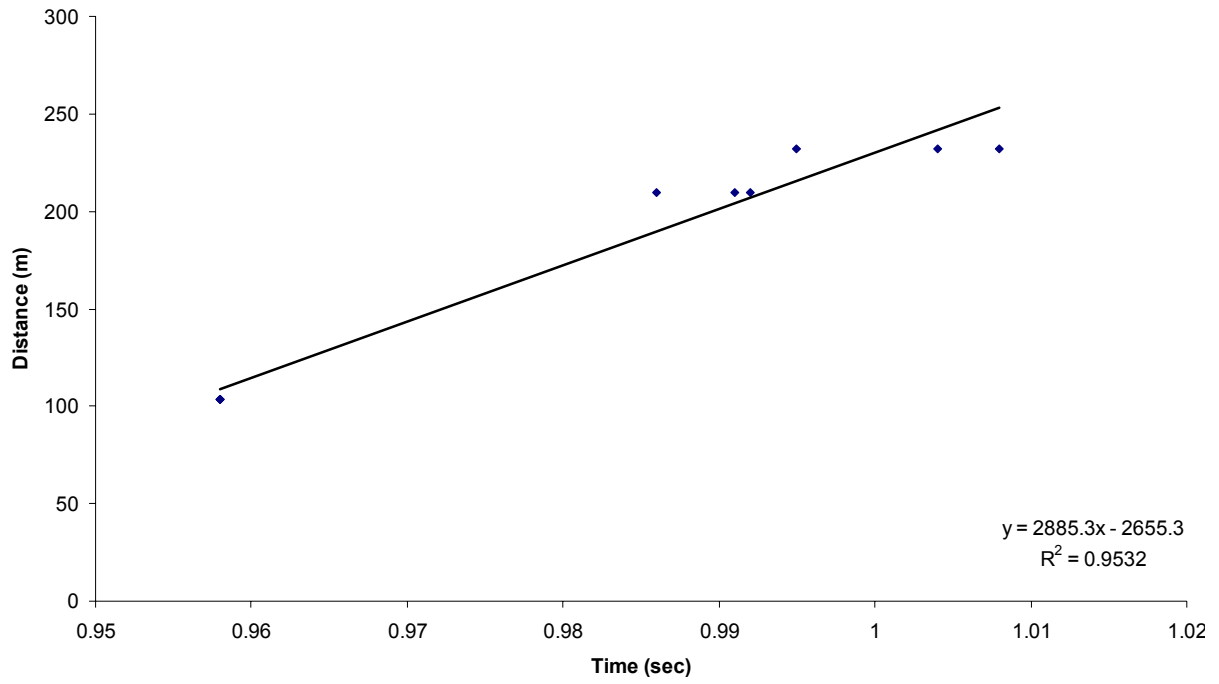


Figure G.22 – Distance-time plot for mine shot #537.



**Figure G.23** – Distance-time plot for mine shot #538.

# **Appendix H:**

**Summary of Radiated Seismic Energy and  
Moment Magnitude Estimates from Mine Shots  
#503 – 524**

**Table H.1 – Moment magnitude and radiated seismic energy summary from Geophone 1.**

Test	Gas Zone (ft)	Gas Zone (m)	Cross-Sectional Area (m <sup>2</sup> )	Methane Gas (%)	Amount of Methane (kg)	Amount of Coal Dust (lb)	Amount of Coal Dust (kg)	Initial Energy (MJ)	Average Magnitude	Seismic Energy (MJ)	Seismic/Initial Energy %
Mine Shot #503	47	14	11.6	9.5%	10.58	8	4	710	1.15	0.28	0.04%
Mine Shot #504	47	14	11.6	9.5%	10.58	8	4	710	1.47	1.91	0.27%
Mine Shot #505	47	14	11.6	9.5%	10.58	8	4	710	2.05	5.91	0.83%
Mine Shot #506	71	22	11.6	9.5%	15.98	0	0	799	2.22	21.51	3%
Mine Shot #507	47	14	11.6	9.5%	10.58	8	4	710	2.17	53.37	8%
Mine Shot #509	71	22	11.6	9.5%	15.98	32	15	1525	2.14	26.12	2%

**Table H.2 – Moment magnitude and radiated seismic energy summary from Geophone 2.**

Test	Gas Zone (ft)	Gas Zone (m)	Cross-Sectional Area (m <sup>2</sup> )	Methane Gas (%)	Amount of Methane (kg)	Amount of Coal Dust (lb)	Amount of Coal Dust (kg)	Initial Energy (MJ)	Average Magnitude	Seismic Energy (MJ)	Seismic/Initial Energy %
Mine Shot #503	47	14	11.6	9.5%	10.58	8	4	710	1.18	0.26	0.04%
Mine Shot #504	47	14	11.6	9.5%	10.58	8	4	710	1.49	1.69	0.24%
Mine Shot #505	47	14	11.6	9.5%	10.58	8	4	710	1.89	5.91	0.83%
Mine Shot #506	71	22	11.6	9.5%	15.98	0	0	799	2.13	9.78	1.22%
Mine Shot #507	47	14	11.6	9.5%	10.58	8	4	710	1.76	3.69	0.52%
Mine Shot #509	71	22	11.6	9.5%	15.98	32	15	1525	2.17	26	1.715%
Mine Shot #510	40	12	12.5	10.0%	10.21	0	0	511	1.21	0.708	0.139%
Mine Shot #513	40	12	12.5	10.0%	10.21	0	0	511	1.10	0.574	0.112%
Mine Shot #514	40	12	12.5	10.0%	10.21	0	0	511	1.25	2.666	0.522%
Mine Shot #516	40	12	12.5	10.0%	10.21	0	0	511	1.20	0.368	0.072%
Mine Shot #517	40	12	12.5	10.0%	10.21	0	0	511	1.24	2.959	0.580%
Mine Shot #518	40	12	12.5	10.0%	10.21	0	0	511	1.15	0.242	0.047%
Mine Shot #519	85	26	12.5	10.0%	21.70	0	0	1085	1.49	4.293	0.396%
Mine Shot #520	40	12	12.5	10.0%	10.21	0	0	511	1.66	6.262	1.227%
Mine Shot #522	40	12	12.5	10.0%	10.21	0	0	511	1.63	3.020	0.592%

**Table H.3 – Moment magnitude and radiated seismic energy summary from Geophone 3.**

Test	Gas Zone (ft)	Gas Zone (m)	Cross-Sectional Area (m <sup>2</sup> )	Methane Gas (%)	Amount of Methane (kg)	Amount of Coal Dust (lb)	Amount of Coal Dust (kg)	Initial Energy (MJ)	Average Magnitude	Seismic Energy (MJ)	Seismic/Initial Energy %
Mine Shot #505	47	14	11.6	9.5%	10.58	8	4	710	1.55	0.67	0.0946%
Mine Shot #506	71	22	11.6	9.5%	15.98	0	0	799	1.57	37.56	4.7010%
Mine Shot #507	47	14	11.6	9.5%	10.58	8	4	710	1.49	0.35	0.0492%
Mine Shot #508	47	14	11.6	9.5%	10.58	8	4	710	1.62	0.15	0.0212%
Mine Shot #509	71	22	11.6	9.5%	15.98	32	15	1525	1.64	1.42	0.0929%
Mine Shot #510	40	12	12.5	10.0%	10.21	0	0	511	1.11	0.03	0.0051%
Mine Shot #513	40	12	12.5	10.0%	10.21	0	0	511	1.12	0.01	0.0013%
Mine Shot #514	40	12	12.5	10.0%	10.21	0	0	511	1.17	0.02	0.0035%
Mine Shot #516	40	12	12.5	10.0%	10.21	0	0	511	1.13	0.07	0.0136%
Mine Shot #517	40	12	12.5	10.0%	10.21	0	0	511	1.17	0.01	0.0021%
Mine Shot #519	85	26	12.5	10.0%	21.70	0	0	1085	1.41	1.50	0.1378%
Mine Shot #520	40	12	12.5	10.0%	10.21	0	0	511	1.10	0.20	0.0401%
Mine Shot #521	40	12	12.5	8.5%	8.68	0	0	434	0.59	0.00	0.0008%
Mine Shot #523	50	15	12.5	10.0%	12.76	0	0	638	1.34	0.59	0.0924%
Mine Shot #524	85	26	12.5	10.0%	21.70	0	0	1085	1.46	0.58	0.0531%

**Table H.4 – Moment magnitude and radiated seismic energy summary from Geophone 4.**

Test	Gas Zone (ft)	Gas Zone (m)	Cross-Sectional Area (m <sup>2</sup> )	Methane Gas (%)	Amount of Methane (kg)	Amount of Coal Dust (lb)	Amount of Coal Dust (kg)	Initial Energy (MJ)	Average Magnitude	Seismic Energy (MJ)	Seismic/Initial Energy %
Mine Shot #510	40	12	12.5	10.0%	10.21	0	0	511	1.11	0.1410	0.02761%
Mine Shot #513	40	12	12.5	10.0%	10.21	0	0	511	0.79	0.0016	0.00031%
Mine Shot #514	40	12	12.5	10.0%	10.21	0	0	511	1.00	0.0076	0.00149%
Mine Shot #518	40	12	12.5	10.0%	10.21	0	0	511	0.80	0.0042	0.00082%
Mine Shot #520	40	12	12.5	10.0%	10.21	0	0	511	1.09	0.4120	0.08070%
Mine Shot #522	40	12	12.5	10.0%	10.21	0	0	511	1.10	0.412	0.081%

**Table H.5 – Moment magnitude and radiated seismic energy summary from Geophone 5.**

Test	Gas Zone (ft)	Gas Zone (m)	Cross-Sectional Area (m <sup>2</sup> )	Methane Gas (%)	Amount of Methane (kg)	Amount of Coal Dust (lb)	Amount of Coal Dust (kg)	Initial Energy (MJ)	Average Magnitude	Seismic Energy (MJ)	Seismic/Initial Energy %
Mine Shot #505	47	14	11.6	9.5%	10.58	8	4	710	1.71	0.67	0.09%
Mine Shot #506	71	22	11.6	9.5%	15.98	0	0	799	1.57	37.56	4.70%
Mine Shot #507	47	14	11.6	9.5%	10.58	8	4	710	1.59	0.22	0.03%
Mine Shot #508	47	14	11.6	9.5%	10.58	8	4	710	1.60	0.22	0.03%
Mine Shot #509	71	22	11.6	9.5%	15.98	32	15	1525	1.80	24.89	1.63%
Mine Shot #513	40	12	12.5	10.0%	10.21	0	0	511	1.06	0.01	0.0022%
Mine Shot #516	40	12	12.5	10.0%	10.21	0	0	511	1.06	0.07	0.0141%
Mine Shot #517	40	12	12.5	10.0%	10.21	0	0	511	1.16	0.02	0.0032%
Mine Shot #518	40	12	12.5	10.0%	10.21	0	0	511	1.05	0.03	0.0050%
Mine Shot #519	85	26	12.5	10.0%	21.70	0	0	1085	1.23	0.74	0.0678%
Mine Shot #521	40	12	12.5	8.5%	8.68	0	0	434	0.58	0.00	0.0006%
Mine Shot #523	50	15	12.5	10.0%	12.76	0	0	638	1.40	0.46	0.0722%
Mine Shot #524	85	26	12.5	10.0%	21.70	0	0	1085	1.40	0.76	0.0698%



**Table H.6 – Moment magnitude and radiated seismic energy summary from Geophone 6.**

Test	Gas Zone (ft)	Gas Zone (m)	Cross-Sectional Area (m <sup>2</sup> )	Methane Gas (%)	Amount of Methane (kg)	Amount of Coal Dust (lb)	Amount of Coal Dust (kg)	Initial Energy (MJ)	Average Magnitude	Seismic Energy (MJ)	Seismic/Initial Energy %
Mine Shot #505	47	14	11.6	9.5%	10.58	8	4	710	1.35	0.40	0.06%
Mine Shot #506	71	22	11.6	9.5%	15.98	0	0	799	2.46	885	110.77%
Mine Shot #508	47	14	11.6	9.5%	10.58	8	4	710	1.90	28	4.00%
Mine Shot #509	71	22	11.6	9.5%	15.98	32	15	1525	2.09	44	2.91%
Mine Shot #513	40	12	12.5	10.0%	10.21	0	0	511	1.02	0.003	0.0006%
Mine Shot #514	40	12	12.5	10.0%	10.21	0	0	511	1.02	0.011	0.0022%
Mine Shot #518	40	12	12.5	10.0%	10.21	0	0	511	0.93	0.006	0.0012%
Mine Shot #520	40	12	12.5	10.0%	10.21	0	0	511	1.09	0.017	0.0033%
Mine Shot #522	40	12	12.5	10.0%	10.21	0	0	511	1.08	0.020	0.004%

**Table H.7 – Moment magnitude and radiated seismic energy summary from Geophone 8.**

Test	Gas Zone (ft)	Gas Zone (m)	Cross-Sectional Area (m <sup>2</sup> )	Methane Gas (%)	Amount of Methane (kg)	Amount of Coal Dust (lb)	Amount of Coal Dust (kg)	Initial Energy (MJ)	Average Magnitude	Seismic Energy (MJ)	Seismic/Initial Energy %
Mine Shot #506	71	22	11.6	9.5%	15.98	0	0	799	2.10	1.44	0.18%
Mine Shot #507	47	14	11.6	9.5%	10.58	8	4	710	1.83	46	6.49%
Mine Shot #508	47	14	11.6	9.5%	10.58	8	4	710	1.56	0.11	0.02%
Mine Shot #509	71	22	11.6	9.5%	15.98	32	15	1525	2.07	14	0.89%

**Table H.8 – Moment magnitude and radiated seismic energy summary from Geophone 9.**

Test	Gas Zone (ft)	Gas Zone (m)	Cross-Sectional Area (m <sup>2</sup> )	Methane Gas (%)	Amount of Methane (kg)	Amount of Coal Dust (lb)	Amount of Coal Dust (kg)	Initial Energy (MJ)	Average Magnitude	Seismic Energy (MJ)	Seismic/Initial Energy %
Mine Shot #506	71	22	11.6	9.5%	15.98	0	0	799	2.69	434	54%
Mine Shot #507	47	14	11.6	9.5%	10.58	8	4	710	2.92	6450	908%
Mine Shot #508	47	14	11.6	9.5%	10.58	8	4	710	1.85	0.93	0.13%
Mine Shot #509	71	22	11.6	9.5%	15.98	32	15	1525	2.33	34	2.26%

**Table H.9 – Moment magnitude and radiated seismic energy summary from Geophone 10.**

Test	Gas Zone (ft)	Gas Zone (m)	Cross-Sectional Area (m <sup>2</sup> )	Methane Gas (%)	Amount of Methane (kg)	Amount of Coal Dust (lb)	Amount of Coal Dust (kg)	Initial Energy (MJ)	Average Magnitude	Seismic Energy (MJ)	Seismic/Initial Energy %
Mine Shot #508	47	14	11.6	9.5%	10.58	8	4	710	1.58	0.00265	0.000373%
Mine Shot #509	71	22	11.6	9.5%	15.98	32	15	1525	2.01	1.441	0.09%

**Table H.10** – Moment magnitude and radiated seismic energy summary from Geophone 13.

Test	Gas Zone (ft)	Gas Zone (m)	Cross-Sectional Area (m <sup>2</sup> )	Methane Gas (%)	Amount of Methane (kg)	Amount of Coal Dust (lb)	Amount of Coal Dust (kg)	Initial Energy (MJ)	Average Magnitude	Seismic Energy (MJ)	Seismic/Initial Energy %
Mine Shot #509	71	22	11.6	9.5%	15.98	32	15	1525	1.54	0.003531	0.0002%